

JOURNAL OF THE MYANMAR ACADEMY OF ARTS AND SCIENCE



Physics

Vol. XVI, No.2, October 2018

Myanmar Academy of Arts and Science

Journal of the Myanmar Academy of Arts and Science

Vol. XVI, No. 2

Contents

Physics

<u>Sr. No.</u>	<u>Title</u>	<u>Page</u>
1	Mg Zayar Pyae Phyo Aung , *Growth and Characterization of Electrospun SnO ₂ Nanofibers by Electrospinning Technique	1
2	Naw Htoo Lar Phaw , Investigation on Environmental Benefits of Local Resources from Loikaw, Kayah State	17
3	Hla Toe , Temperature Dependent Characterization of Al doped TiO ₂ Particles	33
4	Cho Cho San , Comparison of the form Factors of Tin Isotopes	51
5	Mi Mu Mu Khaing , The Influence of Different Reducing Agents on the Polyol Synthesis of Copper Nanoparticles	63
6	Aye Aye Min , Δ Single-particle Energy Levels in ^{13}C , ^{14}C and ^{15}C	75
7	Aung Zaw Oo , Server Based Real-Time Environmental Parameters Logging and Monitoring System	89
8	Hla Hla Win , Resonance States of α -n System by Applying Complex Scaling Method	105
9	Nyunt Win , Effects of Monomer on the Electrically Conductive Polymer	119
10	Min Maung Maung , The Occurrence and Crystal Structure of Tungsten Bearing Ores-Mineral at Kanbouk, Tanintharyi Region (Myanmar)	129
11	Sint Ohnmar , Structural, Electrical and Magnetic Properties of Wolframite (FeMnWO ₄) from Pharchaung Mine in Tanintharyi Region	139
12	Soe Soe Thin , Measurement of Earth Resistance In Pyay University Compound Using Model 2720 <i>er</i> Earth Resistance Tester	149
13	Kyauk Khe Sein , Fabrication of Porous Silicon for MEMS Devices Application	163

<u>Sr. No.</u>	<u>Title</u>	<u>Page</u>
14	Khin Su Myat Phone, Study on Structural, Morphological, Optical and Photovoltaic Performance of CdS _{1-x} Se _x (x=0.2 mol) Thin Films By Chemical Bath Deposition Technique	181
15	Phyu Phyu Khine, Study On Characterization of Mg _{0.5} Cu _{0.5} Fe ₂ O ₄ Ferrite Compound	195
16	Shwe Sin Oo, Study of DNA Sequence in Human Genes with Statistical Mechanics	211
17	Win Win Maw, Theoretical Analysis on J-PARC E31 Experiment	221
18	Thet Thet Cho, Sensitivity and Application to Low – Z Elements by X – Ray Detection System	235
19	Hnin Hnin Hlaing, Theoretical Interpretation on D(π^+ , K $^+$)X Inclusive Missing Mass Spectrum of J-PARC E-27 Experiment	247
20	Htet Naing Lwin, Study on Temperature Dependent Electrical Properties of Cobalt-Zinc Nanoferrites	265
21	Khin Moe War, Elemental Analysis of Rice Husk Ash Using Edxrf Method	281
22	Theint War War Khaing, Preparation and Characterization of SnO ₂ Nanorods at Different Temperatures	295
23	Khin Thida Aung, Fabrication of Two Cells, Three Cells and Four Cells Meander Type Dye-Sensitized Solar Cell Modules	309
24	Myint Myint Soe, Characterization of Nickel Sodium Sulphate Hexahydrate (NSSH) Crystal	329
25	Aye Thandar, Study on Physical and Chemical Characterization of Bamboo Based Biochar	337
26	ThinzarWut Yee, Study on Electrical Properties of Nickel-Zinc-Cobalt Ferrites Humidity Sensors	347
27	Hnin Hlwar Nu, Gas Sensitivity of Nanocrystalline Cobalt Doped Nickel Ferrites	359
28	Khin Sandar Soe, Structural Analyses, Microstructural Characteristics and Electrical Conductivity of Copper-Cobalt Ferrites	381
29	Win Win Mon, Structural, Thermal and Electrical Characteristics of Nickel Potassium Sulphate Hexahydrate (NPSH) Crystal	397

<u>Sr. No.</u>	<u>Title</u>	<u>Page</u>
30	Saw Shine Ko , Investigation of ZnO/ITO Thin Films on Structural, Optical and Electrical Properties	409
31	Win Pa Pa Khaing , Growth and Characterization of ZnTiO ₃ PerovskiteFilm on Si Substrate	427
32	Hnin Thu Zar , Study on Dielectric Properties and Charge Conduction Mechanism of Zinc Sulphide Films by Chemical Bath Deposition Method	443
33	Moe Swe , Fabrication Mechanism and Optical Properties of pure ZnO and ZnS-ZnO Nanocomposite Films	453
34	Su Su Lwin , Synthesis, Structural and Optical Properties of ZnO-TiO ₂ -GO Nanocomposite	469
35	Zar Zar Myint Aung , Studies on Effect of Ytterbium Substitution in Zinc Ferrite	493
36	Ei Cherry Hlaing , Laser Raman, FTIR Spectroscopic Investigation and Infrared Light Testing of M ₂ SO ₄ (M = K, NH ₄ , Li) Doped Triglycine Sulphate (TGS) Crystals	509
37	July Oo , Study on Humidity Sensitive Electrical Properties of Barium Ferrite	529
38	Shwe Yee Win , Dye-Sensitized Solar Cell Based on TiO ₂ -MgO Composite Electrodes by Using Combined Dye	553

GROWTH AND CHARACTERIZATION OF ELECTROSPUN SnO₂ NANOFIBERS BY ELECTROSPINNING TECHNIQUE*

Zayar Pyae PhyoAung,¹ Mar Lar Wai², Than Than Win³ and Yin Maung Maung⁴

Abstract

Tetragonal tin oxide (SnO₂) nanoparticles of the range 80 nm have been successfully synthesized by a direct precipitation from an aqueous solution in the presence of stannous chloride dehydrate (SnCl₂.2H₂O) and ammonium hydroxide. The final products was ground into a fine powder and then annealed at 650°C for 6 h. Characterization of the materials was carried out using technique such as scanning electron microscope and the optical studies were carried by UV-Vis absorption. SnO₂ nanofibers were fabricated by home-made electrospinning with vertical experimental set up. The electrospinning solution was prepared by homogeneous viscous solution of tin acetate in polyvinyl alcohol (PVA). The electrospinning were under taken by applying a DC voltage of 20 kV to the tip of a syringe and maintaining the tip to collector distance (TCD) of 5 cm, 7 cm, 10 cm and 12 cm. The spinning or running time interval was set to 4 h. The green nanofibers were calcined at 600°C for 1 h. The XRD analysis revealed that nanofibers were phase pure and all materials exhibited a tetragonal rutile structure of SnO₂. The nanofibers treated at 600°C was examined by field emission scanning electron microscope (FESEM). The functionalize sample surface at a nanometer range of SnO₂ nanofibers were examined by Atomic Force Microscopy (AFM). The SEM and AFM shows cylindrical fibers with diameter in the range of 47 – 100 nm. In general, average diameter of the fibers decreased with decrease in TCD.

Keywords: Tin acetate, polyvinyl alcohol, Nanofibers, TCD, Electrospinning

¹ Demonstrator, Department of Physics, Myeik University

² Lecturer, Department of Physics, University of Yangon

³ Associate Professor, Department of Physics, Mandalay University of Distance Education

⁴ Associate Professor, Department of Physics, University of Yangon

* Best Paper Award Winning Paper in Physics (2017)

Introduction

Nano-sized tin oxide (SnO_2) is an interesting semiconducting material with a wide band gap and one of the most widely used due to its chemical and mechanical stabilities [H. Kose et al and Lucky M Sikhwivhilu et al]. Tin oxides (SnO_2) are widely used in transparent conductive electrode for solar cells, a gas sensing material for gas sensors devices, transparent conducting electrodes, photochemical and photoconductive devices in liquid crystal display, gas discharge display, lithium-ion batteries and many other application [Asama. N. Naje et al, Nehru L.C. and V. Senthilkumar et al]. Many process have been developed to the synthesis of tin oxide (SnO_2) nanostructures, for example, spray pyrolysis, hydrothermal method, evaporation tin grain in air, chemical vapor deposition (CVD), thermal evaporation of oxide powders, rapid oxidation of elemental tin, the sol-gel method and etc. [Ganesh E Patil]. One-dimensional nanostructure, tin oxide nanowires, nanobelts, nanorods and nanofibers, with a high surface to volume ratio has attracted special attention in the last years. Currently, there are three techniques available for the synthesis of nanofibers: electrospinning, self-assembly and phase separation. Of these, electrospinning is the most widely studied technique and also seems to exhibit the most promising results. Moreover this technique also has important advantages such as simplicity, low cost, and easy mass production. It is one of the most useful methods for the fabrication of 1-D composite nanofibers by electro stretching [Jose Pedro Santos et al and Rajesh Vasita et al]. Electrospinning is a very simple and popular technique for fabrication of sub-micron to nanometer range fibers. It is one of the simplest method to form continuous one-dimensional nanofibers under the electrostatic force of the charges on the surface of a liquid droplet in a sufficiently high electric field, which is applied between the capillary nozzle and the metal collector [M. Chandraiah et al and Zunxian Yang et al]. In this research SnO_2 nanopowders were prepared by precipitation method and the resulting powders were characterized by UV-Vis and FESEM. Then SnO_2 nanofibers were prepared by electrospinning homogeneous viscous solution of tin acetate in polyvinyl alcohol (PVA). The SnO_2 nanofibers were also characterized by XRD, FESEM and AFM.

Experimental Procedure

Sample Preparation of SnO₂Nanopowder

In this research, Stannous chloride dehydrate (SnCl₂.2H₂O) was used as starting materials. The block diagram of sample investigation was described in figure 1. All chemicals were analytically pure and directly used as received without further purification. Distilled water was used as a solvent. SnO₂nanopowders have been prepared by using precipitation method. SnO₂nanopowders were prepared by means of dissolving of 2 g (0.1 M) stannous chloride dehydrate (SnCl₂.2H₂O) in 100 ml distilled water. 10% ammonium hydroxide was slowly added to the solution for complete precipitation of tin hydroxide in the pH range 7.5 - 9. Then the solution was put into thermostat water bath, in which the temperature was kept about 80 °C, for 15 minutes until white depositions came out. Then the precipitate was centrifuged and washed several time with distilled water to reduce the amount of ammonium chloride. The resulting gels was filtered and dried at 100 °C for 3 h. The obtained powder was collected and grounded in an agate mortar and it is referred “as – prepared”. The color of the as-prepared sample is gray. Finally the as-prepared sample was heated in a muffle furnace at 650 °C for 6 h in an atmosphere, then the color turned into white. Optical absorption spectra of the sample were taken with UV-1800 UV-Vis Spectrometer. Field emission scanning electron microscopy (FESEM) was employed for morphological study using JEOL JSM-5610. Atomic force microscope (AFM) (Bruker N8 Rados) was used to examine the surface morphology.

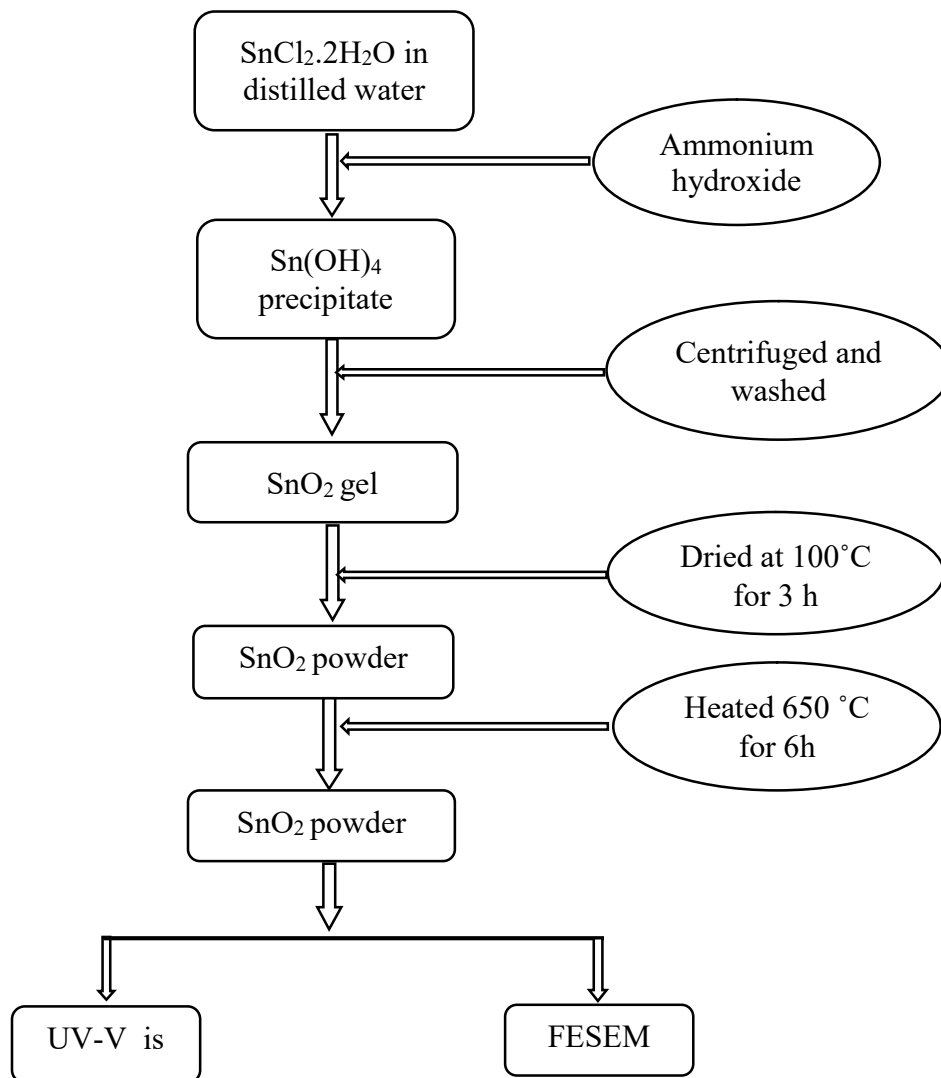


Figure 1. Block diagram of preparation for SnO₂ powder

Sample Preparation of SnO₂ Nanofibers

In this study, the flow chart of experimental procedure is shown in figure 2. Tin dioxide (SnO₂), Poly Vinyl Alcohol (PVA) and distilled water were chosen as the starting chemicals and solvent. SnO₂ nanofibers were prepared by sol-gel process. 1 g of SnO₂ was dissolved in 2 ml of acetic acid with constant stirring for 10 min to obtain a clear solution of tin acetate in the pH range 1-2. This solution was mixed with 4 ml of 10 % PVA solution. The solution was stirred for 4 h by a magnetic stirrer and a viscous sol-gel was obtained with viscosity in the range of 1100-1180 cP. The solution gel was expected to be viscous enough for electrospinning. Nearly 5 ml of the viscous solution was taken in a 20 ml syringe. The distance of 5 cm, 7 cm, 10 cm and 12 cm were maintained between the collector plate and the tip of the needle. Al-substrate was then struck on the collector.

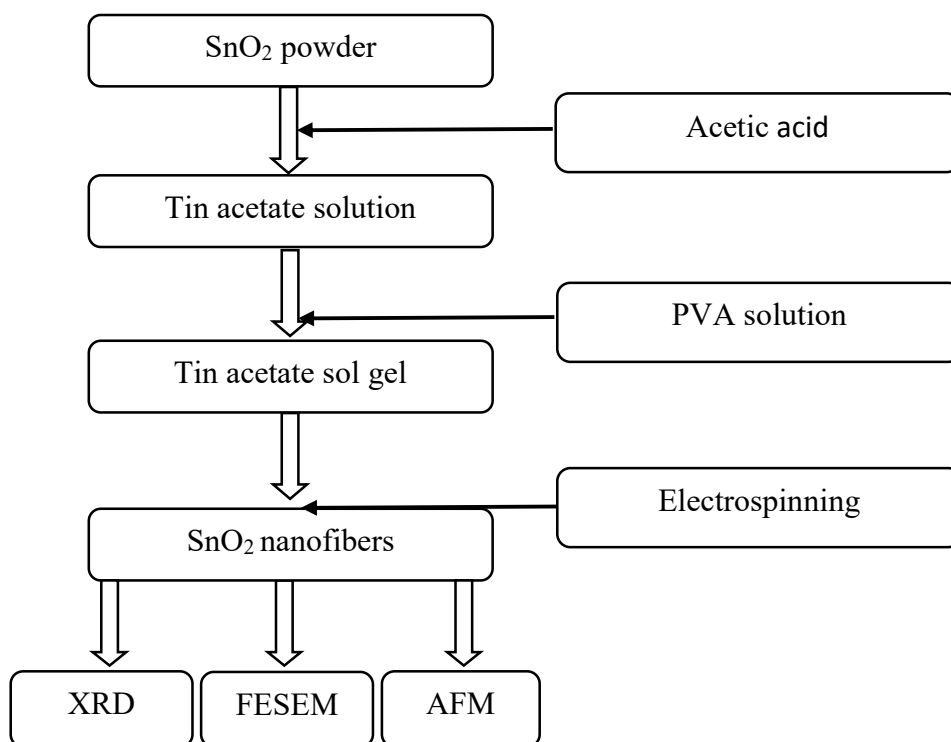


Figure 2. The flow chart of experimental procedure for SnO₂ nanofibers

Electrospinning Setup

The home-made electrospinning device consisted of a syringe, stand, high voltage DC source and a ground collector plate. The high voltage source was taken from 21" fly pad (219 x 6M, Toshiba) indirectly and the output voltage is 20 kV. The positive terminal of the DC source was connected with a needle and the Al-substrate (collector) was connected with the negative terminal to ground it. When the voltage was applied a stream of solution came out through the needle which was subdivided into a number of nano to submicron sized jets and were deposited in the form of nanofibers on the collector plate. The green nanofibers were calcined at 600 °C for 2 h. A typical electrospinning set up is shown in figure 3. The electrospinning conditions are mentioned in table 1. The morphology of the fibers was measured by field emission gun-scanning electron microscope (FESEM).

Table 1. The electrospinning conditions of SnO₂ sample

Syringe capacity	20 ml
Tip to collector distance (TCD)	5 cm, 7 cm, 10 cm and 12 cm
Voltage	20 kV
Running Time	5 hr
Colling time	5 hr
Annealing temperature	600 °C
Annealing time	2 h

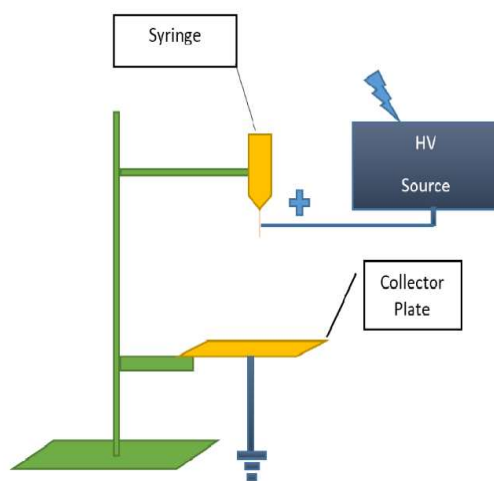


Figure 3. Schematic drawing of the electrospinning process set up

Results and Discussion

Characterization of tin oxide nanofiber by XRD analysis

According to the XRD analysis, pure tin oxide nanofiber were matched with standard library of PDF 77-0447 cassiterite tin oxide. The X-ray diffraction (XRD) pattern of SnO₂ nanoparticles fiber from SnCl₂.2H₂O is shown on figure 4. There are four peaks and all of the peaks can be indexed to be pure tin oxide structure of tetragonal due to the lattice parameters agreement with the literature. The average crystallite size is 31.5 nm.

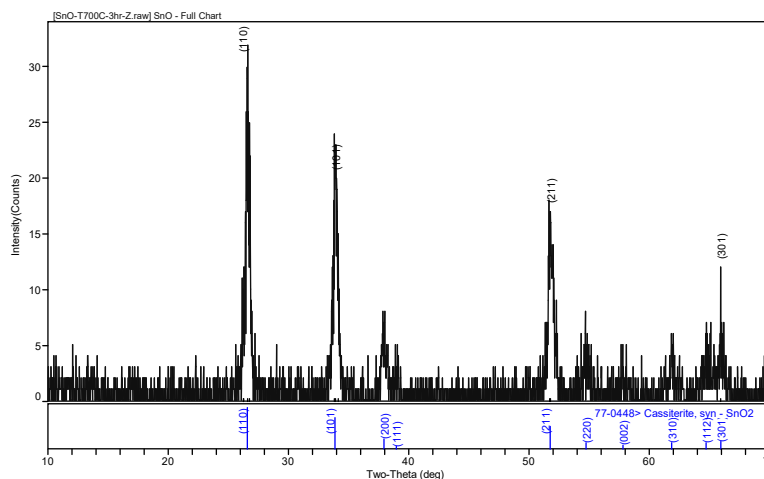


Figure 4. XRD diffractogram of tin oxide nanofiber

UV-Visible analysis of SnO₂ nanopowder

The UV-Vis spectra of SnO₂ powder was recorded with respect to the glass substrate placed in the reference beam using beam spectrometer in the range 190 to 1100 nm. The absorption spectrum of SnO₂ deposited on glass substrate is shown in figure 5. The figure shows high absorption coefficient in the UV region. It's transparent coefficient also in the UV region. The optical band energy (E_g) of the semiconductor is calculated from the relation.

$$\alpha h\nu = A (h\nu - E_g)^n$$

where α is the absorption coefficient, A is a constant (independent from ν), n is the exponent that depends upon the quantum selection rules for the

particular material, h is the planck's constant and E_g the energy band gap. A plot of $(\alpha h\nu)^2$ versus $h\nu$ shows intermediate linear region, the extrapolation of the linear part can be used to calculated the E_g from intersect with $h\nu$ axis. The resultant values of E_g for SnO_2 is found to be about 3.82 eV. The value may be related to the formation of nanostructures of SnO_2 and the bulk SnO_2 , these value show a good agreement with the values published by other researchers.

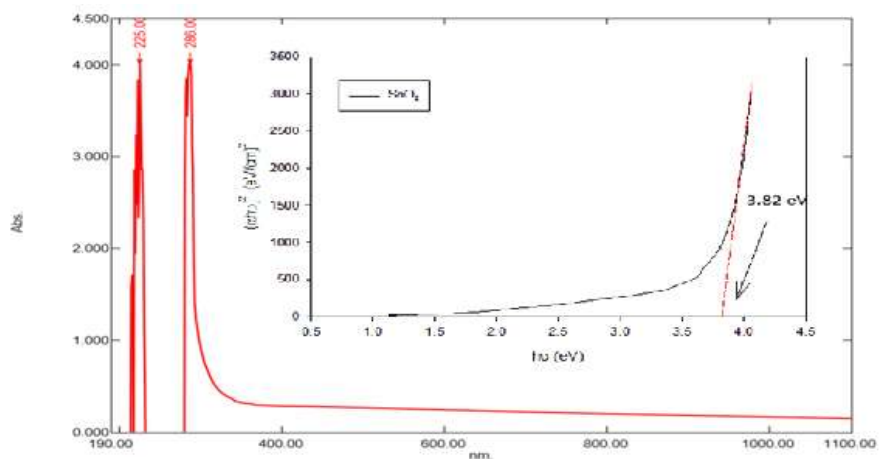


Figure 5. The absorption spectrum of SnO_2 powder

Characterization of tin oxide nanoparticles and nanofibers by FESEM

The SnO_2 powder was obtained from directed precipitation method. Figure 7 shows the FESEM analysis of the SnO_2 powder. The grain sizes were calculated by using well known bar code system. Bar code size was $1 \mu\text{m}$. According to the calculation the grain size is 80 nm. The powders morphology was spherical in shape and then the surface was rough.

The SnO_2 fibers on aluminum foil were carried out to examine by FESEM image. In order to study the morphology and the nano structural properties of fabricated SnO_2 nanofibers for different tip to collector distance (TCD) 5 cm, 7 cm, 10 cm and 12 cm are shown in figure 8 (a) (b), figure 9 , figure 10 (a) (b) and figure 11 (a) (b). According to the FESEM analysis SnO_2 nanofibers from all TCD distance reveal the retention of cylindrical shape but with surface roughness. And then, the fibers form TCD 5 cm and

TCD 7 cm are straighter and smaller diameter than TCD 10 cm and TCD 12 cm. But most of the fibers of TCD 10 cm TCD 12 cm are uniform but TCD 5 cm and TCD 7cm are not. The average diameter of the SnO₂nanofibers of TCD 5 cm are 47 - 80 nm, TCD 7 cm are 50-75 nm, TCD 10 cm are 80-85 nm and TCD 12 cm are 100 nm – 102 nm. So, tip to collector distance (TCD) 5 cm is the best position to produce nanofibers because its fibers diameter are the smallest in all position. The fibers diameter for all TCD position are listed in table 2.

Table 2. The fibers diameter for all tip to collector distance (TCD) position

Sample	Fiber diameter (nm)
TCD 5 cm	47
TCD 7 cm	50
TCD 10 cm	80
TCD 12 cm	100

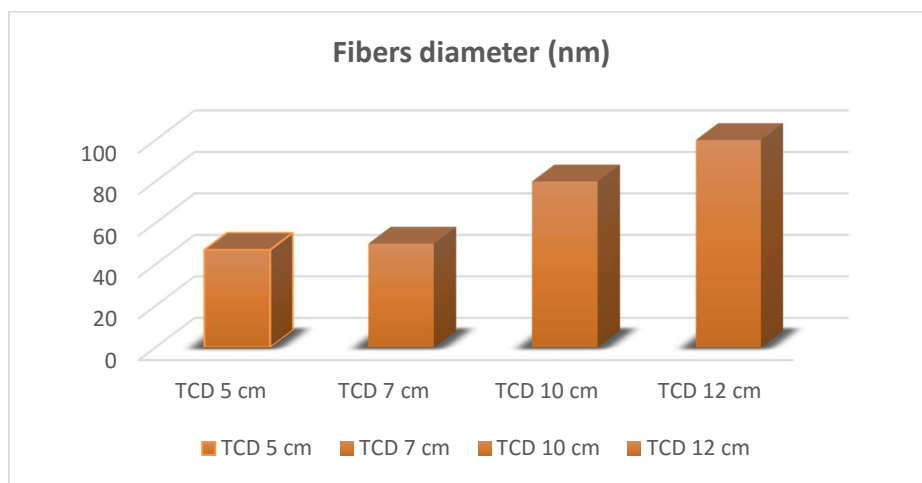


Figure 6. Tip to collector distance (TCD) dependence of fiber diameter

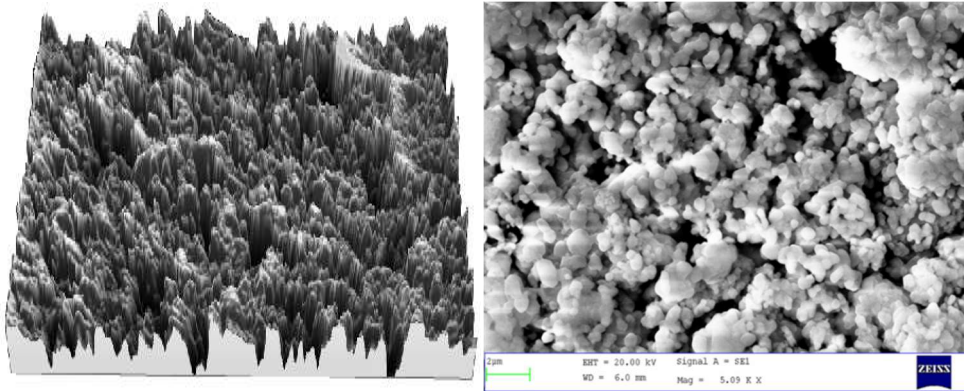


Figure 7. FESEM image of SnO₂ nanopowder

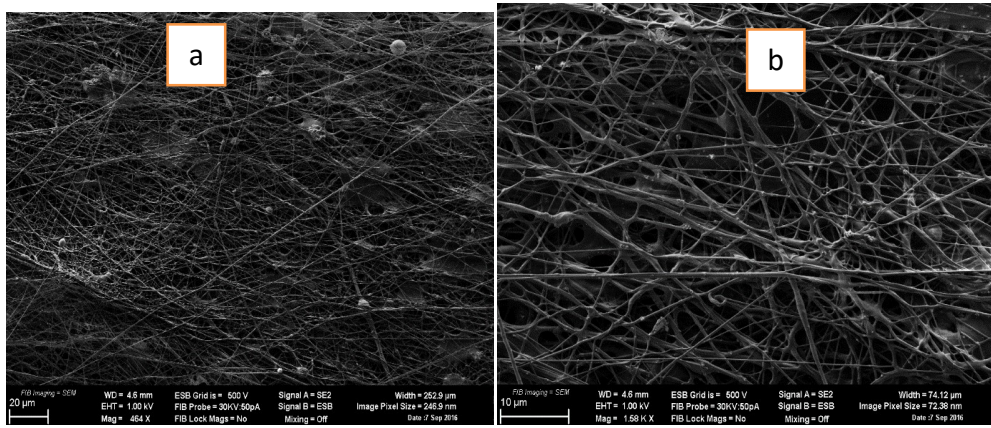


Figure 8. The FESEM photograph of SnO₂ nanofibers for 5cm (TCD) (a) 20μm (b) 10μm

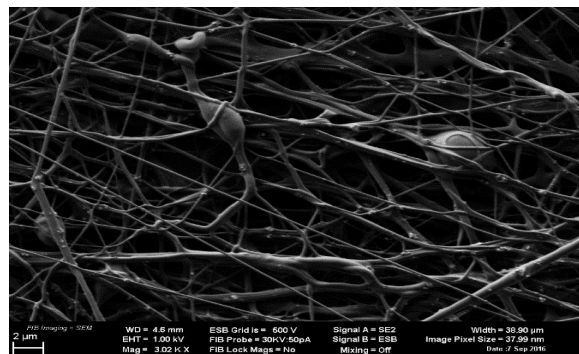


Figure 9. The FESEM photograph of SnO₂ nanofibers for 7cm (TCD)

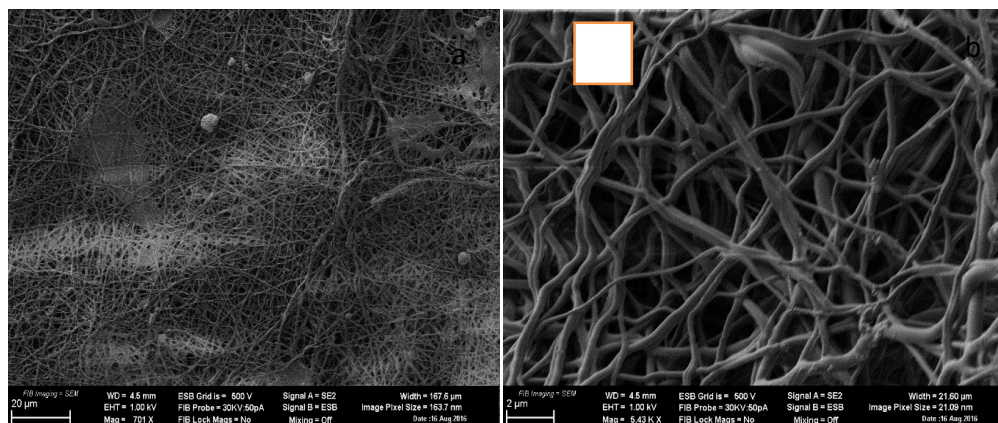


Figure 10. The FESEM photograph of SnO₂ nanofibers for 10cm (TCD) (a) 20 μm (b) 2 μm

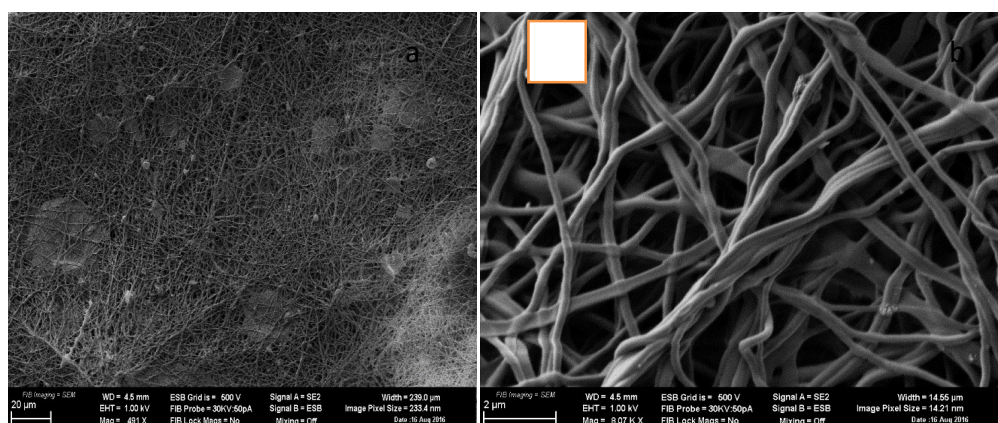


Figure 11. The FESEM photograph of SnO₂ nanofibers for 12cm (TCD) (a) 20 μm (b) 2 μm

Characterization of tin oxide nanofibers by AFM analysis

Atomic force microscope (AFM) is a technique for analyzing the surface of a rigid material all the way down to the level of the atom. AFM uses a mechanical probe to magnify surface features up to 1×10^8 times, and it produces 3-D images of the surface. The AFM consists of a cantilever with a sharp tip (probe) at its end that is used to scan the specimen surface. The cantilever is typically silicon or silicon nitride with a tip radius of curvature on the order of nanometers. The AFM image of TCD 5 cm, 7 cm and TCD 10 cm

are shown in figure 12, 13 and 14. Fiber diameter is estimated from fiber height to avoid tip-convolution effects. According to the line profile, the average fibers diameter for TCD 5 cm are 40 nm – 70 nm and TCD 10 cm are 84 nm – 95 nm.

Table 3 The comparison of fibers diameter between the FESEM and AFM results

TCD (cm)	Fiber diameter (nm)	
	FESEM	AFM
5	47 - 80	40 - 70
10	80 - 85	84 - 95

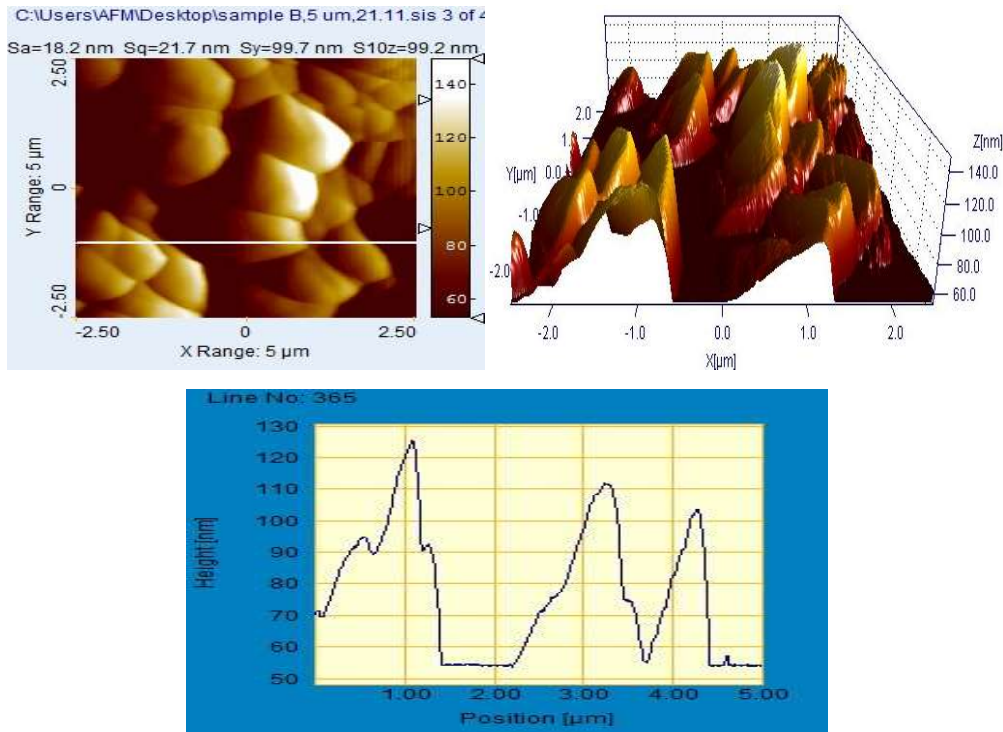


Figure 12. The amplitude, the 3D image and line profile for TCD 5 cm

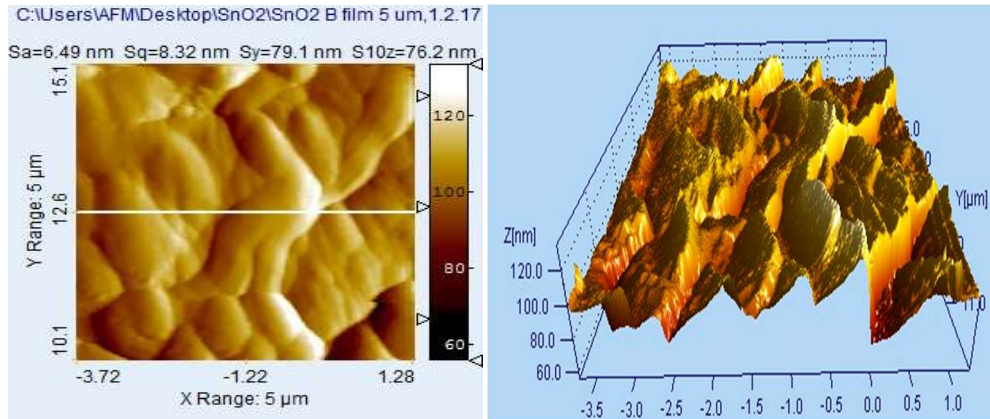


Figure 13. The amplitude and the 3D image for TCD 7 cm

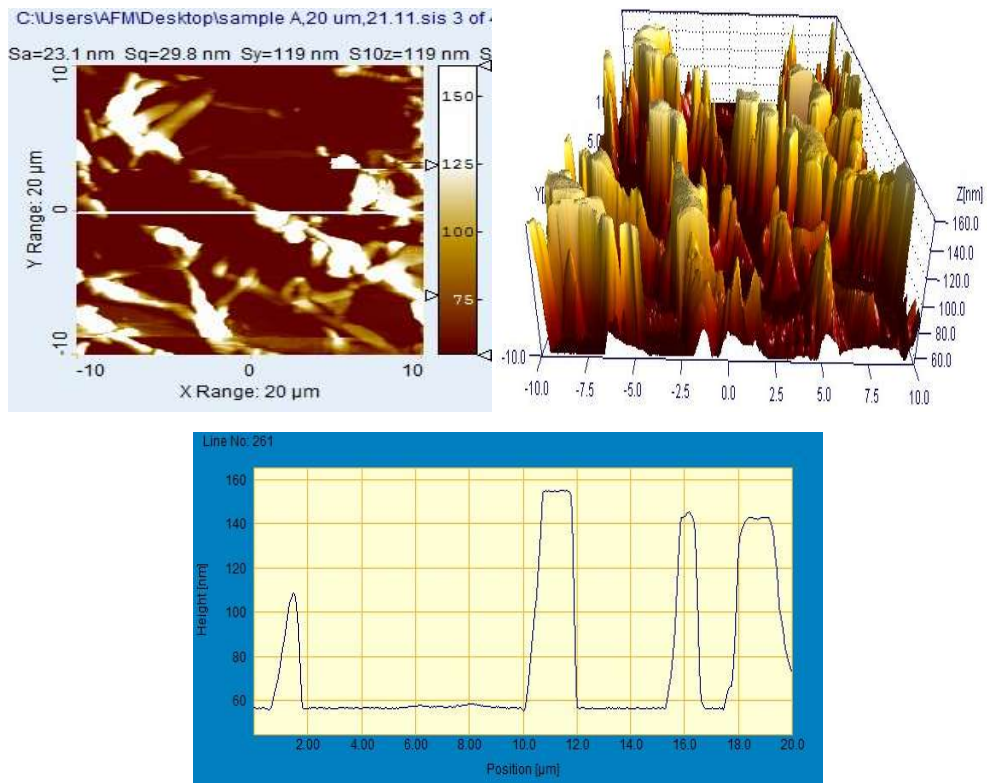


Figure 14. The amplitude, the 3D image and line profile for TCD 10 cm

Conclusion

Tin oxide powders were prepared by direct precipitation method from starting material $\text{SnCl}_2 \cdot 2\text{H}_2\text{O}$. According to the XRD and SEM analysis the resulting SnO_2 powder was indicated the good crystalline nature of the powder. The SEM images indicated the presence of predominantly spherical shape having grain size 80 nm. The optical absorption spectrum showed the sharp absorption edge at 225 nm and 286 nm. And then SnO_2 nanofibers were fabricated by home-made electrospinning with vertical experimental set up. Moreover the tip to collector distance (TCD) was changing in 5 cm, 7 cm, 10 cm and 12 cm. According to the FESEM image the structural properties of fibers are changing depending upon the (TCD). The SnO_2 nanofibers from all TCD distance reveal the retention of cylindrical shape but with surface roughness. And then, the fibers from TCD 5 cm and TCD 7 cm are straighter and smaller diameter than TCD 10 cm and TCD 12 cm. But most of the fibers of TCD 10 cm TCD 12 cm are uniform but TCD 5 cm and TCD 7 cm are not. The average diameter of the SnO_2 nanofibers of TCD 5 cm are 47 - 80 nm, TCD 7 cm are 50 - 75 nm, TCD 10 cm are 80-85 nm and TCD 12 cm are 100 nm – 120 nm. The fiber diameter is influenced by the tip to collector distance (TCD). Moreover the AFM profiles reveal the fibers diameter of TCD 5 cm are 40 nm – 70 nm and TCD 10 cm are 84 nm – 95 nm. So, tip to collector distance (TCD) 5 cm is the best position to produce nanofibers because its fibers diameter are the smallest in all position. This home-made high voltage power supply and electrospinning set-up are quite simple, easily made and low cost than the others but it can produce fine nanofibers.

Acknowledgements

The author also acknowledge the support of Professor Dr Khin Khin Win, Head of Department of Physics, University of Yangon. I wish to express my profound thanks to Dr Si Si Hla Bu, Rector of Myeik University for her kind permission to carry out this work. Moreover, I am greatly indebted to Professor Dr Myint Myint Moe, Head of Department of Physics, Myeik University, for her help with experimental work and discussion.

References

- Asama. N. Naje, Azhar S. Norry, Abdulla. M. Suhail (2013) "Preparation and Characterization of SnO₂ Nanoparticles" IJRSET, Vol. 2, Issue 12.
- C. Zhong, A. Cooper, A. Kapetanovic (2010) "A facile bottom-up route to self-assembled chitinnanofiber" The Royal Society of Chemistry, Vol. 4, Issue 17.
- E. SURESH¹ and K. SUNDARAM¹ (2016) "Electrolysis Of Ibuprofen on conduction Nanofibers" Int J Curr Pharm Res, Vol 8, Issue 4, 44-48 Review Article.
- Ganesh E Patil, Dnyaneshwar D Kajale and Gotan H Jain (2012) "Preparation And characterization of SnO₂ nanoparticles by hydrothermal route", International Nano Letters, Vol. 2, 17.
- H. KOSE, A.O.AYDIN and H. AKBULUT (2013) "The Effect of Temperature on of Grain Size of SnO₂ Nanoparticles Synthesized by Sol-Gel Method", ACTA PHYSICA POLONICA, Vol. 125 (2014).
- Jose Pedro Santos, Maria Jesus Fernandez and LsabelGracia (2014) "Nanocrystalline Tin Oxide Nanofibers Deposited by a Novel Focused Electrospinning Method", Sensors, 24231-2423.
- Lucky M Sikhwivhilu, Sreejarani K Pillai, Thembela K Hillie (2012) "Influence Of Citric Acid on SnO₂ Nanoparticles Synthesized by Wet Chemical Process", Journal of Nanoscience and Nanotechnology" Revised Version.
- Nehru L.C. (2014) "Preparation and Characterization of Nanosize SnO₂ Nanopowders by Precipitation Method", IJAN, Vol. 1, Issue 1.
- M. Chandraiah, Benudhar Sahoo and Prasanta Kumar Panda (2014) "Preparation and Characterization of SnO₂ Nanofibers by Electrospinning", Trans. Ind. Ceram. Soc., Vol. 73, 266-269.
- Rajesh Vasita, Dharendra S Katti (2006) "Nanofibers and their applications in tissue Engineering", International journal of Nanomedicine, Vol. 1, 15-30.
- V. Senthilkumar, P. Vickraman, M. Jayachandran and C. Sanjeeviraja (2015) "Synthesis and Characterization of SnO₂ Nanopowder Prepared by Precipitation Method", Journal of Dispersion Science and Technology, Vol. 31, 1178-1181.
- Zunxian Yang, Guodong Du and Zaiping Guo (2009) "Easy Preparation of SnO₂@carbon Composite nanofibers with improved lithium ion storage properties", Cambridge Journal, Vol. 25, 8.

INVESTIGATION ON ENVIRONMENTAL BENEFITS OF LOCAL RESOURCES FROM LOIKAW, KAYAH STATE

Naw htoo Lar Phaw*

Abstract

This research is preliminary proposing level to investigate how the addition of fly-ash affects the compressive strength of traditional bricks and the radon concentration of local resources. For this work dolomite, fly-ash and cement were used as raw materials to make brick samples. Before making bricks, they were analyzed by EDXRF and XRD techniques. Ten brick samples were prepared by dolomite and cement only without fly-ash as the ratio of 18:1(They have been currently used in Kayah State) and 6:1 in five of each. Other eight brick samples were prepared with different weight ratios of dolomite, fly-ash and cement. The compressive strengths of obtained bricks were determined by using Compressive Testing Machine (RBU-250). From results the sample made by the mixture of dolomite, fly-ash and cement with the weight ratio of 2:1:1 shows the best compressive strength of 1325.59 PSI, which is significantly higher than that of traditional brick samples made by the mixture of dolomite and cement with the weight ratio of 18:1 (424.80 PSI). So that fly-ash (regional source) is an appropriate addition to make bricks with higher compressive strength. To study the radon concentration measurements in dolomite, fly-ash were examined by using LR 115 type II SSNTDs which were used as track recording materials.

Introduction

In the Kayah State , people are using traditional bricks which are made by the dolomite (Demawsore) and cement (KanBawZa) as the ratio of 18:1 in construction of buildings. If the concentration of them as the ratio of 6:1 are used instead of the ratio of 18:1 , the construction materials should be modified by using the higher compressive strength level. But cost will become high.

The addition of fly- ash (Tigyit) to cement, concrete and bricks can improve their mechanical properties such as compressive strength as well as reducing the cost of bricks.

*. Dr, Professor, Department of Physics, Pyay University

In this research, dolomite, fly-ash and cement were used as raw materials to make brick samples and they were examined by EDXRF and XRD methods. And then the compressive strength of the brick samples were determined by compressive strength testing machine (RBU-250) from the structural laboratory at department of civil engineering in Yangon Technology University.

In the present work, the raw materials were collected and analyzed the radon concentration to estimate the levels of radon in order to guaranty the safety of people and surrounding atmosphere. The aim of this work is to avoid the health risk in buildings.

Experimental Procedures

2.1 Determining the concentrations of elements

The raw materials which are dolomite (Demawsore, Loikaw), fly-ash (Tigyit, southern Shan State) and cement(Kan Baw Za) were collected and analyzed by EDXRF for determining the concentrations of elements. And then XRD analysis was carried out to probe the crystal structures of raw materials. For EDXRF and XRD analysis, the raw materials were ground by using agate motor and pestle to get the fine powder and pressed under uniaxial pressure of 5 tons per cm³ to obtain pellets.

2.2 Measuring the compressive strength

At first, the five bricks which having the ratio as those currently used in local construction and other five bricks which are made with the dolomite (Demawsore) and cement (Kan Baw Za) as the ratio of 6:1 were investigated to determine their compressive strength by compressive strength testing machine.



Figure 1. Five bricks samples as 18:1 ratio **Figure 2.** Five bricks samples as 6:1 ratio

The three elements such as dolomite, fly- ash and cement were weighted by using digital balance in the various ratio and listed in Table1. And then, the eight brick samples were made in such way that each pair of bricks, namely A₁ and A₂ , B₁ and B₂ ,C₁ and C₂ , D₁ and D₂ are the same in weight. When the eight bricks were got, they were dried by the sun for 28 days (25.6.2016 to 22.7.2016) and the temperatures were also recorded day by day. The average temperature is found to be 25.46°C.

Table 1. The weighted values of brick samples with various ratios

Sample	Dolomite (g)	Fly-ash (g)	Cement (g)
A ₁ , A ₂	3840	3840	-
B ₁ , B ₂	3840	1920	1920
C ₁ , C ₂	3840	2304	1536
D ₁ , D ₂	3840	3072	768



Figure 3. Making Bricks



Figure 4. Eight samples as brick



Figure 5. Compressive testing machine (250)

2.3 For measuring radon concentration

In this measurement, can technique was to find out the radon concentration. LR-115 plastic film was used as track detector. Raw materials were air dried and ground in pulverized form. A known amount (100g) of each raw material was placed in plastic can of dimensions 7.5cm height and 7.5cm diameter. A piece of LR-115 detector with area of (1.5cm by 1.5cm) was fixed on the bottom of the lid of each can. The cans were tightly closed from the top and sealed. The detectors were left inside the cans for 100 days of exposure time (13.8.2016 to 21.11.2016). During this time, alpha particles from the decay of radon and its daughter bombard the detectors in the air volume of the can. At the end of exposure time, the detectors were etched chemically in 6.25N solution of NaOH at 60°C for 1hour. Then, the detectors were washed and dried.

After chemical treatment, the tracks were counted by using optical microscope with objective having the same magnification 40 was used for all detectors. Fifty different views scanned to reduce statistical errors.

Experimental Results

3.1 EDXRF Results

The raw materials were examined by EDXRF (EDX-720) analysis. They are depicted in Fig 6 and Fig 7 respectively. The concentrations of elements are shown in Table 2.

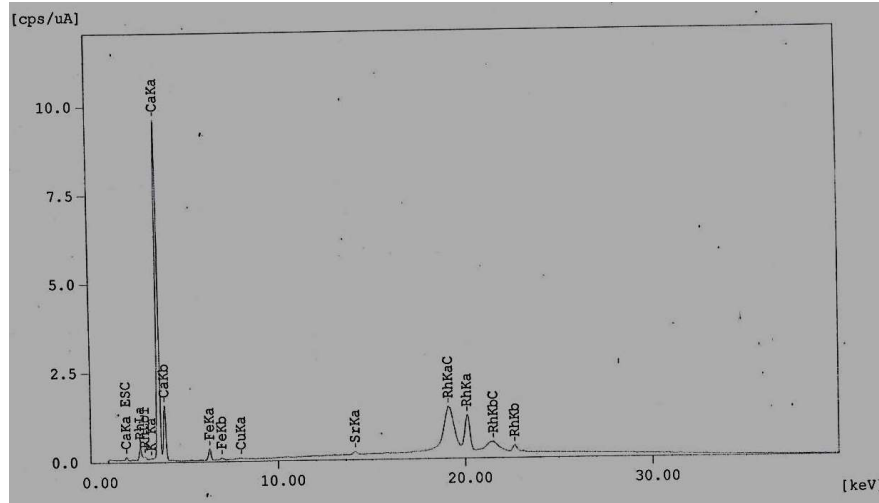


Figure 6. EDXRF analysis for dolomite

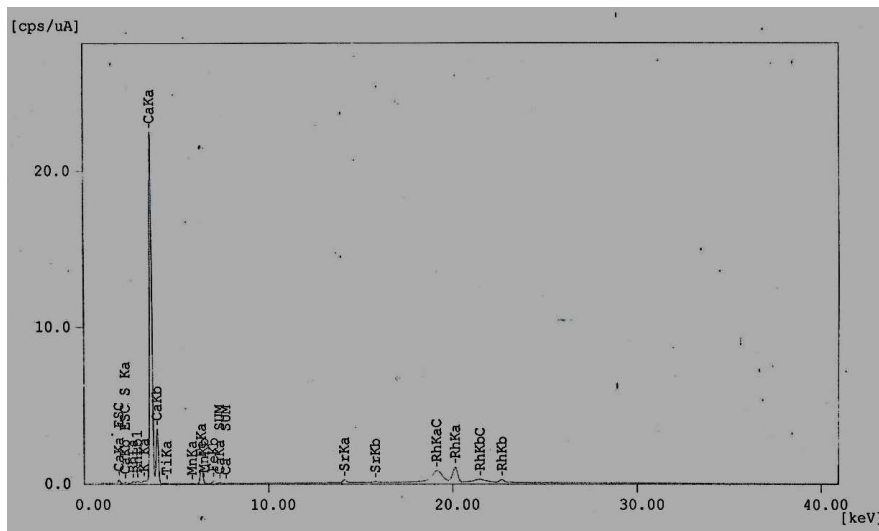


Figure 7. EDXRF analysis for fly- ash

Table 2. Concentrations of elements in dolomite and fly- ash

Elements	Dolomite	Fly - ash
Fe	1.838%	2.802%
Ti	ND	0.141 %
K	0.622 %	0.961 %
Ca	97.257 %	95.680 %
Mn	ND	0.068 %
Cu	0.165 %	ND
Sr	0.119 %	0.095 %
S	ND	0.259 %

3.2 XRD analysis

The results from XRD are shown in Fig 8, Fig 9 and Fig 10 and their properties are shown in Table 3 ,4 and 5 respectively.

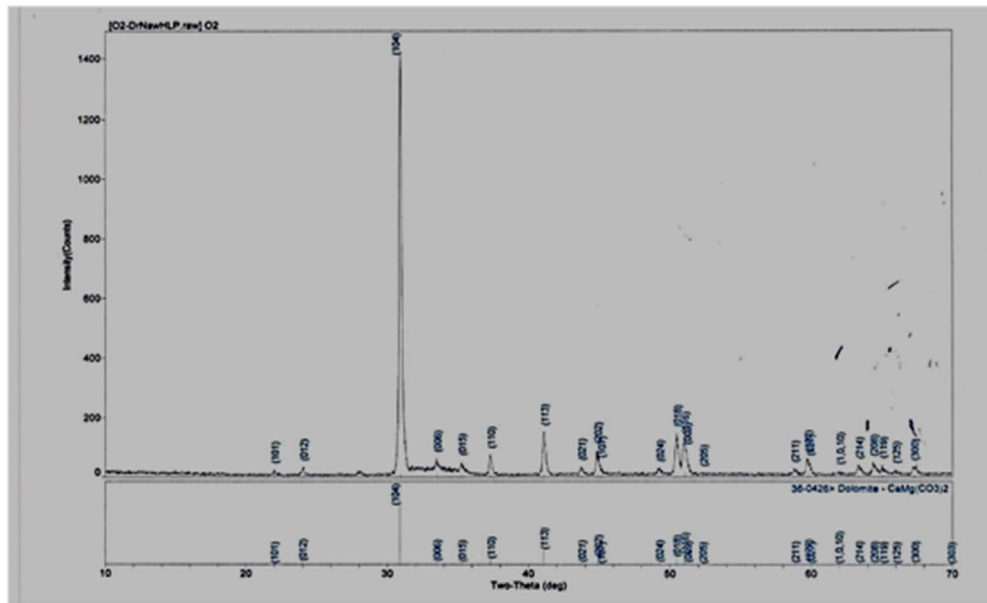


Figure 8. XRD pattern of dolomite

Table 3. XRD results of dolomite

Planes	(CaMg(CO ₃) ₂)	SiO ₂	Al ₂ O ₃
(104)	(104)	-	-
(110)	(110)	-	-
(113)	(113)	-	-
(202)	(202)	-	-
(018)	(018)	-	-

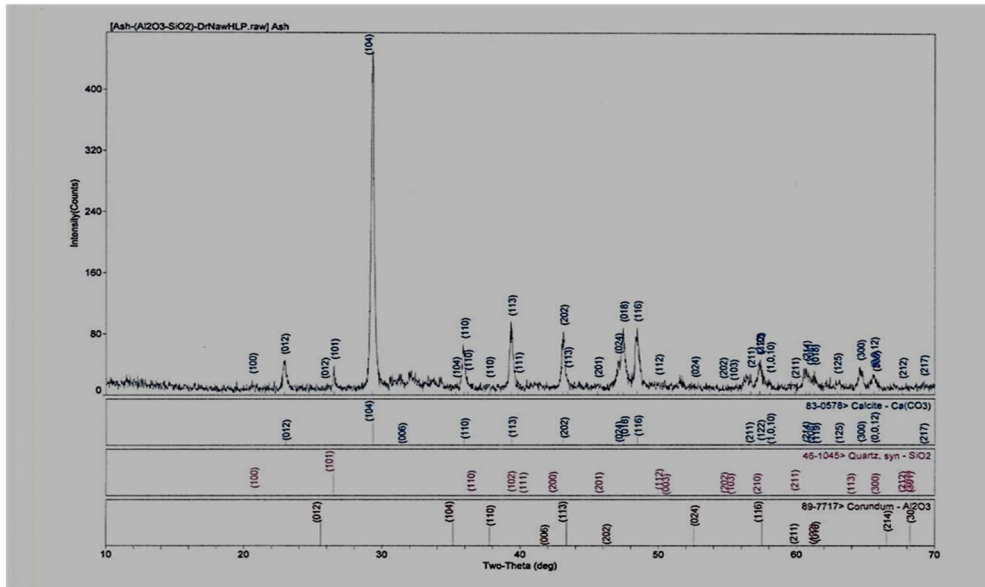
**Figure 9.** XRD pattern of fly-ash

Table 4. XRD results of fly - ash

Planes	Ca(CO ₃)	SiO ₂	Al ₂ O ₃
(100)	-	(100)	-
(012)	(012)	-	(012)
(101)	-	(101)	-
(104)	(104)	-	(104)
(110)	(110)	(110)	(110)
(113)	(113)	(113)	(113)
(202)	(202)	(202)	(202)
(116)	(116)	-	(116)
(211)	(211)	(211)	(211)
(300)	(300)	(300)	(300)

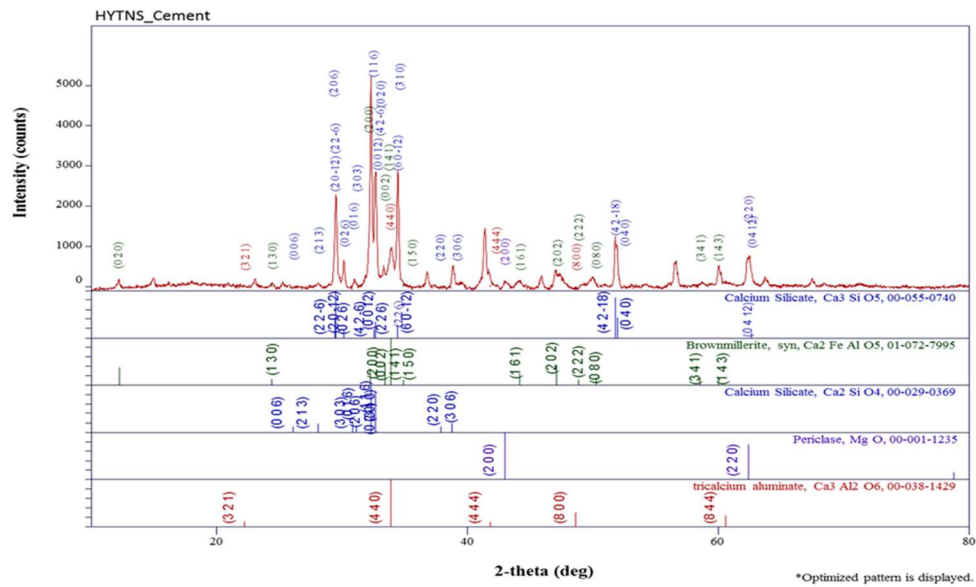


Figure 10. XRD pattern of cement

Table 5. XRD results of cement

Planes	Ca ₃ SiO ₅	Ca ₂ SiO ₄	Ca ₂ FeAlO ₅	Ca ₃ Al ₂ O ₆	MgO
(20 $\bar{1}2$)	(20 $\bar{1}2$)	-	-	-	-
(026)	(026)	-	-	-	-
(116)	-	(116)	-	-	-
(200)	-	-	(200)	-	-
(00 $\bar{1}2$)	(00 $\bar{1}2$)	-	-	-	-
(440)	-	-	-	(440)	-
(141)	-	-	(141)	-	-
(60 $\bar{1}2$)	(60 $\bar{1}2$)	-	-	-	-
(306)	-	(306)	-	-	-
(444)	-	-	-	(444)	-
(202)	-	-	(202)	-	-
(42 $\bar{1}8$)	(42 $\bar{1}8$)	-	-	-	-
(040)	(040)	-	-	-	-
(143)	-	-	(143)	-	-
(04 $\bar{1}2$)	(04 $\bar{1}2$)	-	-	-	-
(220)	-	-	-	-	(220)

3.3 Results for Compressive Strength

The compressive strengths were determined by compressive strength testing machine (RBU-250) of the structural laboratory at department of civil engineering in Yangon Technology University. The results are shown in Table 6(a) and 6(b) as the various ratio of dolomite, fly- ash and cement.

Table 6(a) Compressive strength for ten bricks as the various ratio

Items / Samples		Dolomite and cements as raw materials									
		18 : 1					6:1				
Weight (g)		6910	6760	6690	6890	6300	6860	6860	6760	6830	6660
Length (cm)		28.91	28.91	28.91	28.91	28.91	26.17	26.17	26.17	26.17	26.17
Width (cm)		13.17	13.17	13.17	13.17	13.17	12.15	12.15	12.15	12.15	12.15
Height (cm)		10.33	10.33	10.33	10.33	10.33	10.47	10.47	10.47	10.47	10.47
Unit Weight (lb/ft ³)		129.4	126.6	125.3	129.0	118.0	157.4	157.4	155.1	156.1	152.8
Maximum load (p) (N)		9443	10934	10437	8449	8946	44233	46221	42742	43736	40257
Compressive Strength	lb/in ²	416	482	460	372	394	2421	2530	2339	2394	2230

Table 6(b) Compressive strength for eight bricks as the various ratio

Items / Samples		Dolomite , fly- ash and cement as raw materials							
		A ₁	A ₂	B ₁	B ₂	C ₁	C ₂	D ₁	D ₂
Weight (g)		6120	6120	6880	7060	6820	6740	6800	6700
Length (cm)		26.0	25.5	26.0	26.0	26.0	26.0	26.0	26.0
Width (cm)		9.5	10.0	10.0	10.0	10.0	13.0	10.0	10.0
Height (cm)		12.0	12.5	13.0	13.5	13.0	13.5	13.0	13.5
Unit Weight (lb/ft ³)		130.97	121.79	129.11	127.58	127.99	93.69	127.61	121.08
Maximum load (p) (N)		71550	65770	16460	110620	158700	215120	216090	159930
Compressive Strength	lb/in ²	420.18	374.12	918.28	1732.90	885.36	923.17	1205.53	892.22

3.4 Microscope Results

Photomicrographs of alpha tracts in LR- 115 for raw materials such as dolomite and fly- ash are shown in Fig 11 and Fig 12 respectively.



Figure 11. Photomicrographs of alpha tracks for dolomite

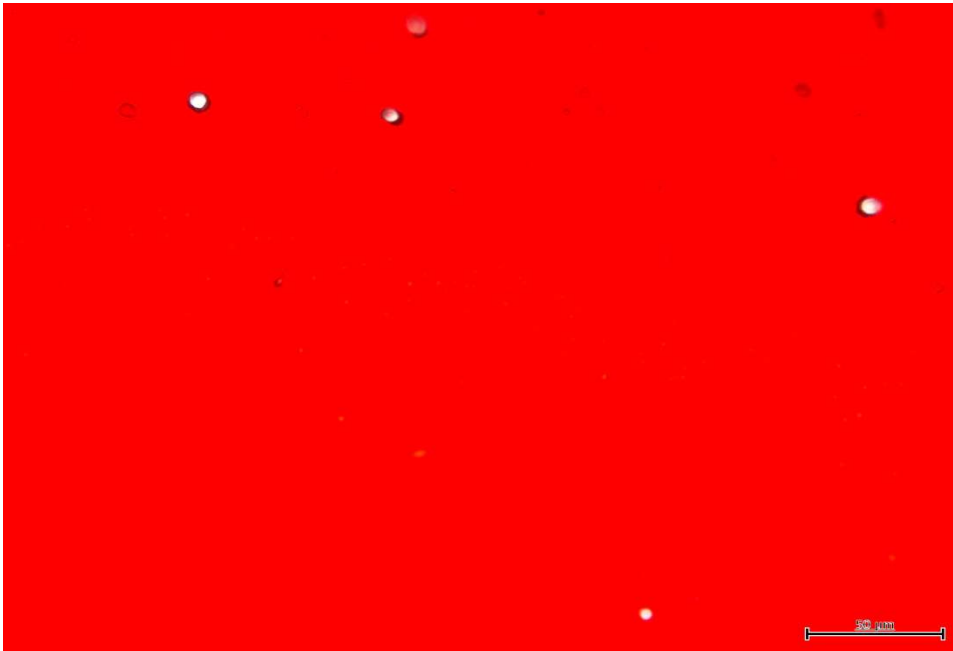


Figure 12. Photomicrographs of alpha tracks for fly- ash

The calculated values of radon concentration in dolomite and fly- ash are listed in Table 7.

Table 7. Results from radon concentration

Sample	Average net Tracks	Track Density (track $\text{cm}^{-2}\text{day}^{-1}$)	Radon concentration (Bq m^{-3})	Annual Effective Dose (mSv yr^{-1})	Activity (Bq $\text{m}^{-3}\text{h}^{-1}$)	Mass Exhalation Rate (mBq $\text{kg}^{-1}\text{h}^{-1}$)	Surface Exhalation Rate (mBq $\text{m}^{-2}\text{h}^{-1}$)
Dolomite	1.28 \pm 0.226	0.146 \pm 0.026	6.952 \pm 1.238	0.1196 \pm 0.0213	(1.668 \pm 0.297) 10^4	0.138 \pm 0.025	3.114 \pm 0.554
Fly - ash	2.88 \pm 0.718	0.329 \pm 0.082	15.667 \pm 3.905	0.2695 \pm 0.067	3.760 \pm 0.937	0.310 \pm 0.077	7.019 \pm 1.750

Discussion and Conclusion

4.1 Discussion

The EDXRF results show that Ca contains the highest concentration of 97.257% in dolomite and 95.680% in fly- ash.

The XRD results show that in dolomite, the planes (104), (110), (113), (202) and (018) identify with the planes of dolomite. All of the planes can be attributed to dolomite ($\text{CaMg}(\text{CO}_3)_2$) phase, which is matched well with the library file no 36-0426 .

In fly-ash, the planes (110), (113), (202), (211) and (300) identify with the planes in calcite; silicate and aluminum oxide respectively. The planes (012), (104) and (116) identify with that of in calcite and aluminum oxide. Also the planes (100) and (101) identify with the planes in silicate from library file in XRD.

In cement, the presence of calcium silicate (Ca_3SiO_5), calcium silicate (Ca_2SiO_4), brownmillerite ($\text{Ca}_2\text{FeAlO}_5$), tricalcium aluminate ($\text{Ca}_3\text{Al}_2\text{O}_6$) and periclase(MgO) are observed. The planes $(20\bar{1}2)$, (026) , $(00\bar{1}2)$, $(60\bar{1}2)$, $(42\bar{1}8)$, (040) and $(04\bar{1}2)$ are corresponding to the major phase of monoclinic structure Ca_3SiO_5 . Other planes are represented by the minor phases such as Ca_2SiO_4 , $\text{Ca}_2\text{FeAlO}_5$, $\text{Ca}_3\text{Al}_2\text{O}_6$ and MgO , respectively.

The measurement of compressive strengths of brick samples are summarized in Table 6(a) and (b). As listed in Table 6(a), dolomite and cement were used as raw materials. The average compressive strength of five bricks prepared by the mixture of dolomite and cement with the weight ratio of 18:1 (according to the conventional brick that currently used in Loikaw township, Kayah State in Myanmar) is 424.8 lb in⁻². The average compressive strength of five bricks prepared by the mixture of dolomite and cement with the ratio of 6:1 is 2382.8 lb in⁻². In Table 6(b), dolomite, fly-ash and cement were used as raw materials as the various ratios. The average compressive strength of A₁ and A₂ made by the mixture of dolomite and fly-ash as the ratio of 1:1 is 397.15 lb in⁻².

The average compressive strength of B₁ and B₂ made by the mixture of dolomite, fly-ash and cement as the ratio of 2: 1:1 is 1325.59 lb in⁻². When dolomite, fly-ash and cement were mixed with 5:3:2 ratio, the average compressive strength of obtained bricks C₁ and C₂ is 904.27 lb in⁻². For samples D₁ and D₂, dolomite, fly-ash and cement were mixed with 5:4:1 and the average compressive strength of D₁ and D₂ is 1048.88 lb in⁻².

According to the radon concentration results, the alpha track density is 0.146±0.026 tracks cm⁻² day⁻¹, radon concentration is 6.952±1.238 Bqm⁻³, annual effective dose is 0.120±0.021 mSvyr⁻¹, activity is 1.668±0.297 Bqm⁻³h⁻¹, mass exhalation rate is 0.138 ±0.025 mBqkg⁻¹h⁻¹ and surface exhalation rate is 3.114 ±0.554 mBqm⁻²h⁻¹ are found in dolomite. In fly-ash, the alpha track density is 0.329±0.082 tracks cm⁻² day⁻¹, radon concentration is 15.667±3.905 Bqm⁻³, annual effective dose is 0.270±0.067mSvyr⁻¹, activity is 3.760±0.937 Bqm⁻³h⁻¹, mass exhalation rate is 0.310 ±0.077 mBqkg⁻¹h⁻¹ and surface exhalation rate is 7.019 ±1.750 mBqm⁻²h⁻¹.

4.2 Conclusion

The XRD results show that the Portland from Demawsore township, Kayah State is the type of dolomite which has the properties of cement. The fly-ash from Tigyt in Southern Shan State also has the properties of cement.

The average value of compressive strength of brick samples which were made by the mixture of dolomite and cement as the ratio of 18:1 is 424.8 PSI. This value is very lower than the standard values (1000~2500PSI). So

that kind of bricks, currently used in Loikaw township, is not safe in constructing high buildings.

When dolomite and cement were mixed with the weight ratio as 6:1, the average value of compressive strength of that brick samples is 2382.8 PSI. It is a very perfect value for construction materials. But their prices become high.

In addition to use the fly-ash to mixture of dolomite and cement with the various weight ratio, the average values of compressive strength of that brick samples are 1325.59PSI (2:1:1) and 1048.88PSI (5:4:1).

From the above mentioned results, it can be concluded that fly-ash is an appropriate additive to prepare bricks with higher compressive strengths as well as it can be used especially in reducing the use of cement.

From International Commission on Radiological Protection (2010), the radon concentration data, annual effective doses are much lower than the limited level 300 Bqm^{-3} and 17 mSvyr^{-1} respectively. So in construction materials which were made by using regional sources (dolomite, fly-ash) the level of indoor radon are well within acceptable values for the people and free from exposure to radon and radon daughters.

And also it can be concluded that the present work has primarily been focused upon the radon concentration and annual effective dose that will be a significant support for further studies concerning the environmental safety and health protection.

Acknowledgements

I would like to thank Pro-rectors from Pyay University Dr Nyunt Soe and Dr Nilar Myint, Professor Dr Pyone Pyone Shein, Head of Department of Physics, Pyay University, for their kind permission to do this work.

I also would like to thank Rector (YU) Dr Pho Kaung, Professor Dr Khin Khin Win (Head of Department of Physics, YU) and Professor Dr Soe Soe Nwe (YU) for their permission to present this research report.

I am also grateful to Dr Zeya Oo, Visiting Professor, Department of Engineering, Physics, Yangon Technological University for sharing the knowledge on Geopolymer which is a great motivation to initiate this paper.

References

- Alton Wade.F., Richard Mattox.B., (1960) *Elements of Crystallography and Mineralogy* (Harper and Brothers, Publishers, New York)
- Callister.W.D., (1997) *Materials Science and Engineering* (Toronto : Wiley)
- Chris Pellant, (1992) *Rocks and Minerals* (Dorling Kindersley Limited, London)
- Guy.A.G., (1972) *Introduction to Materials Science* (London : Mc Graw-Hill)
- <http://www.Introduction to Cement.com>
- <http://www.Introduction to Polymers.com>
- <http://www.Introduction to Geopolymer.com>

TEMPERATURE DEPENDENT CHARACTERIZATION OF AL DOPED TiO₂ PARTICLES

Hla Toe¹, Khin Khin Kyaw², Nyein Nyein Ei³

Abstract

The research describes the structural and optical properties of Aluminium Al_x, TiO₂ (1-x) (Al 5, 10 and 15 wt %) doped Titanium dioxide thin films prepared by thermal diffusion technique. The Aluminium and Titanium dioxide mixed samples are annealed in temperature controller furnace at different temperature scale for each sample are 400°C, 500°C, 600°C, 700°C and 800°C for two hours. The samples are characterized by X-ray diffraction technique (XRD). The band gap energy of all doped sample are studied by Ultra-Violet visible absorption spectroscopy (UV-Vis). The surface morphology and grain size of samples are measured by Scanning Electron Microscopy (SEM). X-ray diffraction result reveal the tetragonal structure of samples with secondary phase formation changed depend on increasing temperatures. The Ultra-violet visible absorption spectroscopy studies Aluminium doped Titanium dioxide show the band gap differs from Titanium dioxide anatase form. The Aluminium doped Titanium dioxide samples are deposited on glass and p-type Si (100) substrates by screen printing method. The Aluminium doped Titanium dioxide deposited on glass thin films are heating temperature 200°C for 30 minutes. The Aluminium doped Titanium dioxide deposited on p-type Si substrate thin films are heating temperature 300°C to 800°C for one hour. The electrical properties of Aluminium doped Titanium dioxide deposited on glass and Si substrate thin films are measured by standard electrical devices.

Introduction

TiO₂ is one of the most commonly used semiconductors in photocatalytic and photovoltaic applications because of its different properties, such as low cost, low toxicity, chemical stability, and so on. It is used in photovoltaic application as a semiconductor in dye-sensitized solar cells (DSSCs). Doping TiO₂ is an interesting strategy used to improve its properties as a semiconductor and, thus, its efficiency in many applications. However, only a few studies on the doping of TiO₂ with Al have been

¹. Associate Professor, Department of Physics Pyay University

². Associate Professor, Department of Physics Pyay University

³. Demonstrator, Department of Physics, University of Medicine, Taungyi

performed, and in these cases, the percentage of doping was low, at around (5,10 and 15wt%) in Al doped TiO₂, which is 15wt%,the maximum doping obtained by using dissolution methods for synthesis. Al doped TiO₂particles were synthesized by using two methods (named methods: Thermal Diffusion method and Co-precipitation method) to produce levels of doping(5,10 and 15wt%) while maintaining the crystallinity of the samples in most cases. The synthesized samples were extensively characterized through XRD methods, which enabled the study of the characteristic and phase changes as a function of the annealing temperature, the percentage of doping, and the method of synthesis used. With both methods of synthesis, the formation of the rutile phase was display of the doping was increased, so the anatase phase was predominant in most cases.

Experimental Procedure

Sample Preparations

TiO₂ powder and Al powder are used as starting material for Al doped TiO₂. The first method synthesis of Al powder and TiO₂ powder were mixed by Al powder of weight ratio (5, 10 and 15 wt%) and Al is x and TiO₂ powder is (1-x) ratios are stirred with ceramic mortar for two hours as shown in Figure-1 to 5. The mixtures of Al doped TiO₂ powders were heated at 400°C to 800°C for two hours by thermal diffusion method. The second method of the Al doped TiO₂ samples have been prepared by co-precipitation method are as shown in Figure 6 and 7. Analytical grade of pure TiO₂, the various ratio of aluminium nitrate Al(NO₃)₃.9H₂O are used as a main chemicals and ammonia and distilled water (DI) were used as agent materials. In a typical experiment were dissolved of distilled water (DI) in TiO₂, aluminium nitrate Al(NO₃)₃.9H₂O and ammonia(drop by drop) stirring for two and half hours with heated temperatures 150°C then the white precipitation powder were drop on the bottom of the flask. The mixture powder was filtered and the white solid was collected and washed several times with distilled water (DI) and ethanol as shown in Figure-4.After washing process, for precipitation of the final samples were dry in air for 120 hours and calcine temperature is 600°C for 2 hours in furnace. The final samples doped TiO₂ with Al concentrations are (5, 10 and 15 wt%) respectively by using co-precipitation

method. In these two process, the best ratio of Al doped TiO₂ powder were placed into the beaker and mixed with 2-methoxyethanol, propylene glycol (PPG) and stirred homogeneously for 1 hour. After that Al doped TiO₂ solvent were obtained to use for deposited on glass and silicon substrates. The p-type silicon (100) and glass substrates were cleaned with standard process and used for the deposition of the Al doped TiO₂ solvent by screen printing method. Finally, Al doped TiO₂ deposited on Si thin films were annealed at different temperatures for 300°C to 800°C. The electrical properties of Al doped TiO₂ deposited on Si thin films were examined by standard electrical equipment.

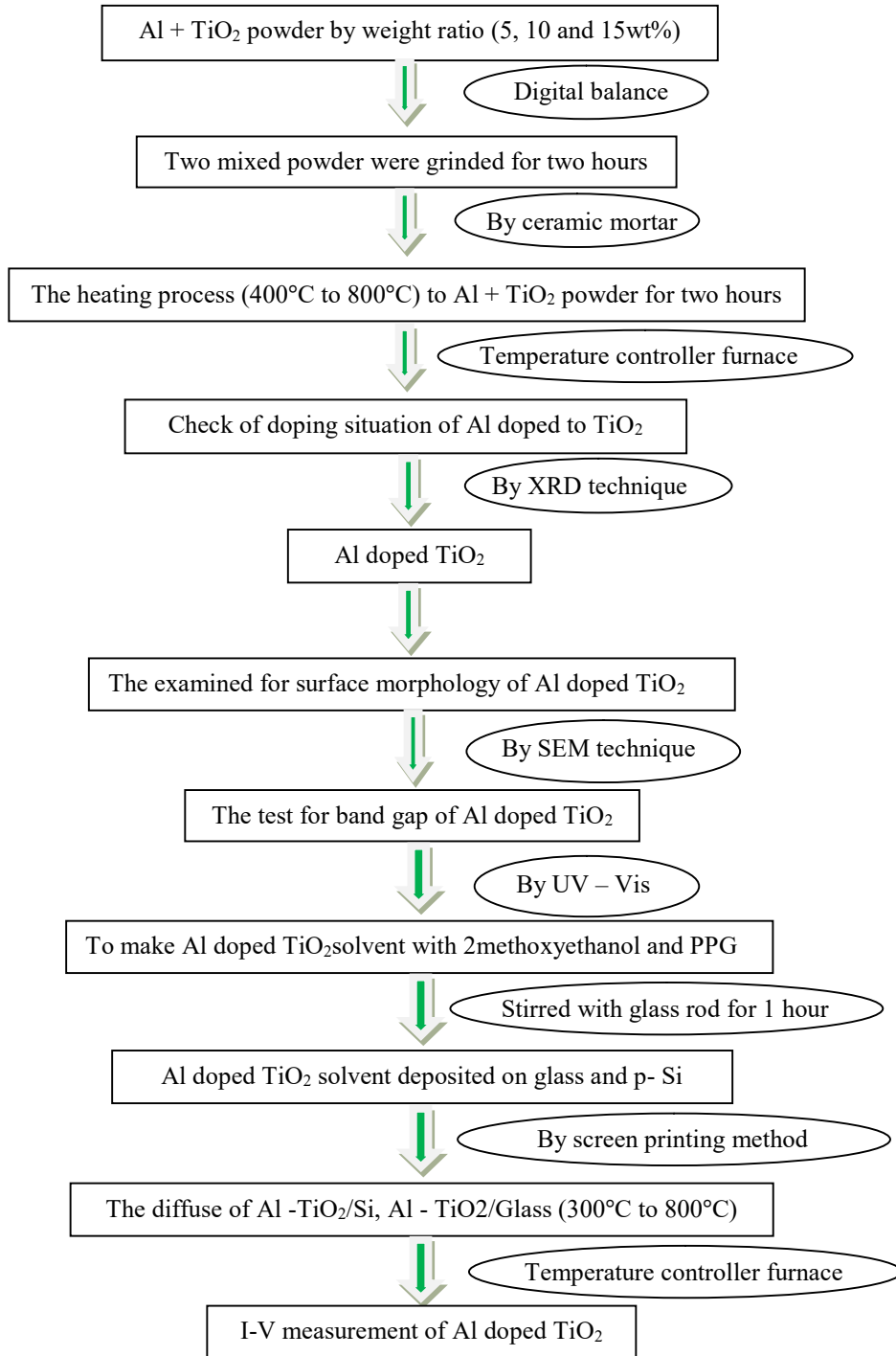


Figure 1. The sample preparation scheme of Al doped TiO₂ for thermal diffusion method

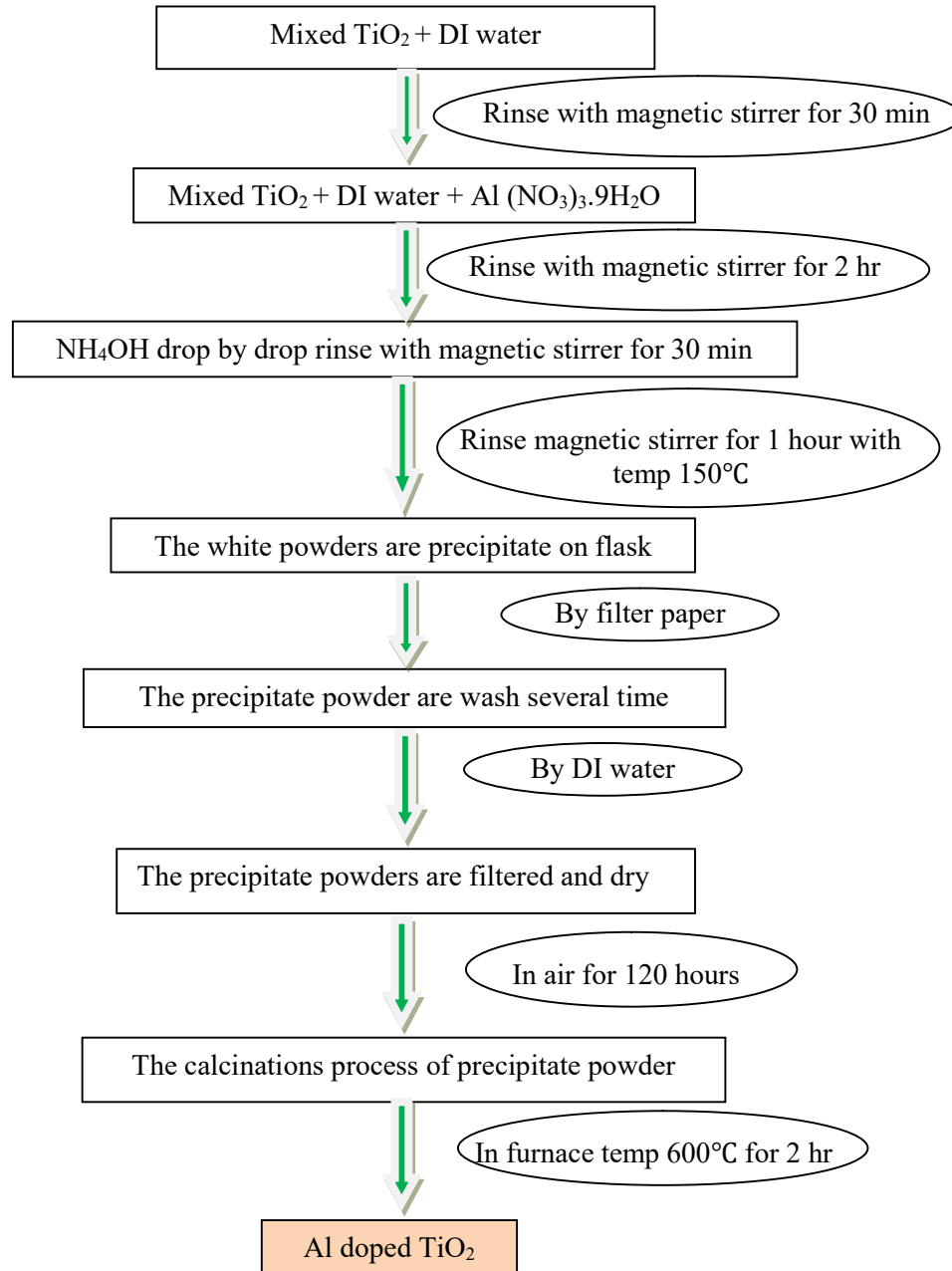


Figure 2. The sample preparation scheme of Al doped TiO₂ for co-precipitation method

Sample Preparation Photos

Figure 3. Weighing of chemicals with digital balance and grinding with aggregate mortar



Figure 4. Heat treatment to mixed powder of Al and TiO₂, Al doped TiO₂ deposited on Si and glass by screen printing method



Figure 5. Sample deposition process by the screen printing method and heat treatment at different temperatures



Figure.6 Different doping ratio of Al doped into TiO₂ by co-precipitation method



Figure 7. Al doped TiO₂ sample precipitate on flask, filter and dry in air for 120 hours

Experimental Data

The x-ray diffraction (XRD) analysis of Al doped TiO₂

The typical XRD patterns of pure TiO₂ and Al doped TiO₂ were shown in Figure-8 to 11. Major peaks of Al doped TiO₂ is (101) can be attributed to tetragonal structure anatase form at doping temperature 400°C to 700°C. The diffraction major peaks of Al doped TiO₂ at 800°C (15 wt%) are (110) and (101). The diffraction peaks of all samples were quite matching with the tetragonal TiO₂ data [JCPDS card, No-71-1167 and 87-0920] but different form. In XRD pattern, (101) diffraction peak observed 2θ degree range between 25.055° to 25.335° for anatase form and rutile form 2θ degree is 27.225° to 27.487°. The variation of 2θ is depending on the Al doping concentration and 2θ degree of Al doped TiO₂ is smaller than pure TiO₂ for anatase phase. In rutile phase, 2θ degree of Al doped TiO₂ is wider than pure TiO₂. The 2θ degree is increase with decrease intensity of XRD peak for anatase form and reverse situation for rutile form. The XRD pattern intensity of TiO₂ (101) peak is decrease with increasing Al doping ratio for anatase form and intensity peak increase with increasing doping ratio for rutile form. The lattice parameter “c” of Al doped TiO₂ depicts as a function of Al doping concentration. The crystal structure of TiO₂ is the same but change the anatase form to rutile form, it is depends on the doping temperature. As could

be seen, the lattice parameter “c” is 9.5204 Å for pure TiO₂ and other “c” vales. With the increase in the Al concentration (5, 10 and 15 wt%), the lattice parameter “c” is differ from pure TiO₂ and changes with randomly 9.5191 Å, 9.5279 Å and 5.4910 Å respectively for doping temperature 500°C.The increase in the lattice parameter “c” could be attributed to the Al atoms substitute in the Ti atoms in the lattice, and radius of the Al ion was smaller than that of the Ti ion.

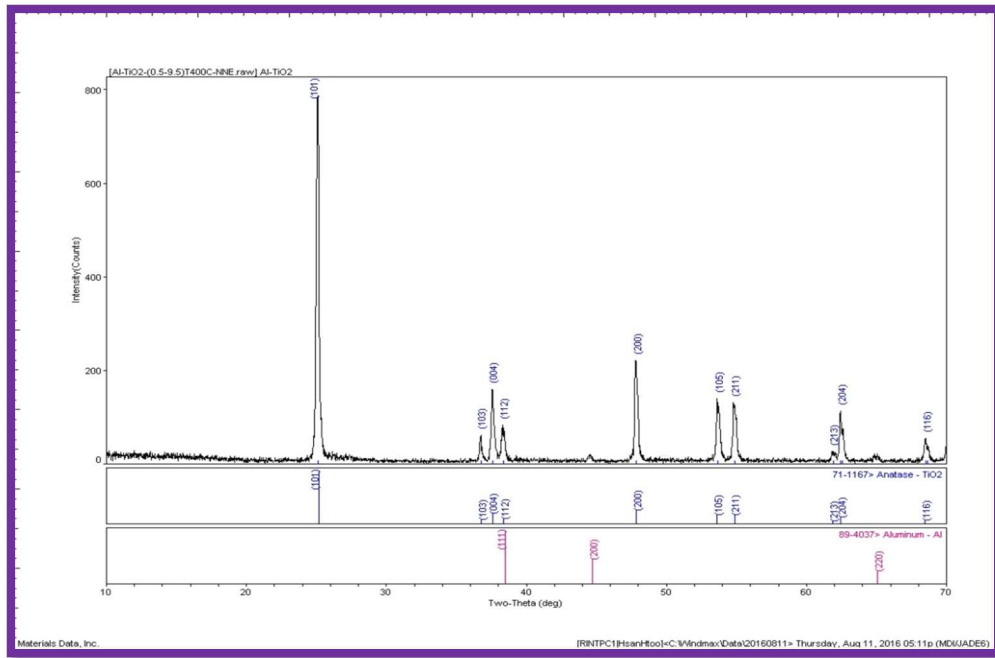


Figure 8. XRD analysis of Al doped TiO₂ (5wt% Temp 400°C)

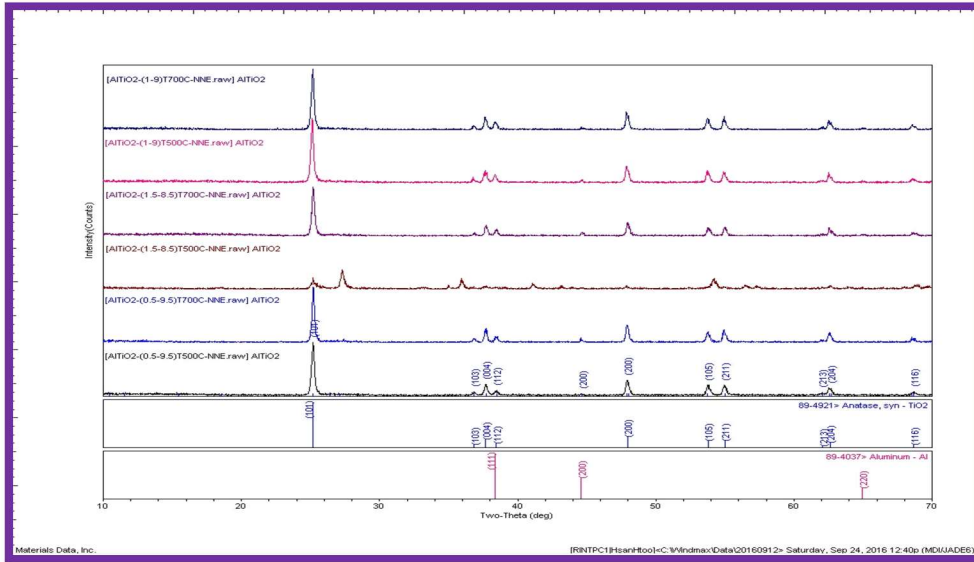


Figure 9. XRD analysis for comparison of pure TiO₂ and Al doped TiO₂ at different doping ratios and temperatures

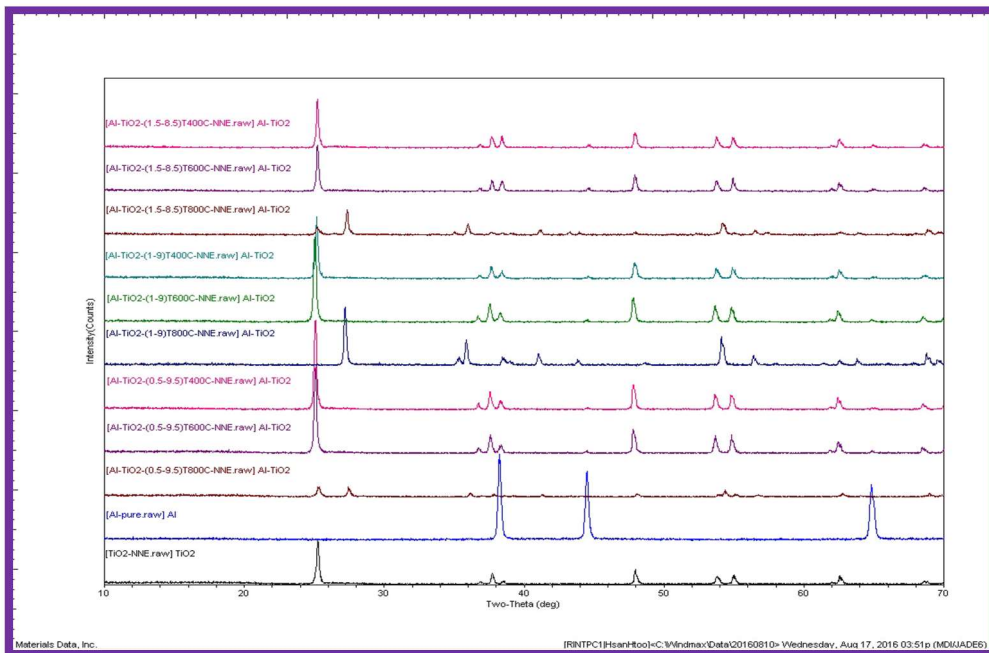


Figure 10. XRD analysis for comparison of Al doped TiO₂ and pure TiO₂ at different doping ratios and temperatures

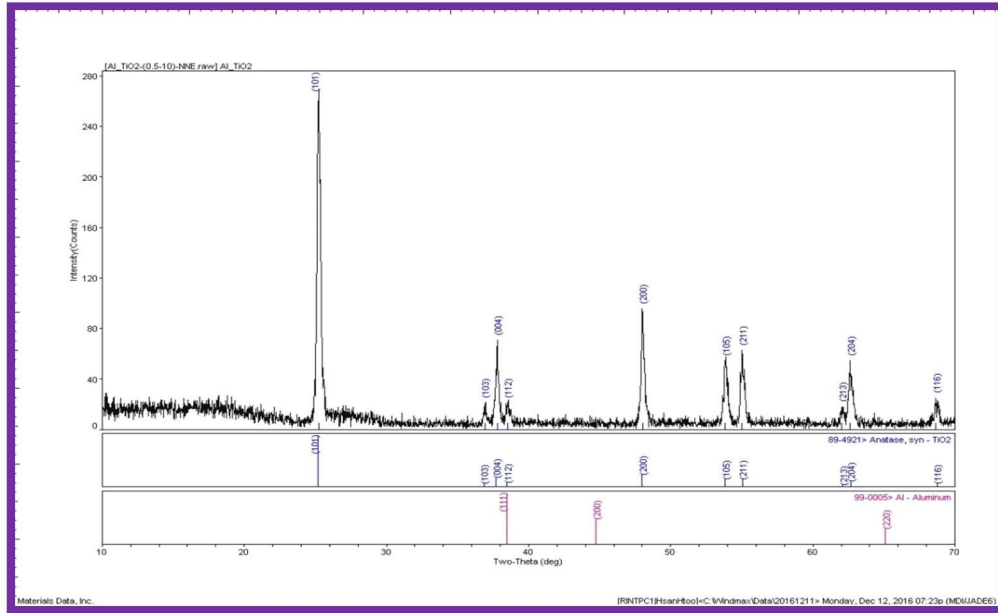


Figure 11. XRD analysis of Al doped TiO₂ by co-precipitation method (5 wt%)

The scanning electron microscopy (SEM) analysis of Al doped TiO₂

The surface morphology of the samples was investigated by scanning electron microscope (SEM) as shown in Figure-12. Al doped TiO₂ (5wt%) particles appear several shape and grain size of these particles present in the size range between 30 nm- 60 nm. The surfaces morphology of Al doped TiO₂ powders for different doping temperatures are 400°C, 500°C, 600°C, 700°C and 800°C respectively. The SEM images are show generally uniform for doping temperatures 500°C, 600°C and 700°C not only doping temperature 400°C but also 800°C are different morphology forms. Doping temperature 500°C image is more uniform, sharp and clearly structure of other Al doped TiO₂ images.

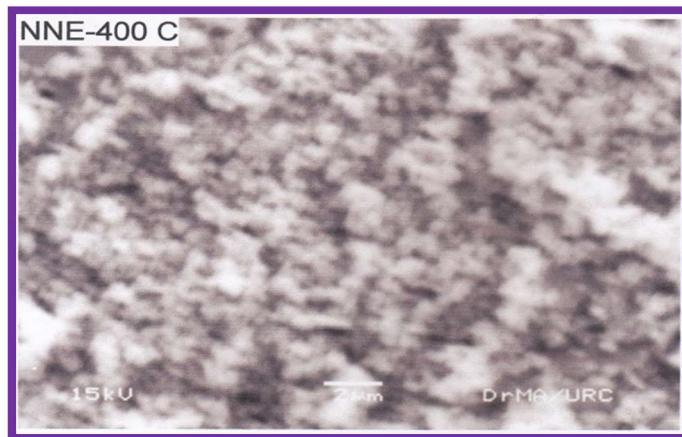


Figure.12 SEM analysis of Al doped TiO₂ (5wt%) at 400°C

The ultraviolet spectroscopy UV-Vis analysis of Al doped TiO₂

The measurement of the bandgap of materials is important in the semiconductor and solar industries. The term “bandgap” refers to the energy difference between the top of the valence band to the bottom of the conduction band. The electrons are able to jump from one band to another. In order for an electron to jump from a valence band to a conduction band, it requires a specific minimum amount of energy for the transition, the bandgap energy.

UV-Vis analysis of Al doped TiO₂ particles are shown in Figure-13. The bandgap is vary with Al doping concentration for constant temperature 400° C as shown in fig 14. In this case, pure TiO₂ has a bandgap 3.2 eV for anatase form as compared to bandgap of Al doped TiO₂ are (1.944 eV, 2.431 eV, 1.525 eV, 1.395 eV, 1.893 eV) for doping ratio 5wt% at doping temperatures 400°C, 500°C, 600°C, 700°C and 800°C respectively. Al doping concentration is reduced the bandgap of pure TiO₂. The bandgap of Al doped TiO₂ is depending on different doping ratio in constant doping temperature 400°C as shown in Table-1. The bandgap of undoped TiO₂ and Al doped TiO₂ could be determined by finding the wavelength turning edge of the UV-Vis absorbance peak and equation as follow;

$$E_g = \frac{hc}{\lambda_{edge}}$$

Where, E_g = the bandgap energy h = Plank's constant

λ_{edge} = the wavelength of absorption edge c = the velocity of light

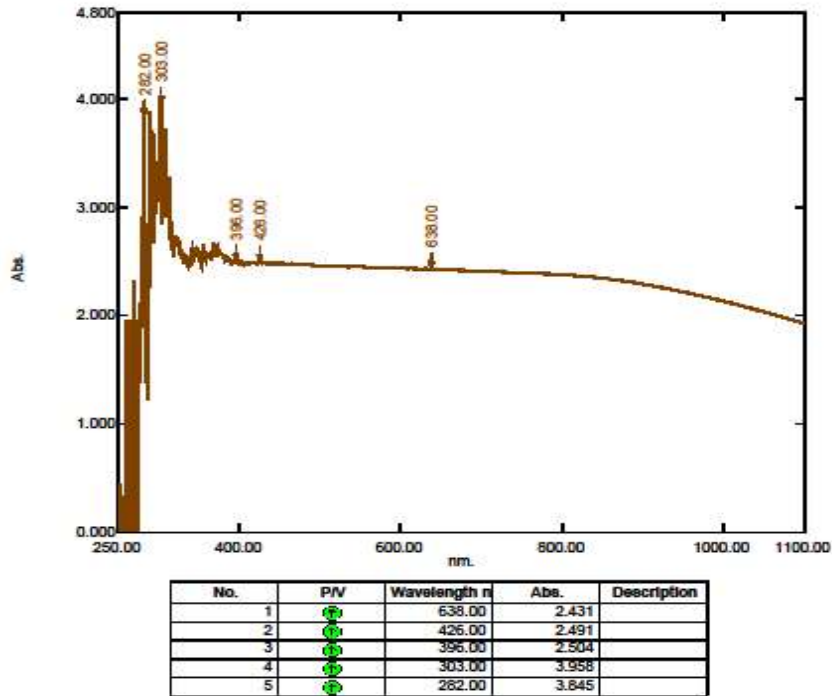


Figure 13. UV analysis of Al doped TiO₂ (5wt%) at 400°C

Table 1. UV analysis of Al doped TiO₂ of different doping ratios and same doping temperature

serial	Doping ratio (wt%)	Doping Temperature (°C)	Wavelength edge (nm)	Bandgap energy (eV)
1	5	400	638.00	1.944
2	10	400	412.00	3.009
3	15	400	378.00	3.280

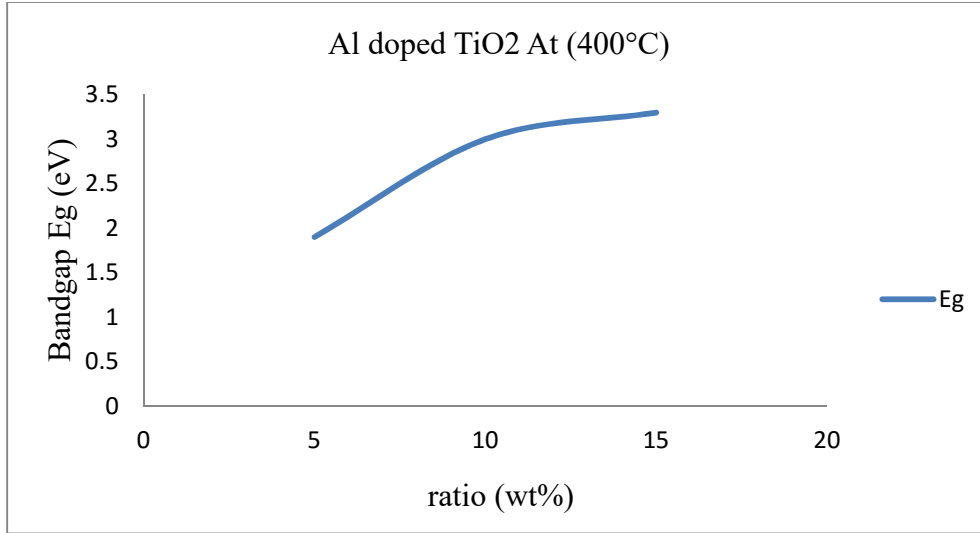


Figure 14. Bandgap energy of Al doped TiO₂

Current-Voltage Characteristics under Illumination Condition

Figure 15 exhibits the photovoltaic behavior of the junction under the illumination condition. It is understood that the photoelectric effect is resulted from light induced electron-hole generation at the junction and particularly at the depletion region of the p-type silicon. The results of current-voltage (I-V) measurements for Al doped TiO₂ deposited on Si films prepared at different diffusion temperatures. Photovoltaic properties of Al doped TiO₂ deposited on Si films is depending on the different diffusion temperature and it is vary with light intensity. Photovoltaic of these films are increase with arise of light intensity. Al doped TiO₂ deposited on Si films have been clearly exhibits sensitivity with light intensity.

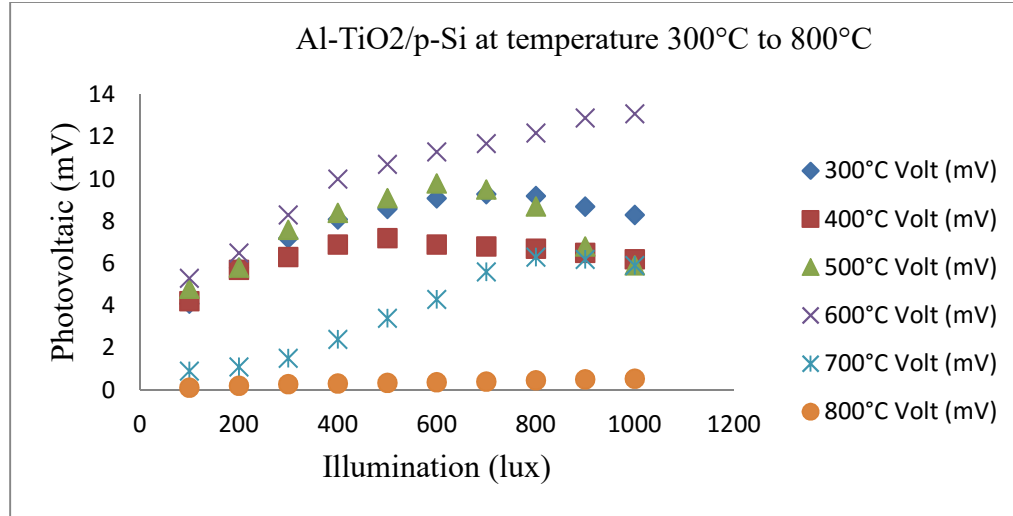


Figure 15. Photovoltaic measurement of Al doped TiO₂ deposited on p-Si at 300°C to 800°C

Discussion

Al powder doped into TiO₂ powder with three different ratio of (5, 10 and 15 wt%) were used by thermal diffusion and co-precipitation methods. Al doping ratio 5wt% is thoroughly doped into TiO₂ and other Al doping ratios (10 and 15 wt%) are not completely doped into TiO₂ in thermal diffusion method and they are examined by the XRD and the results show Al is successfully doped into TiO₂ in 5 wt% samples and other (10 and 15 wt%) samples are not completely doped into TiO₂ in co-precipitation method. Al doped TiO₂ is deposited on glass and p-type Si substrates by screen printing method. In this research screen printing method is use deposition process of Al doped TiO₂ deposited on glass and Si. This method has some advantageous factors such as easy to do, homogeneous deposition and cheaper cost than other deposition techniques. According to the UV-Vis spectra with different doping ratio and temperature of Al doped TiO₂, the band gap energy of Al doped TiO₂ is varied with Al doping concentration. Moreover, it does not depend on doping temperature in same doping ratio. In doping temperature 800°C, XRD pattern of Al doping ratio 5wt% is tetragonal structure of anatase and rutile phase show simultaneously. In XRD pattern, Al doping ratio 10

wt% anatase peak (101) is gradually decrease than doping ratio 5 wt% rutile peak (110). XRD pattern of doping ratio 15 wt% is clearly show dominantly formed rutile phase only.

These two processes were successfully done with home-made equipment and hence cost cheaper price than other deposition techniques. And it is easily done in our laboratory. Al and TiO₂ are promising materials for optoelectronic devices and easy to buy in local market. Thermal diffusion method, co-precipitation method and screen printing method can be done in our laboratory.

Conclusion

Al doped TiO₂ sample of doping temperature 400°C photo was clearer and sharper than other different doping temperature samples-photo has been seen by XRD. Al doped TiO₂ particles were found to be of tetragonal structure, anatase phase of doping temperature 400°C to 700°C. The doping temperature 800°C is critical temperature for phase changes from anatase to rutile phase with same tetragonal crystal structure. Doping ratio (15 wt%) image shows highest intensity peak in co-precipitation method. The samples is clearly shows tetragonal particles with random form from SEM images. Comparing the two doping methods, these two samples have a little difference in XRD. The results of XRD pattern exhibit that thermal diffusion method has higher intensity peak than that result of co-precipitation method. According to the experimental results, thermal diffusion method is better than co-precipitation method for Al doped TiO₂ process. The angle of diffraction (2θ) is increased, varying with increasing doping concentration of Al at 400°C. The interplanar spacing “d” decrease with increasing Al doping concentration. According to the UV analysis pattern and calculation results, bandgap energy of Al doped TiO₂ is narrower than pure TiO₂ (3.2 eV, 3.0 eV) for anatase and rutile phase. The UV results of selected samples are 1.944 eV, 2.431 eV, 1.525 eV, 1.395 eV and 1.893 eV for 5wt% of Al doping temperatures 400°C, 500°C, 600°C, 700°C and 800°C respectively. Bandgap energy of Al doping ratio 10 wt% and 15wt% are 3.009 eV and 3.280 eV respectively. It is slightly different from pure TiO₂ at 400°C. In UV result, Al doped TiO₂ wavelength is between 378 nm to 889 nm and it indicates the inclusion within the range of

visible light and infrared region. Concentrative study on Al doped TiO₂ (5 wt%) ratio is best doping ratio for thermal diffusion method and (15 wt%) for co-precipitation method. I-V characteristic of diffusion temperature 600°C is optimum in this research. The photocurrent, voltage and resistance are varying with different diffusion temperature in constant illumination condition. The main advantages of the proposed synthesis are its simplicity and further work on the optimization of pure TiO₂ and Al doped TiO₂ tetragonal particles growth for electronic and optoelectronic applications in progress. Al doped TiO₂ can be used for gas sensor of NO₂ and CO gas.

Acknowledgements

I would like to thank Professor Dr Khin Khin Win, Head of Department of Physics, University of Yangon, for her kind permission to reading of this paper.

I also deeply thanks Professor Dr Pyone Pyone Shein, Head of Department of Physics, Pyay University, for kind permission to carry out of this research.

References

- C. KITTEL, (1995), "Introduction to Solid State Physics" Seventh Edition, John Wiley & Sons (Asia) Pte. Ltd- Singapore.
- H.P.MYERS, (1998), "Introductory Solid State Physics" Second Edition, VIBA BOOKS PRIVATE LIMITED, New Delhi 110 002.
- Jenny Nelson,(2013), "The Physics of Solar Cells" Imperial College Press, 57 Shelton Street, Covent Garden, London WC2H 9HE.
- J.P. Srivastava, (2011), "Elements of Solid State Physics" Third Edition, PHI Learning Private Limited, New Delhi 110 001.
- R.K.PURI and V.K.BABBAR, (2003), "Solid State Physics and Electronics" Second Revised Edition, S. CHAND AND COMPANY LTD, New Delhi 110 055.

COMPARISON OF THE FORM FACTORS OF TIN ISOTOPES

Cho Cho San¹, Khin Swe Myint²

Abstract

The purpose of this research is to obtain the form factors of ^{116}Sn , ^{118}Sn and ^{124}Sn nuclei using two parameter Fermi model (2PF) . The structural parameters, namely radius parameter (c) and the skin thickness parameter (z) of ^{116}Sn , ^{118}Sn and ^{124}Sn taken from the experimental data are used to get the charge density distribution. After getting the charge density distribution, the root mean square radius and the form factors are calculated.

Key words: Charge density distribution, form factor, root mean square radius.

Introduction

There are two types of nuclear distributions which are nuclear charge distribution and nuclear matter distribution. We are dealing with nuclear charge density distribution. In theory, nuclear charge density distributions are expressed in various form factors depending upon nuclear model. In the present work nuclear distribution on charge distribution are given in two parameter Fermi model (2PF) and three parameter Fermi model (3PF) respectively. The parameters consist in these models are obtained from scattering experiments. A study of electron scattering would be a method of measuring the distribution of the static electromagnetic field of the nucleus. The scattering of β -particles are not monoenergetic, they have low momentum and suffer, in addition to large single scatters, severe multiple scattering effects. This property prevented clear results being obtained from early measurements of electron scattering. However, the scattering of more energetic electrons (>100 MeV) is a very important tool in the investigation of the nuclear size.

In atomic physics, the boundary of an atom is not sharp since the wave function of the outer electrons decreases monotonically: therefore we should expect a similar situation to occur in nuclear physics. As we have seen, when Rutherford was investigating the scattering of α -particle by gold, his scattering

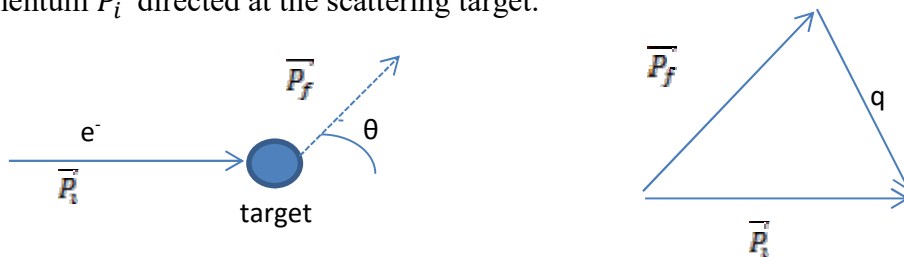
¹ Department of Physics, Mandalay University of Distance Education, Mandalay, Myanmar.

² Department of Physics, Mandalay University, Mandalay, Myanmar.

measurements were in agreement with the predictions found assuming that the interaction was the Coulomb potential between two point charges. Thus for gold at the classical distance of closest approach that could be reached with the α -particle energies that Rutherford had available, he was unable to detect any deviations which might indicate that the charges on α -particle and the gold nucleus were point like. However, using light nuclei as target, Rutherford found deviations which indicated a breakdown in the Coulomb's law when the classical distance of closest approach was about 10^{-4} m. These deviations occur at short distances of approach, because the finite charge density distributions overlap and the strong nuclear forces which exist between the α -particle and nucleus come into play. It is necessary to distinguish between the distribution of the source of electric fields (proton) and the source of nuclear fields (protons and neutrons), although these sources are probably strongly linked. To make progress we should use a probe for one which does not feel the other. The electron is coupled to an electric field due to charge sources but does not experience the nuclear force. Conversely, the neutron is electrically neutral but does not experience the nuclear force. Thus separate scattering experiments with these two particles should, in principle, go some way to measuring these two distributions. So, electron scattering experiments are tools to obtain charge density distribution of nuclei while neutron scattering experiments are used to get matter distribution.

Relation between Cross Section and Form Factor

Form Factors are an intuitive and simple tool used to describe the scattering particles from extended targets. Here we will show how the Form Factor comes about in the context of the scattering of spinless electrons. A discussion of the more rigorous description, which includes electron spin and magnetic moment, will follow. The typical set up has an electron beam with initial momentum \vec{P}_i directed at the scattering target.



The electrons are deflected through an angle θ with a final momentum \vec{P}_f . We define the momentum transfer as the vector $\vec{q} = \vec{P}_i - \vec{P}_f$. As with many scattering experiments, the quantity we are interested in is the differential cross section $\frac{d\sigma}{d\Omega}$ of our scattered electrons off our target. This quantity can be measured in the lab and easily connected to QM scattering theory in order to confirm theory and provide insight to the physical processes at play. Earlier we had shown that the differential cross section is related to the scattering amplitudes through the relation:

$$\frac{d\sigma}{d\Omega} = \frac{k}{k_i} |f(\theta, \phi)|^2 \tag{1}$$

The scattering amplitudes $f(\theta, \phi)$ can be obtained in approximate form using the Born Approximation. To first order (and up to a normalization) the Born Approximation can be written as:

$$f_{B1} = \langle \phi_{\vec{k}_f} | V | \phi_{\vec{k}_i} \rangle \tag{2}$$

$$\int \phi_{\vec{k}_f}^*(\vec{r}) V(\vec{r}) \phi_{\vec{k}_i}(\vec{r}) d^3(\vec{r}) \tag{3}$$

In the first Born Approximation the initial incoming wave and the outgoing waves are assumed to be plane waves of the form:

$$\phi_{\vec{k}_i}(\vec{r}) = e^{i\vec{k}_i \cdot \vec{r}}$$

$$\phi_{\vec{k}_f}(\vec{r}) = e^{i\vec{k}_f \cdot \vec{r}}$$

We will also define the momentum transfer as $\frac{\vec{q}}{\hbar} = \vec{k}_i - \vec{k}_f$. Making use of these definitions the first Born Approximation can be written as:

$$f_{B1} = \int e^{\frac{i\vec{q} \cdot \vec{r}}{\hbar}} V(\vec{r}) d^3\vec{r} \tag{4}$$

This result is still quite general; in order to proceed we will need to assume a specific form for the potential, $V(\vec{r})$. We can describe an extended charge distribution by $Ze \rho(\vec{r})$ with

$$\int \rho(\vec{r}) d^3\vec{r} = 1 \tag{5}$$

In this case, the potential experienced by an electron located at (\vec{r}) is given by the Coulomb potential:

$$V(\vec{r}) = \frac{-ze^2}{4\pi\epsilon_0} \int \frac{\rho(\vec{r}')}{|\vec{r}-\vec{r}'|} d^3\vec{r}' \quad (6)$$

Substitute this potential into the general expression for the first Born Approximation to the scattering amplitudes $f(\theta, \phi)$ in (eq. 4)

$$f_{B1} = \frac{-ze^2}{4\pi\epsilon_0} \int e^{\frac{i\vec{q}\cdot\vec{r}}{\hbar}} \frac{\rho(\vec{r}')}{|\vec{r}-\vec{r}'|} d^3\vec{r}' d^3\vec{r} \quad (7)$$

Make the substitution $\vec{R} = \vec{r} - \vec{r}'$ and noting that $d^3\vec{R} = d^3\vec{r}'$,

$$f_{B1} = \frac{-ze^2}{4\pi\epsilon_0} \int e^{\frac{i\vec{q}\cdot\vec{r}}{\hbar}} \frac{\rho(\vec{r}')}{|\vec{R}|} d^3\vec{r}' d^3\vec{R} \quad (8)$$

$$\frac{-ze^2}{4\pi\epsilon_0} \int e^{\frac{i\vec{q}\cdot\vec{r}}{\hbar}} \frac{\rho(\vec{r}')}{|\vec{R}|} d^3\vec{r}' d^3\vec{R} \quad (9)$$

$$\frac{-ze^2}{4\pi\epsilon_0} \int \frac{e^{\frac{i\vec{q}\cdot\vec{R}}{\hbar}}}{|\vec{R}|} d^3\vec{R} \left[\int e^{\frac{i\vec{q}\cdot\vec{r}'}{\hbar}} \rho(\vec{r}') d^3\vec{r}' \right] \quad (10)$$

This bracket factor is known as the 'Form Factor', $F(q)$.

$$F(q) = \int e^{\frac{i\vec{q}\cdot\vec{r}'}{\hbar}} \rho(\vec{r}') d^3\vec{r}' \quad (11)$$

It can be shown that when the expression for f_{B1} is used to determine $\frac{d\sigma}{d\Omega}$,

$$\frac{d\sigma}{d\Omega} = \frac{k}{k_i} f_{B1}^2 |F(q)|^2 \quad (12)$$

$$\left(\frac{d\sigma}{d\Omega} \right)_{point} = \frac{k}{k_i} f_{B1}^2 \quad (13)$$

So, Relation between cross section and form factor is

$$\frac{d\sigma}{d\Omega} = \left(\frac{d\sigma}{d\Omega}\right)_{point} |F(q)|^2 \tag{14}$$

To provide some insight into the meaning of form factors and probability distribution, we shall connect $F(q^2)$ to nuclear radius and give examples of the relation between form factor and probability distribution. For $qR \ll 1$, where R is approximately the nuclear radius, the exponential in equation (11) can be expanded, and $F(q^2)$ becomes

$$F(q^2) = 1 - \frac{1}{6\hbar^2} q^2 \langle r^2 \rangle + \dots \tag{15}$$

where $\langle r^2 \rangle$ is defined by

$$\langle r^2 \rangle = \int d^3r r^2 \rho(r) \tag{16}$$

and is called the mean-square radius.

Two Parameter Fermi Model

In our calculation, two parameter Fermi model is used to calculate the root mean square radius and charge density distribution.

For two parameter Fermi model, charge density distribution is

$$\rho(r) = \frac{\rho_0}{(1 + e^{(r-c)/z})} \tag{17}$$

Where, c = the radius parameter

z = the skin thickness parameter

The variation of form factor with momentum transfer is

$$F(q) = \frac{4\pi}{qZe} \int \rho(r) r \sin(qr) dr \tag{18}$$

The parameters of two parameter Fermi model are expressed in Table.

No.	Nucleus	c (fm)	z (fm)
1	¹¹⁶ Sn	5.358	0.550
2	¹¹⁸ Sn	5.412	0.560
3	¹²⁴ Sn	5.490	0.534

Calculation of Charge Density Distribution, Form Factor and RMS for Two Parameter Fermi Model

Density distribution for two parameter Fermi model is

$$\rho(r) = \frac{\rho_0}{(1 + e^{(r-c)/z})} \quad (19)$$

Where, c = the radius parameter

z = the skin thickness parameter

The normalization condition is

$$\int \rho(r) 4\pi r^2 dr = Ze \quad (20)$$

$$\int \rho(r) r^2 dr = \frac{Ze}{4\pi} \quad (21)$$

By substituting equation (19) in equation (21),

Let,
$$TERM = \int \frac{1}{(1 + e^{(r-c)/z})} r^2 dr \quad (22)$$

$$\rho_0 = \frac{1}{TERM} \times \frac{Ze}{4\pi} \quad (23)$$

By substituting equation (23) in equation (19),

$$\rho(r) = \frac{1}{(TERM)^2} \left(\frac{Ze}{4\pi} \right) \quad (24)$$

The variation of form factor with momentum transfer is

$$F(q) = \frac{4\pi}{qZe} \int \frac{\rho_0}{(1 + \exp((r-c)/z))} r \sin(qr) dr \quad (25)$$

$$F(q) = \frac{1}{q} \frac{1}{TERM} \int \frac{1}{(1 + \exp((r-c)/z))} r \sin(qr) dr \quad (26)$$

Root mean square radius is

$$\begin{aligned} \langle r^2 \rangle^{1/2} &= \frac{4\pi}{Ze} \int \rho(r) r^4 dr \\ \langle r^2 \rangle^{1/2} &= \frac{4\pi}{Ze} \int \frac{1}{(TERM)^2} \frac{Ze}{4\pi} r^4 dr \\ \langle r^2 \rangle^{1/2} &= \int \frac{r^4}{(TERM)^2} dr \quad (27) \end{aligned}$$

The charge density distributions, the form factors and root mean square radii are solved numerically by using a FORTRAN code.

Results and Discussion

The charge density distribution, form factor and the root mean square radius of ^{116}Sn , ^{118}Sn and ^{124}Sn are calculated by using two parameter Fermi model (2PF). The parameters we used in our calculation for Sn isotopes are shown in Table (1).

Table 1. The parameters of two parameter Fermi model

No.	Nucleus	c (fm)	z (fm)
1	^{116}Sn	5.358	0.550
2	^{118}Sn	5.412	0.560
3	^{124}Sn	5.490	0.534

By using these parameters, charge density distributions are calculated and the resultant distributions are displayed in figure (1), (2) and (3). From these distributions, we calculated the form factors and root mean square radii for the Sn isotopes. The calculated form factors are displayed in figure (4), (5) and (6). The root mean square radii are displayed in Table (2).

Table 2. Comparison for RMS value for ^{116}Sn , ^{118}Sn and ^{124}Sn

No.	^{116}Sn	^{118}Sn	^{124}Sn
RMS radii	4.530609	4.576880	4.596027
Experimental Value	4.53	4.58	4.60

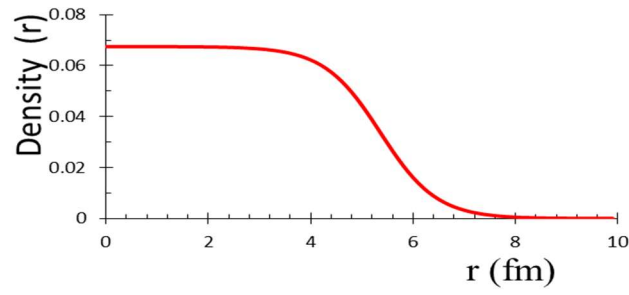


Figure 1. Charge density distribution of ^{116}Sn

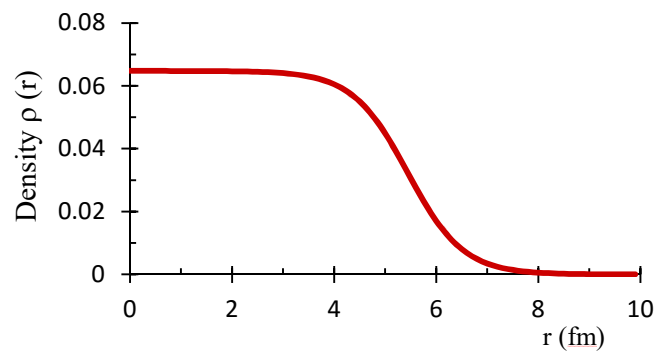


Figure 2. Charge density distribution of ^{118}Sn

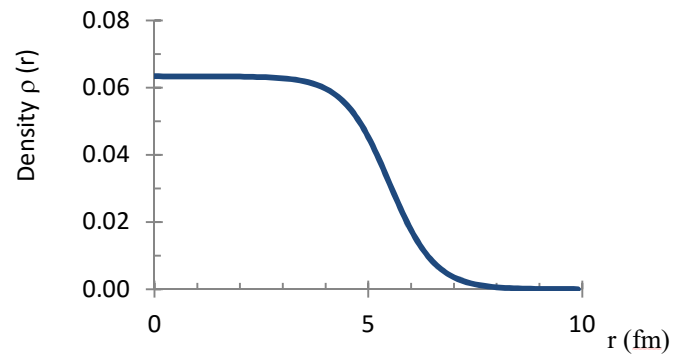


Figure 3. Charge density distribution of ^{124}Sn

Variation of Form factor with momentum transfer for ^{116}Sn

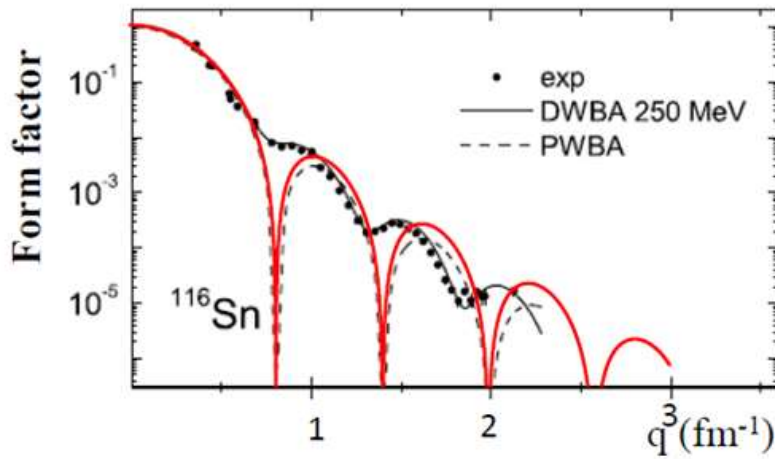
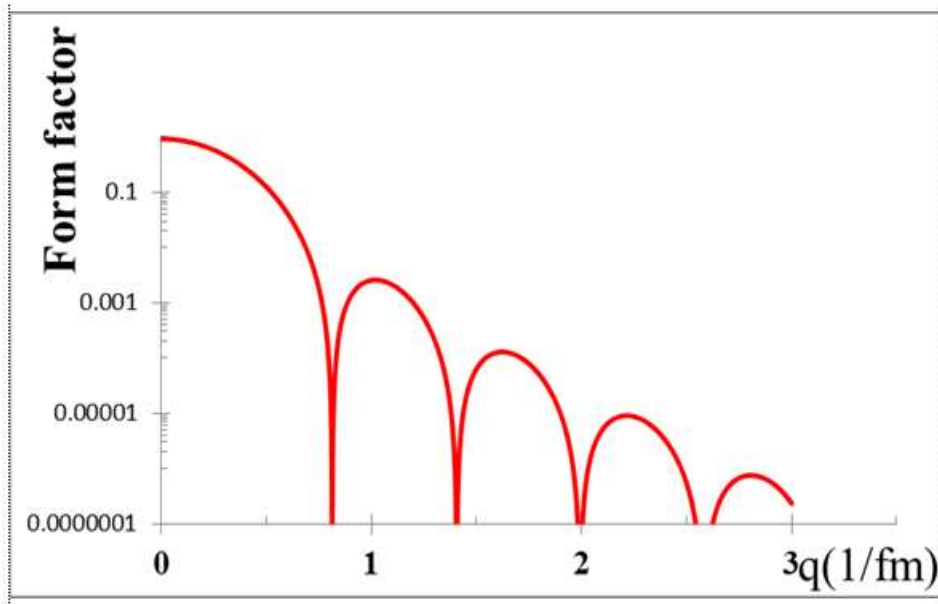


Figure 4. Comparison of experimental and calculated results of form factor for ^{116}Sn

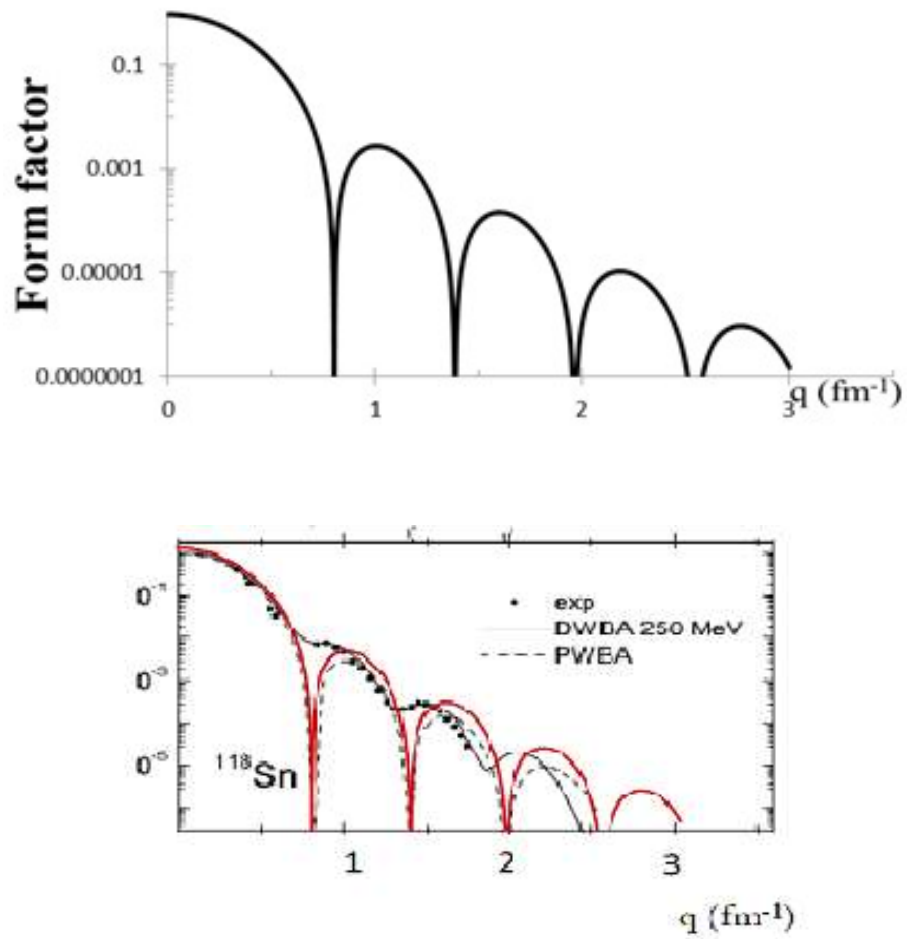
Variation of Form factor with momentum transfer for ^{118}Sn 

Figure 5. Comparison of experimental and calculated results of form factor for ^{118}Sn

Variation of Form factor with momentum transfer for ^{124}Sn

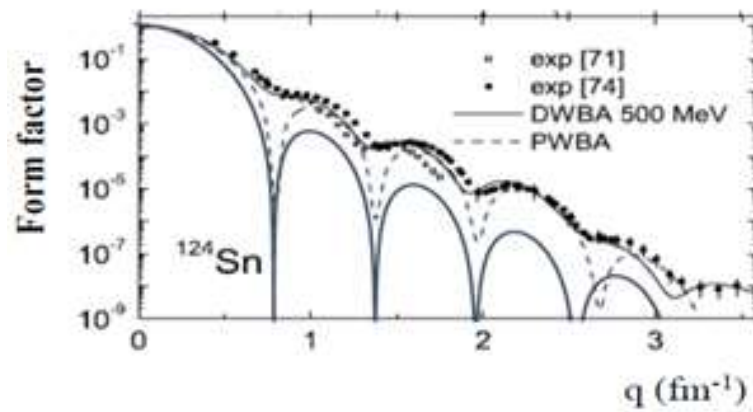
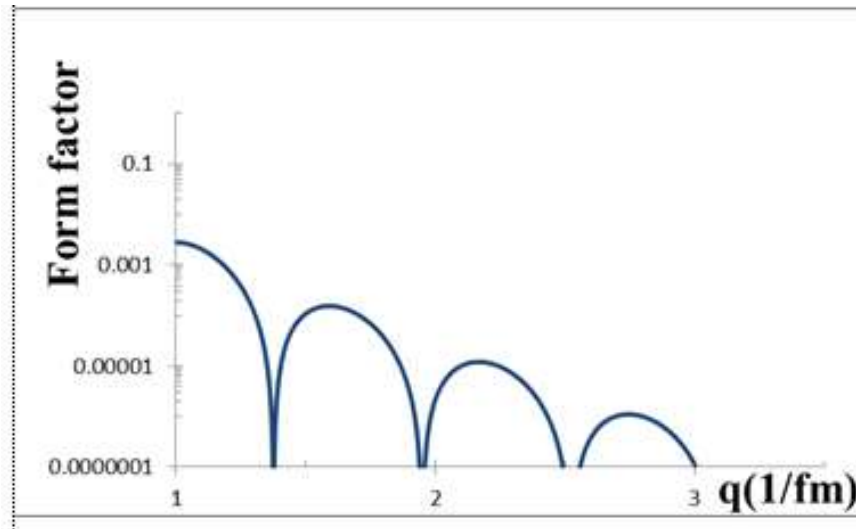


Figure 6. Comparison of experimental and calculated results of form factor for ^{124}Sn

Conclusion

In our calculation, we have calculated the charge density distributions in two parameter Fermi model for Sn isotopes. From these density distributions, we calculated the form factors and root mean square radii of Sn isotopes. In our results, we concluded that charge form factors and rms values which are calculated using the charge density of two parameter Fermi model is good agreement with the experimental value.

Acknowledgements

I would like to thank Dr Tin Maung Hla, Rector, Mandalay University of Distance Education for his encouragement. I am grateful to the full support of Professor Dr Kay Thi New, Head of Department of Physics, Mandalay University of Distance Education. I am deeply indebted to Professor Dr Khin Swe Myint, Rector (Rtd), Emeritus Professor, Department of Physics, University of Mandalay for all her enthusiastic discussion, collaboration and encouragement. I also would like to thank Dr Hla Myat Thanda, Lecturer, University of Mandalay and Dr Aye Aye Min, Lecturer, University of Mandalay for their discussions.

References

- E.M. Henlay, (1991) "Subatomic Physics".
- E.R Schneuwly, H.Vuilleumier, J.L Walter, et.al., (1974), "Charge-Distribution parameters, Isotope shifts and Isomer shifts".
- H. Vries, C.W Jager and C. Vries, (1987) , "Atomic Data and Nuclear Data Tables", **36**.
- H.D. Vires, C.W.D Jager and C.D Vires, (1987), "Nuclear Charge Density Distribution Parameters from Elastic Electron Scattering".
- L. Angeli and K.P Marinova, (2013) , "Atomic Data and Nuclear Data Tables" **99**.
- W.S.C Williams, (1991), "Nuclear and Particle Physics".

THE INFLUENCE OF DIFFERENT REDUCING AGENTS ON THE POLYOL SYNTHESIS OF COPPER NANOPARTICLES

Mi Mu Mu Khaing¹, Nan Thidar Chit Swe², Lwin Ko Oo³, Myo Aung⁴,
Ye Chan⁵

Abstract

This paper focused on the preparation of copper (Cu) nanoparticles from copper nitrate as metal precursor by Polyol reduction. Ethylene glycol, Glycerol and Glycerine were used as a reducing agent and stabilizer. The copper particles formed were identified by EDXRF, XRD and SEM. The effect of solvent showed that small spherical copper nanoparticles and the good dispersion of nanoparticles are found by using solvent either glycerol or glycerine. EDXRF spectrum also informed that there was no other metal impurity in the formation of Cu NPs. From XRD pattern, the average crystallize size of Cu NPs was found to be 38 nm as each particle observed from SEM is not a single crystallite of Cu but the agglomerates of many single crystallites. The aggregation of nanoparticles caused the inhomogeneous size distribution.

Keywords: Copper nanoparticles, spherical shaped nanoparticles, inhomogeneous size distribution

Introduction

Metals and their compounds such as Copper (Cu), Gold (Au), Silver (Ag), Palladium (Pd) and Platinum (Pt) are widely used these days (Bell *et al*, 2001) (Hutter *et al*, 2001). Nanoparticles of these metals and metal compounds have been interested extensively in recent years because of their unexpected physical and chemical properties shown at nanoscale (Ozin, 1992). Among various nanoparticles, the copper nanoparticles can be utilized in several applications. Owing to extremely small size, copper nanoparticles exhibit enhanced properties when compared with the bulk material including

¹ Lecturer, Department of Physics, Hpa-an University

² Lecturer, Universities' Research center, University of Yangon

³ Assistant Lecturer, Universities' Research center, University of Yangon

⁴ Lecturer, Universities' Research center, University of Yangon

⁵ Professor, Universities' Research center, University of Yangon

large surface area relative to their volume, ability to easily interact with other particles and increased antibacterial efficiency (Carrol et al, 2011). Because of its excellent electrical conductivity, catalytic behaviour, good compatibility and surface enhanced Raman scattering activity, Cu nanoparticles have drawn the attention of scientists to be used as essential component in the future nano-devices (Wu et al., 2006). The general problems like aggregation and oxidation of copper nanoparticles limit their usage. However, the usage of suitable separate stabilizing agent in the preparation rectifies this problem easily. Copper nanoparticles have been synthesized by different methods. To date, thermal reduction, thermal decomposition, direct electrochemical reduction from CuO nanoparticles, mechano-chemical process, polyol process, chemical reduction, *in-situ* synthesis in polymers, electro-exploding wire (EEW) and ion beam radiation have all been developed to prepare nanostructured copper (Dang et al, 2011).

In this paper, a polyol reduction method to synthesize copper colloids in different solvent without protective gas is presented. Ethylene glycol, glycerin and glycerol mixed with and without water were used as solvents. Their influence on the different reducing agent affects the nanoparticle solutions will be discussed.

2. Experimental

2.1 Materials

Analytical grade (BDH, England) Copper Nitrate $\text{Cu}(\text{NO}_3)_2$, Sodium Hydroxide (NaOH) and different solvent such as Ethylene Glycol $(\text{CH}_2\text{OH})_2$, Glycerol $(\text{C}_3\text{H}_8\text{O}_3)$ and Glycerin $(\text{C}_3\text{H}_8\text{O}_3)$ were used as starting precursor. All chemicals were used as purchased without further purification.

2.2 Synthesis of copper nanoparticles

The copper nanoparticle was prepared by polyol reduction of copper nitrate with sodium hydroxide solution. Copper nitrate was used as starting material and glycerol was used as solvent, reducing agent and a stabilizer. Sodium Hydroxide is used for faster the chemical reaction. $\text{Cu}(\text{NO}_3)_2$ (0.5 M) was dissolved in 2 ml double distilled water. To this solution, 10 ml of

ethylene glycol was added. NaOH (2.5 M) was dissolved in 2 ml double distilled water. Ethylene glycol 10 ml was added to Sodium Hydroxide and water solution. Then mixture of NaOH and $\text{Cu}(\text{NO}_3)_2$ solution was heated on a hot plate stirrer at temperatures of 135°C for half an hour. The change in colour of test solution from dark blue to reddish brown colour was observed visually. The reddish brown coloured solution was removed from the heating magnetic stirrer and cooled down. Then, the colloidal solution was separately centrifuged for 15 mins at 6000 rpm, washed three times with double distilled water (DDW) and ethanol. The wet precipitates were dried at 70°C overnight to obtain the Cu nanoparticles. Cu NPs have been prepared by polyol reduction of copper nitrate as precursor using water and ethylene glycol, water and glycerine, water and glycerol as reducing agent until the dark blue coloured solution turns to reddish brown colour. Another experiment was carried out by using the same precursor and solvents without water. The obtained colloid solution is shown in figure 2(a, b and c) with a deeper red colour.



Figure 1. Color changes (blue , green, red to dark brown) of solution after mixing NaOH 2.5 M CuNO_3 of 0.5 M

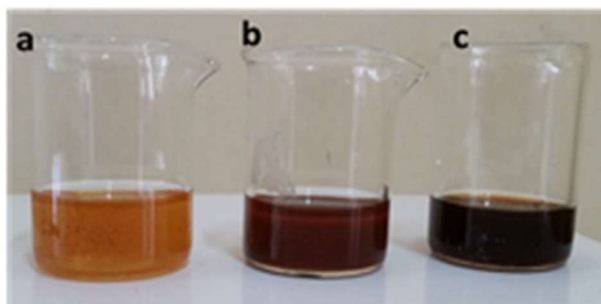


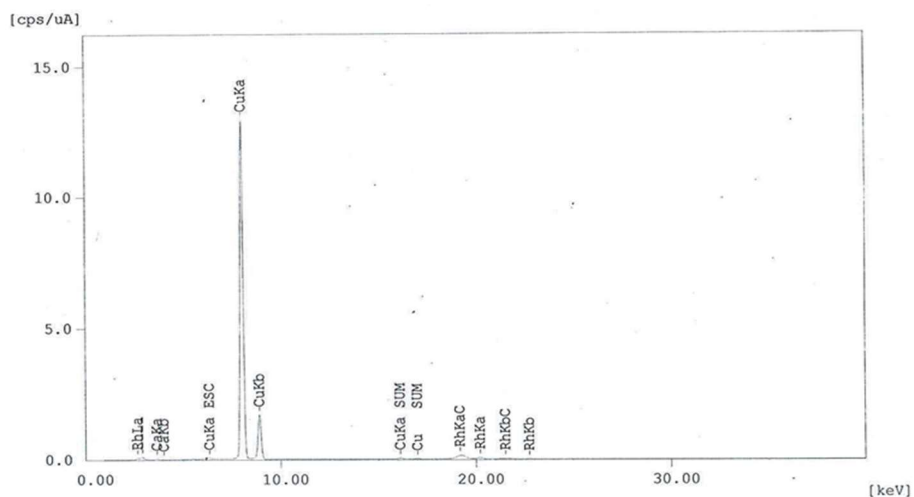
Figure 2. Fresh Colloid solutions of Cu nanoparticles in (a) glycerol (b) glycerin and (c) ethylene glycol

2.3 Characterization

Centrifuge machine (Kokusen H-200 series) was used to separate the colloid from the solutions. The influence of solvent on formation of Cu NPs was confirmed EDXRF Energy Dispersive X-rays Spectrometer (EDX 720), X-ray powder diffractometer (Type: RIGAKU-RINT 2000), and SEM (Type: JEOL 15 kV).

3. Results and Discussions

3.1 EDXRF and XRD analysis of Cu NPs



Quantitative Result

Analyte	Result	[3-sigma]	Proc.-Calc. Line	Int.(cps/uA)
	12.745 mg/cm2	[-----]	Total	-----
Cu	17141.54 mg/l	[42.337]	Quan-FP	CuKa 116.3318
Ca	150.424 mg/l	[6.078]	Quan-FP	CaKa 0.2983
C 6H10 O5	12.500 mg/cm2	[-----]	Fix	-----

Figure 3. EDXRF Cu nanoparticles by using ethylene solvent, after centrifugation and drying Cu nanoparticles obtained from different solvent shows same EDXRF spectrum.

EDXRF of all samples show similar spectrum. EDXRF analysis shows a very rich copper composition for metal. No other chemical impurities is detected. The weak calcium (Ca) signals may be due to some impurities that surrounds the Cu particles.

To confirm the crystalline structure of the copper (Cu) nanoparticles was analyzed on X-ray diffractometer (Model RIGAKU-RINT 2000). The polycrystalline properties for drop coated glass thin film of Cu powder were analyzed by using Cu / K- α_1 radiation (40 kV, 40 mA) in 2θ range from 10° to 70° on a Rigaku powder X-ray diffractometer equipped with a diffracted-beam graphite monochromator. The crystallite domain diameters D were obtained from XRD peaks according to the Scherrer equation:

$$D = \frac{0.89 \lambda}{\Delta W \cos \theta}$$
, where λ is the wavelength of the incident X-ray beam (1.5405 Å for Cu / K- α_1), λ is the Bragg's reflection angle, ΔW is the width of X-ray pattern line at peak half peak height in radians. The Miller indices in XRD pattern of Cu NPs (upper spectrum) and standard Cu particles (lower) were shown in Figure 4 and 5.

XRD graph of Cu powder synthesized from Copper nitrate precursor and different solvent such as ethylene glycol, glycerin, glycerol mixed with water has been shown in Figure 4. The pattern in Figure 4 shows that three XRD peaks appeared at 38.8° , 43.163° due to strong Bragg reflections from (111), (200) and (222) planes of Copper (I) Oxide and Copper (II) Oxide respectively. All reflections are agreed with standard library file (ICDD-PDF#99-041) of with Copper (I) Oxide and (ICDD-PDF#78-0428) of Copper (II) Oxide. Based on Scherrer equation, the average crystallite size of Cu NPs was found to be 38 nm.

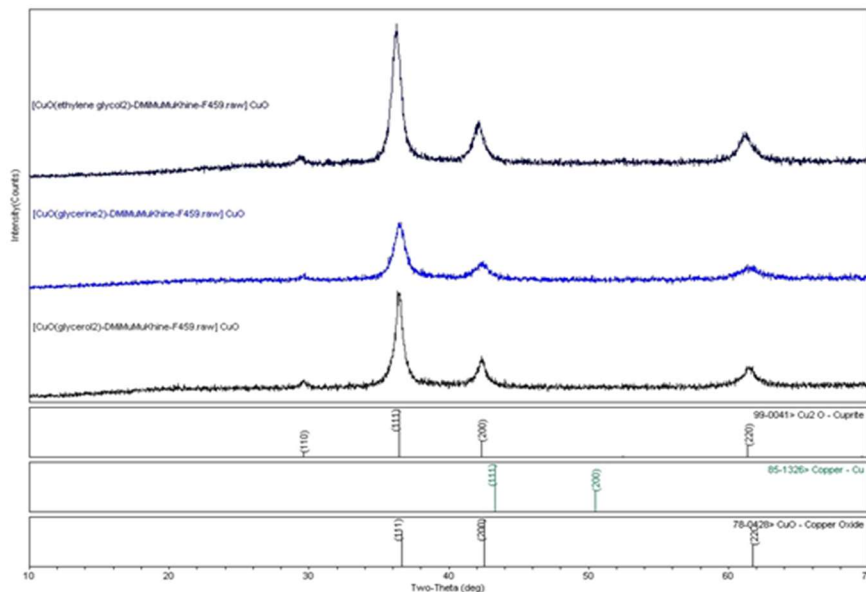


Figure 4. XRD Cu nanoparticles synthesized by using different solvents such as ethylene glycol, glycerin and glycerol. In this reaction all solvents and precursor mixed with water.

XRD graph of Cu powder synthesized from same precursor with different solvent such as ethylene glycol, glycerin and glycerol which are not mixed with water is shown in Figure 5. The XRD patterns of sample synthesized with glycerol and glycerin appeared at 43.5° , 50.163° , due to strong Bragg reflections from (111) and (200) planes of copper respectively. All reflections are agreed with standard library file (ICDD-PDF#04-0836) of pure copper metal with fcc (face centred cubic) symmetry. The XRD patterns of sample synthesized with Ethylene glycol give the Cu₂O peaks. Based on Scherrer equation, the average crystallite size of Cu NPs was found to be around 35- 38 nm.

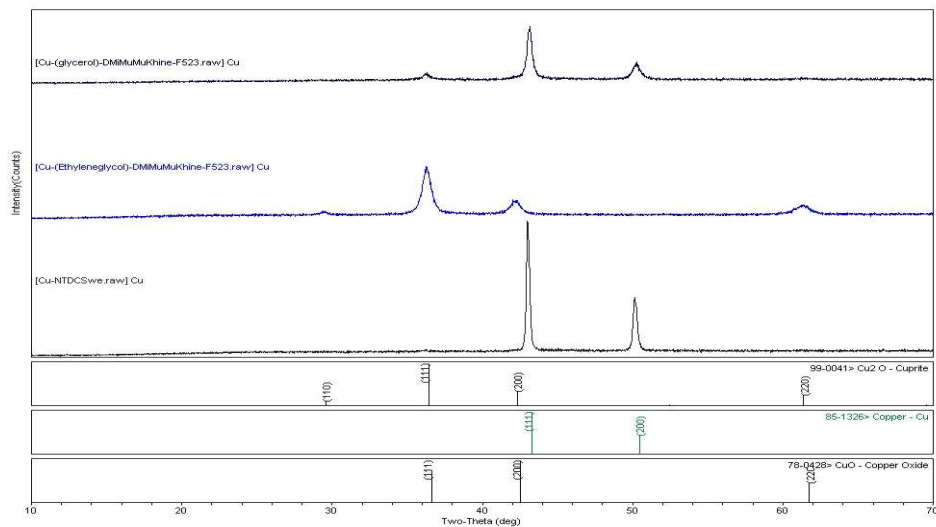
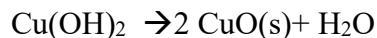


Figure 5. Figure 4. XRD Cu nanoparticles synthesized by using different solvents such as ethylene glycol, glycerin and glycerol. In this reaction, all solvents and precursor do not mixed with water.

From the XRD results, it is obviously appeared that the reaction included water gives the oxide nanoparticles. In this case, copper and copper oxide nanoparticles by the reaction of copper with water can be explained according to the reaction at 135 °C. As the concentration of Cu^{2+} and OH^- ions exceed a critical value, the precipitation of hydroxide nuclei starts.



The Cu OH can be transformed into the Cu_2O crystals via the sample chemical reaction. The Cu metal on reaction with water slowly gives out hydrogen and the liberated oxygen reacts with metal to give oxides as shown in above reaction. The Cu react with oxygen and forms nuclei, which further serve as seed for CuO and Cu_2O nanoparticles growth. The growth nanoparticles could be occurring at small oxide nuclei that may be present on the metal surface.

SEM analysis

After the preparation of the nanoparticles, SEM analysis was performed on dried nanoparticles to investigate the size and surface morphology of the samples using different solvents such as ethylene glycol, glycerin and glycerol (The samples obtained the reaction without water). Figure 6(a)–(b), 7(a)–(b) and 8(a)–(b) show the top-view SEM images of the prepared Cu samples after centrifugation and drying at 70 °C. The size of particles observed with SEM is extremely different from the XRD calculated crystallite size (35 nm or 38 nm), as each particle observed from SEM is not a single crystallite of Cu but the agglomerates of many single crystallites. The aggregation of nanoparticles caused the inhomogeneous size distribution.

Figure 6(a)–(b) As-prepared Cu precipitations using ethylene glycol are found to be mixed with big square-like structure particles and sphere form in SEM images. The size of particles are larger than 2 μm . The non-uniform size distribution is found in this sample. Figure 7(a)–(b) and 8 (a)-(b) shows that dried Cu precipitations using either glycerol or glycerin are in good dispersion and found to be small spherical-like structure. In some regions, it is noticed that big nanoparticles (having average diameter of 100nm) which are surrounded by smaller nanoparticles. The surface morphology and size distribution of the samples by using glycerol and glycerin are better in those samples compare with the sample using solvent, ethylene glycol.

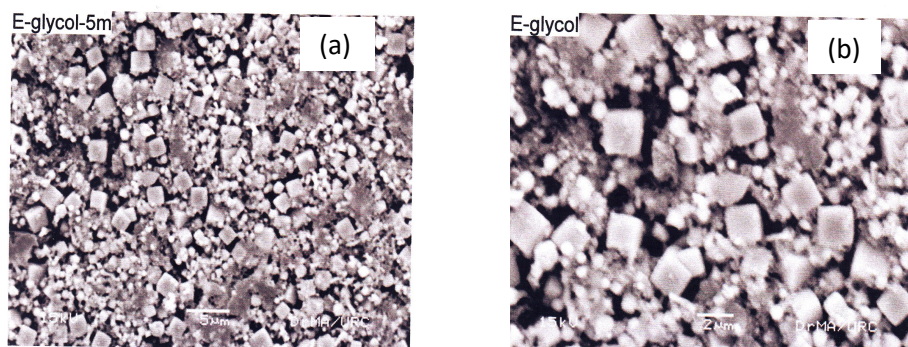


Figure 6. (a) high and (b) high magnification top-view SEM images of as prepared Cu nanoparticles by using ethylene glycol

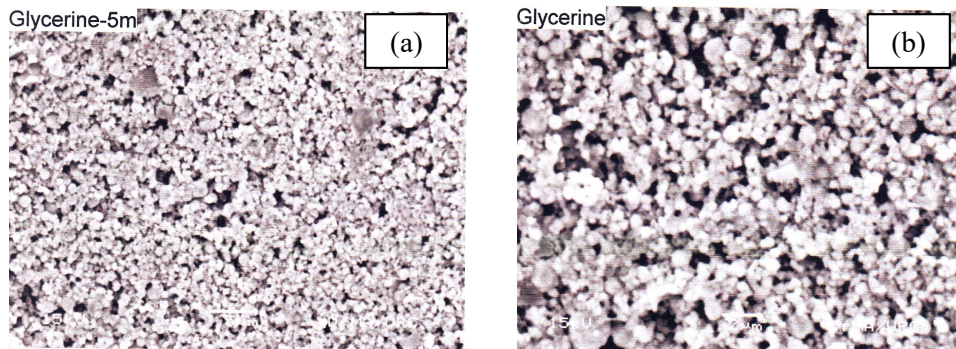


Figure 7. (a) Low and (b) high magnification top-view SEM images of as prepared Cu nanoparticles by using glycerin

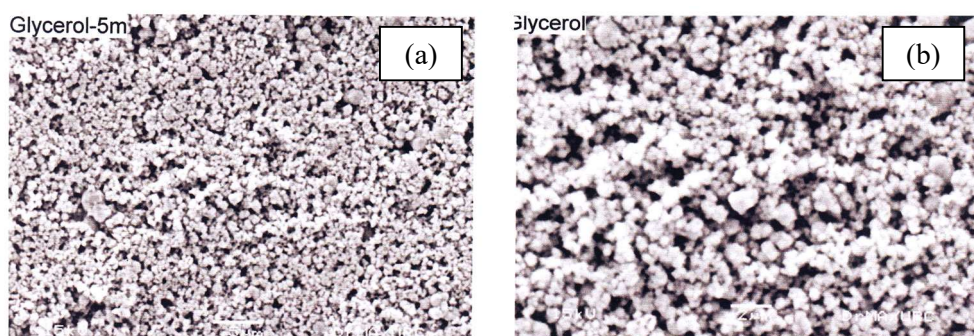


Figure 8. (a) low and (b) high magnification top-view SEM images of as prepared Cu nanoparticles by using glyceol

The following table shows the brief description of all experiments with different solvents.

Table1. List of chemical reaction by using polyol method

Sr	Solvent/Reducing agent	Cu Precursor	Shape (SEM)	Product (XRD)
1.	Water+ Glycerol	CuNO ₃	-	Cu+ CuO
2.	Water+ Glycerin	CuNO ₃	-	Cu+ CuO
3.	Water+ Ethylene Glycol	CuNO ₃	-	Cu+ Cu ₂ O
4.	Glycerol	CuNO ₃	Spherical	Cu
5.	Glycerin	CuNO ₃	Spherical	Cu
6.	Ethylene Glycol	CuNO ₃	Square	Cu+ CuO

4. Conclusion

In this paper, it was also found that the optimum size and distribution for the formation of Cu NPs was to be using the solvent such as glycerol and glycerin. The effect of solvent showed that small spherical copper nanoparticles and the good dispersion of nanoparticles are found by using solvent either glycerol or glycerin. EDXRF spectrum also informed that there was no other chemical impurities in the formation of Cu NPs. From XRD pattern the average crystallize size of Cu NPs was found to be 38 nm as each particle observed from SEM is not a single crystallite of Cu but the agglomerates of many single crystallites. The aggregation of nanoparticles caused the inhomogeneous size distribution. From the XRD results, it is obviously appeared that the reaction included water gives the oxide nanoparticles.

Acknowledgement

The authors are grateful to Dr Khin Khin Win, Professor and Head of the Department of Physics, University of Yangon for her kind permission to carry out this work.

References

1. Bell, W. C., and Myrick, M. L. (2001), 'Preparation and characterization of nanoscale silver colloids by two novel synthetic routes', *Journal of Colloid and Interface Science*, 242, 300 – 305
2. Choi, S. H., Zhang, Y. P., Gopalan, A., Lee, K. P., and Kang, H. D. (2005), 'Preparation of catalytically efficient precious metallic colloids by γ -irradiation and characterization colloids and surfaces A', *Physicochemical and Engineering Aspects*, 256, 165 – 170
3. D. V. Goia and E. Matijevic, (1998), "Preparation of monodispersed metalparticles," *New J.Chem.*, vol. 22, no.11, pp. 1203-1215.
4. Hutter, E., Fendler, J. H., and Roy, D. (2001), ' Surface plasmon resonance studies of gold and silver nano particles linked to gold and silver substrates by 2-aminoethanethiol and 1,6 Hexanedithiol' *J. Phys. Chem. B*, 105, 11159-11168
5. K. J. Carroll, J. U. Reveles, M. D. Shultz, S. N. Khanna, and E. E. Carpenter, (2011), "Preparation of elemental Cu and Ni nanoparticles by the polyol method: An experimental and theoretical approach," *J. Phys.Chem. C*, vol. 115, no. 6, pp. 2656–2664.
6. Kuo, C.H., Chen, C.H., Huang, M.H. (2007): Seed-mediated synthesis of monodispersed Cu₂O nanocubes with five different size ranges from 40 to 420 nm. *Adv. Funct. Mater.* 17, 3773–3780
7. S. P. Wu and S. Y. Meng, (2006), "Preparation of micron size copper powder with chemical reduction method," *Materials Letters*, vol. 60, no. 20, pp. 2438–2443
8. T. M. D. Dang, T. T. T. Le, E. Fribourg-Blanc, and M. C. Dang, (2011), "Synthesis and optical properties of copper nanoparticles prepared by a chemical reduction method," *Adv. Nat. Sci: Nano-sci. Nanotechnol.*, vol.2, no.1, pp. 1-6.
8. Ozin, G.A. (1992), 'Nanochemistry – Synthesis in diminishing dimensions' *Advanced. Materials*, 4, 612

A SINGLE-PARTICLE ENERGY LEVELS IN

${}_{\Lambda}^{13}\text{C}$, ${}_{\Lambda}^{14}\text{C}$ AND ${}_{\Lambda}^{15}\text{C}$

Aye Aye Min¹, Chit Oo² and Khin Swe Myint³

Abstract

In this research work, the single-particle energy levels of Λ -hypernuclear carbon isotopes, namely ${}_{\Lambda}^{13}\text{C}$, ${}_{\Lambda}^{14}\text{C}$ and ${}_{\Lambda}^{15}\text{C}$ was investigated. The folding Λ -nucleus potential based on effective Λ -nucleon interaction which is constructed by Akaishi is used. The calculated binding energies of ${}_{\Lambda}^{13}\text{C}$ and ${}_{\Lambda}^{14}\text{C}$ by applying folding Λ -nucleus potential are two times larger than the experimental results. In the folding process, only Hartree potential called direct term is considered but Fock term which can give the repulsive effect is neglected. The correction term $\Delta V(r)$ of spin and charge dependence of the effective Λ -N interaction is not taken into account. In addition, we assume that the proton density distribution and neutron density distribution are the same. Moreover, the Λ single-particle energy levels of these hypernuclei have also been calculated by using Woods-Saxon potential including spin-orbit interaction. In this calculation, Λ single particle energy levels of s-state and p-state are -11.57 MeV, -1.32 MeV for ${}_{\Lambda}^{13}\text{C}$, -12.10 MeV, -1.81 MeV for ${}_{\Lambda}^{14}\text{C}$ respectively. The Λ single-particle energy levels of s-state for ${}_{\Lambda}^{13}\text{C}$ and ${}_{\Lambda}^{14}\text{C}$ are in good agreement with the experimental and theoretical results. The Λ single-particle energy levels of ${}_{\Lambda}^{15}\text{C}$ are estimated to be -12.59 MeV for s-state and -2.29 MeV for p-state.

Key words: effective Λ -nucleon interaction, Woods-Saxon potential, Λ single-particle energy, Λ -hypernuclei

Introduction

Hypernuclear physics is an interesting subject and the study of short-lived hypernuclei can provide new information and dynamical features such as hyperon-nucleon interaction and hyperon-hyperon interaction. These interactions are indispensable for the understanding of high-density nuclear

¹ Lecturer, Department of Physics, University of Mandalay

² Master of Research Student, Department of Physics, University of Mandalay

³ Rector (Rtd.), University of Mandalay

matter inside neutron stars where hyperons are possibly mixed and playing extremely important roles. Generally, the scattering experiments are the most suitable experiments to provide the determination of any interaction. However, in hypernuclear physics, hyperon–nucleon (YN) scattering experiment are quite difficult to carry out as in nucleon-nucleon (NN) case due to the short life of hyperons. It is impossible to create either the incident hyperon beams or hyperon targets. Therefore, the information of Y-N interaction could be deduced only from the existing data of hypernuclei. As the experimental motivation, the strangeness hypernuclei could be produced from the emulsion experiments and counter experiments (Danysz, M. et al., (1953), Prowse, D.D.J., (1966), Milner, C. et al., (1985), Dluzewski, P. et al., (1988), Hashimoto, A. et al., (1989), Chrien, R.E. et al., (1989) & Dover, C.B. et al., (1989)). The experimental and theoretical investigations of hypernuclear physics, the understanding of the hyperon-nucleon interaction and its role in few-body systems, were made the summary reports (Bando, H. et al., (1990) & Gibson, B.F. and Hungerford III, E.V., (1995)). However, there was still a problem to understand hyperon-nucleon interaction and hyperon-hyperon interaction deeply.

Thus, a new spectroscopic study of ${}_{\Lambda}^{12}\text{C}$ by the (π^+, K^+) reaction was reported by Hasegawa (Hasegawa, T. et al., (1996)). The information of some p-shell Λ -hypernuclei observed from (π^+, K^+) reaction with the use of Ge detector array Hyperball was interpreted by employing shell-model calculations. In this calculation, both Λ and Σ channels are included (Millener, D.J., (2008)). From theoretical investigation of the neutron-rich Λ -hypernuclei, new information of hypernuclear physics such as a strong attractive mechanism due to coherent Λ - Σ coupling for single Λ -hypernuclei and the significance of $\Lambda\Lambda$ - ΞN coupling effect in formation of double strangeness Λ -hypernuclei could be explained (Akaishi, Y. et al., (2000) & Myint, K.S., et al., (2003)). Moreover, from the theoretical point of view, the structure analysis of Λ -hypernuclei is investigated by applying various models such as a single-particle model, shell model and cluster model. The binding energies of p-shell Λ -hypernuclei such as ${}_{\Lambda}^6\text{He}$, ${}_{\Lambda}^{7,8,9}\text{Li}$ and ${}_{\Lambda}^{12,13,14}\text{C}$ were calculated by using folding potential (Kolesnikov, N.N. and Kalachev, S.A., (2006)).

The structure calculation of ${}^9_{\Lambda}\text{Be}$, ${}^{13}_{\Lambda}\text{C}$ and ${}^{20,21}_{\Lambda}\text{Ne}$ were investigated by Kimura. Their calculated ground state binding energy of ${}^{13}_{\Lambda}\text{C}$ with the use of an effective ΛN interaction is 11.6 MeV (Kimura, M. et al., (2011)). Thus, we also would like to investigate the structure analysis of Λ -hypernuclei namely, ${}^{13}_{\Lambda}\text{C}$ and, ${}^{14}_{\Lambda}\text{C}$ and ${}^{15}_{\Lambda}\text{C}$.

Mathematical Formulation

Derivation of Energy Matrix Elements

In order to calculate the structure analysis of Λ -hypernucleus, we will start the radial part time-independent Schrödinger equation for two-body system as follows.

$$\left[-\frac{\hbar^2}{2\mu} \frac{d^2}{dr^2} + \frac{\hbar^2}{2\mu} \frac{\ell(\ell+1)}{r^2} + V(r) \right] u(r) = E u(r). \quad (1)$$

In this equation, μ is the reduced mass of Λ hyperon and core nucleus. For our calculation, Gaussian basis wave function with expansion coefficients (c_j) and range parameters (b_j) is used,

$$u(r) = r^{(\ell+1)} \sum_j c_j e^{-(r/b_j)^2} \quad (2)$$

The Schrödinger equation becomes as,

$$\left\{ -\frac{\hbar^2}{2\mu} \frac{d^2}{dr^2} + \frac{\hbar^2}{2\mu} \frac{\ell(\ell+1)}{r^2} + V(r) \right\} \sum_j c_j r^{(\ell+1)} e^{-(r/b_j)^2} = E \sum_j c_j r^{(\ell+1)} e^{-(r/b_j)^2}. \quad (3)$$

The above equation was multiplied both sides of the equation by $r^{(\ell+1)} e^{-(r/b_i)^2}$ from the left and integrated through the equation;

$$\begin{aligned} \int r^{(\ell+1)} e^{-(r/b_i)^2} \left\{ -\frac{\hbar^2}{2\mu} \frac{d^2}{dr^2} + \frac{\hbar^2}{2\mu} \frac{\ell(\ell+1)}{r^2} + V(r) \right\} \sum_j c_j r^{(\ell+1)} e^{-(r/b_j)^2} dr \\ = E \int r^{(\ell+1)} e^{-(r/b_i)^2} \sum_j c_j r^{(\ell+1)} e^{-(r/b_j)^2} dr. \end{aligned} \quad (4)$$

We, therefore, can define the above equation as

$$\sum_j H_{ij} c_j = E \sum_j N_{ij} c_j,$$

where, $H_{ij} = T_{ij}^\ell + F_{ij}^\ell + V_{ij}^\ell$.

In this equation, T_{ij}^ℓ and F_{ij}^ℓ are the kinetic energy, centrifugal potential energy matrix elements and V_{ij}^ℓ is potential energy matrix elements which are described as follows:

$$T_{ij}^\ell = \int r^{(\ell+1)} e^{-(r/b_i)^2} \left\{ -\frac{\hbar^2}{2\mu} \frac{d^2}{dr^2} \right\} r^{(\ell+1)} e^{-(r/b_j)^2} dr \quad (5)$$

$$F_{ij}^\ell = \frac{\hbar^2}{2\mu} \int r^{(\ell+1)} e^{-(r/b_i)^2} \frac{\ell(\ell+1)}{r^2} r^{(\ell+1)} e^{-(r/b_j)^2} dr \quad (6)$$

$$V_{ij}^\ell = \int r^{(\ell+1)} e^{-(r/b_i)^2} V(r) r^{(\ell+1)} e^{-(r/b_j)^2} dr \quad (7)$$

N_{ij}^ℓ stands for the norm matrix element,

$$N_{ij}^\ell = \int r^{2(\ell+1)} e^{-(r/b_i)^2} e^{-(r/b_j)^2} dr. \quad (8)$$

The N_{ij}^ℓ , T_{ij}^ℓ and F_{ij}^ℓ are analytically solved by using standard integral $\int_0^\infty x^{2n} e^{-a^2 x^2} dx = \frac{(2n-1)!!}{2^{(n+1)}} \frac{\sqrt{\pi}}{a^{(2n+1)}}$, and then the norm matrix element, kinetic energy matrix element, centrifugal potential energy matrix element can be expressed as follows.

$$N_{ij}^\ell = \frac{(2\ell+1)!!}{2^{(\ell+2)}} \frac{\sqrt{\pi}}{\left(\frac{1}{b_i^2} + \frac{1}{b_j^2} \right)^{(\ell+\frac{3}{2})}} \quad (9)$$

$$T_{ij}^\ell = -\frac{\hbar^2}{2\mu} (A - B + C) \quad (10)$$

where

$$A = \frac{4}{b_j^4} \frac{(2\ell + 3)!!}{2^{(\ell+3)}} \frac{\sqrt{\pi}}{\left(\frac{1}{b_i^2} + \frac{1}{b_j^2}\right)^{(\ell+\frac{5}{2})}}$$

$$B = \frac{(4\ell + 6)}{b_j^2} \frac{(2\ell + 1)!!}{2^{(\ell+2)}} \frac{\sqrt{\pi}}{\left(\frac{1}{b_i^2} + \frac{1}{b_j^2}\right)^{(\ell+\frac{3}{2})}}$$

$$C = \ell(\ell + 1) \frac{(2\ell - 1)!!}{2^{(\ell+1)}} \frac{\sqrt{\pi}}{\left(\frac{1}{b_i^2} + \frac{1}{b_j^2}\right)^{(\ell+\frac{1}{2})}}.$$

$$F_{ij}^\ell = \frac{\hbar^2}{2\mu} \ell(\ell + 1) \left(\frac{(2\ell - 1)!! \sqrt{\pi}}{2^{(\ell+1)} \left(\frac{1}{b_i^2} + \frac{1}{b_j^2}\right)^{(\ell+\frac{1}{2})}} \right) \tag{11}$$

The combination of the kinetic energy matrix element and the centrifugal potential matrix element can be written as,

$$T_{ij}^\ell + F_{ij}^\ell = \frac{\hbar^2}{2M} N_{ij}^\ell \frac{(4\ell + 6)}{b_i^2 + b_j^2}. \tag{12}$$

The potential energy matrix element is

$$V_{ij}^\ell = \int r^{(\ell+1)} e^{-(r/b_i)^2} V(r) r^{(\ell+1)} e^{-(r/b_j)^2} dr. \tag{13}$$

In order to solve the above equation, it is necessary to know the Λ -core nucleus interaction $V(r)$.

Interaction between Λ hyperon and Core Nucleus

For the calculation of potential energy matrix element, two types of potential namely folding potential which is based on effective Λ -N interaction and phenomenological Woods-Saxon Λ -core nucleus potential are used.

(a) Folding potential

The effective Λ N interaction derived by Akaishi (Akaishi.Y., Private Communication) will be firstly used. The Λ -nucleon interaction depends on states such as even state, odd state, spin singlet state and spin triplet state and thus this interaction is expressed in five-range Gaussian form as follows;

$$V_{\Lambda N} = \frac{1}{4} V_{\Lambda N}({}^1S_0) + \frac{3}{4} V_{\Lambda N}({}^3S_1),$$

$$\text{where, } V_{\Lambda N}(\vec{R} - \vec{r}) = \sum_{k=1}^5 V_k(k) \exp \left[- \left(\frac{\vec{R} - \vec{r}}{\mu_k} \right)^2 \right] \quad (14)$$

The strength parameters of effective Λ -N interaction in even state and odd state are given in table (1).

Table 1. The strength parameters of effective Λ -nucleon interaction

Even-state		Odd-state	
$V_{\Lambda N-\Lambda N}({}^1S_0)$ (MeV)	$V_{\Lambda N-\Lambda N}({}^3S_1)$ (MeV)	$V_{\Lambda N-\Lambda N}({}^1S_0)$ (MeV)	$V_{\Lambda N-\Lambda N}({}^3S_1)$ (MeV)
47.99645	-46.25826	23.462	230.12
-272.7777	-43.83829	-257.22	-614.76
679.7185	493.1045	33.823	855.15
-160.1574	-136.9770	-57.307	-66.964
-2.274696	-0.568783	-0.19762	1.7357

The schematic diagram of a relation between Λ hyperon and core nucleus is shown in Fig. 1.

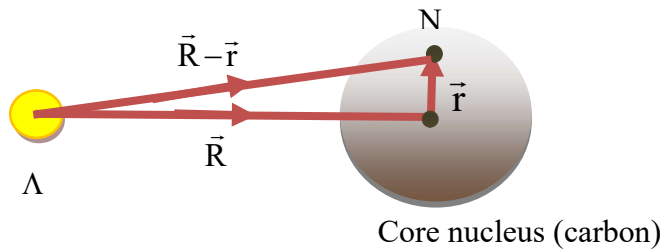


Figure 1. The schematic diagram of a relation between Λ and core nucleus

And thus the Λ -core nucleus interaction is obtained by folding the effective ΛN interaction with the density distribution $\rho(r)$ of core nucleus. Therefore, the effective interaction between Λ and the core nucleus can be written as

$$V_{\Lambda\text{-core}}(\mathbf{R}) = \int V_{\Lambda N}(\mathbf{R} - \mathbf{r})\rho(\mathbf{r}) d(\mathbf{r}). \tag{15}$$

For the density distribution, we will use the proton density or charge density distribution in harmonic oscillator model and we will assume that the proton density distribution is the same as the neutron density distribution. Thus, the density distribution $\rho(r)$ (Dejager, C.W. et al., (1974)) for core nucleus is

$$\rho(\mathbf{r}) = \rho_0 \left(1 + \frac{\alpha}{a^2} r^2 \right) e^{-(r/a)^2}. \tag{16}$$

The values of α and a are 1.067 fm, 1.687 fm for ${}^{13}_{\Lambda}\text{C}$, 1.403 fm, 1.635 fm for ${}^{14}_{\Lambda}\text{C}$ and 1.38 fm, 1.73 fm for ${}^{15}_{\Lambda}\text{C}$ respectively. By substituting the density distribution $\rho(r)$, effective interaction in equation (13) and solving it, the Λ -core nucleus interaction can be obtained as

$$V_{\Lambda\text{-core}}(\mathbf{R}) = \sum_{k=1}^5 V_k(\mathbf{k}) \rho_0 e^{-\left(\frac{\mathbf{R}}{\mu_k}\right)^2} \left(\frac{\pi}{\frac{1}{\mu_k^2} + \frac{1}{a^2}} \right)^{\frac{3}{2}} \exp\left(-\frac{\mathbf{R}^2}{\mu_k^2 + \frac{\mu_k^4}{a^2}} \right)$$

$$\left[1 + \frac{\alpha}{a^2} \left\{ \frac{3}{2 \left(\frac{1}{\mu_k^2} + \frac{1}{a^2} \right)} + \frac{R^2}{\mu_k^4 \left(\frac{1}{\mu_k^2} + \frac{1}{a^2} \right)^2} \right\} \right] \quad (17)$$

The above equation (17) is the folding potential or Λ -core nucleus interaction for the interested system. After getting the Λ -core nucleus interaction, the potential energy matrix element can be computed by using equation (13) and the result is as follows.

$$V_{ij}^\ell = \sum_k^5 V_k \rho_0 \left(\frac{\pi}{\frac{1}{\mu_k^2} + \frac{1}{a^2}} \right)^{\frac{3}{2}} \frac{(2\ell+1)!! \sqrt{\pi}}{2^{\ell+2} \left(\frac{1}{b_i^2} + \frac{1}{b_j^2} \frac{1}{\mu_k^2} - \frac{1}{\left(\mu_k^2 + \frac{\mu_k^4}{a^2} \right)} \right)^{\ell+\frac{3}{2}}} Q \quad (18)$$

$$\text{where } Q = \left[1 + \frac{\alpha}{a^2} \left\{ 1 + \frac{3}{2 \left(\frac{1}{\mu_k^2} + \frac{1}{a^2} \right)} + \frac{1}{\mu_k^4 \left(\frac{1}{\mu_k^2} + \frac{1}{a^2} \right)^2} \frac{(2\ell+3)}{2 \left(\frac{1}{b_i^2} + \frac{1}{b_j^2} \frac{1}{\mu_k^2} - \frac{1}{\left(\mu_k^2 + \frac{\mu_k^4}{a^2} \right)} \right)} \right\} \right]$$

Thus the folding potential energy matrix element is

$$V_{ij}^\ell = \frac{1}{4} V_{ij}^\ell ({}^1S_0) + \frac{3}{4} V_{ij}^\ell ({}^3S_1) \quad (19)$$

(a) Woods-Saxon potential

For this potential, a Λ hyperon moves independently in an average potential well generated by the other nucleons. The phenomenological

Woods-Saxon potential (Dudek, J. et al., (1981)) having the interaction strength $V_0 = 30$ MeV and the nuclear density $\rho(r)$ is

$$V_{w-s}(r) = -V_0\rho(r) \tag{20}$$

where, $\rho(r) = \frac{1}{1 + e^{\frac{r-R}{a}}}$, the nuclear radius $R = r_0 A^{\frac{1}{3}} = 1.1 A^{\frac{1}{3}}$ fm and the

diffuseness parameter $a=0.6$ fm. The mass number A is for the core nucleus. We will also consider spin-orbit interaction which is mentioned as followed;

$$V_{ls}(r) = V_{so} \left(\frac{\hbar}{m_\pi c} \right)^2 (\mathbf{l}\cdot\mathbf{s}) \frac{1}{r} \frac{d\rho(r)}{dr} \text{ and}$$

Thus the potential becomes;

$$V(r) = -V_0\rho(r) + V_{so} \left(\frac{\hbar}{m_\pi c} \right)^2 (\mathbf{l}\cdot\mathbf{s}) \frac{1}{r} \frac{d\rho(r)}{dr}. \tag{21}$$

In this equation, $\frac{\hbar}{m_\pi c}$ is Compton wavelength and spin-orbit constant V_{so} is

chosen as 4 MeV. The scalar product of LS coupling is

$$\mathbf{l}\cdot\mathbf{s} = \frac{1}{2} \left(j(j+1) - \ell(\ell+1) - \frac{3}{4} \right).$$

There are two possible states, $j = \ell + \frac{1}{2}$ and $j = \ell - \frac{1}{2}$, which represents for stretch case and Jackknife case. For stretch case, $j = \ell + \frac{1}{2}$ state, the potential is

$$V(r) = \frac{-V_0}{1 + e^{\frac{(r-R)}{a}}} - V_{so} \left(\frac{\hbar}{m_\pi c} \right)^2 \left(\frac{1}{2} \ell \right) \left(\frac{1}{r} \frac{e^{(r-R)/a}}{(1 + e^{(r-R)/a})^2} \frac{1}{a} \right) \text{ and}$$

For Jackknife case, $j = \ell - \frac{1}{2}$, the potential becomes as

$$V(r) = \frac{-V_0}{1 + e^{(r-R)/a}} + V_{so} \left(\frac{\hbar}{m_\pi c} \right)^2 \left(\frac{1}{2} (\ell + 1) \right) \left(\frac{1}{r} \frac{e^{(r-R)/a}}{(1 + e^{(r-R)/a})^2} - \frac{1}{a} \right).$$

By using the above two equations, we can calculate the potential energy matrix elements which are described as follows.

$$V_{ij}^\ell = \int r^{(2\ell+2)} e^{-\left(\frac{1}{b_i^2} + \frac{1}{b_j^2}\right)r^2} \left[\frac{-V_0}{1 + e^{(r-R)/a}} + V_{so} \left(\frac{\hbar}{m_\pi c} \right)^2 \left(\frac{1}{2} \ell \right) \left(-\frac{1}{r} \frac{e^{(r-R)/a}}{(1 + e^{(r-R)/a})^2} - \frac{1}{a} \right) \right] dr \quad (22)$$

$$V_{ij}^\ell = \int r^{(2\ell+2)} e^{-\left(\frac{1}{b_i^2} + \frac{1}{b_j^2}\right)r^2} \left[\frac{-V_0}{1 + e^{(r-R)/a}} + V_{so} \left(\frac{\hbar}{m_\pi c} \right)^2 \left(-\frac{(\ell + 1)}{2} \right) \left(-\frac{1}{r} \frac{e^{(r-R)/a}}{(1 + e^{(r-R)/a})^2} - \frac{1}{a} \right) \right] dr \quad (23)$$

Equations (17), (22) and (23) are the potential energy matrix elements for the two interaction types. Although the folding potential energy matrix element can be computed analytically, the phenomenological Woods-Saxon potential energy matrix elements cannot be find out the solution. Thus, the latter potential energy matrix element have been solved numerically. In order to calculate the binding energy of ${}_{\Lambda}^{13}\text{C}$, ${}_{\Lambda}^{14}\text{C}$ and ${}_{\Lambda}^{15}\text{C}$ and Λ -single particle energy levels, power inverse iteration method is used as the numerical calculation for solving nonrelativistic Schrödinger equation.

Results and Discussions

We have calculated Λ single-particle energy in carbon isotopes, ${}_{\Lambda}^{13}\text{C}$, ${}_{\Lambda}^{14}\text{C}$ and ${}_{\Lambda}^{15}\text{C}$, by solving Schrödinger equation with the use of Gaussian basis wave function. Two types of potential namely folding potential and phenomenological Woods-Saxon central potential including spin-orbit coupling are applied in this calculation. The effective Λ -N interaction and phenomenological Woods-Saxon potential which are shown in Fig. 2 have been plotted in order to understand the behavior of the interaction. According to this figure, the effective Λ -N interaction strength for singlet state is appreciably stronger than that in triplet state.

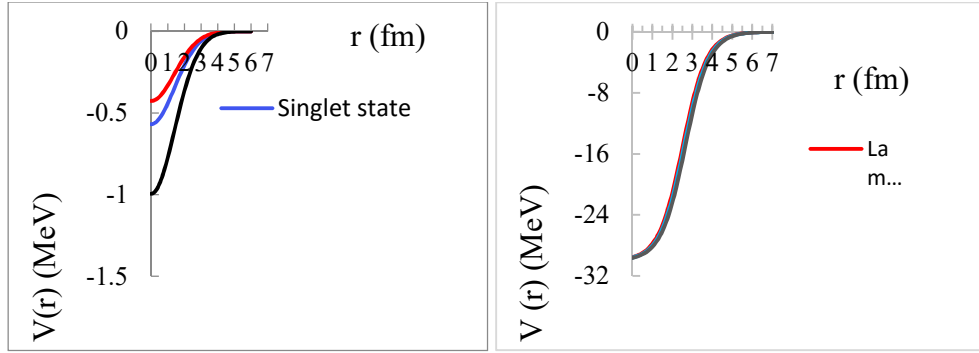


Figure 2. The two potential types; state-dependent effective Λ -N interaction and phenomenological Woods-Saxon potential

In addition, we have also investigated the density distribution of the core nuclei, carbon isotopes, ^{12}C , ^{13}C and ^{14}C which is displayed in Fig. 3. From this graph, we can clearly see that the density distribution of ^{12}C is smoother than that of ^{13}C and ^{14}C .

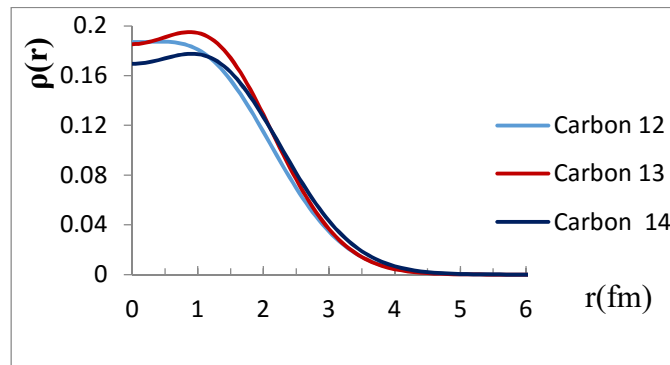


Figure 3. Density distribution of carbon isotope

The Λ single-particle energy levels of $^{13}_{\Lambda}\text{C}$, $^{14}_{\Lambda}\text{C}$ and $^{15}_{\Lambda}\text{C}$ are investigated by using folding potential based on effective Λ -N interaction. The calculated results are shown in Table (2). The calculated results for $^{13}_{\Lambda}\text{C}$ and $^{14}_{\Lambda}\text{C}$ are two times larger than the experimental results (Ajimura, S. et al., (2001) & Kohri, H. et al., (2002)). This is due to the fact that only Hartree term (or) direct term is considered but Fock term or exchange term which can

give the repulsive effect is neglected. In addition, the correction term of spin and charge dependence of Λ -N interaction $\Delta V(\mathbf{r})$ is not taken into account in our calculation. We used the proton density distribution or charge density distribution in harmonic oscillator model and we assume that this proton density distribution is also the same as the neutron density distribution for our system, ${}_{\Lambda}^{13}\text{C}$, ${}_{\Lambda}^{14}\text{C}$ and ${}_{\Lambda}^{15}\text{C}$.

Table 2. The Λ single-particle energy levels of ${}_{\Lambda}^{13}\text{C}$, ${}_{\Lambda}^{14}\text{C}$ and ${}_{\Lambda}^{15}\text{C}$ by using folding potential

Λ single-particle energy state (MeV)	${}_{\Lambda}^{13}\text{C}$	${}_{\Lambda}^{14}\text{C}$	${}_{\Lambda}^{15}\text{C}$
s-state	-23.89	-27.68	-27.61
Experimental result (s-state): (Ajimura, S. et al., (2001) & Kohri, H. et al., (2002))	-11.69 ± 0.12	-12.17 ± 0.33	-

Moreover, the Λ single-particle energy levels of ${}_{\Lambda}^{13}\text{C}$, ${}_{\Lambda}^{14}\text{C}$ and ${}_{\Lambda}^{15}\text{C}$ by using phenomenological Woods-Saxon central potential including spin-orbit coupling are displayed in Table (3). By using Woods-Saxon potential including spin-orbit interaction, the Λ single-particle energy levels of s-state and p-state are -11.57 MeV, -1.32 MeV for ${}_{\Lambda}^{13}\text{C}$, -12.10 MeV, -1.81 MeV for ${}_{\Lambda}^{14}\text{C}$ and -12.59 MeV, -2.29 MeV for ${}_{\Lambda}^{15}\text{C}$, respectively. The binding energy of single Λ -hypernucleus, ${}_{\Lambda}^{13}\text{C}$ was also investigated by Kimura and his group by using an effective ΛN interaction. Their calculated result is 11.6 MeV (Kimura, M. et al., (2011)). Our calculated results by using Woods-Saxon central potential including spin-orbit interaction are in good agreement with Kimura's result and the experimental results (Ajimura, S. et al., (2001) & Kohri, H. et al., (2002)).

Table 3. The Λ single-particle energy levels of ${}^{13}_{\Lambda}\text{C}$, ${}^{14}_{\Lambda}\text{C}$ and ${}^{15}_{\Lambda}\text{C}$ by using Woods-Saxon potential including spin-orbit interaction

Λ Single-Particle Energy States (MeV)	${}^{13}_{\Lambda}\text{C}$	${}^{14}_{\Lambda}\text{C}$	${}^{15}_{\Lambda}\text{C}$
s-state	-11.57	-12.10	-12.59
$p_{\frac{3}{2}}$ -state	-1.32	-1.81	-2.29
Experimental result (s-state) (Ajimura, S. et al., (2001) & Kohri, H. et al., (2002))	-11.69 ± 0.12	-12.17 ± 0.33	-

Conclusion

The Λ single-particle energy levels of ${}^{13}_{\Lambda}\text{C}$, ${}^{14}_{\Lambda}\text{C}$ and ${}^{15}_{\Lambda}\text{C}$ have been investigated by solving time-independent Schrödinger equation. Gaussian basis wave function is used for our consideration systems. The folding Λ -nucleus potential based on effective Λ -nucleon interaction and Woods-Saxon potential including spin-orbit interaction are used. The calculated binding energy of ${}^{13}_{\Lambda}\text{C}$ and ${}^{14}_{\Lambda}\text{C}$ by applying folding Λ -nucleus potential are two times larger than the experimental results. In this folding potential, only Hartree potential or direct term which can give the attractive effect is considered but Fock potential which can give the repulsive effect is neglected. The correction term $\Delta V(r)$ of spin and charge dependence of Λ -N interaction is not taken into account. Moreover, we also assume that the proton density distribution and neutron density distribution are the same. By using Woods-Saxon potential including spin-orbit interaction, the Λ single-particle energy levels of s-state and p-state are -11.57 MeV, -1.32 MeV for ${}^{13}_{\Lambda}\text{C}$, -12.10 MeV, -1.81 MeV for ${}^{14}_{\Lambda}\text{C}$ and -12.59 MeV, -2.29 MeV for ${}^{15}_{\Lambda}\text{C}$, respectively. The Λ single-particle energy levels of s-state for ${}^{13}_{\Lambda}\text{C}$ and ${}^{14}_{\Lambda}\text{C}$ are in good agreement with the experimental results.

Acknowledgements

The authors would like to thank Dr Thida Win, Rector, University of Mandalay, for her encouragement. The authors also would like to acknowledge to Professor Dr Lei Lei Win, Head of Department of Physics, University of Mandalay, for her valuable advice and permission.

References

- Ajimura, S. et al., (2001). *Phys. Rev. Lett.* **86** 4255.
- Akaishi, Y. et al., (2000). *Phys. Rev. Lett.* **84** 3539.
- Bando, H. et al., (1990). *Intl. J. Mod. Phys. A* **5** 4023.
- Chrien, R.E. et al., (1989). *Ann. Rev. Nucl. Part. Sci.* **39** 113.
- Danysz, M. et al., (1953). *Phil. Mag.* **44** 348.
- Dejager, C.W. et al., (1974). *Atomic Data and Nuclear Tables* **14** 489
- Dluzewski, P. et al., (1988). *Nucl. Phys. A* **484** 520.
- Dover, C.B. et al., (1989). *Phys. Rpt.* **184** 1.
- Dudek, J. et al., (1981). *Phys. Rev. C* **23** 23.
- Gibson, B.F. and Hungerford III, E.V., (1995). *Phys. Rep.* **257** 349.
- Hasegawa, T. et al., (1996). *Phys. Rev. C* **53** 1210.
- Hashimoto, A. et al., (1989). *Nuovo Cimento* **102 A** 679.
- Kimura, M. et al., (2011). *Phys. Rev. C* **83** 1.
- Kohri, H. et al., (2002). *Phys. Rev. C* **65** 034607.
- Kolesnikov, N.N. and Kalachev, S.A., (2006). *Russ. J. Phys.* **69** 2020.
- Millener, D.J., (2008). *Nucl. Phys. A* **804** 84.
- Milner, C. et al., (1985). *Phys. Rev. Lett.* **54** 1237.
- Myint, K.S., et al., (2003). *Nucl. Phys. A* **721** 21.
- Prowse, D.D.J., (1966). *Phys. Rev. Lett.* **17**, 782.

SERVER BASED REAL-TIME ENVIRONMENTAL PARAMETERS LOGGING AND MONITORING SYSTEM

Aung Zaw Oo¹

Abstract

This research work presents the real-time environmental parameters monitoring system using Wi-Fi network in order to create a remote environmental monitoring solution. DHT22 sensor and BMP085 pressure sensor are used to measure the environmental parameters such as temperature, relative humidity, atmospheric pressure, dew point and heat index. ENC28J60 Ethernet module is used to read the sensor data from Arduino and send the measured data to database server. Measured data are logged in a database file using WAMP web server which enables immediate access to sensor readings through Wi-Fi network. Router is used to assign IP address of server and Ethernet module. Users can view the real-time environmental data on web pages. The measured values are also recorded in a database file for historical review and data analysis. The recorded data are displayed in line graph by using Java script chart. To monitor the recorded data remotely, router connects the multiple wireless devices via the Wi-Fi network.

Keyword: Environmental parameters, WAMP web server, Wi-Fi network

Introduction

Environmental monitoring establishes the processes and activities of environment. The measurement of environmental parameters such as temperature, relative humidity, atmospheric pressure, dew point, heat index, becomes an integral part of the study to observe the change in global climate, species, plants and animal populations.

In this research work, real-time environmental parameters (temperature, relative humidity, atmospheric pressure, heat index and dew point temperature) measuring and logging system is constructed. To sense temperature and relative humidity, DHT22 sensor is used. BMP085 sensor measures atmospheric pressure of environment. Heat index and dew point temperature are calculated from measured temperature and relative humidity.

¹. U, Lecturer, Department of Physics, Pyay University

Arduino microcontroller senses the data from two sensors in every fifteen minutes and puts these data to server computer through Wi-Fi network by using ENC28J60 Ethernet module and router. The collected data are store in database file in My SQL database.GSM router sets up the IP addresses of Ethernet module and server computer.

The router connects multiple wireless devices such as smart-phone, tablet and laptop. Logged data can be viewed from web browser by using Wi-Fi devices which are all connected within the same LAN (local area network). Real-time data and logged data are shown in line graph in web page. Functional block diagram is shown in Figure 1.

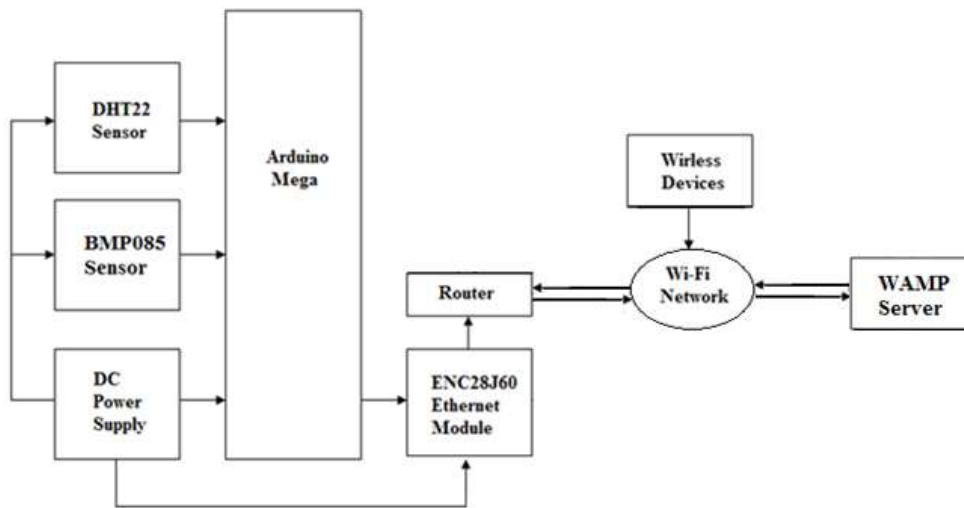


Figure 1. Functional block diagram of *constructed system*

Material and Method

Constructed system is based on Arduino platform and the system is designed to monitor the real-time environmental parameters over the Wi-Fi network. This monitoring system is a combination of hardware and software components. Arduino Mega 2560 microcontroller board, *DHT22* temperature and humidity sensor, *BMP085* pressure sensor, *ENC28J60* Ethernet module and Huawei GSM Router are hardware components. Hardware components are divided in three parts: main controller, sensor devices and Wi-Fi

accessible modules. Arduino IDE software and WAMP software are used as software components.

Main Control Devices

Arduino Mega 2560 microcontroller board is used as main controller device. Arduino Mega is based on Atmel ATmega2560 microcontroller. Mega 2560 board has 54 digital input/output pins, 16 analog inputs, 4 UARTs (hardware serial ports), a 16 MHz crystal oscillator, a USB connection, a power jack, an ICSP header (In-Circuit Serial Programming), and a reset button. Photograph of Arduino Mega board is shown in Figure 2. (Arduino Mega 2560 Datasheet)



Figure 2. Photo of Arduino Mega 2560 microcontroller board

DHT22 Temperature and Humidity Sensor

The DHT22 is a low-cost digital temperature and humidity sensor. It uses a capacitive humidity sensor and a thermistor to measure the surrounding air, and spits out a digital signal on the data pin. Sensor readings can be up to 2 seconds long. It has an operating temperature range of -40°C to $+80^{\circ}\text{C}$ and $\pm 0.5^{\circ}\text{C}$ accuracy. It has an operating humidity range of 0 to 100% RH and $\pm 2\%$ to $\pm 5\%$ accuracy. Figure 3 shows the photo of DHT22 temperature and humidity sensor.

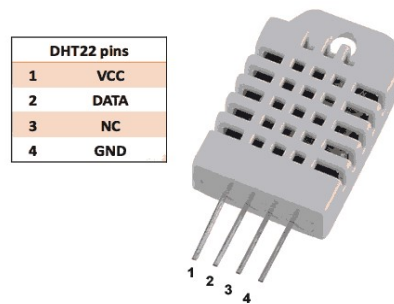


Figure 3. Photo of DHT22 temperature and humidity sensor

BMP085 Barometric Presser Sensor

BMP085 is a high-precision, low-power digital barometer. The BMP085 offers a pressure measuring range of 300 to 1100 hPa with accuracy down to 0.02 hPa. It's based on piezo-resistive technology for high accuracy and long term stability. These come factory-calibrated, with the calibration coefficients already stored in ROM. Photo of BMP085 presser sensor is shown in Figure 4.

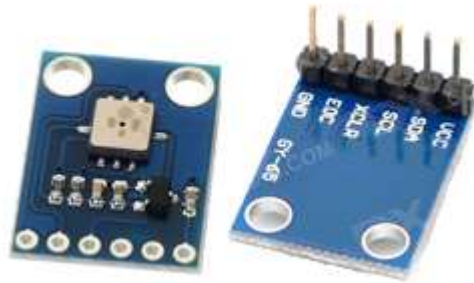


Figure 4. BMP085 barometric presser sensor

ENC28J60 Ethernet Module

The **ENC28J60** Ethernet module allows an Arduino board to connect to the internet. This chip has 28 pins and contains a stand-alone Ethernet controller for a 10BASE-T network connection with an SPI interface. The Ethernet module has a standard RJ-45 connection. This Ethernet chip provides

a network IP address which connects to the internet via an Ethernet cable (RJ45) connection. Figure 5 shows the photo of ENC28J60 Ethernet module.



Figure 5. ENC28J60 Ethernet module

Huawei GSM Router

A router is a networking device that forwards data packets between computer networks. Routers perform the traffic directing functions on the Internet. The Huawei GSM router easily connects multiple devices such as smart-phone, tablet and laptop. This can be done via the fast Wireless network or the LAN ports. WLAN is usually password protected, but may be open, which allows any device within its range to access the resources of the WLAN network. Figure 6 shows Wi-Fi connection of router and wireless devices.



Figure 6. Huawei GSM Router

Software Preparation

WAMP Server is installed to computer to create and manage the database. It allows creating the web applications with Apache2, PHP and a MySQL database.

Pushing Data to PHP Server

To record the measured data of temperature and relative humidity, atmospheric pressure, heat index and dew point temperature, Arduino has to connect to MySQL server. Measured data are pushed to database file in server. In the created sketch, Arduino is set as a client and its IP address of Ethernet module is determined by DHCP(Dynamic Host Configuration Protocol). The MAC address of **ENC28J60** Ethernet module is manually assigned in Arduino sketch. IP address of server is 192.168.1.2 and subnet mask is 255.255.255.0. **ENC28J60** Ethernet module is connected to Huawei GSM router. Software flowchart of Arduino sketch is shown in Figure 7.

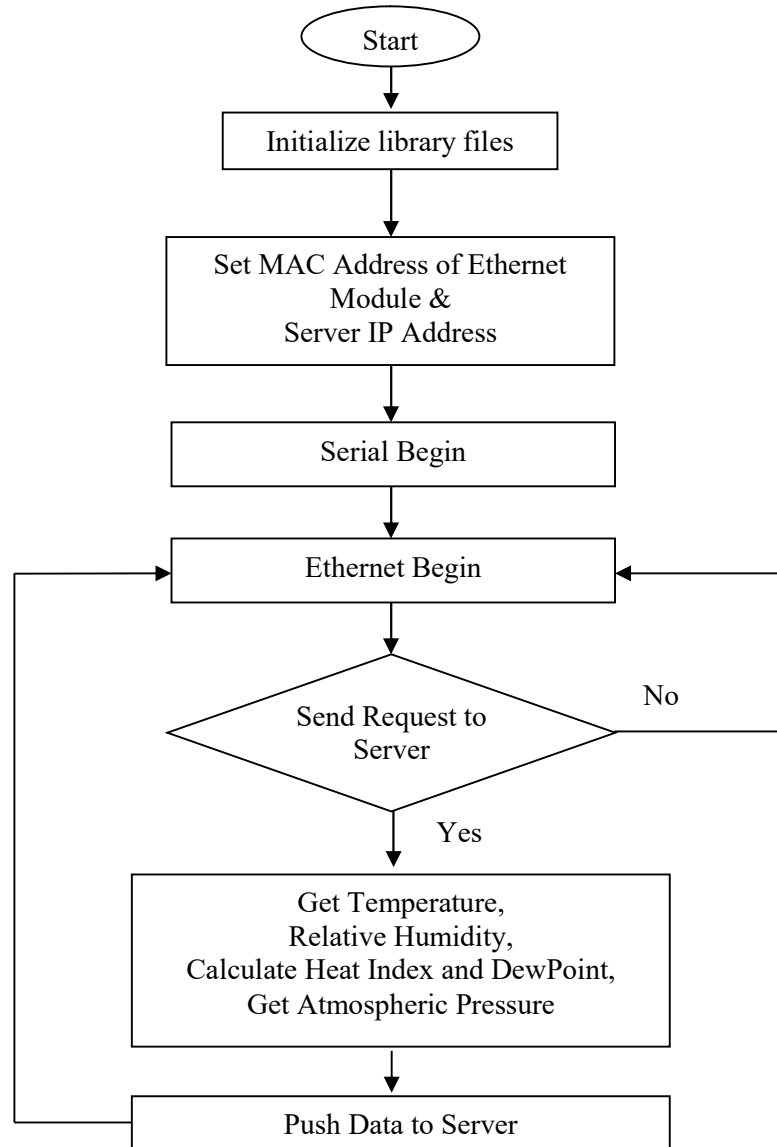


Figure 7. Software flowchart

Creating MySQL Database in WAMP Server

To record and review the measured sensor data send from Arduino, MySQL database and a web development environment is required. Firstly, it has to be established a database connection using **PHP** code on a web page. This code sends incoming data to MySQL database table Figure 8 shows the menu of MySQL database in WAMP server. WAMP server is a Windows web development environment. To push recorded data to database file, MySQL server address, username, password and database name is created in a PHP page. MySQL server address is set to static IP of 192.168.1.2.

A php file of **data_TRH.php** is created with user name of “root”. Password is set to “env”. MySQL database is managed with phpMyAdmin. Database name is “test” and database table is “inout_temp_rh”. Constructed database field in MySQL database is shown in Figure 9. Figure 10 shows the recorded data in MySQL database.



Figure 8. Menu of MySQL database in WAMP server

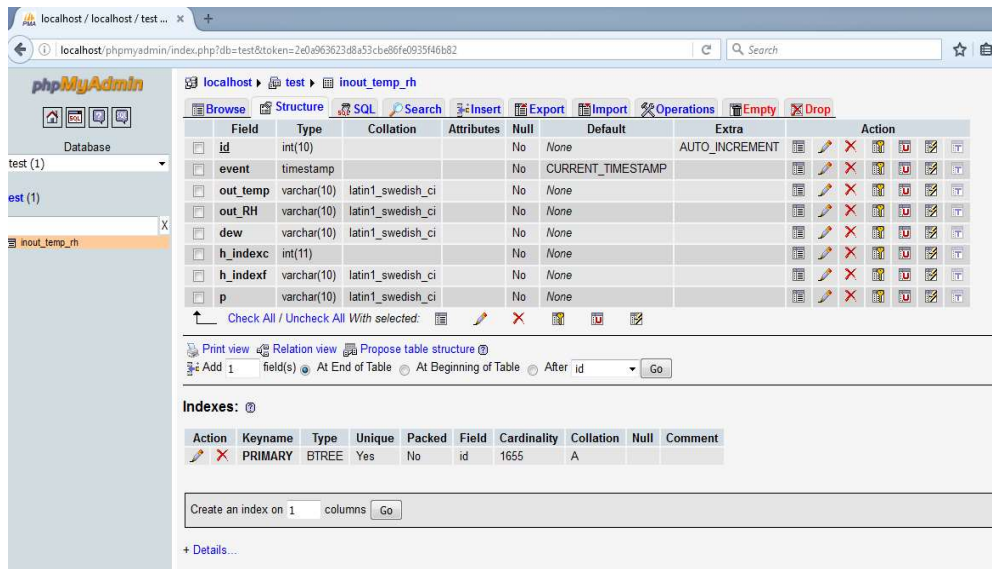


Figure 9. Database field in MySQL database

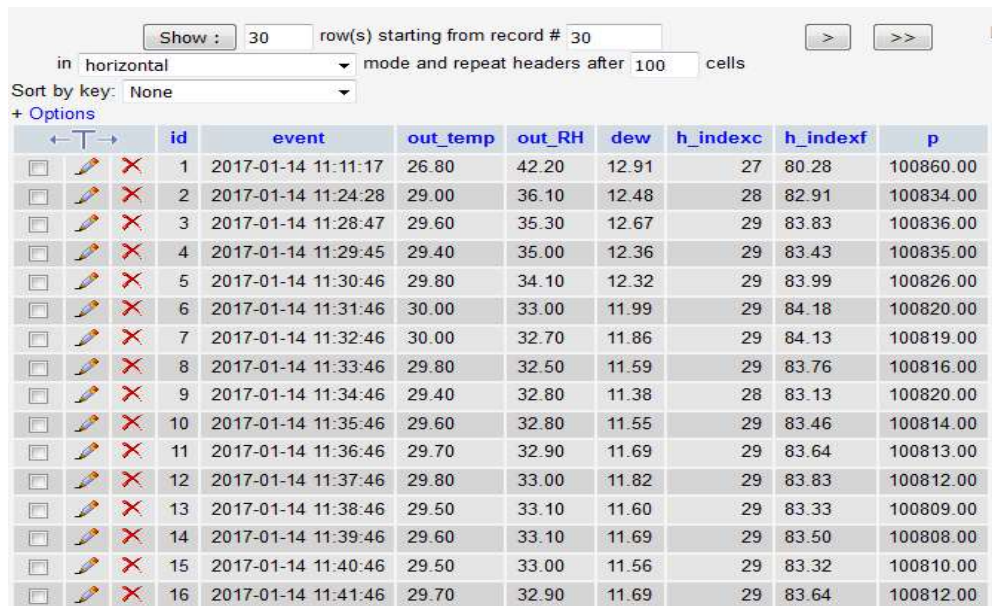


Figure 10. Example of recorded data in MySQL database.

Creating Chart

AmCharts is a JavaScript-based interactive chart for data visualization. Web page is created with PHP script that connects to MySQL server, loads the data and shows data in chart. PHP code for chart is shown in Figure 11.

```
<!DOCTYPE HTML PUBLIC "-//W3C//DTD HTML 4.01//EN" "http://www.w3.org/TR/html4/strict.dtd">
<html>

<head>

  <meta http-equiv="Content-Type" content="text/html; charset=utf-8">
  <title>Environmental</title>

  <meta http-equiv="refresh" content="60"; url=http://192.168.1.2/envdata/view_G_TRH8.php">
  <link rel="stylesheet" href="style.css" type="text/css">
  <script src="../amcharts/amcharts.js" type="text/javascript"></script>
  <script src="../amcharts/serial.js" type="text/javascript"></script>
  <h1 align="center">Environmental Data of Pyay</h1>

  <script>
AmCharts.loadJSON = function(url) {
  // create the request
  if (window.XMLHttpRequest) {
    // IE7+, Firefox, Chrome, Opera, Safari
    var request = new XMLHttpRequest();
  } else {
    // code for IE6, IE5
    var request = new ActiveXObject('Microsoft.XMLHTTP');
  }
}
```

Figure 11. Using AmChart library in PHP code

Managing Router

Wireless broadband routers establish a wireless network using a name called a Service Set Identifier (SSID). A router's SSID can be accessed from its administrator configuration pages shown in Figure 12. SSID name of constructed system in Wi-Fi access is “pyayenv” with dynamic IP address of 192.168.1.3. Figure 13 shows SSID name and password of constructed WI-Fi access. Figure 14 shows the IP address of Ethernet module connected with Arduino.



Figure 12. Administrator configuration pages of router

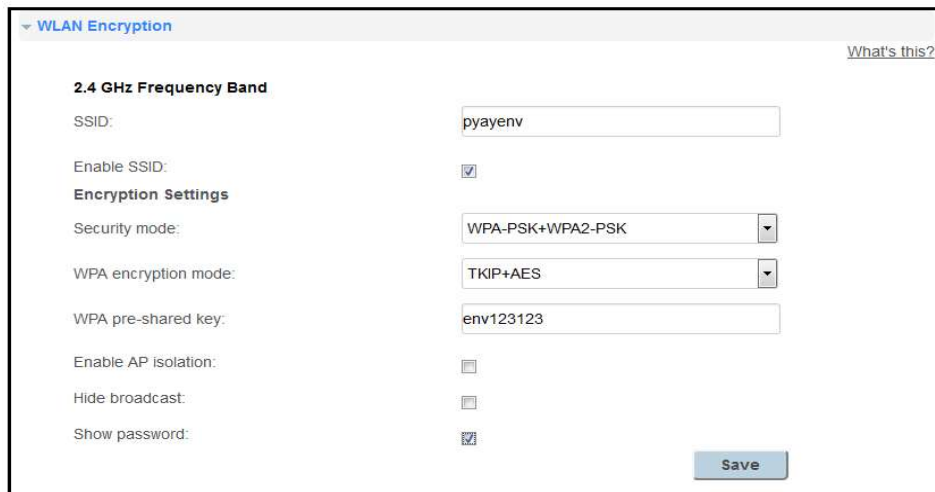


Figure 13. SSID name and password created in router configuration



Figure 14. IP address of Ethernet module

Results and Discussion

To show detailed visualizations of data over the periods of time, measured data are record in database server. Record data are logged in a database file and these data are viewed by web page written in php code. The http address is http://localhost/envdata/data_log.php. Figure 15 shows the data logger of measured data shown from web page, updated with the received sensors data. All Wi-Fi accessible devices can view the data logger page by joining Wi-Fi network. The browser was made to refresh every 15 minutes so that newly received data from the web page could be seen on the browser. Figure 15 shows recorded data in data logger web page.

Recorded database table in MySQL server can be exported to Excel file and every day data can be stored in computer. Table 1 shows the sample of exported Excel file. Each of these *line graphs* shows a change in *data* over time. *Line graph* is useful for *displaying data* or information which changes continuously over time. The multiple line graph with different zoom is created using Amchart library. It is shown in Figure 16 and address of this PHP page is 192.168.1.2/envdata/envdat8.php. This chart page shows real time value of temperature, relative humidity, due point temperature and heat index. *Historical data can also be viewed by clicking the mouse pointer on the graph*. Figure 17 shows complete circuit diagram of constructed system. Photograph of constructed system is shown in Figure 18.

ID	Date and Time	Outside Temp(C)	Outside RH(%RH)	Dew Point(C)	Heat Index(C)	Heat Index(F)	Pressure(Pa)
1482	2017-01-15 19:10:49	24.20	56.40	15.00	24	75.47	100772.00
1481	2017-01-15 19:09:48	24.20	55.80	14.83	24	75.44	100780.00
1480	2017-01-15 19:08:48	24.20	55.40	14.72	24	75.42	100771.00
1479	2017-01-15 19:07:48	24.20	55.10	14.64	24	75.41	100773.00
1478	2017-01-15 19:06:48	24.30	54.70	14.62	24	75.58	100772.00
1477	2017-01-15 19:05:48	24.30	54.50	14.56	24	75.58	100770.00
1476	2017-01-15 19:04:48	24.40	54.40	14.62	24	75.77	100767.00
1475	2017-01-15 19:03:48	24.70	54.30	14.87	25	76.36	100766.00
1474	2017-01-15 19:02:48	24.90	54.20	15.03	25	76.75	100767.00
1473	2017-01-15 19:01:48	24.70	54.30	14.87	25	76.36	100764.00
1472	2017-01-15 19:00:48	24.10	54.30	14.32	24	75.17	100762.00
1471	2017-01-15 18:59:48	24.20	54.10	14.35	24	75.36	100762.00
1470	2017-01-15 18:58:48	24.10	53.90	14.20	24	75.15	100761.00
1469	2017-01-15 18:57:48	24.20	53.40	14.15	24	75.33	100756.00
1468	2017-01-15 18:56:47	24.30	53.20	14.19	24	75.51	100761.00
1467	2017-01-15 18:55:47	24.40	52.90	14.19	24	75.70	100757.00
1466	2017-01-15 18:54:47	24.50	52.60	14.20	24	75.88	100756.00
1465	2017-01-15 18:53:47	24.50	52.40	14.14	24	75.87	100751.00

Figure 15. Data logger web page in PHP format

Table 1. Temperature, relative humidity, dew point temperature and heat index data in excel file (Sample)

id	event	out_temp	out_RH	dew	h_indexc	h_indexf	p
1	2017-01-14 11:11:17	26.8	42.2	12.91	27	80.28	100860
2	2017-01-14 11:24:28	29.0	36.1	12.48	28	82.91	100834
3	2017-01-14 11:28:47	29.6	35.3	12.67	29	83.83	100836
4	2017-01-14 11:29:45	29.4	35.0	12.36	29	83.43	100835
5	2017-01-14 11:30:46	29.8	34.1	12.32	29	83.99	100826
6	2017-01-14 11:31:46	30.0	33.0	11.99	29	84.18	100820
7	2017-01-14 11:32:46	30.0	32.7	11.86	29	84.13	100819
8	2017-01-14 11:33:46	29.8	32.5	11.59	29	83.76	100816
9	2017-01-14 11:34:46	29.4	32.8	11.38	28	83.13	100820
10	2017-01-14 11:35:46	29.6	32.8	11.55	29	83.46	100814
11	2017-01-14 11:36:46	29.7	32.9	11.69	29	83.64	100813
12	2017-01-14 11:37:46	29.8	33.0	11.82	29	83.83	100812
13	2017-01-14 11:38:46	29.5	33.1	11.60	29	83.33	100809

id	event	out_temp	out_RH	dew	h_indexc	h_indexf	p
14	2017-01-14 11:39:46	29.6	33.1	11.69	29	83.5	100808
15	2017-01-14 11:40:46	29.5	33.0	11.56	29	83.32	100810
16	2017-01-14 11:41:46	29.7	32.9	11.69	29	83.64	100812
17	2017-01-14 11:42:46	29.8	33.0	11.82	29	83.83	100810
18	2017-01-14 11:43:47	29.9	33.1	11.95	29	84.02	100797
19	2017-01-14 11:44:47	30.0	32.9	11.95	29	84.16	100800
20	2017-01-14 11:45:47	29.9	32.7	11.77	29	83.96	100800
21	2017-01-14 11:46:47	29.7	32.5	11.50	29	83.59	100789
22	2017-01-14 11:47:47	30.0	32.4	11.72	29	84.09	100795
23	2017-01-14 11:48:47	30.3	32.0	11.79	29	84.56	100787
24	2017-01-14 11:49:47	30.3	31.7	11.65	29	84.51	100789
25	2017-01-14 11:50:47	30.8	31.8	12.13	30	85.45	100789

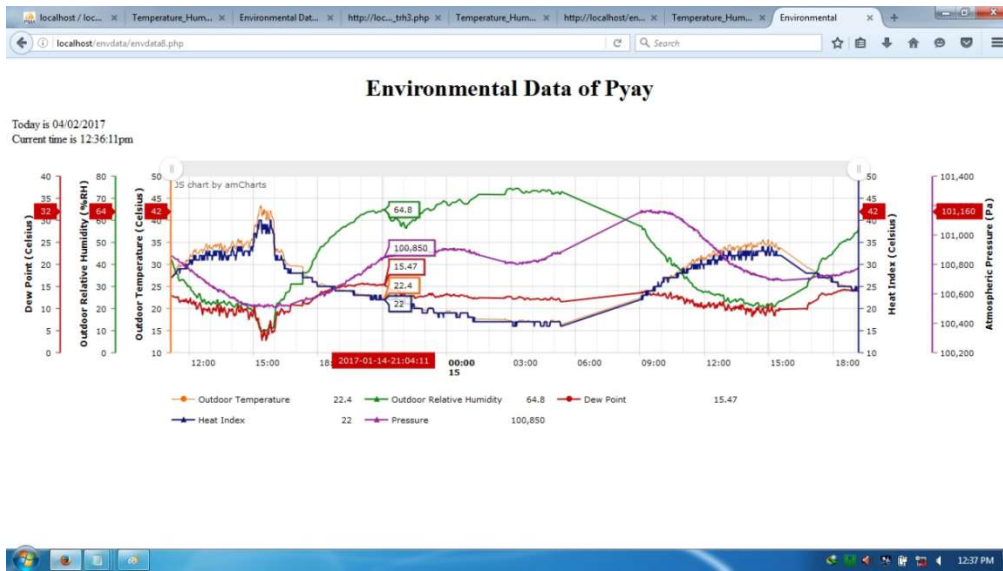


Figure 16. Real time information of data displayed on web page

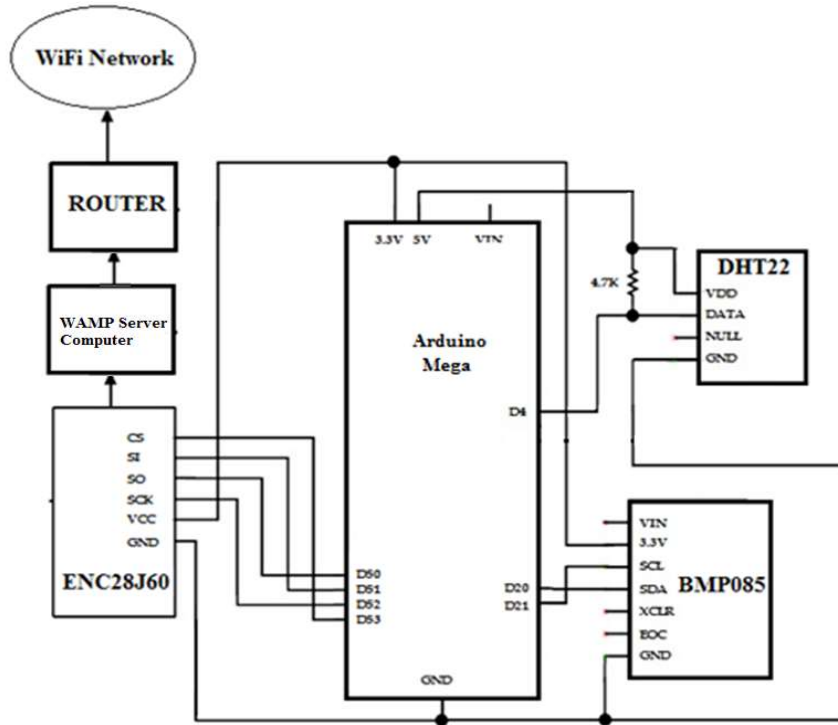


Figure 17. Circuit diagram of constructed system

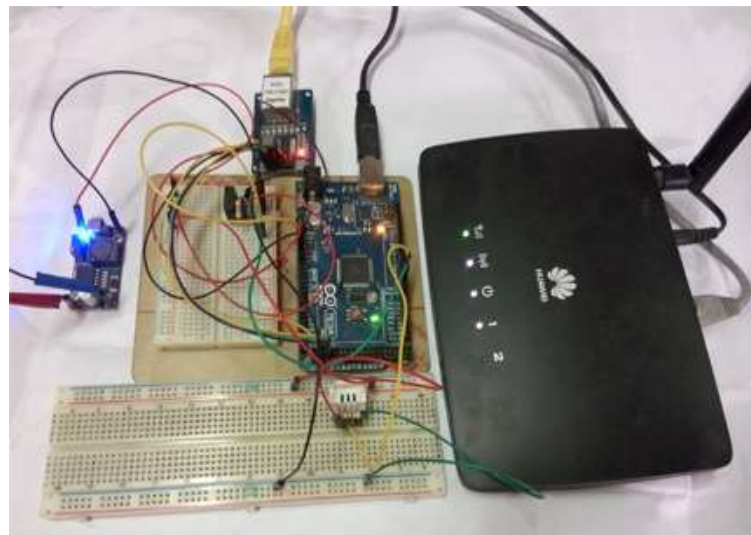


Figure 18. Photograph of constructed system

Conclusion

In this research work, server based real-time environmental parameters monitoring system has been constructed for logging and monitoring of environmental parameters. Constructed system offers a large range of data loggers for long-term recording of measurement data by using database server. For monitoring purpose, Wi-Fi accessible web page is developed using PHP code. This page shows real time data in multiple line graphs. The system can be used as remote temperature monitoring device by using smart phone or tablet by accessing Wi-Fi connection, browsing web page and entering URL of page.

Any change in the climate of an area can affect the plants and animals living there, as well as the makeup of the entire ecosystem. Constructed real-time environmental parameters monitoring system can be used in environmental research fields such as global temperatures warming and climate changing effect on ecosystems.

Acknowledgements

I would like to thank Professor Dr Pyone Pyone Shein, Head of Department of Physics, Pyay University, Professor Dr Naw Htoo Lar Phaw, Pyay University, Pro-rectors from Pyay University Dr Nyunt Soe and Dr Nilar Myint for their kind permission to do this work.

I also would like to thank Rector (YU) Dr Pho Kaung, Professor Dr Khin Khin Win (Head of Department of Physics, YU) and Professor Dr Soe Soe Nwe (YU) for their permission to present this research report.

I am also indebted to Dr Ye Chan, Professor of Physics, Universities' Research Center, University of Yangon, for his guidance and thought to complete this research work.

References

1. Delisle M., (2008) *Mastering php My Admin 2.11 for Effective MySQL Management* (Packt Publishing)
 2. Gertz E., Di Justo P. , (2012)*Environmental Monitoring with Arduino* (Sebastopol, California: O'Reilly Media)
 3. Paul Du Bois, (2013) *MySQL* (Addison-Wesley)
 4. Sklar D., Trachtenberg A., (2003) *PHP Cookbook* (Sebastopol, California: O'Reilly Media)
- <https://dev.mysql.com/doc/refman/5.1/en/what-is-mysql.html>
<http://www.microchip.com/downloads/en/devicedoc/39662a.pdf>
<http://php.net/manual/en/index.php>

RESONANCE STATES OF α -n SYSTEM BY APPLYING COMPLEX SCALING METHOD

Hla Hla Win¹, Su Su Hlaing², Theingyi³

Abstract

The purpose of this research is to study the resonance energy of ${}^5_2\text{He}$ (α , n) system by solving the two body Schrödinger equation with complex scaling method. The Gaussian basis wave function is used to solve the two body Schrödinger equation for ($J^\pi = 3/2^-$) state and ($J^\pi = 1/2^-$) state in spin-orbit coupling. The calculated resonance energies and level widths for ($J^\pi = 3/2^-$) state and ($J^\pi = 1/2^-$) state are (0.747, 0.596) MeV and (2.147, 5.533) MeV respectively. Comparison is made with the experimental data and good agreement is found.

Key words: resonance energy, complex scaling method, spin-orbit coupling

Introduction

The nuclear structure is roughly homogeneous distribution of neutrons and protons. Binding energy curve is the experimental evidence about the nuclear structure. The shape of this curve is the reflection of structure of nucleus. Hence every theory which evolved from 1930s till this time was trying to reproduce the binding energy curve. It started from the Liquid Drop Model (LDM), Alpha Clustering Model and now it reaches at the shell model, which is the most successful model in describing the structure of nucleus so far. However, the clustering phenomena is important to determine the structure of light nuclei.

LDM could fit smoothly with the binding energy curve and explain the fission mechanism successfully, but could not explain why there is a large binding energy for even nuclei such as ${}^4\text{He}$, ${}^{12}\text{C}$, etc. The success of the shell model is that it could explain the reason behind the large binding energy for even nuclei. According to the simplest shell model, every nuclei is spherical in

¹. Lecturer, Department of Physics, University of Mandalay

². Master of Research student, Department of Physics, University of Mandalay

³. Lecturer, Department of Physics, University of Mandalay

structure. But many experimental results revealed that 90% of the nuclei are not spherical. Therefore, the extension of the shell model for the deformed nuclei shape is given first by S.G. Nilsson in 1955. Some experimental studies at CERN (Gaffney, 2013) show that the structure of Rn(Radon) is not spherical but pear shaped and they expect to see more such nuclei near Th(Thorium). These results show that there is a need for a new theory to well explain the structure of nuclei. There is the interaction between nucleons (as it is in reality) in the model approach, it can expect the formation of clusters. Clustering is a natural energy minimization mechanism. There is a large scale, it can see Galaxy clusters, star clusters, planets, etc. There are the small scales, it can also see clustering, quarks clustered to form molecules.

The idea of alpha clustering has a history back to 1930s. By observing alpha decay from nucleus, people speculated that nuclei are made up of alpha particles. ^8Be has one bond between two alpha particles and they dumbbell-like shape, ^{12}C has three alpha bonds and triangular shape, and ^{16}O has six alpha bonds and tetrahedral shape.

Resonances

The first resonance in particle physics was discovered by H. Anderson, E. Fermi, E. A. Long, and D. E. Nagle, working at the Chicago Cyclotron in 1952. Resonance states are formed when quantum particles collide at certain (resonant) energies. Before moving apart, they stay together for a while. During the resonance lifetime, the particles move around each other and “forget” the direction from which they came. Therefore, when the resonance eventually decays, the particles “choose” the direction to move away at random.

A resonance can be viewed and approached from two different angles, as a delay connected with an enhanced phased shift in a scattering process or as a long-lived but decaying state of a compound system. The main observable characteristics of a resonance are position and the width. The real and imaginary parts of the energy give the position and width of the resonance, respectively.

A resonance energy is $E_{res} = E_r - i\frac{\Gamma}{2}$ has a negative imaginary part, which is called resonance width. The use of a complex energy allows a classification of the energy levels of a quantum system.

Spin-Parity States of ${}^5_2\text{He}$ Resonance

In shell-model, shells are filled according to Pauli principle. This independence particle model further assumes a strong spin-orbit coupling so that each individual nucleon has a total angular momentum $j = \ell \pm \frac{1}{2}$ except in case $\ell = 0$ when j has only one value $\ell + \frac{1}{2} = \frac{1}{2}$. Thus each energy levels splits up into two sub-levels with $j \uparrow = \ell + \frac{1}{2}$ (s and ℓ parallel) and $j \downarrow = \ell - \frac{1}{2}$ (s and ℓ anti-parallel). The sub-level $j + \frac{1}{2}$ has a lower energy than the sub-level $j - \frac{1}{2}$. Each sub level of $N=1$ can have a maximum of $(2j+1)$ nucleons of the same kinds.

For odd mass nuclei, spin and parity is determined by orbital of the last unpaired nucleon. Parity is related to the orbital quantum number ℓ and is given by $P = (-1)^\ell$.

The relative orbital angular momentum of alpha and nucleon is 1. Spin and parity of lowest lying states are $(3/2^-)$ state and $(1/2^-)$ state and shown in Fig. (1).

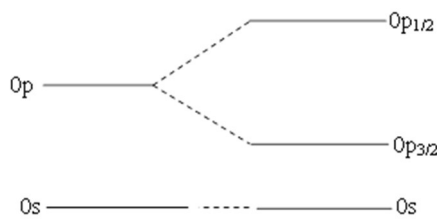


Figure 1. Energy levels of unpaired neutron in ${}^5_2\text{He}$ system

Complex Coordinate Rotation Method

The method of complex coordinate rotation is used to investigate the resonance states. Under this treatment a resonance is considered as an extension of the concept of a bound state which is solution to the Schrödinger equation with purely outgoing asymptotic belonging to the complex energy. The real and imaginary parts of the energy give the position and width of the resonance, respectively. Thus complex resonance energy is written as

$$E_{\text{res}} = E_R - i \frac{\Gamma}{2} \quad (1)$$

where E_R is energy level and Γ is the level width. In the asymptotic region, the resonance wave function is described by purely outgoing radial part as

$$\Psi(r) \xrightarrow{r \rightarrow \infty} e^{iKr} \quad (2)$$

where the wave vector $K = K_R - iK_I$ ($K_R > 0$ and $K_I > 0$) and satisfies

$$E = \frac{\hbar^2 K^2}{2\mu}.$$

Thus

$$\begin{aligned} \Psi(r) \xrightarrow{r \rightarrow \infty} e^{i(K_R - K_I)r} &= e^{iK_R r} e^{-K_I r} \\ &= e^{K_I r} \{ \cos(K_R r) + i \sin(K_R r) \} \end{aligned} \quad (3)$$

which shows that the asymptotic radial part is oscillating between exponentially growing amplitudes of $e^{K_I r}$.

The asymptotic divergence of the resonant wave function has caused difficulties in the resonance calculations. This resonance wave function cannot be solved by using the bound state type wave function.

According to complex rotation method, the following transformation

$$r \rightarrow r e^{i\theta} \quad (4)$$

where θ is a rotation angle. The complex scaling operator $\hat{U}(\theta)$ acting on a single particle wave function is defined as

$$\Psi(r) \rightarrow \Psi(re^{i\theta}) = \Psi_0(r) = \hat{U}(\theta) \Psi(r) \tag{5}$$

Let us see the transformed Schrödinger equation under complex rotation,

$$H(r) \Psi(r) = E \Psi(r) \tag{6}$$

$$H(re^{i\theta}) \Psi(re^{i\theta}) = E \Psi(re^{i\theta}) \tag{7}$$

$$H(re^{i\theta}) \hat{U}(\theta) \Psi(r) = E \hat{U}(\theta) \Psi(r)$$

$$\hat{U}^{-1}(\theta) H(re^{i\theta}) \hat{U}(\theta) \Psi(r) = E \hat{U}^{-1}(\theta) \hat{U}(\theta) \Psi(r)$$

$$\hat{U}^{-1}(\theta) H(re^{i\theta}) \hat{U}(\theta) \Psi(r) = E \Psi(r) \tag{8}$$

By comparing Eq.(6) and (8)

$$H(r) = \hat{U}^{-1}(\theta) H(re^{i\theta}) \hat{U}(\theta)$$

$$\text{(or)} \quad \hat{U}^{-1}(\theta) H(r) \hat{U}(\theta) = H(re^{i\theta}) = H_0(r) \tag{9}$$

Under this transformation, the energy eigenvalue remains unchanged

$$H_0(r) \Psi_0(r) = E \Psi_0(r)$$

Then the asymptotic resonance wave function is transformed as

$$\begin{aligned} \Psi_0(r) &\xrightarrow{r \rightarrow \infty} e^{i(K_R - iK_I)r} e^{i\theta} \\ &\xrightarrow{r \rightarrow \infty} e^{-(K_R \sin \theta - K_I \cos \theta)r} e^{i(K_R \cos \theta + K_I \sin \theta)r} \end{aligned} \tag{10}$$

and oscillating with amplitude $e^{-(K_R \sin \theta - K_I \cos \theta)r}$. From the above equation, if $K_R \sin \theta > K_I \cos \theta$ (or) $\tan \theta > \frac{K_I}{K_R}$, the resonance wave functions becomes convergent at the asymptotic region.

Thus the resonance state can be solved with bound state type wave functions. According to the relation of the complex resonance energy and wave vector,

$$E_R - iE_I = \frac{\hbar^2}{2\mu} (K_R - iK_I)^2 \quad (11)$$

If $E_R \gg E_I$ ($K_R \gg K_I$), the boundary condition for resonance state can be expressed as

$$\tan \theta > \frac{K_I}{K_R} \sim \frac{E_I}{2E_R}$$

The rotation parameter θ has an upper limit, $\theta_c = \pi/4$. The Gaussian basis wave functions are transformed under complex rotation.

By introducing r' as $r' = r e^{i\theta}$ (12)

$$r = r' e^{-i\theta} \quad (13)$$

Eq. (7) is written as $H(r e^{i\theta}) \Psi(r e^{i\theta}) = E \Psi(r e^{i\theta})$

$$H(r') \Psi(r') = E \Psi(r') \quad (14)$$

The transformed Gaussian basis wave function is

$$\Psi_\theta(r) = \sum_j c_j(\theta) e^{-\left(\frac{r}{b_j}\right)^2} \quad (15)$$

(or) $\Psi(r') = \sum_j c_j(\theta) e^{-\left(\frac{r'}{b_j e^{i\theta}}\right)^2}$ (16)

Eq. (14) becomes

$$H(r') \sum_j c_j(\theta) e^{-\left(\frac{r'}{b_j e^{i\theta}}\right)^2} = E \sum_j c_j(\theta) e^{-\left(\frac{r'}{b_j e^{i\theta}}\right)^2} \quad (17)$$

$$H(r) \sum_j c_j(\theta) e^{-\left(\frac{r}{b_j e^{i\theta}}\right)^2} = E \sum_j c_j(\theta) e^{-\left(\frac{r}{b_j e^{i\theta}}\right)^2} \quad (18)$$

We have to solve the Schrödinger equation which is the same as bound state system except the range parameter b_j becomes $b_j e^{i\theta}$.

The bound states are the same. The positive-energy spectrum of the original Hamiltonian H is rotated down by an angle of 2θ into the complex-energy plane. The resonance states of the eigenvalues $E_{\text{res}} = E_R - i\frac{\Gamma}{2}$ satisfying the condition $E_{\text{res}} \ll 2\theta$, where E_R is the energy and Γ is width of the resonance, respectively. Where the bound states that lies on the negative energy axis remains unchanged, the resonance states located in the fourth quadrant, after the separation from the continuous spectrum, does not vary with θ , the continuum along the positive energy axis rotates clockwise by the angle 2θ . If we do not apply the complex scaling, the original Schrödinger equation gives the continuum spectra, including resonances on the positive energy axis.

Under complex rotation, the resonance for which $\tan\theta > \frac{k_I}{k_R}$ are separated from continuum, and the rotated continuum spectra starting from different threshold energies are separately obtained on different 2θ -lines as shown in Fig. (2).

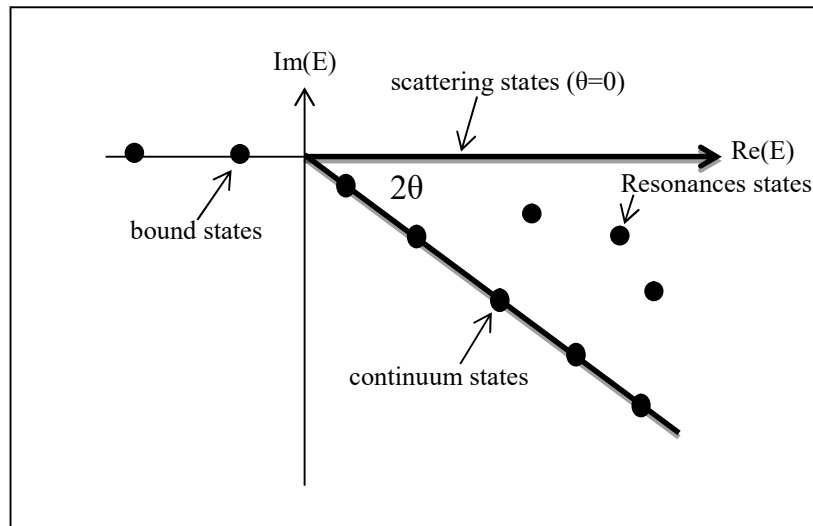


Figure 2. A schematic distribution of the eigenvalues of the bound states and resonance states.

Two-Body Calculation

We use the Gaussian basis wave function as the total wave function of our two-body system which has the following form;

$$u(r) = r^{\ell+1} \sum_j c_j e^{-\left(\frac{r}{b_j e^{i\theta}}\right)^2} \quad (19)$$

where c_j 's expansion coefficient and b_j 's are range parameters.

The Schrödinger equation is written as

$$H\Psi = E\Psi \quad (20)$$

The two body Hamiltonian is

$$H = -\frac{\hbar^2}{2\mu} \frac{d^2}{dr^2} + \frac{\hbar^2}{2\mu} \frac{\ell(\ell+1)}{r^2} + V(r)$$

where reduce mass , $\mu = \frac{m_1 m_2}{m_1 + m_2}$

And then we can write as;

$$\sum_{ij} [T_{ij} + V_{ij}^{\ell} + V_{ij}] c_j = E \sum_{ij} N_{ij} c_j \quad (21)$$

$$\sum_{j=1}^N H_{ij} c_j = E \sum_{j=1}^N N_{ij} c_j \quad (22)$$

Eq.(22) can be written as

$$H_{11} C_1 + H_{12} C_2 + \dots + H_{1N} C_N = E(N_{11} C_1 + N_{12} C_2 + \dots + N_{1N} C_N)$$

$$H_{21} C_1 + H_{22} C_2 + \dots + H_{2N} C_N = E(N_{21} C_1 + N_{22} C_2 + \dots + N_{2N} C_N)$$

.

$$H_{N1} C_1 + H_{N2} C_2 + \dots + H_{NN} C_N = E(N_{N1} C_1 + N_{N2} C_2 + \dots + N_{NN} C_N)$$

The above N equations can be written as a matrix form as follows;

$$\begin{bmatrix} H_{11} & H_{12}\dots & H_{1N} \\ H_{21} & H_{22}\dots & H_{2N} \\ \dots & \dots & \dots \\ H_{N1} & H_{N2}\dots & H_{NN} \end{bmatrix} \begin{bmatrix} C_1 \\ C_2 \\ \dots \\ C_N \end{bmatrix} = E \begin{bmatrix} N_{11} & N_{12}\dots & N_{1N} \\ N_{21} & N_{22}\dots & N_{2N} \\ \dots & \dots & \dots \\ N_{N1} & N_{N2}\dots & N_{NN} \end{bmatrix} \begin{bmatrix} C_1 \\ C_2 \\ \dots \\ C_N \end{bmatrix}$$

$$[H][C] = E [N][C]$$

$$[N]^{-1}[H][C] = E[C]$$

$$[A][C] = E[C]$$

$N_{ij}, T_{ij}, V^{\ell}_{ij}$ are analytically solved by using standard integral. We solved the two body Schrödinger equation to obtain the resonance energies. By diagonalization the Hamiltonian matrix elements, we obtained the complex energy eigenvalues.

Interaction between Alpha and neutron

We have employed the α -n potential which is introduced by Kanada *et al.*, (Kanada, 1979). The α -N potentials are described in the following parity dependent form with the central and spin-orbit terms. Spin-orbit coupling is predominant feature. The α -n potential is expressed in the following Gaussian form,

$$V_{\alpha-n}(r) = \sum_i^{i_{\max}} V_i e^{-\beta_i r^2} + \sum_i^{i'_{\max}} (-)^{\ell} V_i^p e^{-\beta_i^p r^2} + \left[\sum_i^{i''_{\max}} V_i^{\ell,s} e^{-\gamma_i r^2} + i \sum_i^{i'''_{\max}} (-)^{\ell} V_i^{\ell,s,p} e^{-\gamma_i^p r^2} \right] \vec{\ell} \cdot \vec{S}_N \quad (23)$$

where ℓ is the relative angular momentum between α and N, and \vec{S}_N is the spin of N. The spin orbit $\vec{\ell} \cdot \vec{s}$ coupling is calculated by using the following equation;

$$\vec{\ell} \cdot \vec{s} = \frac{j^2 - \ell^2 - s^2}{2} \quad (24)$$

$$\vec{\ell} \cdot \vec{s} = \frac{j(j+1) - \ell(\ell+1) - s(s+1)}{2} \quad (25)$$

The potential strengths and the range parameters are shown in Fig. (3), Fig. (4) and described in Table (1).

Table 1. The size parameters (fm^{-2}) and strength parameters (MeV) of α -n interaction

i	1	2	3
β_i	0.36	0.90	-
β_i^p	0.20	0.53	2.5
γ_i	0.396	0.52	2.2
γ_i^p	0.396	2.2	-
V_i	-96.3	77.0	-
V_i^p	34.0	-85.0	51.0
V_i^{ls}	-20.0	-16.8	20.0
$V_i^{ls,p}$	6.0	-6.0	-

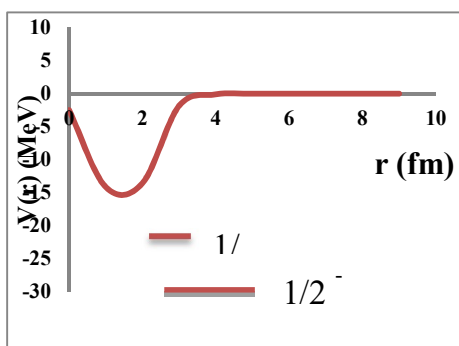


Fig. (3)

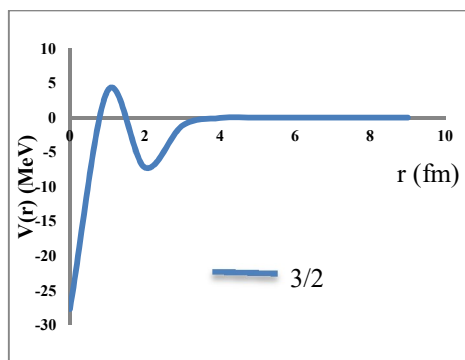


Fig. (4)

Figure 3. The potential for (α -n) system in ($J^\pi = 1/2^-$) state.

Figure 4. The potential for (α -n) system in ($J^\pi = 3/2^-$) state.

Results And Discussion

Resonance Energies of ${}^5\text{He}$ System

Our purpose is to investigate the resonance states of α -n system by using the complex scaling method. The (α -n) system has rather broad resonances but no bound state. The complex-scaled Hamiltonian matrix

elements are diagonalized and we obtained the complex energy eigenvalues. The number of the basis state is determined to converge the solutions.

The complex eigenvalues $E = E_r - i\Gamma/2$ the energy level E_r and level width Γ . From the energy eigenvalue data, we have found that the difference between resonance states and continuum states increases with increasing θ . In complex scaling method, the continuum states vary with the 2θ dependence. This distribution of continuum eigenvalues depends on the choice of the number of basic. In our calculation, the optimum set of parameters are $G_1=0.1\text{fm}$, $CG=1.15$, $N=40$. The resonance states for $(J^\pi = 3/2^-)$ can be seen clearly from the continuum states $\theta=20^\circ$ to 40° . The energy eigenvalue distributions of the ${}^5\text{He} (3/2^-)$ state with $\theta=20^\circ$, $\theta=30^\circ$ and $\theta=40^\circ$ are shown in Fig. (5). The energy eigenvalue distributions of the ${}^5\text{He} (1/2^-)$ state with $\theta=30^\circ$, $\theta=35^\circ$ and $\theta=40^\circ$ are shown in Fig. (6). From our calculation, we found that bound states and resonance states are discrete and obtained independently of θ . The calculated energies and level widths of ${}^5\text{He}(\alpha - n)$ for $(J^\pi = 3/2^-)$ and $(J^\pi = 1/2^-)$ are (0.747, 0.596)MeV and (2.147, 5.533)MeV respectively. Resonance energies for $(\alpha - n)$ system are compared with the experimental results (D.R.Tilley, 2002) in Table (2). Energy levels diagram for each state by comparing with the experimental values are shown in Fig. (7).

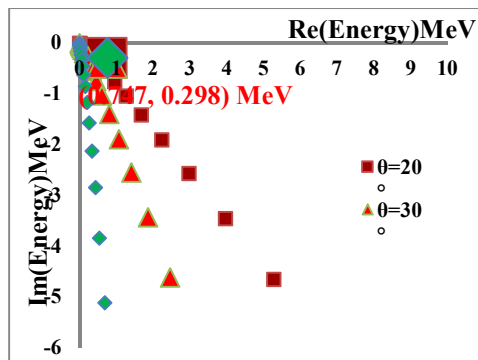


Figure 5

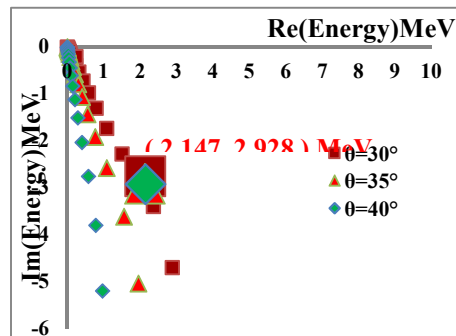


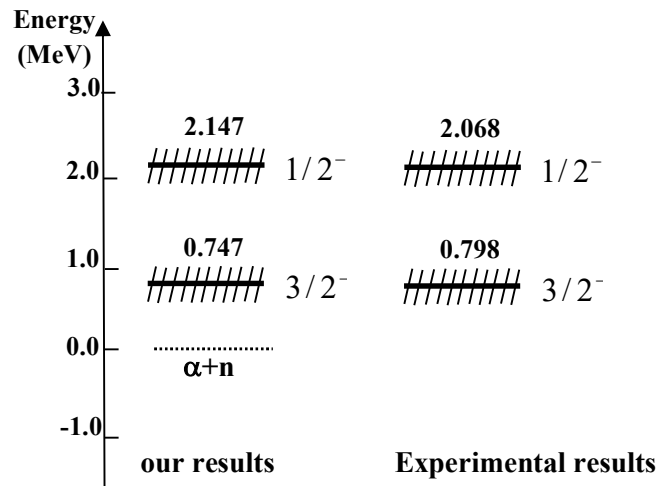
Figure 6

Figure 5. Resonance energy for the ${}^5\text{He} (3/2^-)$ with $\theta=20^\circ$, $\theta=30^\circ$, $\theta=40^\circ$

Figure 6. Resonance energy for the ${}^5\text{He} (1/2^-)$ with $\theta=30^\circ$, $\theta=35^\circ$, $\theta=40^\circ$

Table 2. The energy eigenvalues of ${}^5\text{He}$ system.

States	Energy Level, E (MeV)		Level Width, Γ (MeV)	
	Our Results	Exp: Results (D.R. Tilley, 2002)	Our Results	Exp: Results (D.R. Tilley, 2002)
${}^5\text{He}(3/2^-)$	0.747	0.798 ± 0.008	0.596	0.648 ± 0.006
${}^5\text{He}(1/2^-)$	2.147	2.068 ± 0.021	5.533	5.570 ± 0.056

**Figure 7.** Energy level of ${}^5\text{He}$ system in comparison with experimental values

Conclusion

Studies of resonances are indispensable for understanding the unique properties of drip-line nuclei. We have calculated the $\alpha+N$ two body calculation for ${}^5\text{He}$ resonance states by using complex rotation method. From our calculation, we found that the positions of resonance states in the complex energy plane remains almost unchanged with the variation of rotation angle θ . Our calculated results for the energies and level widths of ${}^5\text{He}$ system are consistent with the experimental results.

Acknowledgement

The authors would like to express their sincere thank to Professor Dr Khin Swe Myint , Rector (Rtd.), Emeritus Professor, Department of Physics, University of Mandalay for her valuable advice and helpful discussion in this research work. The authors would like to thank Dr Lei Lei Win, Professor, Head of Physics Department, University of Mandalay for her encouragement.

References

1. Anderson, H.L. *et al.*, (1952). *Phys. Rev.* **85**, 936.
2. Aguilar, J. and Combes, J.M. (1971). *Commun Math. Phys.* **22**, 269.
3. Bohr, A. (1951) . *Phys. Rev.* **81**, 134.
4. Gyarmati, B. and Kruppa, A.T. (1985) *Phys. Rev. C* **34**, 1.
5. Gaffney, L.P. *et al.*, (2013).*Nature* **497**, 199.
6. Kanada, H. *et al.*, (1979). *Prog. Theor. Phys.* **61**, 1327.
7. Kallunkathariyil, J. and Sosin, Z. (2013). *Int. J. Phys.* **6**.
8. Tilley, D.R. *et al.*, (2002). *Nucl. Phys. A* **708**, 3.

EFFECTS OF MONOMER ON THE ELECTRICALLY CONDUCTIVE POLYMER

Nyunt Win¹, Cho Cho Thet², Ye Chan³

Abstract

The effects of monomers on the electrically conductive polymer films were studied. In the preparation of conductive film, pyrrole (Py) and formyl pyrrole (FPy) were used as the source of monomers. Trifluoroacetic acid (TFA) and chloroform were utilized as a catalyst and solvent. One of the synthesis parameters, mole fractions of FPy against Py, was systematically varied from 0.1, 0.3, 0.5, 0.7 to 0.9 respectively. Then, the effects of monomers on the electrical properties of obtained conductive polymer films were studied. The formation of film was characterized and confirmed by ultraviolet-visible(UV-vis), X-rays diffraction (XRD) and Fourier transform infrared spectrometry(FTIR). Frequency dependent electrical conductivity of the prepare film is increased with the increasing mole fraction of FPy.

Keywords: conductive polymer, pyrrole, formylpyrrole, molar fraction

Introduction

Electrically conductive polymers with conjugated double bonds have been attracting in much attention of advanced materials due to their wide range of electrical conductivity. Such conductivities of polymers can be achieved with various doping levels while maintaining mechanical flexibility and high thermal stability. Among them, polypyrrole (PPy) is commonly used since it can easily be prepared pyrrole monomer in various organic solvents and in an aqueous media by chemical and electrochemical polymerization methods. In these preparation, polymerization condition and introducing additives into the reaction mixture could influence the properties of resultant conductive PPy [1-3]. Besides, using single monomer by chemical polymerization method usually used to obtain polymer powders which have limitations to fabricate the desired shape and size of electrodes [4-6]. Salmon *et al.*, reported chemical polymerization of pyrrole for forming PPy films in

¹. Lecturer, Physics Department, University of Patheingyi

². Lecturer, Universities' Research Centre, University of Yangon

³. Professor and Head, Universities' Research Centre, University of Yangon

the presence of sulfuric acid in ethanol [7]. But, the resultant films were fragile and unstable in their polymer properties. Consequently, very few investigations were examined for single component PPy films prepared by chemical methods. Later, Yusuke *et al.*, successfully synthesized conductive copolymer films by using two monomers, pyrrole (Py) and formylpyrrole (FPy), which could construct conjugated structure between them showing methine group [8]. Recently, Sirilaket *et al.*, modified the work of Yusuke by using surfactant and dopant, sodium dodecylsulfate (SDS) and poly(styrenesulfonate) (PSS)[9]. However, the final product could be obtained only polymer particles when emulsion polymerization method was used. On the other hand, they observed that electrical conductivity increased with the increasing surfactant concentration of SDS. Yusuke *et al.*, studied the effect of acidic catalysts in the polymerization and compare the conductivity of the resultant films. In addition to the different types of carboxylic acids, other important parameter, the amount of monomers, will be the critical role for the copolymer films. In the present work, depending of the formation of films, the effect of monomers in the copolymerization was studied by varying the mole fraction of FPy against Py in order to compare the conductive properties of the resultant films.

Materials and Method

Firstly two monomers solution containing (200 mg, 3 mmol) of Py and (286 mg, 3 mmol) of FPy were mixed and dissolved in 2 mL of chloroform (CHCl_3). They were stirred at room temperature for 30 min. Then, 13 mmol of trifluoroacetic acid (TFA) in 2 mL of CHCl_3 were added to the monomer solution. As a result, the color of the solvent immediately changed from transparent brown to yellowish red. Then, the mixed solution was spin-coated onto 9 cm diameter of the Petri dish at 20 rpm by using a homemade spin coater. The polymerization was carried out for 2 h at room temperature, and finally a film was formed in a Petri dish. The obtained film was a metallic greenish black and insoluble in several solvents. When the polymerization was performed using TFA in CHCl_3 , the mole fraction of FPy was varied from 0.1 to 0.9. Total monomer content in each feed solution was 6 mmol in 2 mL of CHCl_3 in the presence of 13 mmol of TFA system. The synthesis route of polymer films was depicted in Fig.1. It was found out that when only one

monomer Py was used, the color of the monomer Py solution changed from transparent color to a brownish black film when TFA was added and thus a fragile film was obtained without a metallic greenish black color. In contrast, the color of the solution changed from transparent brown to yellowish red and then the formation of the shiny greenish black film was observed when both monomers were mixed. Fig.2 shows the formation of polymer film in the Petri dish. For the measurement of electrical conductivity, chemical doping was performed on the films. Each film was washed with excess water and acetone and then dry 24 h in the desiccator. After that, a small amount of I_2 was put for 24 h in a closed vessel for chemical doping. Then, the electrical conductivity of the doped film was measured by LCR meter.

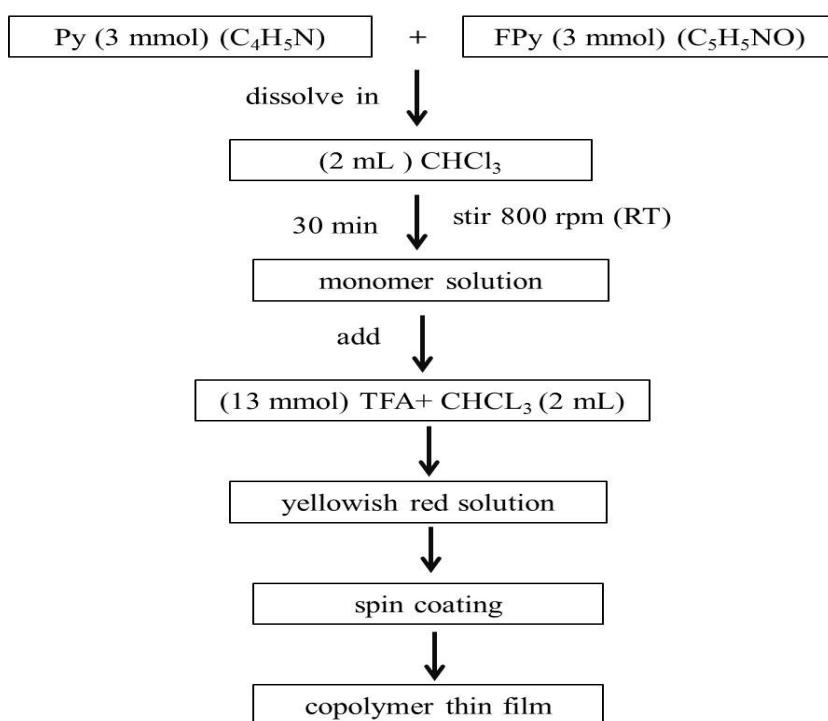


Figure 1. Preparation route of copolymer film



Figure 2. Conductive polymer film

Characterization Techniques

The functional groups of prepared films were investigated by FT-IR NICOLET iS5 spectrophotometer by using the iD7 ATR mode within the wave number from 4000 cm^{-1} to 650 cm^{-1} . The chemical doping of films were analyzed by FTIR 8400 Shimadzu spectrophotometer by using a KBr pallet method in the MIR radiation with the wave number from 4000 cm^{-1} to 400 cm^{-1} range with a resolution of 4.0 cm^{-1} . RIGAKU Miniflux 600 using $\text{CuK}\alpha$ radiation (40 kV, 40 mA) over a 2θ range from 10° to 70° on a powder type X-ray diffractometer equipped with a diffracted-beam graphite monochromator was used to examine the crystal structure of copolymer film. The electrical properties were measured by GW Instek LCR-8110G meter.

Results and Discussion

XRD spectra shown in Fig.3 were the copolymer film before and after Iodine (I_2) doping. No diffraction peaks could be detected except only for the broad peak around at the diffraction angle 23.3° which is corresponding to amorphous polymer. Since the crystallinity is much better after I_2 doping, the intensity is higher than the sample before I_2 doping.

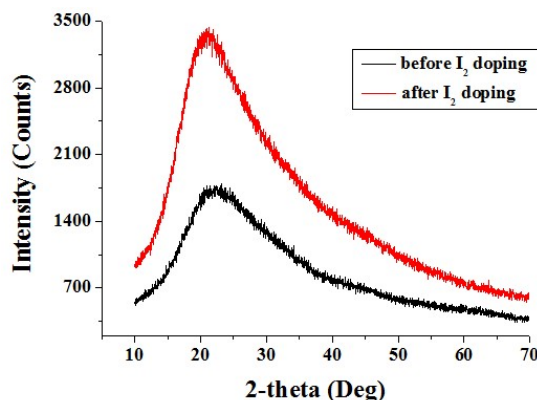


Figure 3. XRD spectra of conductive polymer film before (black) and after (red) I₂ doping

UV-vis spectrum of resultant copolymer film is shown in Fig.4. It was noted that characteristic absorption band of the π - π^* transition of polypyrrole is appeared at around 492 nm. This fact indicated that the FPy group was incorporated into the chemical structure of the conjugated polymer chains. Since Py and FPy had no absorption band at about 500 nm, this could be assigned with π - π^* transition of the C=C double bond, which was formed by the copolymerization. In addition, weaker and broader band was appeared at about 700 nm. This strongly implied that the bipolaron state of polypyrrole was present in the films. This indicated that such strong acid (TFA) strongly interacted with pyrrole segments to form bipolaron state. Fig.4 shows UV-Visible spectrum of Py-FPy copolymer film using by acid catalyst (TFA).

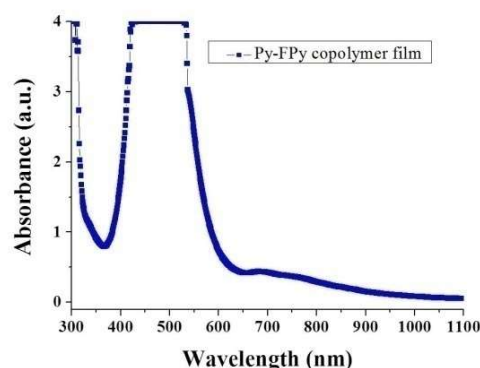


Figure 4. UV-Visible spectrum of Py-FPy copolymer film using by acid catalyst (TFA)

Fig.5 shows FT-IR spectra of the copolymers prepared at each mole fraction of FPy. As indicated by (a), N-H stretching vibrations of two types (3380 and 3260 cm^{-1}) were present in the film. The peaks (b) of saturated C-H stretching at 2935 and 2866 cm^{-1} became very weak when the mole fraction was higher than 0.5 . This indicated that the conjugated structure was increased in the polymer backbone, when the mole fraction of FPy increased. In peaks (c) and (d) for C=C double bond stretching of the pyrrole ring at 1626 and 1538 cm^{-1} and C=N stretching at 1490 cm^{-1} , these were attributed to the formation of conjugated structure in the copolymer. It was noted that the broad peak (e) observed at 1258 cm^{-1} was assigned to -C=CH- stretching from the methine group. Additionally, the peak (f) of C-H out-of-plane deformation vibration from the methine group and peak (g) of the aromatic C-H out-of-plane deformation vibration appeared at 1008 and 836 cm^{-1} , respectively.

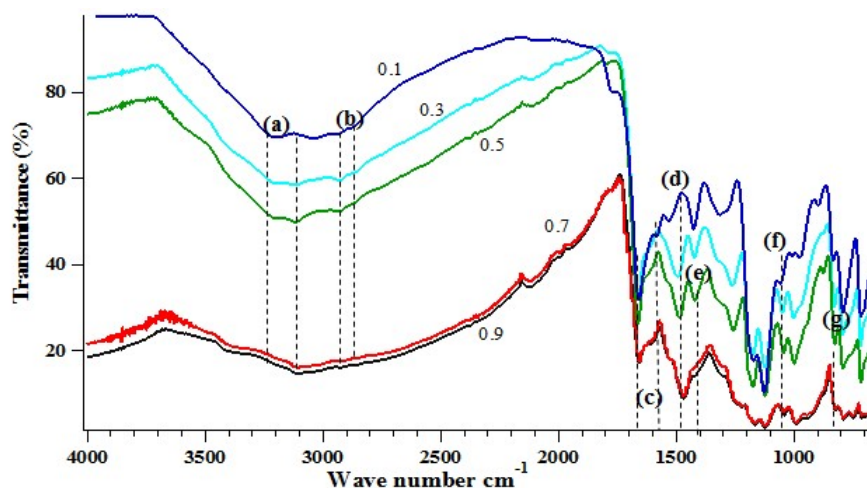


Figure 5. FT-IR spectra of polymer films prepared by various mole fractions of FPy against Py

The doping process was confirmed by FT-IR measurement. Fig.6 shows FT-IR spectra of polymer films before and after I_2 doping. The peak at 3117 cm^{-1} was aromatic C-H stretching. The peaks of C=N stretching at 1494 - 1402 cm^{-1} were attributed to the formation of the conjugated structure in the film. The peak observed at 1263 cm^{-1} was assigned to -C=CH- stretching from methine group of the copolymer. The peak at 1201 cm^{-1} can be related to

C-N stretching of aminegroup. The peak of C=N appeared at 1134cm^{-1} The peak at 1055cm^{-1} can be attributed to C-H in plane deformation. The peak of the aromatic C-H out-of-plane deformation vibration appeared at $1008\text{-}800\text{ cm}^{-1}$, respectively. The two additional peaks occurred at 547 and 486 cm^{-1} were due to the presence of iodine in the analyzed sample. Figure 6 shows FT-IR spectra of conductive polymer film before (black) and after (red) I_2 doping.

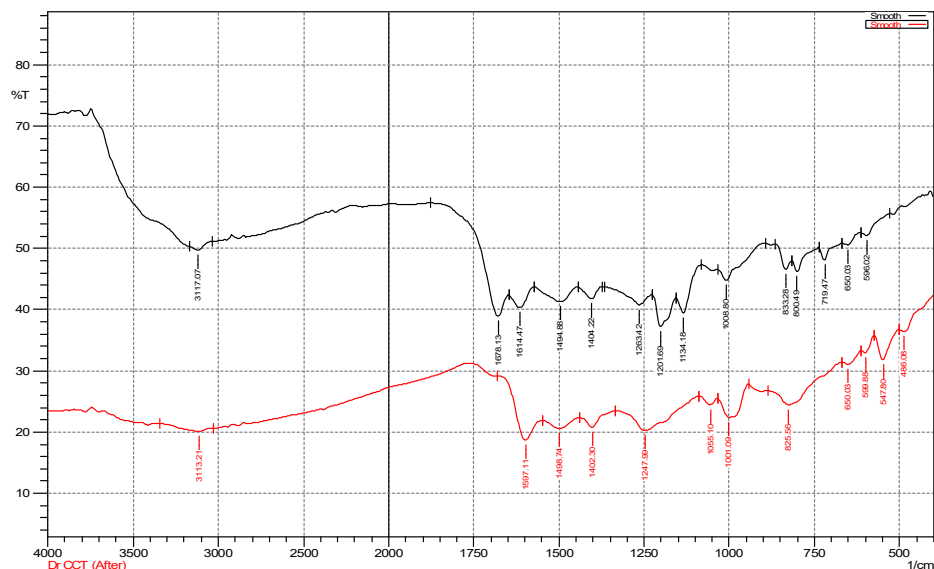


Figure 6. FT-IR spectra of conductive polymer film before (black) and after (red) I_2 doping

The dielectric properties of conductive films were studied by using the LCR meter. The diameter of the sample size is 9.5 mm in a circular shape for each film. The parameters including capacitance and dielectric loss in the frequency range $0.1\text{ Hz-}1\text{ MHz}$ are measured. Dielectric constant (κ) was calculated by using the formula:

$$\kappa = \frac{Cd}{\epsilon_0 A} \quad (1)$$

Where, κ is dielectric constant of the medium, C is the capacitance, d is the thickness of the sample, and A is the cross sectional area of the sample and ϵ_0

is the permittivity of vacuum ($8.854 \times 10^{-12} \text{Fm}^{-1}$). Then dissipation factor ($\tan \delta$) is determined by the formula:

$$\tan \delta = \frac{D}{\kappa} \quad (2)$$

Where D is the dielectric loss obtained from LCR measurement. Finally, the AC conductivity (σ_{ac}) was determined by using the relationship:

$$\sigma_{ac} = 2\pi f \tan \delta \varepsilon_0 \kappa \quad (3)$$

Where, f is the frequency of applied field.

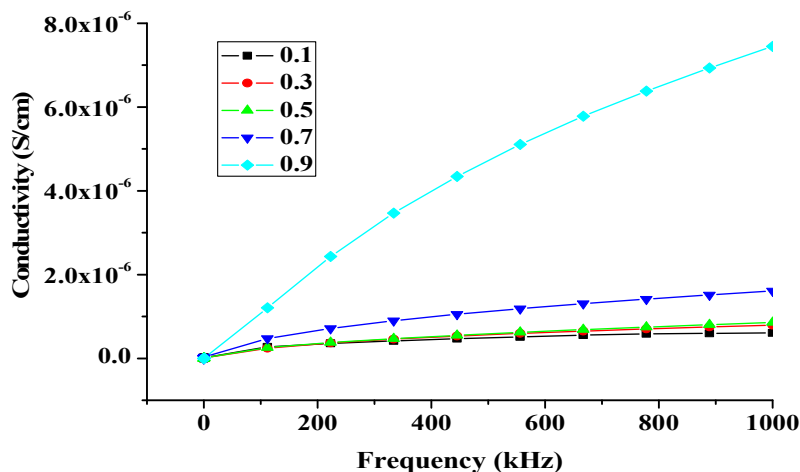


Figure 7. The electrical conductivity of I₂ doped copolymer films dependence on frequency for various mole fractions.

AC conductivity dependence on frequency was studied in the frequency range of 0.1 Hz -1000 kHz. As shown in Fig.7, the ac conductivity of the films increased with an increasing amount of FPy for all films. Among the films, the film prepared the mole fraction 0.9 FPy amount has the highest conductivity. On the other hand, mole fraction 0.7 FPy has the second highest conductivity. In addition, the films prepared the mole fraction 0.1, 0.3 and 0.5 has lower conductive properties than the others. Thus, it is remarkable that the mole fractions was the important parameters for the enhancing the

conductivities of the polymer films. Therefore, it can be concluded that polymer films can enhance the conductivity with an increasing amount of mole fraction of FPy against Py. Fig.8 shows the average electrical conductivity of films prepared by various amount of FPy. It can be clearly see that the values abruptly increased when the mole fraction is larger than 0.7 and becomes the highest for 0.9 mole fraction. As a result, monomers are one of the critical parameters for determining the electrical properties of polymer films.

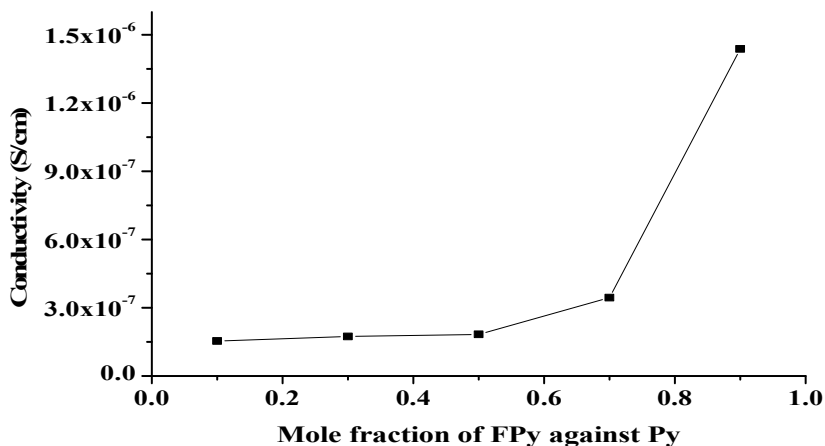


Figure 8. Average electrical conductivity of I₂ doped P(Py-co-FPy) films prepared by various mole fractions of FPy against Py.

Conclusion

The conductive polymer films have been successfully prepared by chemical polymerization method. The characterizations of formation and electrical properties are performed for different mole fractions of FPy and Py. The π - π^* transition of polypyrrole in UV-vis spectrum at around 492 nm is evident that the formation of polymer and indicates that the FPy group is incorporated into the chemical structure of the conjugated polymer chains. The broad peaks around 23° in XRD spectra and stretching vibrations in FT-IR spectra show the characteristic of polymer and effect of I₂ on the film formation. In the observation of electrical properties, it is found that ac

conductivity of the film is significantly increased at mole fraction of 0.9. The interesting results would be anticipated for use in several applications as a new conductive polymeric material.

Acknowledgements

I would like to acknowledge to Professor Dr Khin Khin Win, Head of Department of Physics, University of Yangon, for giving me the chance to participate in this event. My thanks go to Professor Dr Soe Soe Nwe for her encouragement of this work. I do specially thank you to my Supervisor, Dr Ye Chan, Professor and Head of URC, for his guidance of my work. I am also indebted to my Co-supervisor, Dr Cho Cho Thet, Lecturer, Universities' Research Centre, who gives me valuable comments and suggestions to this work and for a large number of excellent discussions.

References

1. H. D. Tran, K. Shin, w. G. Hong, J. M. D'Arcy, R. W. Kojima, B. H. Weiller and R. B. Kaner, "A Template- Free Route to Polypyrrole Nanofibers," *Macromolecular Rapid Communications*, Vol. 28. No. 24, 2007, pp. 2289- 2293.
2. K. S. Jang, H. Lee and B. Moon, "Synthesis and Characterization of Water Soluble Polypyrrole Doped with Functional Dopants," *Synthetic Metals*, Vol. 143. No. 3, 2004, pp. 289-294.
3. K. Ishizu, H. Tanaka and R. Saito, "Microsphere Synthesis of Polypyrrole by Oxidation Polymerization," *Polymer*, Vol. 37. No. 5, 1996, pp. 863-867.
4. M. Omastová, M. Trchová, J. Kovářová and J. Stejskal, "Synthesis and Structural Study of Polypyrroles Prepared in the Presence of Surfactants," *Synthetic Metals*, Vol 138. No. 3, 2003, pp. 447-455.
5. M. Salmon, K. K. Kanazawa, A. F. Diaz and M. Krounbi, "A Chemical Route to Pyrrole Polymer Films," *Journal of Polymer Science: Polymer Letters Edition*, Vol. 20. No. 3, 1982, pp. 187-193.
6. R. E. Myers, "Chemical Oxidative Polymerization as a Synthetic Route to Electrically Conducting Polypyrroles," *Journal of Electronic Materials*, Vol. 15. No. 2, 1986, pp. 61-69.
7. Sirilak Arunsawad, Kawee Srikulkit and Sarintorn Limpanart "Effect of surfactant on conductivity of Poly(pyrrole-*co*-formylpyrrole) via Emulsion Polymerization" *Journal of Metals, Materials and Minerals*, Vol.24 No.2 pp.29-34, 2014.
8. Y. Kudoh, "Properties of Polypyrrole Prepared by Chemical Polymerization Using Aqueous Solution Containing Fe₂(SO₄)₃ and Anionic Surfactant," *Synthetic Metals*, Vol. 79. No. 1, 1996, pp. 17-22.
9. Yusuke Hoshina, Takaomi Kobayashi "Effect of Acidic Catalyst on Properties of Novel Conductive Copolymer Films Made of Pyrrole and Formyl Pyrrole" *Engineering*, 2012, 4, 139-145.

THE OCCURRENCE AND CRYSTAL STRUCTURE OF TUNGSTEN BEARING ORES-MINERAL AT KANBOUK, TANINTHARYI REGION (MYANMAR)

Min Maung Maung¹, Sint Ohnmar²

Abstract

Tungsten is a metal of superlatives and the lowest vapour pressure and the lowest expansion coefficient of all metals. The quality and the costs of producing the metal greatly depends on the efficiency of the concentrating steps performed at the rather limited number of mining sites. In this work, the tungsten (W) and tin (Sn) were produced in wolframite ore from Kanboug mine by calcinations process and their structural properties were analyzed by using X-ray diffraction method. The elemental analysis was done by Energy Dispersive X-rays Fluorescence (EDXRF) method. The electric and magnetic properties of these samples were also observed PERMAGRAPH L and LCR meter.

Keywords: Tungsten, LCR meter, Wolframite, X-ray diffraction

Introduction

Tungsten ore is a rock from which the element tungsten can be economically extracted. The ore minerals of tungsten include wolframite, scheelite, and ferberite. Materials processing is one of the most important and active areas of research in heat transfer today. With growing international competition, it is has become crucial to improve the present processing techniques and the quality of the final product. Heat transfer is extremely important in a wide range of materials processing techniques such as crystal growing, casting, glass fiber drawing, chemical vapor deposition, spray coating, soldering, welding, polymer extrusion, injection molding, and composite materials fabrication.

The flows that arise in the molten material in crystal growing due to temperature and concentration differences, for instance, can affect the quality of the crystal and, thus, of the semiconductors fabricated from the crystal. Therefore, it is important to understand these flows and develop methods to minimize or control their effects. As a consequence of the importance of heat

¹ Dr, Associate Professor, Department of Physics, Dawei University.

² Dr, Lecturer, Department of Physics, Dawei University.

and mass transfer in materials processing, extensive work is presently being directed at this area. But what is often lacking is the link between the basic mechanisms that govern diverse processing techniques and the thermal systems needed to achieve the given process.

Tungsten is an economically important metal, being widely used in light-bulb filaments, electron and television tubes, abrasives and special alloys such as tool steels. Tungsten carbide is of great importance to the metal-working, mining and petroleum industries. Contamination from these sources is, therefore, possible in industrial and urban areas.

Experimental

Rock samples were purchased from Wolframite mine (Kanbouk), Tanitharyi region. Firstly, tungsten-ores alloys were divided and collected from rock sample according to their raw group formations (colour). The obtained raw samples were grounded with agate mortar and heated at 150°C, 300°C, 400°C and 500°C in furnace 3 hrs each and slightly cold down to room temperature. The samples were grounded again and again to form homogeneous powder. The powder samples were then added into the internal mixer 3 min after the blending started and allowed to mix for 4 min and were charged into the internal mixer. The powder samples were prepared with XRD holder to determine the structure and lattice parameter.

Small amount of annealed powder was characterized by XRD using Cu-K α radiation at room temperature in order to check the phase purity and calculated average crystallite size. Once a homogeneous mixture is assumed after 13 min, the samples were pressed by hydraulic press machine into a measurement cell (1.3 cm diameter). The pellet samples were cured in a mold with a spacer approximately 0.5 mm thick and 1.3 cm in diameter. Dielectric measurements were carried out by a digital RLC meter (GWInstek LCR821) at room temperature. The dielectric constant and loss factor was measured over the frequency range 10 to 200 kHz. The measurements were performed applying a voltage of 1.5 V rms between the electrodes no. 1 and electrode no. 2. Capacitive and resistance effects were determined through the measurements of permittivity and resistivity. The room temperature

ferroelectric hysteresis loop measurement demonstrated the coexistence of ferroelectricity and magnetism was done by permagraph L equipment.

Results and Discussion

Structural characterization and elemental concentration

Figure 1.1 showed the XRD (X-ray diffraction) patterns of the powder samples. It was found that the powders were in tetragonal structure having $p4_2/m\ n\ m$ space group. The average lattice constants are calculated to be $a = 4.737\text{\AA}$ and $c = 3.185\ \text{\AA}$ from the refinement of the XRD data. The prominent peaks in the plot are indexed to various (hkl) planes of Cassiterite (Tin(IV)oxide (SnO_2)). The secondary peaks were observed in the form of wolframite (Fe, MnWO_4). The sample calcined at 400°C and 500°C are having stronger peak of (211) plane compared with other samples, but there have more other planes and impurities.

From the elemental analysis of wolframite ore samples, Tin (Sn), Tungsten (W), Iron (Fe), Manganese (Mn) were observed as major elements. When increasing of the treatment of annealing temperature, the concentration of Tin (Sn) element was decreased and the concentration of Tungsten (W) and Iron (Fe) were increased. Table 1.1 was shown the elemental concentrations of wolframite ore samples with heat treatment.

Surface morphology analysis

Figure 1.2 showed the scanning electron microscope (SEM) images of wolframite ore samples with different annealing temperatures. It was analyzed in a JEOL JSM-6400 scanning electron microscope at accelerating voltage of 20KVA, real time of 21-36 and live time of 60 seconds. There were two different types of morphological feathers along with voids are visible. The unreacted MnWO_4 grains which exhibit flowery feathers depict breaking up morphology, evenly distributed on the whole pellet surface. The increase in the furnace temperature enhances the rate of reaction and the images were formed faceted particles and agglomerated rods.

Dielectric measurements at room temperature

Figure 1.3 showed the dielectric constant measurements with respect to frequency in the region of (10 Hz-200 kHz) of wolframe pellets produced using PVA as a binder and applying pressure of 15 ton/cm² and using LCR meter. It was found that dielectric constant was higher in the lower frequency region. It decreases with increasing frequency and becomes almost constant at higher frequency region. It can be seen that the dielectric constant decreases with increasing frequency. It means that the dielectric constant of these samples were the strong function of frequency. The average dielectric constant of wolframe samples in the range 10Hz to 200 kHz at room temperature found to be $\epsilon_r = 35, 30, 25, 20, 10$ respectively.

Resistivity measurement at room temperature

Figure 1.4 showed the electrical resistivity decreases and their electrical conductivity increases with increasing frequency applied. It can be said that the possibility of uses to these materials in high frequency device applications.

Magnetic hysteresis loop measurement

Figure 1.5 showed the magnetization of the wolframe simples as a function of applied magnetic field. Magnetization and magnetic hysteresis results confirm the absence of canted ferromagnetic behaviour in these simples. The measurement was carried out on the simples at room temperature. It is evident that magnetization is a linear function of applied magnetic field. Their magnetic remanences, normal coercivity and maximum energy products were decreased but their intrinsic coercivity values were increased with increasing annealing temperatures. It was said that this behaviour is the typical of antiferromagnetic materials.

Conclusion

Although the availability and quality of tungsten ores are limited and the price of the metal greatly fluctuates, its special physical properties and applications pose a reliable demand for production. The low tungsten content

and the interference of the gangue minerals in the ore make it complicated and costly to provide a suitable concentrate for the metallurgical processing.

The primary objective of this work was the characterization of an ore bearing wolfrinite mineral from Kanbouk mine, Tanintharyi region. The XRD phase patterns confirmed the availability of minerals such as Cassiterite, Hubnerite and manganocolumbite. The chemical elemental composition determined by EDXRF was Tin (Sn), Tungsten (W), Iron (Fe), Manganese (Mn) as major elements and other trace elements were also found. The mineralogical studies carried out with SEM point imaging showed the presence of different aggregates of minerals.

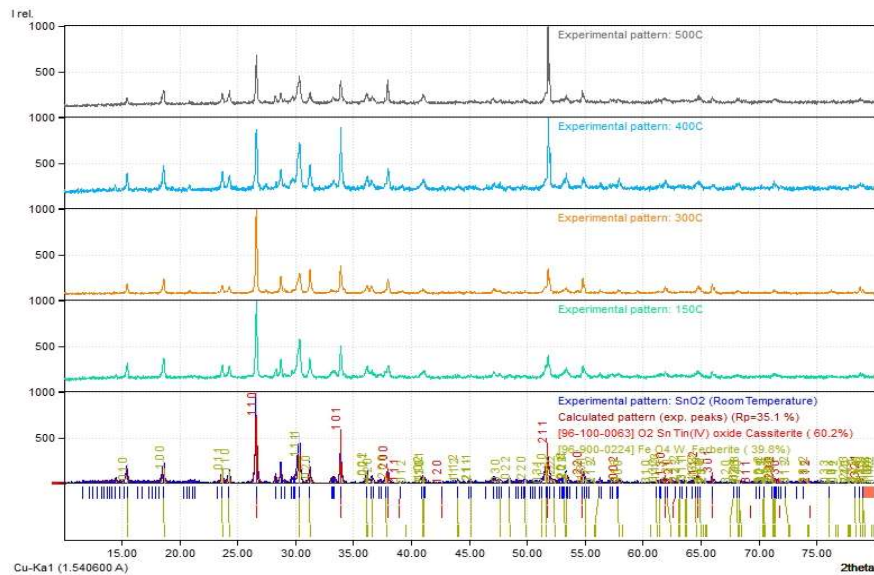
A decrease in dielectric constant with increase of frequency was observed. This decrease was rapid at lower frequency ranges and slower at higher frequency ranges. It is observed that the dielectric structure is formed into two layers namely, the well conducting grains and poorly conducting grain boundaries. At very low frequencies, the oxide grain boundaries were more active and this contributes to the very high dielectric constant at low frequencies. Thus, it was found that they were a promising material for dielectric applications. B-H loop confirms that the antiferromagnetic nature of the wolframite samples. Since the calculation values of permeability of these samples, it was said that their magnetic properties would transformed from diamagnetism to paramagnetism in sample annealing with temperature above 500°C.

Table 1.1: The elemental concentration in wolframite ore samples.

Elements	Concentration (%)				
	room temperature	Calcinations for 1 hour			
		150°C	300°C	400°C	500°C
Tin (Sn)	34.251	44.331	31.878	26.737	25.965
Tungsten (W)	26.949	25.390	26.330	26.897	28.353
Iron (Fe)	30.21	22.644	32.290	36.015	36.082
Manganese (Mn)	7.053	5.402	6.989	7.298	7.530

Table 1.2: The characteristic quantities of magnetic field in wolframite ore samples.

Sample	Remanence (B _r)(T)	Intrinsic coercivity (H _{cJ}) (kA/m)	Normal coercivity (H _{cB}) (kA/m)	Maximum Energy Product (BH) _{max} (kJ/m ³)
Room Temperature	0.00391	11.6	3.2	0.00032
Annealing with 150°C	0.00349	37.6	2.89	0.00009
Annealing with 300°C	0.00237	66.4	1.91	0.0011
Annealing with 400°C	0.00196	72.08	1.57	0.00114
Annealing with 500°C	0.000951	90.9	0.749	0.00001

**Figure 1.1:** The XRD patterns of wolframite samples

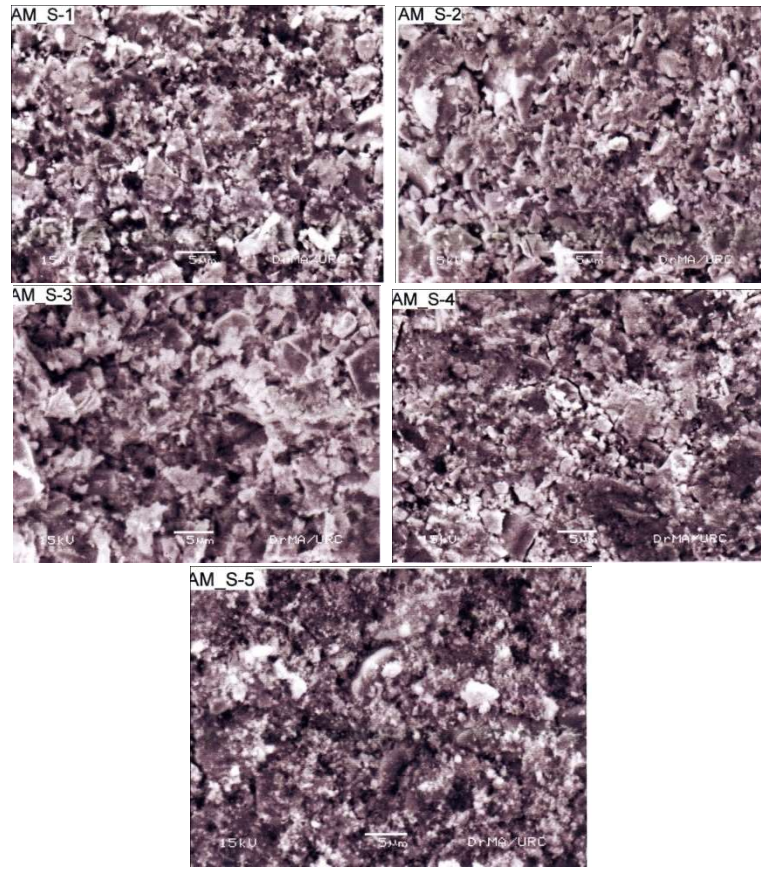


Figure 1.2: The SEM image of wolframite samples with different annealing temperatures.

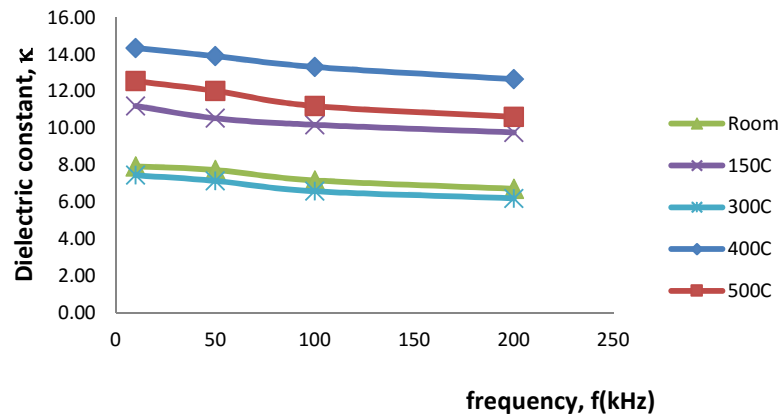


Figure 1.3: The capacitive effects of wolframite samples

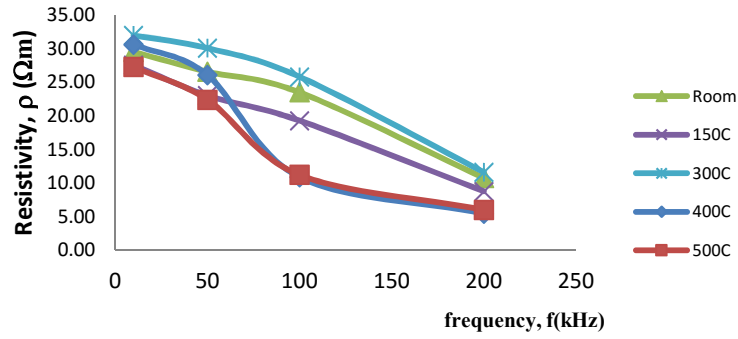


Figure 1.4: The frequency dependence resistivity of wolframite samples.

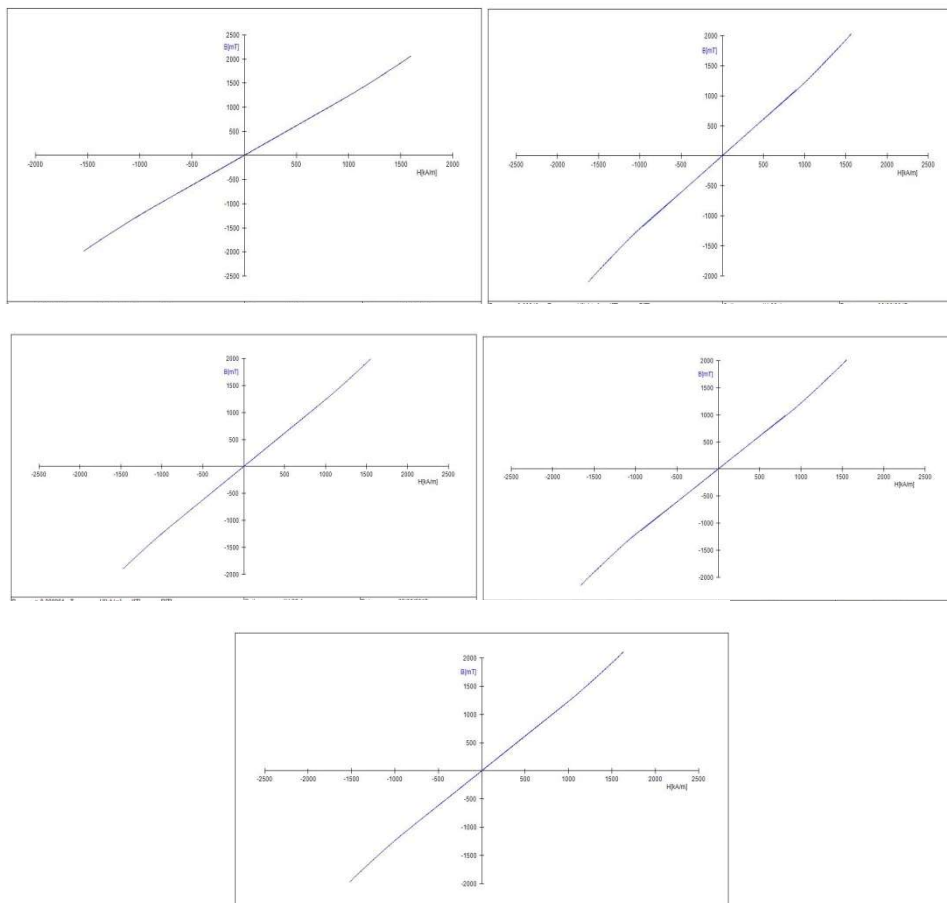


Figure 1.5: The Magnetic properties of wolframite samples

Acknowledgements

I would like to express appreciation to Pro-rector Dr Ba Han, Pro-rector Dr Khin May Aung, Dawei University and Pro-rector Dr Aung Myat Kyaw Sein, Mawlamyine University for their encouragement and kind permission to undertake the present research. I also would like to express my profound thanks to Professor Dr Than Tun, Head of Department of Physics, and Professor Dr Sanda Dwe, Department of Physics, Mawlamyine University, for their kind permission to use material science research lab apparatus in Mawlamyine University and Professor Dr Aung Myat Kyaw, Department of Physics, Dawei University for encouragement and help during this work.

References

1. Ahmad S et al, (2004), *Ferroelectric Ceramics Processing Properties and Applications*, Department of Ceramic Science and Engineering, Rutgers University: USA
Instruction Manual LCR meter GW 820, USA. JCM 6000 Plus, Scanning Electron Microscope.
2. Moulson A J & Herbert J M, (1997), *Electroceramic Materials Properties Applications*, New Delhi: Thomson Press
3. Rajagopal K. (2009) *Textbook of engineering physics part II*. New Delhi-110001.
4. Steingroever GmbH. Dr.,(2010), *Computer controlled permagraph® L*” Cologne-Germany
5. Suryanarayana C. and Norton M. G. (1998), *X-ray Diffraction A Practical Approach*, (New York: Plenum).
6. Tyagi M S, (1991), *Introduction to Semiconductor Materials and Devices*, New York: Wiley
7. Xu Y, (1991), *Ferroelectric Materials and their Applications*, New York: Elsevier Science Publishing Co. Inc.
8. Yadav M S, (2003), *A Textbook of Spectroscopy*, New Delhi: Anmol Publication
<http://www.digibridge-ab.ca/ceramic material/86.html>
<https://en.m.wikipedia.org/wiki/Hysteresis>

STRUCTURAL, ELECTRICAL AND MAGNETIC PROPERTIES OF WOLFRAMITE (FeMnWO₄) FROM PHARCHAUNG MINE IN TANINTHARYI REGION

Sint Ohnmar¹, Min Maung Maung²

Abstract

The sintering process of ore mineral which is important for designing scientific and economic sintering schedule. The sintering behavior of electrical conductivity and a structural tile were investigated using thermal analysis techniques. In this paper, the conductivity of FeMnWO₄ sample was determined by annealing method and the activation energy was observed 0.4147 eV. And also the thermal loop was observed in the temperature range between 303K-623K-303K. The weight loss was observed 4.599% from TGA curve and the oxidation process occurred from the exothermic peak at 464.56 °C. The crystal structure and the morphology of FeMnWO₄ powder were observed by XRD and scanning electron microscope. The magnetic properties of wolframite was also observed by PERMAGRAPH L.

Keywords: Sintering process, TGA curve, Wolframite, electrical conductivity

Introduction

Materials science uses the laws of physics (e.g. thermodynamics, heat and mass transfer, fluid dynamics) to understand how various physical phenomena influence materials behavior. Mineral, Wolframite, is a principal ore of tungsten. It is an iron and manganese tungstate mineral. It has a hardness of 5 to 5.5 mhos, specific gravity of 7.1 to 7.5, is dark gray, reddish brown, brownish black, or iron black in color. Wolframite is commonly found in granite and pegmatite dikes, and is often associated with cassiterite; it also occurs in sulfide veins and placer deposits. Because heat causes tungsten to expand at about the same rate as glass, the metal is widely used to make glass-to-metal seals. Tungsten or its alloys are used for filaments for electric lamps, electron and television tubes, electrical contact points for automobile distributors, heating elements for electrical furnaces, and space, missile, and high-temperature applications. Other important tungsten compounds are

¹ Dr, Lecturer, Department of Physics, Dawei University

² Dr, Associate Professor, Department of Physics, Dawei University

calcium and magnesium tungstates, which are used in fluorescent lighting, and tungsten disulfide, which is used as a high-temperature lubricant at temperatures up to 500 deg C. It has been suggested that the name ferberite be limited to mixtures containing not more than 20 per cent of the hubnerite molecule and the name hubnerite to those containing not more than 20 per cent of the ferberite molecule. This would leave the name wolframite for mixtures containing more than 20 per cent of both FeWO_4 and MnWO_4 . Scintillators for dark matter search, semiconducting photoelectrodes for photoelectrolysis or humidity sensors for meteorology are some of the direct applications that wolframite-type compounds with chemical formula AWO_4 present. On top of that, an especially interesting case is the one with the divalent magnetic ion $A=\text{Mn}^{2+}$, which shows three different antiferromagnetic phases below 13.7 K, with the intermediate one presenting an incommensurate magnetic structure able to lift the center of inversion in MnWO_4 originating a polar moment. The high-pressure (HP) behavior of these materials has attracted a lot of attention in recent years, with the search of new structures with enhanced scintillating properties being the major cause. At ambient pressure, wolframites crystallize in a monoclinic structure with $Z = 2$ and space group $P2/c$. A theoretical work has shown that the monoclinic ($P2/c$) wolframite structure is energetically competitive with a triclinic ($P1$) one of CuWO_4 -type.

When a material is heated its structural and chemical composition can undergo changes such as fusion, melting, crystallization, oxidation, decomposition, transition, expansion and sintering. Using Thermal Analysis such changes can be monitored in every atmosphere of interest. The obtained information is very useful in both quality control and problem solving. Thermal Analysis is the term applied to a group of methods and techniques in which chemical or physical properties of a substance, a mixture of substances or a reaction mixture are measured as function of temperature or time, while the substances are subjected to a controlled temperature programme. For specific application, the magnetic properties are important. Non-magnetic materials have to be used whenever the magnetic fields can be perturbed in radiation equipment or when shielding is positioned near electrical sensors.

Experimental

Characterization Techniques

Electrical Conductivities with Temperatures: To measure the variation of electrical conductivity with temperature, a simple home-made apparatus was developed in the laboratory. The apparatus consists of a sample holder attached with the 300 W heater and the steel chamber. The desired temperature of the samples was maintained with the help of a temperature controller. The sample was sandwiched between two copper plates that are in contact with two copper rods. These two copper rods serve as two electrodes. To ensure better electrical contact, silver paste was applied evenly on both surfaces of the sample. The sample in the sample holder was placed on the copper cylinder that was heated by 300 W heater. Thermal conducting mica shield is used between the sample holder and the copper cylinder to protect from electrical conduction. The apparatus was immersed in a heating steel chamber surrounded by asbestos to reduce the thermal flow from the environment. The resistances were measured using FLUKE 45 digital resistance-meter. The capacitances were measured using FUKE DM6013A CAPACITANCE METER. The K-type thermocouple was inserted near the sample to record its temperature.

X-ray diffraction (XRD): In this work, X-ray diffraction were carried out using a Rigaku x-ray powder diffractometer which employs Cu-K α x-radiation of wavelength $\lambda = 1.54056 \text{ \AA}$ between a 2θ angle of 5° to 70° . X-ray diffraction was carried out to determine the crystalline structure of the materials

Scanning Electron Microscopy (SEM): The SEM provides useful analysis of surface structures and morphology. SEM was carried out using the JSM-5610 scanning electron microscope at the Research Center, Yangon University. Scanning electron microscopy was performed in order to understand further the results obtained from other techniques such as XRD.

Thermogravimetry (TG) and Differential Thermal Analysis (TDA) : The instrument used in thermogravimetry (TG) is called a thermobalance. Under controlled and reproducible conditions, quantitative data can be extracted from the relevant TG curves. Most commonly, the mass change is related to

sample purity or composition. TGA also provides information about the temperature range over which a particular sample appears to be stable or unstable. The heat changes within a material are monitored by measuring the difference in temperature (T) between the sample and the inert reference. This differential temperature is then plotted against temperature or time to get DTA curve. TG and DTA was carried out using the DTG-60H thermal analyser at the Research Center, Yangon University.

Magnetic Measuring Techniques: The measurement was carried out on the sample at room temperature. The magnetization (hysteresis graph) of FeMnWO_4 was also identified by computer controlled PERMAGRAPH L system.

Results and Discussions

The investigation of the relationship among processing, structure, properties, and performance of materials. The phase transition between two allotropic forms can be exploited in a smart way to obtain sensors or actuators (especially to obtain thermal or strain sensors). As an illustration, our team has focused for many years on the CuMoO_4 and CoMoO_4 phase transitions for thermochromic or piezochromic properties. More extensively, the ABX_4 compounds exhibit numerous crystalline forms and the phase transitions between some of them were shown to be of great interest. In this paper, we concentrate on the FeMnWO_4 compounds; respectively, with orthorhombic structure. In the literature, it is known that FeMnWO_4 monoclinic structure crystallize in the wolframite structure when synthesized between 400°C and 500°C . As-obtained FeMnWO_4 (70%) at room temperature was finally investigated by X-ray diffraction. Characterization of the sample are structural analysis by XRD as shown in Figure.1. The crystal structure was observed orthorhombic. The average lattice parameters were observed $a = 4.7535 \text{ \AA}$, $b = 5.6818 \text{ \AA}$ and $c = 5.0120 \text{ \AA}$. SEM investigations on FeMnWO_4 (70%) at room temperature as-synthesized with orthorhombic form in Figure 2. SEM investigations are not adequate to confirm or otherwise the presence of deleterious phase. The temperature induced phase transition exhibited by a single compound make it suitable as a shock detector and a thermal sensor.

Thermal properties are related to transmission of heat and heat capacity. To measure the variation of electrical conductivity with temperature, a simple home-made apparatus was developed in the laboratory. Thermal analysis by TG-DTA as shown in Figure.3, the weight loss was observed 4.599% from TGA curve and the oxidation process occurred from the exothermic peak at 464.56 °C from DTA. Figure.4 shows the $\ln\sigma$ versus $1000/T$ curve of the FeMnWO_4 in the temperature range 303 K–623 K -303K.

Differential thermal analysis is well established as a technique for the characterization and control of materials which undergo characteristic changes on heating. It is less well established as a method for investigating the products obtained when such a material is heated, since equilibrium is an inherent impossibility of the method. However, the latter is not an obstacle when thermodynamic considerations control the design of the apparatus and when good recording equipment is employed. With the addition of dynamic atmosphere control much useful information about the products of heating can be assembled in a short time. Because differential thermal analysis is most useful when the apparatus is designed so that several different techniques can be employed.

The most important class of magnetic materials is the ferromagnets: iron, nickel, cobalt and manganese, or their compounds. The magnetization curve looks very different to that of a diamagnetic or paramagnetic material. Ferromagnetism is distinguished from paramagnetism by more than just permeability because it also has the important properties of remnance and coercivity. Although susceptibility is seldom directly important to the designer of wound components which explain the theory of magnetism. The non-ferromagnetic substances the permeability is so close to μ_0 that characterizing them by μ is inconvenient. Instead use the magnetic susceptibility, χ - via the permeability. The paramagnetic substances have positive susceptibilities and the diamagnetic substances have negative susceptibilities. The susceptibility of a vacuum is then zero.

The magnetic properties of a material is likely to include the type of graph known as a magnetization or B-H curve. The magnetic field strength as the horizontal axis and the magnetic flux density as the vertical axis. The magnetization curve of FeMnWO_4 is shown in Figure.5. The linear

dependence between applied field H and magnetic induction B proves that at room temperature is paramagnetic. The measurement of the magnetic properties could be a method for on line testing or estimating the properties of produced heavy alloys which is routinely done in the case of cemented carbides. In that work saturation coercivity as well as several composites were determined.

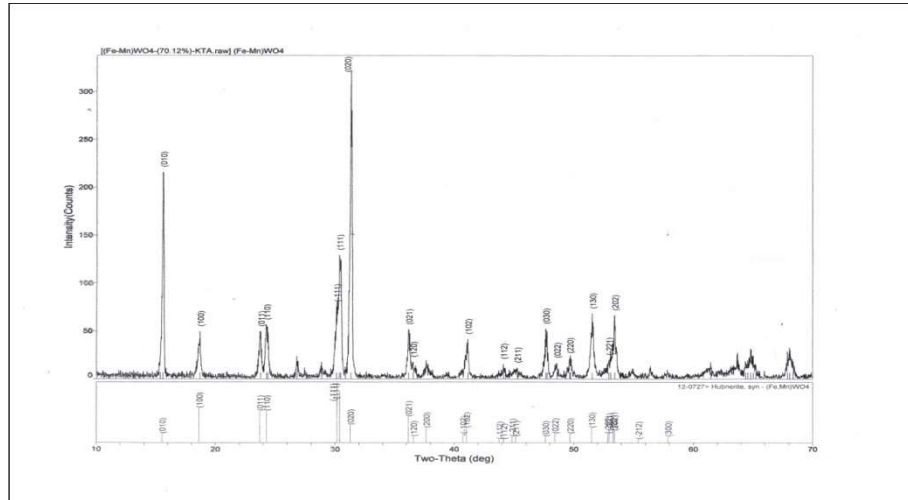


Figure 1. XRD pattern of wolframite (FeMnWO_4)

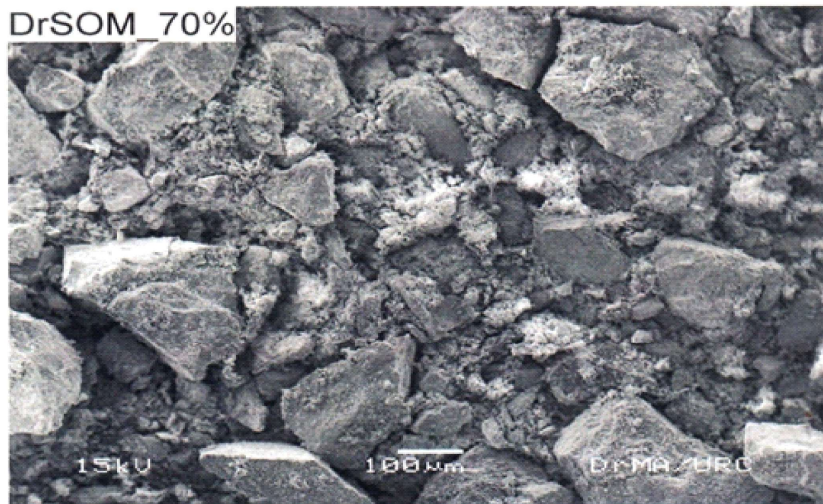


Figure 2. SEM micrograph of wolframite (FeMnWO_4)

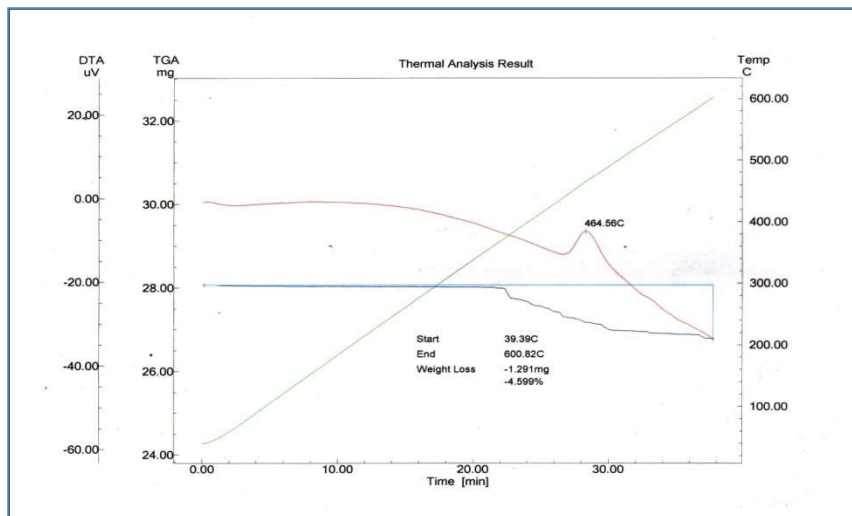


Figure 3. TGA and TDA curve of the FeMnWO_4

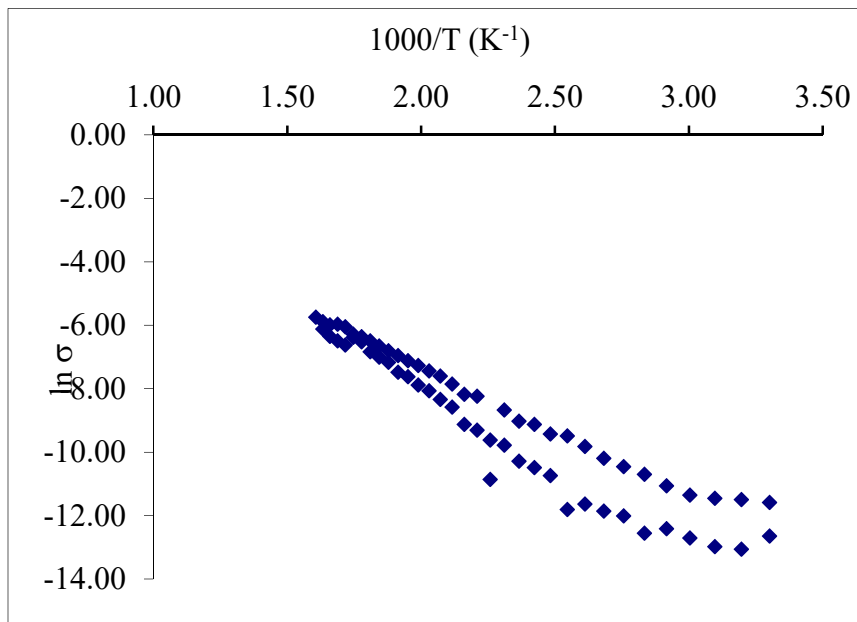


Figure 4. Plot of the $\ln \sigma$ versus $1000/T$ curve of the FeMnWO_4 in the temperature range 303 K – 623 K -303 K

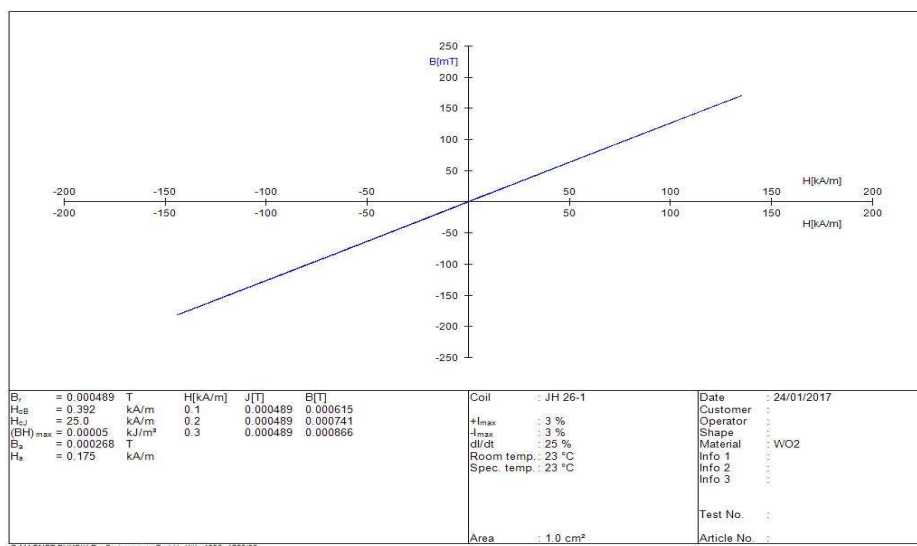


Figure 5. Magnetization curve of FeMnWO₄

Conclusion

Based on the analysis of electrical and magnetic properties, it may be safely suggested that the wolframite can be efficiently used as natural materials for production of pellets and sinters. In the present work, the crystal structure of FeMnWO₄ was observed orthorhombic from XRD analysis. SEM investigations on FeMnWO₄ (70%) at room temperature as-synthesized with orthorhombic form. SEM investigations are not adequate to confirm or otherwise the presence of deleterious phase. The conductivity of FeMnWO₄ sample was determined by annealing method and the activation energy was observed 0.4147 eV. And also the thermal loop was observed in the temperature range between 303K-623K-303K. A thermoanalysis test aids in understanding the behaviour of the wolframite when subjected to raised temperatures. The DTA analysis highlights the endothermic and exothermic effects and temperature ranges, which are correlated with the removal of physically present in the wolframite. It further highlights the occurrence of phase transformations. The values of weight loss during heating of the FeMnWO₄ sample was observed 4.599% from TGA curve and the oxidation process occurred from the exothermic peak at 464.56 °C DTA curve. The

phase transition of 70% wolframite (FeMnWO_4) can be changed orthorhombic to monoclinic structure, it should be analysed the temperature between 400°C and 500°C . The humidity sensors for meteorology is the direct applications that wolframite-type compounds with chemical formula FeMnWO_4 . The phase transformation is associated with a drastic thermochromic behavior and the marked temperature can be tuned with the tungsten concentration. Hence, the study opens up the window for the use and the optimization of a new generation of shock sensors and thermal sensors. In the magnetic properties of FeMnWO_4 was examined no hysteresis loop was registered. The dependency between magnetic field and magnetization was linear. B_r (remanent flux density) and H_c (coercive field) were observed 0.000489 T and $0.392 \times 10^3\text{ A/m}$ from B-H graph. The results obtained for this grade confirmed that the material in the examined was in a paramagnetic state. The relative permeability (μ_r) was obtained 1.2193, so the susceptibility value was 0.2193. The results obtained for this grade confirmed that the material in the examined was in a paramagnetic state.

Acknowledgement

I would like to express appreciation to Rector Dr Ba Han, Pro-rector Dr Khin May Aung, Dawei University for their encouragement and kind permission to undertake the present research. I also would like to express my profound thanks to Professor Dr Aung Myat Kyaw, Head of Department of Physics, and Professor Dr Marlar Myint, Department of Physics, Dawei University, for their kind permission to carry out this work, their encouragement and help during this work.

References

1. Braham J.B. Muwanguzi et al.,(2012), “Characterisation of the Physical and Metallurgical Properties of Natural Iron Ore for Iron Production”, Department of Material Science and Engineering, KTH Royal Institute of Technology, Brinellvägen 23, 100 44 Stockholm: Sweden.
2. Grega Klančnik, (2009), “Differential thermal analysis (DTA) and differential scanning calorimetry (DSC) as a method of material investigation”, University of Ljubljana, Faculty of natural science and engineering, Department of materials and metallurgy, Aškerčeva 12, SI-1000 Ljubljana, Slovenia.
3. Janusz J. Bucki, (2011), “ Magnetic Properties of Tungsten Composites”, Department of Material Science and Engineering, Warsaw University of Technology, Poland.
4. Ruiz-Fuertes J. “Room-temperature vibrational properties of multiferroic MnWO₄ under quasi-hydrostatic compression up to 39 GPa” Abteilung Kristallographie, Geowissenschaften, Goethe-Universität, 60438 Frankfurtam Main, Germany.
5. Veronica Blanco-Gutierrez, Alain Demourgues, Eric Lebreau, and Manuel Gaudon*, (2016), “Phase transitions in Mn(Mo_{1-x}W_x)O₄ oxides under the effect of high pressure and temperature”, Universite de Bordeaux, France.

www.Wolframite_mineral_info.htm

**MEASUREMENT OF EARTH RESISTANCE
IN PYAY UNIVERSITY COMPOUND
USING MODEL 2720 ER EARTH RESISTANCE TESTER**

Soe Soe thin *

Abstract

The purpose of this research work was to find out the temperature would have an effect on the earth resistance (resistivity). The earth resistance tester (Model 2720 ER) which containing three electrodes were used to measure the earth resistance. The earth resistance data were collected for different temperatures (actually different times). The electrodes were driven down to the same depth and equal distances apart in a straight line. According to the data, it was found that the earth resistance depends on temperature and seasonal variation. From the results, the values of earth resistance were less than 5Ω . According to the IEEE standard, this area is suitable for telecommunication facilities and distribution substation.

Key words; Earth resistance, Earth resistance tester, Fall of potential method.

Introduction

"Earth resistance" is the resistance of soil to the passage of electric current. Actually the earth is a relatively poor conductor of electricity compared to normal conductors like copper wire. But if the area of a path for current is large enough, resistance can be quite low and the earth can be a good conductor. It is the earth's abundance and availability that make it an indispensable component of a properly functioning electrical system.

Soil resistivity is the key factor that determines what the resistance of a grounding electrode will be, and to what depth it must be driven to obtain low ground resistance. The resistivity of the soil varies widely throughout the world and changes seasonally. Soil resistivity is determined largely by its content of electrolytes, which consist of moisture, minerals and dissolved salts. A dry soil has high resistivity if it contains no soluble salts.

Measurements of earth resistivity are useful also for finding the best location and depth for low resistance electrodes. Such studies are made, for example, when a new electrical unit is being constructed; a generating station,

¹. Dr, Lecturer, Department of Physics, University of Pyay

substation, transmission tower, or telephone central office. Finally earth resistivity may be used to indicate the degree of corrosion to be expected in underground pipelines for water, oil, gas, gasoline, etc.

2. Measuring Earth Resistance

Earth resistance meter is connected with the special ground components introduced on the earth by mean of the checking cables. Ground components will be put in a straight line (place the green cable for ground rod, then connect the yellow one and the red cable for the second ground rod). All measurements are done in dry earth condition. Everything is ready to connect the earth resistance meter to check the earth connection of building. Data collecting is started from 9:00 AM and 12:00 noon exactly. Surrounding temperature is known using thermometer and read in Celsius scale. This can be also used inside a building to check that water connections with earth work properly. This meter has been developed according to IEC 1010-1 standard and fulfills all the safety conditions for control electronic mechanism.

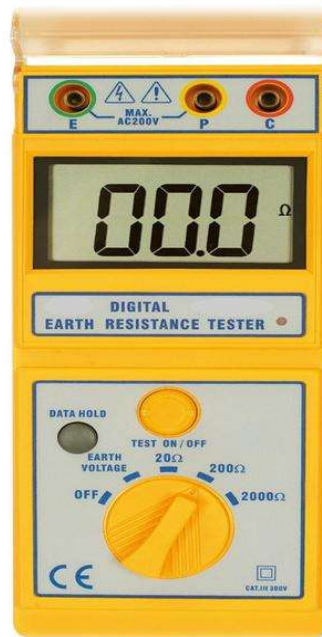


Figure 2.1: Earth resistance tester (Model 2720 ER)



Figure 2.2: Earth resistance measuring area (Palae hostel, Pyay University)



Figure 2.3: Setting up to measure the earth resistance

3. Experimental Results

The measurement data of the earth resistance (using 2720 ER earth tester) is shown in table 3.1 to 3.4. The data are collected two times daily (9:00 am and 12:00 am).

Table 3.1 Measurement data for 2016 October

Date	9:00 AM		12:00 AM(noon)	
	Temperature (°C)	Resistance (Ω)	Temperature (°C)	Resistance (Ω)
12-Oct			34	3.72
13-Oct	32	3.69	34	3.66
14-Oct	32	3.65	34	3.6
15-Oct	31	3.67	34	3.64
16-Oct	32	3.62	34	3.64
17-Oct	31	3.66	32	3.64
18-Oct	30	3.61	32	3.62
19-Oct	31	3.6	32	3.59
20-Oct	31	3.57	33	3.55
21-Oct	32	3.65	33	3.56
22-Oct	31	3.59	33	3.56
23-Oct	31	3.6	33	3.59
24-Oct	30	3.6	33	3.6
25-Oct	30	3.61	32	3.57
26-Oct	30	3.58	31	3.62
27-Oct	29	3.55	31	3.53
28-Oct	29	3.6	31	3.57
29-Oct	30	3.64	32	3.58
30-Oct	29	3.63	31	3.62
31-Oct	30	3.54	32	3.62

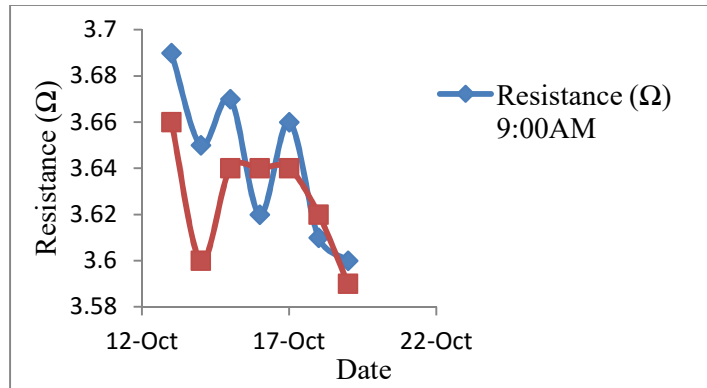


Figure 3.1: Resistance vs date and time graph (13 October 2016 to 19 October 2016)

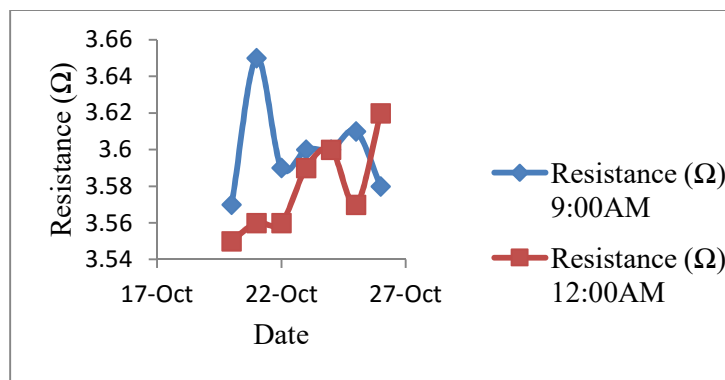


Figure 3.2: Resistance vs date and time graph (20 October 2016 to 26 October 2016)

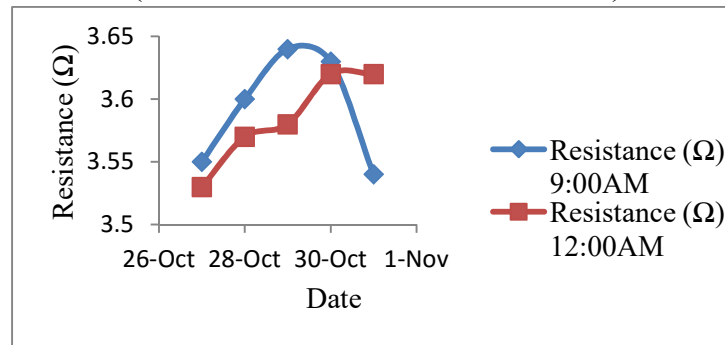


Figure 3.3: Resistance vs date and time graph (27 October 2016 to 31 October 2016)

Table 3.2. Measurement data for 2016 November

Date	9:00 AM		12:00 AM(noon)	
	Temperature (°C)	Resistance (Ω)	Temperature (°C)	Resistance (Ω)
1-Nov	29	3.57	32	3.57
2-Nov	31	3.62	31	3.62
3-Nov	29	3.65	31	3.65
4-Nov	29	3.71	33	3.64
5-Nov	30	3.69	32	3.64
6-Nov	30	3.66	32	3.66
7-Nov	30	3.61	31	3.66
8-Nov	30	3.65	32	3.62
9-Nov	30	3.69	33	3.6
10-Nov	31	3.6	32	3.54
11-Nov	30	3.55	31	3.55
12-Nov	30	3.6	32	3.55
13-Nov	29	3.6	31	3.58
14-Nov	29	3.64	31	3.58
15-Nov	28	3.68	31	3.64
16-Nov	28	3.64	30	3.63
17-Nov	28	3.68	30	3.65
18-Nov	28	3.65	30	3.63
19-Nov	27	3.7	29	3.7
20-Nov	27	3.7	29	3.68
21-Nov	25	3.74	28	3.77
22-Nov	25	3.73	27	3.74
23-Nov	25	3.72	28	3.73
24-Nov	23	3.82	27	3.75
25-Nov	24	3.78	26	3.75
26-Nov	25	3.77	27	3.78
27-Nov	25	3.8	27	3.58
28-Nov	25	3.81	28	3.94
29-Nov	25	3.83	28	3.78
30-Nov	27	3.74	30	3.74

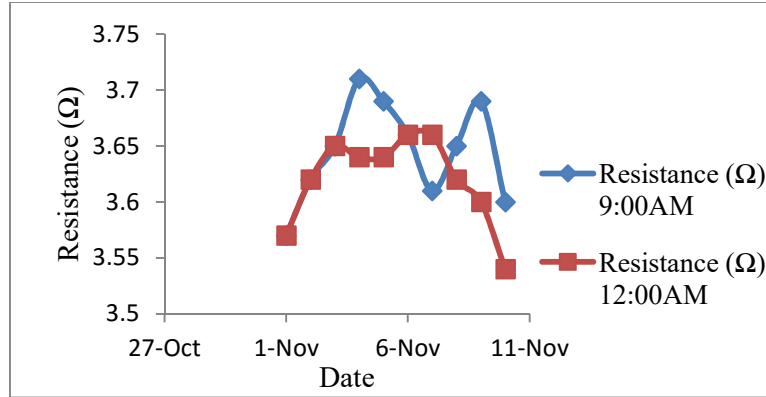


Figure 3.4: Resistance vs date and time graph (1 November 2016 to 10 November 2016)

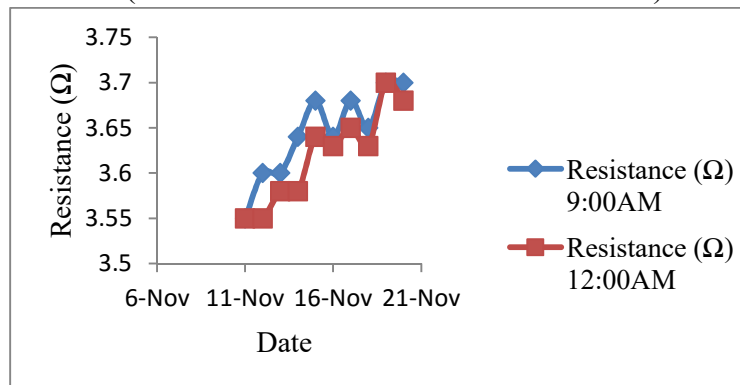


Figure 3.5: Resistance vs date and time graph (11 November 2016 to 20 November 2016)

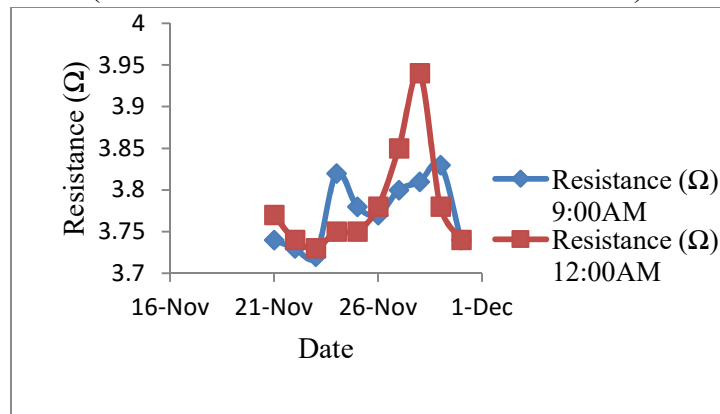


Figure 3.6: Resistance vs date and time graph (21 November 2016 to 30 November 2016)

Table 3.3. Measurement data for 2016 December

Date	9:00 AM		12:00 AM(noon)	
	Temperature (°C)	Resistance (Ω)	Temperature (°C)	Resistance (Ω)
1-Dec	26	3.82	29	3.77
2-Dec	27	3.84	30	3.81
3-Dec	27	3.86	30	3.84
4-Dec	27	3.84	30	3.92
5-Dec	26	3.88	29	3.9
6-Dec	26	3.87	29	3.87
7-Dec	26	3.96	29	3.82
8-Dec	25	3.84	29	3.86
9-Dec	25	3.87	29	3.96
10-Dec	25	3.97	29	3.93
11-Dec	25	3.91	29	3.94
12-Dec	25	3.96	29	3.91
13-Dec	26	3.96	29	3.87
14-Dec	25	3.96	28	3.91
15-Dec	23	3.95	28	3.93
16-Dec	25	3.95	28	3.95
17-Dec	25	3.98	28	3.96
18-Dec	26	3.94	30	3.9
19-Dec	26	3.94	30	3.89
20-Dec	25	3.9	29	3.91
21-Dec			27	3.9
22-Dec	22	3.98	26	3.93
23-Dec	23	3.95	28	3.95
24-Dec	26	4		
25-Dec	26	3.92	27	3.95
26-Dec	26	3.91	30	3.96
27-Dec	26	3.95	30	3.94
28-Dec	27	3.97	29	3.91
29-Dec	24	3.97	29	3.97
30-Dec	25	3.96	28	3.98

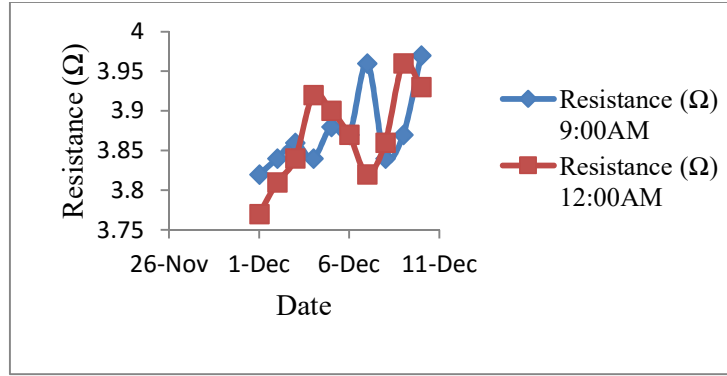


Figure 3.7: Resistance vs date and time graph (1 December 2016 to 10 December 2016)

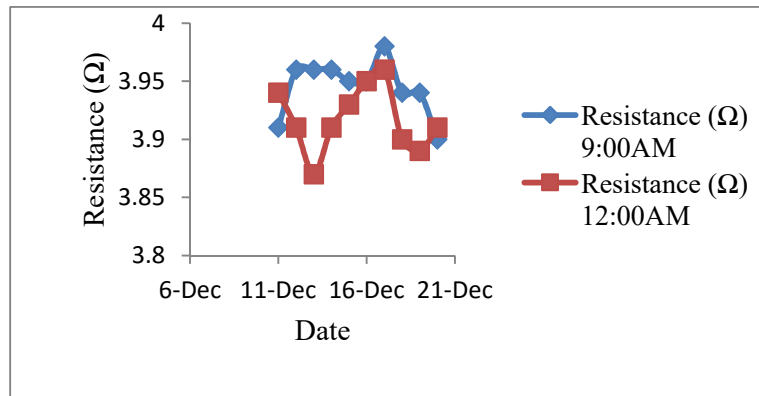


Figure 3.8: Resistance vs date and time graph (11 December 2016 to 20 December 2016)

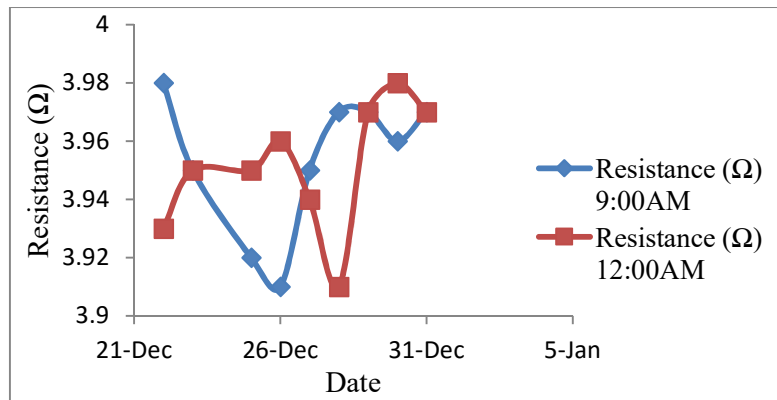


Figure 3.9: Resistance vs date and time graph (22 December 2016 to 31 December 2016)

Table 3.4. Measurement data for 2017 January

Date	9:00 AM		12:00 AM(noon)	
	Temperature(°C)	Resistance (Ω)	Temperature(°C)	Resistance (Ω)
1-Jan	24	4		
2-Jan				
3-Jan	24	3.49	26	3.48
4-Jan	24	3.48	28	3.49
5-Jan	25	3.49	29	3.49
6-Jan	25	3.49	29	3.49
7-Jan	24	3.51	27	3.5
8-Jan	23	3.52	28	3.51
9-Jan	24	3.53	28	3.52
10-Jan	25	3.53	30	3.52
11-Jan	24	3.54	28	3.53
12-Jan	23	3.54	27	3.53
13-Jan	22	3.55	27	3.55
14-Jan	21.5	3.57	27	3.56
15-Jan	22	3.58	27	3.57
16-Jan	21	3.59	26	3.59
17-Jan	21	3.59	26	3.59
18-Jan	22	3.6	28	3.59
19-Jan	23	3.6	27	3.6
20-Jan	22	3.6	28	3.59
21-Jan	24	3.6	29	3.59
22-Jan	23	3.6	29	3.6
23-Jan	24	3.6	30	3.6
24-Jan	25	3.59	30	3.59
25-Jan	26	3.59	30	3.58
26-Jan	26	3.58	30	3.58
27-Jan	24	3.58	29	3.58
28-Jan	24	3.58	28	3.59
29-Jan	23	3.59	30	3.59
30-Jan	23	3.6	28	3.59
31-Jan	23	3.6	29	3.61

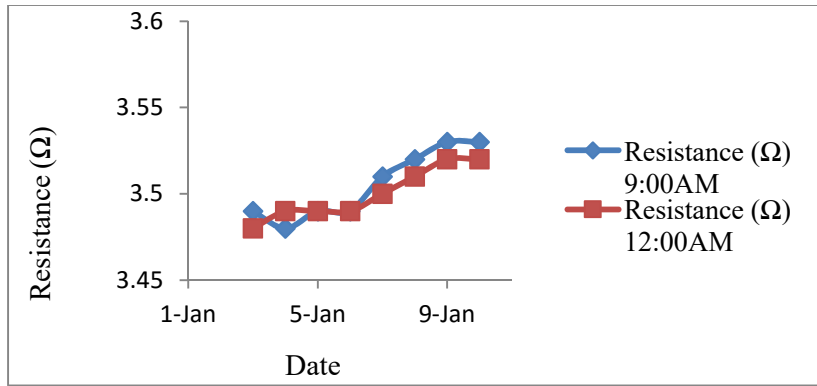


Figure 3.10: Resistance vs date and time graph (3 January 2017 to 10 January 2017)

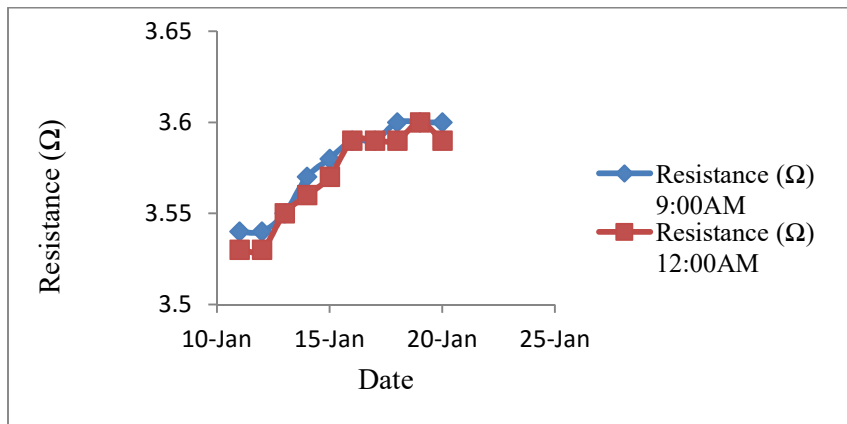


Figure 3.11: Resistance vs date and time graph (11 January 2017 to 20 January 2017)

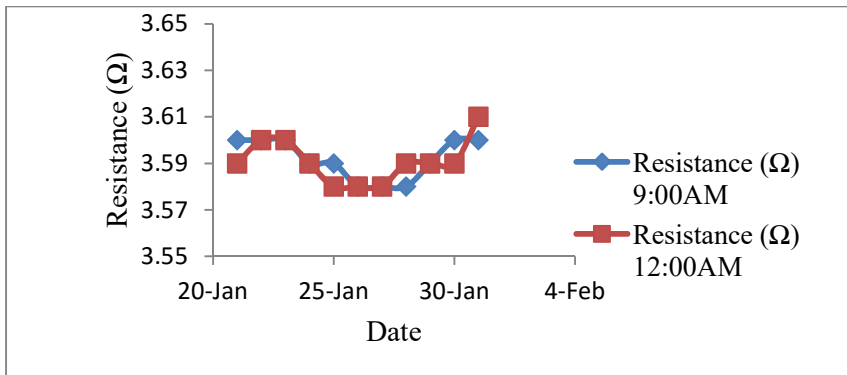


Figure 3.12: Resistance vs date and time graph (21 January 2017 to 31 January 2017)

Discussion and Conclusion

Discussion

In this research work, the earth resistance datum have been collected since mid- October (13 October, 2016) to the end of January (31 January, 2017). The datum were collected two times for every day. Collected parameters are environ- mental temperature, electrode temperature, ground temperature and earth resistance. From those data, earth resistivity can be calculated by using the equation of $2\pi AR$. Where, A is the distance between each pair of electrodes.

According to the collected datum and calculated values, the earth resistance changes proportionally with temperatures. From the graph of figure 4.1 shows, the value of earth resistance is decreased and stable from the first week of January 2017. This means that earth resistance is affected upon temperature and moisture of the environment. So, the earth resistivity of the soil depends on seasonal variations also. From the results, the values of each resistance are lower than 4Ω (collected data results). According to the IEEE standard, the area is suitable for telecommunication facilities, distribution substation and industrial plant.

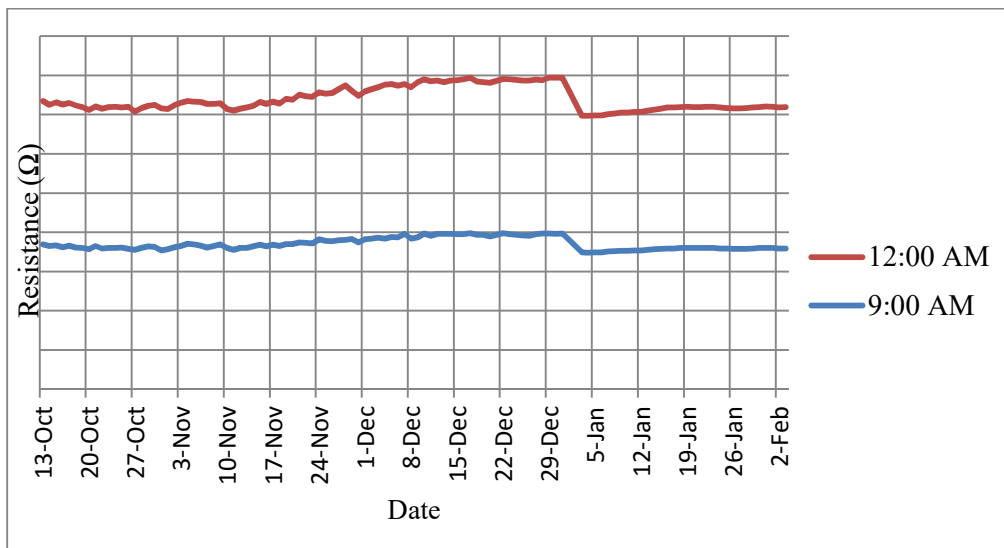


Figure 4.1: Date and temperature dependence of resistance graph

Conclusion

It is important for a facility to have a good grounding system. The safety of all personnel and equipment is at stake. In order to be sure that a good grounding system is in place, it is necessary to maintain a low resistance of all the electrodes and a low resistivity of the local soil. There are different methods for obtaining these measurements. Due to variations in electrodes and soil, a number of repeated measurements should be taken and evaluated for a consistency.

Acknowledgements

I would like to thank Professor Dr Pyone Pyone Shein, Head of Department of Physics, Pyay University, Professor Dr Naw Htoo Lar Phaw, Department of Physics, Pyay University, Pro-rectors from Pyay University Dr Nyunt Soe and Dr Nilar Myint for their kind permission to do this work.

I also would like to thank Rector(YU)Dr Pho Kaung, Professor Dr Khin Khin Win(Head of Department of Physics, YU) and Professor Dr Soe Soe Nwe (YU) for their permission to present this research report.

Finally, I would like to express my gratitude to all teachers for their kind advices and help in completing this research work.

References

- E.D. Sunde, (1968), "Earth Conduction Effects in Transmission System", Dover Publications, New York.
- C. Arnovx, "Understanding Ground Resistance Testing", AEMC Instruments, <http://www.aemc.com>.
- G.F. Tagg, George, (1964), "A Practical Guide to Earth Resistances", Newnes Limited, London.
- S.K. Pole and A.K. Sharma, "Analysis on the Factors Affecting Resistance of the Earth Electrode", International Journal of Engineering Research & Technology (IJERT), Vol. 2 Issue 5, Received May – 2013, <http://www.ijert.org>.

FABRICATION OF POROUS SILICON FOR MEMS DEVICES APPLICATION

Kyauk Khe Sein¹, Ye Chan²

Abstract

The porous layers can be used as sacrificial layers due to the high reactivity of the material which leads to a new class of micromachined MEMS devices. The porous silicon (PS) has been fabricated on p-type silicon wafers by anodization, photolithographic metal assisted etching and metal assisted chemical etching techniques. The surface and cross-sectional inspections of the silicon wafers were performed with a Scanning Electron Microscope (SEM) and the porosity of wafers is determined Fourier Transform Infrared Spectroscopy (FTIR). It is found that the porous formation in silicon can control with adjustable metal concentration and time by metal assisted etching method. According to the characterization results the metal assisted chemical etching method gives better porous morphological structure which is suitable for MEMS and sensor applications.

Keywords: porous silicon, MEMS, microsensor

1. Introduction

With the development of micro systems, there is an increasing demand for integrable porous materials. In addition to those conventional applications, such as filtration, wicking, and insulating, many new micro devices, including micro reactors, sensors, actuators, and optical components, can benefit from porous materials [Natalya Tokranova, 2003]. Conventional porous materials, such as ceramics and polymers, however, cannot meet the challenges posed by micro systems, due to their incompatibility with standard micro-fabrication processes.

Porous Si and its modifications are allowed to fabricate a number of sensors for MEMS [Wolfgang Benecke]:

- gas-sensitive sensors of impedance (conductivity, capacity) or so-called “electrophysical sensors”;

¹. Assistant Lecturer, Universities’ Research Centre, University of Yangon

². Professor, Head of Universities’ Research Centre, University of Yangon

- optical and optoelectronic sensors (for example, luminescent photovoltaic, photoresistivity ones);
- sensors of mechanical strains (change of volt- ampere characteristics of p-n junctions on porous silicon);
- sensors for determination of changing the intensity of magnetic field in which the change of magnetic permeability is used.

In general, the sponge-like structure of PS is formed by an electrochemical etching process of a silicon substrate in hydrofluoric acid (HF) based electrolytes. The mechanism of pore generation depends on the availability of positive charge in the substrate. Positive charge carriers react at the silicon surface with fluorine ions. Thereby, a parasitic oxidation is an important aspect to release silicon atoms with HF from the substrate to create pores. The free standing porous skeleton retains the same chemical properties as the bulk silicon and the crystalline structure of the silicon is not changed. The new resulting surface is enlarged and very reactive compared to the original silicon surface. Various pore dimensions can be formed and tuned by the fabrication parameters [Jin Zheng, 2006].

The different types of porous silicon formed due to variations formed in the etching/ deposition conditions can be classified (IUPAC classification) into three categories viz.:

	<u>Pore size range</u>
1. Micro porous silicon	< 2 nm
2. Meso porous Silicon and	2 - 50 nm
3. Macro porous silicon.	> 50 nm

In this paper, porous silicon (PS) has been fabricated on p-type silicon wafers by anodization with different HF ratio and different current density, lithographic metal assisted chemical etching, and Ag assisted chemical etching.

1.1 Porous Formation Mechanisms in Anodization

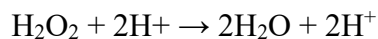
In order to produce and optimize porous silicon materials for each application, it is important to understand the fundamentals of porous silicon formation. The most common method of forming porous silicon is electrochemical dissolution of silicon in a hydrofluoric acid (HF) based electrolyte. In the dissolution process, a silicon wafer serves as the anode, while any HF resistant conducting material, such as Pt, is used as the cathode. For this reason, the dissolution process is often called anodization.

Details of the chemical reactions of pore formation are not fully understood yet. Several theories suggest that two types of dissolution processes may be involved. The first one is direct dissolution, where the presence of holes weakens Si-Si backbonds and Si-H surface bonds, allowing them to be attacked by negative F⁻ ions in the HF solution. A compound (SiF₄) is then formed at the surface and breaks away from the substrate. In this reaction path, 1,2,3, or 4 holes may be involved. In the other dissolution process, the anodically biased silicon surface is first oxidized. The silicon dioxide is then dissolved by HF. This reaction path requires four holes. Since in the overall reaction the valence, the number of consumed holes for each dissolved silicon atom, is around 2.7, it is believed that the two dissolution processes must coexist. The actual occurrence percentage of each process is self adjusting, decided by the anodization conditions. Since the direct dissolution path etches silicon anisotropically while the oxidation path is more isotropic, any shift of the balance between two processes may cause change in morphologies of the resulting porous silicon [Bisis, et. al., 2000].

1.2 Pore Formation Mechanism in Metal-Assisted Chemical Etching

As far as the mechanisms and reactions involved in the formation of PS structures produced by metal-assisted etching is concerned, it is well-known that chemical and electrochemical reactions occur near the interface between the noble metal and the silicon substrate when the system is immersed in an etchant composed of HF and H₂O₂. So far, several reaction models have been proposed to describe the electrochemical reactions taking place during the formation of porous silicon by metal-assisted etching [Chunlin He, et. al., 2016]. In this system, the noble metal works as a cathode,

where hydrogen peroxide is reduced at the metal surface following these electrochemical reactions while the silicon works as the anode:



In summary, metal-assisted etching of porous silicon can be divided into four stages Figure 1.

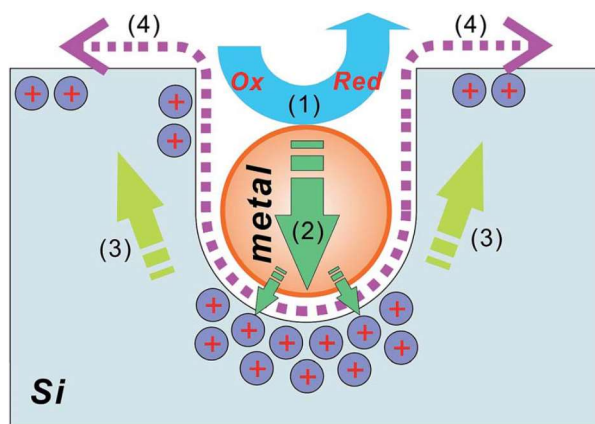


Figure 1. Illustration of the metal-assisted chemical etching process:

- (1) Reduction of an oxidative agent (such as H_2O_2) catalyzed by a noble metal particle;
- (2) Injection of the holes generated during the reduction reaction, into the silicon substrate, with the highest hole concentration underneath the metal particle;
- (3) Migration of holes to silicon sidewalls and surfaces; and
- (4) Removal of oxidized silicon via HF.

2. Experimental

2.1 Porous Silicon Preparation by Anodization Method

There are two types of anodization cells which is single tank and double tank cells that are commonly used to produce porous silicon. In the single-tank cell, a metallic contact is made to the backside of the wafer. An O-ring is used to seal around the edge of the wafer so that only the front side of

the sample is exposed to the electrolyte. Due to its simple configuration, single-tank cell is the most commonly used arrangement.

All of the etching cells are made of HF resistant materials, such as Teflon and polypropylene. Since HF is a very dangerous and aggressive chemical, safety has been given highest priority in the designs of all etching cells. Figure 2 shows anodization in a single-tank Teflon holder with Pt electrode for etching small samples. The schematic diagram for assembling and using this fixture is shown in Figure 3. The cover piece and the bottom piece of the holder are bolted together during the etching process to hold a silicon sample in place.



Figure 2. Anodization set up by single-tank Teflon holder with Pt electrode for etching small samples

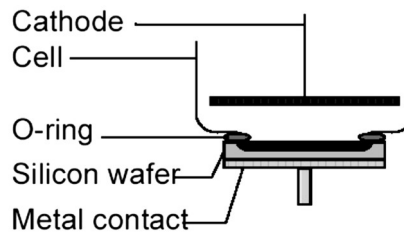


Figure 3. Schematic diagram for assembling of anodization

2.2 Porous Silicon Preparation by Metal Assisted Chemical Etching Method

Si wafers were etched into a single tank cell with a different concentration and amount of AgNO_3 solution by adding in a solution of 1:1:2 (V:V:V) 40%HF:30% H_2O_2 : H_2O . The remaining Ag is removed from the textured Si surface by etching in aqueous solution of 30% HNO_3 at room temperature for 20 min.

On the other technique, the silicon wafers were washed with ethanol and acetone under ultrasonic wave, then a silver particle thin layer was electroless deposited by immersing the silicon wafers in a 5 mM AgNO_3 salt solution for 5 min at room temperature, after the Ag-covered Si wafers were slightly rinsed in deionized water, they were immersed in a solution of 1:1:2 (V:V:V) 40%HF:30% H_2O_2 : H_2O in ultrasonic bath for 30min. Finally, the etched Si wafers were rinsed thoroughly with deionized water, ethanol and acetone, respectively, and dried.

2.3 Selected Porous Silicon Preparation by Photolithography Method

PS structures with precisely controlled and exquisitely defined morphology and geometric features can be produced when the surface of the silicon wafer is patterned by lithographic techniques prior to the etching step. In particular, some lithographic methods have demonstrated outstanding results when combined with metal-assisted etching in this work.

3. Results and Discussion

3.1 Characterization of Porous Silicon Prepared by Anodization

Table 1 shows comparison of porous formation with different current density and electrolyte solution ratio and same etching time by anodization method. The size of porous increased with HF ratio according to the SEM images.

Scanning electron microscope (SEM) has been used to analysis surface morphology and cross sectional view of the PS layers produced with different formation parameters. It is found that porous formation in silicon as shown in Figure 4 by anodization. Although porous formation is uniform in electrolyte

HF: ethanol = 2:1 ratio, it is not uniform in HF: ethanol = 1:1 ratio at current density 10mA/cm² and porous formation is low.

Another porous formation is shown in Figure 5 at same ratio (HF: ethanol: water = 1:2:3) with different current density 10mA/cm² and 25mA/cm². The porous formation using 25mA/cm² is better than 10mA/cm² according to the SEM images.

Figure 6 shows the porous silicon formation with different electrolyte ratio and current density. It is also found that the porous formation depends on electrolyte ratio and current density. Thus porous silicon making by anodization is difficult to control porous formation and to find optimum point.

Table 1. Comparison of porous formation with different electrolyte ratio and current density by anodization method

Method	Electrolyte Solution	Current Density (mA/cm ²)	Etching Time (min)	Porous Formation	Average Pore Size(μm)
A1	HF:ethanol (1:1)	10	10	Non-uniform	1
A2	HF:ethanol (2:1)	10	10	Uniform	3
A3	HF:ethanol:H ₂ O (1:2:3)	10	10	Uniform	Unobservable
A4	HF:ethanol:H ₂ O (1:2:3)	20	10	Uniform	5
A5	HF:ethanol:H ₂ O (1:1:3)	10	10	Non uniform	4
A6	HF:ethanol:H ₂ O (1:1:3)	20	10	Uniform	Unobservable

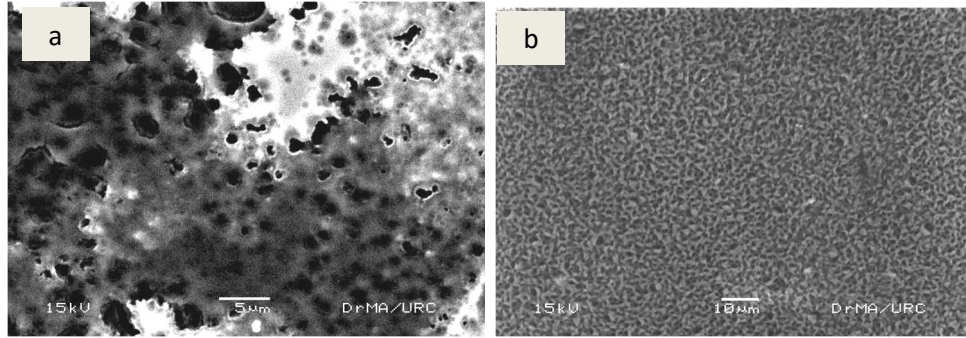


Figure 4. SEM photographs of porous formation using (a) A1 and (b) A2 method

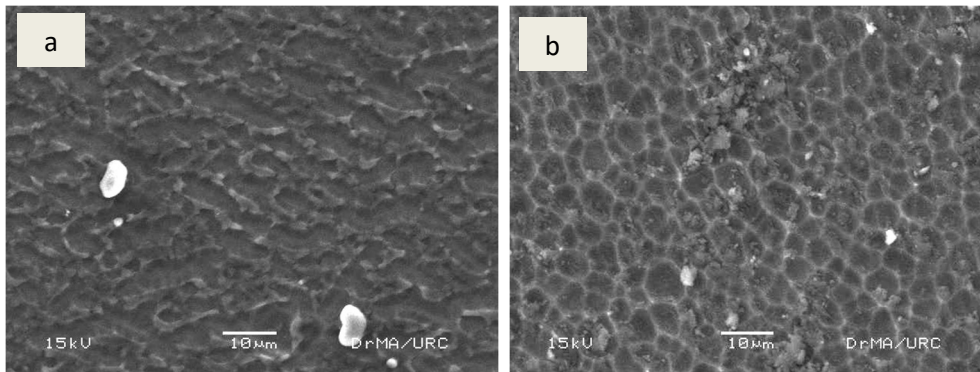


Figure 5. SEM photographs of porous formation using (a) A3 and (b) A4 method

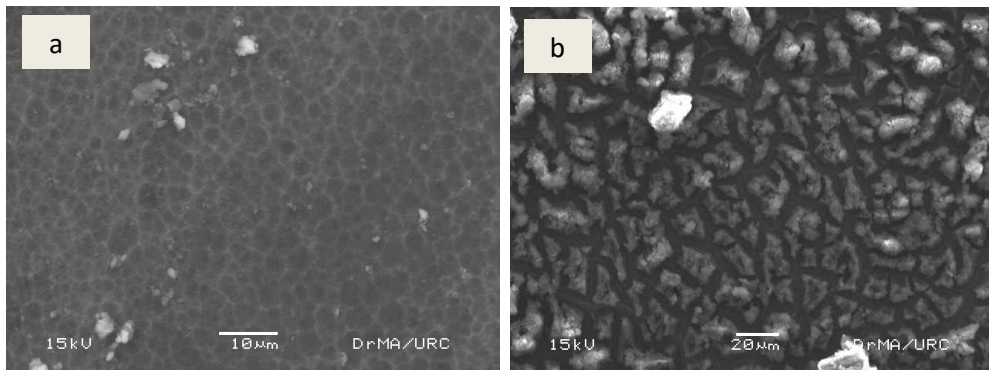


Figure 6. SEM photographs of porous formation using (a) A5 and (b) A6 method

3.2 Characterization of Porous Silicon prepared by Metal Assisted Chemical Etching

Another technique to make porous silicon is metal assisted chemical etching. In this research, silver is used as novel metal for metal assisted etching. Table 2 shows the comparison of porous formation with different chemical ratio and etching time by metal assisted chemical etching.

It is found that the porous formation is very uniform in 4.7mM of AgNO_3 concentration solution with hydrofluoric acid, hydrogen peroxide and water (1:1:2) volume ratio according to SEM images (Figure 7 – 9). It is also found that the pore size depend on the etching times. The average pore sizes are 2 μm for 1 hour, 3 μm for 2 hours and 4 μm for 3 hours etching time as shown in Table 3. Figure 15 shows the porous thickness or pore length using C1 method after 3 hours etching time. Therefore, this etching method was used to fabricate micro sensor in this work.

From the Figure 12, it is found that nano porous formation in low AgNO_3 ratio but porous formation is low. In strong AgNO_3 ratio, the porous formation is uniform but it is found that silicon is strong etched by this ratio (Figure 13). Thus, it is found that porous formation can control by changing of AgNO_3 concentration and amount.

The next method is silver-layer deposition before etching (SDBE). The silicon substrate deposited by electroless plating. Figure 14 is the SEM surface morphology of PS wafer produced by SDBE method in which 5 mM AgNO_3 salt solution used for 15 min at room temperature for plating. It is found that the density and thickness of the Ag nanoparticle layer increase with prolonged immersion time (plating time), however, the size of the Ag particles remains almost the same. Fine, uniform and single dispersed Ag nanoparticles benefits to prepare homogenous meso porous structure on the Si surface. It estimates porous size is less than 0.5 μm . Thus, it is difficult to measure accuracy pore size with current facility.

Table 2. Comparison of porous formation with different chemical ratio and etching time by metal assisted chemical etching

Method	HF:H ₂ O ₂ :H ₂ O	AgNO ₃	Etching (hour)	Porous Formation	Average Pore size (μm)
C1	1:1:2	0.2 mL (4.7mM)	1	Uniform	2
C2	1:1:2	0.3 mL (4.7mM)	1	Uniform	3
C3	1:1:2	0.6mL (4.7mM)	1	Uniform	Unobservable
C4	1:1:5	0.2 mL (2.3mM)	5	Uniform	1
C5	1:1:5	0.1 mL (2.3mM)	5	Uniform	Unobservable
C6	5:5:0	1mL (5mM)	15min	Uniform	0.5
C7	1:1:0	1mL (0.2M)	15min	Uniform	Unobservable

Table 3. Comparison of pore formation for different etching time using C1 method

Method	HF:H ₂ O ₂ :H ₂ O:AgNO ₃ (40%V:30%V:V: 4.7mM of V)	Etching time (hour)	Average Pore Size (μm)
C1	5:5:10:1	1	2
C1	5:5:10:1	2	3
C1	5:5:10:1	3	4

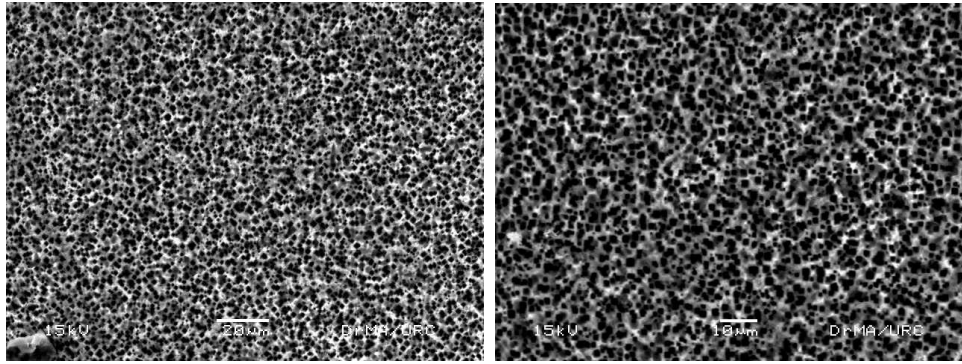


Figure 7. SEM photographs of porous formation using C1 method

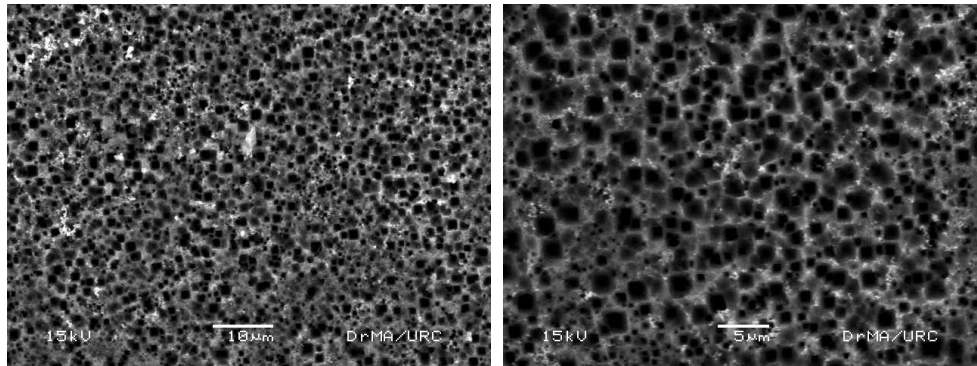


Figure 8. SEM photographs of porous formation using C2 method

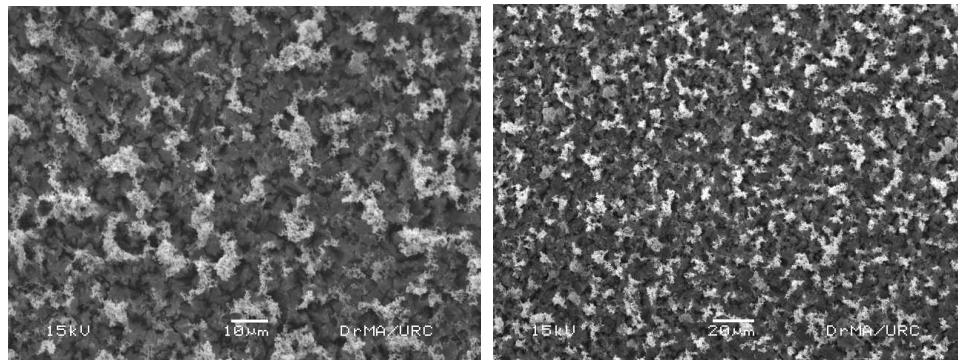


Figure 9. SEM photographs of porous formation using C3 method

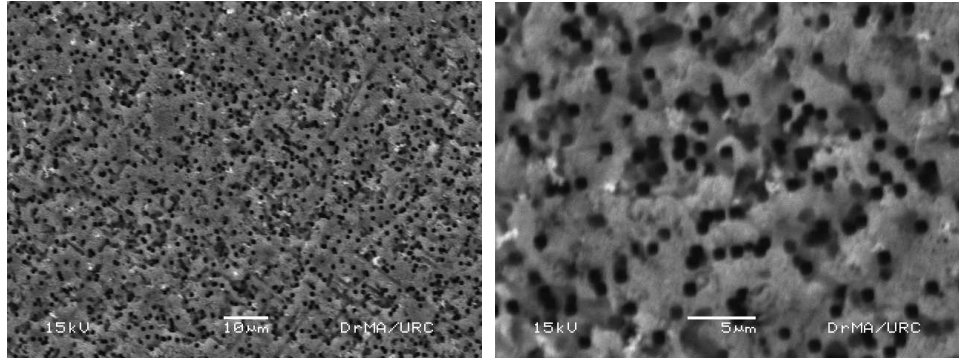


Figure 10. SEM photographs of porous formation using C4 method

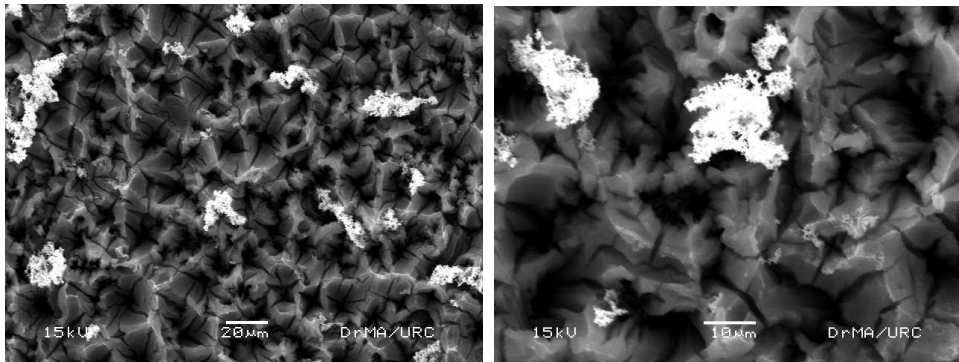


Figure 11. SEM photographs of porous formation using C5 method

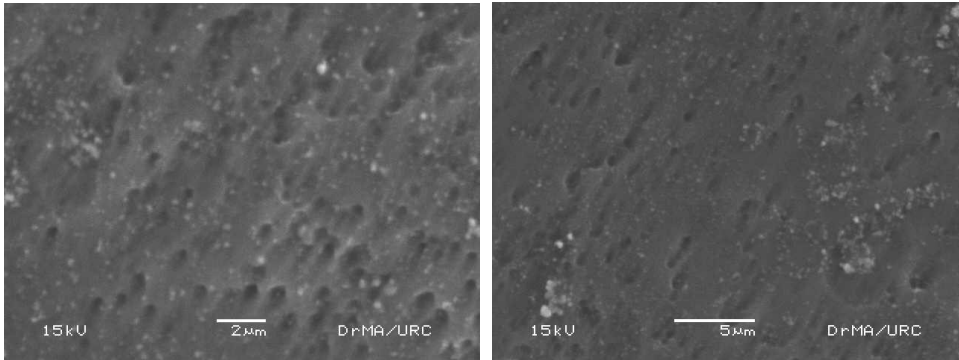


Figure 12. SEM photographs of porous formation using C6 method

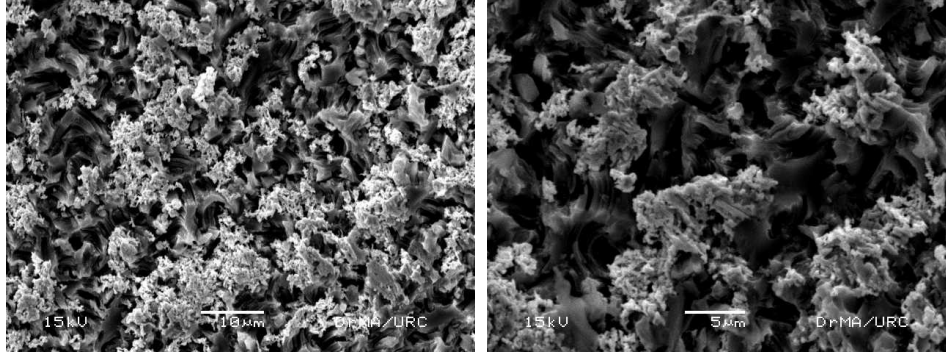


Figure 13. SEM photographs of porous formation using C7 method

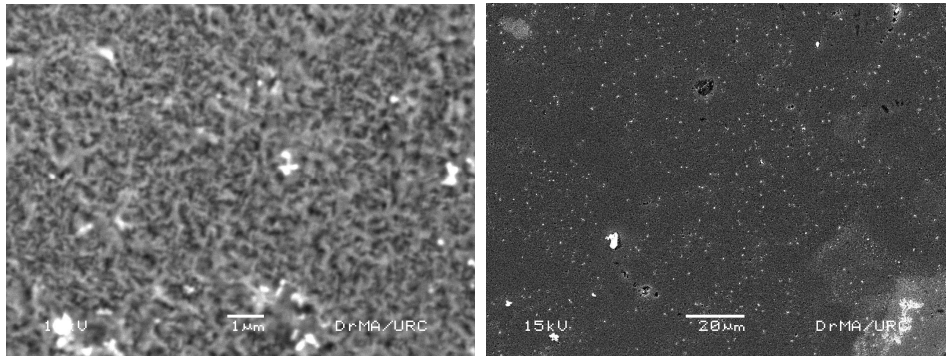


Figure 14. SEM images of porous formation using SDBE method

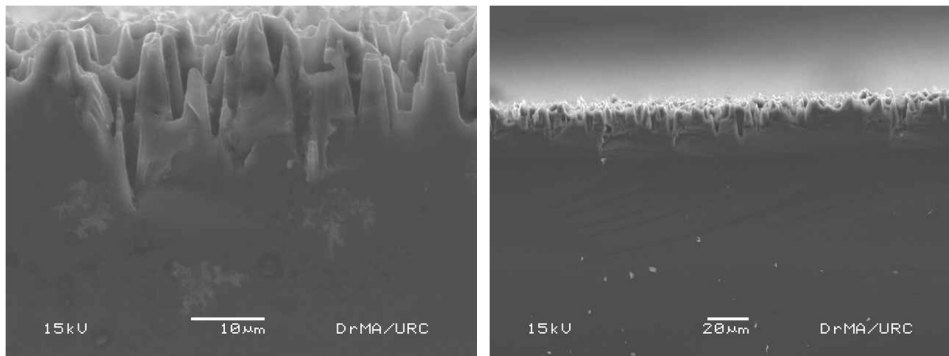


Figure 15. SEM images of porous thickness or pore length using C1 method after 3 hours etching time

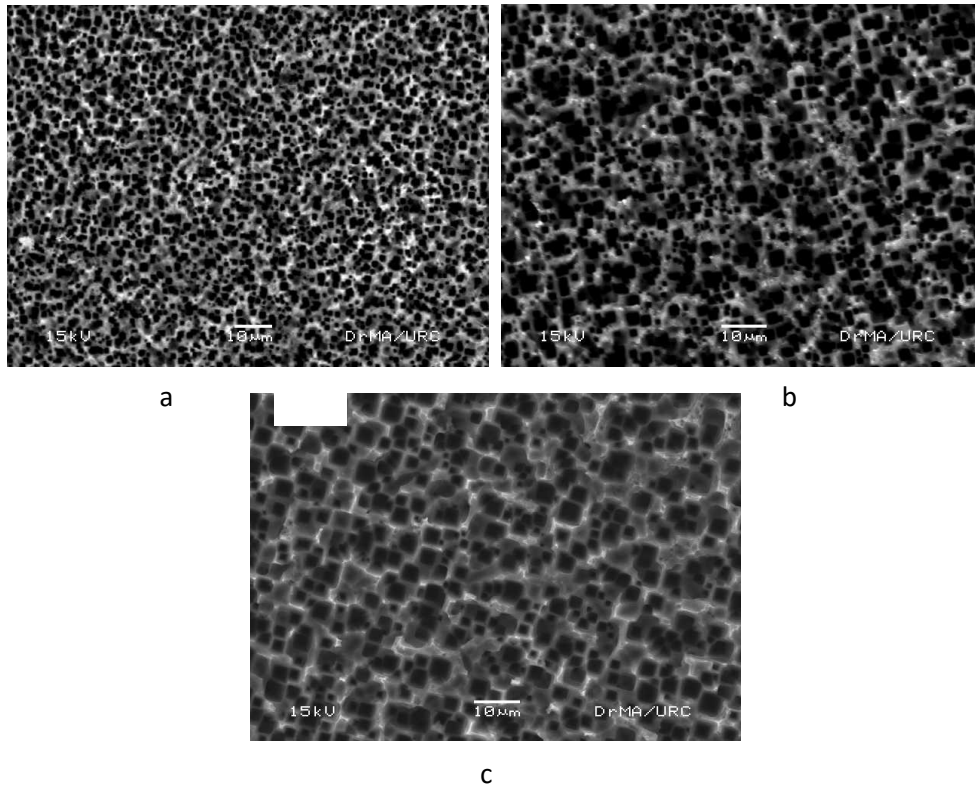


Figure 16. SEM photographs of porous size formation using C1 method for (a) 1 hour (b) 2 hours (c) 3 hours

3.3 Characterization of Porous Silicon prepared by Hybrid Method

The lithographic approach makes it possible to produce porous silicon on specific area with controlled geometry, morphology and size. The mask design is limited to get sub micron size and the mask is used with 40 μm resolution. Therefore, lithographic approach can select that porous area. The porous formation with Ag assisted chemical etching using lithographic approach is shown in Figure 17. A rounded porous size area is about 250 μm². This method can make a nano porous formation in the specific area.

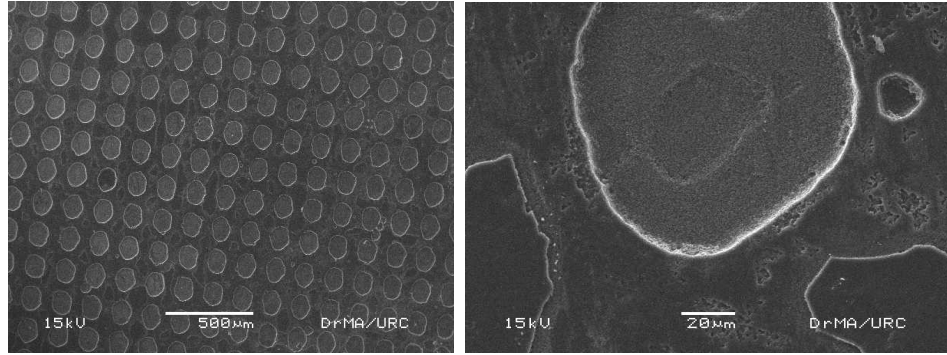


Figure 17. SEM photographs of porous formation using lithographic metal assisted chemical etching

3.4 Characterization of Porous Silicon by XRD

One important property of porous silicon is that its skeleton maintains the structure of silicon crystalline after anodization by X-ray topography studies. The X-ray beam is diffracted at specific angular positions with respect to the incident beam depending on the phases of the sample. When crystal size is reduced toward nanometric scale, then a broadening of diffraction peaks is observed and the width of the peak is directly correlated to the size of the nanocrystalline domains [Lorusso A., et. al. 2009]. The broadening peak of the PS can be compared with bulk silicon as shown in Figure 18.

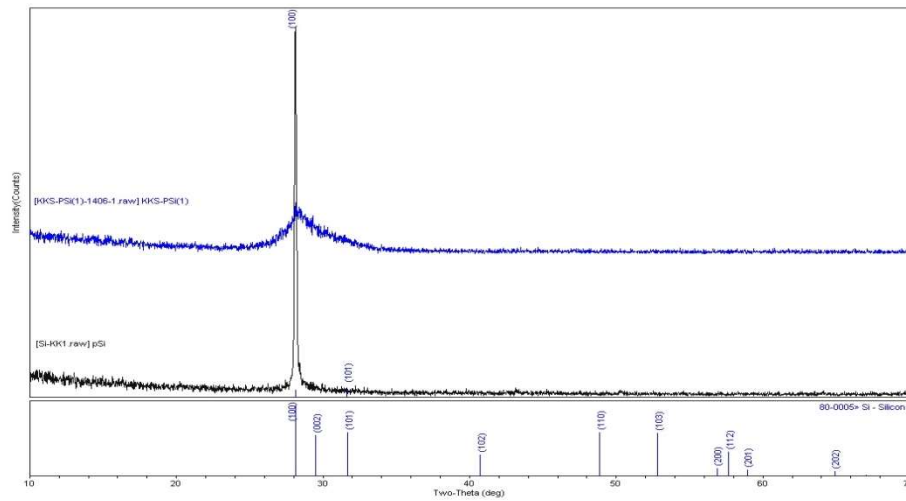


Figure 18. XRD characterizations of bulk silicon and porous silicon

3.5 Characterization of Porous Silicon by FTIR

Surface chemical composition of PS is best probed with Fourier Transform Infrared (FTIR) spectrophotometer. The FTIR spectra of the p-type porous silicon are shown in Figure 19. In the transmittance spectrum, peak at 624.96 cm^{-1} represents Si-H bending (Si_3SiH), peak at 852.56 cm^{-1} shows Si-H₂ wagging mode and peak at 910.23 cm^{-1} illustrates Si-H₂ scissor mode [Bisis et.al.2000]. The peak at around 1074.30 cm^{-1} is due to Si-O-Si stretching modes [Yue Zhao et. al. 2005], which are depended on the oxidation degree of porous silicon. Furthermore, 2096.69 cm^{-1} and 2922.25 cm^{-1} are, respectively, related to Si-H stretch ($\text{Si}_3\text{-SiH}$) and C-H stretch (CH_2) [Andrea Edit PAP, 2005 and Dimova D., 2000]. Chemical bonds and their IR resonance positions detected in PS are shown in Table 4. Si-H bonds play an important role in regulating optical electrical and gas sensing properties of porous silicon.

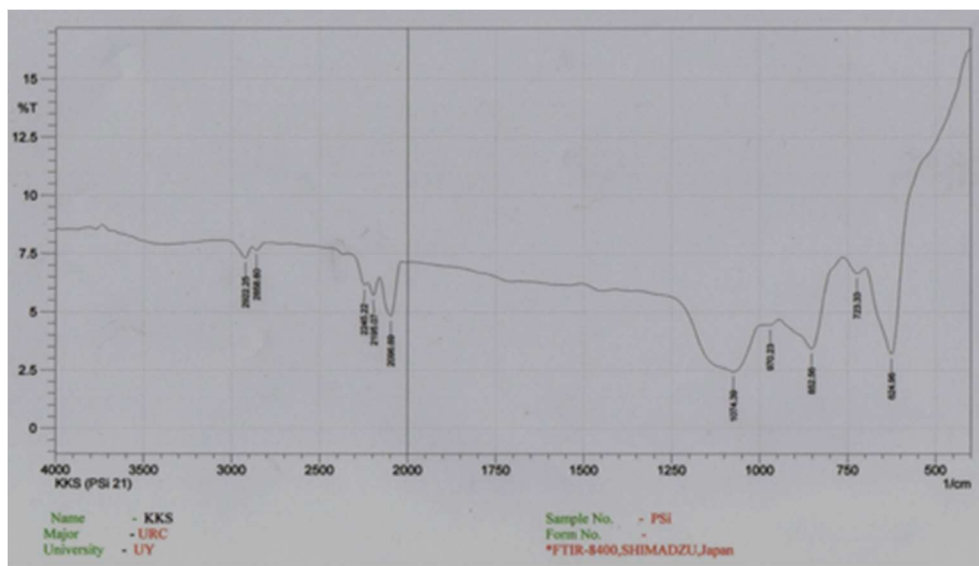


Figure 19. FTIR transmittance spectrum of a PS layer

Table 4. Peaks of PS sample observed FTIR spectrum

Peak position (cm ⁻¹)	Attribution
624.96	Si-H bending
852.56	Si-H ₂ wagging
910.23	Si-H ₂ scissor
1074.30	Si-O-Si stretching
2096.69	Si-H stretch (Si ₃ -SiH)
2922.25	C-H stretch (CH ₂)

Conclusion

Porous silicon has been fabricated in p-type silicon by anodization, metal assisted chemical etching and lithographic metal assisted etching. Although porous formation by anodization technique is more than another technique, it is difficult to make uniform porous silicon. It is found that the porous formation in silicon can control with adjustable metal concentration and time by metal assisted chemical etching method. Lithographic approach method can select uniformly porous area with metal assisted etching but the minimum porous selected area is 250 μm^2 . According to the characterization results the metal assisted chemical etching method gives better porous morphological structure which is suitable for MEMS and sensor applications.

References

1. Andrea Edit PAP, (2005), "Investigation of Pristine and Oxidized Porous Silicon", University of Oulu.
2. Bisio, Ossicini S. and Pavesi L., (2000), "Porous silicon: a quantum sponge structure for silicon based optoelectronics", *Surface science reports* 264.
3. Chunlin He, Xuefei Yang, Guofeng Ma, Jianming Wang, Zhaofu Du, Dongliang Zhao, Qingkui Cai, (2016), "Fabrication of Anti-reflecting Silicon Surfaces for Solar Cells Using Ag Assisted Chemical Etching", Liaoning Provincial Key Laboratory of Advanced Materials, Shenyang University, Shenyang University, 110044, China.
4. Jin Zheng, Wallner, (2006), "Porous silicon technology for integrated Microsystems", Dissertation, Michigan Technological University.
5. Lorusso A., Nassisi V., Congedo G., Lovergine N., Prete P., (2009), "Pulsed plasma ion source to create Si nanocrystals in SiO₂ substrates", *Applied Surface Science*.
6. Natalya Tokranova, Xiaojun Feng, Steve Olson, Tang Tang, Bai Xu, James Castracane, (2003), "Fabrication of MEMS Devices with Macroporous Silicon Membrane Embedded with Modulated 3D Structures for Optimal Cell Sorting", School of Nanosciences and Nano Engineering, University at Albany (SUNY), 251 Fuller Rd, Albany, New York
7. Wolfgang Benecke and Alexandra Splinter, "MEMS Applications of Porous Silicon", Institute for Microsensors, -actuators and -systems (IMSAS), University of Bremen _ Dept. 1 Physics/Electrical Engineering, Kufsteiner Str. _ D-28359 Bremen GERMANY
8. Yue Zhao, Deren Yang, Dongsheng Li, Minghua Jiang, (2005), "Annealing and amorphous silicon passivation of porous silicon with blue light emission", *Applied Surface Science* 252, 1065–1069.
9. Zhipeng Huang, Nadine Geyer, Peter Werner, Johannes de Boor, and Ulrich Gösele in memory of Prof. Ulrich Gösele, 2013, "Metal-Assisted Chemical Etching of Silicon: A Review", Max Planck Institute of Microstructure Physics Weinberg 2, D-06120 Halle, Germany, Functional Molecular Materials Centre Scientific Research Academy, Jiangsu University, China.

STUDY ON STRUCTURAL, MORPHOLOGICAL, OPTICAL AND PHOTOVOLTAIC PERFORMANCE OF CdS_{1-x}Se_x (x=0.2 mol) THIN FILMS BY CHEMICAL BATH DEPOSITION TECHNIQUE

Khin Su Myat Phone ¹, Yar Zar Tun ², Than Than Win ³
and Yin Maung Maung ⁴

Abstract

The CdS_{1-x}Se_x (x = 0.2 mol) sol-solution was prepared by Chemical Bath Deposition(CBD) Technique. The temperature treatment in the water bath was at 100 °C for 1 h. CdSSe thin films were formed onto the pure glass substrates by chemical bath deposition method. Phase identification and crystallographic properties of CdSSe thin films were examined by X-ray diffraction (XRD) technique while the surface appearances (morphology) of fabricated films were also identified by Scanning Electron Microscope (SEM). Optical properties of CdSSe films were used by UV-Vis spectroscopy. The electrical properties of CdSSe thin film solar cells have been studied the photovoltaic (PV) performances with a focus on the influence of temperature treatment at 350 °C and 400 °C. The capacitance-voltage characteristics of CdSSe thin films deposited at room temperature and the effect of different thermal annealing were carried out. The maximum power output, series resistance, shunt resistance and built in voltage were calculated from the I-V and C-V measurements. This research has been focused on the investigation of structural, optical and photovoltaic performances of CdS_{1-x}Se_x (x=0.2 mol) thin films by chemical bath deposition technique.

Keywords: CBD, XRD, SEM, UV-Vis spectroscopy, PV

Introduction

Nowadays, II–VI chalcogenide semiconducting compounds and alloys have received the attraction of many researchers due to the considerable progress in the epitaxial growth techniques as well as because of their

¹. Assistance Lecturer, Department of Physics, West Yangon University

². Assistance Lecturer, Department of Physics, West Yangon University

³. Associate Professor, Department of Physics, Mandalay University of Distance Education

⁴. Associate Professor, Department of Physics, University of Mandalay

potential usages in several optical devices operating in the visible and near infrared ranges. [Hassanien, A. S., Akl, A. A., 2015].

The synthesis of binary metal chalcogenide of II-VI semiconductors in thick film, thin film, and nanocrystalline form has been rapidly growing area in the material research due to their important non-linear optical, photo luminescent and other physical and chemical properties. It is found that the band gap of CdSe material is 1.7 eV whereas of cadmium Sulphide is 2.4 eV, both these are suitable for solar spectrum. This feature makes these materials useful for solar energy conversion in photovoltaic form. These materials can be synthesized in thin film form from several methods [Patil, L. A., & Rane, D. S., et al, 2015].

The II-VI group cadmium sulphoselenium is an important alloy with excellent properties like, good photo conductivity material, response time and band gap. CdS (Cadmium Sulfite) and CdSe (Cadmium Selenite) are two very important wide band gap semiconductors, because of their wide applications in optoelectronics, such as non-linear optics, visible-light emitting diodes and lasers. For optoelectronic applications, it is very important to tune the emission wavelength. For the efficient optoelectronic device application, the material should be between CdS in which very high sensitivity is possible but response time is high. CdSe as a great material for electrochemical solar cell has a narrower bandgap than CdS. Instead of incorporating cation, anion doping such as Se doping in CdS could bring promising improvement for both light absorption and photoactivity [Rui Xie, Jinzhan Su, Ya Liu, Liejin Guo, et al, 2013].

In CBD method, the film can be grown on any suitable substrate by dipping it in appropriate solution of metal salt. The deposition may occur either by homogenous or heterogeneous chemical reaction. The cation of respective metal, complexed with suitable complexing agent is allowed to react with chalcogen ion. The cations and anions were to generate slowly by increasing temperature of reacting bath. The ions produced combine on substrate via nucleation. The growth usually takes place by ion-by-ion condensation process. Typically, a liquid solution containing precursors to the eventual film was prepared and a substrate was exposed the solution. Over the course of second or minutes (depending on the reagents and their

concentrations), the precursors reacted to produce a solid material that grows, atom by atom, on all the surfaces exposed to the bath. Chemical bath deposition is regularly used in the photovoltaic industry to deposit thin films of cadmium sulfite. The growth of thin films strongly depended on growth conditions, such as duration of deposition, composition and temperature of the solution, and topographical and chemical nature of the substrate.

Experimental Procedure

$\text{CdS}_{1-x}\text{Se}_x$ ($x = 0.2$ mol) was deposited onto a glass substrate at 80°C by using chemical bath deposition method. Starting materials used for preparing of $\text{CdS}_{1-x}\text{Se}_x$ thin films were Cadmium Chloride (CdCl_2), Selenium (Se), Thiourea $\text{SC}(\text{NH}_2)_2$, Sodium sulphite (Na_2SO_3) and Ammonia (NH_3). Thiourea $\text{SC}(\text{NH}_2)_2$ was used as anionic precursor solution. Sodium sulphite (Na_2SO_3) was used as a solvating agent for anionic precursor solution. Selenium (Se), Sodium Sulphite (Na_2SO_3) and Ammonia (NH_3) were mixed in a beaker by using magnetic stirrer and annealed with water bath at 80°C for about 7 h. A solution of sodium selenosulphate (Na_2SeSO_3) was obtained. It was sealed and kept overnight, on cooling, small quantity of selenium settles down at the bottom of the solution. It was then filtered to obtain a clear solution. H_2O was used as a cationic precursor solution. Thiourea $\text{SC}(\text{NH}_2)_2$, Cadmium Chloride (CdCl_2) and Ammonia were mixed into another beaker by using magnetic stirrer. This mixture solution was added into the previous sodium selenosulphate solution and stirred by magnetic stirrer for 1 h. For maintaining the pH of the precursor solution was 10 to 11, 25 % concentrated NH_3 solution was used. All solutions were prepared in deionized water. This mixture final solution (Cadmium sulphoselenide solution) was put onto the water bath at 100°C for 1 h. The color of this solution was found to be orange color. Glass slides of dimension (1cmx1cm) were used as the substrates for deposition of $\text{CdS}_{1-x}\text{Se}_x$ thin films. The glass substrates were dipped into the orange color Cadmium sulphoselenide solution and heated at 120°C for 1h. After that they were annealed at 350°C and 400°C for 1h to change from oxide layer into CdSSe thin films respectively.

In this research work, preparation of $\text{CdS}_{1-x}\text{Se}_x$ ($x = 0.2$ mol) thin films were reported. The properties of the thin films and aspects of growth mechanism can be well understood by its characterization of the films. The $\text{CdS}_{1-x}\text{Se}_x$ thin films were characterized for their structural, surface morphological, optical, electrical properties, and photosensitivity of the films. I-V characteristics in dark and under illumination with in visible range were studied for the measurement of photosensitivity of $\text{CdS}_{1-x}\text{Se}_x$ thin films. The structural analyses of the films were made by an X-ray diffractometer. The surface morphology was studied by scanning electron microscopy (SEM). UV-Vis spectrophotometer (automatic computer data acquisition) was employed to record optical spectra over the wavelength range of 400-1100 nm.

Results and Discussion

Structural properties of $\text{CdS}_{1-x}\text{Se}_x$ thin films by XRD

X-ray diffraction (XRD) technique is one of the most important analytical tools for the thin film structural analysis. The Rigaku RINT 2000-Multi Flex 2kW X-ray diffractometer was used in this work. "d" values were determined using the Cu-K_α radiation with wavelength of 1.54056 Å. In diffractographs of powders not free from phase shift, several diffraction patterns of different crystalline fractions could be superimposed. The X-ray diffraction data obtained is printed in tubular form on paper and is compared with Joint Committee on Powder Diffraction Standard (JCPDS) or American Standard Testing for Materials (ASTM) data cards. The crystallite size (G) was determined by Debye-Scherrer formula.

From Figure 1, three of nine distinct peaks were formed on observed spectrum. Three of nine diffracted peaks were matched with those of angle CdSSe standard. From Figure 2, five distinct were formed on observed spectrum. Five of nine diffracted peaks were matched with those of CdSSe Standard. On the XRD pattern from Figure 1, the (100), (101) and (110) peaks and from Figure 2, (100), (002), (101), (110) and (112) were clearly observed. They were compared the data with the library (or) standard file. The most dominant peak was also occur at (101) for 350 °C and (100) for 400 °C. According to the observed XRD, the dopant material (modifier) Se^{2-} ion

doped into S^{2-} ion of the CdS lattice with hexagonal structure. The crystallographic phases of samples were in good agreement with the typical hexagonal structure. The polycrystalline structure $CdS_{1-x}Se_x$ thin film was considered to be an alloy of hexagonal CdS and CdSe crystallite grains. $CdS_{1-x}Se_x$ was successfully formed onto substrate at given temperatures for both samples. The observed XRD profile (upper side) and JCPDF library or reference XRD profile (lower side) were partially matched. FWHM and crystallite size of $CdS_{1-x}Se_x$ ($x = 0.2$ mol) thin films at $350^\circ C$ and $400^\circ C$ were listed in Table 1 and 2. Annealing temperature, lattice constants (a & c) and lattice parameter (c/a) ratio of $CdS_{1-x}Se_x$ ($x = 2$ mol) thin films were calculated and listed in Table 3.

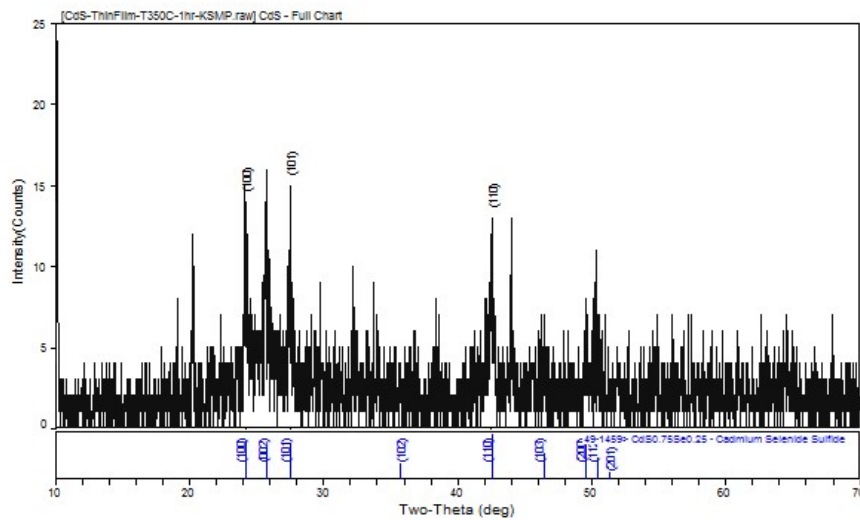


Figure 1. XRD spectrum of $CdS_{1-x}Se_x$ ($x = 0.2$ mol) thin film at $350^\circ C$

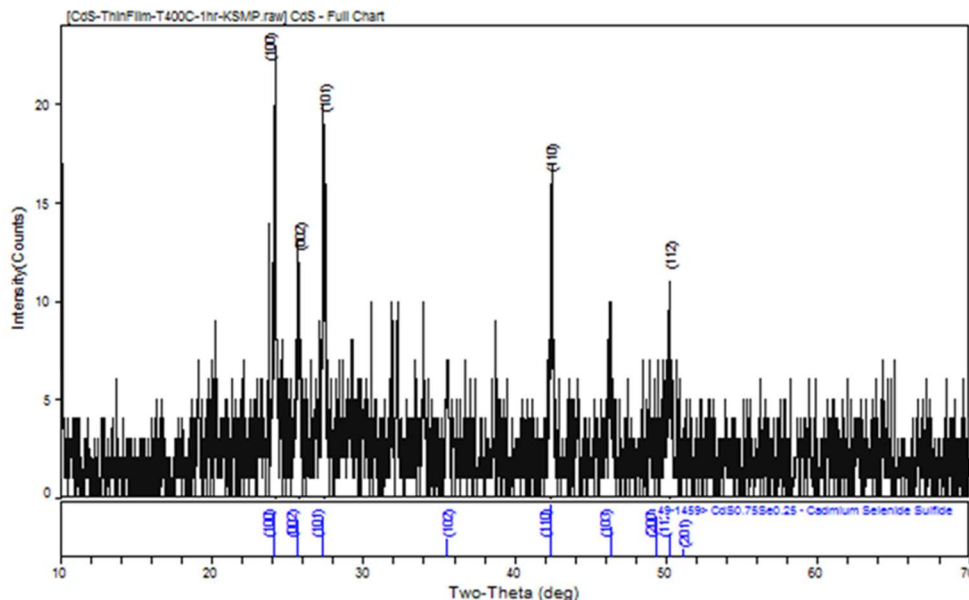


Figure 2. XRD spectrum of $\text{CdS}_{1-x}\text{Se}_x$ ($x = 0.2$ mol) thin film at 400°C

Table 1. Crystallite size of $\text{CdS}_{1-x}\text{Se}_x$ ($x = 0.2$ mol) thin film for all identified peaks at 350°C

No	Peaks	FWHM(degree)	Crystallite Size (nm)
1	(100)	0.26	31.48
2	(101)	0.26	31.69
3	(110)	0.16	55.04
Average crystallite size			39.40

Table 2. Crystallite size of $\text{CdS}_{1-x}\text{Se}_x$ ($x = 0.2$ mol) thin film for all identified peaks at 400°C

No	Peaks	FWHM(degree)	Crystallite Size (nm)
1	(100)	0.19	44.26
2	(002)	0.11	74.77
3	(101)	0.16	50.92
4	(110)	0.25	33.76
5	(112)	0.07	127.44
Average crystallite size			66.23

Table 3. Annealing temperature, lattice constants (a and c) and lattice parameter (c/a) ratio of CdS_{1-x}Se_x (x = 0.2 mol) thin films

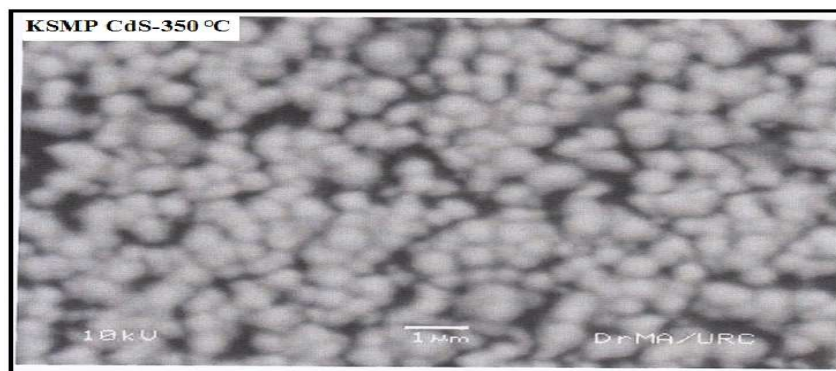
Annealing Temperature(°C)	Average Lattice Constant, a (Å)	Average Lattice Constant, c (Å)	Lattice Parameter (c/a) ratio
350	4.24	6.86	1.62
400	4.25	6.94	1.63

Scanning Electron Microscopy (SEM)

SEM is one of the most versatile instruments available for the examination and analysis of the microstructure characteristics of a solid. The Scanning Electron Microscope generated a beam of electrons in a vacuum. The scanning electron microscope (JEOL, JSM- 5610 LV) with acceleration voltage 10 and 15 kV and magnification 5500x and 10000x which was used in this research work. Table 4 shows average grain size of CdS_{1-x}Se_x (x = 0.2 mol) thin films at 350 °C and 400 °C. Figure 3 and 4 show the SEM image of CdS_{1-x}Se_x (x = 0.2 mol) thin film at 350 °C and 400°C.

Table 4. Average grain size of CdS_{1-x}Se_x (x = 0.2 mol) thin films at 350 °C and 400 °C

Annealed Temperature (°C)	Grain size (nm)
350	405
400	684

**Figure 3.** SEM image of CdS_{1-x}Se_x (x = 0.2 mol) thin film at 350°C

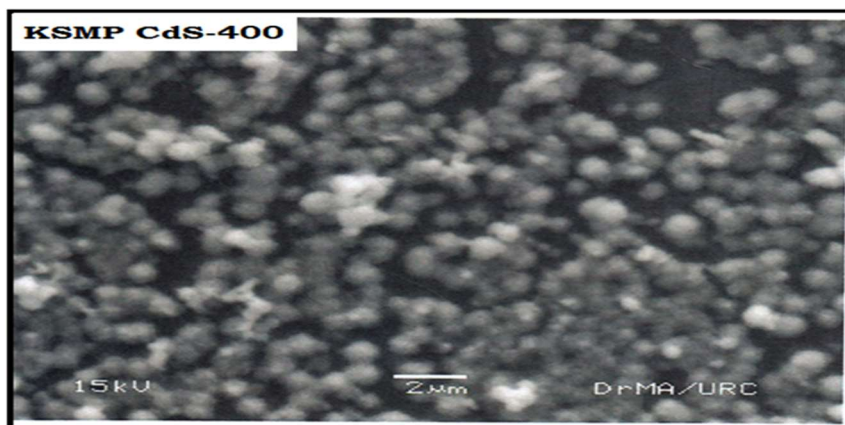


Figure 4. SEM image of $\text{CdS}_{1-x}\text{Se}_x$ ($x = 0.2$ mol) thin film at 400°C

UV-Visible optical absorption studies

Ultra-violet radiation is the part of the electromagnetic radiation spectrum below visible light. The band gap properties of a semiconductor can be controlled by using different semiconductor allays. The spectral absorption was taken by using UV-Vis spectrometer (UV-1800 SHIMADZU UV SPECTROPHOTOMETER). Table 4 shows the optical band gap energy of CdSSe thin films at 350°C and 400°C . Fig. 5 and 6 show the plot of $(\alpha h\nu)^2$ vs $h\nu$ for CdSSe thin film at 350°C and 400°C .

Table 4. Optical band gap energy of CdSSe thin films at 350°C and 400°C

Temperature ($^\circ\text{C}$)	Optical band gap energy (eV)	Standard band gap energy (eV)
350	1.44	1.67-2.35 [Rui Xie et al]
400	1.67	

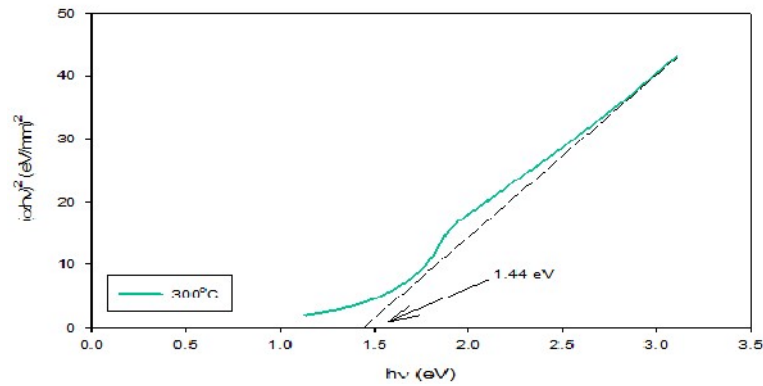


Figure 5. Plot of $(\alpha hv)^2$ vs hv for CdSSe thin film at 350 °C

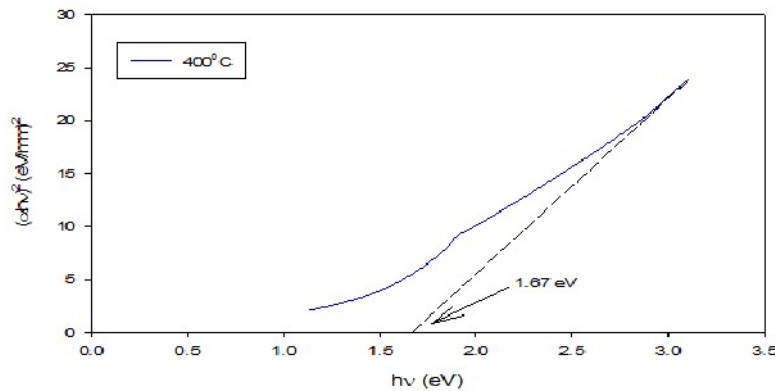


Figure 6. Plot of $(\alpha hv)^2$ vs hv for CdSSe thin film at 400 °C

I-V Measurement

The basic characterization tool for a solar cell was the current-voltage (IV) measurement under illumination and dark. The main parameters were the open-circuit voltage (V_{oc}), the short-circuit current (I_{sc}), the fill factor (F), maximum power point (P_{max}), the energy conversion efficiency, (η_{con}) and the conversion efficiency, (η_{con}). Variation of photovoltaic voltage and photovoltaic current with illumination intensity were also investigated. Most solar cell parameters can be obtained from the simple I-V measurement. Figure 7 shows current Vs. voltage characteristic graph for $CdS_{1-x}Se_x$ ($x = 0.2$ mol) thin films at 350°C and 400°C under dark condition. Fig. 8 In I

Vs. Voltage characteristic graph for $\text{CdS}_{1-x}\text{Se}_x$ ($x = 0.2$ mol) thin films at 350°C and 400°C under dark condition. Fig.9 and 10 show photocurrent Vs. cell voltage curves for CdSSe thin film at at 350°C and 400°C . Table 5 shows saturation current, ideality factor and zero bias barrier height for $\text{CdS}_{1-x}\text{Se}_x$ ($x = 0.2$ mol) thin films at 350°C and 400°C under dark condition. Table 6 shows photovoltaic parameters of $\text{CdS}_{1-x}\text{Se}_x$ ($x = 0.2$ mol) thin films at 350°C and 400°C under illumination. Table 7 shows Efficiency and Fill Factor of $\text{CdS}_{1-x}\text{Se}_x$ ($x = 0.2$ mol) thin films at 350°C and 400°C under illumination.

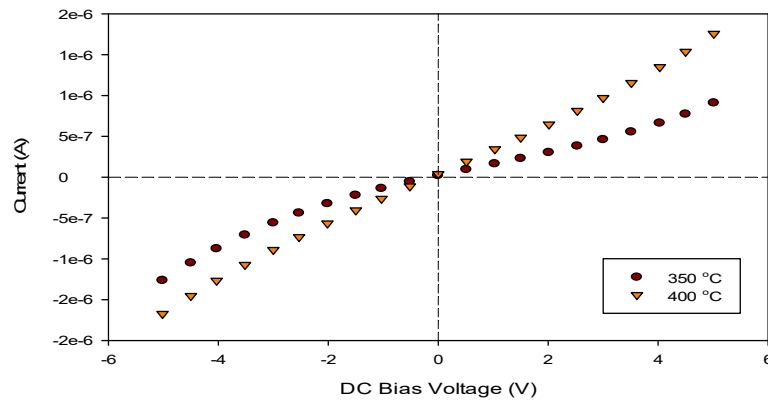


Figure 7. Current Vs. Voltage characteristic graph for $\text{CdS}_{1-x}\text{Se}_x$ ($x = 0.2$ mol) thin films at 350°C and 400°C under dark condition

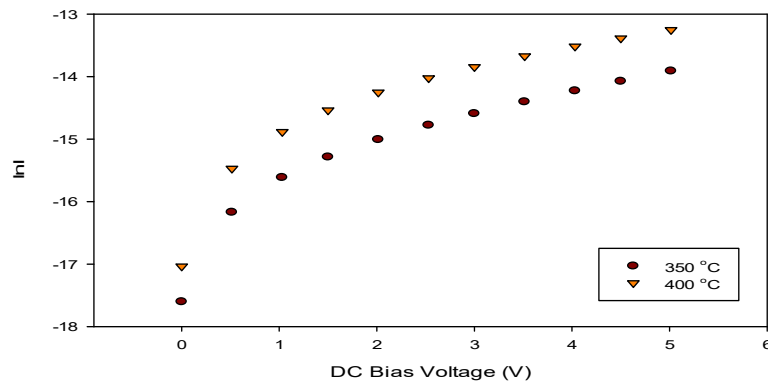


Figure 8 . $\ln I$ Vs. Voltage characteristic graph for $\text{CdS}_{1-x}\text{Se}_x$ ($x = 0.2$ mol) thin films at 350°C and 400°C under dark condition

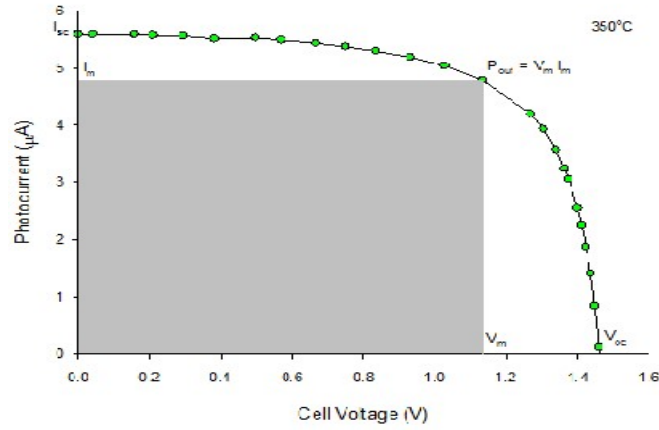


Figure 9. Photocurrent Vs. Cell voltage curves for CdSSe thin film at 350°C

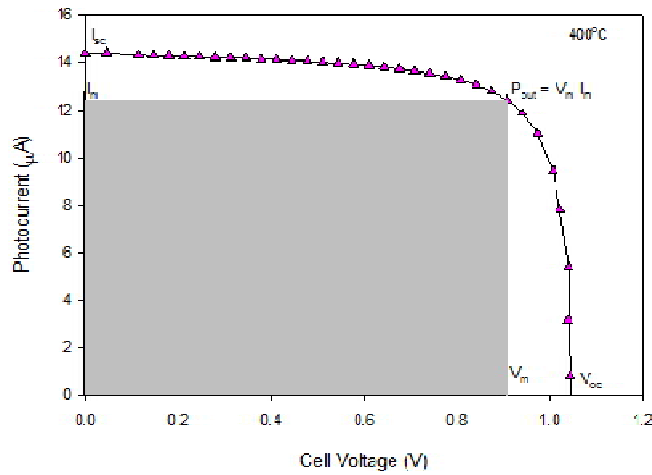


Figure 10. Photocurrent Vs. Cell voltage curves for CdSSe thin film at 400°C

Table 5. Saturation current, ideality factor and zero bias barrier height for CdS_{1-x}Se_x (x = 0.2 mol) thin films at 350 °C and 400 °C under dark condition

Temperature (°C)	I _s (A)	φ _{bo} (eV)	η
350	6.30x10 ⁻⁸	0.39	1.64
400	1.27x10 ⁻⁷	0.37	1.59

Table 6. Photovoltaic parameters of CdS_{1-x}Se_x (x = 0.2 mol) thin films at 350 °C and 400 °C under illumination

Temperature (°C)	I _m (μA)	V _m (V)	I _{sc} (μA)	V _{oc} (V)	P _{max} (μW)
350	4.83	1.13	5.61	1.45	5.48
400	12.42	0.90	14.40	1.07	11.27

Table 7. Efficiency and Fill Factor of CdS_{1-x}Se_x (x = 0.2 mol) thin films at 350 °C and 400 °C under illumination

Temperature (°C)	η _{con} (%)	FF	Standard η _{con} (%) and FF
350	1.18	0.67	η _{con} = 0.59%, 0.67% and FF = 0.55, 0.56 (PUJARI V.B et al, 2013)
400	2.42	0.73	η _{con} = 0.79%, 2.12% and FF = 0.46, 0.49 (Abhijit A .Yadav et al, 2011)

Conclusion

Fabrication and characterization of CdS_{1-x}Se_x thin films have been successfully investigated. The XRD results showed a polycrystalline films with hexagonal structure and lattice distortions (c/a) of 1.61 and 1.63 at 350°C and 400°C. The crystallite sizes of CdS_{1-x}Se_x thin films were calculated to be 39.40 nm and 66.23 nm at the growth temperature 350°C and 400°C. SEM photographs showed homogeneous film and spherical shape. The average grain size of the films varied with annealing temperature. The grain sizes of CdS_{1-x}Se_x thin films were estimated to be 405 nm and 684 nm at 350°C and 400°C. The films had a direct band gap with an optical value of 1.44 eV and 1.48 eV at 350°C and 400°C from the absorption spectrum. According to the band gap energy obtained by the absorption method, all optical band gaps in this study were 1.44 eV and 1.48 eV, nearly ranged between the standard values of CdS_{1-x}Se_x thin films (1.67 - 2.35 eV). All films were found the good absorbance, low transmittance in the visible/ near infrared region from about 400 nm to 1100 nm. Conversion efficiency of

CdS_{1-x}Se_x thin films were 1.18 % and 2.42 % at 350°C and 400°C. Fill factor of CdS_{1-x}Se_x thin films were determined to be 0.67 and 0.73 at 350°C and 400°C. The maximum power outputs were 5.48 μW and 11.27 μW at 350°C and 400°C. Finally, V_{bi} obtained for different temperatures are 0.45 V and 0.55 V at 350°C and 400°C. These values of band gap were in good agreement with the value reported by others. These results also suggest that the chemical bath deposition method is quite appropriate to produce CdS_{1-x}Se_x thin films solar cell. Photocurrent increased with applied voltage and showed ohmic behavior in nature for both temperatures. The dark current and photocurrents were measured at -5 to +5 V and the plot showed diode characteristic. Annealing temperatures were fairly influence on photoconductive properties of the films. CdS_{1-x}Se_x thin films with different composition of Se at different annealing temperatures will be investigated in future research. The investigation of CdS_{1-x}Se_x thin films will be focused on the other applications such as optical filters, signal memory devices, optoelectronic switches and radiation protection field.

Acknowledgements

I am greatly indebted to professor Dr Khin Khin Win, Head of Department of Physics, University of Yangon, for her kind permission to carry out this research.

I would like to thank Professor Dr Moe Ohnmar, Head of Department of Physics, West Yangon University, for her kind permission to carry out this research.

I would like to express my warmest thanks to Dr Yin Maung Maung, Associate Professor, Department of Physics, University of Yangon, for his valuable advice throughout in this research.

I would like to deeply grateful to Dr Than Than Win, Associate Professor, Department of Physics, Mandalay University of Distance Education, for her valuable supervising throughout I this research.

References

1. Abhijit, A., Yadav et al 2011 Journal of Electrochimica Acta
2. Hassanien, A.S., & Akl, A.A., 2015. Effect of Se addition on optical and electrical properties of chalcogenide CdSSe thin films, Super lattices and Microstructures, doi: 10.1016/j.spmi.2015.10.044
3. Patil, L. A. & Rane, D. S., et al, 2015. International Journal of Engineering, Science and research Technology 4(7) 2277-9655
4. Pujari V B et al 2013 International Journal of application or Innovation in Engineering and Management (IJAIEEM) 2 4847
5. Rui Xie, Jinzhan Su, Ya Liu, Liejin Guo et al, 2013. International Journal of hydrogen energy xxx (2013) I-II

STUDY ON CHARACTERIZATION OF $Mg_{0.5}Cu_{0.5}Fe_2O_4$ FERRITE COMPOUND

Phyu Phyu Khine¹, May Soe Myint² & Win Kyaw³

Abstract

Magnesium-Copper mixed spinel ferrite, $Mg_{0.5}Cu_{0.5}Fe_2O_4$, was prepared by usual ceramic method at 1100°C for 10 h in vacuum chamber (160 mmHg). Starting materials of Analar (AR) grade Magnesium Oxide (MgO), Copper Oxide (CuO), and Iron Oxide (Fe_2O_3) with desired stoichiometric composition were used to prepare the sample. The X-ray analysis was carried out to investigate the phase formation. The crystallite size was estimated by using collected XRD lines to examine the nanosized ferrite particles. SEM method was used to investigate the microstructural properties of the sample. D.C electrical conductivities of the sample were investigated in the temperature range 303 K – 1218 K to study the electrical conductivity.

Key word: $Mg_{0.5}Cu_{0.5}Fe_2O_4$ Ferrite Compound, Dc electrical conductivity, Activation energy.

Introduction

Ferrite, a ceramic-like material with magnetic properties and they are useful in many types of electronic devices, such as cell phones and wireless devices.

Ferrites are hard, brittle, iron-containing, and generally gray or black and are polycrystalline, *i.e.*, made up of a large number of small crystals. They are composed of iron oxide and one or more other metals in chemical combination. A ferrite is formed by the reaction of ferric oxide (iron oxide or rust) with any of a number of other metals, including magnesium, aluminum, barium, manganese, copper, nickel, cobalt, or even iron itself. A ferrite is usually described by the formula $M(Fe_xO_y)$, where M represents any metal that forms divalent bonds, such as manganese (Mn^{2+}), nickel (Ni^{2+}), cobalt (Co^{2+}), zinc (Zn^{2+}), copper (Cu^{2+}), or magnesium (Mg^{2+}). Nickel ferrite, for instance, is $NiFe_2O_4$, and Magnesium ferrite is $MgFe_2O_4$.

¹. Dr, Assistant Lecturer, Department of Physics, Pyay University

². Assistant Lecturer, Department of Physics, Pyay University

³. Assistant Professor, Department of Physics, Sagaing University

The physical properties of ferrites are dependent on several factors, such as preparation method, sintering process and constituent elements. Several methods can be used to prepare ferrites, such as solid state reaction, mechanical milling, co-precipitation. The effect of various substituting cations on the structural, electrical, dielectric and magnetic properties of ferrites was the subject of an extensive research work which used techniques such as X-ray and neutron diffraction, thermal analysis, magnetization and electrical conductivity.

In the present work Magnesium-Copper mixed spinel ferrite, $Mg_{0.5}Cu_{0.5}Fe_2O_4$ was prepared by usual ceramic method. Structural, microstructural, and its related temperature dependent electrical property of the sample were reported.

Experimental Procedures

2.1 Measurement

The present experimental work include the preparation of the $Mg_{0.5}Cu_{0.5}Fe_2O_4$ mixed ferrite, structural analysis by powder X-ray diffraction measurement, microstructural investigation by SEM measurement and D.C electrical conductivities of the sample were investigated in the temperature range 303 K – 1218 K.

2.2. Preparation of $Mg_{0.5}Cu_{0.5}Fe_2O_4$ Mixed Ferrite

Magnesium-Copper mixed ferrite, $Mg_{0.5}Cu_{0.5}Fe_2O_4$, was prepared by usual ceramic method. The starting materials of Analar (AR) grade Magnesium Oxide (MgO), Copper Oxide (CuO), and Iron Oxide (Fe_2O_3) were weighed with stoichiometric composition to prepare the sample.

The weighed powders were mixed and ground by an agate motor for 1 h to be homogeneous and to obtain fine grain powders. The powders were annealed at 1100°C for 10 h in vacuum chamber (160 mmHg) by using DELTA A Series Temperature Controller DTA4896. The K-type thermocouple was used as the temperature sensor.

Photographs of the experimental setup of sample preparation system, DELTA A Series Temperature Controller DTA-4896 and flow diagram of the Mg-Cu ferrite sample preparation are shown in Fig 1(a - c).

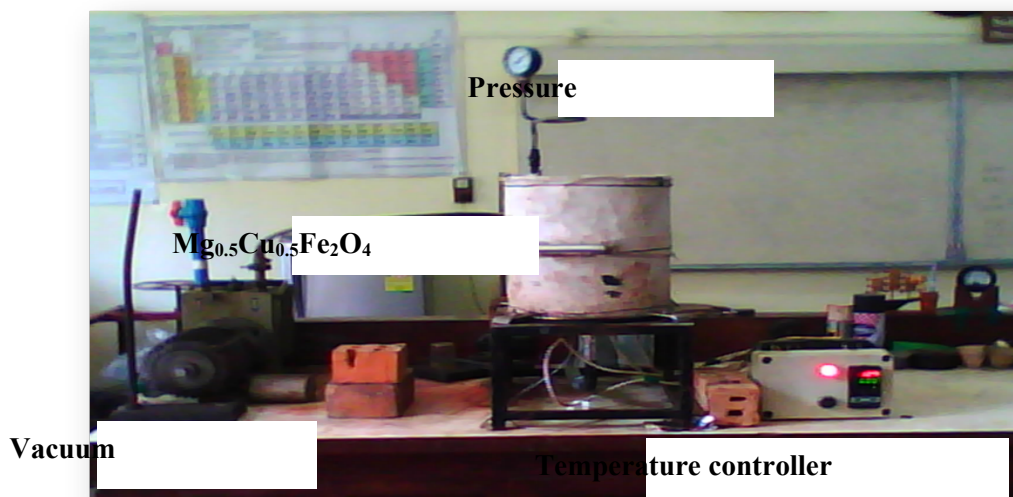


Figure 1(a) Photograph of the experimental setup of sample preparation



Figure1(b). Photograph of DELTAA SERIES DTA-4896 temperature controller

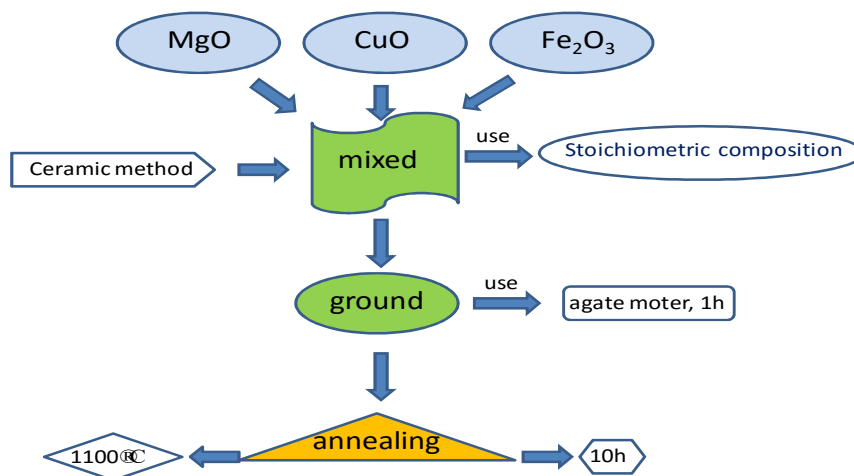


Figure 1(c). Flow diagram of the Mg-Cu ferrite sample preparation

2.3 X-ray Diffraction Measurement

Structural analysis and single phase examination of $\text{Mg}_{0.5}\text{Cu}_{0.5}\text{Fe}_2\text{O}_4$ were investigated by RIGAKU MULTIFLEX X-ray diffractometer using Ni-filter with CuK_α radiation, $\lambda = 1.54056 \text{ \AA}$. The main reflections in the range $10^\circ < 2\theta < 70^\circ$ were observed, and the collected data were used to refine the unit cell parameters from the observed 2θ values with JCPDS (Joint Committee on Powder Diffraction Standards). Photograph showing the front-panel of the RIGAKU MULTIFLEX X-Ray Diffractometer is shown in Fig 2.

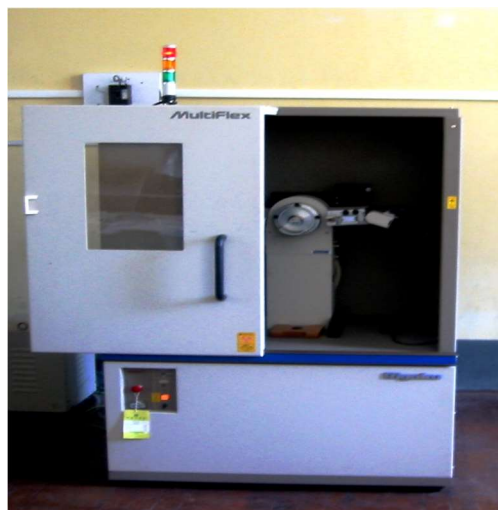


Figure 2. Photograph of the RIGAKU MULTIFLEX X-Ray Diffractometer

2.4 Characterization of Surface Morphology

The microstructure and morphology have an important role in determining the magnetic and electrical transport properties and those were examined by a high resolution scanning electron microscope. Morphological features of $Mg_{0.5}Cu_{0.5}Fe_2O_4$ mixed ferrite were investigated by using JEOL JSM-5610LV SEM. Photograph of the JEOL JSM-5610LV Scanning Electron Microscope is shown in Fig 3.



Figure 3. Photograph of the JEOL JSM-5610 LV Scanning Electron Microscope (SEM)

2.5 Conductivity Measurement

The dc electrical resistivity measurement on the ferrite was carried out by using digital multimeter. To measure the temperature variation of resistivity, a sample homemade apparatus was developed in the laboratory. The sample was placed in a sample holder that was immersed in a heating steel chamber surrounded by asbestos. Thermal conducting mica shield was used between the sample and the chamber to have a good thermal conductivity and to protect from electrical conduction.

The resistances were measured over a temperature range from 303 K to 1218K. The variation of the temperature was sensed by k-type

thermocouple. The dc conductivity σ of the sample is determined from the measured value and sample dimension using the relation: $\sigma = l/RA$, where l is the thickness of the sample, A is the area of the sample and R is the dc resistance. Photograph of the temperature dependent electrical conductivity measurement is shown in Fig 4(a) and the internal arrangement for the temperature dependent dc resistivity measurement is shown in Fig 4(b).



Figure 4(a) Photograph of the experimental setup of electrical resistance measurement

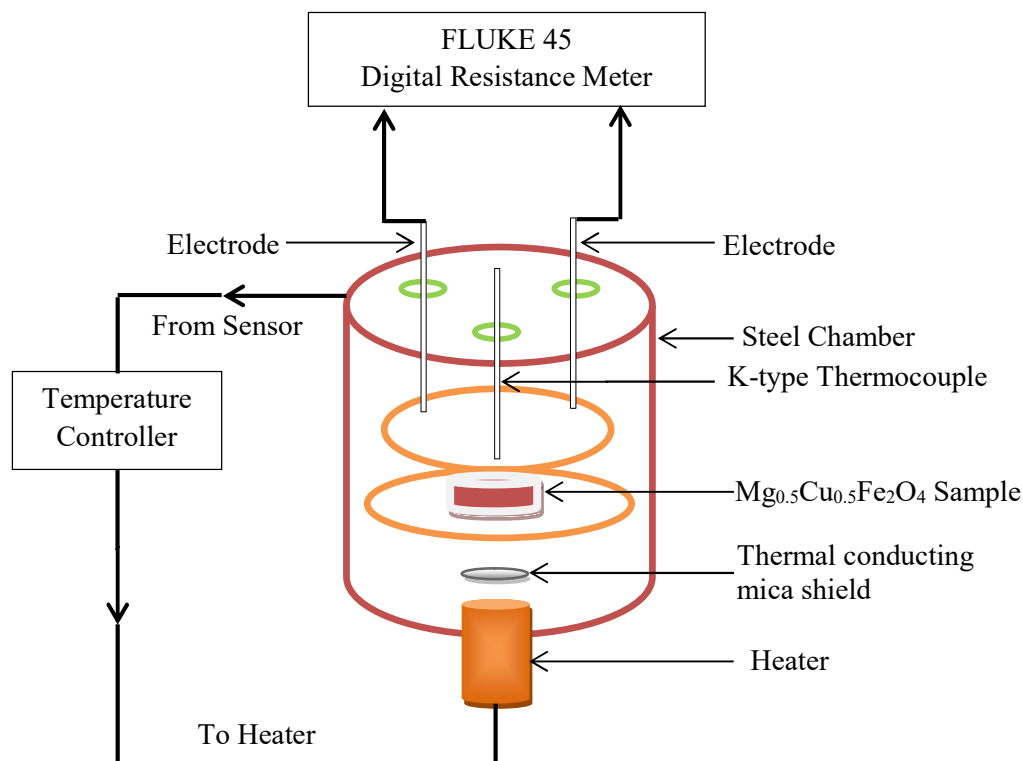


Figure 4(b). Sample chamber for temperature dependent electrical resistance measurement

Experimental Results

3.1 XRD Results

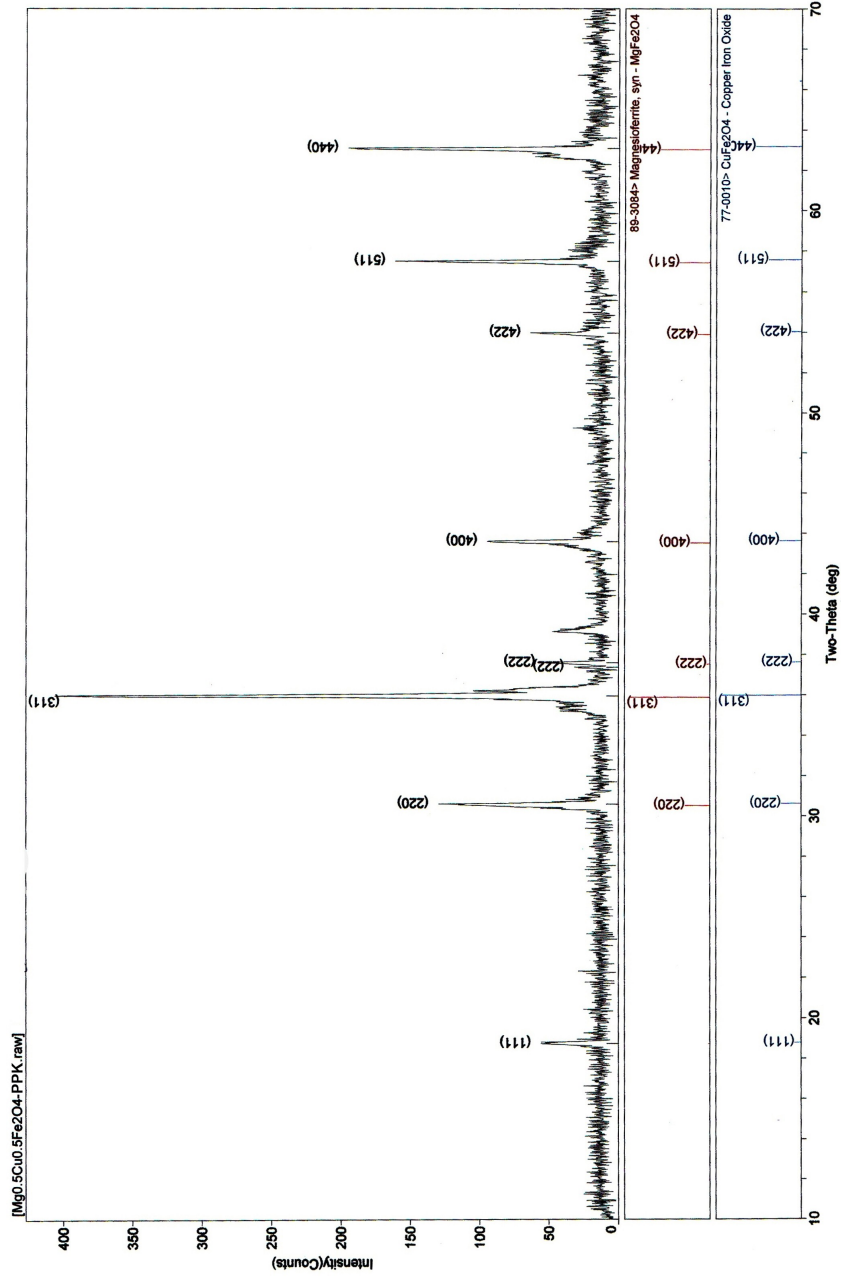
Structural analysis of the Magnesium-Copper mixed ferrite, $Mg_{0.5}Cu_{0.5}Fe_2O_4$, was investigated by powder X-ray diffraction (XRD) method. XRD pattern of the sample was collected on PC-controlled RIGAKU MULTIFLEX X-ray Diffractometer in the diffraction angle range $10^\circ - 70^\circ$ and as shown in Fig 5. The collected XRD lines were identified by JCPDS data library files of (1) Cat. No. 89-3084> Magnesioferrie, syn – $MgFe_2O_4$ and (2) Cat. No. 77-0010> $MgFe_2O_4$ – Copper Iron Oxide. XRD data are tabulated in Table 1.

The diffraction lines at 37.35° or (222) plane is represented by the Magnesium ferrite, $MgFe_2O_4$ and the line at 37.58° is represented by the

Copper ferrite, CuFe_2O_4 . The diffraction line of small intensity at the diffraction angle of 38.46° is not assigned with JCPDS files. This may be attributed to small crystallite effects, crystal defects or chemical heterogeneity of the samples.

Table 1. XRD data of Magnesium-Copper mixed ferrite, $\text{Mg}_{0.5}\text{Cu}_{0.5}\text{Fe}_2\text{O}_4$

[Mg0.5Cu0.5Fe2O4-PPKHi.raw] MgCuFe2O4 - Full Chart								Peak ID Report		
SCAN: 10.0/70.0/0.02/0.12(sec), Cu(40kV,40mA), I(max)=407, 09/03/10 17:55										
PEAK: 25-pts/Quartic Filter, Threshold=3.0, Cutoff=0.1%, BG=1/0.7, Peak-Top=Summit										
NOTE: Intensity = Counts, 2T(0)=0.0(deg), Wavelength to Compute d-Spacing = 1.54056Å (Cu/K-alpha1)										
#	2-Theta	d(Å)	Height	Height%	Phase ID	d(Å)	I%	(h k l)	2-Theta	Delta
1	18.743	4.7305	44	11.2	Magnesioferrit...	4.7348	0.8	(1 1 1)	18.726	-0.017
2	30.596	2.9195	120	30.5	CuFe2O4	2.9177	23.7	(2 2 0)	30.615	0.019
3	35.939	2.4968	394	100.0	CuFe2O4	2.4938	100.0	(3 1 1)	35.983	0.045
4	37.346	2.4059	22	5.6	Magnesioferrit...	2.3951	2.4	(2 2 2)	37.520	0.174
5	37.578	2.3915	44	11.2	CuFe2O4	2.3890	9.3	(2 2 2)	37.620	0.042
6	43.579	2.0751	80	20.3	Magnesioferrit...	2.0776	23.2	(4 0 0)	43.524	-0.055
7	53.950	1.6981	51	12.9	Magnesioferrit...	1.6997	14.3	(4 2 2)	53.896	-0.055
8	57.478	1.6020	148	37.6	Magnesioferrit...	1.6033	37.4	(5 1 1)	57.426	-0.053
9	63.073	1.4727	181	45.9	Magnesioferrit...	1.4738	61.3	(4 4 0)	63.019	-0.054



<C:\Winmax\Data\20100805- (MDUJDE6)

Fig 5 XRD pattern of Magnesium-Copper mixed ferrite, Mg_{0.5}Cu_{0.5}Fe₂O₄

3.2 Microstructural Analysis

Scanning Electron Microscopy (SEM) was employed for morphological features of grain shape, grain size and sample homogeneity of Magnesium-Copper mixed ferrite, $Mg_{0.5}Cu_{0.5}Fe_2O_4$ powders. SEM micrograph of Magnesium-Copper mixed spinel ferrite, $Mg_{0.5}Cu_{0.5}Fe_2O_4$ is shown in Fig 6. As shown in figure, the grain shape of the sample is block. The grain sizes of the sample are about $0.20\ \mu m - 1.80\ \mu m$. Some pores are found. Most of the samples are found to be well-crystallized grains.

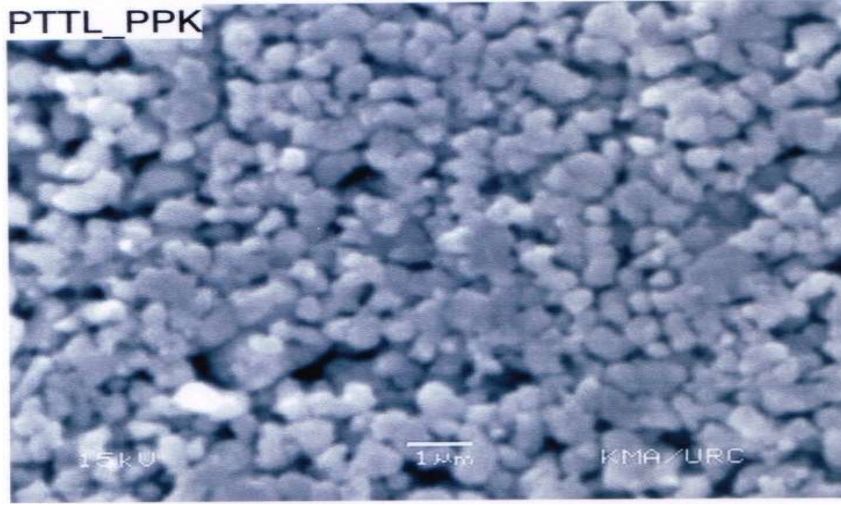


Figure 6. SEM image of Magnesium-Copper mixed ferrite, $Mg_{0.5}Cu_{0.5}Fe_2O_4$

3.3 Temperature Dependent Electrical Conductivity Study

The electrical nature of a material is characterized by its conductivity (or, inversely, its resistivity) .

Electrical conductivity of a ferrite obeys the following Arrhenius expression.

$$\sigma = \sigma_0 \exp(-E_a / kT)$$

where σ is the conductivity, σ_0 is the pre-exponential factor, E_a is the activation energy for electrical conduction, k is the Boltzmann constant and T is the absolute temperature.

Arrhenius plot of Magnesium-Copper mixed ferrite, $Mg_{0.5}Cu_{0.5}Fe_2O_4$ in the temperature range of 303 K - 1218 K is shown in Fig 7(a-b). The experimental data are tabulated in Table 2. The electrical conductivity of the sample was found to be clearly increased at 1068 K and it indicated with the ellipse shape ring.

The electrical conductivity (σ) of the sample can be written as the form:

$$\begin{aligned}\sigma_{dc} &= \sigma_0 \exp(-E_a / kT) \\ \ln \sigma_{dc} &= -E_a / kT + \ln \sigma_0 \\ &= (-E_a / k)(1/T) + \ln \sigma_0\end{aligned}$$

Comparing the above equation with the experimental linear equation, $y = mx + c$, then the value of slope will give the value of $(-E_a/k)$. From Fig 7(b), the activation energy E_a can be obtained by using the slope of the $\ln(\sigma)$ versus $1000/T$ graph.

$$\begin{aligned}E_a/k &= 7.5578 \times 1000 \\ E_a &= 7.5578 \times 1000 \times k \\ E_a &= 7.5578 \times 1000 \times 1.38E-23 \\ E_a &= 1.0430 \times 10^{-19} \text{ J} \\ E_a &= 0.6519 \text{ eV}\end{aligned}$$

Electrical conductivities of the sample are obtained as $1.9232 \times 10^{-6} \text{ S m}^{-1}$ at 303 K (start temperature) and $8.3840 \times 10^{-6} \text{ S m}^{-1}$ at 1218 K (end temperature) respectively. Temperature dependent electrical conductivity results show that the $Mg_{0.5}Cu_{0.5}Fe_2O_4$ sample exhibited as a normal ionic conductor due to its electrical conductivity is found as $\sigma < 10^{-3} \text{ S m}^{-1}$.

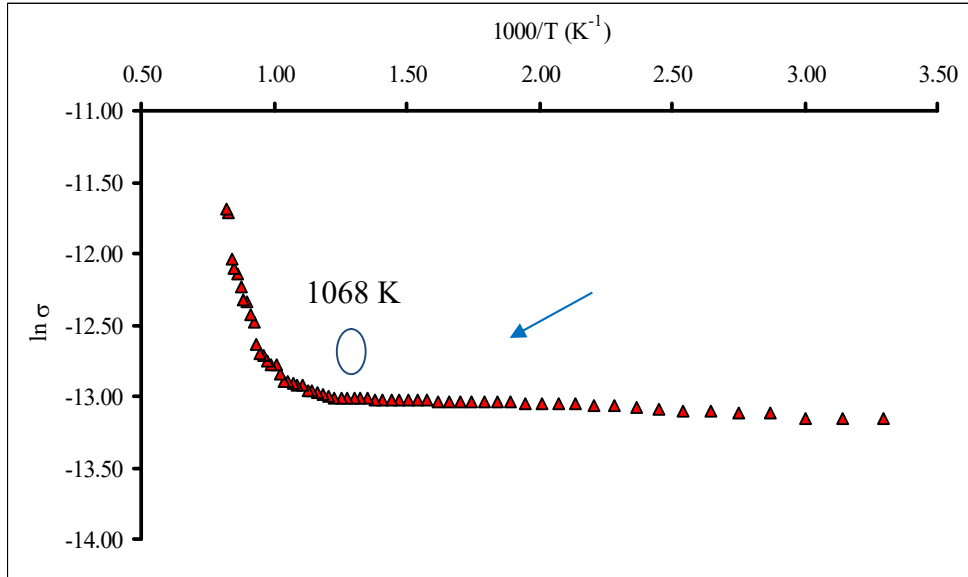


Figure 7(a) Arrhenius's plots of the conductivity with reciprocal temperature of the Magnesium-Copper mixed ferrite, $Mg_{0.5}Cu_{0.5}Fe_2O_4$ (303 K – 1218 K)

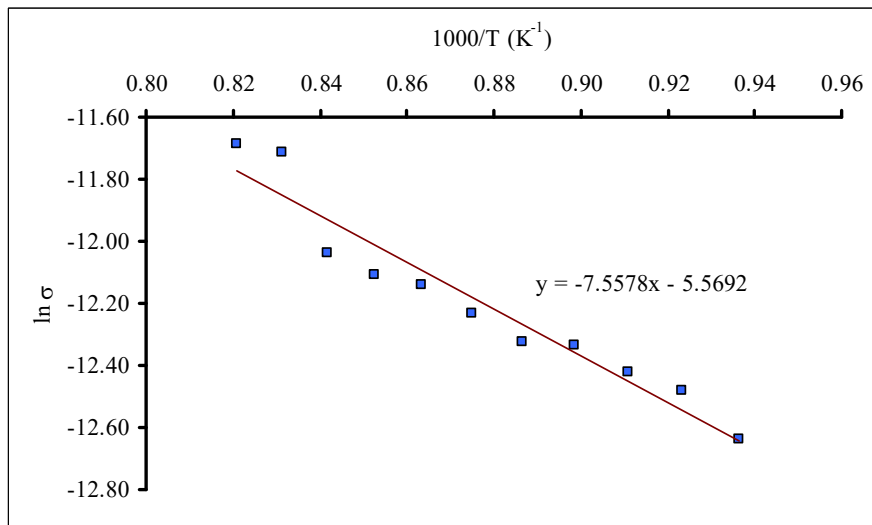


Figure 7(b) Arrhenius's plots of the conductivity with reciprocal temperature of the Magnesium-Copper mixed ferrite, $Mg_{0.5}Cu_{0.5}Fe_2O_4$ (1068 K – 1218 K)

Table 2. The experimental data of the Magnesium-Copper mixed ferrite, $Mg_{0.5}Cu_{0.5}Fe_2O_4$

T(K)	1000/T (K⁻¹)	R (Ω)	σ (S m⁻¹)	ln σ
303	3.3003	2.2460E+07	1.9232E-06	-13.1615
318	3.1447	2.2449E+07	1.9242E-06	-13.1610
333	3.0030	2.2242E+07	1.9421E-06	-13.1518
348	2.8736	2.1485E+07	2.0105E-06	-13.1171
363	2.7548	2.1396E+07	2.0189E-06	-13.1130
378	2.6455	2.1201E+07	2.0374E-06	-13.1038
393	2.5445	2.1192E+07	2.0383E-06	-13.1034
408	2.4510	2.1000E+07	2.0569E-06	-13.0943
423	2.3641	2.0633E+07	2.0935E-06	-13.0767
438	2.2831	2.0400E+07	2.1174E-06	-13.0653
453	2.2075	2.0364E+07	2.1212E-06	-13.0635
468	2.1368	2.0243E+07	2.1339E-06	-13.0576
483	2.0704	2.0154E+07	2.1433E-06	-13.0532
498	2.0080	2.0146E+07	2.1441E-06	-13.0528
513	1.9493	2.0068E+07	2.1525E-06	-13.0489
528	1.8939	1.9986E+07	2.1613E-06	-13.0448
543	1.8416	1.9972E+07	2.1628E-06	-13.0441
558	1.7921	1.9935E+07	2.1668E-06	-13.0422
573	1.7452	1.9895E+07	2.1712E-06	-13.0402
588	1.7007	1.9878E+07	2.1730E-06	-13.0394
603	1.6584	1.9840E+07	2.1772E-06	-13.0375
618	1.6181	1.9817E+07	2.1797E-06	-13.0363
633	1.5798	1.9736E+07	2.1887E-06	-13.0322
648	1.5432	1.9723E+07	2.1901E-06	-13.0316
663	1.5083	1.9720E+07	2.1905E-06	-13.0314
678	1.4749	1.9681E+07	2.1948E-06	-13.0294
693	1.4430	1.9592E+07	2.2048E-06	-13.0249
708	1.4124	1.9540E+07	2.2106E-06	-13.0222
723	1.3831	1.9493E+07	2.2160E-06	-13.0198
738	1.3550	1.9473E+07	2.2182E-06	-13.0188

T(K)	1000/T (K⁻¹)	R (Ω)	σ (S m⁻¹)	ln σ
753	1.3280	1.9458E+07	2.2199E-06	-13.0180
768	1.3021	1.9427E+07	2.2235E-06	-13.0164
783	1.2771	1.9406E+07	2.2259E-06	-13.0153
798	1.2531	1.9290E+07	2.2393E-06	-13.0094
813	1.2300	1.9284E+07	2.2400E-06	-13.0090
828	1.2077	1.9147E+07	2.2560E-06	-13.0019
843	1.1862	1.8785E+07	2.2995E-06	-12.9828
858	1.1655	1.8542E+07	2.3296E-06	-12.9698
873	1.1455	1.8485E+07	2.3368E-06	-12.9667
888	1.1261	1.8420E+07	2.3450E-06	-12.9632
903	1.1074	1.7674E+07	2.4440E-06	-12.9219
918	1.0893	1.7644E+07	2.4482E-06	-12.9202
933	1.0718	1.7427E+07	2.4787E-06	-12.9078
948	1.0549	1.7307E+07	2.4959E-06	-12.9009
963	1.0384	1.7130E+07	2.5216E-06	-12.8906
978	1.0225	1.6419E+07	2.6308E-06	-12.8482
993	1.0070	1.5400E+07	2.8049E-06	-12.7841
1008	0.9921	1.5370E+07	2.8104E-06	-12.7822
1023	0.9775	1.4873E+07	2.9043E-06	-12.7493
1038	0.9634	1.4398E+07	3.0001E-06	-12.7169
1053	0.9497	1.4252E+07	3.0309E-06	-12.7067
1068	0.9363	1.3325E+07	3.2417E-06	-12.6394
1083	0.9234	1.1390E+07	3.7924E-06	-12.4825
1098	0.9107	1.0733E+07	4.0246E-06	-12.4231
1113	0.8985	9.8317E+06	4.3935E-06	-12.3354
1128	0.8865	9.7073E+06	4.4498E-06	-12.3226
1143	0.8749	8.8663E+06	4.8719E-06	-12.2320
1158	0.8636	8.1033E+06	5.3306E-06	-12.1420
1173	0.8525	7.8235E+06	5.5213E-06	-12.1069
1188	0.8418	7.2950E+06	5.9213E-06	-12.0370
1203	0.8313	5.2669E+06	8.2014E-06	-11.7112
1218	0.8210	5.1522E+06	8.3840E-06	-11.6892

Conclusion

4.1 Conclusion

Magnesium-Copper mixed ferrite, $\text{Mg}_{0.5}\text{Cu}_{0.5}\text{Fe}_2\text{O}_4$, was prepared by usual ceramic method at 1100°C for 10 h in vacuum chamber (160 mmHg). Structural analysis and lattice parameters determination of the sample were investigated by XRD method. XRD pattern showed that $\text{Mg}_{0.5}\text{Cu}_{0.5}\text{Fe}_2\text{O}_4$ mixed ferrite belongs to cubic structure at room temperature. The lattice parameters are obtained as $a = b = c = 8.28 \text{ \AA}$. The crystallite size was also obtained as 37.95 nm. It is consistent with the ceramically prepared ferrite.

SEM micrograph shows that sample exhibited the fine grained microstructure with small grain size of block shape. Most of the samples were found to uniform and obtained as $0.20 \mu\text{m} - 1.80 \mu\text{m}$. Some pores are found and most of the samples are found to be well-crystallized grains.

Electrical conductivities of the sample were increased with increasing temperatures. The sample exhibited as a normal ionic conductor due to its electrical conductivity is found as $\sigma < 10^{-3} \text{ S m}^{-1}$.

Magnesium-Copper ferrite device can be used for many application such as chlorine gas sensors, color imaging, cores of audio frequency, microwave absorber, high frequency transformers coils and medical diagnosis.

Acknowledgements

I wish to express my special thanks to Professor Dr Khin Khin Win, Head of Department of Physics, University of Yangon, for her kind permission to carry out this work.

I wish to express my special thanks to Dr Nyunt Soe, Pro-Rector of Pyay University and Dr Nilar Myint, Pro-Rector of Pyay University, Bago Division for their kind permission to carry out this paper.

I am deeply indebted to Dr Pyone Pyone Shein, Professor, Head of Physics Department, Pyay University to support my paper.

I am also grateful to Dr Naw Htoo Lar Phaw, Professor, Department of Physics Pyay University for her invaluable assistance in presentation my paper.

Reference

1. Cullity B D (1978) "Elements of X-Ray Diffraction" (Reading: Wesley)
2. Goldstein et al (1981) "Scanning Electron Microscopy and X-Ray Microanalysis Manuals" (Singapore: Plenum)
3. Marder M P (2000) "Condensed Matter Physics" (New York: Wiley)
4. Moulson A J & Herbert J M (1997) "Electroceramics Materials, Properties & Applications" (London: Chapman & Hall)
5. Patil S M et al (2013) International Journal of Advanced Research in Electrical, Electronics and Instrumentation Engineering 2 (8) 3814
6. Rana M et al (2002) Pakistan Journal of Applied Sciences 2 (12) 1110
7. Rietveld H M (1969) Journal of Applied Crystallography 2 65
8. Ross S D (1972) "Inorganic Infrared and Raman Spectra" (New York: McGraw-Hill)
9. Spilde M N & Adcock C (1999) "Scanning Electron Microscope: Operator's Manual" Department of Earth and Planetary Science, University of New Mexico
10. Vaingankar A F et al (1997) Journal of Physics 4 (C1) 155

STUDY OF DNA SEQUENCE IN HUMAN GENES WITH STATISTICAL MECHANICS

Shwe Sin Oo*

Abstract

All living things have DNA. Human DNA contains about 38,000 genes. Characteristics of these living things depend on DNA sequence. Each gene sequence is determined by the way the base amino acid pairs (AT and CG) are arranged. In this work, human DNA base pairs were studied by statistical mechanics to investigate if the existing arrangement of these base pairs in human genes are in statistical equilibrium according to Maxwell-Boltzmann statistics.

Key words: DNA, base amino acid pairs (AT and CG), Maxwell-Boltzmann statistics

Introduction

Statistical Mechanics and the Structure of DNA

In a system of N particles where each particle can access to different energy levels $E_1, E_2, E_3, \text{ etc.}$, one can talk about the most probably partition where n_1 number of particles are in E_1 , n_2 number of particles in E_2 etc. When the system is in this most probable partition, we say that the system is in statistical equilibrium. In classical statistical mechanics, Maxwell-Boltzmann distribution determines the number of particles in each energy levels for the statistical equilibrium. For the system to be in statistical equilibrium, Maxwell-Boltzmann distribution says that the number of particles in energy level E_i is given by

$$n_i = g_i \exp(- a - b E_i)$$

Where a and b are constants and g_i is the intrinsic probability of a particle to be in the state with energy E_i If all the energy levels are equally accessible, we will take $g_1 = g_2 = g_3 = \dots = g$ etc.. The constant b is related to temperature by

$$b = 1/kT$$

*. Assistant Lecturer, Department of Physics, Loikaw University

Where k is the Boltzmann constant and T is the temperature. In order to understand how to determine if a system of N particles is in statistical equilibrium, consider a system of $N=5000$ particles with available energies $E_1=0$, $E_2=E$, and $E_3=2E$ where E is some known energy. Now let us suppose that we know how many particles are in each energy levels. For example, let us take $n_1=1000$, $n_2=3500$ and $n_3=500$. Since the total number of particles is $N=5000$ and, to be in the statistical equilibrium we must use the expression for each n_i given by the Maxwell-Blotzmann distribution. i.e.

$$5000 = n_1 + n_2 + n_3 \quad (A)$$

At statistical equilibrium, we get (for simplicity, in this example we take $g=1$ without loss of generality)

$$5000 = \exp(-a - b E_1) + \exp(-a - b E_2) + \exp(-a - b E_3)$$

Recall that, in this example, $E_1 = 0$, $E_2 = E$ and $E_3 = 2 E$. Now by naming $y = \exp(-bE)$, $n_1 = \exp(-a)$, $n_2 = \exp(-a - bE) = n_1 y$, and $n_3 = \exp(-a - 2bE) = n_1 y^2$

Equation (A) becomes

$$5000 = n_1 + n_1 y + n_1 y^2 \quad (B)$$

The total energy is given by

$$E(\text{total}) = n_1 E_1 + n_2 E_2 + n_3 E_3$$

From the given numbers

$$E(\text{total}) = (1000 \times 0) + (3500 \times E) + (500 \times 2E) = 4500 E$$

Now, to be in statistical equilibrium (SE), the total energy is given by

$$E(\text{total-SE}) = \exp(-a - b E_1) E_1 + \exp(-a - b E_2) E_2 + \exp(-a - b E_3) E_3$$

$$4500 E = E (n_1 y) + 2E (n_1 y^2) \text{ which leads to}$$

$$4500 = n_1 y + 2 n_1 y^2 \quad (C)$$

We can eliminate n_1 between (B) and (C) and get

$$11y^2 + y - 9 = 0$$

Which gives $y = +0.86$ where we have taken only the positive root since $y = \exp(-bE)$.

We can then find n_1 from either (B) or (C) and obtain $n_1=1923$. We also obtain $n_2 = n_1 y = 1653$ and $n_3 = n_1 y^2 = 1422$. Therefore we have found the populations of each energy level at statistical equilibrium. We also note that, the given configuration $n_1=1000$, $n_2=3500$ and $n_3=500$ is not the most probable partition. That means it was not in statistical equilibrium. If we found that the original n_i s are very close to the calculated ones using Maxwell-Boltzmann distribution, we can conclude that the system is in statistical equilibrium.

At this point, we introduce the most basic ideas about DNA (Deoxyribo Nucleic Acid) and its structure. The discovery and the study of the structure of DNA has been one of the most exciting and challenging experiences that scientists have faced. As early as 1940s scientists started using bacteria and viruses in the study of genetics. The rapid reproduction rate of these simple life forms allowed the scientists to make a detail study of the structure of the genes. Even at that time, there were evidence that DNA played the role of a storage for genetic information. In 1953, James Watson and Francis Crick discovered the double helix structure of DNA. Now it is well known that DNA has a double helix structure with two sugar-phosphate backbones with rungs consisting of amino-acid base pairs. [1] In DNA, there are four types of amino-acids. (i) A (Adenine) (ii) T (Thymine) (iii) C (Cytosine) (iv) G (Guanine). Thymine (T) always pairs up with Adenine (A) and Guanine (G) always pairs up with Cytosine (C), hence AT and CG pairs. This DNA molecule is very long and the human DNA if stretched out would be about 2 meters long. It is like a long ladder with the two side rails made out of sugar and phosphate molecules and the rungs are entirely made out of AT (Adenine and Thymine) and CG (Cytosine and Guanine) pairs. Human DNA contains billions of these amino- acid pairs. There are approximately about 30,000 genes in human DNA. Each gene has a distinct sequence of AT and CG base pairs. Depending on the sequence of these base pairs, different types and amounts of proteins are produced in the organism. Each gene can contain from a couple of hundred base pairs to millions of base pairs. In between the genes in the DNA there are sequences which are the reminiscence of our evolution.

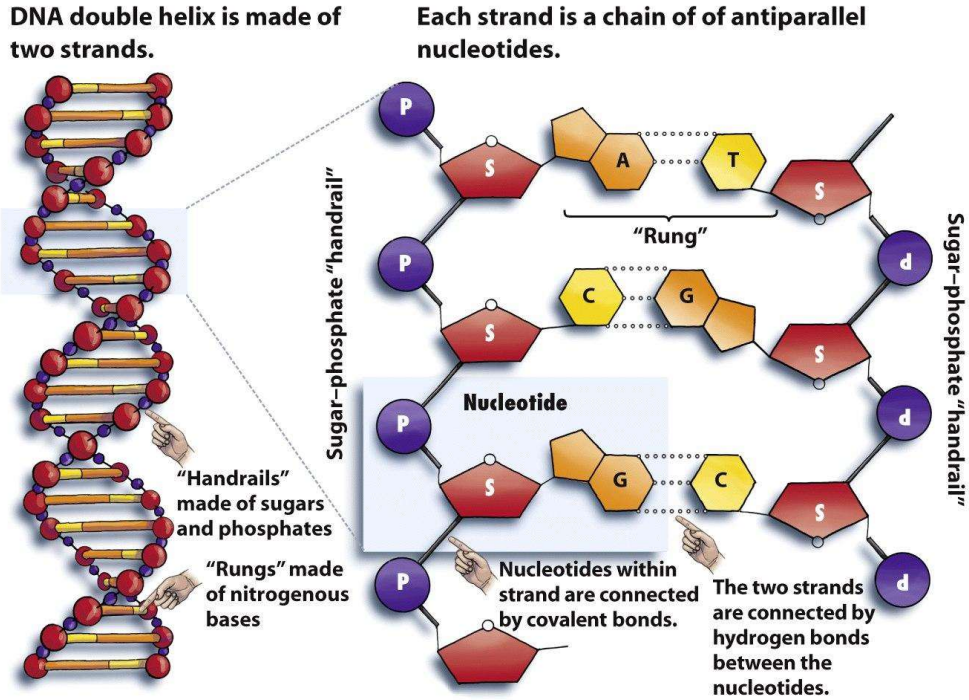


Figure 2-13ab Biology: Science for Life, 2/e © 2007 Pearson Prentice Hall, Inc.

Figure 1. Structure and replication of DNA.

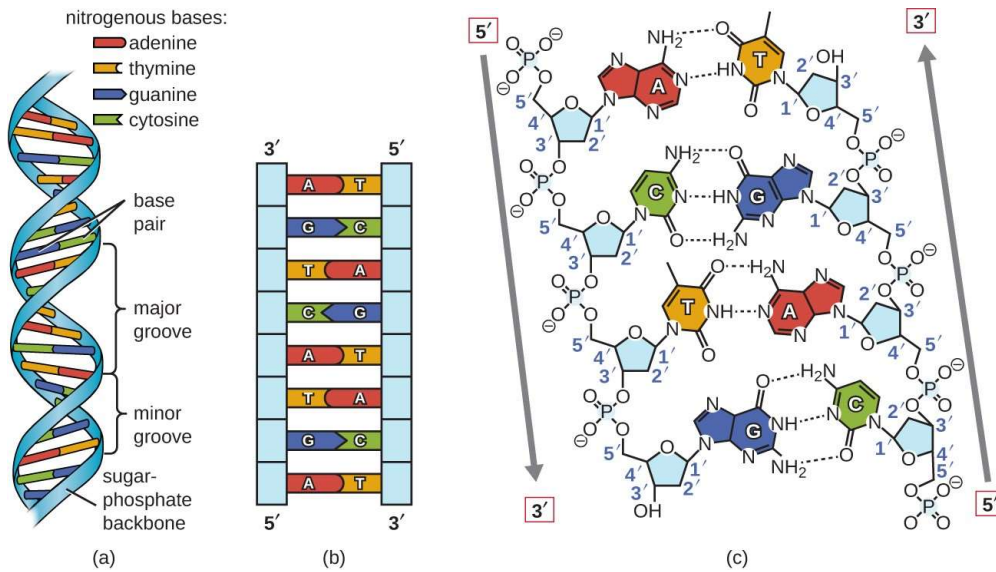


Figure 2. Structure and function of DNA.

All living things have DNA which stores the genetic information. The material that make DNA is the same regardless of whether it comes from a tree or an insect or a human. What is important is the sequence of these base pairs (amino acid pairs). The difference in the sequence makes each organism different.

Materials and Methods

DNA and Statistical Equilibrium

Now, we look at DNA from the point of view of statistical mechanics which is a very powerful tool in studying many particle systems. Let suppose a given gene has a total of 1000 base pairs with 375 pairs of ATs and 625 pairs of CG. Obviously there are millions of possible ways to arrange these base pairs in this gene. The following is one possible segment of a gene.

```

A T T T G C C G T G A T G C T T G G A T G
| | | | | | | | | | | | | | | | | |
T A A A C G G C A C T A C G A A C C T A C
    
```

Since these amino acids A, T, C and G interact with each other, an AT pair between a CG and an AT will have different energy than an AT pair between CG and GC. Since an A is always attached to a T and a C is always attached to a G, we can consider AT as a single particle and a GC as a single particle. Since their energies will depending on what their nearest neighbors, each AT and CG have different accessible energy levels. There are ten possible ways to sandwich a base pair. For example, an AT base pair can be in between

```

AAA      AAT      AAC      AAG
| | |    | | |    | | |    | | |
TTT      TTA      TTG      TTC

      TAT      TAC      TAG
      | | |    | | |    | | |
      ATA      ATG      ATC
    
```



Similarly we can sandwich a CG base pair the same way and we will get ten different possibilities again.

Since the interactions between different amino acids vary, the net energy for each AT base pair for the above sandwiching possibilities are all different. This gives us ten different energy levels for AT pair and ten levels for a CG pair.

Now, for a given gene sequence, we have a known number of AT base pairs and CG base pairs and they are arranged in a specific sequence. The natural question to ask is, if the sequence put this many particle system in a statistical equilibrium. As far as we are aware, no one has studied the question of statistical equilibrium regarding a gene sequence.

In the following, we outline our method for finding out if a DNA gene sequence is in statistical equilibrium.

First, we take each base pair AT and CG as single particles. This is justified because, A and T are always together and C and G are always together. We take AT and CG to be two different types of particles. The number of AT s and CG s can simply be obtained by counting them from the gene sequence under study. Next we need to consider the energies of each AT and CG. The change in free energies (Gibb free energy) of the base pairs which takes the nearest neighbor in to account is given by John Santa Lucia [3]. In his work, Lucia obtained the energies by making a comparison among the experimental results from seven different laboratories. [3]. There exists many other studies of base pair stacking and parameterization of the energies.

First consider the case of the base pair AT. Now for the total number NT of ATs we can write at equilibrium

$$NT(AT) = g_1 \exp(-a - b E_1) + g_2 \exp(-a - b E_2) + g_3 \exp(-a - b E_3) + \dots$$

By assuming that intrinsic probabilities for all levels to be the same, i.e. $g_1 = g_2 = \dots = g = 1$ we can write

$$NT(AT) = \exp(-a - b E_1) (1 + \exp(-b (E_2 - E_1)) + \exp(-b (E_3 - E_1)) + \dots)$$

$$NT(AT) = n_1 (1 + \exp(-b (E_2 - E_1)) + \exp(-b(E_3 - E_1)) + \dots) \tag{D}$$

Here the value of NT(AT) is obtained from counting the numbers of ATs in the gene sequence.

Now for the total energy of ATs, we write

$$ET(AT) = g_1 E_1 \exp(-a - b E_1) + g_2 E_2 \exp(-a - b E_2) + g_3 E_3 \exp(-a - b E_3) + \dots$$

Again, we take $g_1 = g_2 = g_3 = \dots = g = 1$, we write

$$ET(AT) = \exp(-a - b E_1) (E_1 + E_2 \exp(-b(E_2 - E_1)) + E_3 \exp(-b(E_3 - E_1)) + \dots)$$

$$ET(AT) = n_1 (E_1 + E_2 \exp(-b(E_2 - E_1)) + E_3 \exp(-b(E_3 - E_1)) + \dots) \tag{E}$$

The value of ET(AT) on the left hand side of equation (E) is obtained from

$$ET(AT) = E_1 n_1 + E_2 n_2 + E_3 n_3 + \dots$$

Where all the n_i are obtained from counting the gene sequence.

Now, if our gene sequence is in statistical equilibrium, equations (D) and (E) must be consistent for a given temperature. Note that NT(AT) is obtained from counting and $(E_i - E_1)$ are obtained experimentally. Since $b = 1/kT$, temperature comes in through the value of b. Therefore for a given temperature, we can obtain n_1 from equation (D). (The most appropriate temperature to use here is the normal human body temperature which is about 37 degree C.) This n_1 value must also satisfy equation (E) if the system is in statistical equilibrium. A similar set of equations for CG can also be written and the same set of criteria must be applied to test statistical equilibrium.

Results and Discussion

In order to test our method of determining if a DNA sequence is in statistical equilibrium, we obtain a gene sequence from data base provided by The National Center for Biotechnology Information under the National Institute of Health, United States of America. [2]

Species: Homo sapiens (human)

Chromosome:1

Gene : S100A10

Number of rungs: 294

ATGCCATCTCAAATGGAACACGCCATGGAAACCATGATGTTTACAT
 TTCACAAATTCGCTGGGGATAAAGGCTACTTAACAAAGGAGGACC
 TGAGAGTACTCATGGAAAAGGAGTTCCTGGATTTTTGGAAAATCA
 AAAAGACCCTCTGGCTGTGGACAAAATAATGAAGGACCTGGACCA
 GTGTAGAGATGGCAAAGTGGGCTTCCAGAGCTTCTTTCCCTAATT
 GCGGGCCTCACCATTGCATGCAATGACTATTTTGTAGTACACATGA
 AGCAGAAGGGAAAGAAGTAG

Species: Homo sapiens (human)

Chromosome: 1

Gene: SPRR4

Number of rungs: 240

ATGTCTTCCCAGCAGCAGCAGCGGCAGCAGCAGCAGTGCCCACCC
 CAGAGGGCCCAGCAGCAGCAAGTGAAGCAGCCTTGTCAGCCACCC
 CCTGTAAATGTCAAGAGACATGTGCACCCAAAACCAAGGATCCA
 TGTGCTCCCCAGGTCAAGAAGCAATGCCACCGAAAGGCACCATC
 ATCCAGCCCAGCAGAAGTGTCCCTCAGCCCAGCAAGCCTCCAAG
 AGCAAACAGAAGTAA

We tested our method on these two genes using the energy values provided by Lucia [3] and we found that the condition for statistical equilibrium is not satisfied as expected. Calculation was done only using a pocket calculator. Here we note that these gene sequences are short, with 294 base pairs and 240 base pairs respectively.

Conclusion

In order to make a more concrete conclusion, we need to test on more genes with more number of base pairs. For long gene sequence where the number of base pairs involved can easily exceeds millions, calculations cannot be performed without the help of computer. We are in the process of developing a computer code which will read very long sequence (in millions) of the base pairs and test the statistical equilibrium. The other logical steps in this research would be to improve upon the energy values of the base pairs. One way would be to make a quantum mechanical model to calculate the energy levels of the base pairs using some well-known interaction potentials such as the harmonic oscillator model or Morse potential.

Acknowledgement

I would like to thank Dr Maung Maung and Dr Soe Myint Thein, Pro- Rectors, Loikaw University and Professor Dr. Than Than Myint, Head of department of Physics, Loikaw University for their kind permission to carry out this work. I am deeply indebted to my Advisor Professor Dr. Khin Maung Maung (Department of Physics and Astronomy, University of Southern Mississippi, USA), for his valuable advices for this work.

References

1. Benjamin A. Pierce , W. H. Freeman and company, NY. (2002) "Genetics"
2. Data Base, National Center for Biotechnology Information under the National Institute of Health, United States of America.
3. John Santa Lucia, Proc. Natl. Acad. Sci. "A unified view of polymer, dumbbell, and oligonucleotide DNA nearest neighbor thermodynamics", USA, Vol 95, pp 1460, 1998
4. NY. McGraw Hill (1997) "McGraw Hill Encyclopedia of Science and Technology"

THEORETICAL ANALYSIS ON J-PARC E31 EXPERIMENT

Win Win Maw¹, Thida Wint², Khin Swe Myint³,
Yoshinori Akaishi⁴, Toshimitsu Yamazaki⁵

Abstract

The research work is to analyze the missing mass and the invariant mass spectra of $D(K^-, n) \Lambda(1405)$ reaction process which was conducted at J-PARC E31 experiment with 1.0 GeV/c incident momentum of K^- . This reaction is expected to enhance a virtual $\bar{K}N$ scattering process, where a K^- beam kicks a neutron out of the deuteron target in a forward angle and is slowing down to form a $\Lambda(1405)$ with a residual nucleon. We have calculated the missing mass spectrum $D(K^-, n) Y$ reaction with Green's function method by using YA potential for $\bar{K}N$ interaction. We have also used the $\bar{K}N \rightarrow \pi\Sigma$ coupled channel Yukawa type separable potential to compute the invariant mass spectrum. We observed that the missing mass spectrum of the $D(K^-, n) Y$ reaction at a neutron forward angle has two peaks below the K^-p threshold and above the threshold respectively. The former peak represents $\Lambda(1405)$ state while the latter is a quasi-free K^-p peak. We have analyzed the invariant mass spectrum of $D(K^-, n)(\Sigma\pi)^{I=0}$ where final state $\Sigma\pi$ is given in $|I=0\rangle$ isospin basis. Our calculated invariant mass spectrum of $\Sigma\pi$ shows the prominent peak below the threshold while quasi-free part is largely suppressed. We have also studied the invariant mass spectrum with final $\Sigma\pi$ charge states separately which are $\Sigma^+\pi^-$, $\Sigma^-\pi^+$, $\Sigma^0\pi^0$

Key words: virtual $\bar{K}N$ scattering, missing mass spectrum, invariant mass spectrum.

Introduction

An antikaon (\bar{K}) and a nucleus may form a bound state (a kaonic nucleus), due to the strong attraction between \bar{K} and nucleon in an isospin $I=0$ state. $\Lambda(1405)$ resonance state is nominally accepted as a bound state of

¹ Assistant lecturer, Physics Department, Mandalay University, Mandalay, Myanmar

² Lecturer, Physics Department, Mandalay University, Mandalay, Myanmar

³ Emeritus Professor, Physics Department, Mandalay University, Mandalay, Myanmar

⁴ Professor, Dr, College of Science and Technology, Nihon University, Chiba, Japan and RIKEN Nishina Center, Saitama, Japan

⁵ Professor, Department of Physics, University of Tokyo, Bunkyo-ku, Tokyo 113-0033, Japan

K^-p system which lies in the continuum region of $\pi\Sigma$, having strangeness $S=-1$, total charge $Q=0$, isospin $I=0$ and spin parity $J^P=1/2^-$.

The updated PDG value of the mass and width of this $\Lambda(1405)$ resonance state or often known as Λ^* is $1405.1_{-1.0}^{+1.3}$ MeV/ c^2 and 50.5 ± 2.0 MeV (Particle Data Group K. A. Olive *et al.*, (2014)) with 27 MeV binding energy with respect to $\bar{K}N$ threshold.

On the other hand, chiral unitary model claims that $\Lambda(1405)$ may have two pole structure; one is mainly coupled to $\pi\Sigma$ state and the other is to $\bar{K}N$ state which are located at different positions, (1390-132i) MeV and (1426-32i) MeV, respectively (T. Hyodo and A. Weise, (2008)). As a consequence, the resonance position of the $\Lambda(1405)$ is 1420 MeV/ c^2 and the binding energy is as shallow as 15 MeV.

The mass and width of $\Lambda(1405)$ resonance were obtained to be 1400.5 ± 4.0 MeV/ c^2 and 50.0 ± 2.0 MeV from production of $\Lambda(1405)$ in K^-p reactions at 4.2 GeV/c (R. J. Hemingway, (1985)) by Dalitz and Deloff (R. H. Dalitz and A. Deloff, (1991)). It is interpreted as a quasi-bound state of $\bar{K}N$ coupled with continuum state of $\pi\Sigma$.

Esmaili *et al.*, (J. Esmaili, Y. Akaishi and T. Yamazaki, (2010), (2011)) analyzed old bubble-chamber of stopped- K^- on ^4He (B. Riley *et al.*, (1975)) with a resonance capture process, and found the best-fit value of mass and width for the $\Lambda(1405)$ are $1405.1_{-1.0}^{+1.3}$ MeV/ c^2 and $24.0_{-3.0}^{+4.0}$ MeV.

Maryam *et al.* (M. Hassanvand, Y. Akaishi, T. Yamazaki, (2015)) have calculated the $\Lambda(1405) \rightarrow (\pi\Sigma)^0$ invariant mass spectra produced in the reaction $K^- + p \rightarrow \Sigma^+(1660) + \pi^-$, followed by $\Sigma^+(1660) \rightarrow \Lambda(1405) + \pi^+ \rightarrow \Sigma\pi + \pi^+$, processes at $p(K^-)=4.2$ GeV/c.

Many experimentalists and theorists have studied the structure of $\Lambda(1405)$ with different reactions by using various methods since nearly 1960's. But, the structure of $\Lambda(1405)$ is still a controversial problem. So, H. Noumi *et al.*, proposed an experiment to study $\Lambda(1405)$ via the D (K^- , n) reaction at J-PARC (E31). In this experiment, missing mass and invariant-mass spectrum of D (K^- , n) at a neutron forward angle were measured. We

analyzed both missing mass and the invariant-mass spectrum of D (K^- , n) Λ (1405) reaction process with K^- momentum 1.0 GeV/c is incident upon the deuteron target.

Formulation of differential cross section for D (K^- , n) Λ (1405)

The mathematical expression for spectral function is the most significant factor to determine the reaction cross-section. Therefore, we are going to determine the differential cross section and spectral function for D (K^- , n) Λ (1405) reaction. The differential cross section is defined as the transition rate per incident flux.

$$d^6\sigma = \frac{L^3}{v_0} \frac{2\pi}{\hbar} \sum_n \delta(E_i - E_f^{(n)}) \left(\frac{L}{2\pi}\right)^3 d\vec{k}_n \left(\frac{L}{2\pi}\right)^3 d\vec{K} |T_{fi}^{(n)}|^2 \tag{1}$$

Where, $\frac{L^3}{v_0}$ = incident flux, incident kaon velocity, $v_0 = \frac{\hbar k_0 c^2}{E_0}$,

$\left(\frac{L}{2\pi}\right)^3 d\vec{k}_n \left(\frac{L}{2\pi}\right)^3 d\vec{K}$ is phase space, $\delta(E_i - E_f^{(n)})$ is energy conservation term and, T=transition operator.

We consider the elementary process of reaction is $K^- + D \rightarrow n + \Lambda(1405)$.

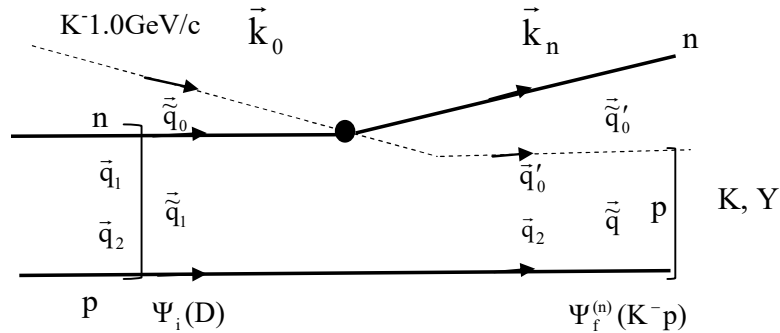


Figure 1. Schematic diagram of the reaction D (K^- , n) Λ (1405) reaction

Transition Matrix Element

We describe, transition matrix for D (K⁻, n) Λ (1405) reaction as follows, $T_{fi} = \langle \text{final state} | T | \text{initial state} \rangle$

$$T_{fi} = \langle \Psi_f^n(\mathbf{K}^- \mathbf{p}), \bar{\mathbf{K}}, \bar{\mathbf{k}}_n | T | \Psi_i(D), \bar{\mathbf{0}}, \bar{\mathbf{k}}_0 \rangle \quad (2)$$

Where, $\Psi_f^n(\mathbf{K}^- \mathbf{p})$ involves $\bar{\mathbf{q}}_2$ and $\bar{\mathbf{q}}'_0$, $\Psi_i(D)$ involves $\bar{\mathbf{q}}_1$ and $\bar{\mathbf{q}}_2$.

The transition matrix element can be expressed as follows;

$$|T_{fi}^{(n)}|^2 = \left| \int d\bar{\mathbf{q}}_1 \langle \Psi_f^{(n)}(\mathbf{K}^- \mathbf{p}) | \bar{\mathbf{q}} \rangle \delta(\bar{\mathbf{K}} + \bar{\mathbf{k}}_n - \bar{\mathbf{k}}_0) [\bar{\mathbf{q}}'_0 | t_{\mathbf{K}^- \mathbf{n}} | \bar{\mathbf{q}}_0] [\bar{\mathbf{q}}_1 | \Psi_i(D)] \right|^2 \quad (3)$$

By substituting equation (4) into equation (1), and then we get,

$$\frac{d^2\sigma}{d\cos(\theta)} = \frac{(2\pi)^5}{\hbar^2 k_0 c^2} E_0 k_n^2 dk_n \left| \langle t_{\mathbf{K}^- \mathbf{n}} \rangle \right|^2 \times \left(-\frac{1}{\pi} \text{Im} \int d\bar{\mathbf{r}}' d\bar{\mathbf{r}} f^*(\bar{\mathbf{r}}') \langle \bar{\mathbf{r}}' | \frac{1}{E - H_{\mathbf{K}^- \mathbf{p}} + i\varepsilon} | \bar{\mathbf{r}} \rangle f(\bar{\mathbf{r}}) \right) \quad (4)$$

Where, $\frac{(2\pi)^5}{\hbar^2 k_0 c^2} E_0 k_n^2 dk_n \left| \langle t_{\mathbf{K}^- \mathbf{n}} \rangle \right|^2$ is the kinematical factor and

$$\left(-\frac{1}{\pi} \text{Im} \int d\bar{\mathbf{r}}' d\bar{\mathbf{r}} f^*(\bar{\mathbf{r}}') \langle \bar{\mathbf{r}}' | \frac{1}{E - H_{\mathbf{K}^- \mathbf{p}} + i\varepsilon} | \bar{\mathbf{r}} \rangle f(\bar{\mathbf{r}}) \right) \text{ is the spectral function } S(E).$$

In this spectral function equation, $\langle \bar{\mathbf{r}}' | \frac{1}{E - H_{\mathbf{K}^- \mathbf{p}} + i\varepsilon} | \bar{\mathbf{r}} \rangle$ is the Green's function.

Green's function can be expressed by coordinate representation

$$G(\bar{\mathbf{r}}', \bar{\mathbf{r}}) = \langle \bar{\mathbf{r}}' | \frac{1}{E - H_{\mathbf{K}^- \mathbf{p}} + i\varepsilon} | \bar{\mathbf{r}} \rangle \quad (5)$$

(H_{K^-p} is Hamiltonian of K^- and p nucleus or K^-p system)

It is satisfies the following equation,

$$(E - H_{K^-p})G^+(\vec{r}', \vec{r}) = \langle \vec{r}' | I | \vec{r} \rangle = \delta(\vec{r}' - \vec{r}) \tag{6}$$

Radial part of Green's function $G^+(r', r)$ satisfies the following equation,

$$[k^2 + \frac{d^2}{dr^2} - \frac{\ell(\ell+1)}{r^2} - \tilde{U}(r)]G_{\ell}^+(r', r) = \frac{2\mu}{\hbar^2} \delta(r' - r) \tag{7}$$

$$k = \sqrt{\frac{2\mu E}{\hbar^2}}, \tilde{U}(r) = \frac{2\mu}{\hbar^2} V_{K^-p}(r)$$

Green's function $G_{\ell}^+(r', r)$ is divided into two regions $G_{\ell_1}^+(r', r)$ and $G_{\ell_2}^+(r', r)$ with,

$$G_{\ell_1}^+(r', r) = C_1 u_{\ell}^{(0)}(r) \quad \text{where, } (0 < r < r')$$

$$G_{\ell_2}^+(r', r) = C_1 u_{\ell}^{(+)}(r) \quad \text{where, } (r' < r < \infty)$$

$u_{\ell}^{(0)}(r)$ and $u_{\ell}^{(+)}(r)$ satisfies,

$$[k^2 + \frac{d^2}{dr^2} - \frac{\ell(\ell+1)}{r^2} - \tilde{U}(r)]u_{\ell}^{(0)}(r) = 0 \text{ with boundary condition } u_{\ell}^{(0)}(0) = 0.$$

$$[k^2 + \frac{d^2}{dr^2} - \frac{\ell(\ell+1)}{r^2} - \tilde{U}(r)]u_{\ell}^{(+)}(r) = 0 \quad \text{with boundary condition}$$

$$u_{\ell}^{(+)}(r \rightarrow \infty) = kr h_{\ell}^+(kr).$$

According to the continuity of Green's function,

$$C_1 u_{\ell}^{(0)}(r) \Big|_{r'} = C_2 u_{\ell}^{(+)}(r) \Big|_{r'} \tag{8}$$

Discontinuity of $\frac{dG}{dr}$ gives

$$C_1 u_\ell^{(0)'}(\mathbf{r})|_{r'} - C_2 u_\ell^{(+)' }(\mathbf{r})|_{r'} = \frac{2\mu}{\hbar^2} \tag{9}$$

We have

$$G_\ell^{(+)}(\vec{r}', \vec{r}) = \frac{2\mu}{\hbar^2} \sum_{\ell=0}^{\infty} \sum_M Y_{\ell M}(\hat{r}') \frac{u_\ell^{(+)}(\mathbf{r}) u_\ell^{(0)}(\mathbf{r}_\zeta)}{W(u_\ell^{(0)}, u_\ell^{(+)})} Y_{\ell M}^*(\hat{r}) \tag{10}$$

The missing mass spectrum from this reaction is calculated by using Green's function method. It can express as follows;

$$\frac{d^2 \sigma}{dY d\cos(\theta)} = \frac{(2\pi)^5}{\hbar^4 k_0} E_0 k_n^2 \left| \langle t_{K^-n} \rangle \right|^2 \frac{Y}{\left(1 + \frac{E_Y}{E_n}\right) k_n - k_0 \cos(\theta)} \times \frac{2\mu}{\hbar^2} \left(\frac{-1}{\pi}\right) \text{Im} \left[\sum_\ell (2\ell+1) \int dr dr' j_\ell^*(Qr') u_i^*(r') \frac{u_\ell^{(+)}(\mathbf{r}) u_\ell^{(0)}(\mathbf{r}_\zeta)}{W(u_\ell^{(0)}, u_\ell^{(+)})} j_\ell(Qr) u_i(\mathbf{r}) \right] \tag{11}$$

Calculation of reaction cross-section with separable potential for $\Sigma\pi$ invariant- mass spectrum from D (K^- , n) reaction

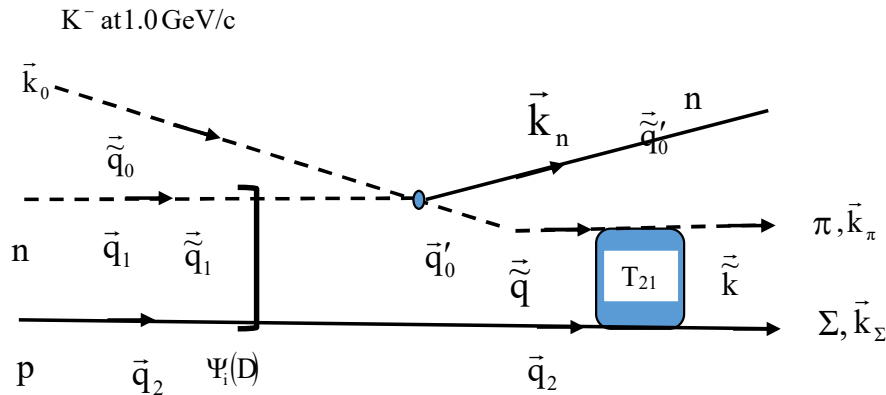


Figure 2. Schematic diagram of D (K^- , n) ($\Sigma\pi$)⁰ decay process

We can express transition matrix element and differential cross-section for $\Sigma\pi$ decay process as follows;

$$T_{fi} = \left[\bar{k}_\pi, \bar{k}_\Sigma, \bar{k}_n \left| T \right| \bar{k}_0, \bar{0}, \Psi_i \right] \tag{12}$$

$$d^3\sigma = \frac{L^3}{v_0} \frac{2\pi}{\hbar} \sum_n \delta(E_i - E_f^{(n)}) \left(\frac{L}{2\pi}\right)^3 d\bar{k}_n \left(\frac{L}{2\pi}\right)^3 d\bar{K} \left(\frac{L}{2\pi}\right)^3 d\tilde{k} \left| T_{fi}^{(n)} \right|^2 \tag{13}$$

$$\begin{aligned} \frac{d^2\sigma}{dYc^2d\cos\theta_n} &= 2 \left(\frac{2\pi}{\hbar c}\right)^6 \left| \langle t_{K^-n} \rangle \right|^2 \frac{E_0}{k_0} \frac{k_n^2 E_Y}{\left(1 + \frac{E_Y}{E_n}\right) k_n - k_0 \cos\theta_n} \\ &\times |F_d(Q)|^2 \left| g(\tilde{k}) T_{21}(Y) \right|^2 \frac{\tilde{E}_\pi \tilde{E}_\Sigma}{\tilde{E}_\pi + \tilde{E}_\Sigma} \tilde{k}(Y) \end{aligned} \tag{14}$$

In equation (2.3), T_{21} is the transition matrix element for $\bar{K}N - \Sigma\pi$ coupled-channel system. So, we have used the $\bar{K}N \rightarrow \pi\Sigma$ coupled channel Yukawa type separable potential to compute the invariant mass spectrum.

$\bar{K}N - \Sigma\pi$ coupled-channel system

We treat the K^*p quasi-bound state as a Feshbach resonance (H. Feshbach, Ann. Phys. (1958), (1962)) embedded in the $\Sigma\pi$ continuum by using Akaishi-Myint-Yamazaki’s (AMY) phenomenological model. In the AMY model, we use a set of separable potentials with a Yukawa-type form factor for the coupled system of $\bar{K}N$ and $\Sigma\pi$ channels.

$$\langle \bar{k}'_i \left| v_{ij} \right| \bar{k}_j \rangle = g(\bar{k}'_i) U_{ij} g(\bar{k}_j), \quad \langle \tilde{k} \left| t_{21} \right| \tilde{q} \rangle = g(\tilde{k}) T_{21}(Y) g(\tilde{q})$$

$$g(\tilde{k}) = \frac{\Lambda^2}{\Lambda^2 + \tilde{k}^2}, \quad U_{ij} = \frac{1}{\pi^2} \frac{\hbar^2}{2\sqrt{\mu_i \mu_j}} \frac{1}{\Lambda} s_{ij}$$

Where, i (j) stands for the $\bar{K}N$ channel, 1, or the $\Sigma\pi$ channel, 2, μ_i (μ_j) is the reduced mass of channel i (j), and s_{ij} are non-dimensional strength parameters. Then, a complex potential with the following strength is derived analytically;

$$s_1^{\text{opt}}(E) = s_{11} - s_{12} \frac{\Lambda^2}{(\Lambda - i\kappa_2)^2 + s_{22}\Lambda^2} s_{21}, E + \Delta M c^2 = \frac{\hbar^2}{2\mu_2} \kappa_2^2$$

$\Delta M = m_{K^-} + M_p - m_{\pi^-} - M_{\Sigma^+} = 103 \text{ MeV}/c^2$ is the threshold mass difference,

κ_2 is a complex momentum in the $\Sigma\pi$ channel.

In this model, we use $s_{22} = -0.66$, which gives $U_{22}/U_{11} = 4/3$ for $\Lambda(1405)$ as in a ‘‘chiral model’’, and $\Lambda = 3.90/\text{fm}$. In this mode, the loop integral is

$$\tilde{G}(E) = \int d\vec{q}' d\vec{q} \frac{\Lambda^2}{\Lambda^2 + \vec{q}'^2} \left\langle \vec{q}' \left| \frac{1}{E - H + i\epsilon} \right| \vec{q} \right\rangle \frac{\Lambda^2}{\Lambda^2 + \vec{q}^2}$$

The transition –matrix of the two coupled channels, $\overline{K}N$ (1) and $\Sigma\pi$ (2), obeys the following equation;

$$\begin{pmatrix} T_{11} & T_{12} \\ T_{21} & T_{22} \end{pmatrix} = \begin{pmatrix} U_{11} & U_{12} \\ U_{21} & U_{21} \end{pmatrix} + \begin{pmatrix} U_{11} & U_{12} \\ U_{21} & U_{21} \end{pmatrix} \begin{pmatrix} G_1 & 0 \\ 0 & G_2 \end{pmatrix} \begin{pmatrix} T_{11} & T_{12} \\ T_{21} & T_{21} \end{pmatrix}$$

The solutions of each matrix are;

$$T_{ii} = \frac{1}{1 - U_{ii}^{\text{opt}} G_i} U_{ii}^{\text{opt}}, \quad T_{ji} = \frac{1}{1 - U_{jj}^{\text{opt}} G_j} U_{ji}^{\text{opt}}$$

The generalized optical potentials are;

$$U_{ii}^{\text{opt}} = U_{ii} + U_{ij} \frac{G_j}{1 - U_{jj} G_j} U_{ji}, \quad U_{ji}^{\text{opt}} = U_{ji} \frac{1}{1 - U_{ii} G_i}$$

It should be noticed that the two-channel coupled equation is divided into four single-channel effective equations without any approximation by the use of the optical potentials. The invariant mass spectrum from $K^- + D \rightarrow n + \Lambda(1405) \rightarrow n + (\Sigma\pi)^{(0)}$ is calculated by using separable potential.

Results and Discussions

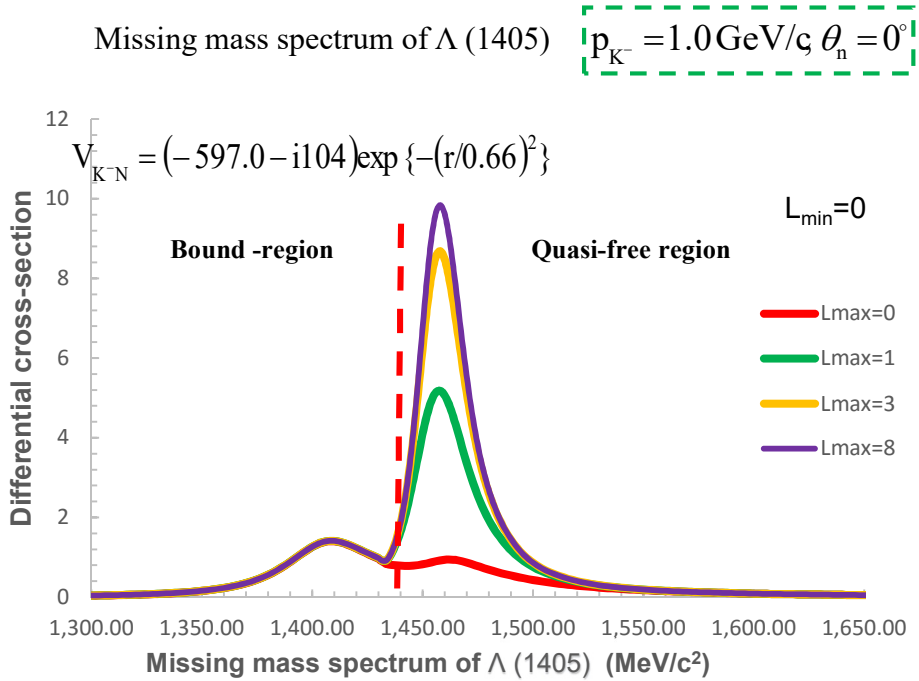


Figure 3. Missing mass spectrum of Λ (1405) with different angular momentum. Red color dotted line represents the $\bar{K}N$ threshold.

The calculated missing mass spectrum of the $D(K^-, n)$ reaction for various angular momentum distribution as shown in fig.(3). Here, we used the YA potential for K-P bound system with $(V_0, W_0) = (-597.0 \text{ MeV}-104.0 \text{ MeV})$. From the calculated missing mass spectrum, it can be seen that $\bar{K}N$ bound state is mainly contributed by $L=0$ while in continuum region, higher angular momentum contributions dominate. According to our analysis, the mass and width of Λ (1405) is about $1409.0 \text{ MeV}/C^2$ and 47 MeV , respectively.

Invariant mass spectrum of $D(K^-, n)(\Sigma\pi)^{(I=0)}$ reaction

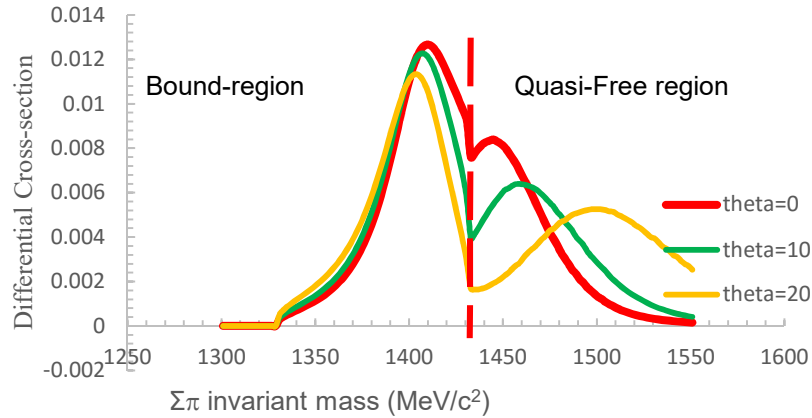


Figure 4. $\Sigma\pi$ invariant mass spectrum with $\theta_n=0^\circ, 10^\circ, 20^\circ$. Red color dotted line represents the $\bar{K}N$ threshold.

Figure (4) shows the $\Sigma\pi$ invariant mass spectrum with emitted neutron angles, $\theta_n=0^\circ, 10^\circ, 20^\circ$. We observe that the peak position in bound state region remain unchanged while the quasi-free peaks shift towards the higher mass region with an increase angle, θ_n . From the calculated invariant mass spectrum, the mass and width of $\Lambda(1405)$ is about $1406.0 \text{ MeV}/c^2$ and 52 MeV , respectively. The value of mass and width of $\Lambda(1405)$ which obtained from missing mass spectrum is nearly consistent that of $\Sigma\pi$ invariant mass spectrum.

Deuteron size effect upon the $\Sigma\pi$ invariant mass spectrum

We studied the deuteron size effect upon the $\Sigma\pi$ invariant mass spectrum by changing the size parameter 'a' of deuteron wave function,

which is given by $\psi_i = \left(\frac{a}{2\pi}\right)^{\frac{3}{4}} e^{-\frac{1}{4}ar^2}$, where smaller 'a' gives larger size.

We have arbitrarily varied the deuteron size by multiplying the size parameter 'a' with a multiplicative factor 'f'. The results are shown in figure (5).

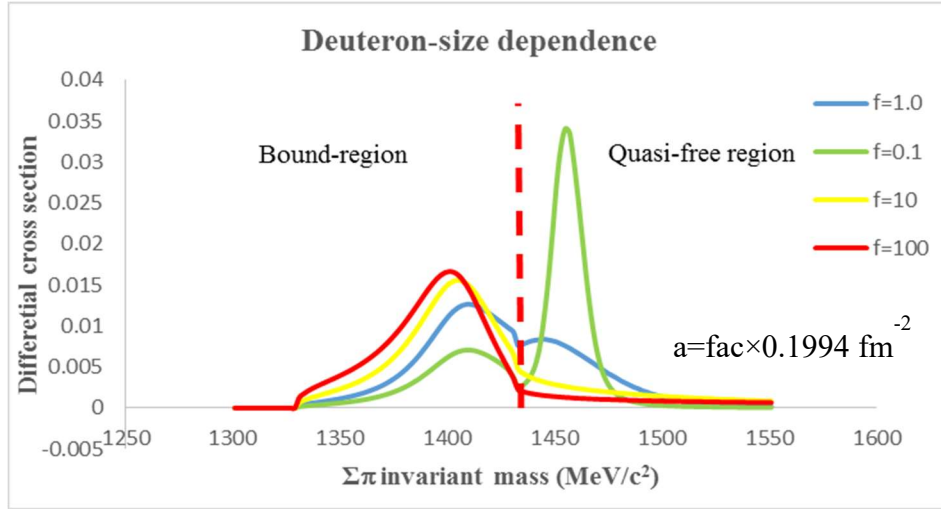


Figure.5 $\Sigma\pi$ invariant mass spectrum depends on deuteron size. Red color dotted line represents the $\bar{K}N$ threshold.

We investigated the deuteron size effect for the cases; $f = 0.1, 1, 10$ and 100 respectively which are shown in the above figure. From this investigation, it is found that the smaller the deuteron size (larger ‘a’), the larger the differential cross-section.

Invariant mass-spectrum of D (K^- , n) $\Sigma\pi$ charge basis

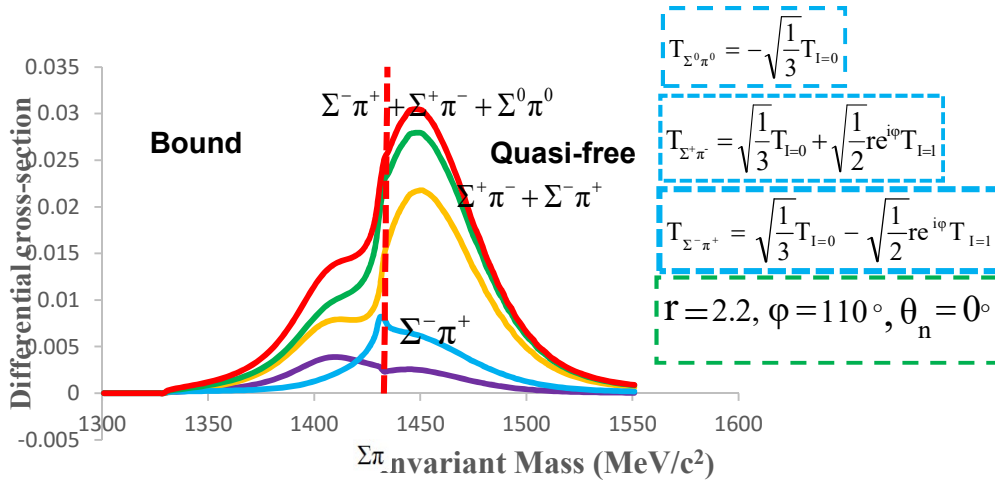


Figure 6. Invariant mass spectrum with final $\Sigma\pi$ charge states. . Red color dotted line represents the $\bar{K}N$ threshold

E 31 experimental data compare with our results and Chiral unity model results

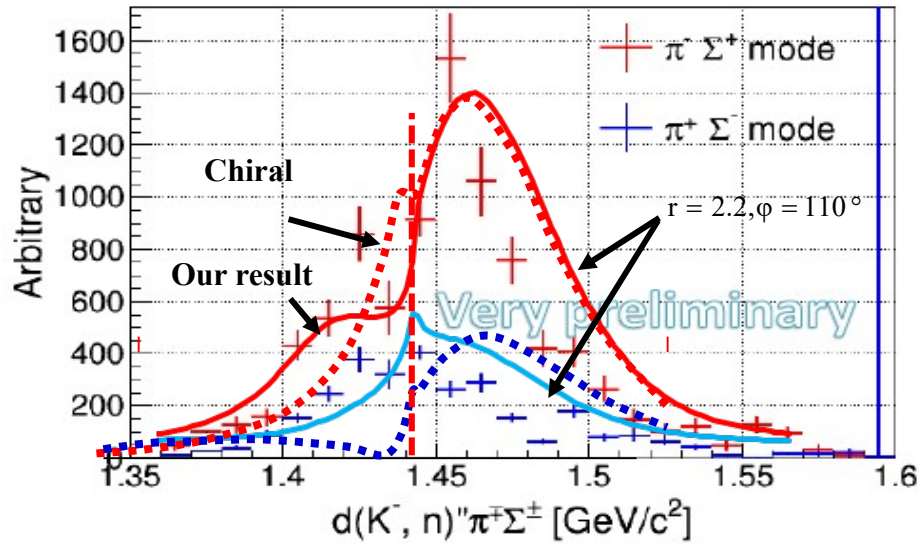


Figure 7. E 31 experimental data compare with our results. . Red color dotted line represents the $\bar{K}N$ threshold

Conclusion

We have analyzed the missing mass and the invariant-mass spectrum of $D(K^-, n) \Lambda(1405)$ reaction at the incident momentum of $K^- 1.0 \text{ GeV}/c$. The calculated results of invariant mass spectrum of $\Sigma^+ \pi^-$ and $\Sigma^- \pi^+$ are in good agreement with the values obtained from a very preliminary experimental data of $D(K^-, n)(\Sigma\pi)^{(0)}$ charge states. Moreover, the calculated results are also consistent with the updated PDG (2016) value

Acknowledgements

I would like to specially thank to my supervisor, Dr Khin Swe Myint, Emeritus Professor, Rector (Rt.d), University of Mandalay, for her invaluable advices and enthusiastic guidance throughout this work.

I do thank Dr Lei Lei Win, Professor and Head of Physics Department, University of Mandalay, for her encouragement and permission.

I also thank my co-supervisor, Dr Thida Wint, Lecturer, Physics Department, University of Mandalay, for her discussions and collaborations.

References

1. B. Riley, I-T. Wang, J. G. Fetkovich and J. M. McKenzie, (1975), Phys. Rev. **D 11** 3065.
2. H. Feshbach, Ann.Phys. (1958) **5** 357; (1962) **19** 287.
3. H. Noumi *et al.*, Spectroscopic study of hyperon resonances below $\bar{K}N$ threshold via the (K^-, n) reaction on deuteron (J-PARC E31), http://j-parc.jp/researcher/Hadron/en/pac_1207/pdf/E31_1202-9.pdf.
4. J. Esmaili, Y. Akaishi and T. Yamazaki, (2010), Phys. Lett. **B 686** 23.
5. J. Esmaili, Y. Akaishi and T. Yamazaki, (2011), Phys. Rev. **C 83** 055207.
6. Maryam Hassanvand, Yoshinori Akaishi, Toshimitsu Yamazaki, (3 Oct 2015), arXiv; **1510.00870v1** [hep-ph].
7. R. H. Dalitz and A. Deloff, (1991), J. Phys. G: Nucl. Part. Phys. **17** 289.
8. R. J. Hemingway, (1985), Nucl. Phys. **B 253** 742.
9. T. Hyodo and A. Weise, (2008), Phys. Rev. **C 77** 035204.
10. Y. Akaishi, K. S. Myint and T. Yamazaki, (2008), Proc. Jpn. Acad. **B 84** 264.
12. Particle Data Group K. A. Olive *et al.*, (2016), Chin. Phys. **C 40** 100001.

SENSITIVITY AND APPLICATION TO LOW Z-ELEMENTS BY X – RAY DETECTION SYSTEM

Thet Thet Cho¹, KathiNwe²,Nyein Nyein³, KalyarThwe⁴

Abstract

The sensitivity of the X ray detection has been investigated for low Z-elements. The sample preparation and measurement were made for low Z elements to determine the influence of the pelletizing pressure on sensitivity. Depending on characteristics of SPECTRO XEPOS Spectrometer, the minimum pelletizing pressure of the sample for low Z element was determined. The results indicated that the minimum pelletizing pressure of the samples is required for the reduction of surface effect and to yield precise results. For aluminum and silicon, the minimum pressed weight of 14 ton is needed, but for potassium, a pressed weight of 12 ton is adequate. For sulfur and calcium, the pressed weight of 10 ton is sufficient. The optimized values have been tested and demonstrated on standard reference material GSR 07. It is observed that in the experimental configurations currently installed, these optimum valued allowed to determine the certified values with an accuracy of 1.33% for low-Z elements.

Key words: XRF, Low Z-element, Sensitivity

Introduction

X-ray fluorescence spectrometry is one of the most widely used routine instrumental methods of elemental analysis of biological, geological and environmental samples. Some factors that are affected on the sensitivity and accuracy of an Energy Dispersive X-Ray Fluorescence (EDXRF) Spectrometer are the excitation source, the instrumental settings and the sample preparation.

In XRF measurement, sample preparation is necessary when the sample is inhomogeneous the surface layer is not representative for the whole sample. As a condition for the reliable analysis by XRF, a flat and even surface of specimen

¹. Dr, Assistant Lecturer, Department of Physics, University of Mandalay

². Dr, Professor, Department of Physics, Mandalay University of Distance Education

³. Dr, Lecturer, Department of Physics, Sagaing University

⁴. Dr, Professor, Department of Physics, University of Mandalay

is required. Particularly for the determination of light elements, the surface should be prepared mirror like, as scattering effect due to rough texture influence the results. An appropriate surface can be normally obtained by pressing the sample into pellet. Accuracy of Calibration Procedure for Energy-Dispersive X-Ray Fluorescence Spectrometry was carried by Markowicz, Haselberger and Mulenga in 1992. The Cnseten EDXRF Spectrometers – Sensitivity, Calibration and Application to Geochemistry were also researched by Rahmani and et al. in 2001. In this work, sample preparation has been done to study the influence of the palletizing pressure of the sample on the measurement sensitivity.

X-Ray Fluorescence Spectroscopy

For each energy region of the electromagnetic radiation, spectrometry has advanced as the associated experimental tools have been developed. The first and crudest detectors often just measure the presence of the radiation, in the second stage, they also measure the intensity of the radiation, but with only a minimum of information on its energy; and the final type measures the intensity as a function of the photon energy, i.e., they generate a spectrum. Williams (1976) give an extensive discussion of the history of spectroscopy for many of the wavelength ranges and of general and specific measurement methods. Historically, the last energy region of electromagnetic radiation to be studied was the high-energy part, the X-ray and γ -ray.

The XRF analysis has been developed by the use of primary excitation source unit, high efficiency detectors, types of spectrometer and measuring electronics. The energy dispersive spectrometers with solid-state detectors are widely used in Energy Dispersive X-ray Fluorescence Analysis.

Experimental Arrangement and Measurement

Sample Collection and Preparation

The elements from aluminum to calcium were chosen to analyze low- Z elements with XRF spectrometer system. Therefore five kinds of samples contained low Z-elements; aluminum oxide (Al_2O_3), silicon dioxide (SiO_2), sulfur (S), potassium carbonate (K_2CO_3) and calcium oxide (CaO) were collected from Academy Chemical Group. The grade of the collected samples

is analytical reagent (AnalaR). The sample matrixes and molecular weight percentage of low- Z elements in the samples used in this experiment are presented in Table (1).

Sample preparation is an important role in XRF measurement because it is crucial to the relationship between spectral line intensity and the elemental concentration. The analysis of sample in the form of powder pellets must represent one of the simplest possible forms of sample preparation. Prepared pellets must be homogenized. If the sample is inhomogeneous, the surface layer is not representative for the whole sample. The solid samples, silicon dioxide and calcium oxide were split and milled into smaller pieces, which were then suitable for further grinding. The subsamples were ground manually with a mortar and a pestle. After grinding, the particle size distributions were determined by using sieves.

The fine powders were prepared as pellets. Then hydraulic press machine (PP-25, Retsch, GmbH) and a 32 mm diameter die set including a die body, base and two polished metal disks were used for pellet sample in our research work. Prior to pelletizing all parts of the die set were carefully cleaned with methylated spirit to prevent contamination. Initially each sample was weighed using digital balance (PW-254) to obtain the needed amount (5 g). Binding agent is added to form stable pellet of the samples. Therefore, binder (1 g) was added to the sample (5 g) and they were mixed to homogenize with each other. In this experiment, Hoechst Wax (HWC) was used as binder. After that weighed sample was poured into the mould and was pressed with 4 ton for 5 minutes by using hydraulic press machine. The pellet was then removed from the die set, taking care not to crack it in the process. For each sample the applied pelletizing pressures are 4 ton, 8 ton, 12 ton, 16 ton and 20 ton respectively. By changing the pelletizing pressure different thickness of pellets were obtained. Pressing time was taken 5 minutes for each pellet. In this procedure three replicated pellets per sample were made (Fig,1 - 5).

Table 1. Sample matrix and molecular weight percentage of low Z-elements in the samples

Sample Matrix	Element	Atomic Number(Z)	Molecular weight (%)
Al ₂ O ₃	Al	13	52.94
SiO ₂	Si	14	46.74
SO ₃	S	16	40.05
K ₂ CO ₃ + KHCO ₃	K	19	47.81
Ca(OH) ₂ +CaCO ₃	Ca	20	47.07



Figure 1. The photograph of pressed pallets of aluminum dioxide samples



Figure 2. The photograph of pressed pallets of silicon dioxide samples



Figure 3. The photograph of pressed pallets of sulfur samples

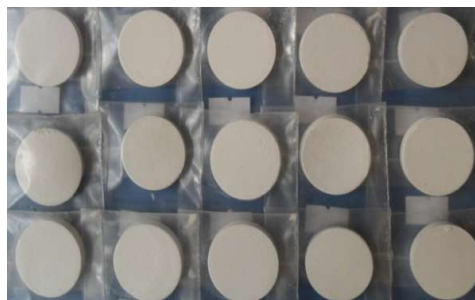


Figure 4. The photograph of pressed pallets of potassium carbonate samples

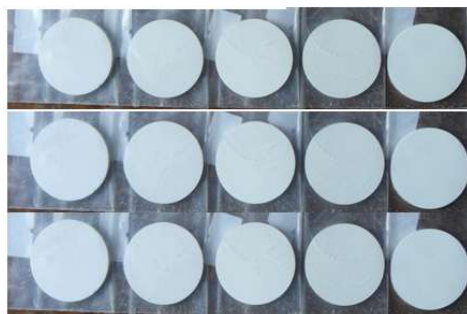


Figure 5. The photograph of pressed pellets of calciumoxide samples

X-ray Fluorescence Spectrometer

The X-ray fluorescence spectrometer used in this work is SPECTRO XEPOS spectrometer at Department of Physics, University of Mandalay. A 50 watt palladium (Pd) anode end-window X-rays tube is used to excite the samples. Three secondary targets used in this spectrometer are Highly Orient Pyrolytic Graphite (HOPG), Molybdenum (Mo) and Aluminum Oxide (Al_2O_3). They offer many different excitation conditions ensuring optimum determination of all elements from aluminum to uranium. HOPG is used for light elements and Mo is used for medium elements. For heavy elements, Al_2O_3 secondary target is applied. The XRF spectrometer consists of a Si (Li) detector with resolution of 160 eV for 5.9 keV ($\text{Mn } k_\alpha$).

X-ray Measurements

X-ray fluorescence is one of the most common techniques for the analysis of the concentrations of many elements contained in the sample by a single measurement. In this research work, all the pelletized samples were measured by using SPECTRO XEPOS spectrometer. Initially, the primary beam from the X-ray tube impinges on one of the secondary targets, molybdenum which emits almost monochromatic X-ray. The monochromatic beam is then used to excite characteristic radiation from the atoms of the sample. The emitted X-ray by the elements presented in the sample is detected by Si (Li) detector. The samples were measured three times for each pellet to determine the precision of the analysis tools. Each measurement has been

carried out for 900 seconds with three secondary targets of the XRF spectrometer system. The obtained X-ray spectra were analyzed using X-LAB Pro 4.5 software to obtain the concentration of each element in the sample. The analyzed X-ray energy range is 0-12.5 keV for light elements presented in the sample. The analyzed X-ray energy lines of the element in the samples, molybdenum target and palladium anode are listed in Table (2).

Table 2. Analyzed X-ray Emission Energies (k eV)

Atomic number	Element	X-ray energies (keV)			
		K _α	K _β	L _α	L _{β1}
13	Al	1.486			
14	Si	1.739	1.829		
16	S	2.307	2.464		
19	K	3.312	3.589		
20	Ca	3.690	4.012		
42	Mo	17.441	19.600	2.293	2.394
46	Pd	21.121	23.806	2.838	2.990

Results and Discussion

The effects of pelletizing pressure on fluorescent intensity of low-Z elements were examined to determine the sensitivity and accuracy of XRF detection system. Experimental data for average concentrations of aluminum, silicon, sulfur, potassium and calcium elements in the samples concerned with different pressed weights are presented in Table (3). The dependence of concentration on pressed weight for aluminum element is shown in Fig. (6). In this figure, for pressed weight between (4 - 12) ton, the concentration values of aluminum element are considerably increased, but for (12 - 20) ton, the concentrations do not change within the error.

For silicon element, the variation of concentration with pressed weight(Fig.7) can be seen that the concentrations are gradually increased in

the pressed weight between (4-12)ton, and then the concentrations are changed unapparently between (12 - 20) ton.

The concentration of sulfur element for five different pressed weights (Fig. 8) is obvious that the concentration values of sulfur are slightly increased in pressed weight between (4 - 8)ton. After that, they remain unchanged within the error between (8 - 20) ton.

For potassium element, the concentration values are markedly increased with an increase in pressed weight from 4 ton to 12 ton then concentrations are gradually increased between (12 - 20) ton in Fig. (9).

In Fig. (10), the concentrations of calcium are slightly increased in pressed weight between (4 - 8) ton, although they do not significantly differ between (8 - 20) ton.

From these results, it is observed that the fluorescent intensity of low- Z elements depends on the pelletizing pressure. The reason for this dependence might be surface effect of the sample.

According to the figures, we found that the minimum pelletizing pressures are 14 ton for aluminum and silicon, 12 ton for potassium and 10 ton for sulfur and calcium.

The accuracy of the XRF detection system with these optimized values was verified by measuring a certified reference material as a routine sample. The linear plots of correlation between certified and measured values of standard reference material for 0 ton to 14 ton pressed weight are also illustrated in Fig. (11)-(15). From these figures, the best value of correlation factor was 0.9829 ($R^2 = 0.9997$) which points out the pressed weight 14 ton is needed for reliable accuracy for low- Z elements in standard reference material GSR 07.

Moreover the measured values of GSR 07 for these minimum pressed weights are compared with the certified values in Table (4). The linear correlation between these values is shown in Fig. (16). The experimental results showed good agreement comparing to the given certified values. It is observed that the relative accuracy values are minimum for 14 ton pressed

weight of aluminum and silicon, 12 ton for potassium and 10 ton for sulfur and calcium.

Table 3. Concentration of low Z - element in the sample at different pressed weights

Pressed weight (ton)	Average Concentration (%)				
	Al	Si	S	K	Ca
4	44.98±2.00	34.76±1.71	36.51±0.89	27.12±0.50	46.33±0.57
8	47.13±1.43	35.60±1.70	38.22±0.62	34.00±0.60	47.46±0.42
12	51.73±2.07	36.78±1.81	38.38±0.86	40.01±0.86	47.38±0.46
16	51.99±2.30	37.12±1.70	38.62±0.67	41.00±0.48	47.48±0.61
20	51.57±2.61	37.15±1.23	38.81±0.52	42.05±0.83	47.45±0.49

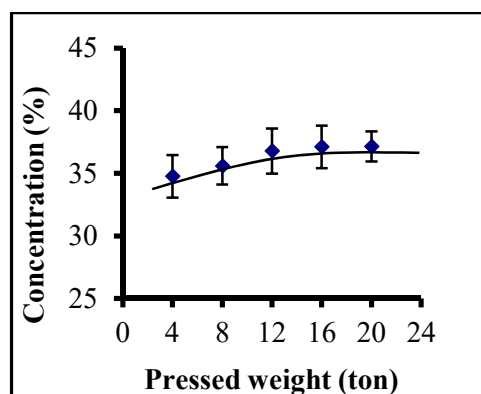
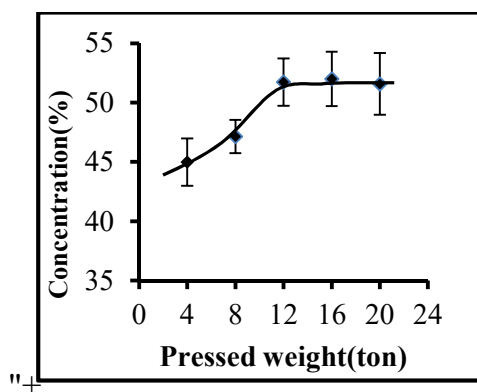


Figure 6. Concentration of aluminum element in the sample at different pressed weights

Figure 7. Concentration of silicon element in the sample at different pressed weights

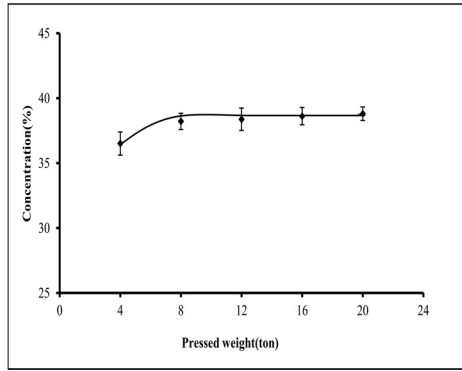


Figure 8. Concentration of sulfur element in the sample at different pressed weights

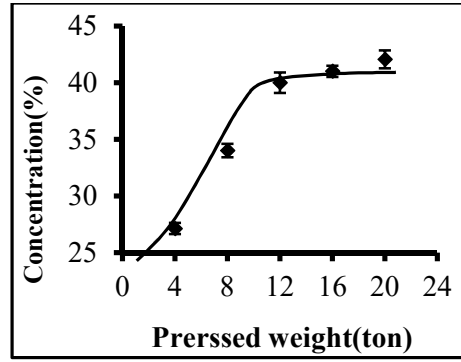


Figure 9. Concentration of potassium element in the sample at different pressed weights

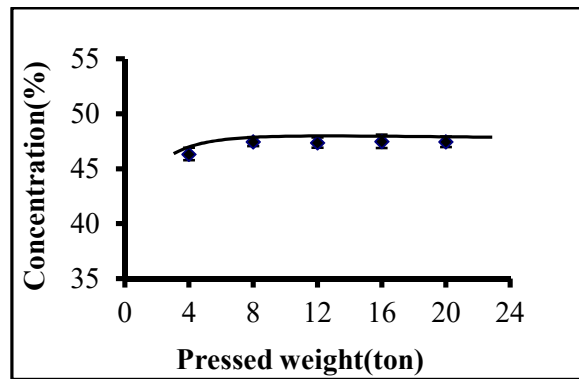


Figure 10. Concentration of calcium element in the sample at different pressed weights

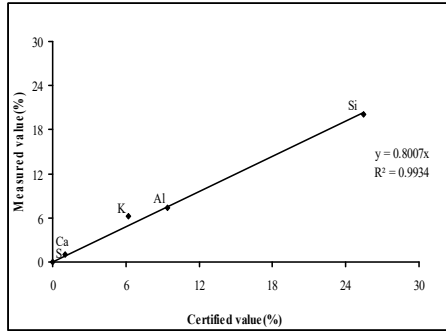


Figure 11. Correlation between certified and measured values of standard reference material GSR 07 for 0 ton pressed weight

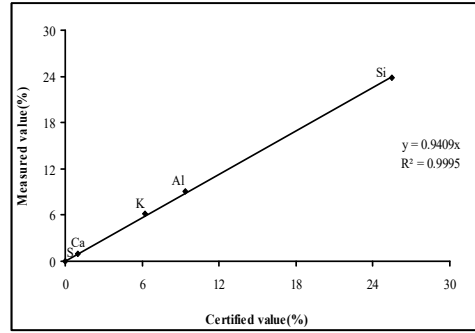


Figure 12. Correlation between certified and measured values of standard reference material GSR 07 for 8 ton pressed weight

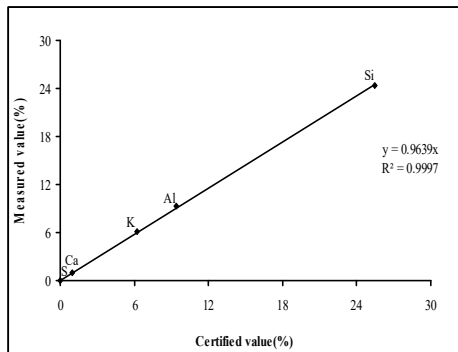


Figure 13. Correlation between certified and measured values of standard reference material GSR 07 for 10 ton pressed weight

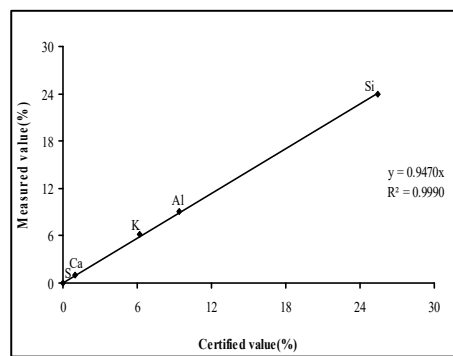


Figure 14. Correlation between certified and measured values of standard reference material GSR 07 for 12 ton pressed weight

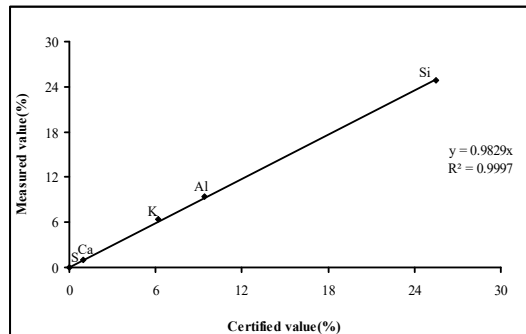


Figure 15. Correlation between certified and measured values of standard reference material GSR 07 for 14 ton pressed weight

Table 4. Analytical results compared to certified values for standard reference material, GSR 07

Element	Concentration (%)		Relative Accuracy (%)	Pressed weight (ton)
	Certified value	Measured value		
Al	9.3742	9.4020	0.2965	14
Si	25.4639	24.8600	2.3715	14
S	0.0100	0.0103	3.0000	10
K	6.2091	6.1880	0.3398	12
Ca	0.9934	0.9996	0.6241	10

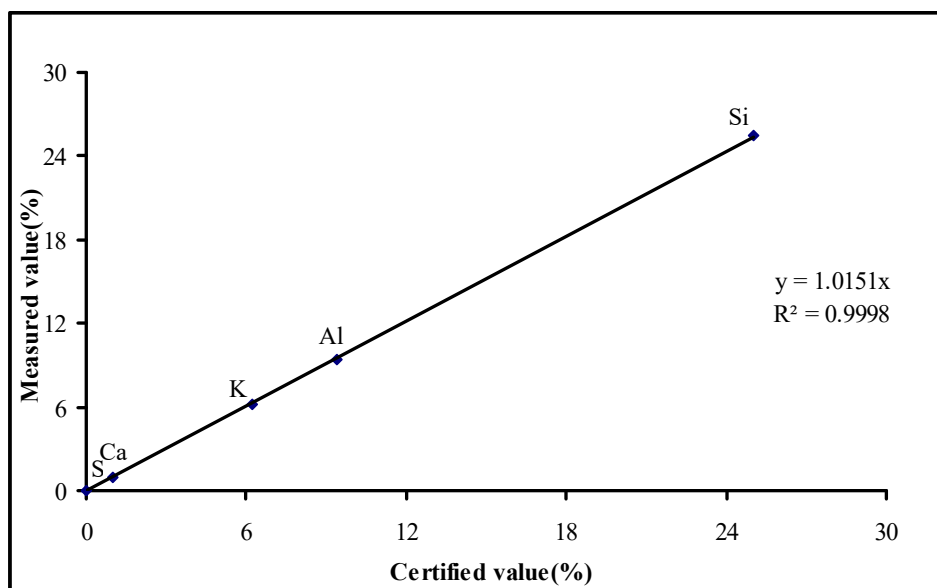


Figure 16. Correlation between certified and measured values for standard reference material GSR 07

Conclusion

The influence of the sample preparation on the elemental sensitivity value in XRF detection system has been studied for light elements. The results show that the choice of pelletizing pressure greatly influence the analysis results for low- Z elements. The results obtained from our research, it can be concluded that this minimum pelletizing pressure can reduce the surface effect. The minimum pelletizing pressure in turn affects the accuracy and precision of the XRF analysis. The correlation factor between certified and measured value of standard reference material GSR 07 with these optimized values is 1.0151. Therefore, these optimized values of pelletizing pressure could be applied and measured with the XRF spectrometer to obtain the accurate results for low- Z elements in any kinds of environmental samples.

Acknowledgements

We express our thanks to Rector Dr Thida Win, University of Mandalay, her permission and encouragement to conduct this research work.

References

1. A. Markowicz, N. Haseberger and P. Mulenga, (1992) "X-ray Spectrometry", **21** 271.
2. A. Rahmaniet al., "The Cnesten EDXRF Spectrometers-Sensitivity, Calibration and Application to Geochemistry"(2001), International Centre for Diffraction Data, **44**.
3. F M. S. Shackely, (2011) "X-Ray Fluorescence Spectrometry in Archaeology", Department of Anthropology, California,.
4. O. Icelli, (2011)"X-ray spectroscopic evaluation of zinc at different applied pressure", International Journal of the Physical Sciences, Turkey, **6**.
5. P. Kregsamer and A. Markowicz, (2003) "Elemental Sensitivity Method in XRF Analysis of PM₁₀Aerosol Filters", Nuclear Science and Technology, Austria, **2** 18.
6. V. Zivanovic, (2011) "XRF Analysis of Mineralogical Matrix Effects and Differences Between Pulverized And Fused Ferromanganese Slag", ERAMET concern laboratory, Norway Birkelands.
7. T. Eivindosnet al., "Problems by Using Pressed Powder Pellets for XRF Analysis of Ferrosilicon Alloys" (2001). International Centre for Diffraction Data, **44**.
8. Y. Maruyama et al., (2008) "Laboratory experiments of particles size effect in XRF and implications to remote X-ray spectrometry of lunar regolith surface", Society of Geomagnetism and Earth, Japan.

THEORETICAL INTERPRETATION ON $D(\pi^+, K^+)X$ INCLUSIVE MISSING MASS SPECTRUM OF J-PARC E-27 EXPERIMENT

Hnin Hnin Hlaing @ Nu Nu Lwin¹, Theingi², Khin Swe Myint³,
Yoshinori Akaishi⁴, Toshimitsu Yamazaki⁵

Abstract

In this research work, the inclusive missing-mass spectrum of $D(\pi^+, K^+)X$ reaction at J-PARC E-27 experiment have been studied. J-PARC E27 experiment was conducted to search for the simplest kaonic nuclear bound state by using $D(\pi^+, K^+)X$ reaction at the beam momentum of 1.7 GeV/c. In the E-27 experiment, high energy pion is incident upon deuteron target and interacts with neutron in the target to produce K^+ , K^- and p. Due to the strong attractive force between K^- and p, $\Lambda^* = \Lambda(1405)$ is formed as a doorway state to populate K^-pp . The missing mass spectrum obtained from E-27 experiment at J-PARC has covered energy regions of quasi free Λ -p, Σ -p, Λ^* -p, Σ^* -p production and K^-pp bound state. The missing mass spectrum of $D(\pi^+, K^+)X$ reaction covering all the above energy regions have been analyzed by using Green's function method.

Keywords: $\Lambda(1405)$ doorway state, quasi-free, inclusive spectrum.

Introduction

The theoretical predictions of possible existence of deeply bound \bar{K} nuclear states in light nuclei have been proposed theoretically by Akasishi and Yamazaki (Akaishi, Y., and Yamazaki, T. (1999)). They constructed $\bar{K}N$ interactions phenomenologically so as to reproduce low energy $\bar{K}N$ scattering data, kaonic hydrogen atom data and the binding energy and decay width of $\Lambda(1405)$, which is asserted to be an $I = 0$ quasi-bound state of $\bar{K}N$. These interactions are characterized by a strongly attractive $I = 0$ part. Yamazaki and Akaishi (Akaishi, Y., and Yamazaki, T. (2002) & Akaishi, Y., and Yamazaki,

¹. Physics Department, Mandalay University of Distance Education, Mandalay, Myanmar

². Physics Department, , Mandalay University, Mandalay, Myanmar

³. Physics Department, Mandalay University, Mandalay, Myanmar

⁴. RIKEN, Nishina Center, Wako, Saitama 351-0198, Japan

⁵. Department of Physics, University of Tokyo, Bunkyo-ku, Tokyo 113-0033, Japan

T. (2002)) have predicted the possible existence of nuclear \bar{K} bound states with narrow widths in (pp), ^3He , ^4He and ^8Be .

Moreover, the importance of the three body dynamics in predicting the resonance energy of strange dibaryon $\bar{K}\text{NN}$ has been investigated by Ikeda and Sato (Ikeda, Y., and Sato, T. (2007)). The binding energy for $\bar{K}\text{NN}$ is obtained to be 60-95 MeV and width to be 45-80 MeV by employing the $\bar{K}\text{N} - \pi\Sigma$ interaction based on the chiral lagrangian.

In search for quasi bound states in the $\text{K}^- \text{pp}$ system, the three-body $\bar{K}\text{NN}$ and $\pi\Sigma\text{N}$ coupled channel Faddeev calculation was also studied by Shevchenko et al. (Shevchenko, N.V., Gal, A., and Mares, J. (2007)). It should be noted that, even for the simplest kaonic nuclear system ($\text{K}^- \text{pp}$ system), different computation techniques and different $\bar{K}\text{N}$ interactions, have produced controversial results. These controversial theoretical issues have led to intensify the experimental search for kaonic nuclear systems.

Among the number of experimental searches for the simplest kaonic nucleus, FINUDA collaboration at DAΦNE (Agnello, M. *et al.*, (2005)) first reported an observation of the $\text{K}^- \text{pp}$ bound state. They investigated the stopped K^- reaction on several kinds of target and observed a number of Λp pairs emitted in back to back. They observed a bump structure in the invariant mass spectrum of these Λp pairs from the ^6Li , ^7Li and ^{12}C targets. By assuming that this structure is due to the $\text{K}^- \text{pp}$ bound state, the binding energy and the decay width were evaluated to be 115_{-5}^{+6} (stat) $_{-4}^{+3}$ (syst) MeV and 67_{-11}^{+14} (stat) $_{-3}^{+2}$ (syst) MeV, respectively, which is more binding than the previously mentioned theoretical values.

Another positive result of the $\text{K}^- \text{pp}$ bound state was also reported by the DISTO collaboration at SATURNE (Yamazaki, T. *et al.*, (2010)). They reanalyzed the data set of the $p + p \rightarrow \Lambda + p + \bar{q}_2$ reaction at $T_p = 2.85$ GeV and observed a bump structure in ΔM_{K^+} missing mass and $M_{\text{p}\Lambda}$ invariant mass spectra in large transverse momentum of protons and kaons. The binding

energy and decay width were determined as $103 \pm 3(\text{stat}) \pm 5(\text{syst})$ MeV and $118 \pm 8(\text{stat}) \pm 10(\text{syst})$ MeV, respectively. In this case the level width is much larger than that of FINUDA. Very recently, J-PARC E-27 experiment was carried out in an attempt to settle this controversial issue.

The J-PARC E-27 experiment has been proposed to search for the K^-pp bound state by using the (π^+, K^+) reaction on a liquid deuterium target at 1.7 GeV/c (Ichikawa, Y. *et al.*, (2013) & Ichikawa, Y. *et al.*, (2015)). In this experiment, there are many background processes of quasi-free hyperon production such as Λ , Σ , $\Lambda(1405)$ and $\Sigma(1385)$ and the signal of K^-pp was predicted to be small compared with the background (Yamazaki, T. *et al.*, (2007) & Akaishi, Y., Dote, A., and Yamazaki, T. (2005)). It was difficult to be observed in inclusive measurements. Therefore, coincidence of a proton from the decay of K^-pp was required to suppress these backgrounds. They have reported a broad peak structure around $2.27 \text{ GeV}/c^2$ in a proton-coincidence spectrum, which is attributed to the K^-pp bound state. Our purpose is to interpret theoretically inclusive missing-mass spectrum from the E-27 experiment. So, we have calculated missing mass spectrum of the E-27 production reaction by using Green's function method.

Mathematical Formulation of Reaction Cross Section

This section is the mathematical formulations of missing mass spectrum of $D(\pi^+, K^+)$ reaction. In this section, we have calculated transition matrix and differential cross section for this reaction by using Green's function method. A schematic diagram of the reaction mechanism is shown in Fig (1).

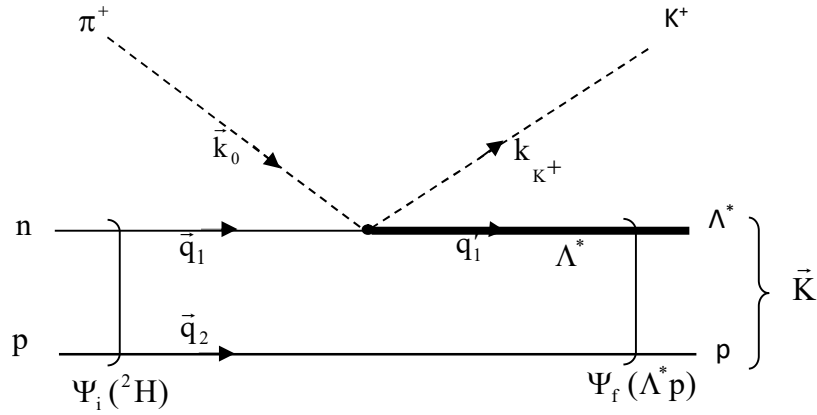


Figure1. Schematic diagram of the $D(\pi^+, K^+)X$ reaction.

Transition Matrix

We can write transition matrix between the initial state $\pi^+ + D$ and the final state $K^+ + \Lambda^* p$ of Fig (1).

$$T_{fi}^{(n)} = \langle \Psi_f^n, \bar{K}, \bar{k}_{K^+} | T | \bar{k}_0, 0, \Psi_i \rangle \tag{1}$$

Equation (1) becomes

$$T_{fi}^{(n)} = \left(\frac{L}{2\pi} \right)^9 \int d\bar{q}_1 \int d\bar{q}_2 \int d\bar{q}'_1 \langle \Psi_f^n, \bar{K} | \bar{q}_2, \bar{q}'_1 \rangle \left[\bar{k}_{K^+}, \bar{q}'_1 | T | \bar{k}_0, \bar{q}_1 \right] \left[\bar{q}_1, \bar{q}_2 | 0, \Psi_i \rangle \right] \tag{2}$$

We can write this equation in terms of relative momentum and center of mass momentum.

Therefore, equation (2) is rewritten as

$$T_{fi}^{(n)} = \left(\frac{L}{2\pi} \right)^9 \int d\bar{q}_1 \int d\bar{q}_2 \int d\bar{q}'_1 \langle \Psi_f^n, \bar{K} | \bar{q}', \bar{Q}' \rangle \left[\bar{q}'_1, \bar{k}_{K^+} | T | \bar{q}_1, \bar{k}_0 \right] \left[\bar{q} | \Psi_i \rangle \right] \left[\bar{Q} | 0 \right] \tag{3}$$

with relative momentum between neutron and pion $\vec{\tilde{q}}_1 = \frac{M_n \vec{k}_0 - m_{\pi^+} \vec{q}_1}{M_n + m_{\pi^+}}$

relative momentum between neutron and proton $\vec{\tilde{q}} = \frac{M_p \vec{q}_1 - M_n \vec{q}_2}{M_n + M_p}$

relative momentum between Λ^* and proton $\vec{\tilde{q}}' = \frac{M_{\Lambda^*} \vec{q}_2 - M_p \vec{q}'_1}{M_{\Lambda^*} + M_p}$

relative momentum between Λ^* and kaon $\vec{\tilde{q}}'_1 = \frac{M_{\Lambda^*} \vec{k}_{K^+} - M_{K^+} \vec{q}'_1}{M_{\Lambda^*} + M_{K^+}}$

Center of mass momentum of Λ^* and proton $\vec{Q}' = \vec{q}_2 + \vec{q}'_1$

and the center of mass momentum of neutron and proton $\vec{Q} = \vec{q}_1 + \vec{q}_2$

Ψ_i and Ψ_f are described by relative momentum only center of mass motion is not affected.

Therefore, equation (3) becomes,

$$T_{fi}^{(n)} = \left(\frac{L}{2\pi}\right)^9 \int d\vec{q}_1 \int d\vec{q}_2 \int d\vec{q}'_1 \overbrace{\langle \Psi_f^n | \vec{\tilde{q}}' \rangle}^1 \overbrace{[\vec{K} | \vec{Q}']}^2 \overbrace{[\vec{\tilde{q}}'_1 | t_{\pi n} | \vec{\tilde{q}}_1]}^3 \overbrace{[k_{K^+} + \vec{q}'_1 | k_0 + \vec{q}_1]}^4 \times \overbrace{[\vec{\tilde{q}} | \Psi_i \rangle]}^5 \overbrace{[\vec{Q} | 0]}^6 \tag{4}$$

Equation (4) becomes,

$$T_{fi}^{(n)} = \int d\vec{q}_1 \int d\vec{q}_2 \int d\vec{q}'_1 \langle \Psi_f^n | \vec{\tilde{q}}' \rangle \delta(\vec{K} - \vec{Q}') [\vec{\tilde{q}}'_1 | t_{\pi n} | \vec{\tilde{q}}_1] \delta(\vec{k}_{K^+} + \vec{q}'_1 - \vec{k}_0 - \vec{q}_1) \times [\vec{\tilde{q}} | \Psi_i \rangle \delta(\vec{Q}) \tag{5}$$

By integrating equation (5) with respect to $d\vec{q}'_1$,

$$T_{fi}^{(n)} = \int d\vec{q}'_1 \int d\vec{q}'_2 \overbrace{\langle \Psi_f^n | \vec{q}' \rangle}^{d\vec{q} d\vec{Q}} \delta(\vec{k}_{K^+} + \vec{K} - \vec{q}_2 - \vec{k}_0 - \vec{q}_1) \left[\vec{q}'_1 | t_{\pi n} | \vec{q}_1 \right] \left[\vec{q} | \Psi_i \rangle \delta(\vec{Q}) \quad (6)$$

After performing the integration with respect to $d\vec{Q}$, we obtained

$$T_{fi}^{(n)} = \delta(\vec{K} + \vec{k}_{K^+} - \vec{k}_0) \int d\vec{q} \langle \Psi_f^n | \vec{q}' \rangle \left[\vec{q}'_1 | t_{\pi n} | \vec{q}_1 \right] \left[\vec{q} | \Psi_i \rangle \quad (7)$$

where $\left[\vec{q}'_1 | t_{\pi n} | \vec{q}_1 \right]$ is the two-body t-matrix for the elementary process $\pi^+ + n \rightarrow K^+ + \Lambda^*$.

Differential Cross Section

Differential cross section of $D(\pi^+, K^+)X$ is calculated as;

$$d^6\sigma = \frac{L^3}{v_0} \frac{2\pi}{\hbar} \sum_n \delta(E_i - E_f^n) \left(\frac{L}{2\pi} \right)^3 d\vec{k}_{K^+} \left(\frac{L}{2\pi} \right)^3 d\vec{K} \left| T_{fi}^{(n)} \right|^2 \quad (8)$$

where, $d^6\sigma$ = the probability of producing this reaction with the emitted particle momentum between \vec{k}_{K^+} and $\vec{k}_{K^+} + d\vec{k}_{K^+}$ and with the kaonic nucleus momentum between \vec{K} and $\vec{K} + d\vec{K}$.

$$\frac{v_0}{L^3} = \text{incident flux, } v_0 = \frac{\hbar k_0 c^2}{E_0} = \text{incident kaon velocity}$$

$\delta(E_i - E_f^n)$ = energy conservation term

$$\left(\frac{L}{2\pi} \right)^3 d\vec{k}_{K^+} \left(\frac{L}{2\pi} \right)^3 d\vec{K} = \text{phase volume (or) phase space}$$

By substituting equation (7) in equation (8), equation (8) becomes,

$$d^6\sigma = \frac{L^3}{v_0} \frac{2\pi}{\hbar} \sum_n \delta(E_i - E_f^n) \left(\frac{L}{2\pi}\right)^3 d\vec{k}_{K^+} \left(\frac{L}{2\pi}\right)^3 d\vec{K} \times \delta^2(\vec{K} + \vec{k}_{K^+} - \vec{k}_0) \left| \int d\vec{q} \langle \Psi_f^n | \vec{q}' \rangle \left[\vec{q}' | t_{\pi n} | \vec{q}_1 \right] \left[\vec{q} | \Psi_i \rangle \right]^2 \right. \quad (9)$$

By integrating equation (9) with $d\vec{K}$, we get

$$d^3\sigma = \frac{(2\pi)^4}{\hbar^2 k_0 c^2} E_0 |\langle t_{\pi n} \rangle|^2 d\vec{k}_{K^+} \sum_n \delta(E_i - E_f^n) \left| \int d\vec{q} \langle \Psi_f^n | \vec{q}' \rangle \left[\vec{q} | \Psi_i \rangle \right]^2 \right. \quad (10)$$

by taking an averaged value $\langle t_{\pi n} \rangle$ as an approximation of $\left[\vec{q}' | t_{\pi n} | \vec{q}_1 \right]$. Now we are going to solve the energy conservation term $\sum_n \delta(E_i - E_f^n)$.

Energy of initial state, $E_i = E_0 + M_n c^2 + M_p c^2 - BE(2H)$

Energy of final state,

$$E_f^n = E_{K^+} + (M_{\Lambda^*} c^2 + M_p c^2) + \left\langle \Psi_f^n \left| H_{\Lambda^* p} \right| \Psi_f^n \right\rangle + \frac{\hbar^2}{2(M_{K^- pp})} (\vec{k}_0 - \vec{k}_{K^+})^2$$

where $\frac{\hbar^2 (\vec{k}_0 - \vec{k}_{K^+})^2}{2(M_{K^- pp})}$ = recoil energy of the product nucleus

$\left\langle \Psi_f^n \left| H_{\Lambda^* p} \right| \Psi_f^n \right\rangle$ = excitation energy of final state

Then $E_i - E_f^n$ is rewritten as;

$$E_i - E_f^n = E - \left\langle \Psi_f^n \left| H_{\Lambda^* p} \right| \Psi_f^n \right\rangle$$

where

$$E = (E_0 - E_{K^+}) + (M_n c^2 - M_{\Lambda^*} c^2) - BE(2H) - \frac{\hbar^2}{2(M_{K^-pp})} (\vec{k}_0 - \vec{k}_{K^+})^2$$

$\delta(E_i - E_f^n)$ is expressed as, $\delta(E_i - E_f^n) = \langle \Psi_f^n | \delta(E_i - E_f^n) | \Psi_f^n \rangle$

$$\delta(E_i - E_f^n) = \left(-\frac{1}{\pi} \right) \text{Im} \left\langle \Psi_f^n \left| \frac{1}{E - H_{\Lambda^* p} + i\varepsilon} \right| \Psi_f^n \right\rangle$$

The following term consists in the right hand side of equation (10) rewritten as

$$\begin{aligned} & \sum_n \delta(E_i - E_f^n) \left| \int d\vec{q} \langle \Psi_f^n | \vec{q} \rangle \langle \vec{q} | \Psi_i \rangle \right|^2 = \\ & \left(-\frac{1}{\pi} \right) \text{Im} \int d\vec{r} \int d\vec{r}' f^*(\vec{r}') \langle \vec{r}' | \frac{1}{E - H_{\Lambda^* p} + i\varepsilon} | \vec{r} \rangle f(\vec{r}) \end{aligned} \quad (11)$$

where $f(\vec{r}) = e^{-i\eta(\vec{k}_0 - \vec{k}_{K^+})\vec{r}} \Psi_i(\vec{r}) = e^{i\vec{q}\vec{r}} \frac{u_i(\vec{r})}{r} \frac{1}{\sqrt{4\pi}}$ with $\eta = \frac{M_p}{M_p + M_{\Lambda^*}}$

$$f^*(\vec{r}') = e^{-i\eta(\vec{k}_0 - \vec{k}_{K^+})\vec{r}'} \Psi_i^*(\vec{r}') = e^{-i\vec{q}\vec{r}'} \frac{u_i^*(\vec{r}')}{r'} \frac{1}{\sqrt{4\pi}}$$

$\Psi_i(\vec{r})$ = wave function of the target nucleus

Substituting equation (11) in equation (10) and it becomes,

$$\begin{aligned} d^3\sigma &= \frac{(2\pi)^4}{\hbar^2 k_0 c^2} E_0 \langle |t_{\pi n}| \rangle^2 k_{K^+}^2 dk_{K^+} 2\pi d\cos\theta_k \left(-\frac{1}{\pi} \right) \\ & \times \text{Im} \left[\int d\vec{r} \int d\vec{r}' f^*(\vec{r}') \left\langle \vec{r}' \left| \frac{1}{E - H_{\Lambda^* p} + i\varepsilon} \right| \vec{r} \right\rangle f(\vec{r}) \right] \end{aligned} \quad (12)$$

The final differential cross-section for missing-mass spectrum of the $D(\pi^+, K^+)X$ reaction is given by

$$\frac{d^2\sigma}{dYc^2d\cos\theta_K} = \frac{(2\pi)^5}{\hbar^2 k_0 c^2} E_0 \frac{k_{K^+} |\langle t_{\pi n} \rangle|^2}{\left\{ \frac{\hbar^2 c^2}{E_{K^+}} + \frac{\hbar^2}{M_{K^-pp}} \left(1 - \frac{k_0}{k_{K^+}} \cos\theta_{K^+}\right) \right\}} \quad (13)$$

$$\times \left(-\frac{1}{\pi} \right) \text{Im} \left[\int d\vec{r} \int d\vec{r}' f^*(\vec{r}') \langle \vec{r}' | \frac{1}{E - H_{\Lambda^*p} + i\epsilon} | \vec{r} \rangle f(\vec{r}) \right]$$

where the first term

$$\frac{(2\pi)^5}{\hbar^2 k_0 c^2} E_0 \frac{k_{K^+} |\langle t_{\pi n} \rangle|^2}{\left\{ \frac{\hbar^2 c^2}{E_{K^+}} + \frac{\hbar^2}{M_{K^-pp}} \left(1 - \frac{k_0}{k_{K^+}} \cos\theta_{K^+}\right) \right\}}$$

is the

kinematical factor and

the second term $\left(-\frac{1}{\pi} \right) \text{Im} \left[\int d\vec{r}' \int d\vec{r} f^*(\vec{r}') \langle \vec{r}' | \frac{1}{E - H_{\Lambda^*p} + i\epsilon} | \vec{r} \rangle f(\vec{r}) \right]$ is the spectral function $S(E)$.

The spectral function $S(E)$ contains Green's function $\left\langle \vec{r}' \left| \frac{1}{E - H_{\Lambda^*p} + i\epsilon} \right| \vec{r} \right\rangle$.

Green-function in coordinate representation is

$$G^+(\vec{r}', \vec{r}) = \left\langle \vec{r}' \left| \frac{1}{E - H_{\Lambda^*p} + i\epsilon} \right| \vec{r} \right\rangle$$

where $H_{\Lambda^*p} = T_{\Lambda^*p}$ and V_{Λ^*p} . H_{Λ^*p} is the Hamiltonian of Λ^*p .

The coordinate representation of Green's function $G^+(\vec{r}', \vec{r})$ which obey

$$\left\{ E - H_{\Lambda^* p} \right\} G^+(\vec{r}', \vec{r}) = \left\langle \vec{r}' \left| \frac{1}{E - H_{\Lambda^* p} + i\epsilon} \right| \vec{r} \right\rangle = \delta(\vec{r}' - \vec{r})$$

Green function and delta function are expressed in partial wave expansion as follows;

$$G^+(\vec{r}', \vec{r}) = \sum_{\ell=0}^{\infty} \sum_M Y_{\ell M}(\hat{r}) \frac{G_{\ell}^+(r', r)}{r r'} Y_{\ell M}^*(\hat{r}') \tag{14}$$

$$\delta(\vec{r}' - \vec{r}) = \sum_{\ell=0}^{\infty} \sum_M Y_{\ell M}(\hat{r}) \frac{\delta(r' - r)}{r r'} Y_{\ell M}^*(\hat{r}') \tag{15}$$

Then the radial part of the Green's function $G_{\ell}^+(\vec{r}', \vec{r})$ is satisfied by solving the following equation;

$$\left[k^2 + \frac{d^2}{dr^2} - \frac{\ell(\ell+1)}{r^2} - \tilde{U}(r) \right] G_{\ell}^+(r', r) = \frac{2\mu}{\hbar^2} \delta(r' - r)$$

$$k^2 = \frac{2\mu E}{\hbar^2}, \quad \tilde{U}(r) = \frac{2\mu}{\hbar^2} V_{\Lambda^* p}(r) \text{ is the potential between } \Lambda^* \text{ and } p.$$

We can write the radial part of the Green's function in the following form;

$$\begin{aligned} G^+(\vec{r}', \vec{r}) &= G_{\ell_1}^+(r', r) = C_1 u_{\ell}^0(r) \quad \text{for } (0 < r < r') \\ G_{\ell_2}^+(\vec{r}', \vec{r}) &= C_2 u_{\ell}^+(r) \quad \text{for } (r' < r < \infty) \end{aligned}$$

We have prepared the two solutions of

$$\left[k^2 + \frac{d^2}{dr^2} - \frac{\ell(\ell+1)}{r^2} - \tilde{U}(r) \right] u(r) = 0, \text{ with the boundary conditions}$$

$$\begin{aligned} u_{\ell}^0(0) &\xrightarrow{r \rightarrow 0} 0 && \text{for } u_{\ell}^0(r) \\ u_{\ell}^+(0) &\xrightarrow{r \rightarrow \infty} k r h_{\ell}^+(kr) && \text{for } u_{\ell}^+(r) \end{aligned}$$

We have $C_1 u_\ell^{(0)}(r') - C_2 u_\ell^{(+)}(r') = 0$

$$C_1 u_\ell^{(0)'}(r') - C_2 u_\ell^{(+)'}(r') = \frac{2\mu}{\hbar^2}$$

We get two parts of the radial part Green's function as

$$G_{\ell 1}^+(r', r) = \frac{2\mu}{\hbar^2} \frac{u_\ell^{(+)}(r') u_\ell^{(0)}(r)}{W(u_\ell^{(0)}, u_\ell^{(+)})} \tag{16}$$

$$G_{\ell 2}^+(r', r) = \frac{2\mu}{\hbar^2} \frac{u_\ell^{(0)}(r') u_\ell^{(+)}(r)}{W(u_\ell^{(0)}, u_\ell^{(+)})} \tag{17}$$

We combine the equation (16) and (17)

$$G_\ell^+(r', r) = \frac{2\mu}{\hbar^2} \frac{u_\ell^{(+)}(r_>) u_\ell^{(0)}(r_<)}{W(u_\ell^{(0)}, u_\ell^{(+)})} \tag{18}$$

Substituting the equation (18) into equation (14), we get

$$G^{(+)}(r', r) = \frac{2\mu}{\hbar^2} \sum_{\ell=0}^{\infty} \sum_M Y_{\ell M}(\hat{r}) \frac{u_\ell^{(+)}(r_>) u_\ell^{(0)}(r_<)}{r r' W(u_\ell^{(0)}, u_\ell^{(+)})} Y_{\ell M}^*(\hat{r}') \tag{19}$$

By substituting the above equation into equation (13), we obtained the final expression as follows;

$$\begin{aligned} \frac{d^2 \sigma}{dY_c^2 d\cos\theta_{K^+}} &= \frac{(2\pi)^5}{\hbar^2 k_0 c^2} \frac{E_0 \bar{k}_{K^+} |t_{m}|^2}{\left\{ \frac{\hbar^2 c^2}{E_{K^+}} + \frac{\hbar^2}{M_{K^+ pp}} \left(1 - \frac{k_0}{k_{K^+}} \cos\theta_{K^+}\right) \right\}} \tag{20} \\ &\times \left(-\frac{1}{\pi} \right) \text{Im} \left[\sum_{\ell=0}^{\infty} (2\ell+1) \int dr \int dr' j_\ell^*(Qr) u_\ell^*(r) \frac{u_\ell^0(r) u_\ell^+(r)}{W(u_\ell^0, u_\ell^+)} j_\ell(Qr) \psi(r) \right] \end{aligned}$$

Results and Discussions

Study on the Quasi-Free Region with Fermi Motion Consideration

We have studied the quasi-free regions namely Λ -p, Σ -p and Λ^* -p, Σ^* -p of the E-27 inclusive spectrum. In order to understand the origins of quasi-free Λ -p, Σ -p, Λ^* -p, Σ^* -p structure, we firstly determine the peak positions and level widths by considering the Fermi motion of neutron in target deuteron. The neutron momentum distribution is taken into account in determining the emitted kaon momentum from which the missing mass of K^0 pp is obtained using the relation $M_x c^2 = \sqrt{(E_{\text{init}} - E_{\text{obs}})^2 - (\mathbf{p}_{\text{init}} - \mathbf{p}_{\text{obs}})^2 c^2}$. We have used the neutron momentum distribution in deuteron as Fermi type and neutron is assumed to be the off-shell mass as $M_n^{*2} = (M_D - \sqrt{M_p^2 + p_n^2})^2 - p_n^2$. Our calculated peak structures of quasi-free production are shown in Figs. (1 - 4) and Table (1). According to our calculations it is found that Λ -p and Σ -p peaks are in good agreement with experimental positions but Λ^* -p and Σ^* -p peaks are quite different from the experimental positions.

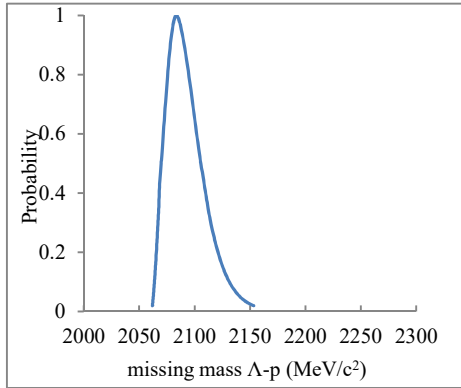


Figure 1. Quasi – free Λ -p production spectrum due to Fermi motion

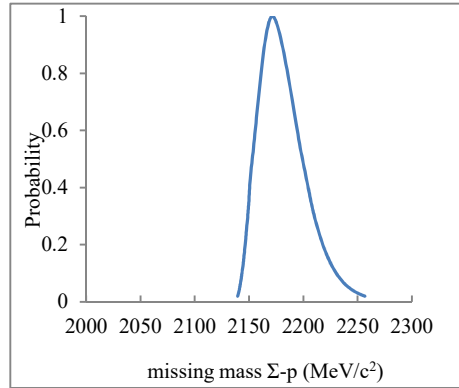


Figure 2. Quasi-free Σ -p production spectrum due to Fermi motion

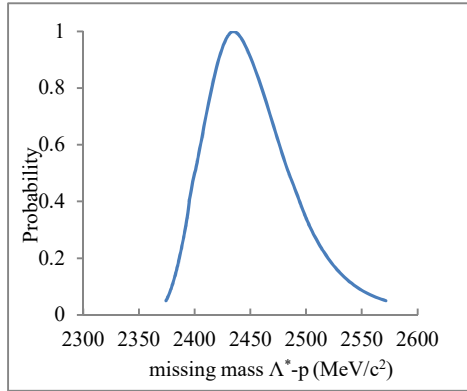


Figure 3. Quasi –free Λ^* -p production spectrum due to Fermi motion

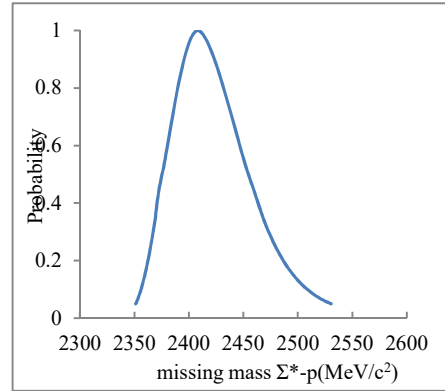


Figure 4. Quasi –free Σ^* -p production spectrum due to Fermi motion

Table 1. The experimental and calculated peak positions and levelwidths for quasi-free process.

Quasi-free production	Peak position Calculated (MeV/c ²)	Peak position Experimental (MeV/c ²)	Level width Calculated (MeV/c ²)	Level width Experimental (MeV/c ²)
Λ -p	2083.6	2085	35.8	50
Σ -p	2171.53	2170	47.5	45
Λ^* -p	2434.85	2389	80	80
Σ^* -p	2408.22	2389	78	80

Inclusive Missing Mass Spectrum of $D(\pi^+, K^+)X$ Reaction

We have studied the quasi-free regions of the inclusive missing mass spectrum for $D(\pi^+, K^+)X$ reaction from J-PARC E-27. We have calculated the missing mass spectrum of this reaction by employing YA and DISTO potential for Y -p (Λ -p and Σ -p) and Y^* -p (Λ^* -p and Σ^* -p) interactions. In the regions of Λ -p and Σ -p, the following optical potential is used;

$$V^{opt}(r) = 5000.0 \exp\left[-\left(\frac{r}{0.4}\right)^2\right] - (V_0 f_R + i W_0 f_I) \exp\left[-(r/1.0)^2\right] \text{ with}$$

$V_0 = -272.6$ MeV, $W_0 = -47$ MeV and $f_R = 0.5$, $f_I = 0.0$ for Λ p and $f_R = 0.9$,

$f_1 = 1.0$ for Σp . It is found that the missing mass spectrum of quasi-free Λ -p production in Fig (5). The peak position and level width are $2083.9 \text{ MeV}/c^2$ and 35.8 MeV . Similarly, Fig.(6) shows the missing mass spectrum of quasi-free Σ -p production. The peak position and level width are found to be $2167.6 \text{ MeV}/c^2$ and 47.5 MeV .

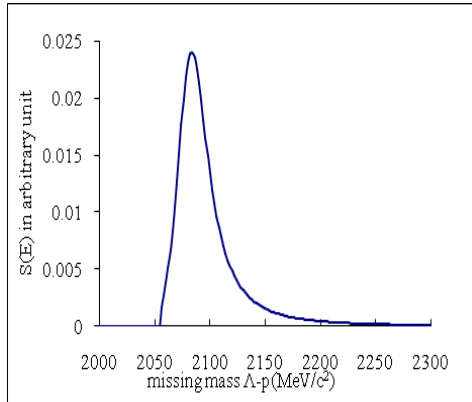


Figure 5. Missing mass spectrum of quasi-free Λ -p production.

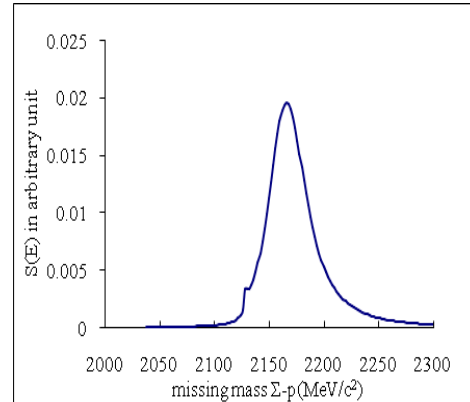


Figure 6. Missing mass spectrum of quasi-free Σ -p production.

In order to see the effect of quasi-free Λ^* -p production on the formation region, we have switched off the Λ^* -p interaction in our calculation. We have considered two cases which are (i) without including the level width of Λ^* and (ii) including the level width of Λ^* . Fig.(7) shows the missing mass spectrum of quasi free Λ^* -p production. The red curve is the missing mass spectrum of quasi free Λ^* -p production for the first case where the level width of Λ^* is not included. It can be seen that the peak position is $2435.4 \text{ MeV}/c^2$ and level width is 90 MeV . The blue curve is the missing mass spectrum of quasi free Λ^* -p production for the second case. The peak position and level width of Λ^* -p are found to be $2423.4 \text{ MeV}/c^2$ and 170 MeV respectively. The effect of Γ_{Λ^*} is slightly shifting the peak position to the lower mass energy region and increasing the level width by 80 MeV .

And then, we have investigated the missing-mass spectrum of the quasi-free Σ^* -p region by turning off the Σ^* -p interaction. We have found the similar characteristics as that of the Λ^* -p. The calculated missing mass spectrum of quasi-free Σ^* -p production is displayed in Fig. (8). The green

curve represented the missing mass spectrum of quasi-free Σ^*-p production which is obtained by giving the level width to be zero. It is found that the peak position and level width are $2405.2\text{MeV}/c^2$ and 70.5 MeV , respectively. When the level width of Σ^* is taken to be 36 MeV , the peak position is $2403.2\text{ MeV}/c^2$ and its width becomes 90 MeV , shown by orange curve. It is seen that the peak position remains unchanged while the level width increases by nearly 20 MeV .

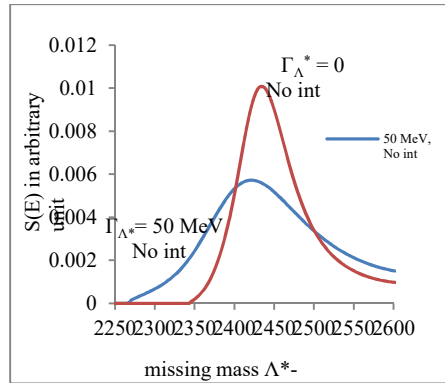


Figure 7. Missing mass spectrum of quasi-free Λ^*-p production; (i) red curve is with $\Gamma_{\Lambda^*} = 0$ and without interaction (ii) blue curve is with $\Gamma_{\Lambda^*}=50\text{ MeV}$ and without interaction

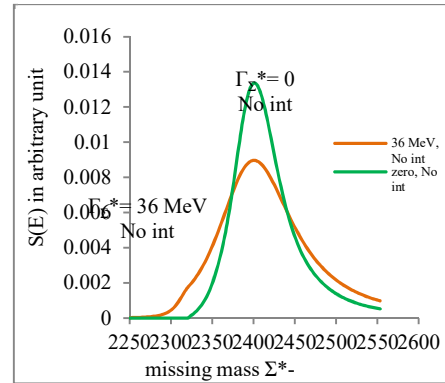


Figure 8. Missing mass spectrum of quasi-free Σ^*-p production; (i) green curve is with $\Gamma_{\Sigma^*}= 0$ and without interaction (ii) orange curve is with $\Gamma_{\Sigma^*}=36\text{ MeV}$ and without interaction

In order to obtain the missing mass spectrum covering all regions of quasi-free Λ -p, Σ -p, Λ^* -p and Σ^* -p as given in the experimental spectrum, we have combined the above mentioned spectra into one spectrum Fig (9).

The upper right of the Fig (9) shows the experimental missing mass spectrum to be compared with our calculated spectrum. In the Y -p region, our calculated spectrum has a cusp peak in $2130\text{ MeV}/c^2$ at the Σ -p threshold which agrees very well with the experimental curve. Our calculated spectrum well reproduced the missing mass spectrum of E-27 experiment including the cusp peak in $2130\text{ MeV}/c^2$ due to $\Sigma N \rightarrow \Lambda N$ conversion in the Y -p region. In the Y^* -p region, our peak is about 30 MeV shifted to the higher mass region compared to the experimental curve. It can be seen from the experimental

spectrum and from the calculated spectrum, there are large quasi-free regions which may obscure the small signal of $K^- pp$ bound state.

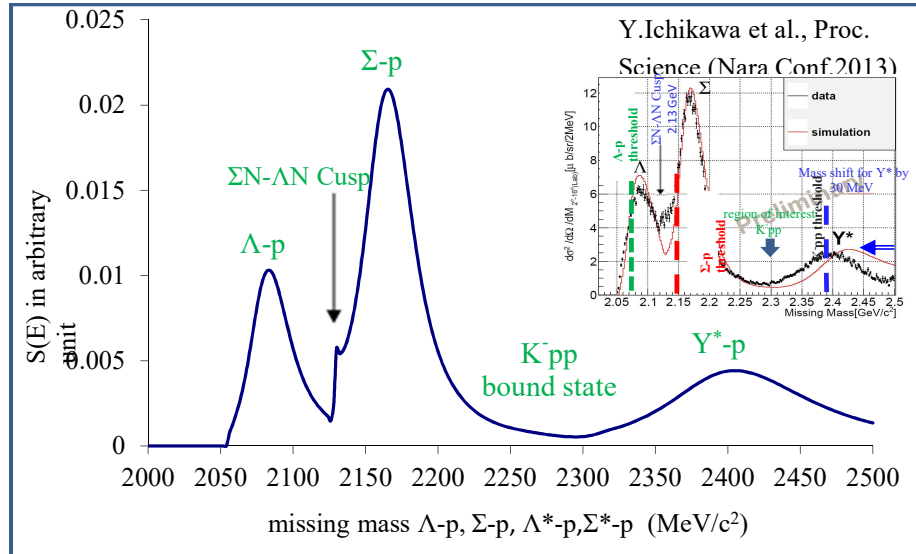


Figure 9. Missing mass spectrum of quasi-free Λ -p, Σ -p, Λ^* -p, Σ^* -p production.

We have obtained the missing mass spectrum of $\Lambda^* p$ production by employing DISTO potential for $\Lambda^* p$ interaction. In our calculation, we used the $\Lambda^* p$ interaction which has the following form

$$V_{Y^*p}^{\text{opt}}(r) = (V_0 + iW_0) \left(\frac{r}{c} \right)^2 \exp[-(r/c)] \quad \text{where } V_0 = -394.0 \text{ MeV},$$

$W_0 = -95.0 \text{ MeV}$ are potential strength parameter and $c = 0.3 \text{ fm}$ is range parameter for DISTO $\Lambda^* p$ interaction. The $\Lambda^* p$ DISTO interaction is obtained by enhancing the YA interaction by 17% which is attributed to partial restoration of chiral symmetry. We have calculated the missing mass spectrum of $\Lambda^* p$ production with angular momentum contributions for $l = 0, l = 1$ to $l = 4$ to study their effect on the production spectrum. Fig. (10) displayed the missing mass spectrum of $\Lambda^* p$. It can be found that the peak position at $l = 0$ indicates the bound state region below the $\Lambda^* p$ threshold. The peak position at

$l = 1$ to $l = 4$ are found in the energy region above the Λ^*p threshold. Thus, quasi-free region is dominated by the higher angular momentum contributions.

Similarly, we have calculated the missing mass spectrum of $\Lambda^* - p$ production with angular momentum contributions for $l_{\min} = 0, l_{\max} = 1$ to $l_{\max} = 4$. In the Fig.(11), the peak position of the bound state region dominates at $l_{\min} = 0$ to $l_{\max} = 0$ below the threshold while the peak position of the quasi-free region dominates at $l_{\min} = 0, l_{\max} = 1$ to $l_{\max} = 4$ above the threshold. The peak at the $l = 0$ is clearly seen bound state. However, it is almost obscured by the large background of quasi-free Λ^*p production, which can be seen in Fig.(11). The quasi-free Λ^*p production is dominant in higher angular momentum contributions.

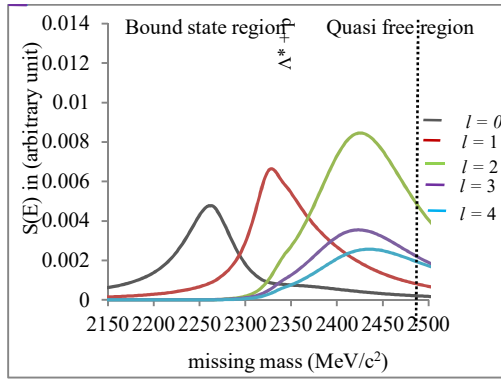


Figure 10. Missing mass spectrum of $\Lambda^* p$ with individual angular momentum contribution

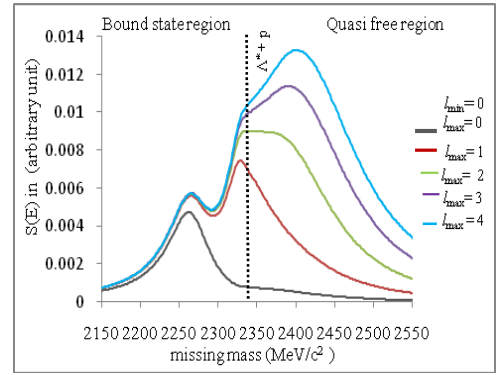


Figure 11. Missing mass spectrum of $\Lambda^* p$ with total angular momentum contribution

Conclusion

We studied the inclusive missing mass spectrum of $D(\pi^+, K^+)X$ reaction from J-PARC E 27 experiment which covers all energy regions of quasi free $Y-p$ ($\Lambda-p, \Sigma-p$), Y^*-p (Λ^*-p, Σ^*-p) production and K^-pp bound state. In order to understand the origins of these quasi-free $Y-p$ and Y^*-p structure, we have investigated the nature of the background processes which are quasi-free regions namely $Y-p$ ($\Lambda-p, \Sigma-p$) and Y^*p (Λ^*-p, Σ^*-p). In our simple consideration, level widths of Λ^* and Σ^* are not taken into account which

might be the discrepancy between our calculated values and the experimental values. It might be conducted that the origin of peak position and level width of quasi-free regions are not due to dynamical aspect but kinematical one. Our calculated quasi free Y - p and Y^* - p spectrum well reproduced the missing mass spectrum of E-27 experiment including the ΣN - ΛN conversion cusp in the Y - p region. In the proton coincidence spectrum, the broad enhancement was observed around the missing mass of $2270 \text{ MeV}/c^2$ which corresponds to a quasi-bound state of K^-pp . Our calculated missing-mass spectrum with the DISTO interaction well reproduced this broad bump structure.

Acknowledgements

I would like to thank Dr Tin Maung Hla, Rector, Mandalay University of Distance Education for his encouragement. I am grateful to the full support of Professor Dr Kay Thi New, Head of Department of Physics, Mandalay University of Distance Education. I am deeply indebted to Professor Dr Khin Swe Myint, Rector (Rtd.), Emeritus Professor, Department of Physics, University of Mandalay for all her enthusiastic discussion, collaboration and encouragement. I also would like to thank Dr Theigin, Lecturer, University of Mandalay for her discussion and collaboration.

References

1. Akaishi, Y., & Yamazaki, T. (1999). Proc. Daphne Workshop, Frascati Physics Series XVI, p. 59; to appear in Phys. Rev. C.
2. Agnello, M. *et al.*, (2005). Phys. Rev. Lett **94** 212303.
3. Akaishi, Y., & Yamazaki, T. (2002). Phys. Rev. C **65** 044005.
4. Akaishi, Y., & Yamazaki, T. (2002). Phys. Lett. **B 535** 70.
5. Akaishi, Y., Dote, A., & Yamazaki, T. (2005). Phys. Lett. **B 613** 140.
6. Dote, A. *et al.*, (2003). arXiv:nucl-th **1** 0310085.
7. Ikeda, Y., & Sato, T. (2007). Phys. Rev. C **76** 035203.
8. Ichikawa, Y. *et al.*, (2013). XV International Conference on Hardon Spectroscopy-Hardon.
9. Ichikawa, Y. *et al.*, (2015). Prog. Theor. Exp. Phys. **021D01**.
10. Shevchenko, N.V., Gal, A., & Mares, J. (2007). Phys. Rev. Lett. **98** 082301.
11. Yamazaki, T. *et al.*, (2007). Phys. Rev. C **76** 045201.
12. Yamazaki, T. *et al.*, (2010). Phys. Rev. Lett **104** 132502.

STUDY ON TEMPERATURE DEPENDENT ELECTRICAL PROPERTIES OF COBALT-ZINC NANOFERRITES

Htet Naing Lwin¹, Thinn Thinn Tun², Cho Cho Aung³ & Win Kyaw⁴

Abstract

Spinel ferrites have been studied extensively because they play a vital role in the technological applications. In the present work, Cobalt-Zinc nanoferrites, $\text{Co}_{1-x}\text{Zn}_x\text{Fe}_2\text{O}_4$ (where $x = 0.0, 0.1, 0.2$ and 0.3) have been prepared by auto-combustion method. Structural and microstructural properties of the samples were characterized by X-ray diffraction (XRD) and Scanning Electron Microscope (SEM) to investigate the single phase nanosized ferrites and morphological features of grain shape, grain size and homogeneity. Variation of the dc electrical resistivities of the Cobalt ferrites with the different concentrations of Zinc was observed by a simple two probe method. Temperature dependent electrical conductivities of the samples were investigated in the temperature range of 303 K – 773 K. The activation energies (E_a) of the samples were evaluated by using the slopes of $\ln\sigma - 1000/T$ relationships.

Keywords: Cobalt-Zinc nanoferrites, auto-combustion method, XRD, SEM, electrical conductivities

Introduction

Spinel ferrites have been studied extensively because they play a vital role in the technological applications. Ferrites have good electric properties and a large number of applications from microwave to radio frequency [Ahmad, (2012)]. The dielectric properties of these ferrites are very sensitive to the method of preparation and sintering condition. Therefore, the selection of an appropriate process is the key to obtain high quality ferrites [Pathan, (2010)].

¹ PhD Candidate, Assistant Lecturer, Department of Physics, University of Yangon

² Dr, Assistant Lecturer, Department of Physics, Dagon University

³ Dr, Associate Professor, Department of Physics, University of Yangon

⁴ Dr, Associate Professor, Department of Physics, Sagaing University

The ability to prepare nanostructures with defined morphologies and sizes in large scale is an essential requirement for applications in nanomaterials [Harris, (2009); Iyer, (2009)]. As a result, extensive efforts have been devoted to develop synthetic capabilities to produce nanomaterials with tailored magnetic and electrical properties. The properties of nanomaterials are remarkably different from that of their bulk counterpart [Marial, (2013)]. The interest in ferrite nanoparticles is due to their important physical and chemical properties and potential for various technological applications such as high density magnetic storage, electronic and microwave devices, sensors, magnetically guided drug delivery etc [Rani, (2013)]. A large number of methods has been developed to prepare $\text{Co}_{1-x}\text{Zn}_x\text{Fe}_2\text{O}_4$ (CZFO) ferrite nanoparticles, such as the Co-precipitation, Auto-Combustion method, Sol-gel method, Solvothermal method, the standard solid-state reaction technique and the hydrothermal method. Further, the electrical and dielectric properties of cobalt-zinc nanoferrites were reported by many workers. In this work, the structural, microstructural and electrical properties of Co-Zn ferrite nanoparticles prepared by solution combustion method and characterized by XRD, SEM and electrical conductivity measurements are reported.

Experimental Details

Preparation of Zinc substituted Cobalt Ferrites

Zinc substituted Cobalt ferrites, $\text{Co}_{1-x}\text{Zn}_x\text{Fe}_2\text{O}_4$ (where $x = 0.0, 0.1, 0.2$ and 0.3) have been prepared by auto-combustion method. The chemical reagents used in this work were Zinc Nitrate Hexahydrate [$\text{Zn}(\text{NO}_3)_2 \cdot 6\text{H}_2\text{O}$], Cobalt (II) Nitrate Hexahydrate [$\text{Co}(\text{NO}_2)_2 \cdot 6\text{H}_2\text{O}$], and Ferric Nitrate Nonahydrate [$\text{Fe}(\text{NO}_3)_3 \cdot 9\text{H}_2\text{O}$]. Urea [$\text{CO}(\text{NH}_2)_2$] was used as a fuel. Sample preparation procedure of the $\text{Co}_{1-x}\text{Zn}_x\text{Fe}_2\text{O}_4$ is shown in Figure 1. Photographs of the preparation of the $\text{Co}_{1-x}\text{Zn}_x\text{Fe}_2\text{O}_4$ samples (e.g., $x = 0.1$), DELTA A SERIES Temperature Controller DTA-4896 and experimental setup of the sample preparation system are shown in Figures 2(a – n).

XRD, SEM and Electrical Properties Measurements

Structural analysis, lattice parameters calculation and crystallite size estimation of the samples were investigated by XRD method. XRD patterns were observed by RIGAKU MULTIFLEX X-ray Diffractometer using Ni-filter with CuK_α radiation, $\lambda = 1.54056 \text{ \AA}$. Microstructural properties of the samples were investigated by using JEOL JSM-5610LV SEM with the accelerating voltage of 15 kV, the beam current of 50 mA and 5500 times photo magnification. For the electrical properties measurement, the samples were made into pellets. The electrical resistances of the samples were observed in the temperature range of 303 K – 773 K by using FLUKE 45 Dual-display digital multi-meter. In this measurement, Autonics TCN4L – 24R Temperature Controller and K-type thermocouple were used as the temperature controller and temperature sensor. Photographs of the experimental setup of electrical conductivity measurement are shown in Figure 3(a) and (b) respectively. Thickness and area of each of the sample were 2.19 mm and $1.14 \times 10^{-4} \text{ m}^2$.

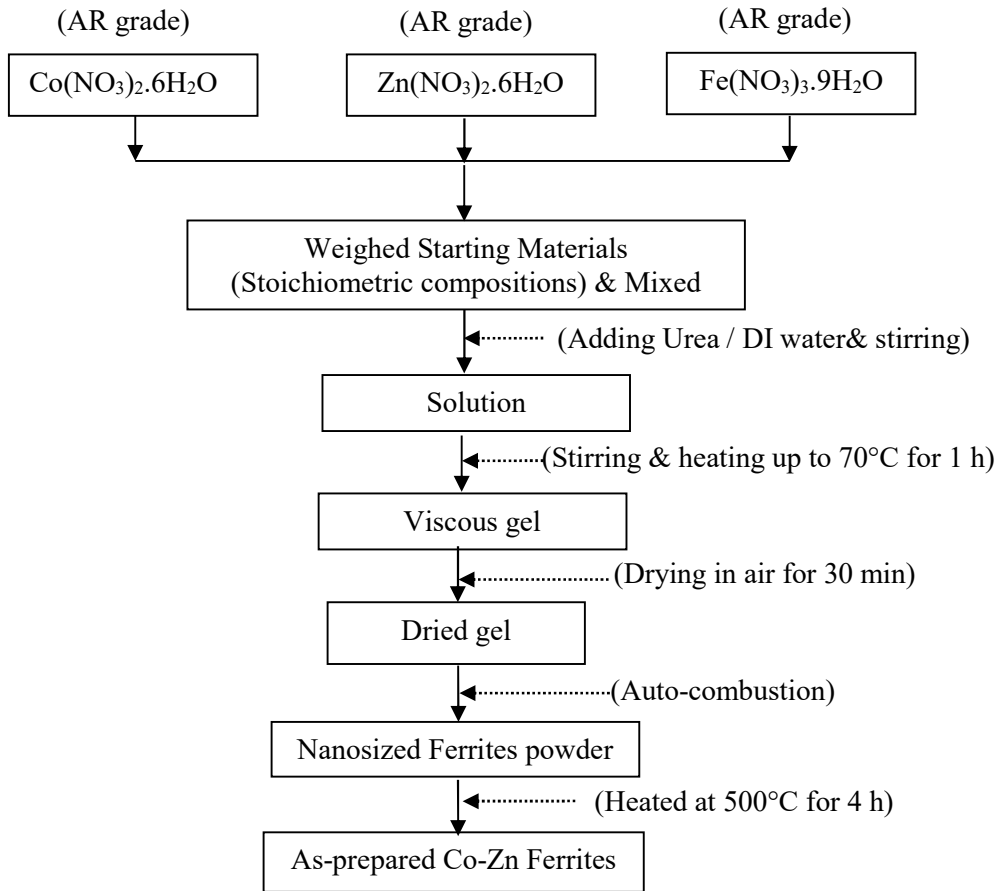


Figure 1. Flow-diagram of the preparation procedure of Co-Zn ferrite



Figure 2. Photographs of the starting materials of AR grade (a)Fe(NO₃)₃·9H₂O, (b) Zn(NO₃)₂·6H₂O, (c) CO(NH₂)₂ and (d) Co(NO₃)₂·6H₂O

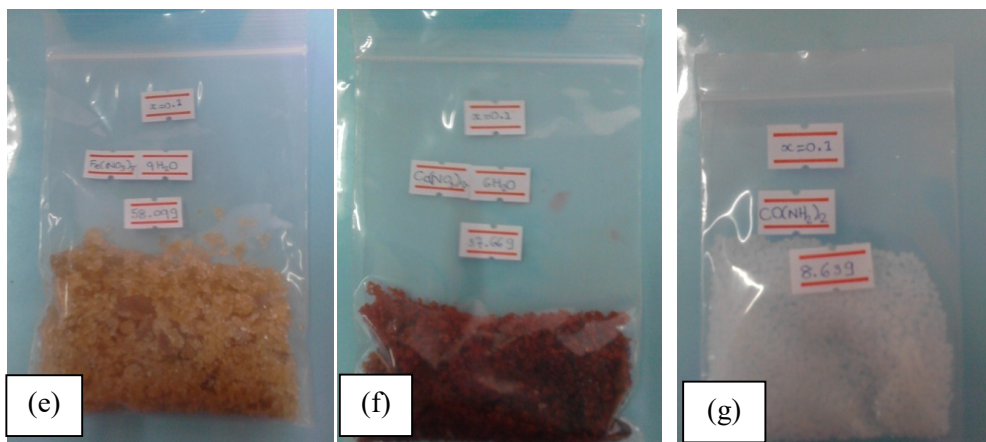


Figure 2. Photographs of the weighed starting materials of (e)Fe(NO₃)₃·9H₂O, (f) Co(NO₃)₂·6H₂O and (g)CO(NH₂)₂

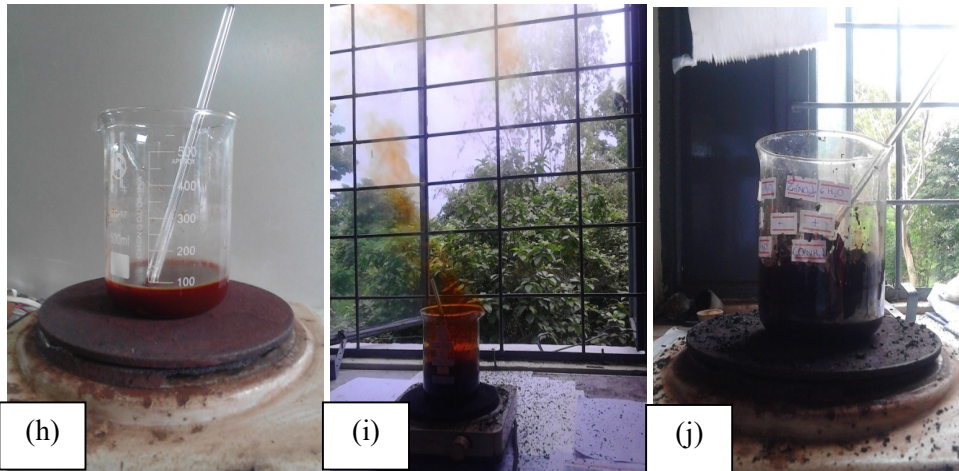


Figure 2. Photographs of the (h) mixed solutions of starting materials, (i) self-combustion occurring and (j) after self-combustion

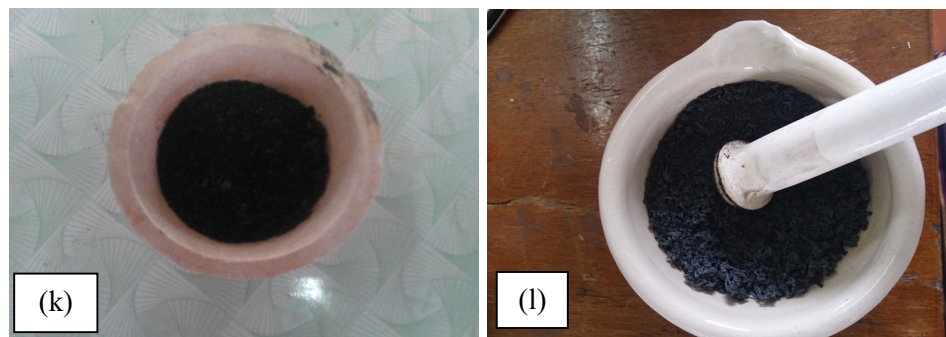


Figure 2. Photographs of the (k) combustion ferrite and (l) crushing of as-prepared ferrite

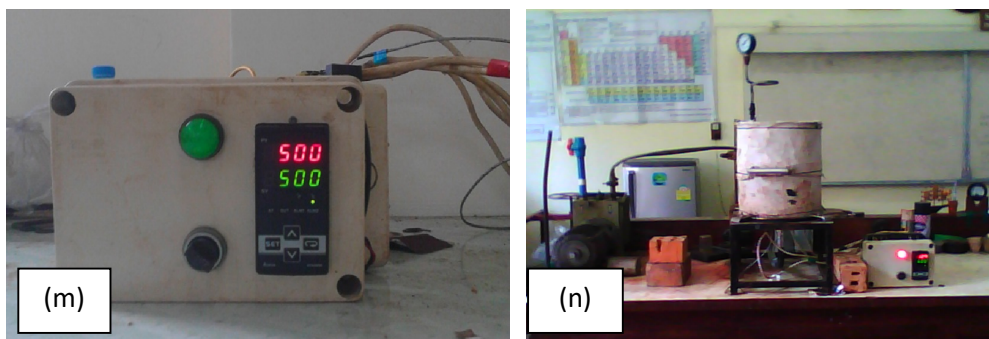


Figure 2. Photographs of the (m) DELTA A SERIES temperature controller DTA-4896 at 500°C and (n) experimental setup of sample preparation system

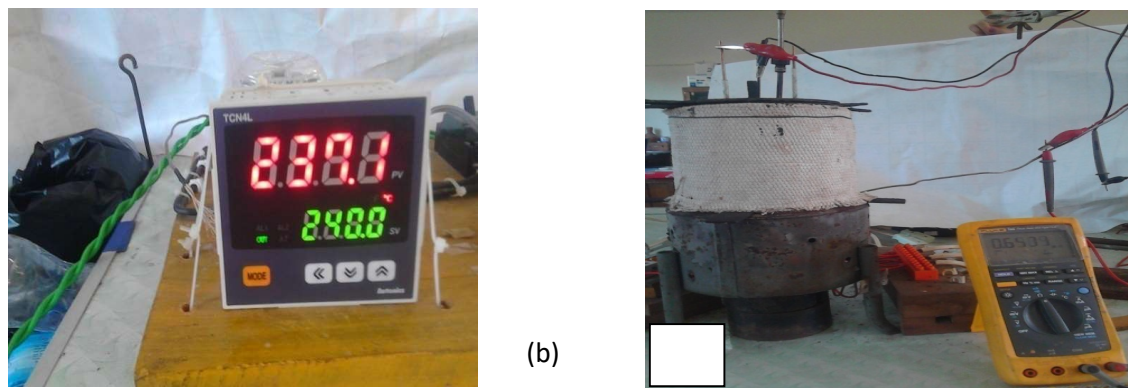


Figure3. Photographs of the (a) temperature controller Autonics TCN4L – 24R and (b) experimental setup of electrical conductivity measurement

Results and Discussion

XRD Study

Powder X-ray diffraction patterns of $\text{Co}_{1-x}\text{Zn}_x\text{Fe}_2\text{O}_4$, (where $x = 0.0, 0.1, 0.2$ and 0.3) samples are shown in Figure 4(a – d). The observed XRD lines were identified by using standard JCPDS data library files of

- (1) Cat. No. 03-0864> CoFe_2O_4 – Cobalt Iron Oxide for CoFe_2O_4 sample and
- (2) Cat. No. 89-7412> Franklinite – ZnFe_2O_4 and Cat. No. 03-0864> CoFe_2O_4 – Cobalt Iron Oxide for $\text{Co}_{0.9}\text{Zn}_{0.1}\text{Fe}_2\text{O}_4$, $\text{Co}_{0.8}\text{Zn}_{0.2}\text{Fe}_2\text{O}_4$ and $\text{Co}_{0.7}\text{Zn}_{0.3}\text{Fe}_2\text{O}_4$.

The entire samples under investigation shows the characteristics peaks of cubic crystalline ferrite material with the most intense peak (311). All the samples show good crystallization with well defined peaks. The observed XRD patterns exclude the presence of any undesirable secondary phase. The slight broadening of the XRD peaks indicates that the samples have nano-crystalline nature.

The lattice parameters were calculated by using crystal utility of the equation: $a = \frac{\lambda}{2 \sin \theta} \sqrt{h^2 + k^2 + l^2}$, where (hkl) is the Miller indices, " λ " is the wavelength of incident X-ray (Å), " θ " is the diffraction angle of the peak ($^\circ$)

and "a" is the lattice parameter (Å). The calculated and observed lattice parameters are tabulated in Table 1. Rani R et al (2013) has

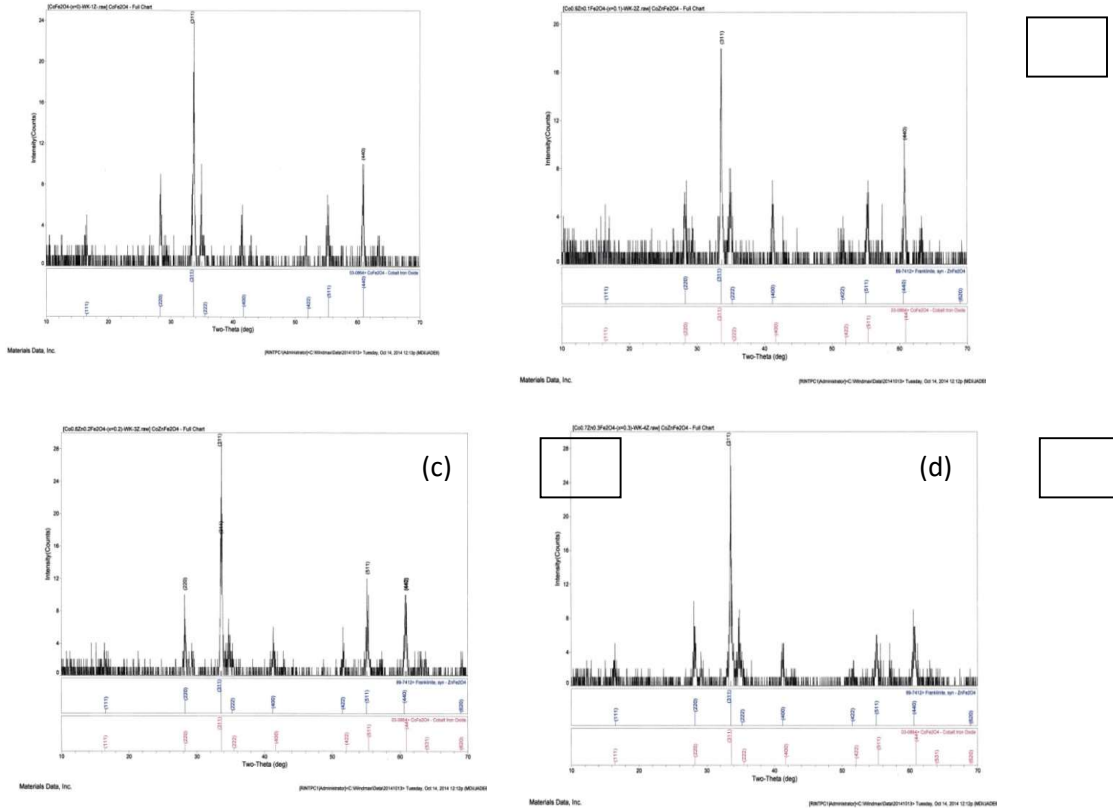


Figure 4. XRD patterns of $\text{Co}_{1-x}\text{Zn}_x\text{Fe}_2\text{O}_4$ where (a) $x = 0.0$, (b) $x = 0.1$, (c) $x = 0.2$ and (d) $x = 0.3$

reported that the $\text{Co}_{1-x}\text{Zn}_x\text{Fe}_2\text{O}_4$ ($x = 0.0, 0.2$ and 0.4) ferrites belong to cubic structure and the lattice parameters are in the range $8.68 \text{ \AA} - 8.91 \text{ \AA}$. In this work, the lattice parameters of the $\text{Co}_{1-x}\text{Zn}_x\text{Fe}_2\text{O}_4$ ($x = 0.0, 0.1, 0.2$ and 0.3) ferrites are obtained as in the range of $8.70 \text{ \AA} - 8.90 \text{ \AA}$ and it almost agreed with that of Rani R et al (2013). Variations of the lattice parameters and crystallite sizes with the concentration of Zn of the samples are shown in Figure 5. The lattice parameters were found to be increased with the increase in concentration of Zn due to the ionic substitution of Zn on Co in the lattice sites.

Crystallite sizes below roughly 100 nm can be evaluated using powder diffraction technique. In this work, the crystallite sizes were estimated by using

the Scherrer formula, $D = \frac{0.9\lambda}{B \cos \theta}$, where "D" is the crystallite size (nm),

" λ " is the wavelength of incident X-ray (Å), " θ " is the diffraction angle of the peak under consideration at FWHM (°) and "B" is the observed FWHM (radians). The obtained average crystallite sizes are also tabulated in Table 1. The obtained average crystallite sizes are nanosized materials.

Table 1. The lattice parameters and crystallite sizes of $\text{Co}_{1-x}\text{Zn}_x\text{Fe}_2\text{O}_4$ (where $x = 0.0, 0.1, 0.2$ and 0.3) ferrites

x	Obs. $a=b=c$ (Å)	Cal. $a=b=c$ (Å)	D (nm)
0.0	8.70	8.70	55.57
0.1	8.71	8.71	41.13
0.2	8.75	8.75	41.97
0.3	8.90	8.90	61.11

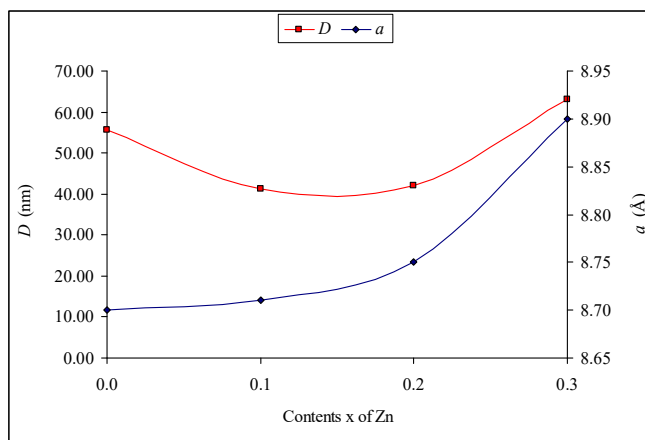


Figure 5. Variations of the lattice parameters and crystallite sizes with increase in Zn concentration of $\text{Co}_{1-x}\text{Zn}_x\text{Fe}_2\text{O}_4$ (where $x = 0.0, 0.1, 0.2$ and 0.3)

Microstructural Analysis

The SEM image is a 2D (2-Dimensional) intensity map in the analog or digital domain. Each image pixel on the display corresponds to a point on the sample, which is proportional to the signal intensity captured by the detector at each specific point. SEM micrograph indicates the microstructural characteristics of the solid materials. SEM micrographs of the samples are shown in Figure 6(a – d) respectively. As shown in figures, the grain shapes of the samples are spherical with poor grain boundary. In all SEM micrographs, some pores are found due to decomposition of starting materials i.e., metal nitrates, water, citric acid and solvent DI water in the sample preparation process. The observed grain sizes of the samples are listed in Table 2. As presented in table, the obtained grain sizes of the samples are different each others. SEM micrographs show that the very fine particles nature.

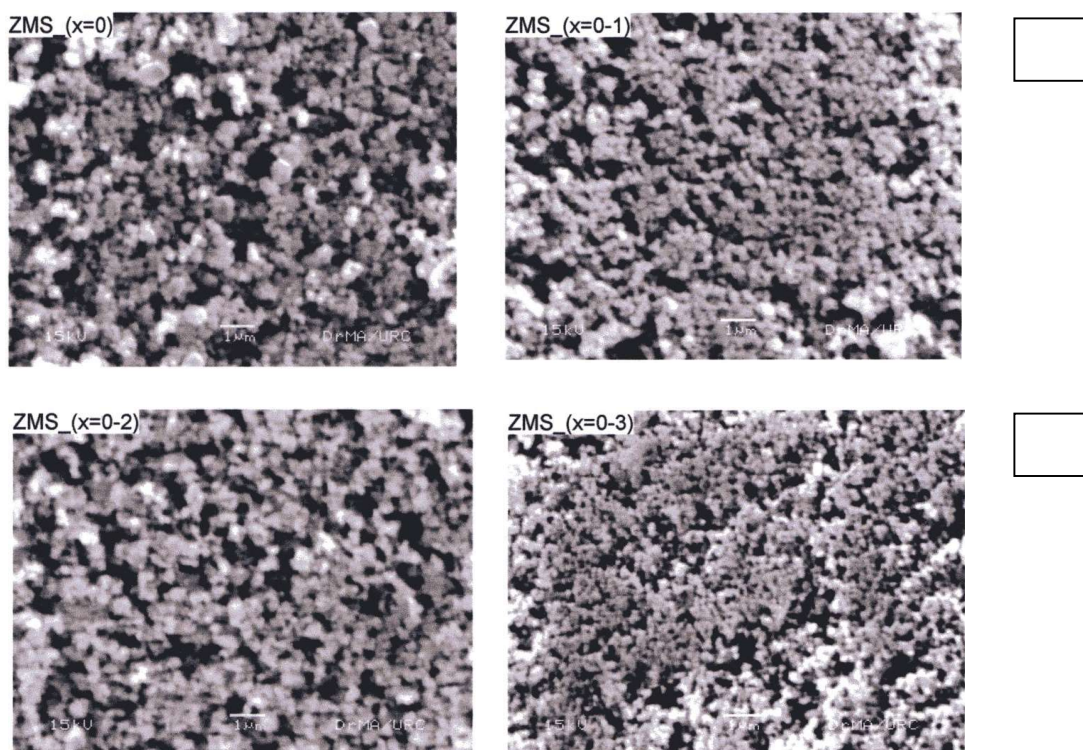


Figure 6. SEM micrographs of $\text{Co}_{1-x}\text{Zn}_x\text{Fe}_2\text{O}_4$ where (a) $x = 0.0$, (b) $x = 0.1$, (c) $x = 0.2$ and (d) $x = 0.3$

Table 2. Grain sizes of $\text{Co}_{1-x}\text{Zn}_x\text{Fe}_2\text{O}_4$ (where $x = 0.0, 0.1, 0.2$ and 0.3) ferrites

x	Grain size (μm)
0.0	0.05 – 0.50
0.1	0.04 – 0.35
0.2	0.06 – 0.50
0.3	0.04 – 0.20

Temperature Dependent Electrical Conductivity Study

The research in the field of Solid-State Ionic encompasses investigations of the physical and chemical behavior of the solids with fast ion movement within the bulk as well as the technological aspects. These materials widely refer to as “Superionic Solids” or “Solid Electrolytes” or “Fast Ion Conductors”, show tremendous scope to develop all solid-state mini/micro electrochemical devices viz. batteries, fuel cells, sensors, etc. The temperature dependent dc electrical conductivity σ of the ferrites obey Arrhenius’s expression: $\sigma = \sigma_0 \exp\left(\frac{-E_a}{kT}\right)$, where, σ_0 is the pre-exponential factor, E_a is activation energy, k is Boltzmann’s constant and T absolute temperature.

Arrhenius’s plots of the dc conductivity of the samples with reciprocal temperature are shown in Figure 7(a – d). The graphs show that the increase in temperature leads to increase in conductivity, which is the normal behaviour of semiconducting materials and it obeys the well known Arrhenius relation. Except the $x = 0.0$ sample, Arrhenius plots of others samples are found to be two portions due to the slope changes in each $\ln \sigma - 1000/T$ curve with the corresponding temperature ranges are shown in Figure 8(a – f). The obtained activation energies of these temperature ranges are listed in Table 3. From the experimental results, the samples exhibited as superionic conductors because their electrical conductivities are greater than 10^{-3} S m^{-1} ($\sigma \geq 1 \times 10^{-3} \text{ Sm}^{-1}$). The superionic phase formation temperatures of the samples are found at 443 K for

$x = 0.0$, 583 K for $x = 0.1$, 753 K for $x = 0.2$ and 643 K for $x = 0.3$ respectively.

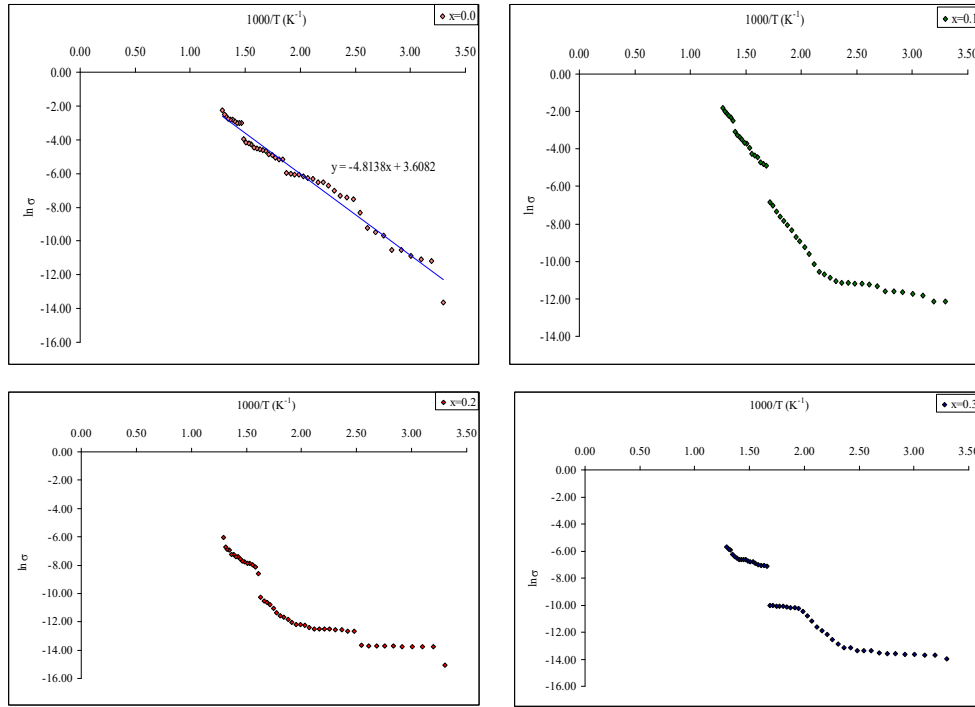


Figure 7. Arrhenius's plots of the dc conductivity with reciprocal temperature of $\text{Co}_{1-x}\text{Zn}_x\text{Fe}_2\text{O}_4$ for (a) $x = 0.0$, (b) $x = 0.1$, (c) $x = 0.2$ and (d) $x = 0.3$

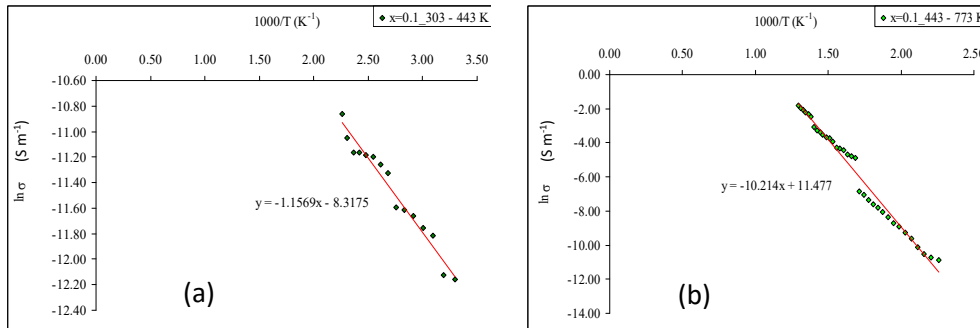


Figure 8. Arrhenius's plots of the temperature dependent electrical conductivities of $\text{Co}_{1-x}\text{Zn}_x\text{Fe}_2\text{O}_4$ (where $x = 0.1$) (a) in 303 K – 443 K and (b) 443 K – 773 K

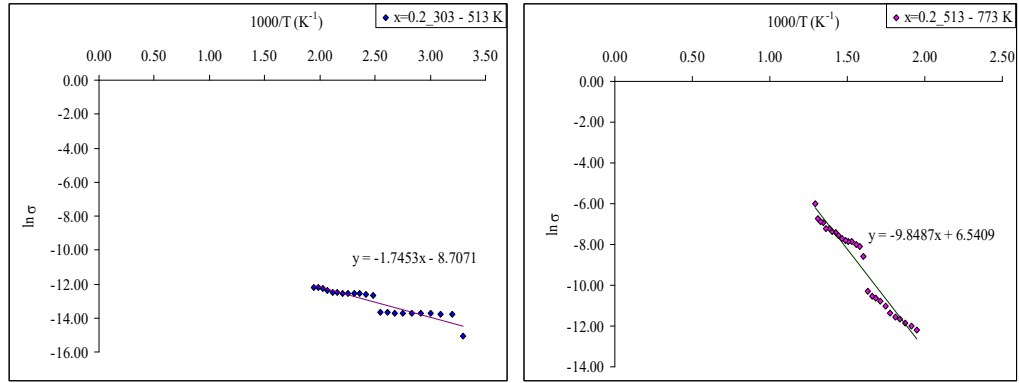


Figure 8. Arrhenius's plots of the temperature dependent electrical conductivities of $Co_{1-x}Zn_xFe_2O_4$ (where $x = 0.2$) (c) in 303 K – 513 K and (d) 513 K – 773 K

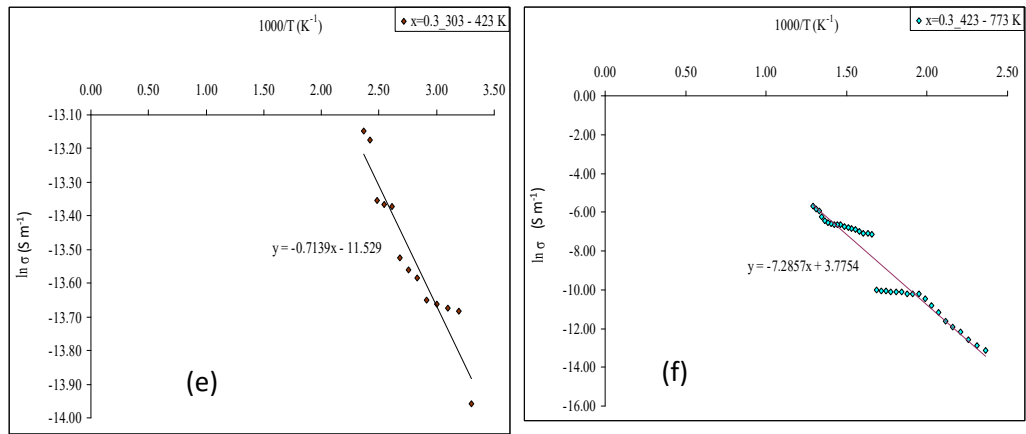


Figure 8. Arrhenius's plots of the temperature dependent electrical conductivities of $Co_{1-x}Zn_xFe_2O_4$ (where $x = 0.3$) (e) in 303 K – 423 K and (f) 423 K – 773 K

Table 3. The activation energies of the $\text{Co}_{1-x}\text{Zn}_x\text{Fe}_2\text{O}_4$ (where $x = 0.0, 0.1, 0.2$ and 0.3)

x	Temperature range (K)	E_a (eV)
0.0	303 - 773	0.42
0.1	303 - 443	0.11
	443 - 773	0.88
0.2	303 - 513	0.15
	513 - 773	0.85
0.3	303 - 423	0.06
	423 - 773	0.63

Conclusion

$\text{Co}_{1-x}\text{Zn}_x\text{Fe}_2\text{O}_4$ (where $x = 0.0, 0.1, 0.2, 0.3$) nanoferrites have been prepared by auto-combustion method. Structural, vibrational and temperature dependent electrical conductivity of the samples were reported in this paper. The X-ray diffraction confirmed the presence of spinel phase cubic crystalline as major phase of the samples. The lattice parameters were found to be increased with the increase in concentration of Zn due to an ionic substitution of Zn^{2+} on Co^{2+} atomic lattice sites. The particle sizes were estimated by using the Scherrer formula and obtained as nanosized ferrite crystallites. SEM micrographs showed that the very fine samples nature. The grain shapes were spherical shapes and they have occurred poor grain boundary. The obtained grain sizes of $\text{Co}_{0.7}\text{Zn}_{0.3}\text{Fe}_2\text{O}_4$ were in the range $0.04 \mu\text{m} - 0.20 \mu\text{m}$ and it was the most homogeneous and the smallest size among the samples. Variation of grain sizes indicated that the grain size depended on Zn concentration. Temperature dependent electrical conductivity results showed that the samples exhibited as the superionic conductors in the high temperatures with the activation energies less than 1 eV. The experimental results can be concluded that the samples can be used as the solid electrolyte materials because they are superionic conductors and their activation energies are obtained as less than 1 eV.

Acknowledgement

The authors would like to acknowledge Professor Dr Khin Khin Win, Head Department of Physics, University of Yangon, for her valuable discussions and comments on this work.

References

1. Ahmad, I. & Farid, M.T. (2012). Characterization of Cobalt Based Spinel Ferrites with Small Substitution of Gadolinium. *World Applied Sciences Journal*, 19, pp. 464-469.
2. Harris, V.G., Geiler, A., Chen, Y., Yoon, S.D., Wu, M., Yang, A., Chen, Z., He, P., Parimi, P.V., Zuo, X., Patton, C.E., Abe, M., Acher O. & Vittoria, C. (2009). Recent advances in processing and applications of microwave ferrites. *Journal of Magnetism and Magnetic Materials*, 321, pp. 2035-2047.
3. Iyer, R., Desai, R. & Upadhyay, R.V. (2009). Low temperature synthesis of nanosized $Mn_{1-x}Zn_xFe_2O_4$ ferrites and their characterizations. *Bulletins Materials Science*, 32, pp. 141-147.
4. Marial, K.H., Choudhury, S. & Hakim, M.A. (2013). Structural phase transformation and hysteresis behavior of Cu-Zn ferrites. *International Nano Letters*, 3, pp. 1-10.
5. Pathan, A.N., Sangshetti, K. & Pangal, A.A.G. (2010). Synthesis and Mossbauer Studies on Nickel-Zinc-Copper Nanoferrites, *Nanotechnology and Nanoscience*, 1(1), pp. 13-16.
6. Rani, R., Kumar, G., Batoor, K.M. & Singh, M.G. (2013). Electric and Dielectric Study of Zinc Substituted Cobalt Nanoferrites Prepared by Solution Combustion Method, *American Journal of Nanomaterials*, 1(1), pp. 9-12.

ELEMENTAL ANALYSIS OF RICE HUSK ASH USING ELEELEMENTAL ANALYSIS OF RICE HUSK ASH USING EDXRF METHOD

Khin Moe War¹, Myint Myint Maw²

Abstract

In this paper, the effect of the different calcinating temperature of rice husk ash (RHA) was studied. Especially the silica content in the RHA was investigated. Rice Husk was collected from rice milling plants of Hlae Gu township, Yangon Region and Pathein township, Ayeyarwaddy Region. For obtaining the pure rice husk, the sieve analysis was done for removing the sand and other impurities. After that the RHA is obtained by calcinating of rice husk at 500 °C, 600°C, 700°C and 800°C respectively for two hours. After that the calcined mass of the different RHA samples was weighted by electronic scientific balance. It was shown that the decreases in mass with increasing calcinating temperature from 500°C to 800°C. Then, each calcinated samples were taken for EDXRF analysis to measure the elemental concentration. According to the results, it was found that the major element, silicon (Si) was contained nearly 80% in each sample at different temperature. The formed rice husk ash is treated with Sodium hydroxide (NaOH) and Hydrochloric acid (HCl) to produce silica. The percentage of extracted silicon lies around 60 %.

Keywords : Rice Husk, Rice husk ash, Sodium Hydroxide, Silica , EDXRF

Introduction

Rice is an important staple food for approximately half of the world population. Rice husk is one of the most widely available agricultural wastes in much rice producing countries around the world. Rice husk (Rice hull) is the hard protecting coverings of grains of rice and removed from rice seed as a by-product during the milling process. Globally, approximately 600 million tons of rice paddies are produced each year. On average 20 % of the rice paddy is husk, giving an annual total production of 120 million ton.

In majority of rice producing countries much of the husk produced from processing of rice is either burnt or dumped as waste. Burning of RH in

¹ Assistant Lecturer, Department of Physics, University of Yangon

² Assistant Lecturer, Department of Physics, University of Yangon

ambient atmosphere leaves a residue, called rice husk ash. For every 1000 kg of paddy milled, about 220 kg (22%) of husk is produced, and when this husk is burnt in the boilers, about 55 kg (25%) of RHA is generated.

Rice husk removal during rice refining creates disposal problem due to less commercial interest. Also, handling and transportation of RH is problematic due to its low density. RHA is a great environment threat causing damage to land and surrounding area where it is dumped.

Therefore, Utilization of rice husk could solve the problem and reduce the cost of waste treatment. Rice Husk and its ash are used directly for manufacturing and synthesizing new materials. It is used as a fuel, fertilizer, substrate and it also used in preparation of activated carbon, pet food fiber, silica and silicon compounds, bricks etc. Rice husk ash used in steel, cement and construction industries. Multiple benefits of rice husks and rice husk ash can be achieved by future critical research efforts to provide new impetus for local and regional sustainable development.

Rice husk ash (RHA) is a term describing all types of ash produce from burning rice husks which vary considerably according to burning techniques. The silica in the ash undergoes structural transformations depending on conditions (time, temperature etc.) of combustion. At 550 to 800°C amorphous ash is formed and at temperature greater than this, crystalline ash is formed.

The change from amorphous to crystalline ash occurs at approximately 800°C, although the process is often 'incomplete' until 900°C is achieved. All the combustion processes devised to burn rice husks remain below 1440°C, which is the rice husk melting point. The rice husk ash obtained at 1000°C will exhibit excellent chemical activities and will be white in colour. These types of silica have different properties and it is important to produce ash of the correct specification for the particular end use. Rice husk ash has so many applications due to its various properties.

Experimental Procedure

Sample collection

Two samples of the rice husk were obtained each from rice milling plants in different places. Sample 1 was sourced from Pathein, Ayeyarwaddy Region (Delta Region) and Sample 2 was from Hlegu, Yangon Region. (Fig: 1) They are different in colour and size due to the difference in soil chemistry of the locations of collection and paddy variety.

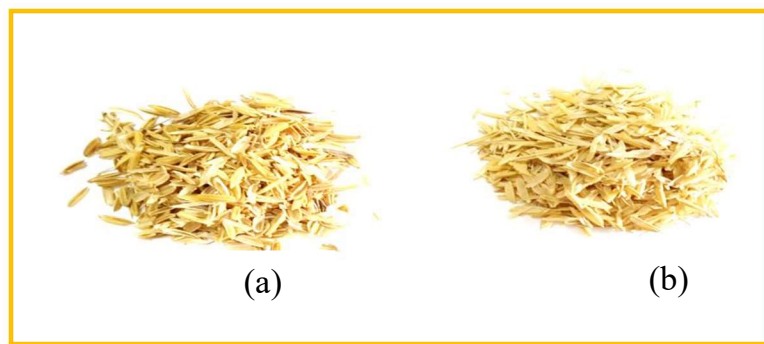


Figure 1: Different Rice Husk (a) in Pathein (b) in Hlae Gu

Sample preparation

At first, all of the samples were burnt in the open air under atmospheric pressure for three days to reduce the carbon content of the rice husk. And then, one of the rice husk samples was washed with water and dried through direct sunlight to remove the sand and other impurities. Fig (2)



Figure 2: The rice husk with sand and other impurities

Sieve Analysis

For obtaining the unnecessary materials and uniform size of rice husk, sieve analysis was done by using mesh. Place a small amount of rice husk is the first mesh. Then do the sieve analysis twice and take the pure rice husk. Fig (3)



Figure 3: Sieve analysis of RHA using with plastic mesh



Figure 4: The obtained pure rice hush after doing seive analysis

Preparation of Rice Husk Ash

5 g of rice husk from each sample was loaded by electronic balance. Each is taken in the crucible and place it in the muffle furnace at a set temperature of 500°C. After reaching 500°C, place it for 2 hours inside the

furnace itself. Then, switch off the furnace. And take the sample out by using tongs. The RHA was left in the furnace to cool for 48 hours. Check the amount of ash retained by using weighing balance. The procedure is repeated for 600°C, 700°C and 800°C respectively. After calcinating, it was found that the more heat it get, the more whitish it is. Therefore, the most whitish RHA include the higher the concentration of the silicon content. And the content of carbon is very low at a higher temperature in calcinating of RHA. Then the weight of the each RHA samples was measured by using an electronic single pan scientific balance. Fig (5).After that X-ray fluorescence method is used to determine the composition of elements in each sample. Fig (7)



Figure 5 : The weight of rice husk is measured by an electronic single pan scientific balance



Figure 6: (i) Before calcinating of Rice Husk



Figure 6: (ii) After calcinating of Rice Husk



Figure 7: Shinmadzu EDX-720 X-ray spectrometer

Production of silica

(i) Preparation of sodium silicate from rice husk ash

2 grams of NaOH pellets is taken and put in a 50 ml of water. This solution is stirred till the pellets get dissolved in water. 1 gram of ash and put in the NaOH solution is taken and mixed it thoroughly by using glass rod. It is placed in the hot air oven at temperature of 100°C. After 1 hour, it is taken from the hot air oven and took the obtained precipitate by using filter paper. Again the residue is dried at 60°C in the hot air oven for half an hour. The obtained product is sodium silicate.



(ii) Preparation of Silica from Sodium Silicate

300ml 1 N HCl solution is prepared and added to sodium silicate. The residue is taken out and dried it in a hot air oven at about 60°C. The obtained product is called silica, the partial replacement of cement.



Results and Discussions

In this present work, the weight for Rice Husk Ash of Hlae Gu calcined at 500°, 600°, 700° and 800°C were 1.156 g, 1.075 g, 1.04 g and

1.029 g respectively and that of Pathein were 0.912 g, 0.848 g, 0.8291g and 0.8273 g respectively. The result is plotted in Table 1 and Fig (8). It can be seen that the weight of RHA decreases with increasing temperature at all calcinating temperature.

Besides, two kind of Rice Husk Ash were analyzed by the EDXRF technique. The concentration of elements contained in the samples were measured by using the SHIMADZU Energy Dispersive X-ray Spectrometer (EDX-720 system). The results are shown in Table (2) and (3). According to the result, it was found that the major elements silicon contained in two sample of rice husk ash at different temperature were shown in Table(4) and Fig(9). From the information as shown in fig (10-17), the concentration of silicon (Si) contained in these all samples are not much different and nearly the same level of quantitative result of RHA.

Moreover, Different normalities of sodium hydroxide are used for different time periods and the weight of sodium silicate has been found and shown in table (5).The pure silica (SiO_2) is obtained by adding 1N Hydrochloric acid. It was shown in table(6) and the extracted silica is 60.2%.

Table 1 : The different mass of RHA from rice husk calcined at different temperature

Samples	Mass of husk(g)	Mass of ash (g)			
		T = 500 °C	T = 600 °C	T = 700 °C	T = 800 °C
Hlae Gu	5	1.156	1.075	1.040	1.029
Pathein	5	0.912	0.848	0.8291	0.8273

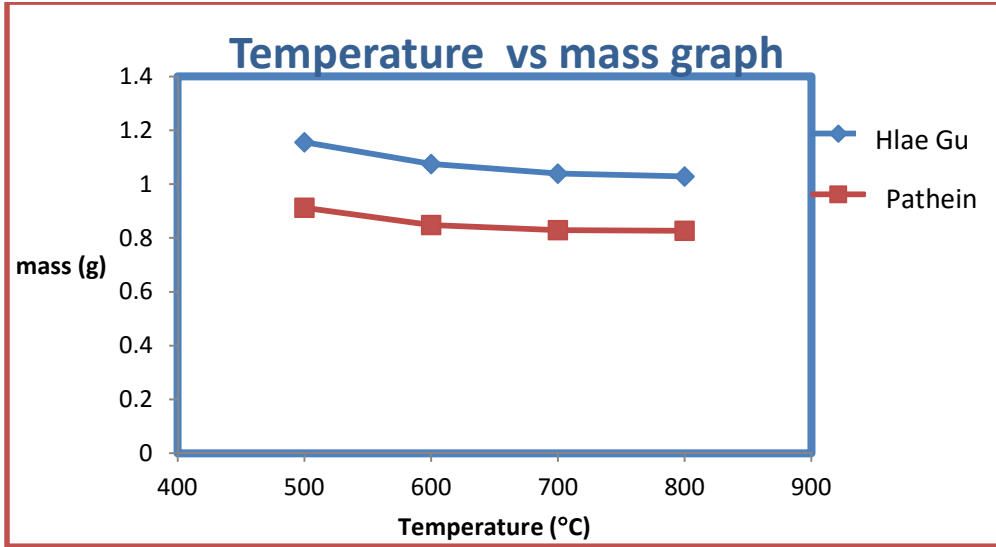


Figure 8: The different mass of RHA from rice husk calcined at different temperature

Table 2: The concentration of elements contained in RHA from Hlae Gu at different temperature

Temperature		500°C	600°C	700°C	800°C
Atomic number(Z)	Elements	Relative concentration of elements (% Wt)			
14	Si	77.156	78.810	79.698	76.728
19	K	14.838	13.149	12.644	12.868
20	Ca	4.130	4.675	3.648	4.818
25	Mn	1.690	1.628	1.543	3.204
26	Fe	1.6240	1.534	1.786	1.619
22	Ti	0.346	-	0.268	0.512
37	Rb	0.093	0.082	0.207	0.084
30	Zn	0.086	0.084	0.094	0.119
38	Sr	0.037	0.038	0.072	0.048
29	Cu	-	-	0.207	-

Table 3: The concentration of elements contained in RHA from Patheinat different temperature

Temperature		500°C	600°C	700°C	800°C
Atomic number(Z)	Elements	Relative concentration of elements (% Wt)			
14	Si	79.586	79.411	80.305	80.801
19	K	10.426	11.646	11.064	10.301
20	Ca	5.740	5.878	5.581	5.560
25	Mn	1.499	1.487	1.442	1.609
16	S	1.254	1.277	-	-
26	Fe	0.979	1.277	1.145	1.166
22	Ti	0.217	-	0.272	-
30	Zn	0.134	0.157	0.131	0.167
29	Cu	0.112	0.078	-	0.325
38	Sr	0.028	0.032	0.028	0.033
37	Rb	0.025	0.033	0.031	0.038

Table 4: Comparison of major element silicon in HlaeGu and Pathein samples at different temperature

Temperature (°C)	Silicon content (% Wt)	
	Hlae Gu	Pathein
500	77.156	79.586
600	78.810	79.411
700	79.698	80.305
800	76.728	80.801

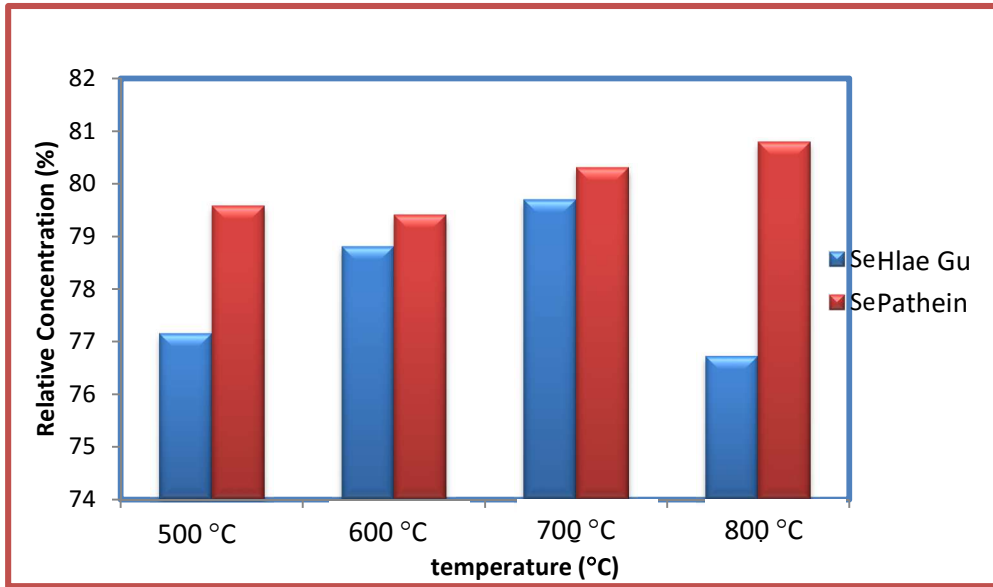


Figure 9 : The comparison of the relative concentration of silicon contents in the two kinds of four conditions of RHA

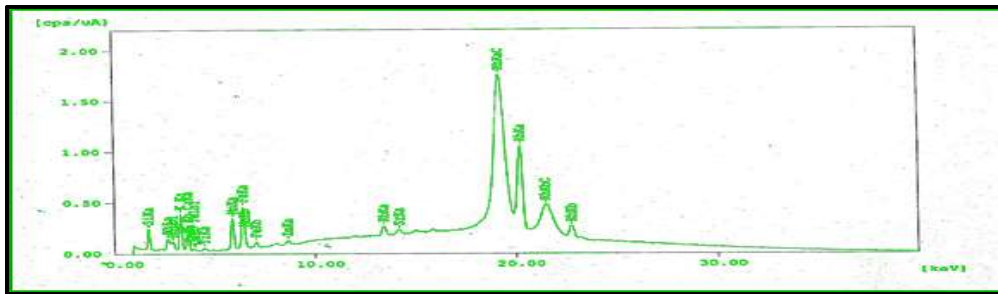


Figure10: The X-ray fluorescence analysis for Rice Husk Ash in Hlaegu for 2hours at 500°C

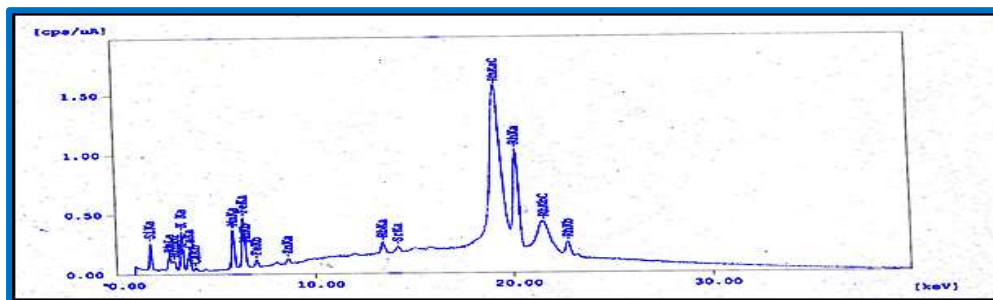


Figure 11: The X-ray fluorescence analysis for Rice Husk Ash in Hlaegu for 2 hours at 600°C

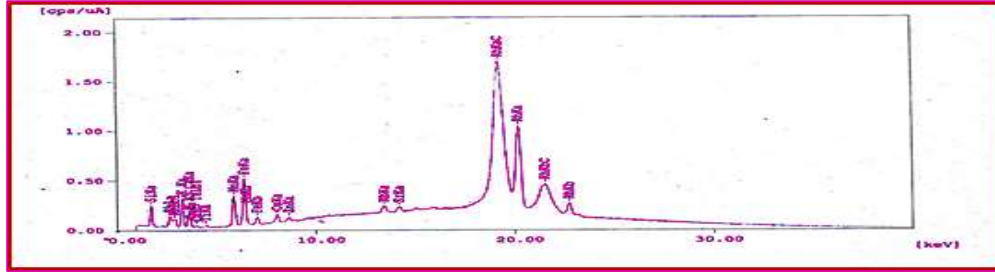


Figure 12: The X-ray fluorescence analysis for Rice Husk Ash in Hlaegu for 2 hours at 700°C

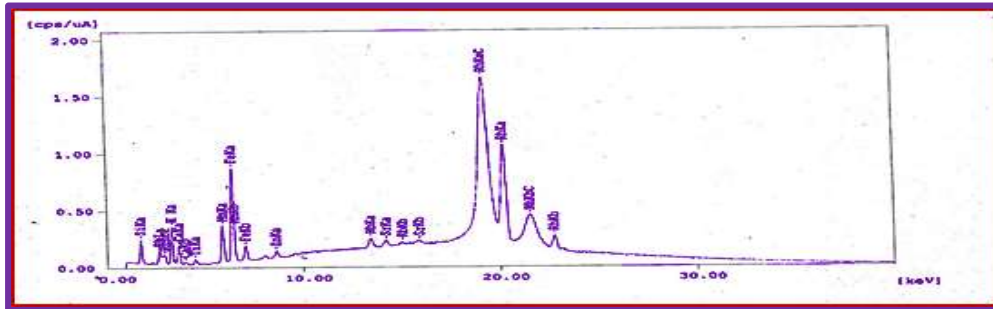


Figure 13: The X-ray fluorescence analysis for Rice Husk Ash in Hlaegu for 2 hours at 800°C

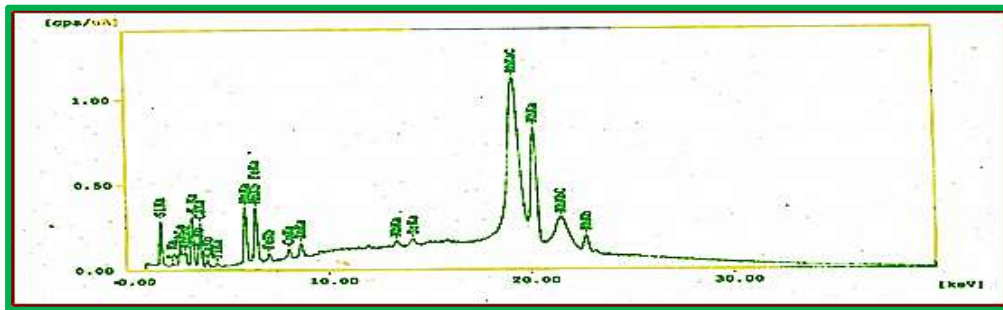


Figure 14: The X-ray Fluorescence analysis for Rice Husk Ash in Pathein for 2 hours at 500°C

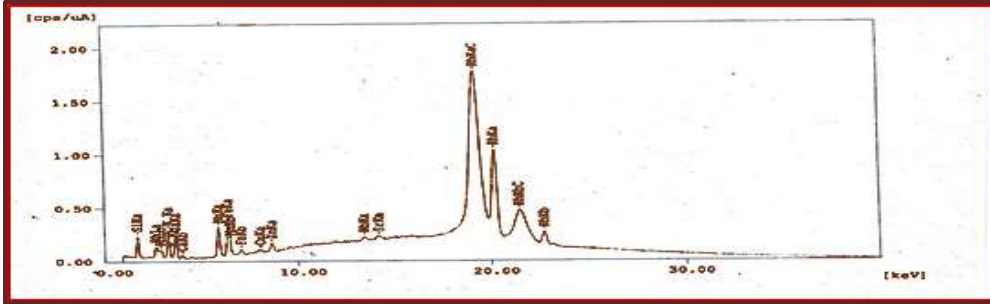


Figure 15: The X-ray Fluorescence analysis for Rice Husk Ash in Pathein for 2 hours at 600°C

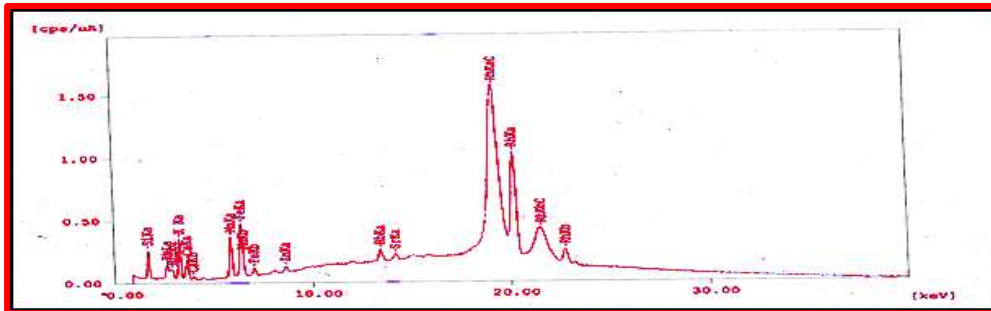


Figure 16: The X-ray Fluorescence analysis for Rice Husk Ash in Pathein for 2 hours at 700°C

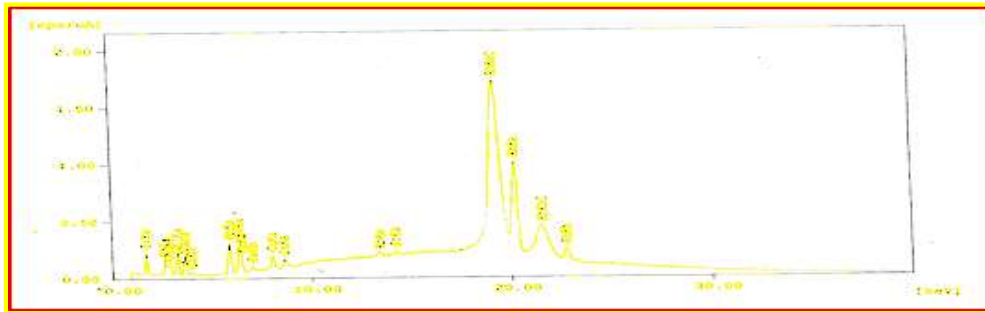


Figure 17: The X-ray Fluorescence analysis for Rice Husk Ash in Pathein for 2 hours at 800°C

Table 5 : Weight of sodium silicate produced for different concentration and time period.

Normality(N)	Time (hour)	Weight of Na_2SiO_3
1	1	0.60
1	2	0.38
2	1	0.50
2	2	0.32

Table 6 : Weight of silica produced for 1N HCl

Normality(N)	Time (hour)	% of Silica
1	1	60.2

Conclusion

From the calcinating of RHS results, it can be observed that the weight of RHA is dependent on the calcinating temperature. The weight of RHA decreases with increasing calcinating temperature for RHA between the temperature 500°C and 800°C.

From the EDXRF results obtained, the major element of each RHA sample is silicon (Si) and the concentration of silicon at the same places in different temperature are nearly 80%. Therefore, the silicon content of RHA between 500°C and 800°C varies slightly with calcinating temperature. Silica has been produced by a two-step process and the percentage extraction lies around 60%.

As a whole, calcination improve the silica content of rice husk ash for use as a pozzolana as well as removes mineral impurities that may affect the pozzolanic properties of the rice husk ash. Moreover, proper utilization of it aims to save the environment, encourages the Government to find solutions regarding disposal to landfills of waste materials and provides new knowledge to the contractors and developers on how to improve the construction industry

by using rice husk, to sustain good product performance and to meet recycling goals.

Acknowledgements

I would like to thank Professor Dr Khin Khin Win, Head of Department of Physics, University of Yangon for her kind permission to carry out this research.

I also would like to thank Dr Soe Soe Nwe, Professor, Department of Physics, University of Yangon, for her allowing me to do this work.

References

1. Adylov G, Faiziev SH, Paizullakhanon M, Mukhsimov S, Nodirmatov E (2003). Silicon Carbide materials obtained from rice husk. *Tech. Phys.Lett.* 29(3): 221 – 223.
2. Bartha P (1995). Biogenous silicic auila growing raw material. *Keramische Zeitschrift* 47 (10), pp 780-785.
3. Dziunikowski, Bohdan.-Amsterdam (1989) Energy dispersive X-ray fluorescence analysis
4. Dziunikowski B, (1989), *Energy Dispersive X-ray Fluorescence Analysis*, (Warszawa: PWN - Polish Scientific)

PREPARATION AND CHARACTERIZATION OF SnO₂ NANORODS AT DIFFERENT TEMPERATURES

Theint War War Khaing¹, Thida Win², Than Than Win³,
Yin Maung Maung⁴

Abstract

In this study, tin oxide (SnO₂) nanorods were fabricated onto FTO substrates via chemical bath deposition (CBD) method. SnO₂ nanorods were prepared by immersing SnO₂ seed layer coated FTO glasses into the aqueous solution. After fabrication process, the substrates were annealed at different temperatures and SnO₂ nanorods were formed. And then, SnO₂ nanorods were characterized by X-ray diffraction to observe crystal structure. Rod's diameter and morphological properties at different temperatures were carried out from SEM analysis. SnO₂ nanorods were obtained as an 1D structure. From this experiment, these nanorods would be used to construct the dye-sensitized solar cells (DSSCs) as photoelectrode. Current density –voltage (J-V) characteristics of DSSC with natural dye was measured. From J-V curve, conversion efficiency (η) and fill factor (FF) were evaluated for DSSC.

Keywords; *SnO₂ nanorods ,CBD method , XRD ,SEM , DSSC, J-V Characteristics*

Introduction

Transparent conducting oxide (TCO) substrates have been extensively used in various electronic and optoelectronic applications, such as solar cells, window heaters and liquid crystal devices [Surawut Chuangchote et al,2011]. Most efforts in TCO have Transparent conducting oxide (TCO) substrates have been extensively used in various electronic focused on the oxides of tin, indium and zinc with small amount of other elements as dopants [Surawut Chuangchote et al,2011]. Nanostructures synthesis with controllable properties is a research desire and still a major challenge for their applications in a wide range[M.A. Batal et al,2012]. Nano architectures of transition semiconductor oxides are getting immense importance because of their

¹. Assistant Lecturer, Department of Physics, West Yangon University

². Lecturer, Department of Physics, University of Yangon

³. Associate Professor, Department of Physics, Mandalay University of Distance Education

⁴. Associate Professor, Department of Physics, Mandalay University

excellent properties and potential applications in energy storage devices [M. Zubair Iqbal et al ,2014] .Tin dioxide (SnO_2) is an n-type semiconducting oxide with a wide bandgap (3.6eV) and well known for its potential applications in dye-based solar cells, semiconductor, photoconductors, and gas sensor [Jr H.He et al ,2006].Tin oxide (SnO_2) thin film is a wide band gap n-type semiconductor with high simultaneous electrical conductivity and optical transparency in visible region of the spectrum [M.A. Batal et al ,2012]. The properties of SnO_2 materials are strongly dependent on their size and shape, it is obvious that the controlled synthesis of the morphologies of SnO_2 materials is very important for special applications [M. Zubair Iqbal et al ,2014].

Inorganic materials with different morphologies and size can exhibit different properties. Accordingly, various structural and morphological forms of SnO_2 materials have been fabricated over the past several years, including nanowires , nanoribbons or nanobelts , nanorods , nanotubes ect [Hyoun Woo Kim et al , 2005]. Several methods and techniques were developed to produce different nanomaterials. Metal oxides having nanostructure forms are of great importance for verity of applications. Among them tin oxide, which has two oxidation states namely stannic (SnO_2) and stannous (SnO). Fabrication of SnO_2 nanorods has been accomplished using several vapor deposition techniques, such as chemical bath deposition, thermal evaporation and hydrothermal [O.Lupan et al, 2009]. However, the preparation of SnO_2 nanostructures with well-controlled morphology and dimension by facile synthesis is still a challenge [M. Zubair Iqbal ,2014].

In this paper , SnO_2 nanorod on FTO substrates were observed by using chemical bath deposition method. One dimensional (1-D) nanomaterials, such as nanowires, nanorods and nanotubes, are regarded as catalysts for oxidation of organic compounds, solid state sensors, biomedicine, ceramics and transparent conductors.

Experimental Procedure

Fabrication of SnO₂ Nanorod

SnO₂ nanopowder was used as starting material. The well-dissolved precursor solution was firstly prepared by mixing SnO₂ powder (3g) and ethanol solvent (40ml). The mixed solution was stirred with magnetic stirrer for 12h figure 1 and put at 110°C for 1h using water bath to remove water of crystallization, reactive with SnO₂ solution and cooled down at room temperature. Finally, SnO₂ precursor solution was obtained.

The substrates was cleaned in the ultrasonic bath with ethanol and deionized water to remove adsorbed dust and surface contamination.

In this study, FTO glass substrates were used for the growth of SnO₂ seed layer by spin coating technique.

The substrates were placed on fragment adapter and the SnO₂ sol solution was poured onto substrates. The spin speed or rotational speed was set 3000 rpm and spinning time was 30 s figure 2. After spin coating, they were annealing at 500°C, 550°C, 600°C for 1h respectively.

For the growth of SnO₂ nanorod, an aqueous solution of tin chloride dehydrate (SnCl₂.2H₂O) was prepared as tin source and hexamethylenetetramine (HTMT) (C₆H₁₂N₄) with water was used as oxygen source.

Next, the seed layer coated FTO glasses were tilted against the wall of the aqueous solution of container as shown in figure 3. Then, the containers were heated at 80°C for 5 h. At the end of fabrication process, the substrates were taken out of the solution and rinsed five times with deionized water and dried at room temperature. After these substrates annealed at 240°C for 1 h respectively, SnO₂ nanorod were obtained.



Figure 1. Magnetic Stirrer



Figure 2. Spin Coating Machine



Figure 3. SnO₂seed layer coated FTO glasses immersed into the aqueous solution

Results and Discussion

X-ray Diffraction Analysis

The XRD pattern shown in figure 4 indicates a high purity of SnO₂ powder. Four obvious peaks were formed at (110), (101), (200), and (211) planes. These diffraction peaks indicate a tetragonal structure of SnO₂ with lattice constants of $a, b = 4.73 \text{ \AA}$ and $c = 3.18 \text{ \AA}$ that agree with documented values for the SnO₂ crystals. Scherrer's equation was used to estimate the size of SnO₂ crystals. It is stated that the crystallite size $D = \frac{0.89\lambda}{\beta \cos\theta}$, where λ is the wavelength for the Cu K $_{\alpha}$ ($= 1.54056 \text{ \AA}$), β is the broadening at half the maximum intensity (FWHM) expressed in radian, and θ is Bragg's angle. The crystallite size is 74.95 nm for SnO₂ powder based on the (110) peak.

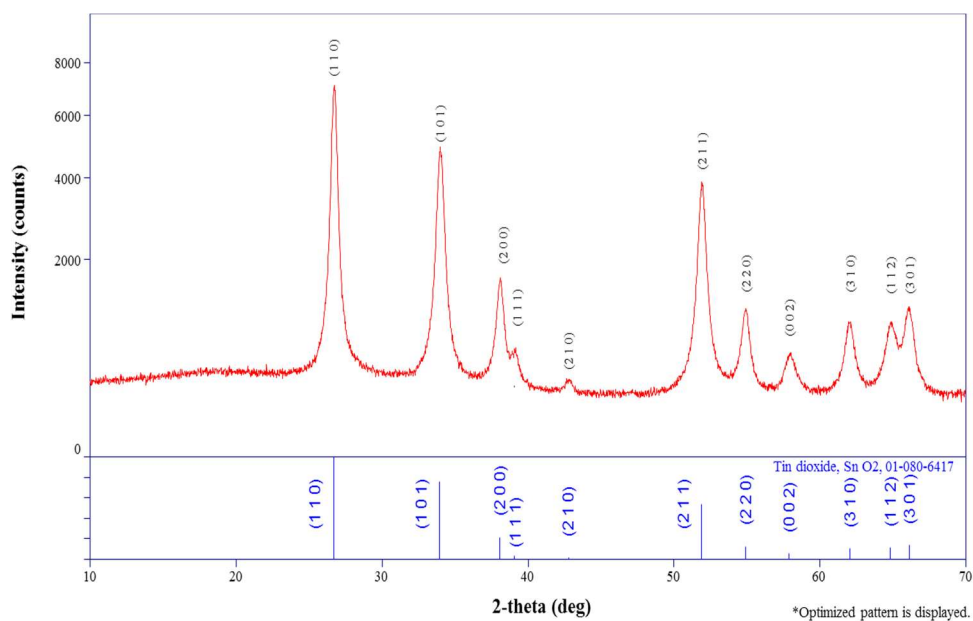


Figure 4. X-ray diffraction pattern of SnO₂ powder

Morphological Characterization

The morphological characterization was analyzed by SEM (Scanning electron Microscope). Figure 5, 6 and 7 showed the SEM image of SnO₂ nanorod at different which a large area of nanorod were formed. The different diameters of SnO₂ was formed between 300-700 nm and length reaches up to around 5 μm as shown in Figure 5,6 and 7. The products consists of nanorod as well as nanoparticles. At 550°C , the SnO₂ nanorod were also temperatures were obtained from seed layer coated substrates were tilted against the wall of container. The SnO₂ nanorod showed 1D structure. After calcinations at 500°C, SnO₂ nanorod onto FTO substrate were obtained 1D structure in formed as nearly same size of the product at 600°C , but they were more smooth than the product at 500°C. The SEM images shows that the growth direction of the nanostructure is randomized. In the SEM images, the products with a closer view comprises straight structures.



Figure 5. SEM image of SnO₂ nanorod annealing at 600°C

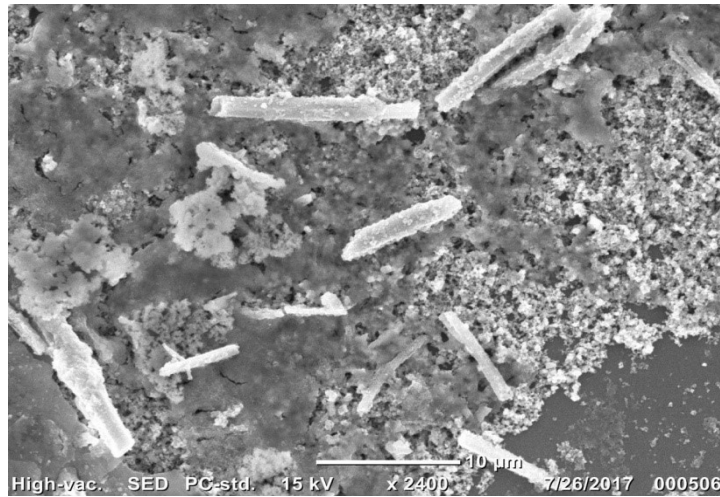


Figure 6. SEM image of SnO₂ nanorod annealing at 550°C

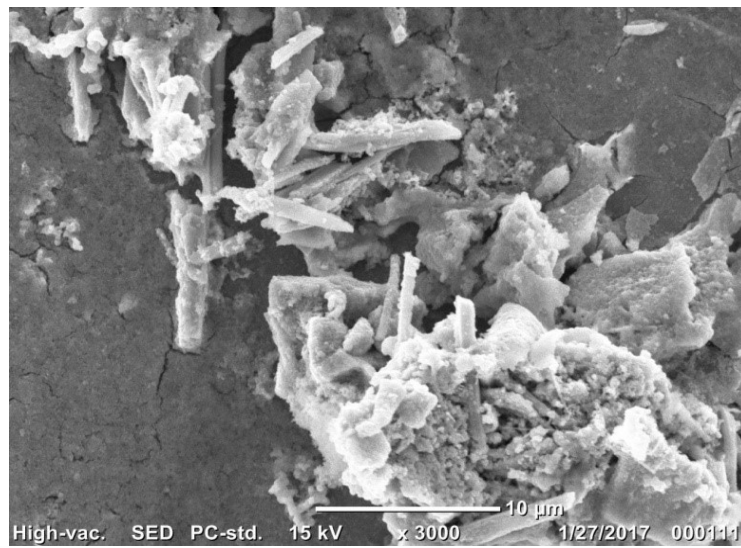


Figure 7 . SEM image of SnO₂ nanorod annealing at 500°C

Application of SnO₂ nanorod

Preparation of natural dye

The natural dye extracted with methanol by the following procedure; Fresh leaves of tamarind (figure 8) were washed with water and dried (figure 9) at room temperature. Then, they were crushed into powder. Each powder (0.8g) was dissolved in the beaker and 25ml of methanol was added. The solution was annealed at 80°C for 1h by using water bath figure10. And then, the residual (solid) parts were filtered out and the resulting filtrates were used as dye solutions.

Next, optical properties of dye in UV and visible regions were analyzed by using Shimadzu UV-170 spectroscopy.



Figure 8. Tamarind dried leaves and powder



Figure 9. Tamarind dried leaves and powder



Figure 10. Annealing dye solution on water bath at 80 °C

UV – Vis Spectroscopic Study

The UV-Vis photospectra of tamarind dye were recorded with respect to the bare substrate placed in the reference beam using beam spectrophotometer in the range 400 to 700 nm.

Figure 11 show the UV visible absorption spectra of tamarind leaves dye at 80 °C. In the figures, chlorophyll dye has absorption features in UV light zone. In the visible light region zone, the absorption peaks of chlorophyll dye extracted from tamarind leaves at 80 °C lie at 674.40 nm. The energy band gap of wavelength was calculated by using Plank’s photoelectric equation.

$$E = \frac{hv}{\lambda} = \frac{hc}{\lambda}$$

where E = energy band gap (eV)

h = Plank’s constant =6.625 x 10⁻³⁴ J-s

c = 2.99 x 10⁸ ms⁻¹

λ = the wavelength (nm)

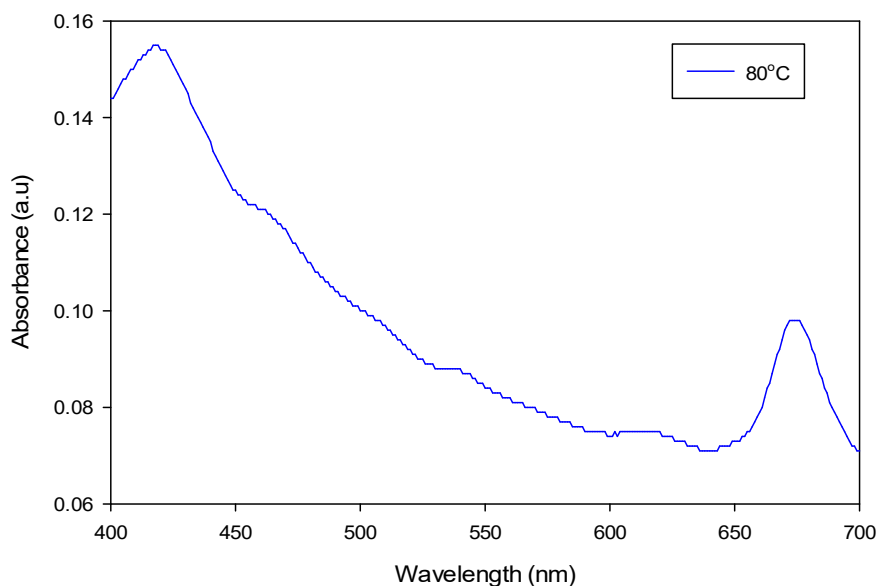


Figure 11. Absorbance spectra of natural dye extracted from tamarind leaves at 80°C

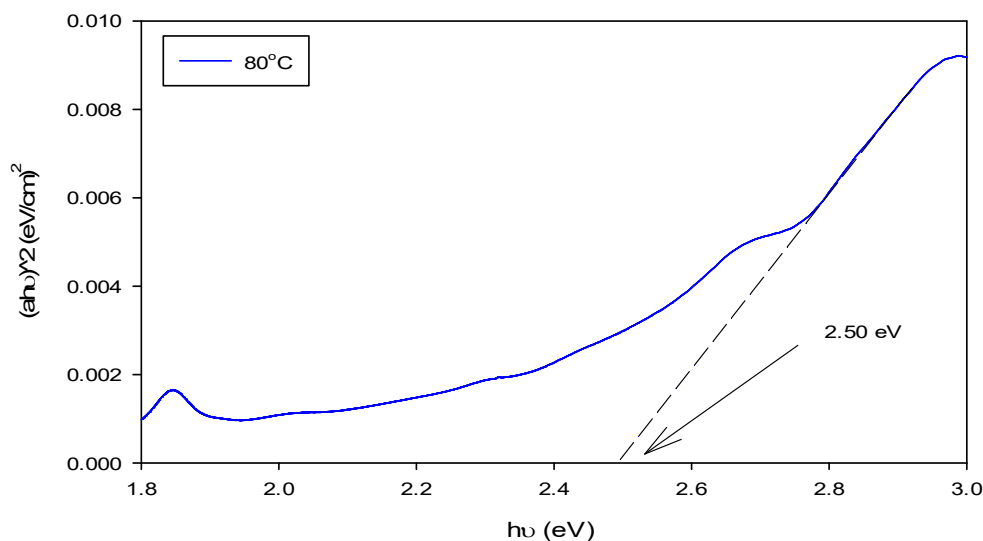


Figure 12. Absorbance spectra of natural dye extracted from tamarind leaves at 80 °C

The transmission spectra were analyzed by plotting $(\alpha h\nu)^2$ Vs $h\nu$, based on following equation.

$$\alpha h\nu = A(h\nu - E_g)^{n/2}$$

Where α is the absorption coefficient A is a constant (independent from ν) and n is the exponent that depends upon the quantum selection rules for the particular material. A straight lines (fig 12) were obtained when $(\alpha h\nu)^2$ is plotted against photon energy ($h\nu$), which indicate that the absorption edge is due to a direct allowed transition ($n=1$ for direct allowed transition). The intercept of the straight line on $h\nu$ axis corresponds to the optical band gap (E_g) and its value was determined.

Fabrication of DSSC

For photoelectrode, SnO₂ nanorod onto FTO glass were immersed into the dye solution for 12h and then took off. For counter electrode, carbon paste was coated onto FTO substrate and annealed at 120 °C for 15 min. SnO₂ nanorod photoanode and carbon counter electrode were sandwiched and two binder clips were used to hold the electrodes together. Iodine was added and it was used as a mediator. Alternately open and close each side of solar cell to draw electrolyte solution in and wet SnO₂ nanorod. Remove excess electrolyte from exposed areas. Fasten alligator clips to exposed sides of solar cell. Photocurrent – Voltage (I-V) curve and photovoltaic properties were investigated.

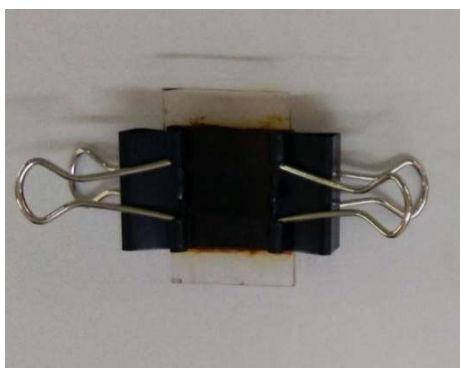


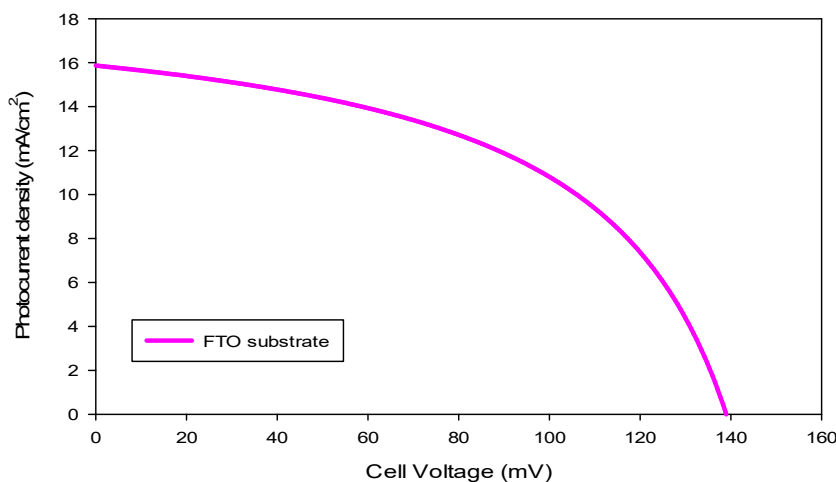
Figure13. Dye sensitized solar cell

Photovoltaic Properties

Figure 14 showed the J-V curves of SnO₂ nanorod for DSSCs with tamarind leaf powder dye solution. From the figure, the maximum power point was obtained by tangential point on J-V curve. By drawing the maximum power point onto X- axis , the maximum voltage (V_m) was obtained. By drawing the maximum power point onto Y- axis , the maximum current (I_m) was obtained. From the analysis, short circuit current (I_{sc}) , maximum current density (J_m), open circuit voltage (V_{oc}), maximum voltage (V_m) , conversion efficiency (η) and fill factor (FF) of dye sensitized solar cell was shown in Table 1.

Table 1. Photovoltaic properties of SnO₂ nanorod DSSC

Substrates	J_{sc} (mA/cm ²)	V_{oc} (V)	FF	PCE (%)
FTO	15.89	0.13870	0.49	1.09

**Figure14 . J-V curve of SnO₂ nanorod DSSC (FTO glass)**

Conclusion

SnO₂ nanorod were obtained by immersing of SnO₂ seed layer coated onto FTO glass substrate into the aqueous solution by using chemical bath deposition method. According to the XRD result, SnO₂ powder were successfully formed with tetragonal symmetry. After calcination at 500°C, the SnO₂ nanorod showed one – dimensional structure with the diameter of 300 nm –700 nm and length reaches up to around 5µm. At 550°C and 600°C , the diameters and lengths were nearly the same as the SnO₂ nanorod at 500°C. In 550°C, very few of SnO₂ nanorod were appeared. In 600°C , a lot of SnO₂ nanorod were appeared and more smooth than the product at 500°C. In the SEM image, the products with a closer view comprises straight structures at different temperature. So, SnO₂ nanorod at 600°C is better than others. When

the SnO₂ nanorod for chlorophyll – based natural dye sensitized solar cell was fabricated, power conversion efficiency (1.09 %) was obtained.

Acknowledgements

I would like to give special thanks to Dr Khin Thida, Rector, West Yangon University, for her kind permission and encouragements to carry out this work.

I would like to give thanks to Dr Moe Ohnmar, Professor(Head), Department of Physics, West Yangon University, for her kind permission and encouragements to carry out this work.

I would like to give thanks to Dr Khin Khin Win, Professor (Head),Department of Physics, University of Yangon, for her kind permission and encouragements to carry out this work.

References

1. Jiawei Gong et al 2015 AIP Advances 5(067134)
2. Jose Pedro Santos et al 2014 Sensors 14 24231-24243
3. II- Doo et al J Electroceram 2010 25 159 – 167
4. M. Zubair Iqbal et al Research Gate 2014 6 1-6
5. M.A. Batal et al JAAUBAS 2014 15 15-20
6. Numan Salah et al 2016 Materials and Design 103 (2016) 339–347
7. Surawut Chuangchote et al 2011 ECS transactions 41(6) 223- 229
8. X.Xia et al 2011 eXPRESS Polymer Letters 6(2) 169 – 176
9. Xin Xia et al 2013 J Master Sci
10. Zunxian Yang et al 2010 CAMBRIDGE JOURNALS 25(8)1516 – 1524

FABRICATION OF TWO CELLS, THREE CELLS AND FOUR CELLS MEANDER TYPE DYE-SENSITIZED SOLAR CELL MODULES

Khin Thida Aung¹, Khin Lay Thwe², Nwe Ni Khin³, Win Win Thein⁴

Abstract

Two cells, three cells and four cells meander type dye-sensitized solar cell modules have been fabricated by using natural dyes extracted from teak leaves as sensitizer. These solar cell modules were assembled with two 20-30 ohms conductive glasses (TEC 15, Dyesol) (one for TiO₂ coated electrode and another for carbon coated electrode), TiO₂ nano-powder (Degussa-P25 powder), iodide electrolyte solution and soft graphite pencil for carbon coating. The silver lines were drawn for series and meander connections. The silicone was drawn as a protective barrier on both sides of the silver line. The performance of all fabricated DSSC modules was evaluated by the open circuit voltage V_{oc} , the short circuit current I_{sc} and the fill factor (FF). The energy conversion efficiency (η) was obtained under the air mass (AM) 1.5 radiation.

Keywords: Meander type DSSC modules, Natural dyes, TiO₂ nano-powder, Electrolyte, Silver line

Introduction

A photovoltaic module refers to an array of identical solar cells which are all interconnected in series or in parallel. Module design can be classified into two categories: strip module design and interdigital meander type module design. A new interdigital meander module design requires fewer holes in the glass substrate for electrolyte filling than the conventional strip design. Furthermore, to achieve a high utilizable current, cells can be connected in series by overlapping the silver grids on the boundary of the cells. This research focuses on the fabrication of a serial interconnected, meander type dye-sensitized solar cell module, one of the categories of third generation solar cells, using dye extracted from teak leaves as sensitizer.

¹. Dr, Demonstrator, Department of Physics, Hinthada University

². Dr, Lecturer, Department of Physics, University of Yangon

³. Dr, Professor (Rtd), Department of Physics, University of Yangon

⁴. Dr, Professor and Head, Department of Physics, Hinthada University

A meander type dye-sensitized solar cell module can be designed as shown in Figure 1(a). The module consists of six cells. Each cell has a width of about 5 cm. Front and counter electrode of a module with meander shaped cells is shown in Figure 1(b). The silver grid of the front electrode is shifted with respect to the silver grid of the counter electrode. The silver grid results in a meander shaped cell area, allowing an easy coloration and filling process via 2 holes per cell. When front and counter electrodes are aligned on top of each other, the silver grids of front and counter electrode only overlap on the boundary of two neighbouring cells as shown in Figure 1(c), thus forming an electrical series connection. The TCO layer of the substrate is structured accordingly. The silicone was drawn as a protective barrier on both sides of the silver line.

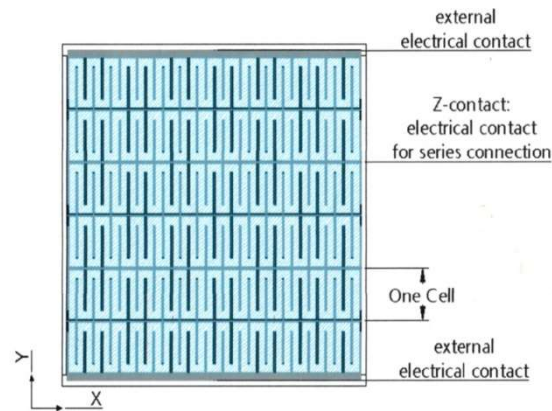


Figure 1(a) A meander type dye-sensitized solar cell module design

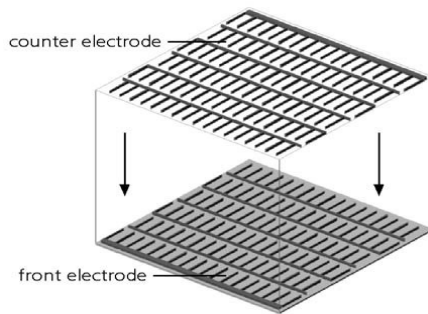


Figure 1(b). Front and counter electrode of a meander type DSSC module

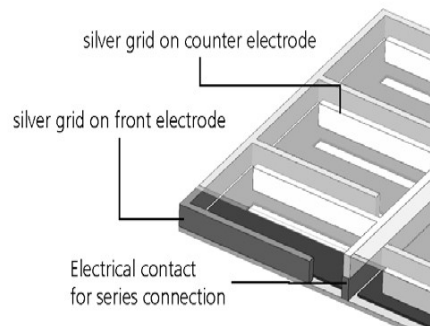


Figure 1(c). Aligning front and counter electrode on top of each other

Experimental Procedures

Figure 2. shows the flow chart for experimental procedures of meander type DSSC modules.

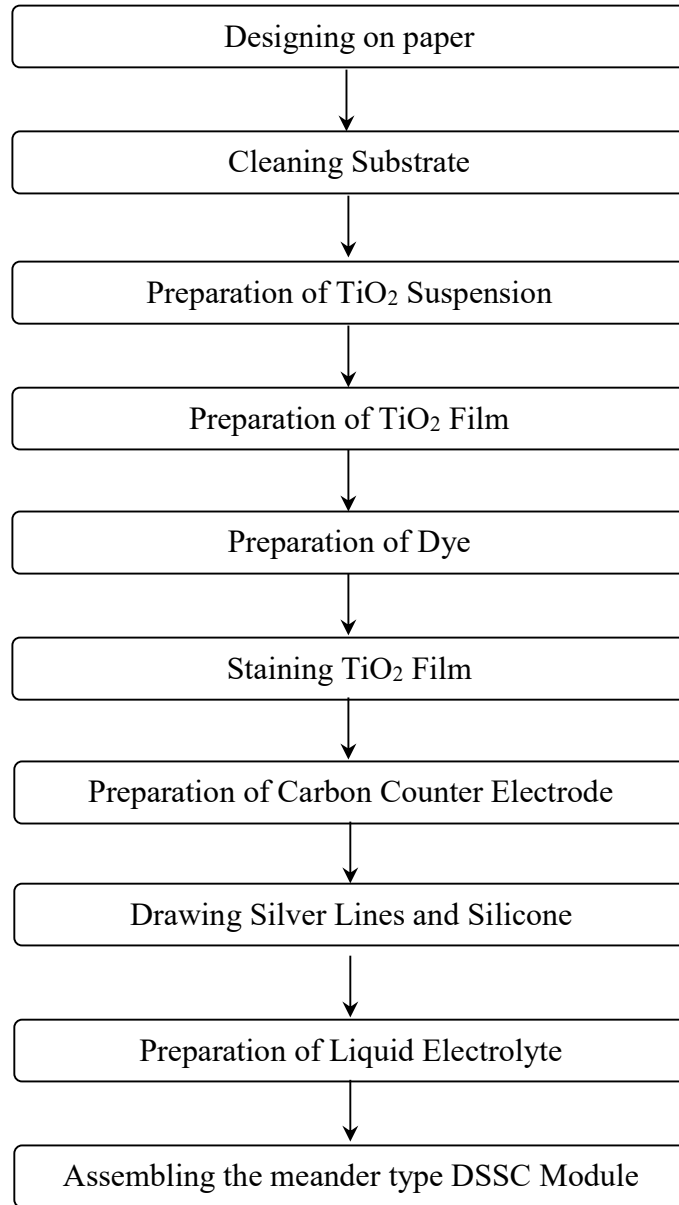


Figure 2. Flow chart for experimental procedures of meander type DSSC modules

Designing on Paper

First the designs of TiO₂ electrode for the two cells, three cells and four cells were drawn on the paper as shown in Figure 3(a), (b) and (c).

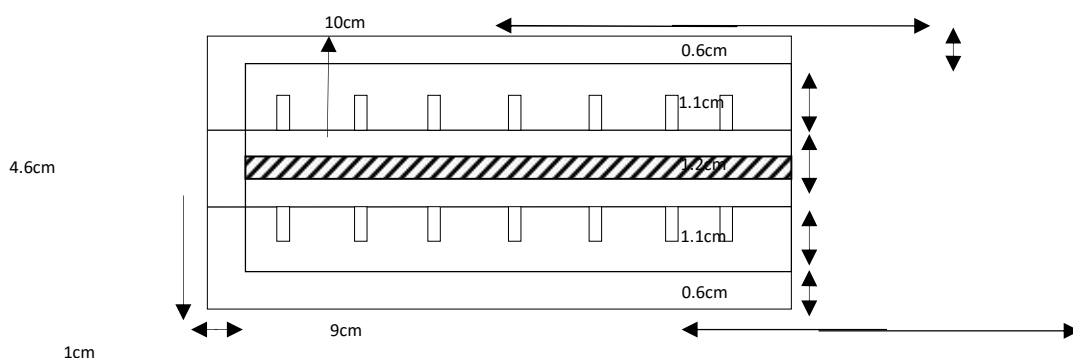


Figure 3(a) The design of TiO₂ electrode for two cells

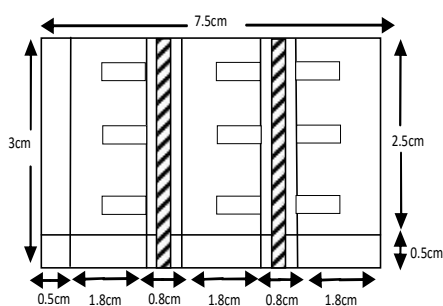


Figure 3(b). The design of TiO₂ electrode for three cells

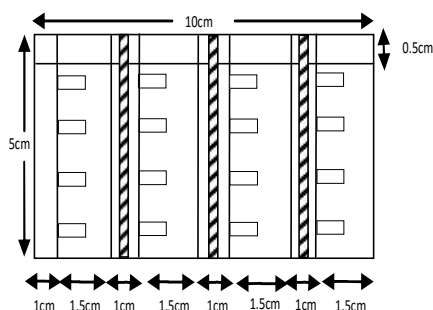


Figure 3(c). The design of TiO₂ electrode for four cells

Cleaning Substrate

The substrates were first dipped into acetone for at least 5 minutes to dissolve unwanted organic materials and to remove dust and contamination material. Another 5 minutes in methanol was followed in order to remove the acetone and materials that are not cleaned or dissolved by acetone. Finally, 5 minutes in isopropyl alcohol (IPA) was needed to further remove the residual particles on the substrates. The cleaned substrates were then put inside the 90°C oven and baked for at least 15 minutes to ensure that the solvents were vaporized and that the remaining particles were removed.

Preparation of TiO₂ Suspension

To fabricate two cells, three cells and four cells meander type DSSC modules, the 5g of TiO₂ nano powder was needed to be used. The TiO₂ nano-powder was put in the mortar and then 1mL nitric acid solution (pH 3 - 4) was added to it while grinding with a pestle until a colloidal suspension with a smooth constancy was obtained. Some clear dishwashing detergent was then added. The mixture was kept to equilibrate at room temperature for about 15 minutes.



Figure 4 (a). Weighing TiO₂ nano-powder **Figure 4(b).** TiO₂ suspension

Preparation of TiO₂ Film for Two Cells, Three Cells and Four Cells Meander Type DSSC Modules

Using a multimeter, the conducting side was identified. According to the designs, TiO₂ paste was put on the glass. The transparent conducting oxide (TCO) layer on the glass substrate was structured.

For two cells, by placing the conducting side of tin oxide coated glass plate up, the two edges which are 0.6 cm wide of the plate were taped with Scotch tape. At the left side of the plate, 1 cm wide was taped and 1.2 cm wide in the middle of the plate was masked by the tape. Moreover, the gaps (0.2 cm x 0.6cm) on the substrate were taped to draw the silver lines.

For three cells, at the bottom, 0.5cm wide of the plate was taped with Scotch tape. At the left side of the plate, 0.5 cm wide was taped and 0.8 cm wide between the cells was masked by the tape. Moreover, the gaps (0.2 cm x 1cm) on the substrate were taped to draw the silver lines.

For four cells, on the top of the glass plate, 0.5cm wide was masked by Scotch tape. At the left side of the plate, 1cm wide was taped. Then, 1.5cm wide between the cells was taped. Moreover, the gaps (0.2 cm x 0.8 cm) on the substrate were taped to draw the silver lines.

Then, some titanium dioxide (TiO_2) suspension was put on the one glass and quickly spread it over the surface using a glass rod (doctor-blade method). The tape was then carefully removed without scratching the TiO_2 coating. The coated plate was dried for 1 minute in a covered Petri dish. The glass plate was heated on the hotplate about 30 minutes until a white titanium dioxide coating was formed. The glass plate was then slowly cool by turning off the hotplate. TiO_2 coated plates for two cells, three cells and four cells were shown in Figure 5(a) and (b).

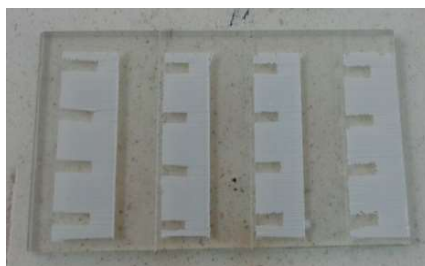
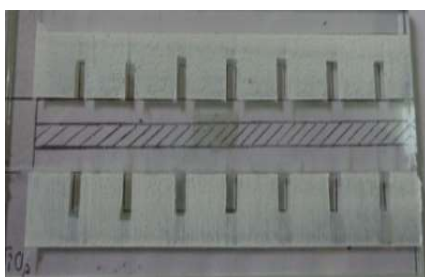


Figure 5(a) TiO_2 coated plates for two cells, three cells and four cells



Figure 5(b). Heating the TiO₂ coated glass plate

Extracting Dye

To extract dyes from teak leaves, the leaves were cut and ground with the mortar and pestle and then 3-5 mL of acetone was added. Then it was squeezed into the Petri dish as shown in Figure 6(a) and (b).



Figure 6(a) Grinding teak leaves with mortar and pestle



Figure 6(b) Squeezing into the Petri dish

Staining TiO₂ Film

The dye solution extracted from teak leaves was poured into a Petri dish. The TiO₂ electrode was dipped into the dye solution with the coated side down for 24 hours until no white TiO₂ can be seen on either side of the glass. The TiO₂ electrodes were dipped into the dye solution for two cells, three cells and four cells as shown in Figure 7. The glass plate then appeared as brownish red color. It was first washed in H₂O and then in ethanol in order to remove water from the porous TiO₂. Any residue was wiped off with a tissue, blotting gently to dry.



Figure 7. Staining TiO₂ films

Preparation of Carbon-Coated Counter Electrode

Firstly, the design for carbon-coated counter electrode was drawn on the paper as the design of TiO₂ electrode. Then, the glass plate was first washed with ethanol. Using a multimeter the conducting side was identified. By scratching thoroughly with a soft graphite pencil, a thin carbon coating was put on the conductive side of the glass plate. The thin carbon coated plates for two cells, three cells and four cells were shown in Figure 8(a), (b) and (c).

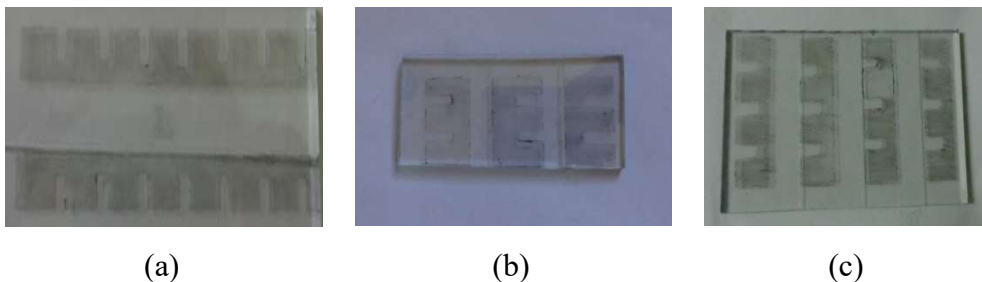


Figure 8. Carbon-coated counter electrodes for two cells, three cells and four cells

Drawing the Silver Lines and Silicone for Two Cells, Three Cells and Four Cells

For series connection, the silver line was drawn in the middle of the substrate. For meander type connection, the silver lines were drawn on the surface of TiO₂ glass substrate and thin carbon coated plate as shown in

Figure 9(a), (b) and (c). The silicone was drawn as a protective barrier on both sides of the silver line. The silver lines of the carbon-coated electrode were shifted with respect to the silver lines of the TiO_2 electrode. These silver lines result in a meander shaped cell area.

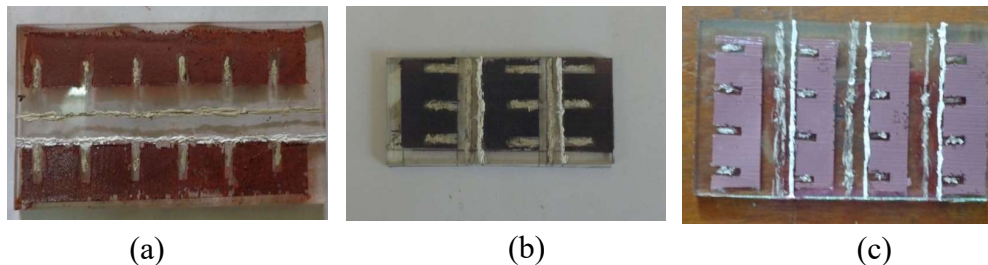


Figure 9. Drawing the silver lines and silicone on the TiO_2 substrate for two cells, three cells and four cells

Preparation of Liquid Electrolyte

0.5 M potassium iodide was mixed with 0.05 M iodine in water-free ethylene glycol. 10 mL of ethylene glycol was put in a container. Then, 0.127 g of I_2 (Iodine) and 0.83 g of KI (Potassium Iodide) was added to it. They were mixed together stirring with a clean glass rod. All the bottles and the containers were kept tightly capped when not in use.

Assembling the Two Cells, Three Cells and Four Cells Meander Type DSSC Modules

The carbon-coated glass plate was placed with the coated-face down on the TiO_2 coated glass plate. The two glass plates were stacked slightly off set. The plates were bound together with the binder clips on each side of the longer edges. Then, two to three drops of iodide electrolyte solution was put on one edge of the plates. Each side of solar cell was then made slightly open and closed alternately so that the electrolyte solution was drawn in and wet the TiO_2 film, thus making all the stained area to be in contact with the electrolyte solution.

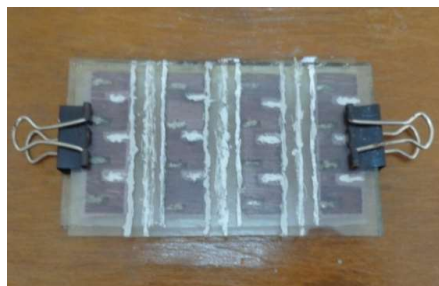
Figure 10(a), (b) and (c) illustrate assembling the two cells, three cells and four cells meander type DSSC modules.



(a)



(b)



(c)

Figure 10. Assembling the two, three and four cells meander type DSSC modules

Results and Discussions

XRD, pH and UV-Vis Measurements

Titanium dioxide (TiO_2) powder was characterized by using RIGAKU-RINT 2000 X-ray Diffractometer. The X-ray diffraction pattern was recorded to different diffraction peaks corresponding to different plane. The resulting XRD pattern was found to be exactly coincide with the reference (78-2486) TiO_2 pattern. This shows that the used TiO_2 nano-powder was pure with no other chemical impurities. By using Scherrer equation, the average crystallite size of TiO_2 powder was found to be 40.81 nm and anatase phase was observed. Figure 11 shows the XRD pattern of TiO_2 nano-powder.

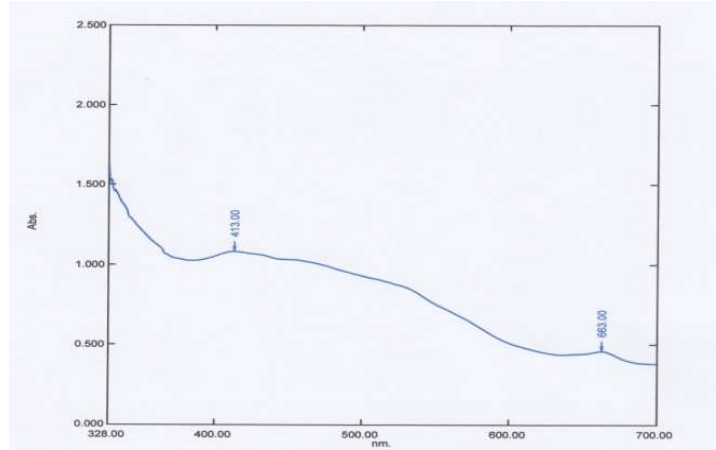


Figure 13. UV-Vis absorption spectra of liquid dye extracting with acetone from teak leaves

The Performance of Meander Type Dye- Sensitized Solar Cell Modules Two Cells Meander Type Dye- Sensitized Solar Cell Module

The open circuit voltage V_{oc} and the short circuit current I_{sc} of two cells meander type DSSC module which connected in series sealing with silicone were measured with the multimeter as shown in Figure 14(a) and (b), giving the results 0.276 V and 0.026 mA respectively.

The extent to which a measured cell deviates from this ideal situation is determined by calculating the cell's 'Fill Factor' (FF) using the following equation:

$$FF = \frac{I_{max} V_{max}}{I_{sc} V_{oc}}$$

where I_{max} and V_{max} are the values of current and voltage measured at the inflection point of the curve shown in Figure 15 and where the 'perfect' cell would have $FF = 1$.

The efficiency of conversion of sunlight to electricity (η) by the tested cell can be determined by the following formula:

$$\eta = \frac{I_{max} V_{max}}{P_{in}}$$

where P_{in} is the power of light incident on the tested cell, which is about 100 mWcm^{-2} for sunlight.

For two cells meander type DSSC module, the fill factor (FF) was obtained 0.659 and the energy conversion efficiency (η) was 0.0048%. The photoelectrochemical parameters of two cells meander type DSSC module are listed in Table 1. From Table 1, the value of Fill Factor (FF) 0.659 was agreed with the typical Fill Factor range from 0.6 to 0.9.

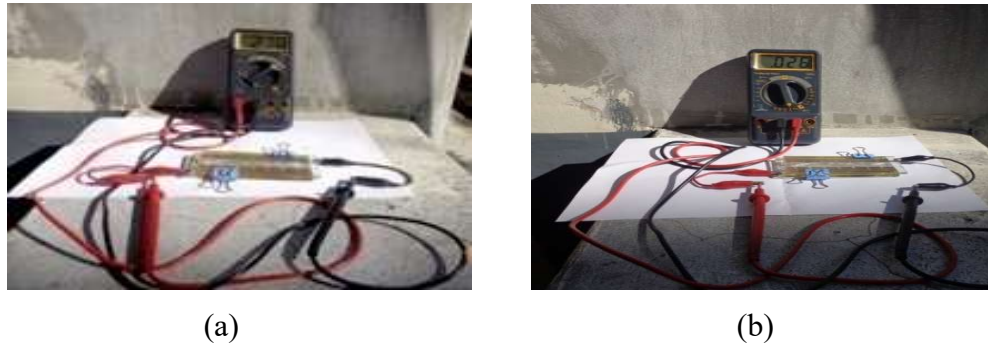


Figure 14 (a) The open circuit voltage V_{oc} (b) The short circuit current I_{sc} for two cells meander type DSSC module

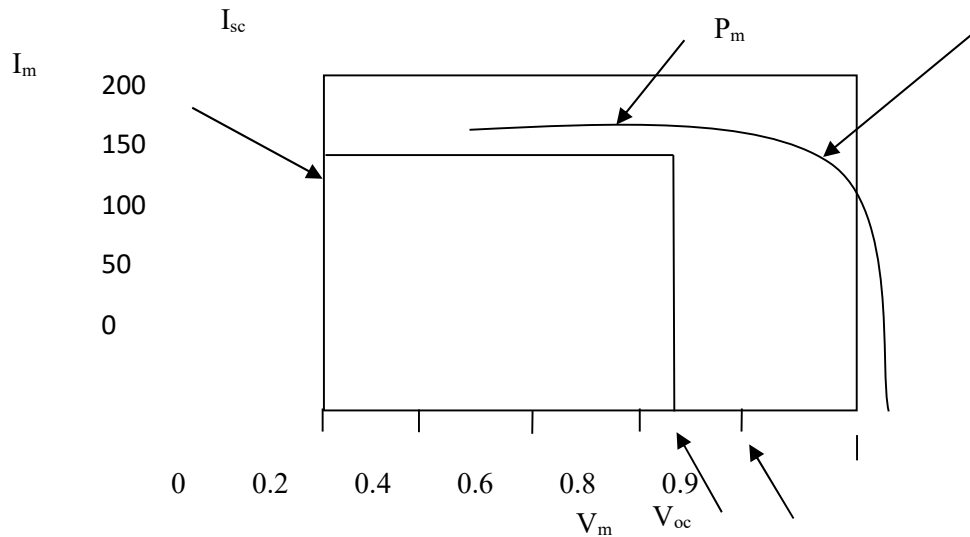


Figure 15. Current-voltage curve of a typical solar cell

Table 1. I-V Characteristics of Two Cells Meander Type DSSC Module

V_{MP} (V)	I_{MP} (mA)	V_{oc} (V)	I_{sc} (mA)	FF	Efficiency(%)
0.2	0.0238	0.28	0.026	0.659	0.0048

Three Cells Meander Type Dye- Sensitized Solar Cell Module

The measuring for the open circuit voltage V_{oc} and the short circuit current I_{sc} of three cells meander type DSSC module were shown in Figure 16(a) and (b). The open circuit voltage V_{oc} was found 0.572 V and the short circuit current I_{sc} was found 0.106 mA. The fill factor (FF) and the energy conversion efficiency (η) were 0.759 and 0.046% respectively. The photoelectrochemical parameters of three cells meander type DSSC module are listed in Table 2.

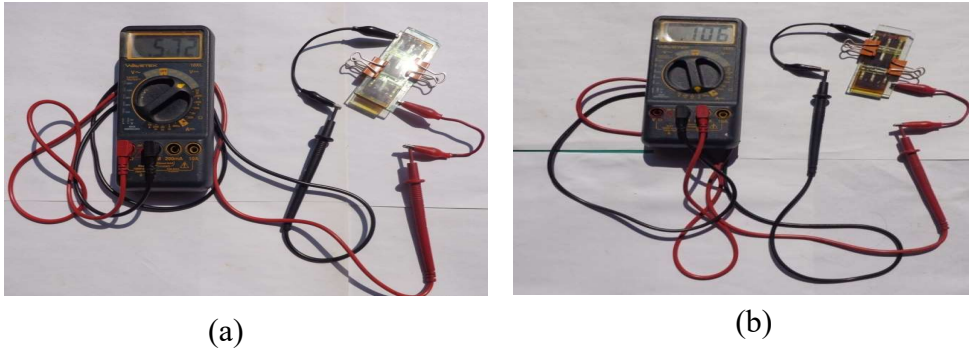


Figure 16 (a) The open circuit voltage V_{oc} (b) The short circuit current I_{sc} for three cells meander type DSSC module

Table 2. I-V Characteristics of Three Cells Meander Type DSSC Module

V_{MP} (V)	I_{MP} (mA)	V_{oc} (V)	I_{sc} (mA)	FF	Efficiency(%)
0.500	0.092	0.572	0.106	0.759	0.046

Four Cells Meander Type Dye- Sensitized Solar Cell Module

The open circuit voltage V_{oc} and the short circuit current I_{sc} of four cells meander type DSSC module were measured with the multimeter as shown in Figure 17(a) and (b), giving the results 0.861 V and 0.119 mA respectively. The fill factor (FF) and the energy conversion efficiency (η) were obtained 0.724 and 0.074%. The photoelectrochemical parameters of four cells meander type DSSC module are listed in Table 3.

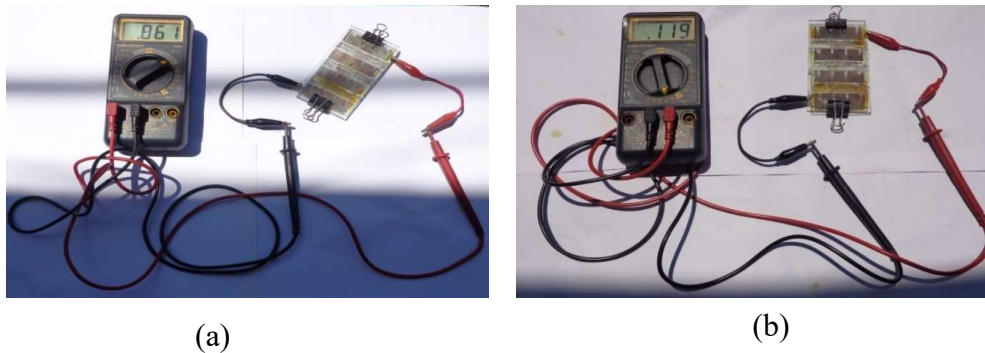


Figure 17 (a) The open circuit voltage V_{oc} **(b)** The short circuit current I_{sc} for four cells meander type DSSC module

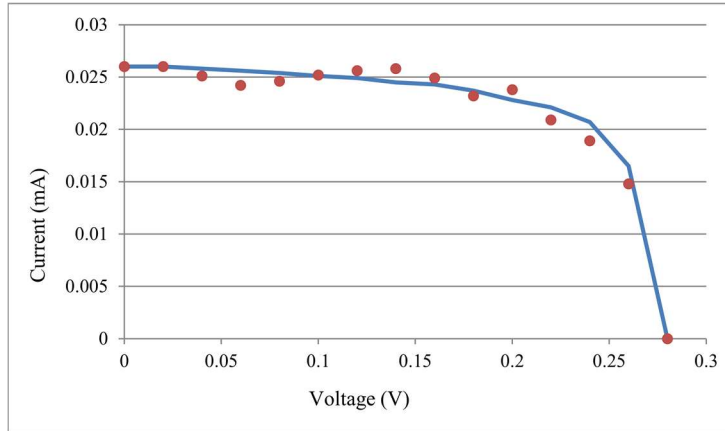
Table 3. I-V Characteristics of Four Cells Meander Type DSSC Module

V_{MP} (V)	I_{MP} (mA)	V_{oc} (V)	I_{sc} (mA)	FF	Efficiency(%)
0.700	0.106	0.861	0.119	0.724	0.074

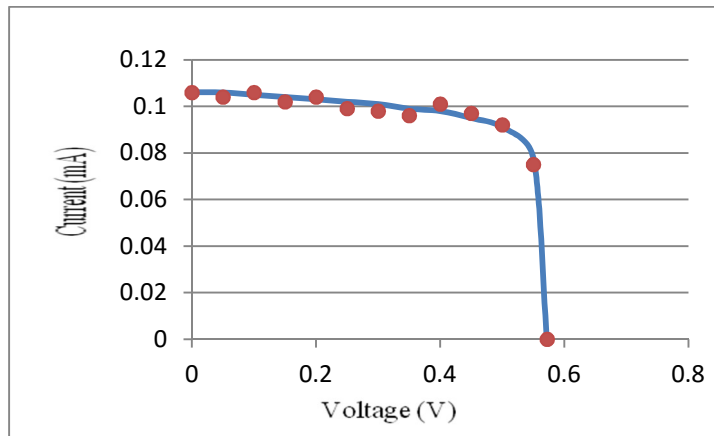
Table 4 shows comparison of I-V characteristics of meander type DSSC module for different number of cells with interconnection. From these comparison results, it was found that the open circuit voltage V_{oc} , the short circuit current I_{sc} and the efficiency of four cells meander type DSSC module were increased than the two cells and three cells meander type DSSC module.

Table 4. Comparison of I-V Characteristics of Meander Type DSSC Module for Different number of Cells

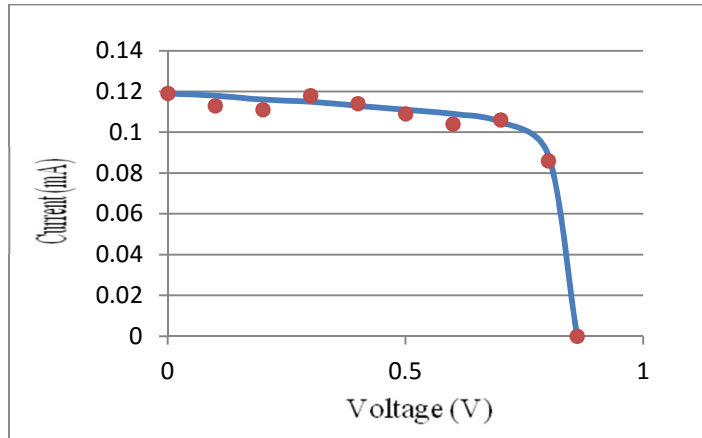
	V_{oc} (V)	I_{sc} (mA)	FF	Efficiency (%)
2 cells module	0.28	0.026	0.659	0.0048
cells module	0.572	0.106	0.759	0.046
4 cells module	0.861	0.119	0.724	0.074



(a)



(b)



(c)

Figure 18. Current-Voltage (I-V) curves for two cells, three cells and four cells meander type DSSC module

Current-Voltage (I-V) curves for two cells, three cells and four cells meander type DSSC modules were shown in Figure 18 (a), (b) and (c) and their I-V characteristics were shown in Table 5, 6 and 7.

Table 5. I-V Characteristic of Two Cells Meander Type DSSC Module

Voltage (V)	Current (mA)	Power (mW)
0.00	0.026	0.0000
0.02	0.026	0.0005
0.04	0.0251	0.0010
0.06	0.0242	0.0014
0.08	0.0246	0.0020
0.10	0.0252	0.0025
0.12	0.0256	0.0031
0.14	0.0258	0.0036
0.16	0.0249	0.0040
0.18	0.0232	0.0042
0.20	0.0238	0.0048
0.22	0.0209	0.0046
0.24	0.0189	0.0045
0.26	0.0148	0.0038
0.28	0.0000	0.0000

Table 6. I-V Characteristic of Three Cells Meander Type DSSC Module

Voltage (V)	Current (mA)	Power (mW)
0.000	0.106	0.000
0.050	0.104	0.005
0.100	0.106	0.011
0.150	0.102	0.015
0.200	0.104	0.021
0.250	0.099	0.025
0.300	0.098	0.030
0.350	0.096	0.034
0.400	0.101	0.040
0.450	0.097	0.044
0.500	0.092	0.046
0.550	0.075	0.041
0.572	0.000	0.000

Table 7. I-V characteristic of Four Cells Meander Type DSSC Module

Voltage (V)	Current (mA)	Power (mW)
0.000	0.119	0.000
0.100	0.113	0.011
0.200	0.111	0.022
0.300	0.118	0.035
0.400	0.114	0.046
0.500	0.109	0.055
0.600	0.104	0.062
0.700	0.106	0.074
0.800	0.086	0.069
0.861	0.000	0.000

Conclusion

Two cells, three cells and four cells meander type dye-sensitized solar cell modules have been fabricated by the use of nano crystalline titanium dioxide TiO_2 photo electrode, carbon counter electrode, dye extracted from teak leaves, redox electrolyte.

The photovoltaic (PV) performance of two cells meander type DSSC module was found that the open circuit voltage (V_{oc}) 0.28 V, the short circuit current (I_{sc}) 0.026 mA, the fill factor (FF) 0.659 and the energy conversion efficiency (η) 0.0048%, respectively.

For three cells meander type DSSC module, it was found that the open circuit voltage (V_{oc}) 0.572 V, the short circuit current (I_{sc}) 0.106 mA, the fill factor (FF) 0.759 and the energy conversion efficiency (η) 0.046%, respectively.

The performance of four cells meander type DSSC module was found that the open circuit voltage (V_{oc}) 0.861V, the short circuit current (I_{sc}) 0.119mA, the fill factor (FF) 0.724 and the energy conversion efficiency (η) 0.074%, respectively.

From the measurement of meander type DSSC modules, the open circuit voltage V_{oc} , the short circuit current I_{sc} and the efficiency of the four cells meander type DSSC module were higher than the two cells and three cells meander type DSSC modules. Therefore, the values of the open circuit voltage V_{oc} and the short circuit current I_{sc} were increased depending on the number of cells. This research shows that natural herbal extract dyes from teak leaves can be used as low cost sensitizer in fabrication of dye-sensitized solar cell module.

Future Prospective

The dye-sensitized solar cell is at present the only serious competitor to solid state junction devices for the conversion of solar energy into electricity. The use of natural herbal extract dyes as sensitizers for these devices could lead to achieve dye solar cells with higher efficiencies holding great potential for further cost reduction and simplification of the manufacturing.

Acknowledgement

We would like to express our particular thanks to Dr Khin Khin Win, Professor and Head of the Department of Physics, University of Yangon for her kind permission to carry out this work.

References

1. Chen L Y (2010) "Fabrication of Dye Sensitized Solar cells on Pre-textured Substrates"
(University of Canterbury: New Zealand)
2. Gong J, Liang J and Sumathy K (2012) "Review on dye-sensitized solar cells (DSSC) : fundamental concepts and novel materials" , Renewable and Sustainable Energy Reviews 16 (8) 5848
3. Jasim K E (2011) "Dye-Sensitized Solar Cells- Working Principles, Challenges and Opportunities" (University of Bahrain: Bahrain)
4. Kay A and Gratzel M (1993) "Photosensitization of TiO₂ Solar Cells with Chlorophyll Derivatives and Related Natural Porphyrins" 97 6272
5. Ojah S, Nair R G and Samdarshi S K (2013) "Recent Development in Dye-Sensitized Solar Cells" 7 (1) 1
6. Sastrawan R (2006) "Photovoltaic modules of dye solar cells" PhD Dissertation (Albert-Ludwigs: Breisgau)

CHARACTERIZATION OF NICKEL SODIUM SULPHATE HEXAHYDRATE (NSSH) CRYSTAL

Myint Myint Soe¹, Wut Hmone Win², Win Kyaw³ & May Thida Win⁴

Abstract

Crystals of Nickel Sodium Sulphate Hexahydrate, $\text{NiNa}_2(\text{SO}_4)_2 \cdot 6\text{H}_2\text{O}$ (abbreviated as NSSH) were grown by slow evaporation method at room temperature. Structural, vibrational and thermal properties of the crystal were investigated by XRD, FTIR and TG-DTA methods. XRD pattern shows that the NSSH crystal belongs to orthorhombic structure with the lattice parameters $a = 15.82 \text{ \AA}$, $b = 9.34 \text{ \AA}$ and $c = 5.21 \text{ \AA}$. FTIR spectrum showed that the vibrational characteristics of SO_4^{2-} and H_2O molecules in the crystalline environments of Ni and Na. TG-DTA thermograms indicated the high temperature phases of dehydration, decomposition and melting of the crystal.

Keywords: Nickel Sodium Sulphate Hexahydrate, XRD, FTIR, TG-DTA

Introduction

Nickel sulphate, NiSO_4 occurs in nature in a hydrated form, such as $\text{NiSO}_4 \cdot \text{H}_2\text{O}$ (monohydrate), $\text{NiSO}_4 \cdot 5\text{H}_2\text{O}$ (pentahydrate), $\text{NiSO}_4 \cdot 6\text{H}_2\text{O}$ (hexahydrate) and $\text{NiSO}_4 \cdot 7\text{H}_2\text{O}$ (heptahydrate), as several minerals, including morenosite and retgersite. The crystalline hexahydrate, for example, form is found in two known phases: α -phase: blue to blue-green tetragonal crystals β -phase: green transparent crystals (stable at 40°C). The α to β phase transition occurs at 53.3°C . Nickel Sulphate Hexahydrate, $\text{NiSO}_4 \cdot 6\text{H}_2\text{O}$ is a water soluble salt which forms hexahydrate (six water) molecules. It is a green colour. [Arivuoli, (2001); Dhandapani, (2006)]

¹ Dr, Demonstrator, Department of Physics, Shwe Bo University

² Dr, Lecturer, Department of Physics, Bago University

³ Dr, Associate Professor, Department of Physics, Sagaing University

⁴ Dr, Professor & HOD, Department of Physics, Shwe Bo University

Sodium sulphate, Na_2SO_4 , is a white crystalline solid or powder. It is obtained by the treatment of sodium chloride with sulphuric acid. The crystallized product is a hydrate, $\text{Na}_2\text{SO}_4 \cdot 10\text{H}_2\text{O}$, commonly known as Glauber's salt. [Dhandapani, (2006); Hulliger, (2001)]

In this paper, crystals of Nickel Sodium Sulphate Hexahydrate, $\text{NiNa}_2(\text{SO}_4)_2 \cdot 6\text{H}_2\text{O}$ (NSSH) were grown by using slow evaporation method and the structural, vibrational and thermal characteristics were studied by X-ray diffraction (XRD), Fourier Transform Infrared (FTIR) and simultaneous Thermogravimetric and Differential Thermal Analysis (TG-DTA) methods.

Crystal Growth and Measurements

Growth of $\text{NiNa}_2(\text{SO}_4)_2 \cdot 6\text{H}_2\text{O}$ (NSSH) Crystal

Most of the single crystals grow from liquid solutions. The liquid is the carrier of the atoms or ions necessary for the growth of the crystal, and may be water or a molten substance at high temperature. If the substance chosen is soluble in water, specimens are usually best prepared by crystallization from the appropriate solvent. Inorganic salts are usually soluble enough in water.

Crystals of Nickel Sodium Sulphate Hexahydrate, $\text{NiNa}_2(\text{SO}_4)_2 \cdot 6\text{H}_2\text{O}$ (NSSH) were grown by slow evaporation method from aqueous equimolar ratio of Nickel Sulphate Hexahydrate, $\text{NiSO}_4 \cdot 6\text{H}_2\text{O}$ and Sodium Sulphate, Na_2SO_4 . Laboratory grade of salt powders and distilled-water were used to grow and synthesis for the crystals. At room temperature $\text{NiNa}_2(\text{SO}_4)_2 \cdot 6\text{H}_2\text{O}$ (NSSH) crystal is green in colour. Photographs of the NSSH crystal growth condition and as-grown NSSH crystal (15.64 mm in length) are shown in Figures 1(a) and (b).

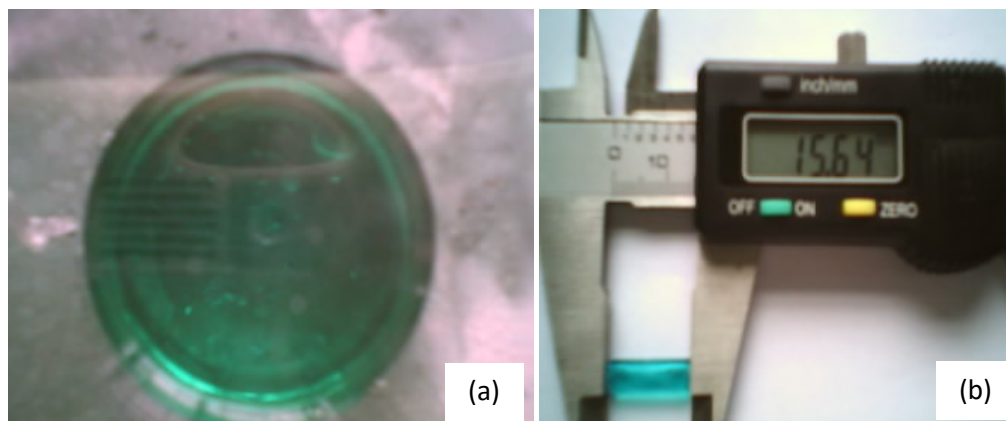


Figure 1. Photographs of the (a) crystal growth condition and (b) as-grown $\text{NiNa}_2(\text{SO}_4)_2 \cdot 6\text{H}_2\text{O}$ (NSSH) crystal

XRD Measurement

Structure analysis and lattice parameters examination of $\text{NiNa}_2(\text{SO}_4)_2 \cdot 6\text{H}_2\text{O}$ (NSSH) crystal were investigated by RIGAKU MULTIFLEX X-ray Diffractometer (Universities' Research Centre (URC), University of Yangon) using Ni-filter with CuK_α radiation, $\lambda = 1.54056 \text{ \AA}$. The main reflections in the range of $10^\circ < 2\theta < 70^\circ$ were observed, and the collected data were used to refine the unit cell parameters from the observed 2θ values with JCPDS (Joint Committee on Powder Diffraction Standards).

FTIR Spectroscopic Measurement

FTIR transmission spectrum of $\text{NiNa}_2(\text{SO}_4)_2 \cdot 6\text{H}_2\text{O}$ (NSSH) crystal was observed by PC controlled SHIMADZU FTIR-8400 spectrophotometer in the wave number range of $400 \text{ cm}^{-1} - 4000 \text{ cm}^{-1}$ using Potassium Bromide, KBr, pellet method.

TG-DTA Measurement

The Differential Thermal Analysis (DTA) measurement with higher accuracy was carried out along with Thermo-Gravimetric Analysis (TGA) using the (SHIMADZU) DTG-60H Thermal Analyzer. This measurement was performed at Universities' Research Centre (URC), University of Yangon. In this work, 8.220 mg powdered sample of the crystal was used to analyze the

high temperature phases. Aluminum (Al) pan was used as the standard sample.

Results and Discussion

Structure Analysis

Powder X-ray diffraction pattern of $\text{NiNa}_2(\text{SO}_4)_2 \cdot 6\text{H}_2\text{O}$ (NSSH) crystal is shown in Figure 2. The observed XRD lines were compared with the JCPDS data library file of Cat. No. 29-1253>Nickelblodite - $\text{Na}_2\text{Ni}(\text{SO}_4)_2 \cdot 6\text{H}_2\text{O}$, to identify the crystalline phase formation and to analyze the crystal structure of the sample.

As shown in XRD pattern, most of the observed diffraction lines were assigned by the use of JCPDS. The diffraction line at 19.58° or (011) plane was found to be the strongest among all lines and it indicated the $(\bar{2}01)$ peak was dominated in the crystal. The diffraction lines of very low in intensities situated in the diffraction angle range of about $46^\circ - 70^\circ$ were not assigned with JCPDS data library.

XRD pattern shows that the NSSH crystal belongs to orthorhombic structure. The lattice parameters were examined by using crystal utility of the equation of $\frac{1}{d^2} = \frac{h^2}{a^2} + \frac{k^2}{b^2} + \frac{l^2}{c^2} = \frac{4 \sin^2 \theta}{\lambda^2}$ where a , b and c are the lattice parameters, λ is the wavelength of incident X-ray and (hkl) is the Miller indices. The lattice parameters of the crystal were obtained as $a = 15.82 \text{ \AA}$, $b = 9.34 \text{ \AA}$ and $c = 5.21 \text{ \AA}$ respectively.

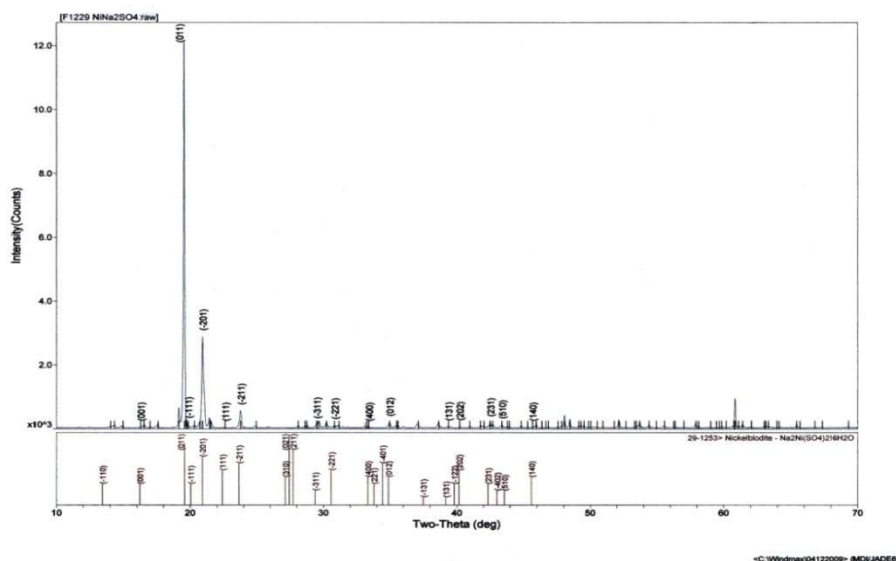


Figure 2. XRD pattern of $\text{NiNa}_2(\text{SO}_4)_2 \cdot 6\text{H}_2\text{O}$ (NSSH) crystal

Vibrational Analysis

FTIR transmission spectrum of $\text{NiNa}_2(\text{SO}_4)_2 \cdot 6\text{H}_2\text{O}$ (NSSH) crystal is shown in Figure 3. The observed wavenumbers and corresponding vibrational characteristics and modes assignments of the molecules in the crystal are tabulated in Table 1. As shown in FTIR spectrum, thirteen absorption lines were observed and identified by using standard data files of free SO_4^{2-} , H_2O , and their molecular networks [Ross, (1972)]. Four fundamental modes of SO_4^{2-} were found in the spectrum and assigned as 982 cm^{-1} (ν_1 -mode; symmetric-stretching), 438 cm^{-1} (ν_2 -mode; bending), $1096 / 1148 \text{ cm}^{-1}$ (ν_3 -mode; dipole) and 623 cm^{-1} (ν_4 -mode; polarization) respectively. The intensity of ν_3 -mode (dipole) was found to dominate on others vibrational modes because in a FTIR transmission spectrum, the intensity of dipole characterization is the strongest one.

The absorption lines at ($1431 \text{ cm}^{-1}/1470 \text{ cm}^{-1}/1688 \text{ cm}^{-1}$) and 3202 cm^{-1} were indicated by the ν_2 -mode (bending) and ν_1 -mode (symmetric-stretching) of H_2O molecule. The ν_3 -mode (asymmetric-stretching) of H_2O was not found. The absorption line at 2206 cm^{-1} is represented by the bending vibration of carbon-dioxide molecule. The lines at 546 cm^{-1} , 745 cm^{-1} and 831

cm^{-1} were represented by the librational wagging, twisting and rocking vibrations of $\text{Ni—H}_2\text{O—Na}$ and $\text{SO}_4\text{—H}_2\text{O—SO}_4$ molecular networks.

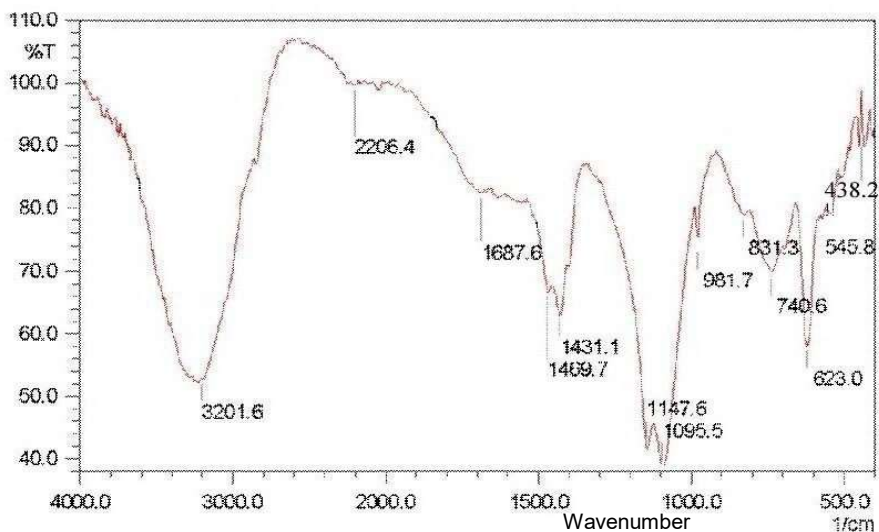


Figure 3. FTIR spectrum of $\text{NiK}_2(\text{SO}_4)_2 \cdot 6\text{H}_2\text{O}$ (NSSH) crystal

Table 1. Wavenumbers and corresponding vibrational mode assignments of molecules in $\text{NiNa}_2(\text{SO}_4)_2 \cdot 6\text{H}_2\text{O}$ (NSSH) crystal

Line No	Wavenumber (cm^{-1})	Vibrational mode & characteristics	Molecule
1	438	ν_2 -mode (bending)	SO_4^{2-}
2	546	ν_ω (librational wagging)	$\text{Ni—H}_2\text{O—Na}$
3	623	ν_4 -mode (polarization)	SO_4^{2-}
4	741	ν_τ (librational twisting)	$\text{SO}_4\text{—H}_2\text{O—SO}_4$
5	831	ν_ρ (librational rocking)	$\text{SO}_4\text{—H}_2\text{O—SO}_4$
6	982	ρ_1 -mode (symmetric-stretching)	SO_4^{2-}
7	1096 / 1148	ν_3 -mode (dipole)	SO_4^{2-}
8	1431 / 1470 / 1688	ν_2 -mode (bending)	H_2O
9	2206	ν_2 -mode (bending)	CO_2
10	3202	ν_1 -mode (symmetric-stretching)	H_2O

Thermal Analysis

TG-DTA thermograms of $\text{NiNa}_2(\text{SO}_4)_2 \cdot 6\text{H}_2\text{O}$ (NSSH) crystal at nitrogen atmosphere in the temperature range of 30°C - 600°C as shown in Figure 4. TGA curve shows the mass variation (weight loss) of the sample recorded during the measurement (heating). In the present work, the first step base line was changed between the temperature 39°C and 328°C in TGA thermogram and it showed the dehydration of six water molecules ($6\text{H}_2\text{O}$) or hydrated compound of $\text{NiNa}_2(\text{SO}_4)_2 \cdot 6\text{H}_2\text{O}$ (NSSH) to anhydrous compound of $\text{NiNa}_2(\text{SO}_4)_2$ (NSS) with the weight loss of the sample was about 36%. In this temperature range, the strong endothermic reaction peak in DTA curve was found at about 130°C and it also indicated by the removal of six water molecules.

Second step base line changes was occurred between 328°C and 600°C in TGA thermogram that showed the decomposition of the anhydrous compound and pre-melting started on the surface of the sample with the mass variation of about 6%. While, one endothermic reaction peak was found at 391°C in DTA thermogram that showed the decomposition and pre-melting started on the surface of the sample.

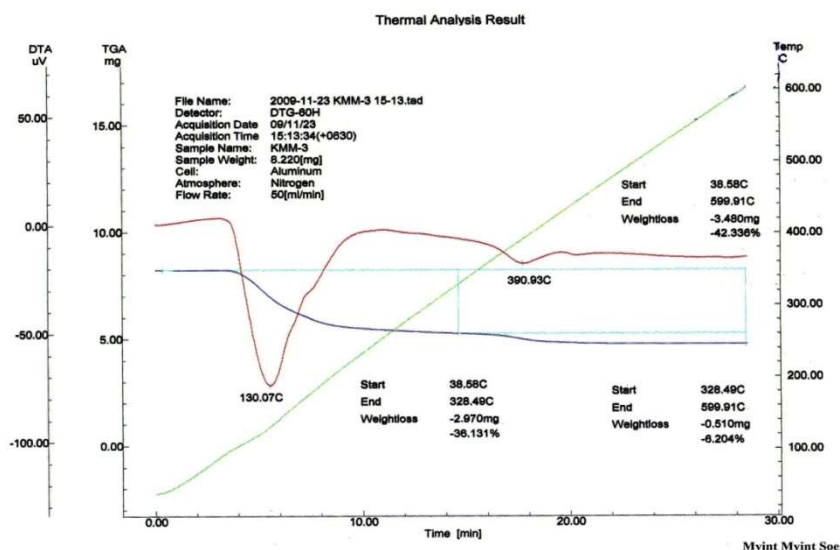


Figure 4. TG-DTA thermograms of $\text{NiK}_2(\text{SO}_4)_2 \cdot 6\text{H}_2\text{O}$ (NSSH) crystal

Conclusion

Crystals of Nickel Sodium Sulphate Hexahydrate, $\text{NiNa}_2(\text{SO}_4)_2 \cdot 6\text{H}_2\text{O}$ (NSSH) were grown by slow evaporation method. Structural, vibrational and thermal characteristics were reported in this paper. XRD pattern shows that the NSSH crystal analogous to orthorhombic structure and the lattice parameters are obtained as $a = 15.82 \text{ \AA}$, $b = 9.34 \text{ \AA}$ and $c = 5.21 \text{ \AA}$ respectively. According to FTIR spectrum, thirteen absorption lines were observed in this spectrum. Four fundamental modes of SO_4^{2-} were found and precisely assigned. The intensity of ν_3 -mode (dipole) of SO_4^{2-} was found to be dominated on others vibrational modes. Only two fundamental modes of H_2O were observed and assigned as ν_1 -mode (symmetric-stretching) and ν_2 -mode (bending). The ν_3 -mode (asymmetric-stretching) of H_2O was not found. Three librational motions of $\text{Ni}-\text{H}_2\text{O}-\text{Na}$ and $\text{SO}_4-\text{H}_2\text{O}-\text{SO}_4$ molecular networks were also observed and assigned. From the TG-DTA thermograms, DTA thermogram confirmed with the result of TG. DTA analysis suggested two phases of the molecular changes of dehydration and pre-melting processes were occurred in the NSSH crystal at about 130°C and 391°C .

Acknowledgement

The authors would like to acknowledge Professor Dr Win Win Thar, Professor and HOD (Rtd.), Department of Physics, Dagon University, for her valuable suggestions and comments.

References

1. Arivuoli, D. (2001). Fundamentals of Nonlinear Optical Materials. *Pramana-Journal of Physics*, 57(5&6), 871-883.
2. Dhandapani, M., Thyagu, L. & Srinivasan, V. (2006). Synthesis and characterization of potassium magnesium sulphate hexahydrate crystals. *Crystal Research Technology*, 41(4), 328-331.
3. Hulliger, J. (2001). Crystal Chemistry and Crystal Growth of Optical Materials. *Chimia*, 55(12), 1025-1028.
5. Theivanayagam, M. & Mahadevan, C. (2001). Lattice variation and thermal parameters of $\text{Ni}_x\text{Mg}_{1-x}\text{SO}_4 \cdot 7\text{H}_2\text{O}$ single crystals. *Bulletins Materials Science*, 24(5), 441-444.

STUDY ON PHYSICAL AND CHEMICAL CHARACTERIZATION OF BAMBOO BASED BIOCHAR

Aye Thandar¹, Marlar Waⁱ², Aye Thandar Oo³ and Yin Maung Maung⁴

Abstract

This paper reports the results of physical and chemical characterization of bamboo based biochar. The bamboo was washed with fresh water to remove impurities such as dust. Bamboo was dried in room temperature. The bamboo ash was obtained in electric furnace at 1000 °C for 3 h and 6 h respectively. Structural properties of bamboo ash were examined by X-ray diffraction (XRD). Scanning electron microscope (SEM) was used to observe the morphology of bamboo ash. Chemical characterization was carried out by X-ray fluorescence (EDXRF) and vibrational characterizations of bamboo ash was studied by FTIR spectroscopy. Each bamboo ash was used to form biochar ceramics by different amount of silica gel, PVA and DIW. These biochar ceramics were annealed at 200 °C for 1 h to be binder burnt out. They were annealed at 600 °C for 1 h to be more rigid. Physical properties such as firing shrinkage, bulk density, biochar yield, pH value of bamboo ash solution, moisture content, specific gravity and hydration capacity of Bio-char ceramics were determined.

Keywords: Bamboo, Bio-char, X-ray diffraction, Morphology, Chemical Properties, Physical Properties

Introduction

Researches all over the world today are focusing on ways of utilizing either industrial or agricultural wastes as a source of raw materials for the industry. These wastes utilization would not only be economical, but may also result to foreign exchange earnings and environmental pollution control [V. S. Aigbodion et al (2010)]. Recent research has focused on wastes generated in different agro-industrial sectors, which are generating serious environmental and social problems, by their accumulation in landfills and uncontrolled burning. One of these sectors is the bamboo with an annual production estimated in 20 million tons all over the world, mainly in Asia and Latin America [Moisés Frías et al (2012)]. Bamboo is natural, cheap,

¹ Dr, Lecturer, Department of Physics, Dawei University

widely available material .It is strong both in tension and compression. [G.N.V Sai Teja et al (2015)]. In recent years there has been increasing interest in utilization of agricultural waste ashes in concrete. If the waste can be reused and recycled, natural resources are used efficiently, wastes are kept out of landfills and the waste disposal costs are saved. Utilization of the waste as cement replacement not only reduces the economic and environmental problems associated with the waste disposal. Therefore , partial replacement of cement with bamboo culm ash (BCAsh) in concrete/mortar has twofold effect; (1) reducing the waste and the problems associated with them and (2) reducing the cement content in concrete and its negative economic and environmental impacts [Sara Soleimanzadeh et al (2015)]. A combination of thermo gravimetric analysis, pH and elemental (ultimate) analysis are necessary [E. Hernandez-Mena*a et al (2014)]. Now a day's concrete are used as the basic materials for the construction works. The concrete is good in compression but weak in the tensile strength. But it has pozzolanic properties, it means that silicate-based material which in itself possesses little or no cementitious value, when silicate-based material (bamboo) is burned under controlled conditions or at in air, it also gives ash having amorphous silica, which has pozzolanic properties. In this study the Bamboo was used as a reinforcing material without any treatment and stirrups. [Jigar K. Sevalia et al (2013)].

Experimental Procedure

The sticks of bamboo were washed with fresh water to remove impurities such as dust and they were dried. The dry pieces of bamboos were ground with a grinding machine. Bamboo powder was obtained by a grinding machine. After firing at 1000 °C for 3 h and 6 h, bamboo ash was obtained. The bamboo ash was shown a gray color. This bamboo ash was characterized by XRD (X-ray Diffraction), Scanning Electron Microscope (SEM) characterization was performed to analyze their microstructural properties. Chemical characterization was carried out X-ray fluorescence (XRF) and vibrational characterizations of bamboo ash were studied by FTIR spectroscopy. The block diagram of bamboo ash preparation was shown in figure 1.

Each ash was mixed thoroughly with silica gel, polyvinyl alcohol (PVA) and distilled water (DIW) to enhance plasticity. The mixed blend was each packed into a mould box and pressed using hydraulic jack. The moulded two samples were dried in an open air at 110 °C for 24 h to expel any moisture and to avoid crack during firing. The dried bricks were then fired in an automatic digital electric furnace (Hood - type furnace) at a preset heating rate at 200 °C for 1 h to be binder burnt-out and then they were annealed at 600 °C for 1 h to be more rigid. Finally, two types of bamboo ash ceramics were annealed at 800 °C for 1 h. After firing, the two samples were allowed to cool in the furnace at a cooling rate of 1°C/min. These samples were removed from the furnace for physical test.

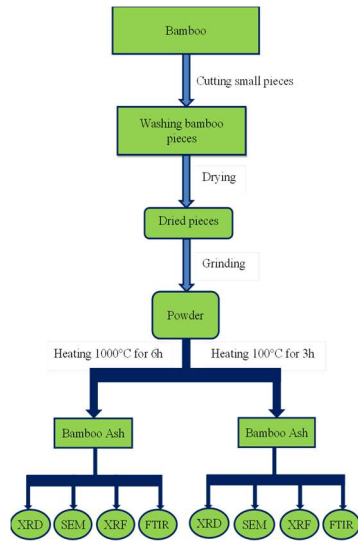


Figure 1. Block diagram of bamboo ash preparation

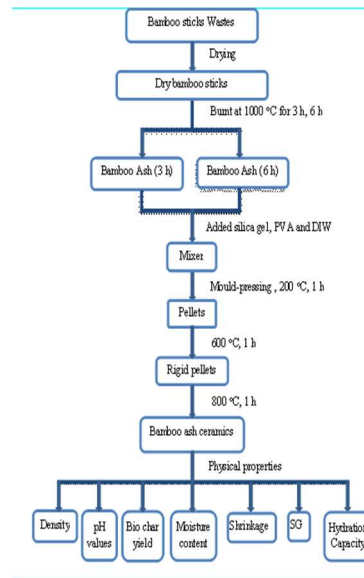


Figure 2. schematic representation of bamboo ash ceramic

Results and Discussion

XRD analysis

Figure 3 (a&b) illustrates the XRD pattern corresponding to the bamboo ash analyzed at 1000 °C for 3 h and 6 h. Structural properties of bamboo ash at 1000 °C for 3 h and 6 h were shown in table (1 & 2).

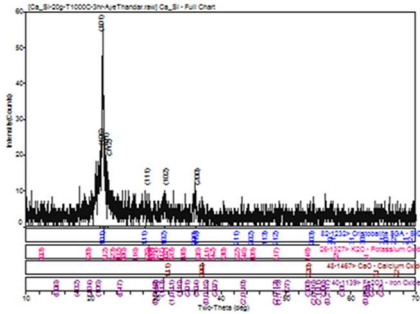


Figure 3(a). The XRD pattern of bamboo ash at 1000 °C for 3 h

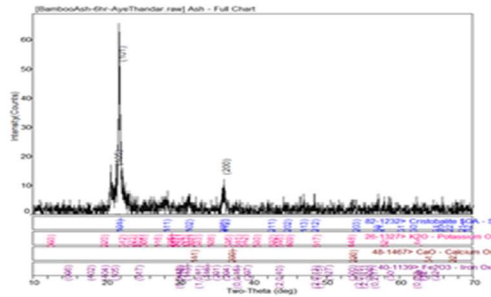


Figure 3(b). The XRD pattern of bamboo ash at 1000 °C for 6 h

Table 1. Diffraction angle of all identified peaks of Cristobalite (SiO_2) at 1000 °C in 3 h

No.	Peaks	Diffraction angles (degree)		FWHM
		observed	standard	
1	(101)	21.993	21.831	0.319
2	(111)	28.452	28.384	0.107
3	(102)	31.326	31.468	0.265
4	(200)	36.102	36.160	0.368

Table 2. Diffraction angle of all identified peaks of Cristobalite (SiO_2) at 1000 °C in 6h

No.	Peaks	Diffraction angles (degree)		FWHM
		observed	standard	
1	(101)	21.331	21.380	0.311
2	(200)	36.102	36.023	0.178

SEM analysis

Fig 4 (a&b) showed irregular forms not well defined and with honey comb like shape, were observed.

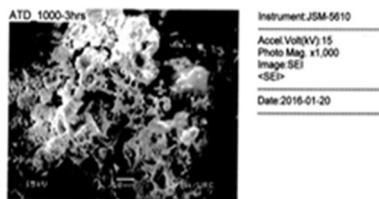


Figure 4(a). SEM image of bamboo ash 1000 °C for 3 h

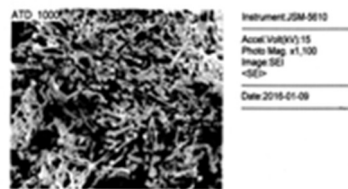


Figure 4(b). EM image of bamboo ash at at 1000 °C for 6 h

EDXRF analysis

Fig 5 (a&b) and table (3&4) shows the chemical compositions by EDXRF corresponding to the bamboo ash samples at 1000 °C for 3 h. The activated bamboo ash analyzed for this study was mainly formed by K₂O and SiO₂ followed by CaO, FeCO₃, MnO, SO₃, ZnO, Rb₂O, CuO, NiO, SrO. These differences would be related to the different species of bamboo, soil, climate and age

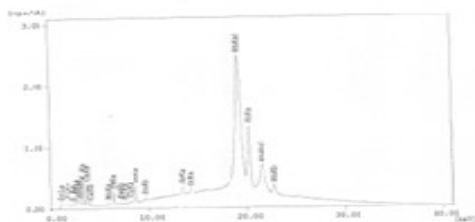


Figure 5(a). EDXRF analysis of bamboo ash at 1000 °C for 3 h

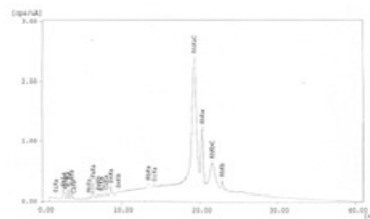


Figure 5(b). EDXRF analysis of bamboo ash at at 1000 °C for 6 h

Table 3. The chemical composition by EDXRF corresponding to the bamboo ash samples at 1000 °C for 3 h.

Analyte	K ₂ O	SiO ₂	CaO	Fe ₂ O ₃	MnO	SO ₃	ZnO	Rb ₂ O	CuO	NiO	SrO
Result	42.96%	42.90%	10.88%	1.775%	0.498%	0.380%	0.364%	0.083%	0.066%	0.047%	0.042%

Table 4. The chemical composition by EDXRF corresponding to the bamboo ash samples at 1000 °C for 6 h.

Analyte	K ₂ O	SiO ₂	CaO	Fe ₂ O ₃	MnO	ZnO	CuO	Rb ₂ O	NiO	SrO
Result	41.36%	36.49%	13.969%	5.909%	0.971%	0.616%	0.235%	0.205%	0.138%	0.098%

FTIR analysis

The FTIR spectrum of the starting bamboo ash figure 6 (a&b) showed two main zones of infrared absorption which are due to the presence of traces of crystalline mineralogical phases such as quartz and cristobalite and mainly of amorphous silica present in the bamboo ash.

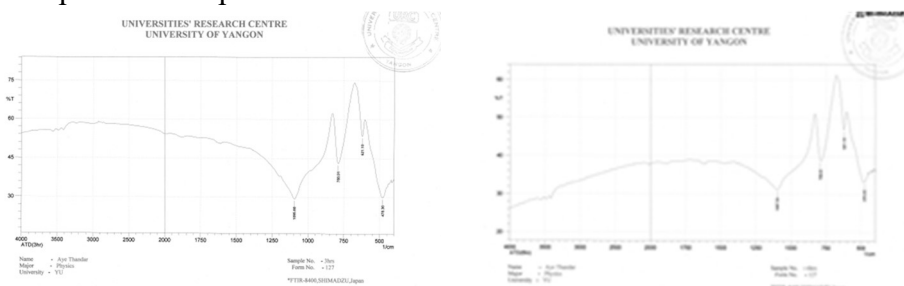


Figure 6(a). FTIR spectrum of bamboo ash at 1000 °C for 3 h of **Figure 6(b).** FTIR spectrum of bamboo ash at at 1000 °C for 6 h

Physical Analysis

In table 5 was showed the weight loss for each reaction bamboo in the different time carried out. Analyzing Table 5, it was verified that there was decline in yields, and hence, an increased loss of weight in function of reaction time.

Table 5. Loss of weight in different time of bamboo ash

Temperature (°C)	Reaction Time (h)	Initial weight (g)	Final weight (g)	Weight (%)
1000	3	49.48	0.88	98.22
1000	6	49.48	0.47	99.04

Firing shrinkage

In Table 6 was showed the weight loss for each reaction of bamboo in different time carried out. Analyzing Table 6, it was verified that there was a decline in yield, and hence, an increased loss of weight in function of reaction time.

Table 6. Firing shrinkage of Bamboo Ash

Temperature (°C)	Reaction Time (h)	(Vo) initial weight (g)	(Vf) final weight (g)	Shrinkage (%)
1000	3 h	0.9466	0.8632	8.81
1000	6 h	1.0490	0.9730	7.81

Density of bamboo ash ceramics

Table 7 represented the calculated parameter of density.

Table 7. Density of bamboo ash ceramics

Temperature (°C)	Reaction Time (h)	Mass (g)	Volume (cm ³)	Density (gcm ⁻³)
1000	3	0.8632	48.5256×10 ⁻²	1.78
1000	6	0.9730	53.0213×10 ⁻²	1.84

pH value of bamboo ash solution

The results of pH values were shown in Table 8.

Table 8. The pH value of bamboo ash ceramics

Temperature (°C)	Reaction Time (h)	pH value of Bamboo ash solution
1000	3	6.74
1000	6	6.76

Measuring moisture contents in bamboo ceramics

The total moisture content results are shown in Table 9.

Table 9. The value of moisture contents in bamboo ash ceramics

Temperature (°C)	Reaction Time (h)	Weight of the sample prior to drying ($W_{initial}$) (g)	Weight of the sample after drying (W_{OD}) (g)	Moisture Contents (%)
1000	3	1.1957	1.0352	13.42
1000	6	1.3836	1.2089	12.53

Determination of Specific Gravity of Bamboo Ash Solution

Specific gravity is defined as the ratio between the weight of a given volume of bamboo ash and weight of an equal volume of water. The values of specific gravity are shown in Table 10.

Table 10. The values of Specific Gravity of Bamboo Ash solution

Temperature (°C)	Reaction Time (h)	Specific Gravity
1000	3	127.71
1000	6	128.56

Hydration Capacity of Bamboo ash

Hydration characteristics of bamboo ash have been determined. The influence of compatibility based on time, temperatures, hydration index and rate were examined for different treatments. The values of hydration capacity are shown in Table 11.

Table 11. The values of Hydration capacity of Bamboo Ash solution

Temperature (°C)	Reaction Time (h)	hydrated mass (g)	dried mass (g)	Hydration Capacity (%)
1000	3h	1.0937	0.9317	17.39
1000	6h	1.2069	1.0463	15.35

Conclusion

A mineralogical study of bamboo ash by XRD revealed the presence of amorphous cristobalite (SiO_2) mainly and, traces of potassium oxide (K_2O), calcium oxide (CaO) and iron oxide (Fe_2O_3) were found at 1000°C for 3 h and 6 h. As a result of SEM investigation was indicated that the structures of bamboo ash heated at 1000°C for 3 h and 6 h were changed. The chemical compositions by EDXRF corresponding to the bamboo ash samples at 1000°C for 3 h and 6 h. The activated bamboo ash analyzed for this study was mainly formed by K_2O and SiO_2 followed by CaO , Fe_2O_3 , MnO , SO_3 , ZnO , Rb_2O , CuO , NiO , SrO . The FTIR spectrum of the starting bamboo ash showed two main zones of infrared absorption: a zone between 1250 and 1000 cm^{-1} and other zone at lower frequencies between 875 and 450 cm^{-1} . The firing shrinkage value of the bamboo ash at 6 h is lower than 3 h. The pH value of bamboo ash for 6 h is little higher than 3 h. Density of the sample at 6 h is 1.835 g/cm^3 which means that bamboo ash is very light material. The value obtained fall within the range of density of carbon and silica which is 1.8 and 2.2 g/cm^3 respectively. The ash can withstand a temperature of up to 1000°C for 6 h. The moisture content is dependent on reaction time. If the specific gravity of cement is greater than 319 g then, the cement is either not minced finely as per the industry standard or it has more moisture content which will affect the mix and bonding and also find lots of chunks while mixing old stock cement replacement. So the interval for heat treatment 6 h of bamboo ash is quite suitable for partially cement replacement application

Acknowledgements

I would like to express my deep appreciation to Dr Ba Han, Rector, and Pro-Rectors, Dr Khin May Aung, Dawei University for their encouragement and kind permission to carry out this work. I also would like to thank Professor Dr Aung Myat Kyaw, Head of Department of Physics, and Professor Dr Malar Myint, Department of Physics, Dawei University, for their kind permission to carry out this work, their encouragement and help during this work.

References

1. Anurag N et al 2013 Journal of Mechanical and Civil Engineering 8 50
2. Dr. Patel Pratima A et al 2013 International Refereed Journal of Engineering and Science 2 55
3. Jagar K S et al 2013 International Journal of Engineering Research and Application 3 1181
4. I.R. Hunter et al An INBAR Working Paper
5. Moises F et al 2012 Cement and Concrete Composites 34 1019
6. P.Asha et al 2014 International Journal of Engineering and Advanced Technology 3 2249
7. Peter M 2002 Bioresource Technology 83 37

STUDY ON ELECTRICAL PROPERTIES OF NICKEL-ZINC-COBALT FERRITES HUMIDITY SENSORS

Thinzar Wut Yee¹, Win Kyaw² & U Win³

Abstract

Nickel-Zinc-Cobalt ferrites with the formula $\text{Ni}_{0.97-x}\text{Zn}_x\text{Co}_{0.03}\text{Fe}_2\text{O}_4$ (where $x = 0.25, 0.50$ and 0.75) and pure NiFe_2O_4 , CoFe_2O_4 and ZnFe_2O_4 have been prepared by conventional ceramic technique. Starting materials of Analytical Reagent (AR) grade Nickel Oxide (NiO), Zinc Oxide (ZnO), Cobalt Oxide (Co_3O_4), and Iron Oxide (Fe_2O_3) with the desired stoichiometric compositions were used to synthesize the samples. The prepared samples were made into circular shape pellets and their electrical properties were investigated in the relative humidity range of 40 RH% – 98RH%. The electrical resistance decreased with increase in relative humidity and the dc voltage and capacitance increased with increase in relative humidity. Sensitivity and sensitivity factor of the samples were examined for the application of humidity sensor.

Keywords: Nickel-Zinc-Cobalt ferrites, $\text{Ni}_{0.97-x}\text{Zn}_x\text{Co}_{0.03}\text{Fe}_2\text{O}_4$, conventional ceramic technique, relative humidity, Sensitivity and sensitivity factor

Introduction

A humidity sensor is a device which can convert the ambient moisture variation into an electrical signal variation. The humidity sensors can be classified as resistive-type and capacitive-type. The sensitive materials will gradually change due to a very slow irreversible reaction with water vapor in atmosphere. The investigation for the problem is focused on improving water-resistive properties of the material. Humidity sensors based on semiconducting oxides have certain advantages compared to other types of humidity sensors (Ahmad, 2012; Harris, 2009; Islam, 1998).

Spinel ferrites, with common formula of MFe_2O_4 (where M is a divalent metal ion), have wide technological applications, e.g., in multilayer chip inductor (MLCI), high-speed digital tape or recording disks, rod antenna, and humidity sensor. Ferrite nanocrystals are also of interest in various

¹. Demonstrator, Department of Physics, Bago University, Myanmar

². Associate Professor, Department of Physics, Sagaing University,

³. Professor & Head, Department of Physics, Bago University, Myanmar

applications, such as inter-body drug delivery, bioseparation, and magnetic refrigeration systems, in particular due to their specific properties, such as superparamagnetism. In addition, among ferrosinels Zinc ferrites are used in gas sensing, catalytic application, and absorbent materials. (Iyer, 2009; Maria1, 2013)

Chemical and structural properties of spinel ferrite nanocrystals are affected by their compositions and synthesis methods, and corresponding electric and magnetic properties depends on cation substitutions. Doping ferrite nanocrystals with various metals, such as Chromium, Copper, Manganese, Cobalt, and Zinc are usually used to improve some of their electric or magnetic properties (Li, 2010). For example, Ni-Zn ferrites have applications as soft magnetic materials with high frequency (due to high electrical resistivity) (Thang, 2005).

This paper is devoted to study the humidity sensitive electrical properties of Ni-Zn-Co ferrites and pure Ni ferrite, Co ferrite and Zn ferrite in the relative humidity range of 40 RH% – 98 RH%.

Materials and Method

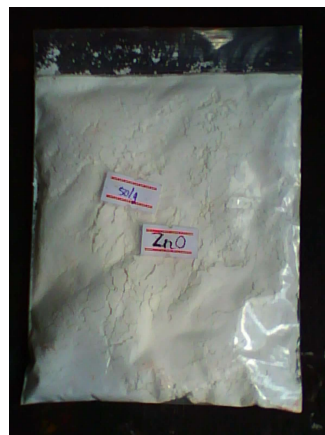
Preparation of Nickel-Zinc-Cobalt Ferrites

Experimental procedures for the preparation of Nickel-Zinc-Cobalt ferrites, $\text{Ni}_{0.97-x}\text{Zn}_x\text{Co}_{0.03}\text{Fe}_2\text{O}_4$ (where $x = 0.25, 0.50$ and 0.75) using conventional ceramic technique were as follows:

First, the raw materials of Analar (AR) grade Nickel Oxide (NiO), Zinc Oxide (ZnO), Cobalt Oxide (Co_3O_4), and Iron Oxide (Fe_2O_3) were weighed according to their desired stoichiometric compositions and mixed together. The mixture of each sample was ground by ball-milling for 3 h using laboratory-made ball-milling machine to a very fine powder and to prepare precursor solution. Then the precursor solid solutions were calcined at 1080°C for 4 h in vacuum chamber. The calcined solid solution was crushed again at room temperature. The crushed powders were pressed into pellets by using laboratory made pellet-maker. The pellets were finally sintered at 1200°C for 4 h to form ferrites. In the sample preparation, DELTA A Series Temperature

Controller DTA4896 and K-type thermocouple (1300°C) were used as the temperature controller and temperature sensor.

Furthermore, pure Nickel ferrite, Cobalt ferrite and Zinc ferrite were prepared by conventional ceramic technique using the above procedure. Photographs of the starting materials, DELTA A Series Temperature Controller DTA4896, laboratory-made ball-milling machine, pellet-maker, and experimental setup of sample preparation system are shown in Fig 1(a - i) respectively.





(e) ball-milling machine



(f) plastic coated stainless-steel ball



(g) temperature controller



(h) temperature controller



(i) experimental setup of sample preparation system

Figure 1. Photographs of the (a – d) starting materials, (e) laboratory-made ball-milling machine, (f) plastic coated stainless-steel ball, (g -h) DELTA A SERIES temperature controller at 1080°C and 1200°C and (i) complete experimental setup of sample preparation system

Humidity Sensitive Electrical Property Measurement

Humidity sensitive electrical properties of the Nickel-Zinc-Cobalt ferrites, $\text{Ni}_{0.97-x}\text{Zn}_x\text{Co}_{0.03}\text{Fe}_2\text{O}_4$ (where $x = 0.25, 0.50$ and 0.75) were investigated in the relative humidity range of 40 RH% - 98 RH%. Firstly, the as-prepared ferrites were made circular shape pellets by using SPECAC hydraulic press with the pressure 5 ton (~ 70 MPa) as shown in Fig 2. Then the pellet was polished by using filtered-paper to get the smoothing surface. Dimensions of the samples were measured by using digital Vernier-Caliper (Taiwan). Thicknesses of the samples are listed in Table 1. Area of the each of the sample was used as $1.14 \times 10^{-4} \text{ m}^2$. The sample was then fixed on glass plate and silver contacts were made over the sample to ensure good electrical contact.

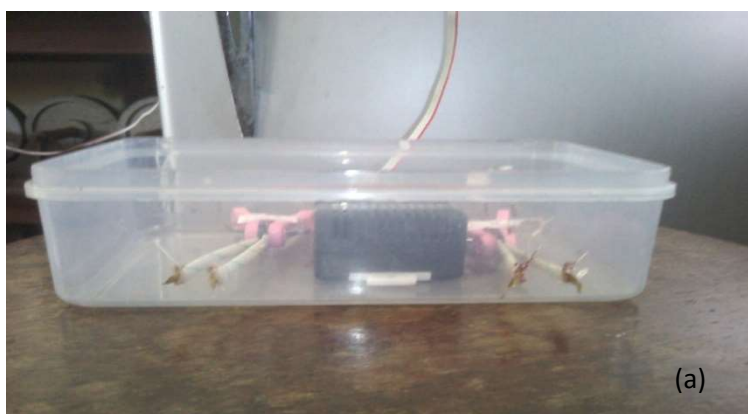
In this measurement, XSW TDK 0302 Humidity Meter was used as the humidity sensing element. Humidity sensitive electrical resistance and voltage of the sample were observed by two probe method by using FLUKE 189 digital multimeter. The refrigerator (TOSHIBA) was used as the humidity generator. Photographs of the experimental setup of humidity sensitive electrical property measurement are shown in Fig 3(a - b). Also, the as-prepared samples pure Nickel ferrite, Cobalt ferrite and Zinc ferrite were made into pellets and their humidity sensitive electrical properties were observed in the above same condition. Thicknesses of the pure Nickel ferrite, Cobalt ferrite and Zinc ferrite pellets are also listed in Table 1.



Figure 2. Photograph of SPECAC hydraulic pellet maker

Table 1. Thickness of the $\text{Ni}_{0.97-x}\text{Zn}_x\text{Co}_{0.03}\text{Fe}_2\text{O}_4$ (where $x = 0.25, 0.50$ and 0.75) and pure Nickel ferrite, Cobalt ferrite and Zinc ferrite pellets

Sr No	Contents x of Zn in $\text{Ni}_{0.97-x}\text{Zn}_x\text{Co}_{0.03}\text{Fe}_2\text{O}_4$ and Pure Ni, Co, Zn Ferrite	Thickness (mm)
1	0.25	2.54
2	0.50	2.51
3	0.75	2.55
4	NiFe_2O_4	2.62
5	CoFe_2O_4	2.57
6	ZnFe_2O_4	2.52



(a)



(b)



(c)

Figure 3. Photographs of the (a) sample and sensor in the same condition, (b) and (c) experimental setup of humidity sensitive electrical property measurement

Results and Discussion

Humidity sensitive electrical resistances R_H versus relative humidity RH%, dc voltage V_H and capacitance C_H versus relative humidity RH% of the investigated Nickel-Zinc-Cobalt ferrites, $Ni_{0.97-x}Zn_xCo_{0.03}Fe_2O_4$ (where $x = 0.25, 0.50$ and 0.75) and pure Nickel ferrite, Cobalt ferrite and Zinc ferrite are shown in Fig 4(a – f) and Fig 5(a – f) respectively.

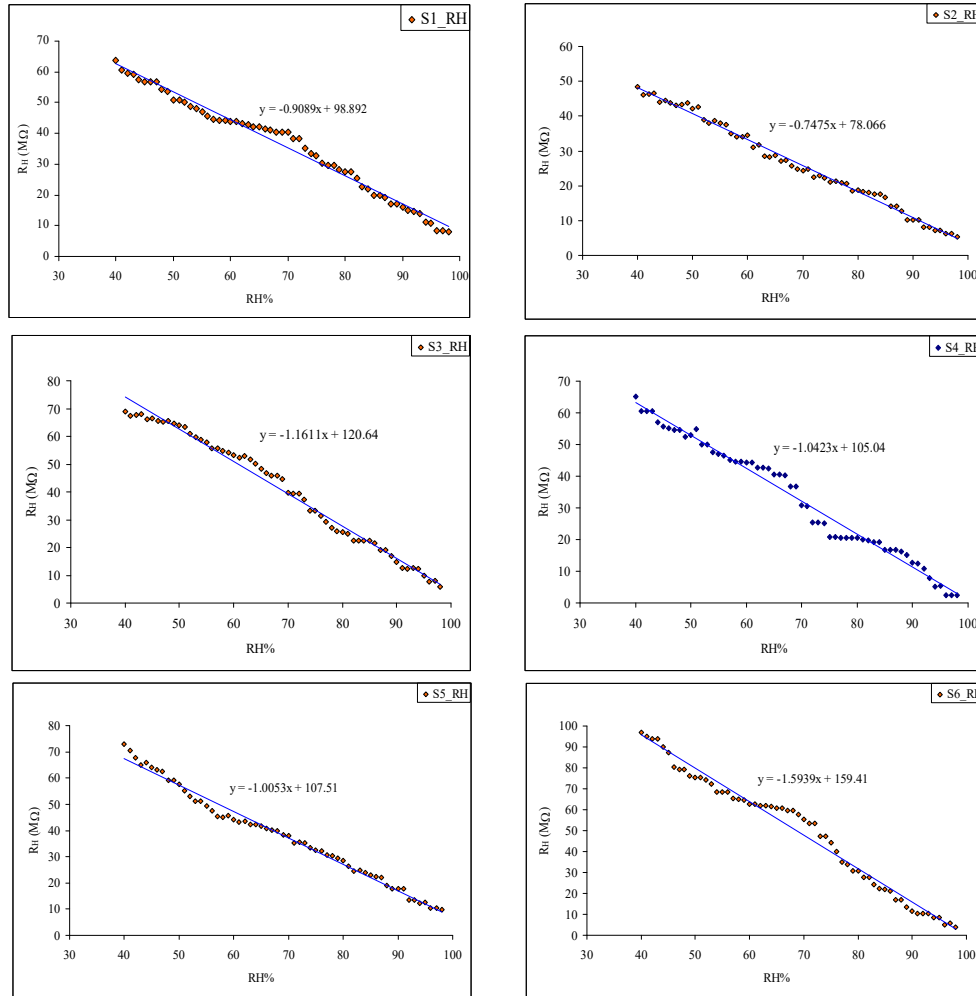


Figure 4. Plots of the variation of electrical resistance R_H with relative humidity RH% of $Ni_{0.97-x}Zn_xCo_{0.03}Fe_2O_4$ where (a) $x = 0.25$, (b) $x = 0.50$, (c) $x = 0.75$ and (d) pure $NiFe_2O_4$, (e) $CoFe_2O_4$ and (f) $ZnFe_2O_4$

(b)

As shown in R_H versus $RH\%$ graphs, the electrical resistance of the $Ni_{0.97-x}Zn_xCo_{0.03}Fe_2O_4$ (where $x = 0.25, 0.50$ and 0.75) and pure Nickel ferrite, Cobalt ferrite and Zinc ferrite decreased with increase in relative humidity and the obtained R_H versus $RH\%$ curves were fitted with linear type to examine the sensitivity of the sample. The slope of the R_H versus $RH\%$ graph can be taken as the sensitivity of the sample. In this work, the obtained sensitivities of the samples are tabulated in Table 2. The sensitivity of the pure $ZnFe_2O_4$ and the largest concentration of Zn in $Ni_{0.97-x}Zn_xCo_{0.03}Fe_2O_4$ or $Ni_{0.97-x}Zn_xCo_{0.03}Fe_2O_4$ (where $x = 0.75$) sample are the most sensitive materials among the investigated samples. The resistance changes in porous spinel type ferrites with increasing of humidity level occur because of adsorption and capillary condensation of water. The sensitivity factor “ S_f ” of the sample can be evaluated by using the following relation,

$$S_f = R_{40\%}/R_{98\%}$$

where $R_{40\%}$ and $R_{98\%}$ are the electrical resistances of the $Ni_{0.97-x}Zn_xCo_{0.03}Fe_2O_4$ (where $x = 0.25, 0.50$ and 0.75) and pure Nickel ferrite, Cobalt ferrite and Zinc ferrite at the relative humidity 40 $RH\%$ (start point) and 98 $RH\%$ (end point) respectively. According to above relation, the sensitivity factors were calculated and obtained as follows.

For $Ni_{0.97-x}Zn_xCo_{0.03}Fe_2O_4$ ($x = 0.25$),

$$S_{f_S1} = R_{40\%}/R_{98\%} = 8.0075$$

For $Ni_{0.97-x}Zn_xCo_{0.03}Fe_2O_4$ ($x = 0.50$),

$$S_{f_S2} = R_{40\%}/R_{98\%} = 9.2205$$

For $Ni_{0.97-x}Zn_xCo_{0.03}Fe_2O_4$ ($x = 0.75$),

$$S_{f_S3} = R_{40\%}/R_{98\%} = 11.9960$$

For pure $NiFe_2O_4$,

$$S_{f_S4} = R_{40\%}/R_{98\%} = 24.3939$$

For pure $CoFe_2O_4$,

$$S_{f_S5} = R_{40\%}/R_{98\%} = 7.5472$$

For pure $ZnFe_2O_4$,

$$S_{f_S6} = R_{40\%}/R_{98\%} = 28.0125$$

The obtained sensitivity factors are also presented in Table 2. As presented in Table 2, the sensitivity factor of the pure ZnFe₂O₄ was the largest one. It can be suggested that microstructure (porosity, grain size, structural defects) has a great role on the electrical resistivity. Smaller grains imply an increase of the grain boundary surface which normally account for high resistivity of a polycrystalline material. The larger the specific surface area and porosity of the specimens the more water vapors can be physically adsorbed, resulting in a larger decrease of the resistivity. One can see that the sensitivity of the pure ZnFe₂O₄ and the largest concentration of Zn in Ni_{0.97-x}Zn_xCo_{0.03}Fe₂O₄ or Ni_{0.97-x}Zn_xCo_{0.03}Fe₂O₄ (where x = 0.75) sample are the most sensitive materials to humidity change.

Table 2. Sensitivity and sensitivity factor of the Ni_{0.97-x}Zn_xCo_{0.03}Fe₂O₄ (where x = 0.25, 0.50 and 0.75) and pure Nickel ferrite, Cobalt ferrite and Zinc ferrite

Sr No	Contents x of Zn in Ni _{0.97-x} Zn _x Co _{0.03} Fe ₂ O ₄ and Pure Ni, Co, Zn Ferrite	Sensitivity (MΩ/RH%)	Sensitivity factor
1	0.25	0.9089	8.0075
2	0.50	0.7475	9.2205
3	0.75	1.1611	11.9960
4	NiFe ₂ O ₄	1.0423	28.0125
5	CoFe ₂ O ₄	1.0053	7.5472
6	ZnFe ₂ O ₄	1.5939	24.3939

As shown in Fig 5(a – f), dc voltage and capacitance increase with increasing humidity due to the water adsorption on sample surface is likely the dominant factor for electrical conduction. Thus, the surface area would provide more sites for water adsorption and produce more charge carriers for electrical conduction.

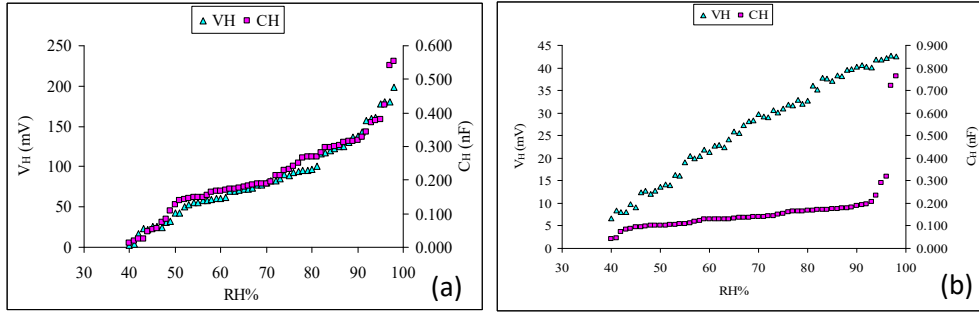


Figure 5. Plots of the variation of dc voltage V_H and capacitance C_H with relative humidity RH% of $Ni_{0.97-x}Zn_xCo_{0.03}Fe_2O_4$ where (a) $x = 0.25$ and (b) $x = 0.50$

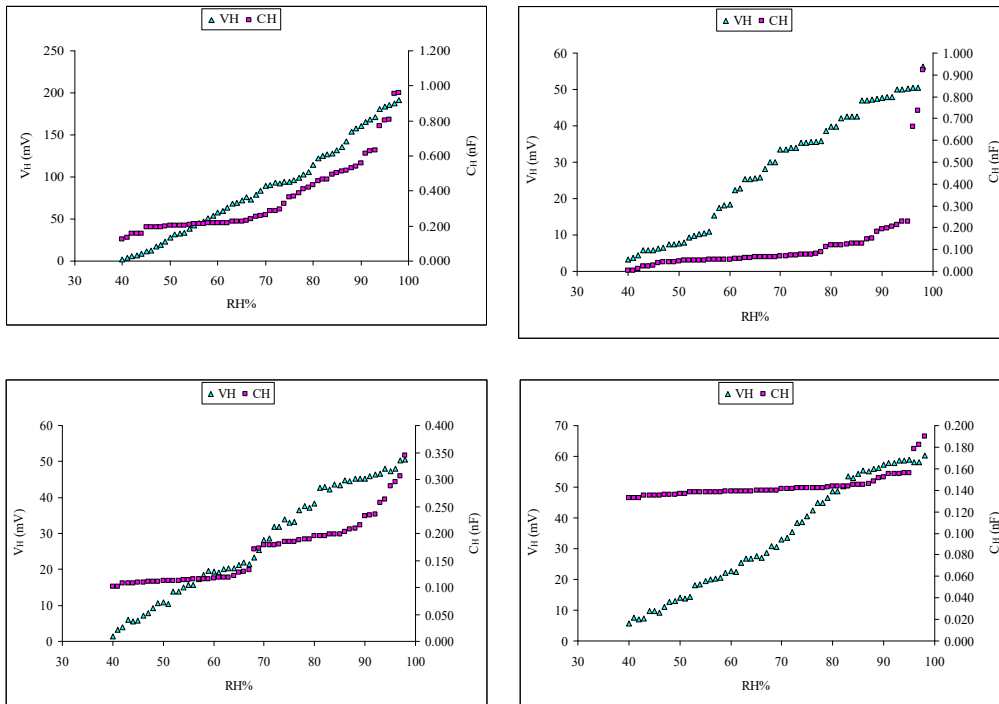


Figure 5. Plots of the variation of dc voltage V_H and capacitance C_H with relative humidity RH% of (c) $Ni_{0.97-x}Zn_xCo_{0.03}Fe_2O_4$ where $x = 0.75$ and (d) pure $NiFe_2O_4$, (e) $CoFe_2O_4$ and (f) $ZnFe_2$

(d)

Conclusion

Nickel-Zinc-Cobalt ferrites, $\text{Ni}_{0.97-x}\text{Zn}_x\text{Co}_{0.03}\text{Fe}_2\text{O}_4$ (where $x = 0.25, 0.50$ and 0.75) and pure NiFe_2O_4 , CoFe_2O_4 and ZnFe_2O_4 were prepared by conventional ceramic technique. Variation of the electrical resistances, dc voltages and capacitances of the as-prepared disc shapes pellets were investigated in the relative humidity range of 40 RH% – 98RH%. From this study, according to experimental results, the pure ZnFe_2O_4 and the largest concentration of Zn in $\text{Ni}_{0.97-x}\text{Zn}_x\text{Co}_{0.03}\text{Fe}_2\text{O}_4$ or $\text{Ni}_{0.97-x}\text{Zn}_x\text{Co}_{0.03}\text{Fe}_2\text{O}_4$ (where $x = 0.75$) sample are the most humidity sensitive materials among the investigated samples. It can be suggested that these samples can be suitable for the application of humidity sensors.

Acknowledgements

The authors feel indebted to Professor Dr. Zeya Oo, Visiting Professor, Department of Engineering Physics, Yangon Technology University, Yangon, Myanmar, for his valuable suggestions and comments for this work.

References

1. Ahmad, I. and Farid, M. T. (2012) "Characterization of Cobalt Based Spinel Ferrites with Small Substitution of Gadolinium", World Applied Sciences Journal, 19, pp. 464-469.
2. Harris, V.G., Geiler, A., Chen, Y., Yoon, S. D., Wu, M., Yang, A., Chen, Z., He, P., Parimi, P. V., Zuo, X., Patton, C. E., Abe, M., Acher, O. and Vittoria, C. (2009) "Recent advances in processing and applications of microwave ferrites", Journal of Magnetism and Magnetic Materials, 321, pp. 2035-2047.
3. Islam, M. U., Rana, M. U. and Abbas, (1998) "Study of Magnetic Interactions in Co-Zn-Fe-O System," Materials Chemistry and Physics, 57, pp. 190-193.
4. Iyer, R., Desai, R. and Upadhyay, R. V. (2009) "Low temperature synthesis of nanosized $\text{Mn}_{1-x}\text{Zn}_x\text{Fe}_2\text{O}_4$ ferrites and their characterizations", Bulletin Materials Science, 32, pp. 141-147.
5. Li, Z. W., Yang, Z. H. and Kong, L. B. (2010) "Ultrabroad bandwidth and matching characteristics for spinel ferrite composites with flaky fillers" Journal of Applied Physics, 108, pp. 06927.

6. Maria1, K. H., Choudhury, S. and Hakim, M. A. (2013) “Structural phase transformation and hysteresis behavior of Cu-Zn ferrites”, *International Nano Letters*, 3, pp. 1-10.
7. Thang, P. D., Rijnders, G. and Blank, D. H. A. (2005) “Spinel cobalt ferrite by complexometric synthesis”, *Journal of Magnetism and Magnetic Materials*, 295, pp. 251-256.

GAS SENSITIVITY OF NANOCRYSTALLINE COBALT DOPED NICKEL FERRITES

Hnin Hlwar Nu¹, Moe Min Min Aye², Win Kyaw³ & Hla Hla Than⁴

Abstract

Gas sensing materials of Cobalt doped Nickel ferrites, $\text{Ni}_{1-x}\text{Co}_x\text{Fe}_2\text{O}_4$ ($x = 0.0, 0.1, 0.2$ and 0.3) were prepared by self-combustion method. A quick combustion was taken as the calcination of metal hydroxides and the reaction between metal oxides. The obtained powders were pressed into disk shapes and subjected to thermal treatment at 1000°C for 30 min. The X-ray diffraction (XRD) analysis was carried out to investigate the crystalline phase formation. Microstructural properties of the samples were investigated by Scanning Electron Microscopy (SEM). The grain size of the samples was found to be varied with the dopant concentration of Co. It was investigated the sensitivities of the samples from the gas-sensitive electrical resistance measurements in acetone, ethanol, octane and liquid petroleum gas (LPG) atmospheres. It was observed that the gas sensitivity depends on the concentration of Co dopant and the test gases to be detected.

Keywords: Cobalt doped Nickel ferrites, self-combustion method, XRD, SEM, gas sensitivity

Introduction

Nanometer-sized materials, which have high surface activity due to their small particle size and enormous surface area, have been widely studied in the field of gas sensors in recent years [Harris, (2009); Kumar, (2009)]. In technologies where ferrites are to be used for magnetic or electrical applications, high-density materials are generally required and the ferrites are often prepared by high temperature solid-state reactions between finely ground powders. Although most applications of ferrites as ceramic materials require high densities to achieve the desired properties, there are many

¹ Dr., Demonstrator, Department of Physics, Meiktila University

² Dr., Lecturer, Department of Physics, University of Yangon

³ Dr., Associate Professor, Department of Physics, Sagaing University

⁴ Dr., Professor & HOD, Department of Physics, Meiktila University

applications for which lower densities and high surface area are preferred [Iyer, (2009); Pathan, (2010)].

Many ferrites are spinels with the formula AB_2O_4 , where A and B represent various metal cations, usually including iron Fe. The magnetic material known as "NiFe" has the formula $NiFe_2O_4$, with Fe^{3+} occupying the octahedral sites and Ni^{2+} occupy the tetrahedral sites, it is an example of a spinel ferrite. Spinel ferrites usually adopt a crystal motif consisting of cubic close-packed (fcc) oxides (O^{2-}) with A cations occupying one eighth of the tetrahedral holes and B cations occupying half of the octahedral holes. If one eighth of the tetrahedral holes are occupied by B cation, then one fourth of the octahedral sites are occupied by A cation and the other one fourth by B cation and it is called the inverse spinel structure [Marial, (2013); Sharma, (2005)]. In the present study, Nickel ferrite doped with small amounts of Cobalt was investigated as gas sensor. An attempt to improve the sensitivity and nanoparticles of Nickel ferrite have been partly replaced with Co on Ni and Fe, respectively.

Materials and Method

Preparation of Cobalt Doped Nickel Ferrites

In this work, nanocrystalline Cobalt Doped Nickel ferrites, $Ni_{1-x}Co_xFe_2O_4$ (where $x = 0.0, 0.1, 0.2$ and 0.3) were prepared by self-combustion method. Analytical Reagent (AR) grade Nickel (II) Nitrate Hexahydrate [$Ni(NO_3)_2 \cdot 6H_2O$], Cobalt (II) Nitrate Hexahydrate [$Co(NO_3)_2 \cdot 6H_2O$] and Iron (III) Nitrate Nonahydrate [$Fe(NO_3)_3 \cdot 9H_2O$] were used as the raw materials. Ammonium Hydroxide [NH_4OH] was used as the fuel. The starting materials were weighed with desired stoichiometric compositions and mixed each others. The obtained precursor solution was heated on a hot plate at room temperature $29^\circ C$ to $100^\circ C$ for 1 h. Then, a quick combustion was taken as the calcination of metal hydroxides and the reaction between metal oxides. The obtained combustion powder was pressed into disk shape pellet and subjected to thermal treatment at $1000^\circ C$ for 30 min in vacuum chamber (160 mmHg) using DELTA A Series Temperature Controller DTA4896. The K-type thermocouple was used as the temperature sensor for read-out the actual or real temperature in the chamber. Flow-diagram of the

preparation procedure of the Cobalt Doped Nickel ferrites using auto-combustion method is shown in Figure 1. Photographs of the sample preparation procedure are shown in Figures 2(a – p).

XRD Measurement

X-ray powder diffraction patterns of the $\text{Ni}_{1-x}\text{Co}_x\text{Fe}_2\text{O}_4$ (where $x = 0.0, 0.1, 0.2$ and 0.3) samples were observed on a RIGAKU MULTIFLEX X-ray Powder Diffractometer using CuK_α radiation ($\lambda = 1.54056 \text{ \AA}$) in 2θ range of $10^\circ - 70^\circ$. The crystallite size was calculated by Scherrer's formula, using the full width at half maximum intensity for (311) plane of the pattern.

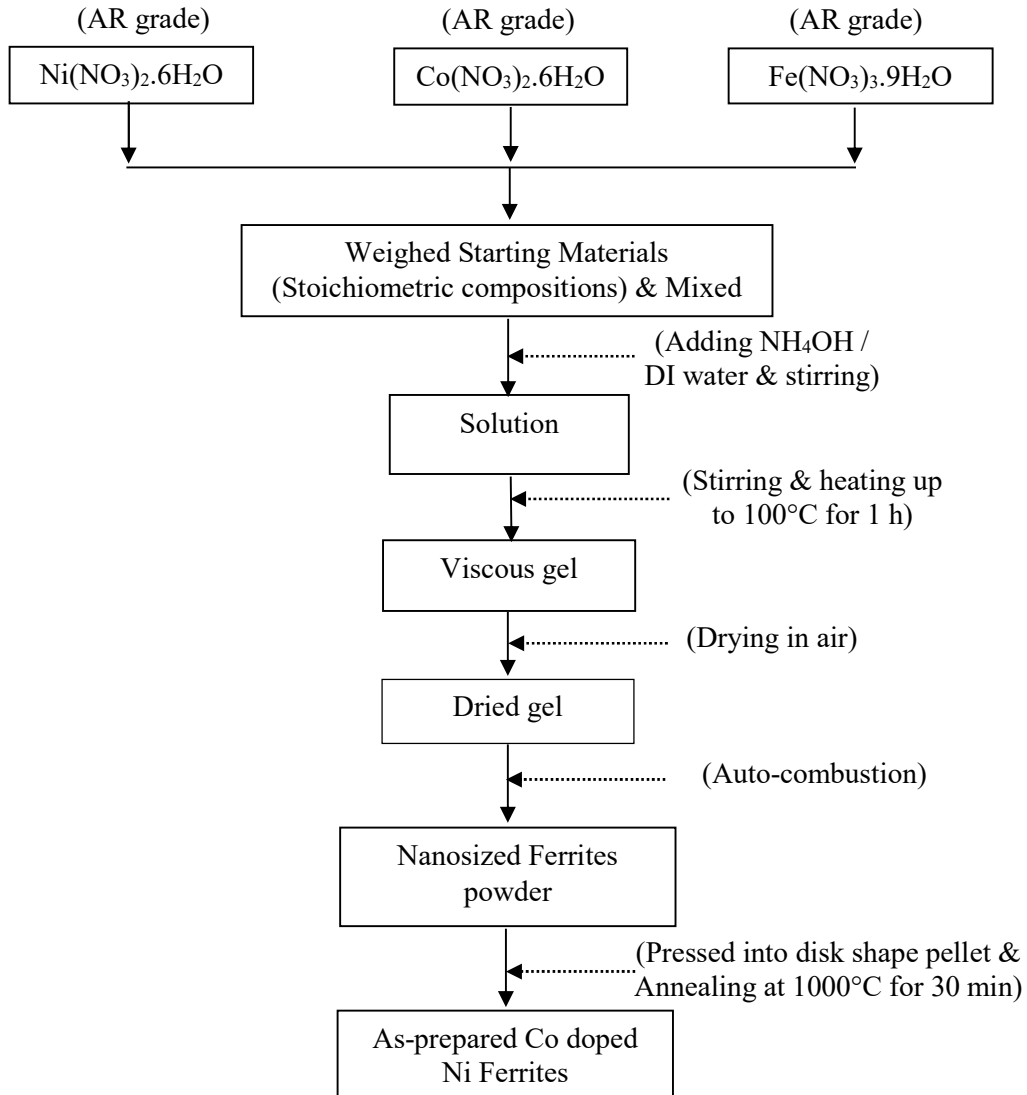


Figure 1. Flow-diagram of the preparation of Cobalt Doped Nickel ferrites



Figure 2. Photographs of the starting materials of (AR) grade (a) $\text{Ni}(\text{NO}_3)_2 \cdot 6\text{H}_2\text{O}$ and (b) $\text{Co}(\text{NO}_3)_2 \cdot 6\text{H}_2\text{O}$

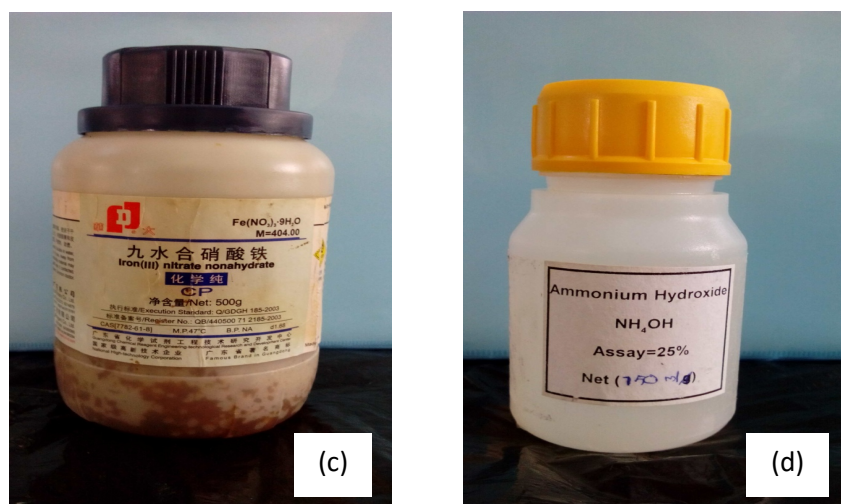


Figure 2. Photographs of the (c) starting materials of (AR) grade $\text{Fe}(\text{NO}_3)_3 \cdot 9\text{H}_2\text{O}$ and (d) NH_4OH



Figure 2. Photographs of the (e) weighed starting materials for $x = 0.0$ sample and (f) mixed solid solutions of starting materials for $x = 0.0$ sample

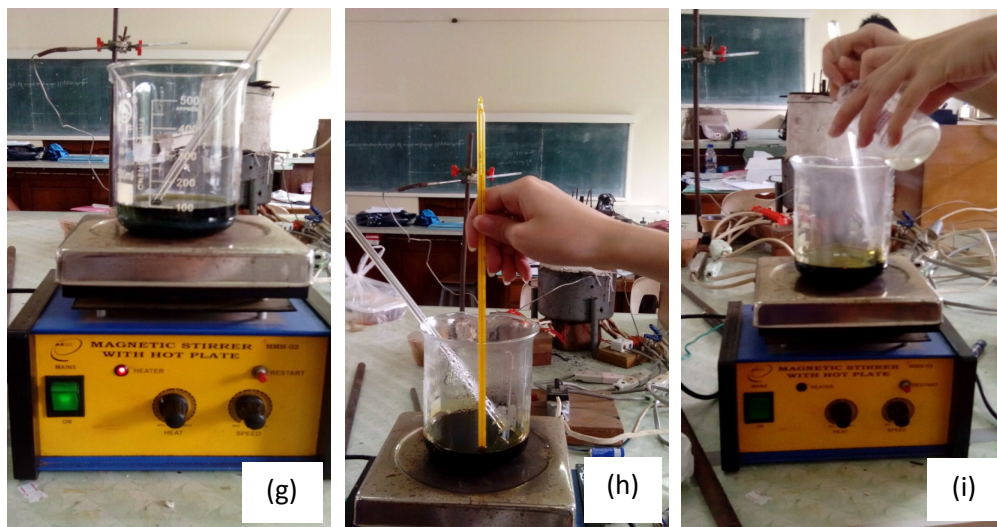


Figure 2. Photographs of the (g) heated and stirred of mixed solution of $x = 0.0$ sample using magnetic stirrer, (h) checked for solution temperature 100°C and (i) NH_4OH solution poured into heated solution

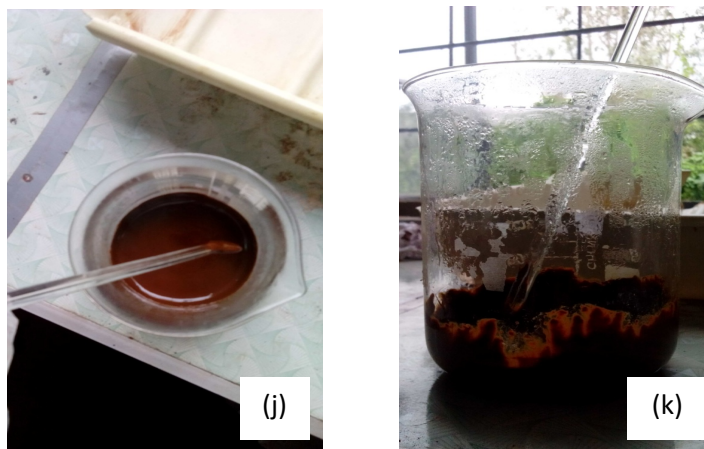


Figure 2. Photographs of the (j) top-view of $x = 0.0$ viscous gel and (k) side-view of combustion $x = 0.0$ ferrite

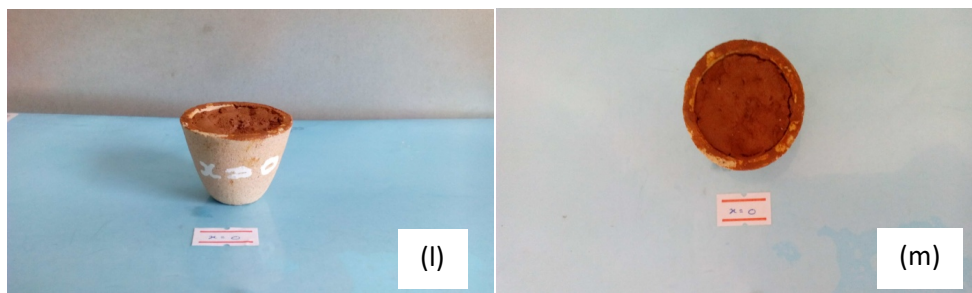


Figure 2. Photographs of the (l) side-view and (m) top-view of combustion $x = 0.0$ ferrite

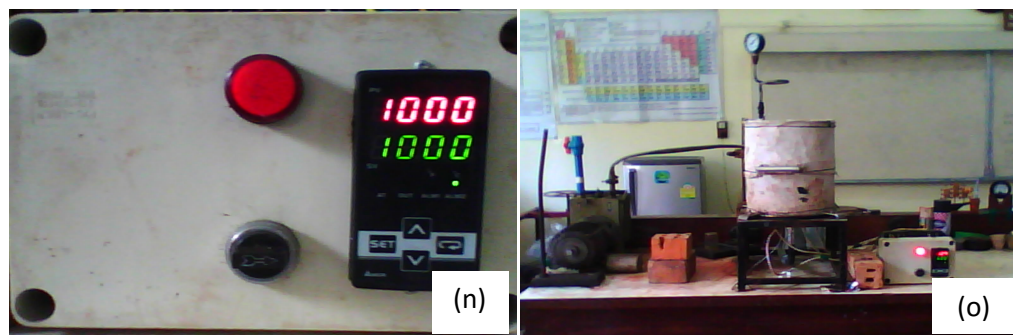


Figure 2. Photographs of the (n) DELTA A Series Temperature Controller DTA4896 at 1000°C and (o) experimental setup of sample preparation system



Figure 2.(p) Photograph of the as-prepared $\text{Ni}_{1-x}\text{Co}_x\text{Fe}_2\text{O}_4$ where $x = 0.0$ ferrite

SEM Measurement

In the present work, the morphological features of $\text{Ni}_{1-x}\text{Co}_x\text{Fe}_2\text{O}_4$ ($x = 0.0, 0.1, 0.2$ and 0.3) powders were investigated by using JEOL JSM-5610LV SEM with the accelerating voltage of 15 kV, the beam current of 50 mA and 5500 times of photo magnification.

Gas Sensitive Electrical Resistance Measurement

The as-prepared Cobalt Doped Nickel ferrites, $\text{Ni}_{1-x}\text{Co}_x\text{Fe}_2\text{O}_4$ ($x = 0.0, 0.1, 0.2$ and 0.3) samples were made pellets by SPECAC hydraulic pellet-maker using 5 ton (~ 70 MPa) to detect gas sensing effects of the samples. The silver paste (conductive pen) was made over the sample to ensure good electrical contacts. Ring-shaped copper electrodes were used to observe the electrical properties of the samples. The electrical resistances of the samples were observed in the ambient condition (air) and acetone, ethanol, octane and liquid petroleum gas (LPG) conditions. The electrical resistances of the samples were measured by using MASTECH digital multi-meter.

In the data collection, firstly, the electrical resistances were observed in air. For the gas sensing measurements, the sensor element (ferrite disk) was placed in a glass chamber. Gas sensing properties were investigated at room temperature. The experiments were performed with four test gases: acetone, ethanol, octane and liquid petroleum gas (LPG).

The sensitivity, S , defined as the ratio:

$$S = \frac{\Delta R}{R_a} = \frac{|R_a - R_g|}{R_a}$$

where R_a and R_g are the sensor resistances in air and in presence of the test gas, respectively.

Electrical resistances of the samples were observed by MASTECH digital multi-meter after the exposure times 3 min and 5 min respectively. Thickness and area of each of the sample were 3.33 mm and $1.14 \times 10^{-4} \text{ m}^2$ respectively. Photographs of the experimental setup of gas sensitive electrical resistances measurements are shown in Figures (a – h) respectively.

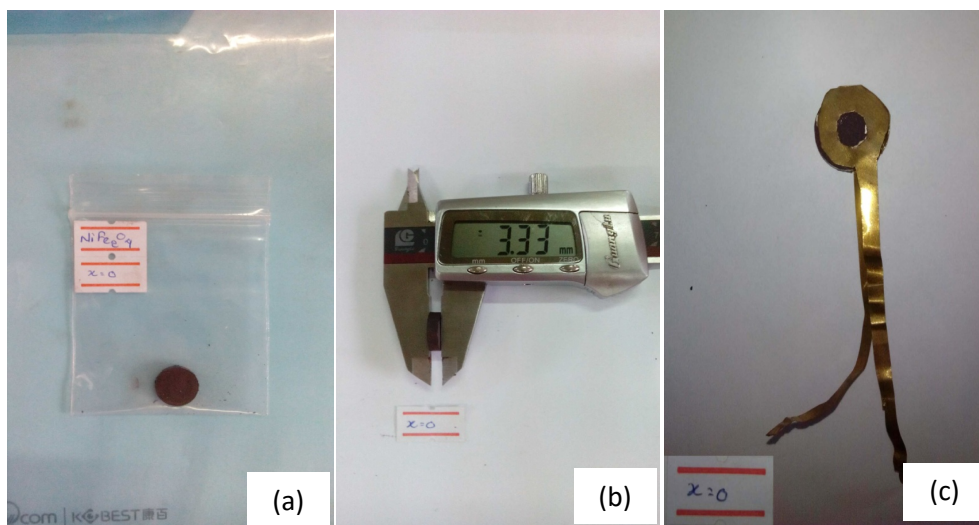


Figure 3. Photographs of the (a) $\text{Ni}_{1-x}\text{Co}_x\text{Fe}_2\text{O}_4$ ($x = 0.0$) ferrite pellet, (b) thickness measurement of $x = 0.0$ sample pellet and (c) ring shape Cu electrode mounted on both-sides of the $x = 0.0$ sample

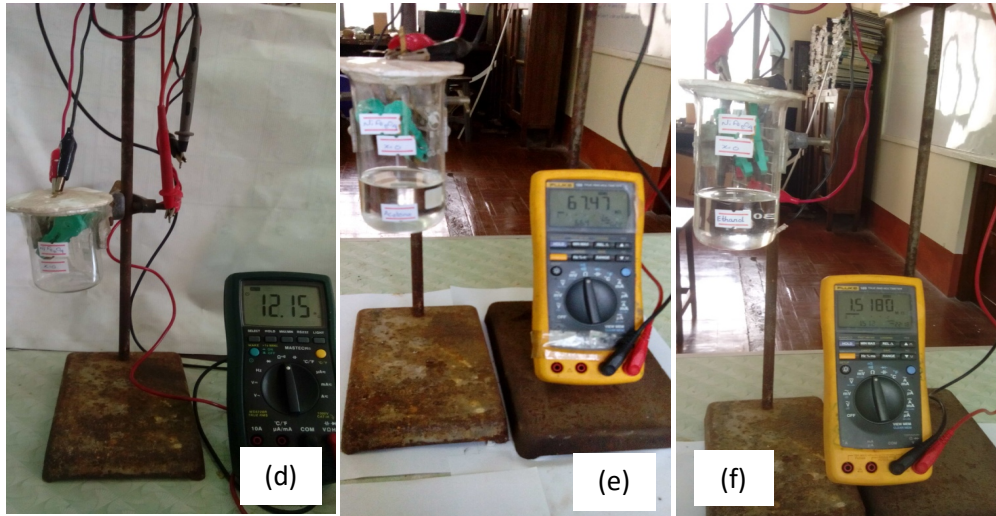


Figure 3. Photographs of the (d) experimental setup of gas-sensitive electrical properties measurements of $x = 0.0$ sample in air, (e) in acetone and (f) in ethanol atmospheres

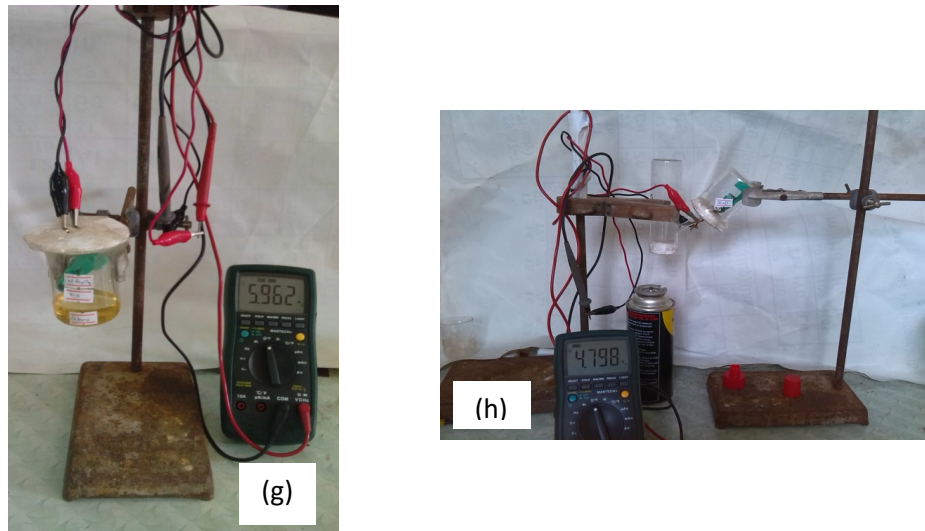


Figure 3. Photographs of the experimental setup of gas-sensitive electrical properties measurements of $x = 0.0$ sample (g) in octane and (h) in LPG atmospheres

Results and Discussion

X-Ray Diffraction Analysis

Powder X-ray diffraction patterns of $\text{Ni}_{1-x}\text{Co}_x\text{Fe}_2\text{O}_4$ ($x = 0.0, 0.1, 0.2$ and 0.3) samples are shown in Figures 4(a – d). The observed XRD lines were identified by using standard JCPDS data library files of

- (1) Cat. No. 86-2267> Trevorite – NiFe_2O_4 for NiFe_2O_4 or $x = 0.0$ sample and
- (2) Cat. No. 86-2267> Trevorite – NiFe_2O_4 and Cat. No. 22-1086> CoFe_2O_4 – Cobalt Iron Oxide for $\text{Ni}_{0.9}\text{Co}_{0.1}\text{Fe}_2\text{O}_4$, $\text{Ni}_{0.8}\text{Co}_{0.2}\text{Fe}_2\text{O}_4$ and $\text{Ni}_{0.7}\text{Co}_{0.3}\text{Fe}_2\text{O}_4$.

As shown in Figure 4(a), five diffraction peaks at 2θ values of 30.275° , 35.639° , 43.319° , 57.397° and 62.905° corresponding to (220), (311), (400), (511) and (440) planes of the sample have been observed and compared with the JCPDS, Cat. No. 86-2267> Trevorite – NiFe_2O_4 - spinel type cubic nickel ferrite phase - standard powder diffraction data file. The collected XRD pattern confirms / indicates that the resultant particles are $\text{Ni}_{1-x}\text{Co}_x\text{Fe}_2\text{O}_4$ ($x = 0.0$) powder.

As shown in Figure 4(b), the collected diffraction lines were found to be agreed with the standard data file. The collected peaks in the sample are (220), (311), (400), (511) and (440) respectively. These lines indicated that the sample was mono-phase or single phase crystalline material.

As shown in Figure 4(c), they can be clearly seen that only the intense peaks of (220), (311), (222), (400), (511) and (440) planes were identified by the standard data files of the same in Cat. Nos. Others lines, e.g., the planes such as (111) and (422) as shown in library files were not identified because the library files were only pure/undoped ferrites materials. Thus, it may be assumed that some of the dopant atoms of Cd^{2+} substituted in the Mg^{2+} lattice sites, then the bond lengths of tetrahedral sites and octahedral sites can be varied due to the lattice substitution of the samples.

Also, as shown in Figure 4(d), six strongest peaks of (220), (311), (222), (400), (511) and (440) planes were identified with standard library files. The lowest intensity of the two lines (111) and (422) as shown in library files were not identified because the library files were only pure/undoped ferrites materials.

In the collected XRD patterns, the appearance of the diffraction peaks demonstrates the Cobalt Doped Nickel ferrites, $\text{Ni}_{1-x}\text{Co}_x\text{Fe}_2\text{O}_4$ ($x = 0.0, 0.1, 0.2$ and 0.3) spinel samples. The experimental results of the samples are presented in Table 1(a – d). According to XRD patterns, the samples belong to cubic structure at room temperature. The lattice parameters were evaluated by using crystal utility of the equation $\frac{\sin^2 \theta}{(h^2 + k^2 + l^2)} = \frac{\lambda^2}{4a^2}$ [5]. The strongest peak was found to be (311) reflection, which indicated the dominated plane of the polycrystalline phase.

The experimental results of the calculated average lattice parameters and the observed lattice parameters are tabulated in Table 2. Variation of the lattice parameters with the dopant concentration of Co is shown in Figure 5. As shown in Figure 5, the lattice parameters of the samples increased with increase in concentration of Co due to the ionic substitution of Co on Ni in the lattice sites. It can be simply explained that the ionic radii of Co^{2+} and Ni^{2+} are 0.82 \AA and 0.78 \AA , thus when the increase in dopant concentration of Co^{2+} on divalent cation sites of Ni^{2+} , then the lattice parameters of the unit cell of undoped NiFe_2O_4 increase.

The crystallite sizes of each of the samples were estimated by using the Scherrer formula, $D = \frac{0.9\lambda}{B \cos \theta}$, where "D" is the crystallite size (nm), " λ " is the wavelength of incident X-ray (\AA), " θ " is the diffraction angle of the peak under consideration at FWHM ($^\circ$) and "B" is the observed FWHM (radians). The ferrite peaks are quite broad as a consequence of the nanometre size of the crystallite domains.

In the present work, the average crystallite sizes are tabulated in Table 2. In the present work, the average crystallite sizes are tabulated in Table 3. The obtained average crystallite sizes are in the range $50.2421 \text{ nm} - 73.5475 \text{ nm}$ and it indicates the nanosized $\text{Ni}_{1-x}\text{Co}_x\text{Fe}_2\text{O}_4$ ($x = 0.0, 0.1, 0.2$ and 0.3) ferrites or it can be said that the nanocrystalline materials. Variation of the crystallite sizes with the dopant concentration of Co of the samples is shown in Figure 5. It was found that the crystallite size of the samples decreased with the increase in dopant concentration of Co.

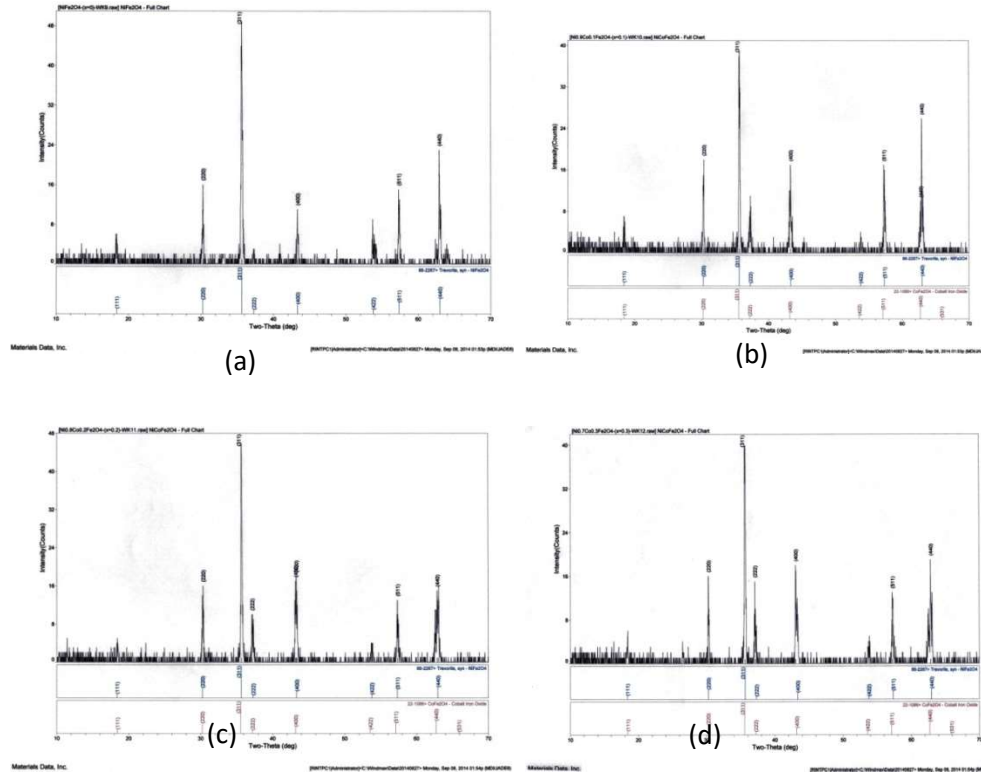


Figure 4. XRD patterns of $Ni_{1-x}Co_xFe_2O_4$ where (a) $x = 0.0$, (b) $x = 0.1$, (c) $x = 0.2$ and (d) $x = 0.3$ ferrites

Table 1.(a) XRD data of $Ni_{1-x}Co_xFe_2O_4$ (where $x = 0.0$) ferrite

[NiFe2O4-(x=0)-WK9.raw] NiFe2O4 - Full Chart										Peak ID Report	
SCAN: 10.0/70.0/0.02/0.06(sec), Cu(40kV,40mA), I(max)=49, 08/27/14 20:04											
PEAK: 11-pts/Quartic Filter, Threshold=1.0, Cutoff=0.0%, BG=1/0.5, Peak-Top=Summit											
NOTE: Intensity = Counts, 2T(0)=0.0(deg), Wavelength to Compute d-Spacing = 1.54056Å (Cu/K-alpha1)											
#	2-Theta	d(Å)	Height	Height%	Phase ID	d(Å)	I%	(h k l)	2-Theta	Delta	
1	30.275	2.9497	16	32.7	Trevorite, syn	2.9476	29.6	(2 2 0)	30.298	0.022	
2	35.639	2.5171	49	100.0	Trevorite, syn	2.5137	100.0	(3 1 1)	35.689	0.050	
3	43.319	2.0870	11	22.4	Trevorite, syn	2.0842	20.3	(4 0 0)	43.378	0.060	
4	57.397	1.6041	13	26.5	Trevorite, syn	1.6045	25.4	(5 1 1)	57.382	-0.015	
5	62.905	1.4762	23	46.9	Trevorite, syn	1.4738	33.1	(4 4 0)	63.021	0.116	
Line Shifts of Individual Phases: PDF#86-2267 - Trevorite, syn <2T(0) = 0.0, d/d(0) = 1.0>											

Table 1.(b) XRD data of Ni_{1-x}Co_xFe₂O₄ (where x = 0.1) ferrite

[Ni0.9Co0.1Fe2O4-(x=0.1)-WK10.raw] NiCoFe2O4 - Full Chart										Peak ID Report
SCAN: 10.0/70.0/0.02/0.06(sec), Cu(40kV,40mA), I(max)=39, 08/27/14 19:59										
PEAK: 13-pts/Quartic Filter, Threshold=1.0, Cutoff=0.0%, BG=1/0.5, Peak-Top=Summit										
NOTE: Intensity = Counts, 2T(0)=0.0(deg), Wavelength to Compute d-Spacing = 1.54056Å (Cu/K-alpha1)										
#	2-Theta	d(Å)	Height	Height%	Phase ID	d(Å)	I%	(h k l)	2-Theta	Delta
1	30.330	2.9445	18	46.2	CoFe2O4	2.9470	30.0	(2 2 0)	30.304	-0.025
2	35.680	2.5143	39	100.0	Trevorite, syn	2.5137	100.0	(3 1 1)	35.689	0.009
3	43.304	2.0876	17	43.6	CoFe2O4	2.0888	20.0	(4 0 0)	43.278	-0.026
4	57.261	1.6076	17	43.6	CoFe2O4	1.6093	30.0	(5 1 1)	57.193	-0.068
5	62.774	1.4790	10	25.6	CoFe2O4	1.4783	40.0	(4 4 0)	62.805	0.031
6	62.937	1.4756	26	66.7	Trevorite, syn	1.4738	33.1	(4 4 0)	63.021	0.084
Line Shifts of Individual Phases:										
PDF#86-2267 - Trevorite, syn <2T(0) = 0.0, d/d(0) = 1.0>										
PDF#22-1086 - Cobalt Iron Oxide <2T(0) = 0.22, d/d(0) = 1.0>										

Table 1.(c) XRD data Ni_{1-x}Co_xFe₂O₄ (where x = 0.2) ferrite

[Ni0.8Co0.2Fe2O4-(x=0.2)-WK11.raw] NiCoFe2O4 - Full Chart										Peak ID Report
SCAN: 10.0/70.0/0.02/0.06(sec), Cu(40kV,40mA), I(max)=46, 08/27/14 19:54										
PEAK: 13-pts/Quartic Filter, Threshold=1.0, Cutoff=0.0%, BG=1/0.5, Peak-Top=Summit										
NOTE: Intensity = Counts, 2T(0)=0.0(deg), Wavelength to Compute d-Spacing = 1.54056Å (Cu/K-alpha1)										
#	2-Theta	d(Å)	Height	Height%	Phase ID	d(Å)	I%	(h k l)	2-Theta	Delta
1	30.263	2.9509	14	30.4	Trevorite, syn	2.9476	29.6	(2 2 0)	30.298	0.035
2	35.664	2.5154	46	100.0	CoFe2O4	2.5159	100.0	(3 1 1)	35.657	-0.007
3	37.138	2.4189	10	21.7	CoFe2O4	2.4102	8.0	(2 2 2)	37.277	0.139
4	43.279	2.0888	18	39.1	CoFe2O4	2.0888	20.0	(4 0 0)	43.278	-0.001
5	57.340	1.6055	13	28.3	Trevorite, syn	1.6045	25.4	(5 1 1)	57.382	0.042
6	62.883	1.4767	15	32.6	CoFe2O4	1.4783	40.0	(4 4 0)	62.805	-0.078
7	63.104	1.4720	16	34.8	Trevorite, syn	1.4738	33.1	(4 4 0)	63.021	-0.083
Line Shifts of Individual Phases:										
PDF#86-2267 - Trevorite, syn <2T(0) = 0.0, d/d(0) = 1.0>										
PDF#22-1086 - Cobalt Iron Oxide <2T(0) = 0.22, d/d(0) = 1.0>										

Table 1.(d) XRD data of Ni_{1-x}Co_xFe₂O₄ (where x = 0.3) ferrite

[Ni0.7Co0.3Fe2O4-(x=0.3)-WK12.raw] NiCoFe2O4 - Full Chart										Peak ID Report
SCAN: 10.0/70.0/0.02/0.06(sec), Cu(40kV,40mA), I(max)=40, 08/27/14 19:49										
PEAK: 13-pts/Quartic Filter, Threshold=1.0, Cutoff=0.0%, BG=1/0.5, Peak-Top=Summit										
NOTE: Intensity = Counts, 2T(0)=0.0(deg), Wavelength to Compute d-Spacing = 1.54056Å (Cu/K-alpha1)										
#	2-Theta	d(Å)	Height	Height%	Phase ID	d(Å)	I%	(h k l)	2-Theta	Delta
1	30.268	2.9504	16	40.0	Trevorite, syn	2.9476	29.6	(2 2 0)	30.298	0.030
2	35.621	2.5183	40	100.0	CoFe2O4	2.5159	100.0	(3 1 1)	35.657	0.035
3	37.082	2.4224	15	37.5	CoFe2O4	2.4102	8.0	(2 2 2)	37.277	0.194
4	43.300	2.0878	12	30.0	CoFe2O4	2.0888	20.0	(4 0 0)	43.278	-0.022
5	57.261	1.6076	12	30.0	CoFe2O4	1.6093	30.0	(5 1 1)	57.193	-0.068
6	62.880	1.4767	19	47.5	CoFe2O4	1.4783	40.0	(4 4 0)	62.805	-0.075
Line Shifts of Individual Phases:										
PDF#86-2267 - Trevorite, syn <2T(0) = 0.0, d/d(0) = 1.0>										
PDF#22-1086 - Cobalt Iron Oxide <2T(0) = 0.22, d/d(0) = 1.0>										

Table 2. The lattice parameters and crystallite sizes of $\text{Ni}_{1-x}\text{Co}_x\text{Fe}_2\text{O}_4$ (where $x = 0.0, 0.1, 0.2$ and 0.3) ferrites

Sample (Contents x of Co)	Obs. $a=b=c$ (Å)	Cal. $a=b=c$ (Å)	D (nm)
0.0	8.3450	8.3450	73.5475
0.1	8.3474	8.3474	70.0537
0.2	8.3532	8.3495	51.4843
0.3	8.3578	8.3578	50.2421

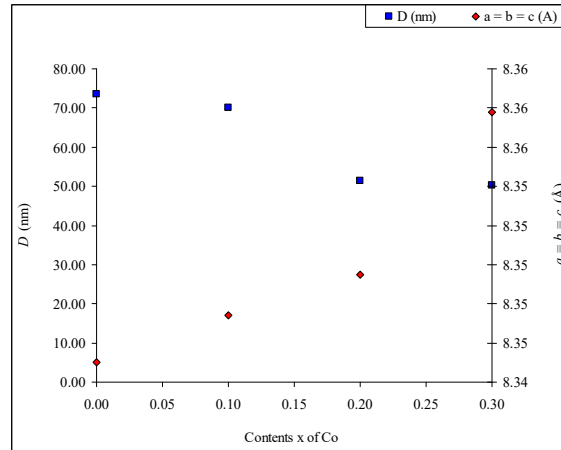


Figure 5. Variations of the lattice parameters and crystallite sizes of $\text{Ni}_{1-x}\text{Co}_x\text{Fe}_2\text{O}_4$ ferrites with the Co concentration

Microstructural Analysis

Grain size and pore structure have a major effect on the properties in polycrystalline materials. Due to the microstructure has a major role in the performance of a ceramic sensor, e.g., gas sensor, in this work, the microstructures of the end products (as-prepared ferrites) by SEM to investigate the external morphology of the grain shape, size and pore formation of the as-prepared ferrite samples. SEM micrographs of $\text{Ni}_{1-x}\text{Co}_x\text{Fe}_2\text{O}_4$ (where $x = 0.0, 0.1, 0.2$ and 0.3) ferrites powders are shown in Figures 6(a – d).

This figures show that the samples consist primarily of irregularly shaped of $0.08 \mu\text{m}$ to $0.70 \mu\text{m}$ aggregates of fine particles. It can be seen that

the crystallite sizes of the samples are extremely fine, on the order 80 nm to 800 nm. The materials are characterized by high intergranular porosities in the observed SEM micrographs; about 20% in $x = 0.0$, 25% in $x = 0.1$, 25% in $x = 0.2$ and 10% in $x = 0.3$ of $Ni_{1-x}Co_xFe_2O_4$ samples. Furthermore, many large and large pores are present in $x = 0.0, 0.1$ and 0.2 samples and many large and small pores are present only in $x = 0.3$ sample. The grain sizes are listed in Table 3.

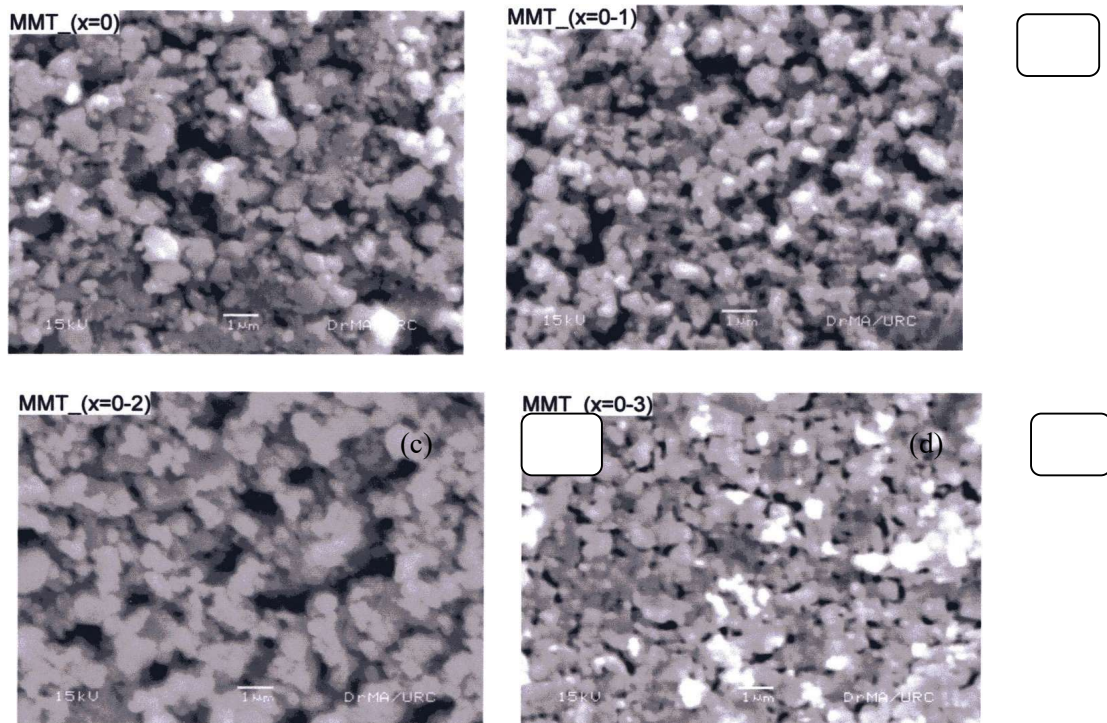


Figure 6. SEM micrograph of $Ni_{1-x}Co_xFe_2O_4$ where (a) $x = 0.0$, (b) $x = 0.1$, (c) $x = 0.2$ and (d) $x = 0.3$ ferrites

Table 3. Grain sizes of $\text{Ni}_{1-x}\text{Co}_x\text{Fe}_2\text{O}_4$ (where $x = 0.0, 0.1, 0.2, 0.3$) ferrites

Sample (Contents x of Co)	Grain size (mm)
0.0	0.08 – 0.70
0.1	0.08 – 0.40
0.2	0.12 – 0.50
0.3	0.10 – 0.70

Gas Sensitive Electrical Property Study

The gas-sensing responses of $\text{Ni}_{1-x}\text{Co}_x\text{Fe}_2\text{O}_4$ (where $x = 0.0, 0.1, 0.2$ and 0.3) samples to different reducing gases like acetone, ethanol, octane and liquid petroleum gas (LPG) at ambient temperature were analyzed for the applications of gas sensing materials.

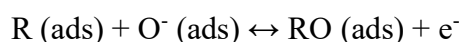
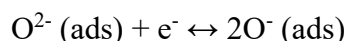
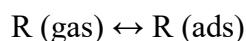
In the present work, gas response characteristics of $\text{Ni}_{1-x}\text{Co}_x\text{Fe}_2\text{O}_4$ ferrites in the acetone, ethanol, octane and liquid petroleum gas (LPG) atmosphere after 3 min and 5 min exposure time are depicted in Figures 7 (a – d) and Figure 8(a – d) respectively. The gas sensitivities of the samples with corresponding test gases after 3 min ($S_{3 \text{ min}}$) and 5 min ($S_{5 \text{ min}}$) exposure time are tabulated in Table 4(a – d). The most sensitive data are high-lighted in the tables.

As presented in tables, the most sensitive samples with corresponding test gases were as follows:

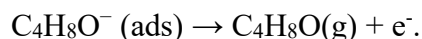
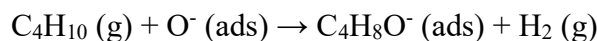
- For $\text{Ni}_{1-x}\text{Co}_x\text{Fe}_2\text{O}_4$ ($x = 0.0$) ferrite after exposure times 3 min and 5 min, the most sensitive test gases are LPG and acetone.
- For $\text{Ni}_{1-x}\text{Co}_x\text{Fe}_2\text{O}_4$ ($x = 0.1$) ferrite after exposure times 3 min and 5 min, the most sensitive test gas is LPG.
- For $\text{Ni}_{1-x}\text{Co}_x\text{Fe}_2\text{O}_4$ ($x = 0.2$) ferrite after exposure times 3 min and 5 min, the most sensitive test gases are acetone and LPG.
- For $\text{Ni}_{1-x}\text{Co}_x\text{Fe}_2\text{O}_4$ ($x = 0.3$) ferrite after exposure times 3 min and 5 min, the most sensitive test gases are ethanol and LPG.

It can be said that the $x = 0.0$ and $x = 0.1$ samples were the most sensitive to LPG and the other samples $x = 0.2$ and 0.3 were the most sensitive to acetone gas and ethanol gas after 3 min exposure time. It can also be said that the $x = 0.0$ or pure NiFe_2O_4 sample was the most sensitive to acetone gas and the other samples ($x = 0.1, 0.2$ and 0.3) were most sensitive to LPG gas after 5 min exposure time.

The gas sensitive processes of the samples, for example LPG sensitive process, can be discussed as follow: The reducing gas R acting on the $\text{Ni}_{1-x}\text{Co}_x\text{Fe}_2\text{O}_4$ surface can be described as



In the absence of R, electrons are removed from $\text{Ni}_{1-x}\text{Co}_x\text{Fe}_2\text{O}_4$ conduction band by the reduction of O_2 , resulting in the formation of O^- species and consequently the resistance of $\text{Ni}_{1-x}\text{Co}_x\text{Fe}_2\text{O}_4$ sensor increases. When R is introduced, it reacts with $\text{O}^- (\text{ads})$ to form RO, and electrons enter the conduction band of $\text{Ni}_{1-x}\text{Co}_x\text{Fe}_2\text{O}_4$ leading to decrease of resistance. The reactions, for example, involved during the butane, C_4H_{10} (LPG) sensing are summarized below:



Thus, the candidate samples of Cobalt Doped Nickel ferrites, $\text{Ni}_{1-x}\text{Co}_x\text{Fe}_2\text{O}_4$ (where $x = 0.0, 0.1, 0.2$ and 0.3) samples can be suitable applied for the LPG, acetone, ethanol and octane gas sensors.

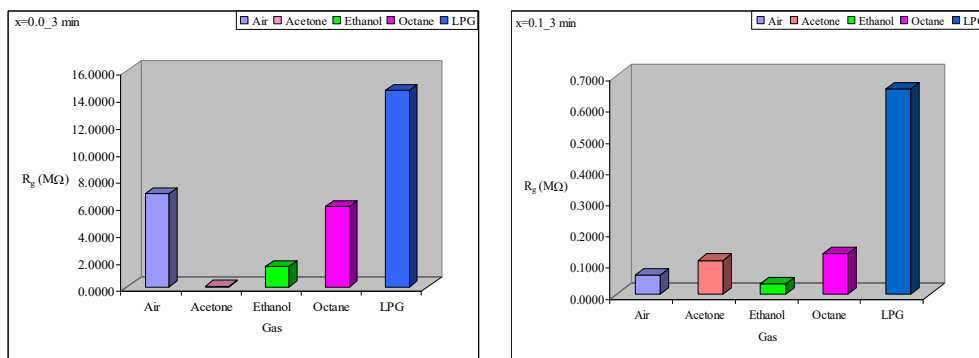


Figure 7. Gas response electrical resistances of $\text{Ni}_{1-x}\text{Co}_x\text{Fe}_2\text{O}_4$ (a) $x = 0.0$ and (b) $x = 0.1$ ferrites after 3 min exposure time

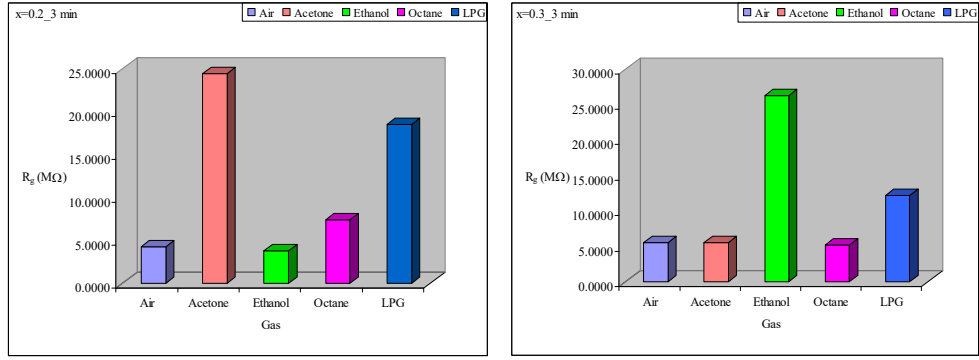


Figure 7. Gas response electrical resistances of $Ni_{1-x}Co_xFe_2O_4$ (c) $x = 0.2$ and (d) $x = 0.3$ ferrites after 3 min exposure time

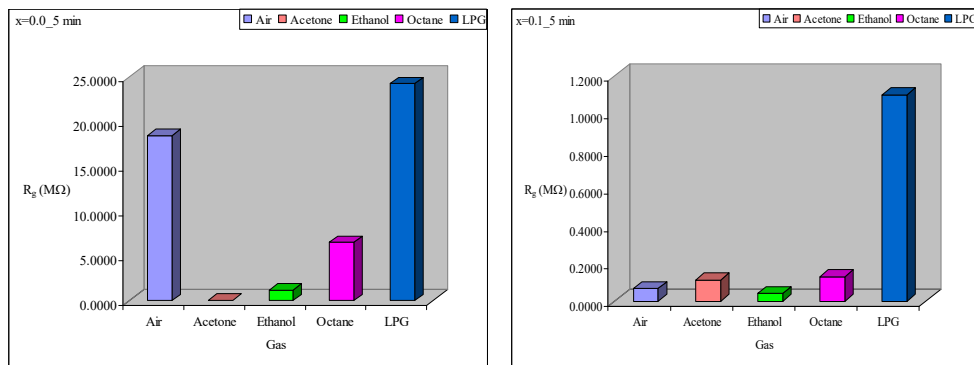


Figure 8. Gas response electrical resistances of $Ni_{1-x}Co_xFe_2O_4$ (a) $x = 0.0$ and (b) $x = 0.1$ ferrites after 5 min exposure time

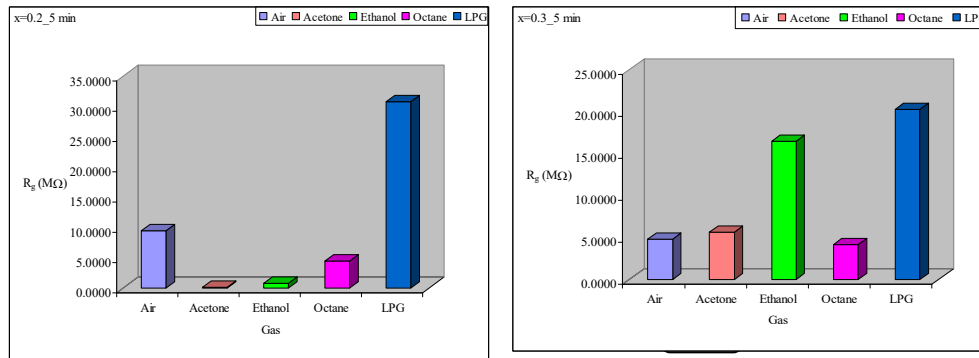


Figure 8. Gas response electrical resistances of $Ni_{1-x}Co_xFe_2O_4$ (c) $x = 0.2$ and (d) $x = 0.3$ ferrites after 5 min exposure time

Table 4.(a) Sensitivities of the $Ni_{1-x}Co_xFe_2O_4$ (where $x = 0.0$) sample after 3 min and 5 min exposure time

Gas	S3 min	S5 min
Acetone	0.9902	0.9962
Ethanol	0.7800	0.9344
Octane	0.1359	0.6457
LPG	1.1057	0.3139

Table 4.(b) Sensitivities of the $Ni_{1-x}Co_xFe_2O_4$ (where $x = 0.1$) sample after 3 min and 5 min exposure time

Gas	S3 min	S5 min
Acetone	0.7659	0.6858
Ethanol	0.4457	0.3924
Octane	1.1350	0.9379
LPG	9.7220	15.2574

Table 4.(c) Sensitivities of the $Ni_{1-x}Co_xFe_2O_4$ (where $x = 0.2$) sample after 3 min and 5 min exposure time

Gas	S3 min	S5 min
Acetone	4.6816	0.9835
Ethanol	0.1050	0.9166
Octane	0.7186	0.5308
LPG	3.3047	2.2749

Table 4.(d) Sensitivities of the $Ni_{1-x}Co_xFe_2O_4$ (where $x = 0.3$) sample after 3 min and 5 min exposure time

Gas	S3 min	S5 min
Acetone	0.0020	0.1568
Ethanol	3.7653	2.3926
Octane	0.0544	0.1337
LPG	1.2105	3.1770

Conclusion

Nanocrystalline Cobalt Doped Nickel ferrites, $\text{Ni}_{1-x}\text{Co}_x\text{Fe}_2\text{O}_4$ (where $x = 0.0, 0.1, 0.2$ and 0.3) samples were successfully prepared by self-combustion method and their structural analysis, microstructural characteristic and gas response electrical property were reported in this work.

The X-ray diffraction patterns of the samples indicated the single-phase spinel type cubic crystalline materials. The lattice parameters of increased with increase in dopant concentration of Co on Ni ferrites in the samples. It was suggested that the lattice substitution of divalent cations of Co^{2+} on Ni^{2+} in each of the unit cell of the samples. It indicated that the presence of Co^{2+} ions causes appreciable change in the structural properties of $\text{Ni}_{1-x}\text{Co}_x\text{Fe}_2\text{O}_4$. The obtained average crystallite sizes showed the nanocrystalline nature of the materials. SEM micrographs indicated that the grains were high intergranular porosities. The pores serve as adsorption sites due to the decomposition of starting materials in the preparation of candidate materials with poor grain boundary. It can also be found that in each of the SEM micrographs, many large and large pores are present in $x = 0.0, 0.1$ and 0.2 samples and many large and small pores are present only in $x = 0.3$ sample. The obtained grain sizes are in the range $0.08 \mu\text{m}$ to $0.70 \mu\text{m}$. From the test gas response and the obtained sensitivities results, the following facts were proposed for the applications of the candidate materials:

- For $\text{Ni}_{1-x}\text{Co}_x\text{Fe}_2\text{O}_4$ ($x = 0.0$) ferrite after the exposure times 3 min and 5 min to the best sensitive gases are LPG and acetone.
- For $\text{Ni}_{1-x}\text{Co}_x\text{Fe}_2\text{O}_4$ ($x = 0.1$) ferrite after the exposure times 3 min and 5 min to the best sensitive gas is LPG.
- For $\text{Ni}_{1-x}\text{Co}_x\text{Fe}_2\text{O}_4$ ($x = 0.2$) ferrite after exposure times 3 min and 5 min to the best sensitive gases are acetone and LPG
- For $\text{Ni}_{1-x}\text{Co}_x\text{Fe}_2\text{O}_4$ ($x = 0.3$) ferrite after exposure times 3 min and 5 min to the best sensitive gases are ethanol and LPG respectively.

According to experimental results, the samples can be used for the applications of gas sensors with the corresponding test gas. Most of the samples should be used for LPG gas sensor. Especially, only the $x = 0.1$ sample is the most suitable for the application of LPG sensor.

Acknowledgement

The authors would like to acknowledge Professor Dr Khin Khin Win, Head of Department of Physics, University of Yangon, for her kind permission to carry out this work.

References

1. Harris, V.G., Geiler, A., Chen, Y., Yoon, S.D., Wu, M., Yang, A., Chen, Z., He, P., Parimi, P.V., Zuo, X., Patton, C.E., Abe, M., Acher O. & Vittoria, C. (2009). Recent advances in processing and applications of microwave ferrites. *Journal of Magnetism and Magnetic Materials*, 321, pp. 2035-2047.
2. Iyer, R., Desai, R. & Upadhyay, R.V. (2009). Low temperature synthesis of nanosized $Mn_{1-x}Zn_xFe_2O_4$ ferrites and their characterizations. *Bulletins Materials Science*, 32, pp.141-147.
3. Kumar, N., Kumar, V., Arora, M., Sharmar, M., Singh, B. & Pant, R.P. (2009). Synthesis of $Mn_{0.2}Zn_{0.8}Fe_2O_4$ particles by high energy ball milling and their applications *Indian Journal of Engineering and Materials Science*, 16, pp. 410-414.
4. Marial, K.H., Choudhury, S. & Hakim, M.A. (2013). Structural phase transformation and hysteresis behavior of Cu-Zn ferrites. *International Nano Letters*, 3, 1-10.
5. Pathan, A.N., Sangshetti, K. & Pangal, A.A.G. (2010). Synthesis and Moussbauer Studies on Nickel-Zinc-Copper Nanoferrites. *Nanotechnology and Nanoscience*, 1(1), 13-16.
6. Sharma, R.K., Suwalka, O., Lakshmi, N., Venugopala, K., Banerjee, A. & Joy, P.A. (2005) Synthesis of Chromium Substituted Nano Particles of Cobalt Zinc Ferrites by Coprecipitation. *Materials Letters*, 59, 3402-3405.

STRUCTURAL ANALYSES, MICROSTRUCTURAL CHARACTERISTICS AND ELECTRICAL CONDUCTIVITY OF COPPER-COBALT FERRITES

Khin Sandar Soe¹, Nyo Nyo Myint², Thida Nyunt Than³ & Win Kyaw³

Abstract

Solid electrolyte materials of Copper-Cobalt ferrites with the general formula, $\text{Cu}_{1-x}\text{Co}_x\text{Fe}_2\text{O}_4$ (where $x = 0.00, 0.33$ and 1.00), were prepared by chemical co-precipitation method. Structural analyses of the samples were investigated by X-ray diffraction (XRD) method. XRD patterns revealed that the samples analogous to cubic structure and the lattice parameters were found to be increased with increase in concentration of Co. The crystallite sizes were obtained in the range of 29.85 nm – 43.44 nm. Scanning Electron Microscopy was used to study the microstructural properties of the sample. SEM micrographs showed that the grain shapes and sizes were affected by the concentration of Co and the most intergranular porosities were found in Cu-Co ferrite of $x = 0.33$ sample among the investigated materials. The electrical conductivities of the samples were investigated in the temperature range of 303 K – 873 K to study the superionic conductivities and to evaluate the activation energies of the samples for the applications of solid electrolyte materials.

Keywords: Copper-Cobalt ferrites, chemical co-precipitation method, XRD, SEM, superionic conductivities

Introduction

Ferrites are electrically ferrimagnetic ceramic compound materials, consisting of various mixtures of iron oxides such as Hematite (Fe_2O_3) or Magnetite (Fe_3O_4) and oxides of other metals like NiO, CuO, ZnO, MnO, CoO [Fang, (2003); Kumar, (2009)]. The prime property of ferrites is that, in the magnetized state, all spin magnetic moments are not oriented in the same direction. Few of them are in the opposite direction. But as the spin magnetic moments are of two types with different values, the net magnetic moment will have some finite value [Harris, (2009); Rani, (2013)].

¹ Dr, Demonstrator, Department of Physics, Monywa University

² Dr, Associate Professor, Department of Physics, Yenanchaung Degree College

³ Dr, Associate Professors, Department of Physics, Sagaing University

Copper ferrite is one of the important spinel ferrites MFe_2O_4 because it exhibits phase transitions, changes semiconducting properties, shows electrical switching and tetragonality variation when treated under different conditions in addition to interesting magnetic and electrical properties with chemical and thermal stabilities [Kumar, (2009); Shutka, (2010)]. It is used in wide range of applications in gas sensing, catalytic applications, Li ion batteries high density magneto-optic recording devices, color imaging, bioprocessing, magnetic refrigeration and Ferro fluids [Tailhades, (1998)]. In this work, $Cu_{1-x}Co_xFe_2O_4$ (where $x = 0.00, 0.33$ and 1.00) were prepared by using chemical co-precipitation method and their structural, microstructural and electrical characteristics were studied by XRD, SEM and temperature dependent electrical resistance measurements for the application of solid electrolyte materials.

Materials and Method

Preparation of Copper-Cobalt Ferrite

$Cu_{1-x}Co_xFe_2O_4$ (where $x = 0.00, 0.33$ and 1.00) were prepared by chemical co-precipitation method from Oxalate precursors. Raw materials of Analytical Reagent (AR) grade Cupric Chloride ($CuCl_2 \cdot 2H_2O$), Cobalt Chloride ($CoCl_2 \cdot 6H_2O$), and Ferric Chloride Hexahydrate ($FeCl_3 \cdot 6H_2O$) with stoichiometric composition were used to prepare the sample.

In the first, a concentrated solution of Cupric, Cobaltous, and Ferric Chlorides were reacted with an Oxalic acid solution to get a precipitate of Oxalates. The metallic salts were initially dissolved in a mixture of water (H_2O), Ethylene Glycol ($C_2H_6O_6$), and Hydrochloric acid (HCl), while the Oxalic acid ($H_2C_2O_4 \cdot 2H_2O$) were also dissolved in the mixture of (95%) Ethyl Alcohol (C_2H_7OH) and (5%) water. Then, the precursor co-precipitated Cu-Co ferrites were slowly decomposed at $700^\circ C$ for 5 h in vacuum chamber. Finally, the candidate material of Copper-Cobalt ferrite was obtained.

The flow-diagram of the $Cu_{1-x}Co_xFe_2O_4$ preparation procedure is shown in Figure 1. Photographs of the starting materials, solutions of starting materials, mixed solution of starting materials, precursor solution and as-prepared Copper-Cobalt ferrite, DELTA A Series Temperature Controller DTA4896 and experimental setup of sample preparation system are shown in Figure 2(a – g).

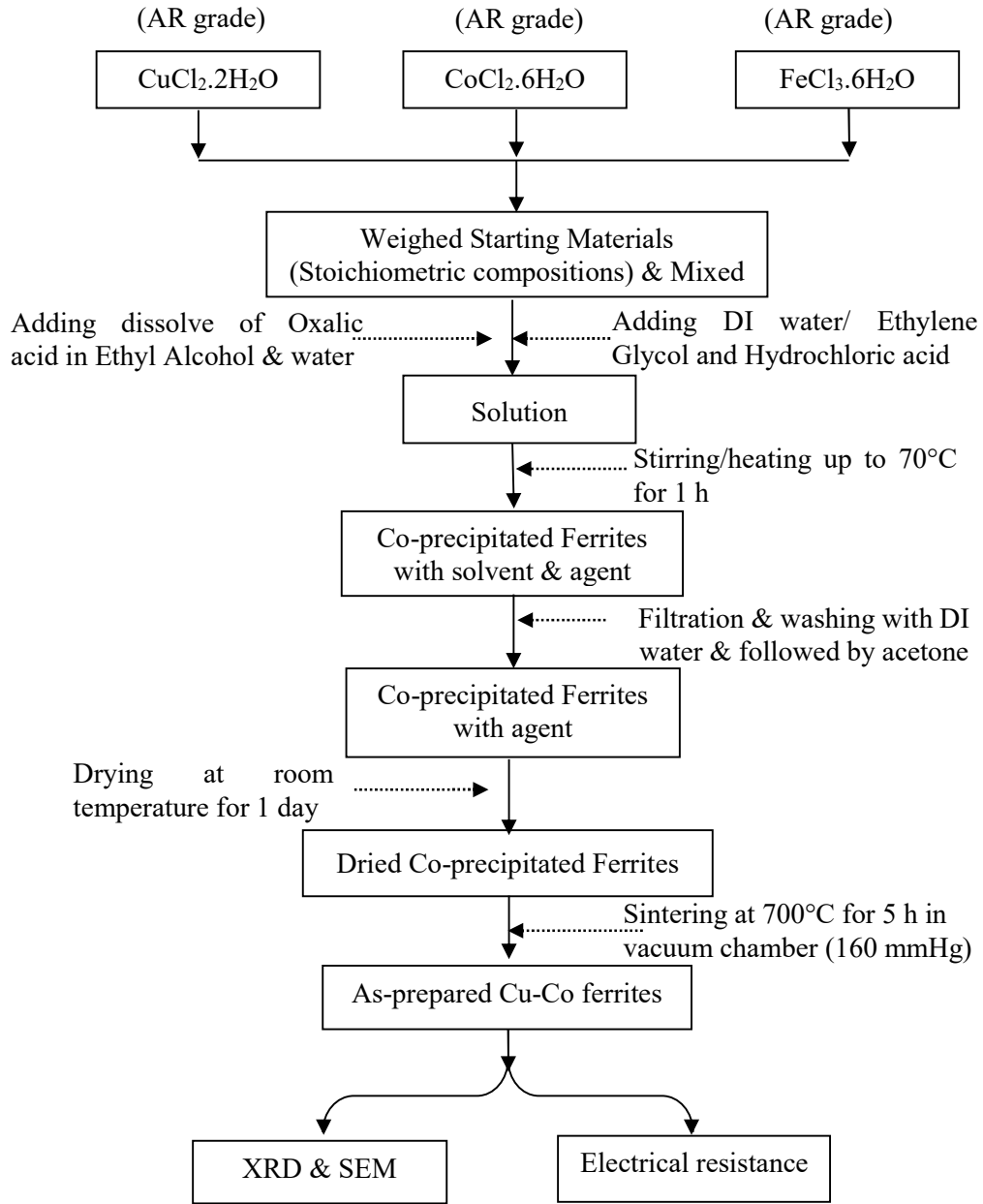


Figure 1. Flow-diagram of Cu-Co ferrite preparation

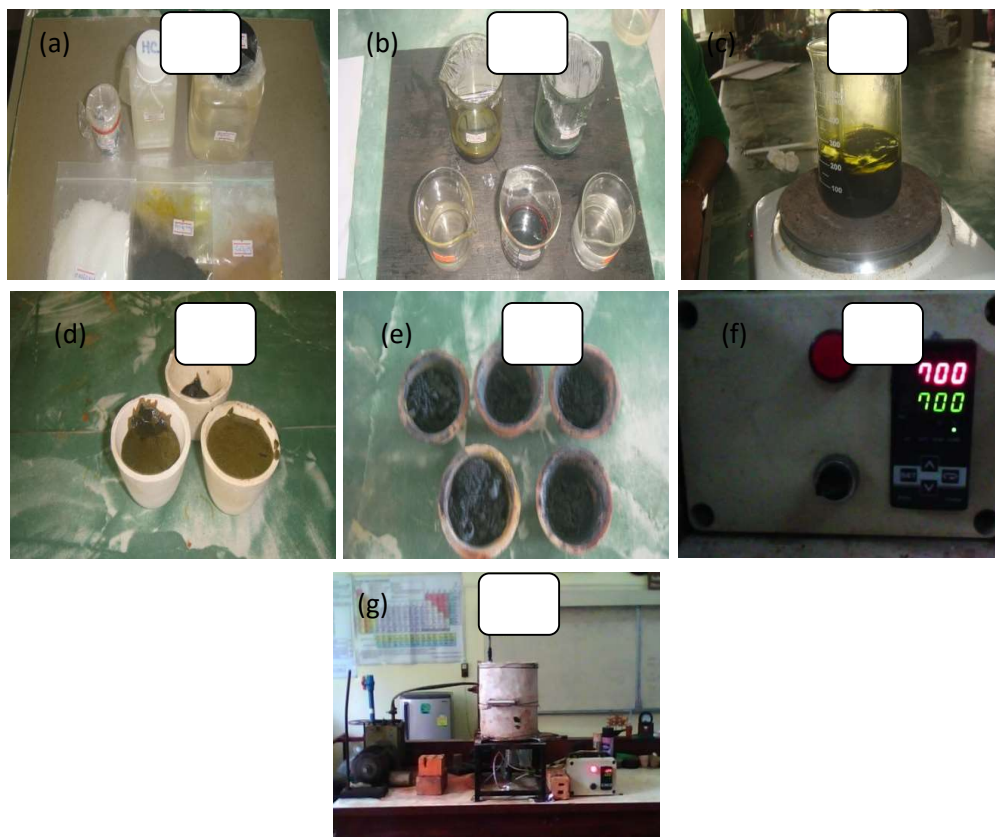
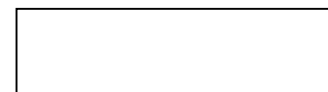
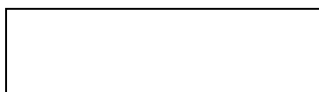


Figure 1. Photographs of the (a) starting materials, (b) solutions of starting materials, (c) mixed solution of starting materials, (d) precursor solution, (e) as-prepared Copper-Cobalt ferrite, (f) DELTA A Series Temperature Controller DTA4896 and (g) experimental setup of sample preparation system

Characteristic Measurement

The XRD spectra of the samples were observed by RIGAKU MULTIFLEX X-Ray Diffractometer to analyse the structural characteristics. Morphological features were investigated by using JEOL JSM-5610LV SEM with the accelerating voltage of 15 kV, the beam current of 50 mA and 5500 times of photo magnification. For the temperature dependent electrical resistance measurement, the as-prepared samples were made into pellets. The



silver paste (conductive pen) was made over the sample to ensure good electrical contacts. The electrical resistances of the samples were observed by using FLUKE 45 Dual-display digital multi-meter in the temperature range of 302 K – 873 K. Photograph of the experimental setup of electrical resistance measurement is shown in Figure 3. The area of pellets are $1.14 \times 10^{-4} \text{ m}^2$ and the thicknesses of the samples are 3.88 mm.



Figure 3. Photograph of the experimental setup of temperature dependent electrical resistance measurement

Results and Discussion

X-Ray Diffraction Analysis

Powder X-ray diffraction patterns of the samples are shown in Figure 4(a – c). The observed XRD lines were identified by using standard JCPDS data library files of

- (i) Cat. No.77-0010 > CuFe_2O_4 – Copper Iron Oxide for $x = 0.00$ sample of pure Cu ferrite,
- (ii) Cat. No.22-1086 > CoFe_2O_4 – Cobalt Iron Oxide and Cat. No. 77-0010 > CuFe_2O_4 – Copper Iron Oxide for $x = 0.33$ sample of Cu-Co ferrite and
- (iii) Cat. No. 22-1086 > CoFe_2O_4 – Cobalt Iron Oxide for $x = 1.00$ sample of pure Co ferrite

XRD patterns show the formation of single phase cubic structure with only one dominant peak corresponding to (311) reflection indicating that the crystallites are preferentially oriented along (311) plane. In the collected XRD patterns, only one diffraction line of (311) plane is found to be identified because the peak heights of the patterns are very low, i.e., peak heights of other lines are less than 10. Thus it cannot be assigned with JCPDS. The lattice parameters are evaluated by using crystal utility of the equation of

$$\frac{\sin^2 \theta}{(h^2 + k^2 + l^2)} = \frac{\lambda^2}{4a^2}$$

where θ is the diffraction angle ($^\circ$), (hkl) is the miller indices, λ is the wavelength of incident X-ray (\AA) and a is the lattice parameter of the samples (\AA). The observed and evaluated lattice parameters and the unit cell volume of the samples are tabulated in Table 1. Figure 5 shows the variation of the lattice parameters and the unit cell volumes with increase in Co concentration of $\text{Cu}_{1-x}\text{Co}_x\text{Fe}_2\text{O}_4$ ferrites. The lattice parameter of the CuFe_2O_4 was found to be increased with increase in Co concentration. The increase in lattice constant and unit cell volume is due to the smaller ionic radii of the doped cation, i.e., Co^{2+} (0.745 \AA) than that of Cu^{2+} (0.730 \AA). The crystallite sizes of the samples were estimated by using the Scherrer formula,

$$D = \frac{0.9\lambda}{B \cos \theta}$$

where D is the crystallite size (nm), λ is the wavelength of incident X-ray (\AA), θ is the diffraction angle of the peak under consideration at FWHM ($^\circ$) and B is the observed FWHM (radians). To examine the nanosized ferrite materials, the FWHM of the strongest peak ($I = 100\%$) of (311) planes of the XRD patterns were used to calculate the crystallite size. The obtained crystallite sizes of $\text{Cu}_{1-x}\text{Co}_x\text{Fe}_2\text{O}_4$ samples are presented in Table 1. It indicates that the as-prepared Cu-Co ferrites powders are nanosized materials and these Cu-Co ferrites are very fine particles nature.

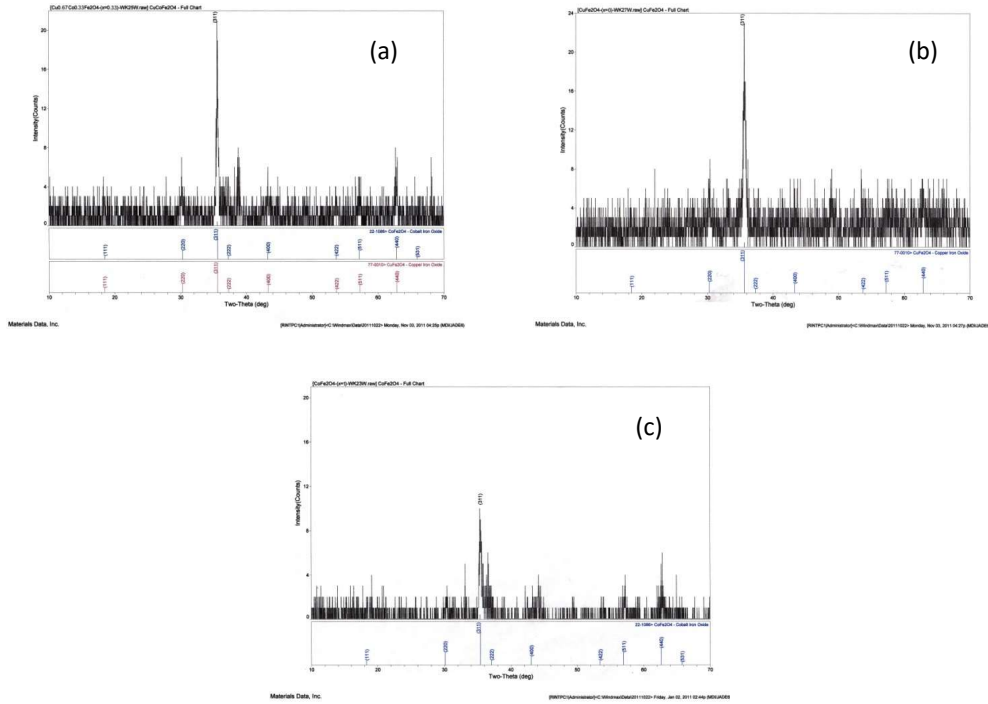


Figure 4. XRD patterns of $\text{Cu}_{1-x}\text{Co}_x\text{Fe}_2\text{O}_4$ for (a) $x = 0.00$, (b) $x = 0.33$ and (c) $x = 1.00$

Table 1. The lattice parameters and crystallite sizes of $\text{Cu}_{1-x}\text{Co}_x\text{Fe}_2\text{O}_4$

x	FWHM (°)	Obs. $a=b=c$ (Å)	Cal. $a=b=c$ (Å)	V (Å) ³	D (nm)
0.00	0.266	8.347	8.347	581.618	29.85
0.33	0.192	8.360	8.360	584.277	43.44
1.00	0.217	8.406	8.407	594.081	38.42

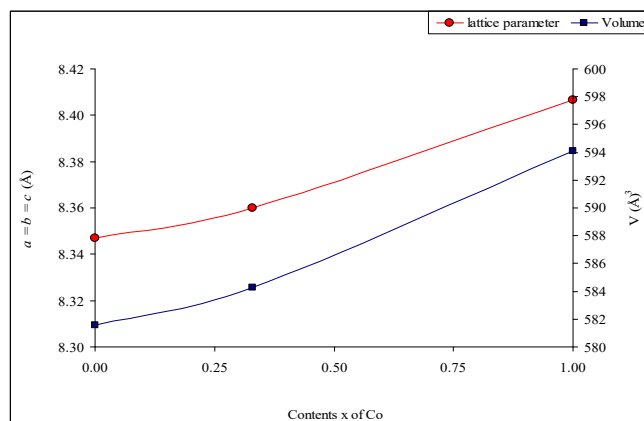


Figure 5. Variations of the lattice parameters and the unit cell volumes with increase in concentration of Co of the $\text{Cu}_{1-x}\text{Co}_x\text{Fe}_2\text{O}_4$ ($x = 0.00, 0.33$ and 1.00) samples

Microstructural Analysis

As more and more attentions have been devoted to the sub-micro magnetic materials for their unique properties compared to their bulk counterparts, the scientific interest on copper-cobalt ferrite is on the rising. SEM micrographs of the $\text{Cu}_{1-x}\text{Co}_x\text{Fe}_2\text{O}_4$ ($x = 0.00, 0.33$ and 1.00) samples are shown in Figure 6(a – c).

In Figure 6(a), the grain shape of the sample is non-uniform rod shape with clear grain boundary. The grain sizes of the sample are in the range of $0.40 \mu\text{m} - 2.00 \mu\text{m}$. As shown in SEM micrograph of Cu-Co ferrite, the grain shape of the sample is non-uniform rectangular shape. The grain sizes of the sample are in the range of $1.00 \mu\text{m} - 8.50 \mu\text{m}$. In Figure 6(a) and (b), some pores are found due to the decomposition of starting materials.

In Figure 6(c), the grain shape of the sample is spherical shape and the grain sizes are in the range of $0.20 \mu\text{m} - 0.75 \mu\text{m}$. Most of samples are found to homogeneous and poor grain boundary. SEM micrographs show that the grain shape of the samples depends on the addition of Co (or composition of desired materials).

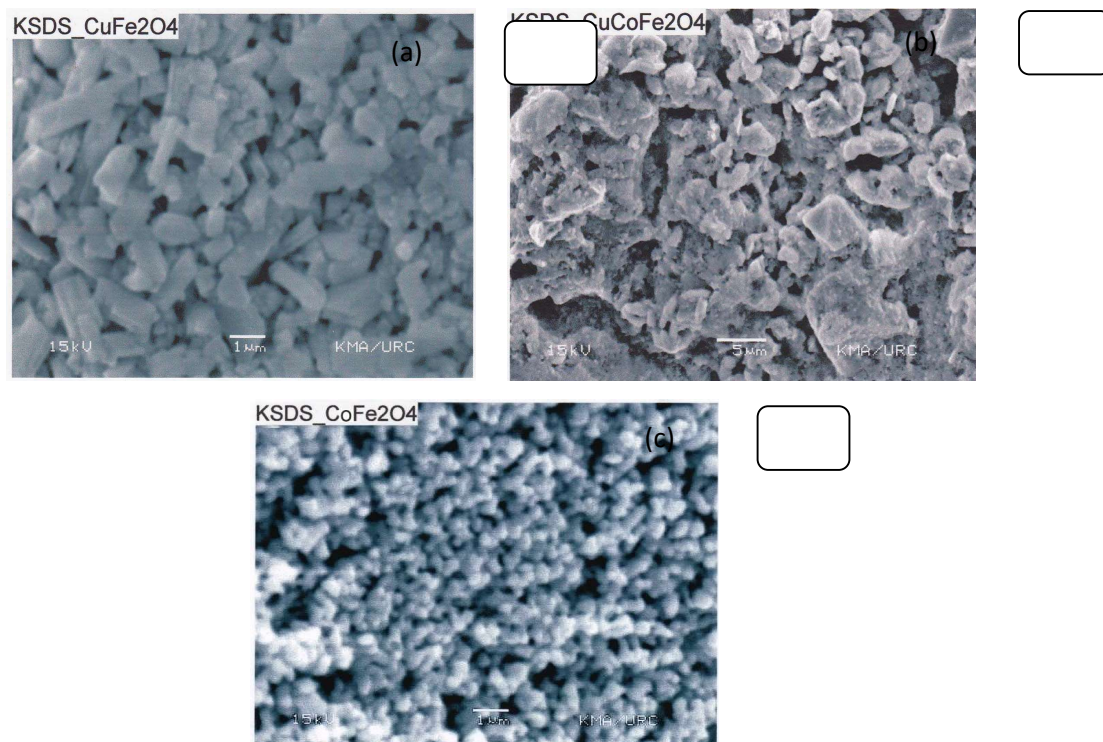


Figure 5. SEM micrographs of $\text{Cu}_{1-x}\text{Co}_x\text{Fe}_2\text{O}_4$ for (a) $x = 0.00$, (b) $x = 0.33$ and (c) $x = 1.00$

Temperature Dependent Electrical Conductivity Study

The research in the field of Solid-State Ionic encompasses investigations of the physical and chemical behavior of the solids with fast ion movement within the bulk as well as the technological aspects. These materials widely refer to as “Superionic Solids” or “Solid Electrolytes” or “Fast Ion Conductors”, show tremendous scope to develop all solid-state mini/micro electrochemical devices viz. batteries, fuel cells, sensors, photoelectrochemical solar cells (PECSC) etc. For all-solid-state electrochemical device applications, these solids should have following characteristic properties:

- Ionic conductivity should be high ($\sim 10^{-1} - 10^{-4} \text{ S cm}^{-1}$) and the electronic conductivity should be negligibly small ($< 10^{-8} \text{ S cm}^{-1}$).
- Activation energy should be low ($< 1 \text{ eV}$).

- Ions should be the principal charge carriers and ionic transference number should be close to unity (i.e. $t_{\text{ion}} \sim 1$). They should be a single ion (preferable cation) conducting solids.

The temperature dependent electrical conductivity σ of the ferrites obeys an Arrhenius's expression, $\sigma = \sigma_0 \exp\left(\frac{-E_a}{kT}\right)$, where, σ_0 is the pre-exponential factor, E_a is activation energy, k is Boltzmann's constant and T absolute temperature. Arrhenius's plots of the dc conductivity with reciprocal temperature of the samples are shown in Figure 7(a – c) in which the temperatures of superionic phase of the samples are indicated with coloured cycles. The graph shows that the increase in temperature leads to increase in conductivity, which is the normal behaviour of superionic materials and it obeys the well known Arrhenius relation. The higher values of temperature for the samples help the trapped charges to be librated and participate in the conduction process which results increase in conductivity. According to the conduction mechanism in ferrites, the decrease in resistivity could also be related to the increase in the drift mobility of the thermally

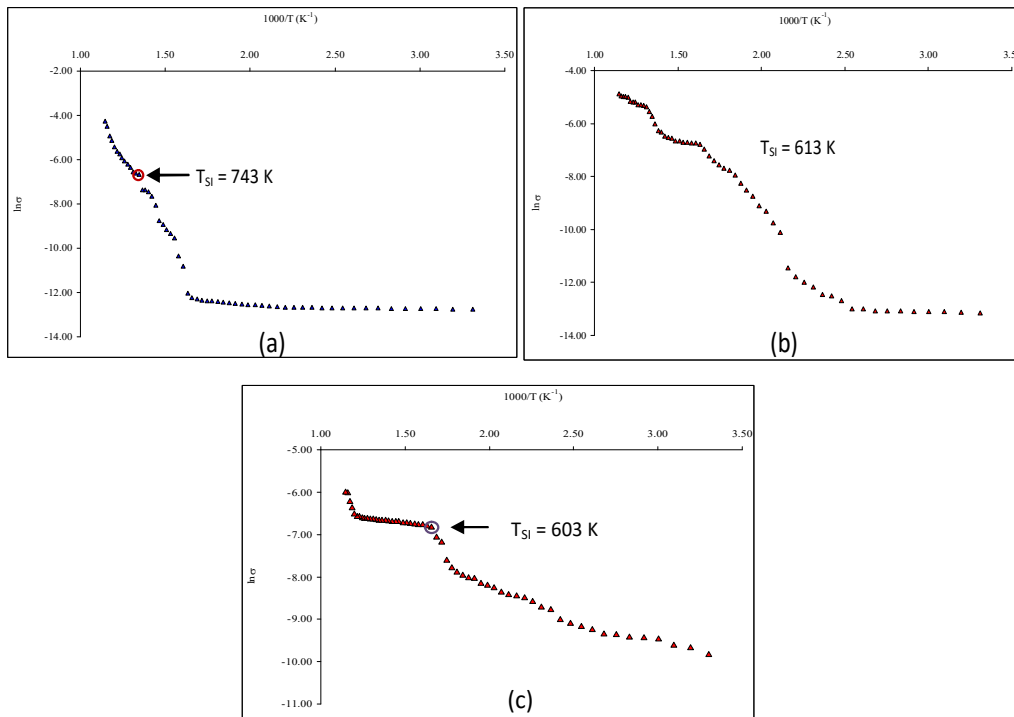


Figure 7. Arrhenius plots of the temperature dependent electrical conductivity of $\text{Cu}_{1-x}\text{Co}_x\text{Fe}_2\text{O}_4$ for (a) $x = 0.00$, (b) $x = 0.33$ and (c) $x = 1.00$

The electrical conductivity curves can be seen with two portions (temperature regions):

- (i) 303 K – 603 K and (ii) 603 K – 873 K for CuFe_2O_4 ($x = 0.00$),
- (i) 303 K – 393 K and (ii) 393 K – 873 K for $\text{Cu}_{0.67}\text{Co}_{0.33}\text{Fe}_2\text{O}_4$ ($x = 0.33$) and
- (i) 303 K – 603 K and (ii) 603 – 873 K for CoFe_2O_4 ($x = 1.00$)

to evaluate the activation energies of the samples. Plots of the variations of electrical conductivity of each of the portion of the samples are shown in Figure 8(a) and (b) for CuFe_2O_4 , Figure 9(a) and (b) for $\text{Cu}_{0.67}\text{Co}_{0.33}\text{Fe}_2\text{O}_4$ and Figure 10(a) and (b) for CoFe_2O_4 respectively. According to the theory of ionic conductivity, the slope of the electrical conductivity in each of the curves corresponding to the activation energy for creating of defect states due to the ionic motions of the sample due to thermal agitation. The activation energies are obtained as:

- (i) 0.02 eV in 303 K – 603 K and 1.20 eV in 603 K – 873 K for CuFe_2O_4 ,
- (ii) 0.0163 eV in 303 K – 393 K and 0.5200 eV in 393 K – 873 K for $\text{Cu}_{0.67}\text{Co}_{0.33}\text{Fe}_2\text{O}_4$ and
- (iii) 0.1344 eV in 303 K – 393 K and 0.0425 eV in 603 K – 873 K for CoFe_2O_4 .

The activation energies are listed in Table 2.

Temperature dependent electrical conductivities of the samples are shown in Figure 11(a – c). The electrical conductivity increases with increase in temperature.

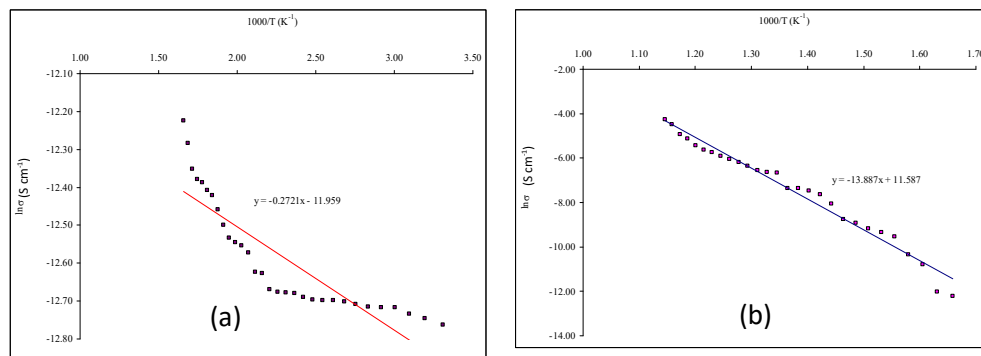


Figure 8. Plots of the variations of electrical conductivity of $\text{Cu}_{1-x}\text{Co}_x\text{Fe}_2\text{O}_4$ for $x = 0.00$ (a) in 303 K – 603 K and (b) 603 K – 873 K

The samples are exhibited as superionic conductors at high temperatures (743 K – 873 K) for CuFe_2O_4 , (613 K – 873 K) for $\text{Cu}_{0.67}\text{Co}_{0.33}\text{Fe}_2\text{O}_4$ and (603 K – 873 K) for CoFe_2O_4 due to their electrical conductivities are found to be $\sigma > 1 \times 10^{-3} \text{ S m}^{-1}$ in each of the temperature range. It can be said that a few solids conduct electricity better by ion motion than by electron motion. These unusual materials are technologically important in making batteries. All batteries have two electrodes separated by an electrolyte, which is a material that conducts ions better than electrons. Furthermore, the superionic phase temperature decreased with increase in concentration of Co on CuFe_2O_4 .

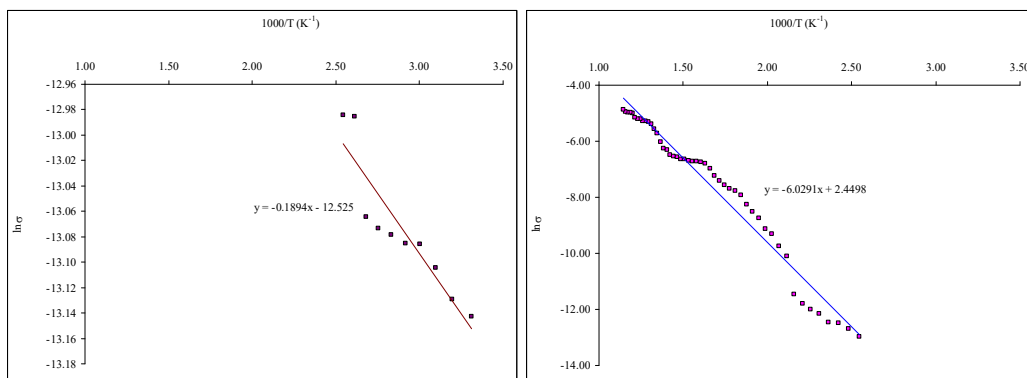


Figure 9. Plots of the variations of electrical conductivity of $\text{Cu}_{1-x}\text{Co}_x\text{Fe}_2\text{O}_4$ for $x = 0.33$ (a) in 303 K – 393 K and (b) 393 K – 873 K

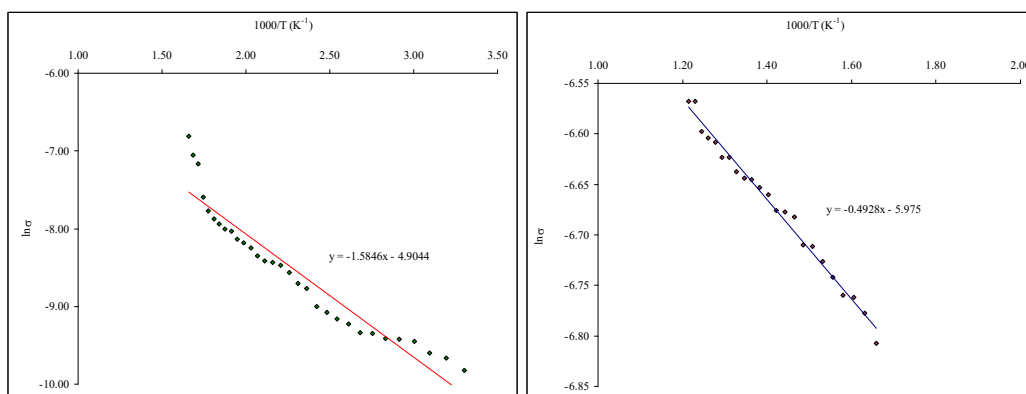


Figure 10. Plots of the variations of electrical conductivity of $\text{Cu}_{1-x}\text{Co}_x\text{Fe}_2\text{O}_4$ for $x = 1.00$ (a) in 303 K – 603 K and (b) 603 K – 873 K

Table 2. The activation energies of $\text{Cu}_{1-x}\text{Co}_x\text{Fe}_2\text{O}_4$

x	Temperature range (K)	E_a (eV)
0.00	303 - 603	0.02
	603 - 873	1.20
0.33	303 - 393	0.02
	393 - 873	0.52
1.00	303 - 603	0.13
	603 - 873	0.04

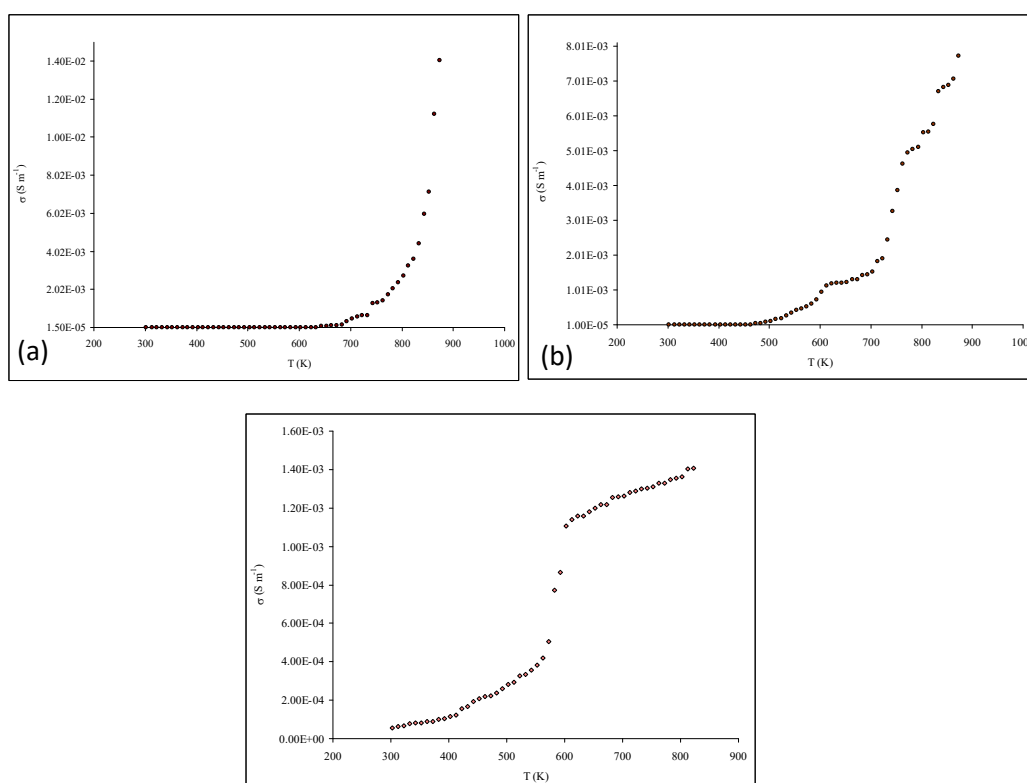


Figure 11. Plots of the variation of electrical conductivity with temperature of $\text{Cu}_{1-x}\text{Co}_x\text{Fe}_2\text{O}_4$ for (a) $x = 0.00$, (b) $x = 0.33$ and (c) $x = 1.00$

Conclusion

$\text{Cu}_{1-x}\text{Co}_x\text{Fe}_2\text{O}_4$ (where $x = 0.00, 0.33$ and 1.00) were prepared by chemical co-precipitation method and their structural, microstructural and electrical conductivities were reported in this work. XRD patterns reveal that the investigated samples analogous to cubic structure. The obtained crystallite sizes indicated that the samples were nanosized materials and very fine particles. SEM micrographs represented three different grain shapes of non-uniform rod for pure Cu ferrite, non-uniform rectangular for Cu-Co ferrite and spherical for pure Co ferrite. Some pores were found in the SEM micrographs due to the decomposition of starting materials in the sample preparation process. The electrical conductivities of the samples were found to be increased with increase in temperature. The samples exhibited as the superionic conductors in the high temperature. The superionic phase temperatures (T_{SI}) of the samples were found to be decreased with increased in Co concentration and found at 743 K for pure Cu ferrite, 613 K for Cu-Co ferrite and 603 K for pure Co ferrite. Except the second portion of the temperature range of pure Cu ferrite, the activation energy of others portions and temperature ranges of the samples were obtained as lower than 1 eV. According to experimental results, the samples can be used as the solid electrolyte materials. Furthermore, from the experimental point of view, pure CoFe_2O_4 is the most suitable for the application of solid electrolyte material because it has the lowest superionic conductor phase temperature.

Acknowledgement

The authors would like to acknowledge Professor Dr Khin Khin Win, Head of Department of Physics, University of Yangon, for her kind permission to carry out this work.

References

1. Fang, J., Sharma, M. & Tang, J. (2003). Ultrafine NiFe₂O₄ powder fabricated from reverse microemulsion process. *Journal of Applied Physics*, 93(10), pp. 7843-7845.
2. Harris, V.G., He, P., Parimi, P.V., Zuo, X., Patton, C.E., Abe, M., Cher, O. & Vittoria, C. (2009). Recent advances in processing and applications of microwave ferrites. *Journal of Magnetization and Magnetic Materials*, 321, pp. 2035-2047.
3. Kumar, N., Kumar, V., Arora, M., Sharmar, M., Singh, B. & Pant, R.P. (2009). Synthesis of Mn_{0.2}Zn_{0.8}Fe₂O₄ particles by high energy ball milling and their applications. *Indian Journal of Engineering and Materials Science*, 16, pp. 410-414.
4. Rani, R., Batoo, K.M. & Singh, M. (2013). Electric and Dielectric Study of Zinc Substituted Cobalt Nanoferrites Prepared by Solution Combustion Method. *American Journal of Nanomaterials*, 1, pp. 9-12.
5. Shutka, A., Mezinskis, G. & Pludon, A. (2010). Preparation of dissimilarly structured ferrite compounds by sol-gel auto-combustion method. *Chemical Technology*, 1(54), pp. 41-46.
6. Tailhades, Ph., Villette, C., & Rousset, A. (1998). Cation Migration and Coercivity in Mixed Copper-Cobalt Spinel Ferrite Powders. *Journal of Solid State Chemistry*, 141, pp. 56-63.

STRUCTURAL, THERMAL AND ELECTRICAL CHARACTERISTICS OF NICKEL POTASSIUM SULPHATE HEXAHYDRATE (NPSH) CRYSTAL

Win Win Mon¹, Aye Aye Lwin², Kywe Kywe Aung³ & Win Kyaw⁴

Abstract

Single crystals of Nickel Potassium Sulphate Hexahydrate, $\text{NiK}_2(\text{SO}_4)_2 \cdot 6\text{H}_2\text{O}$ (NPSH) were grown by slow evaporation of saturated solution containing equimolar ratio of Nickel Sulphate Hexahydrate, $\text{NiSO}_4 \cdot 6\text{H}_2\text{O}$, and Potassium Sulphate, K_2SO_4 , salt powders. Structural analysis of the green colour crystal was investigated by XRD method. The crystal was characterized by simultaneous Thermogravimetric and Differential Thermal Analysis (TG-DTA) method to study the high temperature phases of dehydration and meeting of the crystal. Electrical conductivity with temperature of the crystal was investigated in the temperature range of 299 K – 653 K. Dehydration temperature ($T_{\text{dehydration}}$) of the crystal was determined from the ($\ln \sigma$ vs $1000/T$) relationship. The activation energies of the crystal in the $T \leq T_{\text{dehydration}}$ and $T \geq T_{\text{dehydration}}$ regions were evaluated in this work.

Keywords: Nickel Potassium Sulphate Hexahydrate, XRD, TG-DTA, Electrical conductivity

Introduction

Crystals of Nickel Potassium Sulphate hexahydrate, $\text{NiK}_2(\text{SO}_4)_2 \cdot 6\text{H}_2\text{O}$ (abbreviated as NPSH) have attracted attention recently because of their "order - disorder" dynamics of SO_4^{2-} dipoles. NPSH crystal belongs to the isomorphous series of sulphates of which Nickel Cesium Sulphate Hexahydrate, $\text{NiCs}_2(\text{SO}_4)_2 \cdot 6\text{H}_2\text{O}$ (abbreviated as NCSH) is a member [Dhandapani, (2006); Zhaung, (2006)]. The crystalline hexahydrate, for example, form is found in two known phases: α -phase: blue to blue-green tetragonal crystals β -phase: green transparent crystals (stable at 40°C) [Kasatkin, (2002)]. The α to β phase transition occurs at 53.3°C

¹ Dr, Demonstrator, Department of Physics, Hpa-an University

² Dr, Lecturer, Department of Physics, Bago University

³ Dr, Associate Professor, Department of Physics, Hpa-an University

⁴ Dr, Associate Professor, Department of Physics, Sagaing University

[Theivanayagom, (2001)]. Nickel Sulphate Hexahydrate, $\text{NiSO}_4 \cdot 6\text{H}_2\text{O}$ is a water soluble salt which forms hexahydrate (six water) molecules. It is a green colour. Potassium sulphate, K_2SO_4 is used in the production of fertilizers and potassium alums. It is a water soluble salt and it is white colour powder. In this work, $\text{NiK}_2(\text{SO}_4)_2 \cdot 6\text{H}_2\text{O}$ crystals were grown and characterized by X-ray Diffraction (XRD) Simultaneous Thermogravimetric Analysis and Differential Thermal Analysis (TG-DTA) and temperature dependent electrical conductivity measurements.

Materials and Method

Growth of $\text{NiK}_2(\text{SO}_4)_2 \cdot 6\text{H}_2\text{O}$ (NPSH) Crystal

$\text{NiK}_2(\text{SO}_4)_2 \cdot 6\text{H}_2\text{O}$ (NPSH) Crystals were grown by slow evaporation method from the starting materials of Nickel Sulphate Hexahydrate, $\text{NiSO}_4 \cdot 6\text{H}_2\text{O}$ and Potassium Sulphate, K_2SO_4 . Distilled-water was used as the solvent to grow the crystal. The chemical equation was as follow:



As indicated above chemical reaction, in the present work, the crystals were grown by using equimolar ratio of $\text{NiSO}_4 \cdot 6\text{H}_2\text{O}$ and K_2SO_4 . Firstly, starting materials were weighted and mixed each others. The mixed salt powders were placed into the beaker. Distilled-water was added and stirred with glass stick to occur the chemical reaction and then heat treated to get super saturated solution. The solution was filtered into the beaker and covered with very thin plastic. The solution was placed at room temperature (28°C) for seven days.

The seed crystals may be withdrawn in the saturated solution and collected with tweezers placed on filtered paper to dry. A perfect like (good quality or transparent and homogeneous) seed crystal was selected and placed into the saturated solution to get a large (enough size) crystal. After two months, the enough sized crystal was obtained. At room temperature, $\text{NiK}_2(\text{SO}_4)_2 \cdot 6\text{H}_2\text{O}$ mixed crystal is green in colour. Photograph of the as-grown NPSH crystal (19.90 mm in length) is shown in Figure 1.



Figure 1. Photograph of the as-grown $\text{NiK}_2(\text{SO}_4)_2 \cdot 6\text{H}_2\text{O}$ (NPSH) crystal

XRD Measurement

Structural analysis and lattice parameters evaluation of the crystal were investigated by XRD method. XRD pattern was observed by RIGAKU MULTIFLEX X-ray Diffractometer (Universities' Research Centre (URC), University of Yangon) using Ni-filter with $\text{CuK}\alpha$ radiation, $\lambda = 1.54056 \text{ \AA}$.

TG-DTA Measurement

The Differential Thermal Analysis (DTA) measurement with higher accuracy was carried out along with Thermo-Gravimetric Analysis (TGA) using the (SHIMADZU) DTG-60H Thermal Analyzer. This measurement was performed at Universities' Research Centre (URC), University of Yangon. In this work, 4.510 mg powdered sample was used to analyze the high temperature phases. Aluminum (Al) pan was used as the standard sample.

Electrical Conductivity Measurement

For the electrical conductivity measurement, the crystal was cut to get the dimensions of $(1.29 \times 1.29 \times 0.34) \text{ cm}^3$. Then the crystal was fixed on glass plate and silver contacts were made over the sample to ensure good electrical contacts. Temperature dependent electrical resistances were observed in the temperature range of 299 K – 653 K. Photograph of the

experimental set-up of temperature dependent resistances measurement is shown in Figure 2. The resistances of the sample were measured by using FLUKE 45 DUAL DISPLAY MULTIMETER. CAHO SR-T903 and K-type thermocouple were used as the temperature controller and temperature sensor. 300 W heater coil was inserted into the cylindrical copper holder (2.50 cm in diameter and 12.00 cm in length) that used as the heating element.

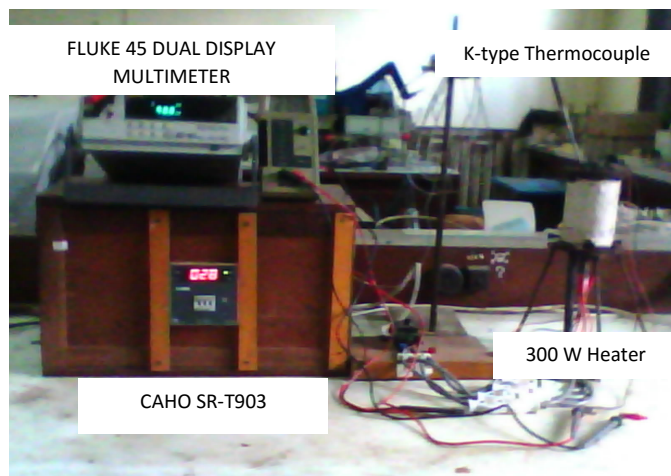


Figure 2. Photograph of the experimental setup for the temperature dependent resistance measurement

Results and Discussion

XRD Study

XRD pattern of the NPSH crystal is shown in Figure 3. The observed diffraction lines were identified by JCPDS to examine the crystal structure and to investigate the lattice parameters. The observed XRD lines were assigned by standard JCPDS data library file of Cat. No. 35-0760 > $K_2Ni(SO_4)_2 \cdot 6H_2O$ - Potassium Nickel Sulphate Hydrate. The appearance of the intensities of the diffraction peaks demonstrates the good crystal quality of NPSH crystal. The line at the diffraction angle 21.54° or (111) plane was the strongest in intensity among the observed XRD lines. XRD pattern shows that the crystal belongs to orthorhombic structure. The lattice parameters are evaluated by using crystal utility of the equation of

$$\frac{1}{d^2} = \frac{h^2}{a^2} + \frac{k^2}{b^2} + \frac{l^2}{c^2} = \frac{4 \sin^2 \theta}{\lambda^2}$$
 where a , b and c are the lattice parameters (Å), d is the atomic spacing (Å), λ is the wavelength of incident X-ray (Å) and (hkl) is the miller indices. The lattice parameters were obtained as $a = 15.80$ Å, $b = 12.19$ Å and $c = 5.91$ Å respectively.

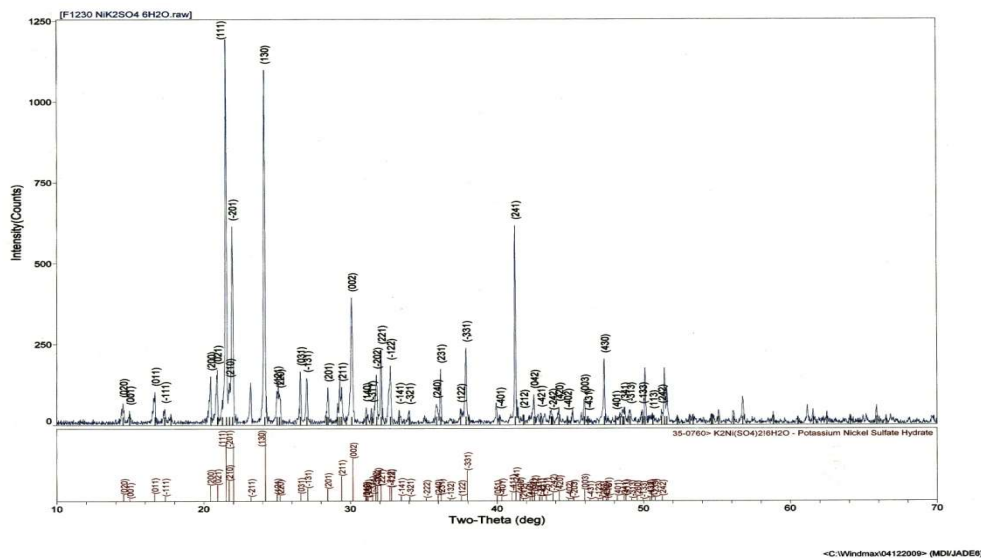


Figure 3. XRD pattern of $\text{NiK}_2(\text{SO}_4)_2 \cdot 6\text{H}_2\text{O}$ (NPSH) crystal

TG-DTA Study

TG-DTA thermograms of NPSH crystal are shown in Figure 4. As shown in observed TGA thermogram, one step mass variation (weight loss) of the $\text{NiK}_2(\text{SO}_4)_2 \cdot 6\text{H}_2\text{O}$ (NPSH) sample occurs between the temperature range of 39°C and 600°C with the weight loss is about 27.85%. This step takes place the dehydration of six water molecules from the $\text{NiK}_2(\text{SO}_4)_2 \cdot 6\text{H}_2\text{O}$ (NPSH) to anhydrous compound of $\text{NiK}_2(\text{SO}_4)_2$ (NPS). The deep endothermic reaction peak in DTA thermogram around 180°C that indicates the dehydration of six water molecules from hydrated to anhydrous compound. One exothermic reaction peak in DTA thermogram around 333°C indicates the irreversible characteristic of the $\text{NiK}_2(\text{SO}_4)_2 \cdot 6\text{H}_2\text{O}$ (NPSH) sample after heating or it is not recovered when cool-down to room temperature.

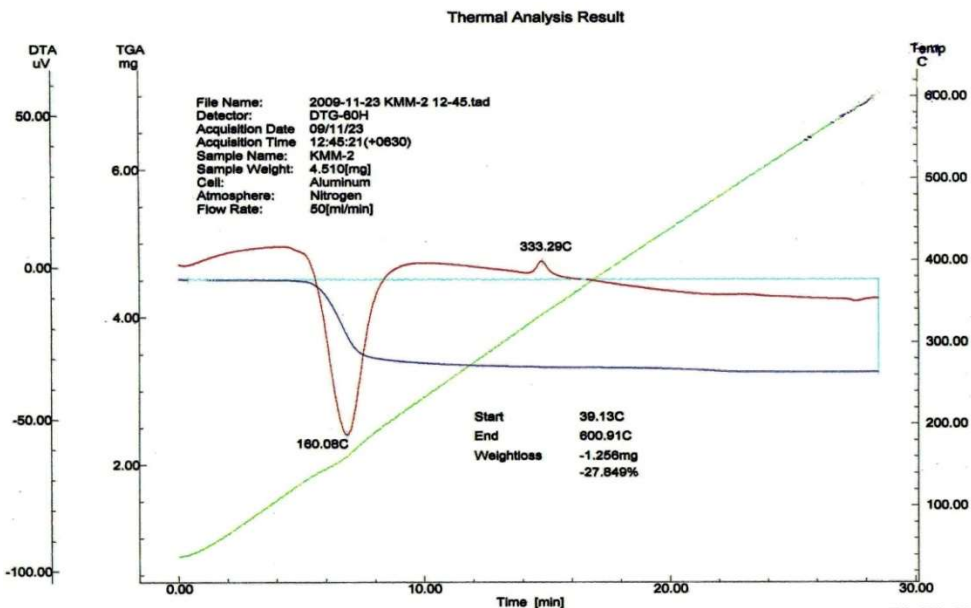


Figure 4. TG-DTA thermograms of $\text{NiK}_2(\text{SO}_4)_2 \cdot 6\text{H}_2\text{O}$ (NPSH) crystal

Temperature Dependent Electrical Conductivity Study

The electrical conductivity of a crystal obeys an Arrhenius formula, $\sigma = \sigma_0 \exp(-E_a/kT)$ where σ is the conductivity (S m^{-1}), σ_0 is the pre-exponential factor, E_a is the activation energy, k is the Boltzmann constant and T is the absolute temperature (K). In the present work, Arrhenius plot of the variation of dc electrical conductivity of the NPSH crystal in the temperature range of 299 K – 653 K is shown in Figure 5. Slope of the curve is found to be changed at 433 K in which the $\text{NiK}_2(\text{SO}_4)_2 \cdot 6\text{H}_2\text{O}$ (NPSH) undergoes to $\text{NiK}_2(\text{SO}_4)_2$ (NPS) and it can be taken as the dehydration temperature ($T_{\text{dehydration}}$) of the crystal.

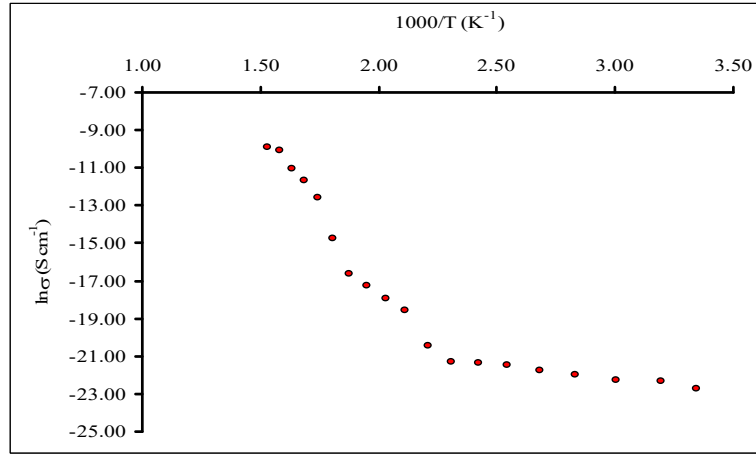


Figure 5. Plot of the variation of dc conductivity of the NPSH crystal in the temperature range of 299 K – 653 K

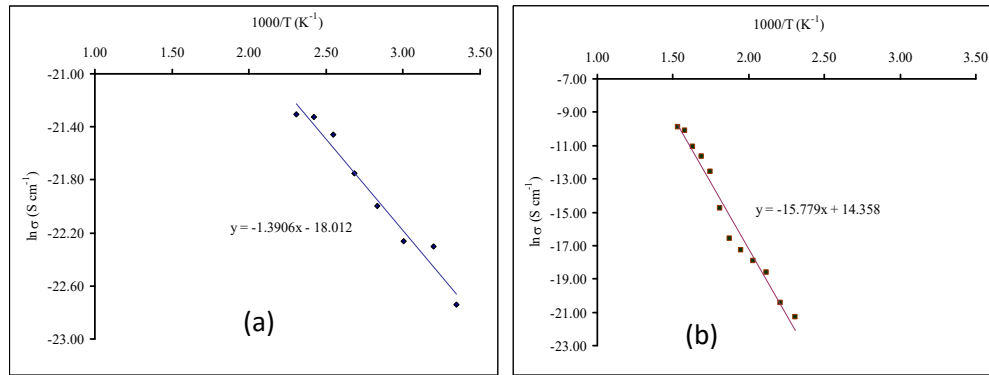


Figure 6. Plots of the variation of dc conductivity of the NPSH crystal in the temperature range of (a) 299 K – 433 K and (b) 433 K – 623 K

The electrical conductivity (σ) of the crystal for $T \leq T_{\text{dehydration}}$ can be written in the form:

$$\begin{aligned} \sigma &= \sigma_0 \exp(-E_a / kT) \\ \ln(\sigma) &= -E_a / kT + \ln(\sigma_0) \\ &= (-E_a / k)(1/T) + \ln(\sigma_0) \end{aligned}$$

Comparing the above equation with the experimental linear equation, $y = mx + c$, where the value of slope will give the value of $(-\frac{E_a}{k})$. From Figure 6(a), the activation energy E_a can be evaluated as follows:

$$\begin{aligned}\frac{E_a}{k} &= 1.3906 \times 1000 \\ E_a &= 1.3906 \times 1000 \times k \\ E_a &= 1.3906 \times 1000 \times 1.38 \times 10^{-23} \\ E_a &= 1.919 \times 10^{-20} \text{ J} \\ E_a &= 0.12 \text{ eV}\end{aligned}$$

The obtained activation energy and electrical conductivity of the crystal over the dehydration temperature ($T \geq T_{\text{dehydration}}$) are greater than that of before ($T \leq T_{\text{dehydration}}$) and as presented in Table 1. From the experimental results, the electrical conductivity of the crystal increased with increase in temperature.

As shown in Figure 6(a), electrical conductivity of the crystal is slowly increased with increasing temperature range about 299 K – 593 K in which the crystal is exhibited as a normal ionic conductor or normal inorganic salt. After reaching the temperature at 593 K, electrical conductivity of the crystal is abruptly increased until up to pre-melting temperature 613 K. The observed value of electrical conductivity at the temperature 613 K is obtained as $1.5608 \times 10^{-5} \text{ S cm}^{-1}$.

However, the activation energy of the sample under the dehydration temperature ($T \leq T_{\text{dehydration}}$) is obtained as 0.12 eV and the electrical conductivity curve over $T \geq T_{\text{dehydration}}$ of the sample is shown in Figure 6(b). Experimental results of conductivity (σ) and $(\ln \sigma)$ are tabulated in Table 2.

Table 1. Activation energies of the NPSH crystal in different temperature regions

<i>Temperature range (K)</i>	<i>Activation energy (eV)</i>
299 - 433	0.1200
433 - 653	1.3616

Table 2. Experimental data of electrical conductivity measurement of the NPSH crystal

T (K)	1000/T (K⁻¹)	R (Ω)	σ (S cm⁻¹)	ln σ
299	3.3445	1.55E+09	1.3262E-10	-22.7435
313	3.1949	9.97E+08	2.0618E-10	-22.3023
333	3.0030	9.57E+08	2.1479E-10	-22.2613
353	2.8329	7.35E+08	2.7967E-10	-21.9974
373	2.6810	5.76E+08	3.5687E-10	-21.7536
393	2.5445	4.29E+08	4.7916E-10	-21.4590
413	2.4213	3.76E+08	5.4670E-10	-21.3271
433	2.3095	3.69E+08	5.5707E-10	-21.3083
453	2.2075	1.57E+08	1.3093E-09	-20.4538
473	2.1142	2.43E+07	8.4453E-09	-18.5897
493	2.0284	1.24E+07	1.6537E-08	-17.9177
513	1.9493	6.49E+06	3.1673E-08	-17.2678
533	1.8762	3.33E+06	6.1729E-08	-16.6005
553	1.8083	5.35E+05	3.8422E-07	-14.7720
573	1.7452	6.02E+04	3.4146E-06	-12.5875
593	1.6863	2.36E+04	8.7175E-06	-11.6502
613	1.6313	1.32E+04	1.5608E-05	-11.0677
633	1.5798	4.94E+03	4.1611E-05	-10.0871
653	1.5314	4.13E+03	4.9772E-05	-9.9081

Conclusion

Crystals of Nickel Potassium Sulphate Hexahydrate $\text{NiK}_2(\text{SO}_4)_2 \cdot 6\text{H}_2\text{O}$ (NPSH) have been grown by the slow evaporation of aqueous solution. Structural, thermal and temperature dependent electrical characteristics were reported in this paper. Experimental results are concluded as follows:

XRD pattern indicates that the $\text{NiK}_2(\text{SO}_4)_2 \cdot 6\text{H}_2\text{O}$ (NPSH) crystal belongs to orthorhombic structure at room temperature. Lattice parameters of the crystals are obtained as $a = 15.80 \text{ \AA}$, $b = 12.19 \text{ \AA}$ and $c = 5.91 \text{ \AA}$ respectively.

TG-DTA thermograms of NPSH crystal give the one step mass variation from NPSH to NPS occurs in the temperature range of $39^\circ\text{C} - 600^\circ\text{C}$ due to the dehydration. The deep endothermic reaction peak in DTA thermogram around 180°C that also indicates the dehydration of six water molecules. One exothermic reaction peak in DTA thermogram around 333°C indicates the irreversible characteristic of the $\text{NiK}_2(\text{SO}_4)_2 \cdot 6\text{H}_2\text{O}$ (NPSH) crystal.

Electrical conductivities with temperatures of the crystal were increased with increasing temperatures. The measurement of σ show anomalous behaviour at the transition point about 433 K. It is the dehydration temperature ($T_{\text{dehydration}}$) of the crystal. The σ -T relationship reveals activation energy of 0.12 eV below ($T \leq T_{\text{dehydration}}$) and 1.3616 eV above ($T \geq T_{\text{dehydration}}$) the dehydration temperature. The observed electrical conductivity at the temperature range about 613 K is $\sim 1.5608 \times 10^{-5} \text{ S cm}^{-1}$ that indicates the superionic conductivity of the sample. Thus $\text{NiK}_2(\text{SO}_4)_2 \cdot 6\text{H}_2\text{O}$ (NPSH) crystal can be used as the solid electrolyte materials at high temperature.

Acknowledgement

The authors would like to acknowledge Professor Dr Win Win Thar, Professor and HOD(Rtd.), Department of Physics, Dagon University, for her valuable suggestions and comments.

References

1. Dhandapani, M., Thyagu, L. & Srinivasan, V. (2006). Synthesis and characterization of potassium magnesium sulphate hexahydrate crystals. *Crystal Research Technology*, 41(4), 328-331.
2. Kasatkin, I.A. (2002). Interferometric Study of $\text{MgSO}_4 \cdot 7\text{H}_2\text{O}$ Single Crystal Growth Kinetics from Solution. *Crystal Research Technology*, 37(2-3), 193-205.
3. Theivanayagam, M. & Mahadevan, C. (2001). Lattice variation and thermal parameters of $\text{Ni}_x\text{Mg}_{1-x}\text{SO}_4 \cdot 7\text{H}_2\text{O}$ single crystals. *Bulletins Materials Science*, 24(5), 441-444.
4. Zhung, X., Su, G., He, U. & Zheng, G. (2006). Growth and characterisation of potassium cobalt nickel sulfate hexahydrate for UV light filters. *Crystal Research Technology*, 41(10), 1031-1035.

INVESTIGATION OF ZnO/ITO THIN FILMS ON STRUCTURAL, OPTICAL AND ELECTRICAL PROPERTIES

Saw Shine Ko¹, Thida Win², Than Than Win³ and Yin Maung Maung⁴

Abstract

The investigations of structural, optical and electrical properties of ZnO/ITO thin films have been presented. The ZnO nanocrystalline thin films were prepared by Chemical Bath Deposition method. Zinc chloride and sodium hydroxide (NaOH) were used as precursor materials. Thin films of ZnO were deposited onto ITO (indium tin oxide) substrate post annealed temperature at 300°C, 400°C in the muffle furnace. X-ray diffraction (XRD) of the ZnO films showed hexagonal structure. Debye Scherrer equation was used to calculate crystallite size. Scanning electron microscopy (SEM) study provides better topographic feature of the sample surface. The optical band gap was analyzed by absorption spectra of ZnO. $1/C^2 - V$ properties of ZnO thin films were determined from C-V measurement. The photovoltaic properties of these films were investigated by current density-voltage characteristic. The photoconversion efficiency was influenced by the open-circuit voltage.

Keywords: *X-ray diffraction, Scanning electron microscopy, Optical band gap, photo conversion efficiency*

Introduction

A solar cell (also called a photovoltaic cell) is an electrical device that converts the energy of light directly into electricity by the photovoltaic effect. It is a form of photoelectric cell (in that its electrical characteristics e.g. current, voltage, or resistance vary when light is incident upon it) which, when exposed to light, can generate and support an electric current without being attached to any external voltage source. By the basic nature of photovoltaic phenomena, it follows that a photovoltaic devices should essentially be comprised of the absorbed layer and the window (buffer layer). In selecting suitable absorber materials, there are three important materials parameters need to be considered, band gap, absorption coefficient and minority carrier

¹. PhD Candidate, Physics Department, University of Yangon

². Physics Department, Mandalay University of Distance Education

³. Physics Department, Mandalay University

diffusion length. Solar cell devices can be divided into three major categories: silicon solar cells, inorganic compound semiconductor solar cells and organic solar cells.

At present, crystalline silicon solar cells have high photovoltaic conversion efficiency, but production cost is high. For amorphous silicon solar cells, the production cost can be significantly reduced, but the main problem is that the photovoltaic conversion efficiency is low. Organic solar cells in general have a severe problem of poor stability. As an alternative, a compound semiconductor solar cells are considered to increase the conversion efficiency and effectively reduce production cost. Chemical Bath Deposition technology is based on slow controlled precipitation of the desired compound from its ions in a reaction bath solution. A ligand or complexing agent acting as a catalysts is usually employed to control the reaction in a suitable medium as indicated by the pH to obtain crystal growth. Otherwise, spontaneous reaction and sedimentation of materials will be obtained. The key point of CBD technique are low cost, large area and relatively low deposition temperature. Accordingly, CBD technique is becoming an important deposition technique for thin film of compound materials like chalcogenides, oxides and halides. However, CBD has some drawbacks in the classical beaker configuration, the material yield for film formation is very low, about a few percent, leading to an un-necessary waste production and increased treatment costs. The reason is that the volume to surface ratio is very high and that only a small part of the solution is contributing to the film formation, the remaining one leading to the formation of colloids in the bulk of the solutions. Also, it suffers from the formation of particles that leads not only to the generation of a lot of waste but also the creation of defects in the deposition film. [Danaher W.J and Lyons L.E ,1978] and [Basol B.M,1984] . Metal oxide semiconductor thin film have been widely researched and have received considerable attention in recent years due to their optical and electrical properties. Because they are good for transparent conducting oxide (TCO) films [Hongxia,2005]. Zinc oxide is a wide band gap ($\sim 3.37\text{eV}$ at $T=300\text{K}$) semiconductor (II-VI) which has been widely investigated in the past years for more literature. ZnO also has a high exciton binding energy of 60meV which is higher than the value of other used band gap materials [Zahedi and Darini ,2012]. ZnO increasingly attracted attention due to its excellent chemical stability, non-toxicity, good electrical,

optical and piezoelectric property. Since, the properties of ZnO strongly depend on its morphology and microstructure, ZnO thin film have been studied as the active channel materials in thin film transistors development because of its exhibiting n-type semiconductor characteristic and excellent thermal stability and can be well oriented crystalline on various substrates. [Masuda,2003] and [Ramamoorthy K , 2004]. Zinc oxide has one of the most promising materials and has a lot of research in interest due to the unique structure and crystallite size dependent electrical, optical and mechanical properties. ZnO nanostructure were studied extensively owing to their potential applications in nano-devices and optical materials. Different techniques to synthesize nano and micro range phosphor such as Spray pyrolysis, plasma enhanced chemical vapour deposition, sol-gel, sputtering, pyrolysis, solid state reaction, co-precipitation and combustion which have been used. In recent time, much interest has been generated around the chemical route technique. This technique is cost, effective, reproducible and the material are readily available material. As compared to other oxide material ZnO is much cheaper and easily available materials. Another advantages of the CBD method over other method is that the film can be deposited at different shapes and size of substrates [Vijayan .T.A, 2008] and [Widoyastuti W,2014]. ITO films have been widely used as Transparent conductive oxide (TCO) in electronic and optoelectronic devices. (such as flat panel solar cells). A series of ITO films are mostly deposited on P-type silicon or glass substrates at room temperature. The carrier concentration in the indium tin oxide film increases, the conductivity of the ITO film will be improved distinctly. In ITO films, the doped tin oxide SnO₂ ions in the ITO films diffuse from grain boundaries and interstitial position into the substitutional position of indium site and the four valence Sn ion is activated and contributes free carriers. ITO film deposited onto the silicon or glass substrate can be used as the antireflection layer. [GAO Mei-Zhen et al.,2008].

Experimental

Film deposition

5.5g of Zinc chloride is dissolved in 100 ml of distilled water. It is stirred continuously with magnetic stirrer and its temperature is raised to 63.8°C. Once the temperature of zinc chloride solution is reached 63.8°C, add 5g of NaOH dissolved in 25ml deionized water solution poured drop by drop touching the walls of the container by using burette. The aqueous solution turned into a milky white colloid without any precipitation. The reaction was allowed to proceed for two hours after complete addition of sodium hydroxide. After the complete reaction, the Indium Tin Oxide (ITO) glass substrate was immersed vertically at the center of reaction bath solution in such a way that it should not touch the walls of the container. Triethanolamine (TEA) 8ml was used drop by drop either directly or as aqueous solution with varying concentration of TEA to prepare various samples. The deposited layer were post annealed or heated inserted into evaporate solvent and organic residuals. The annealing temperature used in this research were 300°C and 400°C respectively.

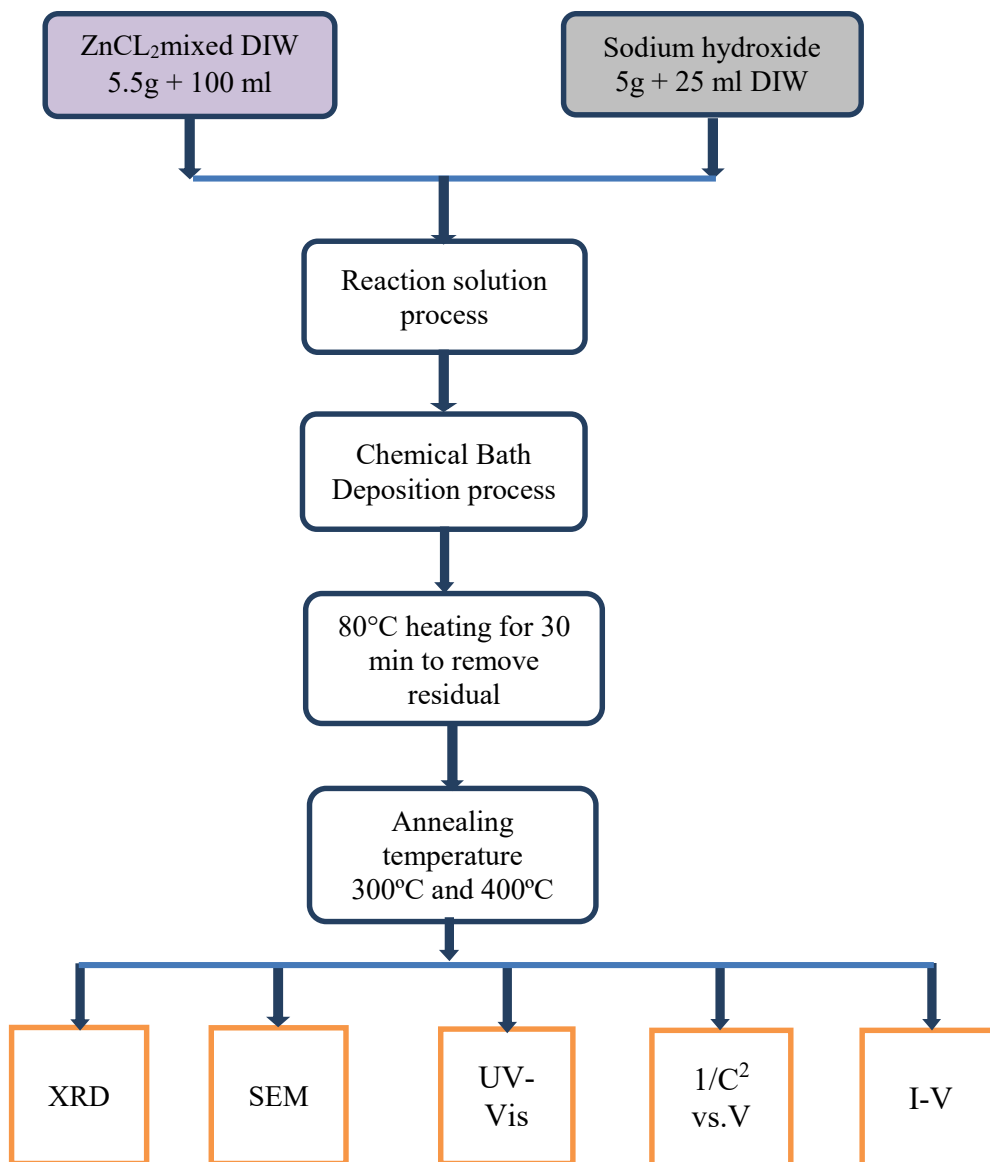


Figure 1. Flow chart of preparation for ZnO/ ITO thin film on ITO glass substrate by using Chemical Bath deposition at various annealing temperature.

Result and Discussion

Structural properties of ZnO/ITO thin film by XRD

To examine the crystal structure and phase formation of ZnO/ITO thin films, they were performed using monochromatic CuK α radiation ($\lambda = 1.54056 \text{ \AA}$) operated at tube voltage 40kV and 40 mA (tube current). The X-ray diffraction patterns for zinc oxide thin films were shown in Fig 2(a). The upper side of XRD profile was represented the observed profile while the lower side showed the standard JCPDS (Joint Committee on Powder Diffraction Standards). From the Fig 2(a), three of nine diffracted peaks between 30° and 40° angle were perfectly matched with those of ZnO standard. On the XRD pattern from Fig 2(b), three distinct were formed on observed spectrum. Three of eight diffracted peaks were perfectly matched with those of Zinc oxide standard. According to the XRD pattern from Fig 2(a), the (1 0 0), (0 0 2), (1 0 1), (1 0 2), (1 1 0) and (1 0 3) peaks and from Fig 2(b), (1 0 0), (0 0 2) and (1 0 1) peaks were clearly observed. They were compared the data with library or standard file. The most dominant peak was also occur at (1 0 1) for both 300°C and 400°C thin films. On the other hand, Table (1) and (2) were also indicated the value of lattice distortion for ZnO/ITO films. Bragg's angle (2θ), interplaner spacing (d-values) and crystallite size of ZnO/ITO thin films. The crystallinity of the ZnO/ITO films determined from the full width half maximum values.

$$D = \frac{k\lambda}{\beta \cos\theta} \quad \text{-----(1)}$$

Where D is the size of the crystallites, β is the full width at half maximum (FWHM) of a diffraction line located at angle θ , λ is the X-ray wavelength and k is a Scherrer's constant (0.9), which depends on the peak breadth, crystallite shape, and crystallite size distribution. The crystallite sizes were found to be increasing with increasing temperature because of the crystallite size for 300°C and 400°C ZnO/ITO thin films were found to be 28nm and 36.904nm. Improved in crystallinity quality with raising annealing temperature. As a result, oxygen defects are favorable to the merging process to form larger grains size while increasing the annealing temperature.

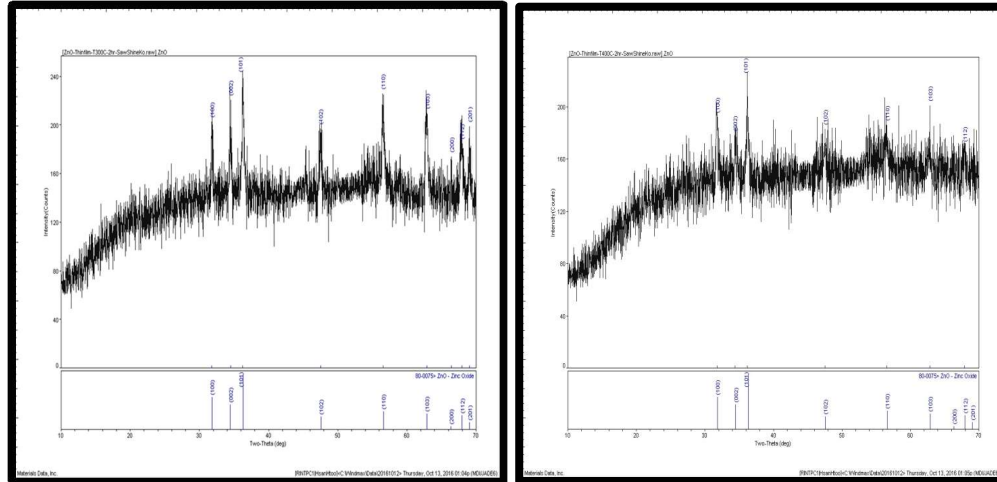


Figure 2(a) and 2(b) XRD patterns of annealed and reference JCPDS file of ZnO/ITO film annealed at 300°C and 400°C

Table 1. The values of lattice distortion for ZnO/ITO thin films

ZnO/ITO	Annealing temperature (°C)	Lattice constant		Hexagonality (c/a)
		a (Å)	c (Å)	
(1 0 1) peak	300	3.2483	5.2108	1.6042
(1 0 1) peak	400	3.2560	5.1963	1.5959

Table 2. Diffraction angle, interplaner spacing and crystallite size for (1 0 1) plane of ZnO/ITO films

ZnO/ITO	Crystallite size (nm) along diffraction planes		
	2θ(rad)	d(Å)	Crystallite size (nm)
(1 0 1) peak	36.260	2.4754	28
(1 0 1) peak	36.215	2.4784	36.904

Morphology and phase analysis

The microstructural properties of Zinc oxide thin films deposited onto ITO glass substrate were observed by SEM analysis. The width of the nanorods were measured by using well known bar code system. Bar code size was formed to be 2 μm with magnification of 13000. SEM images of Zinc oxide thin films on the ITO glass substrate revealed rod shape distribution some portion of the surface of the substrate .Fig 3(a) showed the SEM image of ZnO film at temperature 300 $^{\circ}\text{C}$ and Fig 3(b) provided the rod shape structure on their film. The average width of nanorods would be measured by the bar code system and its width were 105.44 nm for 300 $^{\circ}\text{C}$ and 107.11nm for 400 $^{\circ}\text{C}$.

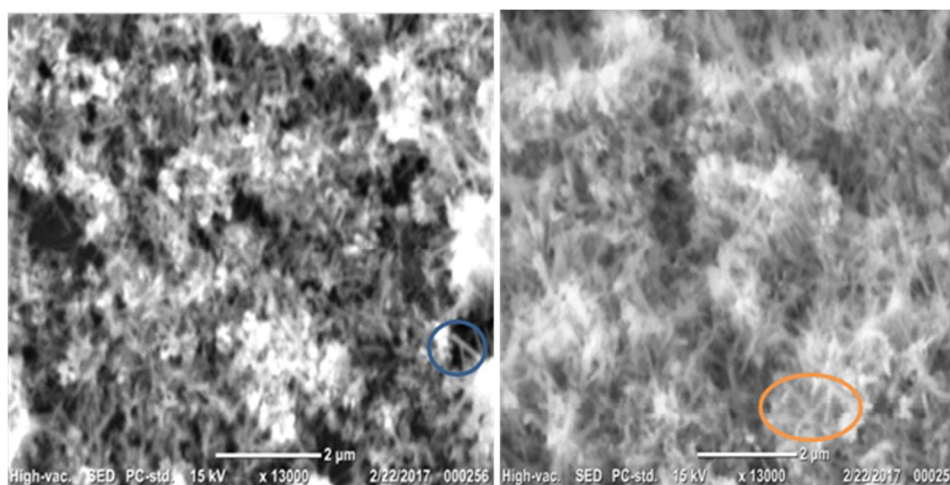


Figure 3(a) and 3(b) showed the SEM photograph of the ZnO/ITO thin film annealed at 300 $^{\circ}\text{C}$ and 400 $^{\circ}\text{C}$

Optical Properties

UV-VIS analysis

The preparation of ZnO/ITO film, ZnO/ITO films were characterized by UV absorbance spectra. The optical properties of ZnO/ITO film are determined from absorbance measurement in the range of 300nm to 800nm for annealing temperature 300C and range 280nm to 800nm for annealing temperature 400C respectively. The maximum absorbance edge was found at 364.5nm for ZnO/ITO films for 300C and 369nm for 400C annealing

temperature. The absorption spectra of ZnO/ITO was shown in figure 4(a). From the dependence of the absorption band edge on wavelength, the energy gap of the material can be determined. When the energy of the incident photon is greater than that of the band gap ($h\nu > E_g$) the absorption coefficient ' α ' is given by

$$\alpha h\nu = A(h\nu - E_g)^{1/2} \text{----- (1)}$$

From the curve $\alpha h\nu^2$ versus $h\nu$, the band gap was identified by extrapolating the linear region of the curve to the energy axis. The energy band gap value of ZnO/ITO film were measured in figure 4(b). In these results, the band gap value of ZnO/ITO film were examined to be 3.66eV and 3.3408 eV for annealing temperature 300°C and 400°C.

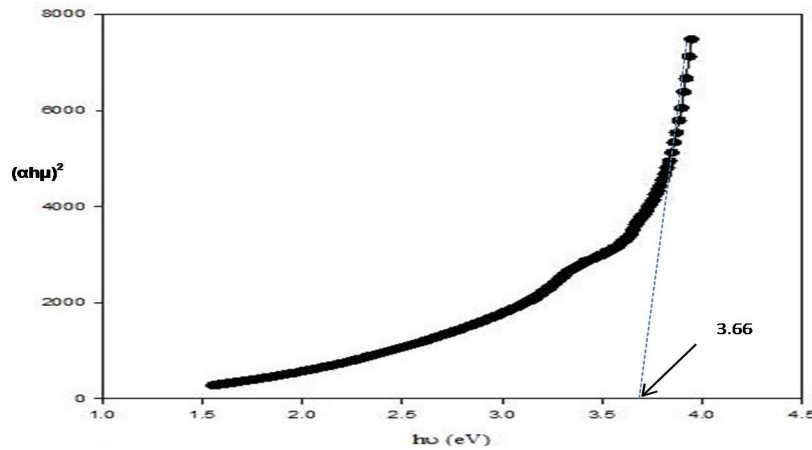


Figure 4(b) Plot of $(\alpha h\nu)^2$ versus photon energy of ZnO/ITO thin film annealed at 300°C

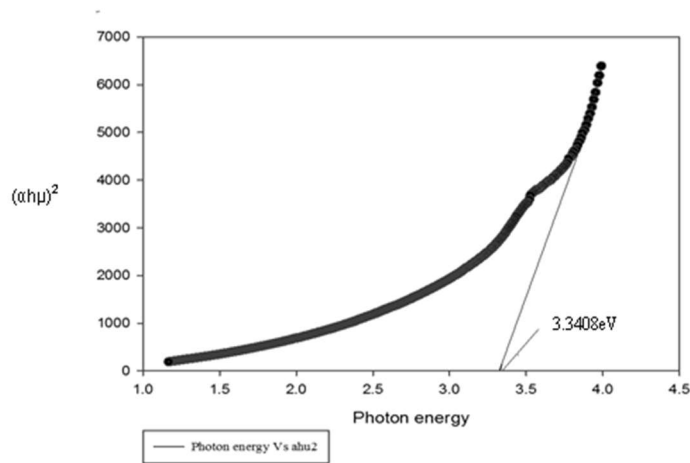


Figure 4(b) Plot of $(\alpha h\nu)^2$ versus photon energy of ZnO/ITO thin film annealed at 400°C

Table 3. Optical band gap (E_g) values for ZnO/ITO thin film

ZnO/ITO thin films	Energy band gap (E_g)	
Annealed at 300°C	3.66 eV	
Annealed at 400°C	3.3408eV	
Reference (Sandeepsanjeev and Dhananjaya ., 2015)	300°C	3.22eV
	400°C	3.16eV

lower band gap of the oxide film annealed at 400 °C may indicate better oxidation since the band gap of bulk ZnO was reported to be ~ 3.37 eV. Moreover, the ZnO/ITO films showed another lower The energy band gap of 3.3408 eV. This lower energy band gap may be due to absorption involving defect states.

Electrical Properties

C-V analysis

In order to examine for more details in electrical behaviors' of ZnO/ITO films, C^2 -V analysis was also studied in this work. The capacitance-voltage (C-V) measurement of ZnO/ITO glass substrate thin film was

accomplished at 50KHz, in the "dc" bias voltage from -5V to +5V. The rate was set 0.5V for all cases. Measurements were performed at room temperature and the quantities of Schottky's contact were estimated from the analysis of the experimental results. Reverse C-V characteristics exhibited a linear $1/C^2$ versus V plot. The slope calculation of C^{-2} -V representations provided to determine the dopant concentrations. The values of built in potential (V_{bi}), acceptor concentration (N_a), donor concentration (N_d) and depletion layer width (W) of Zinc oxide deposited ITO glass substrate films were calculated and summarized. Table 5, $1/C^2$ vs V showed increasing annealing temperature decreasing built in potential. In some references, the induced built in potential reduces the recombination. The $1/C^2$ vs. V intercept is shown to decrease with increase in annealing temperature.

Table 3. $1/C^2$ -V analysis data of ZnO/ITO thin film deposited by Chemical Bath deposition technique

Annealing temperature(°C)	Build in Potential V_{bi} (eV)	acceptor concentration N_a (cm^{-3})	Depletion width W(cm)
300°C	0.3950	1.63E+30	8.131E-11
400°C	0.3250	1.47E+30	8.148E-11

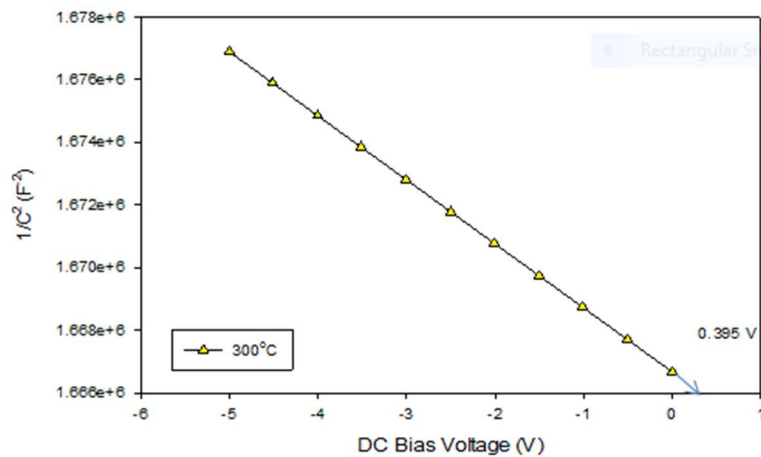


Figure.5(a). $1/C^2$ vs V characteristic of ZnO/ITO thin film annealed at 300°C

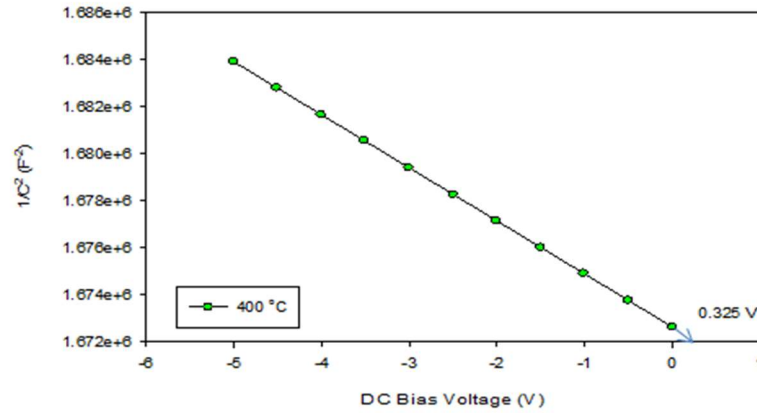


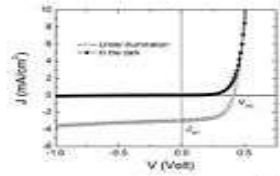
Figure.5(b). $1/I^2$ vs V characteristic of ZnO/ITO thin film annealed at 400°C

Electrical and Photovoltaic properties

Figure 6(a-d) represents the current –voltage (I-V) curve of ZnO/ ITO film solar cell under dark and illumination conditions in the forward and reverse directions with different annealing temperature (300°C and 400°C) respectively. Good rectifying and photovoltaic properties were noticed for this device. It is observed that the ZnO/ITO thin film solar cell device display a great photovoltaic effect and rectifying behavior. The photocurrent caused by $200\text{mW}/\text{cm}^2$ halogen lamp is clearly much greater than dark current. For the (I-V) curve in dark, the current values increases exponentially with increasing in the forward bias voltage. Moreover, it is seen from the figure that the device has high forward current that reverse current . The value of ideality factor of the ZnO/ITO thin film solar cell is gained from the slope of straight line region of the forward bias log I-V characteristics for dark curve. Calculation of the ideality factor, barrier height is shown in Table (4.a.). One can see that the ideality factor of different annealing temperature. I-V characterization of ZnO/ITO thin film solar cell under illumination shown in figure (6c-d). And the open circuit voltage (V_{oc}), short circuit current (I_{sc}), Fill Factor (FF) and conversion efficiency (η) are calculated in Table (4.b.) for different annealing temperature.

Formulae for PV cells, Under illumination condition;

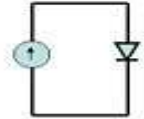
solar cell fundamentals



$$\eta = \frac{P_{max}}{P_{solar}} = FF \frac{J_{sc} V_{oc}}{P_{solar}}$$

$$FF = \frac{J_{max} V_{max}}{J_{sc} V_{oc}}$$

Ideal solar cell: $J = J_0 \left(\exp \frac{qV}{nkT} - 1 \right) - J_{ph}$



Open-circuit voltage: $V_{oc} = \frac{nkT}{q} \ln \left(\frac{J_{ph}}{J_0} + 1 \right)$

Short-circuit current: $J_{sc} = -J_{ph}$

Formula for PV cells, under dark condition,

$$I_s = AR * T^2 \exp \left(-\frac{q\phi}{KT} \right) \text{-----(1)}$$

$$I = I_0 \left(\exp \frac{qV}{kT} - 1 \right) \text{-----(2)}$$

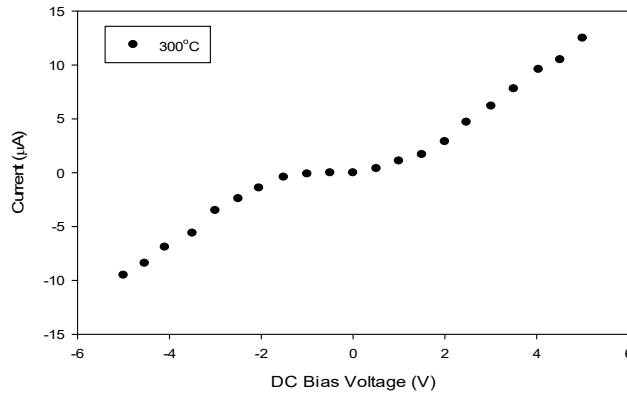


Figure 6(a). I-V characteristic of dark condition ZnO/ITO thin film annealed at 300°C

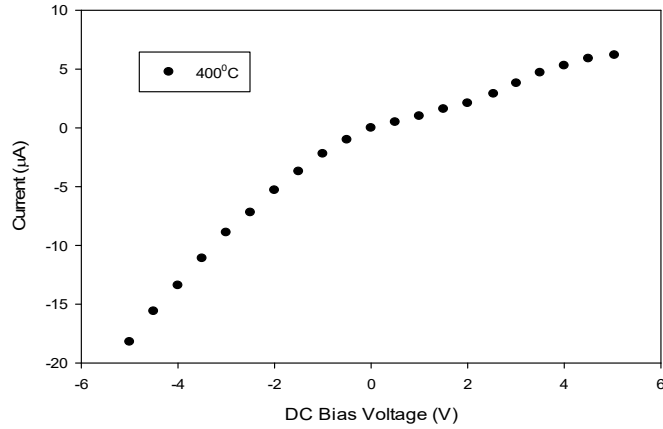


Figure 6(b). I-V characteristic of dark condition ZnO/ITO thin film annealed at 400°C

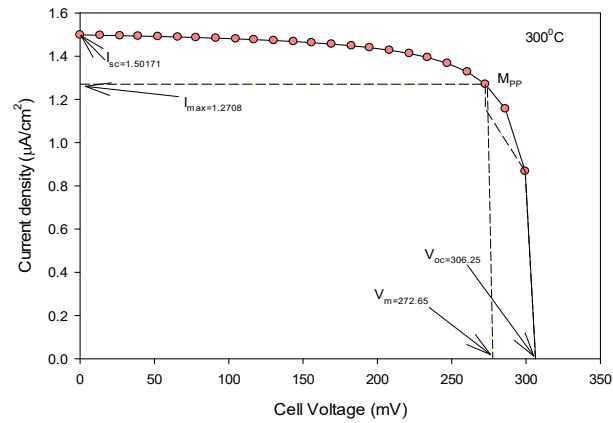


Figure 6(c). I-V characteristic under illuminated condition ZnO/ITO thin film annealed at 300°C

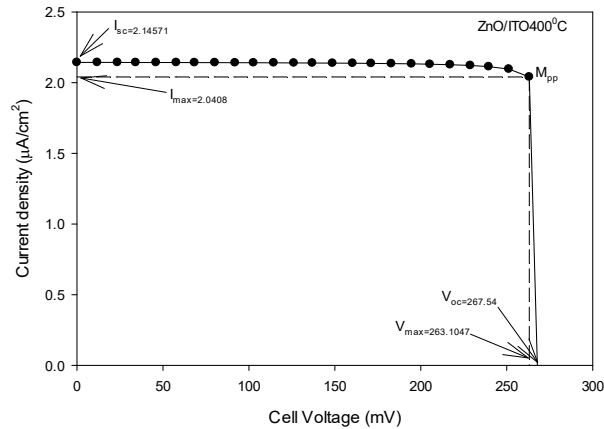


Figure 6(d). I-V characteristic under illuminated condition ZnO/ITO thin film annealed at 400°C

Table 4.a Ideality factor, Barrier height, and Saturation current values for ZnO/ITO thin film solar cells at different annealing temperature

Annealing temperature	Ideality factor	Barrier height(eV)	Saturation current (µAm)
300°C	1.51	0.3371	0.541
400°C	1.55	0.3532	0.291

Table 4.b. Photovoltaic measurement for ZnO/ITO thin films solar cell at different annealing temperature.

Annealing temperature	Voc (mV)	Isc (µAm)	Vmax mV	Imax µAm	FF	Efficiency %
300°C	306	1.50	272.65	1.27	0.75	0.23
400°C	267.54	2.15	263.10	2.04	0.94	0.36

Conclusion

In Summary, deposition of ZnO/ITO thin films prepared by the successive immersion of ITO glass substrate in solutions of NaOH and Zinc chloride reaction solution at 63.5°C ~80°C have been studied. Hexagonal (wurtzite structure) phase can be easily obtained by CBD method. The ZnO/ITO thin films have mainly (101) and (002) crystalline orientations. At temperature of 300°C, the crystallite size was found to be 29.63nm at prominent peak (101) and 400°C provided 38.87 nm respectively. Therefore, we may deduce the crystallite size were found to be increased with increasing annealing temperature. Improved in crystallinity quality with rising annealing temperature. As a result, oxygen defect are favorable to the merging process to form larger grains size while increasing the annealing temperature. The surface morphology of deposited ZnO/ITO thin films on ITO substrate show nanorods shape structure. Optical band gap of the ZnO/ITO films, measured by employing a UV-Vis spectrophotometer, lies at 3.66eV~ 3.3408eV at 300°C and 400°C annealing temperature respectively. This lower energy band gap may be due to absorption involving defect states. According to the C⁻²Vs V measurement, we can deduce that build in voltage for different annealing temperature is slightly different. All I-V characteristics showed the photovoltaic behavior. The fill factor FF for all ZnO/ITO films were flexible for cell design. By the conclusion, the ZnO/ITO film at various annealing temperature were credible and promising use for thin film solar cell by non-expensive and unsophisticated method.

Acknowledgement

I am greatly indebted to Professor Dr Khin Khin Win, Head of Department of Physics, University of Yangon, for her kind permission to carry out this research.

I would like to thank Professor Dr Soe Soe Nwe, Department of Physics, University of Yangon, for her valuable advice in the preparation of this paper.

I wish to express my warmest thanks to Supervisor Dr Thida Win, Lecturer, Department of Physics, University of Yangon, for her valuable advice and supervising throughout in this research.

I am also deeply grateful to Co-supervisor Dr Marlar Wai, lecturer, Department of Physics, University of Yangon, for her valuable advice in my experiment work

References

1. A. vanish S. Deepak ., et al, (2005), “Growth of structural and optical and electrical properties of ZnO thin films deposited by Chemical Bath Deposition techniques”, 8, 189.
2. A. David Adegyoyega., et al, (2016), “ Effect of spin coating speed on some optical properties of ZnO Thin Films”, 4, 1-6.
3. B.M. Basol., et al, (1985), “Effect of heat treatment on the composition and semiconductivity of electrochemically deposited CdSe films”,58, 601.
4. B.Cao and W.Cal., et al, (2008), “ZnO nanorods to nanoplates Chemical Bath Deposition growth and surface related emission”, 112,680.
5. F. Nadir Habubi., et al, (2015), “ Fabrication and Characterization of ZnO/P-Si Heterojunction Solar Cell”,18,118-132.
6. F. A. Kroger ., et al, (1978), “ J. Electrochem. Sci”, 125, 2082.
7. G. Mei-Zhen., et al, (2008), “ Thickness dependence of Resistivity and Optical Reflectance of ITO Films”, 25,no 4.
8. K.Ramamoorthy., et al, (2004), “Material Chemistry and Physics”, 85, 257.
9. S.Masuda., et al, (2003), “ApplPhys”, 93,3.
10. S.Sandeep and Dhananjaya Kekuda., et al,(2015), “ Effect of annealing temperature on the structural and optical properties of Zinc Oxide Thin Fillms Prepared by Spin Coating Process”,73,-
11. J.Mayekar., et al,(2013), “ To Study the Role of temperature and Sodium Hydroxide concentration in the Synthesis of Zinc Oxide Nanoparticles”, 3,11.

GROWTH AND CHARACTERIZATION OF ZnTiO₃ PEROVSKITE FILM ON SI SUBSTRATE

Win Pa PaKhaing¹, Thida Win², Than Than Win³ and Yin MaungMaung⁴

Abstract

Zinc titanate (ZnTiO₃; ZT) powders were successfully prepared by a solid state reaction method. ZT powder were heated at various calcination temperatures ranging from 500 °C to 850 °C for 2h. Powder samples were characterized using thermo gravimetric (TGA), differential thermal analysis (DTA), X-ray diffractometer (XRD), scanning electron microscopy (SEM). The second phases such as ZnO and TiO₂ were detected in the powders calcined below 850 °C. A single perovskite of the ZT powders was found with calcination temperatures at 850 °C. The TGA-DTA results corresponded to the XRD investigation. The crystalline powders were mixed with the solvent and deposited onto the silicon substrates by using spin coating method. Annealing of the deposited films were performed at temperatures ranging from 400°C to 800°C for 1h. The X-ray diffraction, scanning electron microscope and UV-vis spectroscopy have been employed to characterize the deposited films. The obtained 2D materials surface were ZnTiO₃ with cubic structure. The absorbance spectra exhibited visible light emission and optical band gap was 3.7 eV.

Keywords: ZnTiO₃perovskite, solid state reaction, spin coating, optical band gap

Introduction

TiO₂ and ZnO are both wide band semiconductor with excellent properties and extensive application, and have attracted much interest on either single material or ZnO-TiO₂composites .ZnO has attracted intensive research effort for its unique properties and versatile applications in transparent electronics, ultraviolet (UV) light emitters, piezoelectric devices, chemical sensors and spin electronics . One of the most important characteristics of ZnO is that it has a large binding energy (60 meV), which is significantly larger than other materials commonly used semiconductor for

¹ PhD candidate, Department of Physics, University of Yangon

² Lecturer, Department of Physics, University of Yangon

³ Associate Professor, Department of Physics, Mandalay University of Distance Education

⁴ Associate Professor, Department of Physics, University of Mandalay

blue green light-emitters devices, such as ZnSe (22meV) and GaN (25 meV) . On the other hand, titanium dioxide (TiO_2) is one of the most important semiconductors with high photo catalytic activity, being non-toxic, stable in aqueous solution, and relatively inexpensive. The excellent photo catalytic property of TiO_2 is due to its wide band gap and long lifetime of photo generated holes and electrons [Dulin, F.H. et al 1960]. Nowadays, due to the development of microwave dielectrics, zinc-titanates can be used as dielectric resonators and filter in microwave devices [Kim, H.T et al 1999]. Thus, in this work, ultra-fine powders of ZnTiO_3 successfully were obtained via the combustion method. Perovskites are emerging as a new generation of photovoltaic materials. They are abundant in nature and have rapidly increasing power conversion efficiencies (PCE) of above 15% in common hybrid (mixed organic/inorganic) thin-film-based solar cells [Burschka, J et al 2013- Wang, Q et al 2014]. The transition metal oxide such as TiO_2 , their perovskite structures ZnTiO_3 , is widely used in optical and microelectronic applications because of their excellent mechanical, optical and insulating properties. In the past few years zinc-titanium based oxide materials (Zn-Ti-O) have been used widely because of their outstanding properties and potential scientific and technical applications [Sun, D. et al 2011]. Up to now, perovskite films have been formed by film deposition approaches such as spin-coating, sequential deposition of the inorganic and organic precursor, and co-evaporation of the precursors [Burschka, J et al 2013- Liu, M et al 2013]. It has a perovskite-type oxide structure and could be advantageous as a microwave resonator material [Kim, H. T et al 1999]. There are three compounds that exist in the ZnO-TiO_2 system: ZnTiO_3 with a hexagonal limonite structure (h- ZnTiO_3), Zn_2TiO_4 with a cubic spinel crystal structure, and $\text{Zn}_2\text{Ti}_3\text{O}_8$ with a cubic defect spinel structure [Bartram, S.F et al 1961]. $\text{Zn}_2\text{Ti}_3\text{O}_8$ has been observed as a low-temperature form of h- ZnTiO_3 that exists at $T < 820^\circ\text{C}$ [Steinike, U et al 1997], and is only produced based on the Zn_2TiO_4 phase [Kim, H.T et al 2001]. It is known that h- ZnTiO_3 decomposes into Zn_2TiO_4 and rutile TiO_2 at $T > 945^\circ\text{C}$ [Dulin, F.H et al 1960]. However, perovskite crystallizes very rapidly, so it is very challenging to form uniform, continuous, and leakage-free perovskite films by solution methods [Liu, M et al 2013] . In this study, depositions of the ZnTiO_3 thin films were carried out by spin coating method. In addition, the effect of structure

and microstructures and optical properties of ZnTiO₃ thin films were studied, where the deposited films were annealed at temperatures ranging from 400 °C to 800 °C.

Experimental Procedure

In this study, ZnO and TiO₂ were chosen as the starting materials. Firstly ZnO and TiO₂ powder with stoichiometry (ZnO:TiO₂= 1:1 molar ratio) were mixed. Ethanol was added to the mixture powders. And then the mixture solution stirred with the magnetic stirrer and milled with the ball milling machine for 12hr. Thermal behavior of the sample was performed by TG-DTA analyzer in air to investigate the calcination temperature and possible phase transformation from 500 °C to 850 °C for 2h at a heating/cooling rate of 5 °C/min. After the sample annealed at 850 °C, ZnTiO₃ crystals are obtained. When the crystals were dried and sieved uniform particles obtained. X-ray diffraction (XRD) was employed to identify the phase formed. The grain size was directly imaged, using scanning electron microscopy (SEM). The flow chart of preparation of ZnTiO₃ powder as shown in Figure 1. ZnTiO₃ films was prepared using ZnTiO₃ powder and 2-methoxy ethanol as solvent and silicon as substrate. Firstly ZnTiO₃ powder was mixed with the solvent and stirred the mixture for 5h. The preparation of ZnTiO₃ film was shown in figure 5. And then, A few drops of zinc titanate solution were placed on a silicon substrate and spin coated. The ZnTiO₃ films were annealed at 400 °C, 500 °C, 600 °C, 700 °C and 800 °C for 1h in atmosphere. X-ray diffraction (XRD) was employed to identify the phase formed were shown in figure 6(a-e). The grain size were directly imaged, using scanning electron microscopy (SEM) were shown in figure 7(a-e). The absorption spectrum of ZnTiO₃ was shown in figure 8(a). The optical absorbance was measured using UV-VIS spectrometer as shown in figure 8(b).

Result and discussion

Thermal analysis

These are techniques by which the thermal behavior of substances is characterized. Whatever a substrate is heated expands and the variation in the extent of expansion with increasing temperature is dependent on the bond

energy/crystal structure etc. and hence on the type of material. Thus, the changes in crystal structure, coefficient of thermal expansion and melting, can be studied with the help of Differential Thermal Analysis (DTA measures the relative expansion/ contraction between a sample and the standard with varying temperature). Thermo gravimetric analysis (TGA) measures the change in mass of the sample with varying temperature there by indicating the onset, midpoint and completion of a reaction such as oxidation, decomposition, compound formation etc. The reaction of unheated treatment ZT powders taking place during heat treatment was investigated by thermo gravimetric analysis (TGA), differential thermal analysis (DTA). X-ray diffraction (XRD) was employed to identify the phase formed. The TGA and DTA curves of ZT powders prepared by the solid state reaction method. TG-DTA curve of uncalcined powder as shown in figure 2 . The ZT powders demonstrated a three-stage weight loss; the first one was in the temperature range of 100 to 150 °C, the second one from 150 to 280 °C, and the last one began around 300 °C.

XRD analysis

X-ray powder diffraction is a rapid analytical technique used for phase identification of a crystalline material and can provide information on unit cell dimensions. The analyzed material is finely ground, homogenized, and average bulk composition determined. Based on the results of DTA and TGA, calcinations were carried out from 500 to 850 °C for 2 h, at a heating /cooling rate of 5 °C /min for the unheated ZT powders. After anneal from 500 to 700 °C, the precursor of ZnO and TiO₂ were detected. When the temperature went above 700 °C, the minor phase of ZnO remained. A high purity of the cubic perovskite phase was discovered in powders annealed at 850 °C. The XRD patterns of the ZT powders, formed with different calcination temperatures for 2hr at shown in figure 3(a). The XRD patterns of ZT powders after calcination at 850 °C as shown in Figure 3(b).The FWHM and crystalline size of ZnTiO₃ was listed in table 1. Grain size of ZT at various temperature shown in table 2. And then ZntiO₃ powder (850°C) was heated again at various temperatures. Result of the X-ray analysis of ZnTiO₃ powder after heat treatment at 400°C, 500°C, 600°C , 700°C and 800°C for 2h as shown in

in figure 6(a-e). Six diffracted peaks were formed on observed XRD profiles and well matched with those of ZnTiO_3 standard. The most intense peak was examined to be (311) collection. Among them, the highest peak was discovered in films annealed at 400 °C. As the detail of the film analysis by XRD, ZnTiO_3 film was successfully formed on to the Si substrate at different temperatures. Table (3) showed Crystalline size of ZnTiO_3 film at different temperatures.

SEM analysis

The particle morphology and size were directly imaged, using scanning electron microscopy (SEM) and the particle size distribution was determined. The SEM micrographs of ZnTiO_3 powders annealed at different temperatures: 500°C, 600°C, 700°C, 800°C, 850°C for 2 h in air. The sphere like particles seemed to distribute homogeneously. The grain size increase with the increase in the various temperature and caused faster grain growth, thus resulting in better crystallinity as confirmed by the X-ray diffraction analysis. The grain size of ZnTiO_3 powder at different temperature was shown in table 2. They were estimated to be 228.5 nm, at 500°C, 287.5 nm at 600°C, 285.7 nm at 700°C, 406.3 nm at 800°C and 400nm at 850°C. All of SEM images were separated by some porosity. As a result, it was said to be porous structure. The grain size of particle appears to increase in increasing temperature. As discussed earlier, the higher annealing temperature tends to promote phase formation and grain growth. The microstructures of the films were analyzed by using SEM . The zinc titanate films were deposited on silicon substrates at different temperatures. The SEM images of zinc titanate films from 400-800°C were shown in figure 7(a-e). SEM images indicated the normal grain distribution and porous structures. The majority grains on SEM images were ZnTiO_3 . The grain size of the ZnTiO_3 films were measured to be 500 nm, 550 nm, 550nm, 568nm and 587 nm at different temperatures. The annealing temperatures were helpful in increasing gain size. Table (4) showed grain sizes of ZnTiO_3 films at different temperatures.

UV-VIS analysis

The preparation of ZnTiO₃ film, zinc titanate films were characterized by UV absorbance spectra. The optical properties of ZnTiO₃ film are determined from absorbance measurement in the range of 263-982nm. The maximum absorbance was found at 284nm for ZnTiO₃ films. The absorption spectra of ZnTiO₃ was shown in figure 4(a). From the dependence of the absorption band edge on wavelength, the energy gap of the material can be determined. When the energy of the incident photon is greater than that of the band gap ($h\nu > E_g$) the absorption coefficient ' α ' is given by

$$\alpha = \frac{A}{h\nu} (h\nu - E_g)^{1/2} \text{----- (1)}$$

where A is constant and $h\nu$ is the photon energy.

From the curve $\alpha h\nu^2$ versus $h\nu$, the band gap was identified by extrapolating the linear region of the curve to the energy axis. The energy band gap value of zinc titanate film was in figure 4(b). In these results, the band gap value of Zinc titanate film was examined to be 3.7 eV.

$$\alpha = 2.3026 A/t \text{ (2)}$$

where t is thickness of the sample and A is the absorbance.

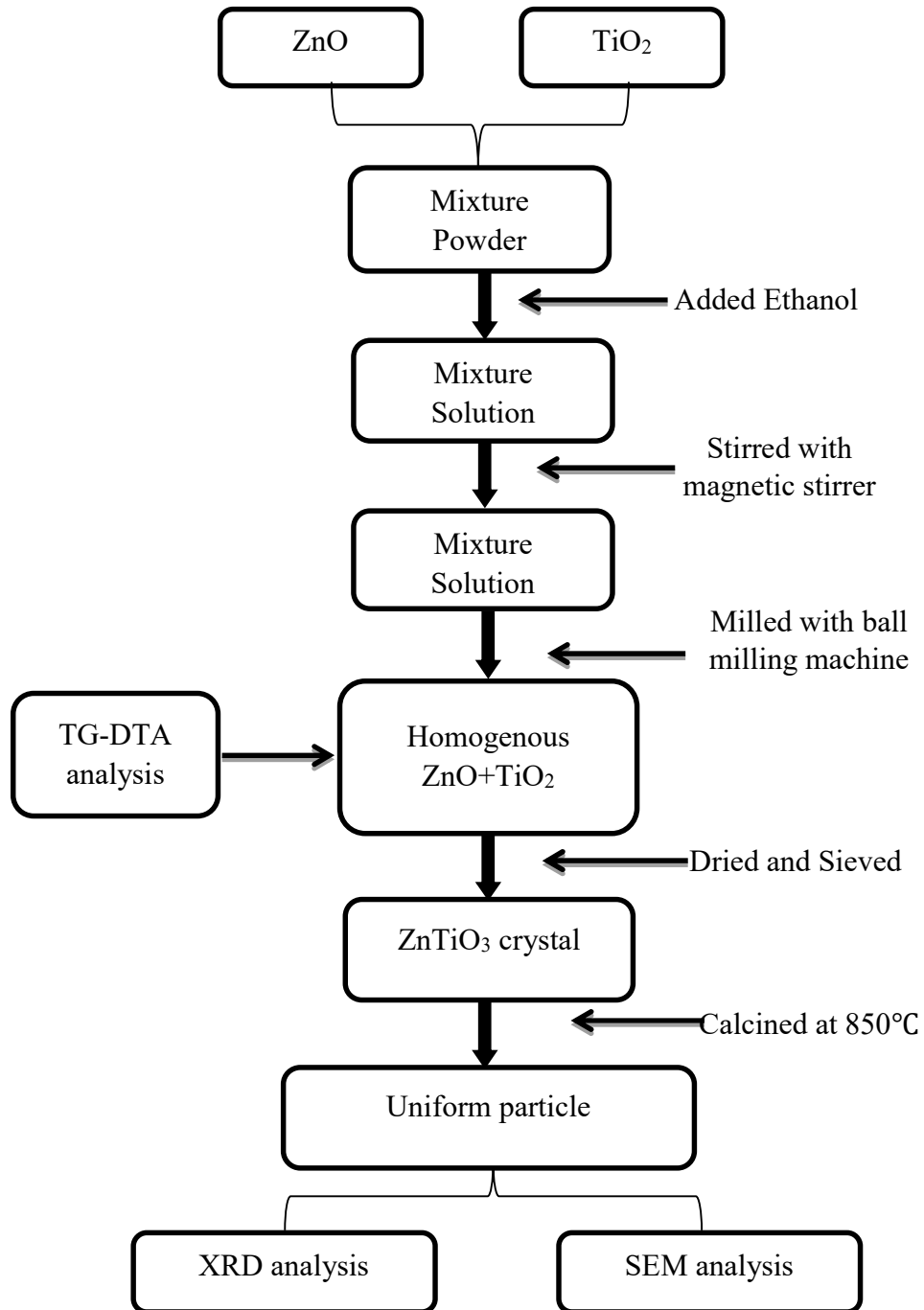


Figure 1. Flow chart for the preparation of ZnTiO₃ powder

Thermal Analysis

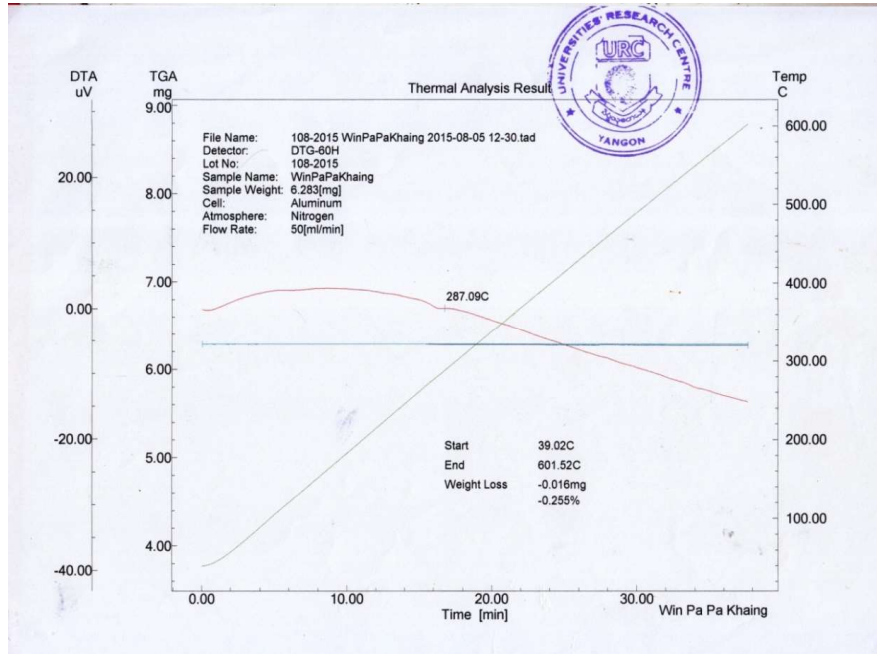


Figure 2. DTA-TG curves of uncalcined ZT powders

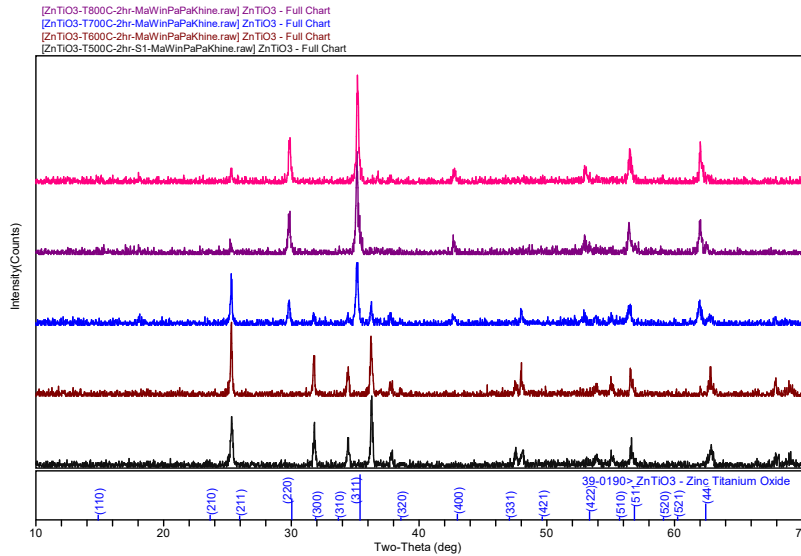


Figure 3(a). XRD patterns of ZT powders with various calcination temperatures for 2hr

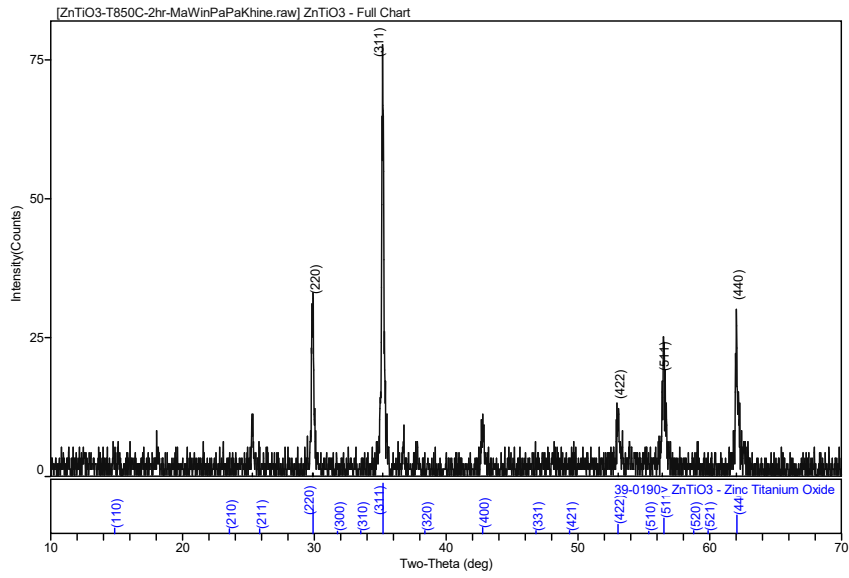


Figure 3(b) XRD patterns of ZT powders after calcination at 850 °C



Figure 4. SEM analysis of ZnTiO₃ powders calcined at 850 °C

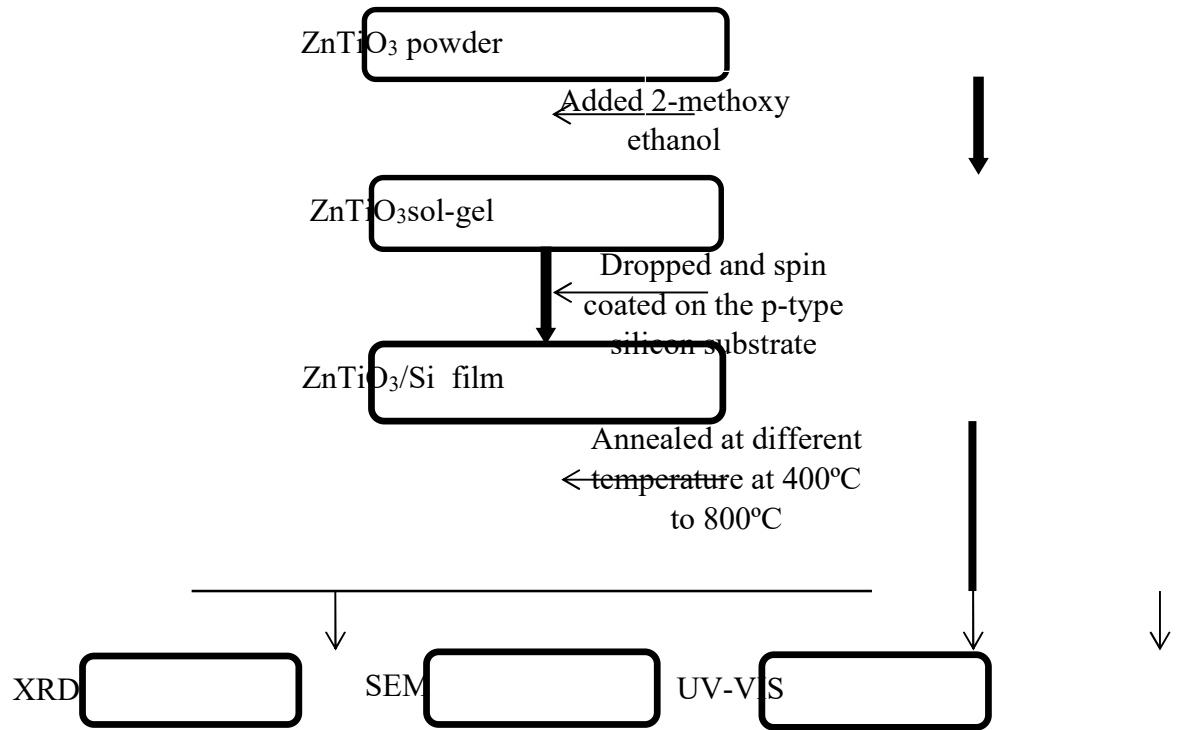


Figure 5 . Flow chart for the preparation of ZnTiO₃ film

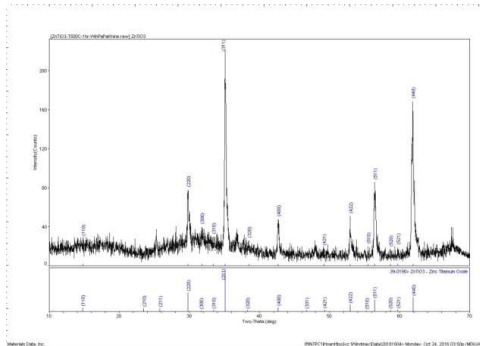


Figure 6 (a). XRD patterns of ZnTiO₃ film at 400 °C

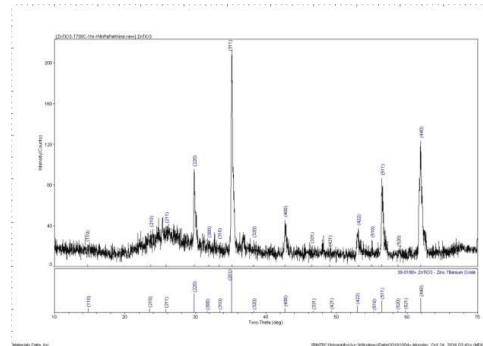


Figure 6 (b). XRD patterns of ZnTiO₃ film at 500 °C

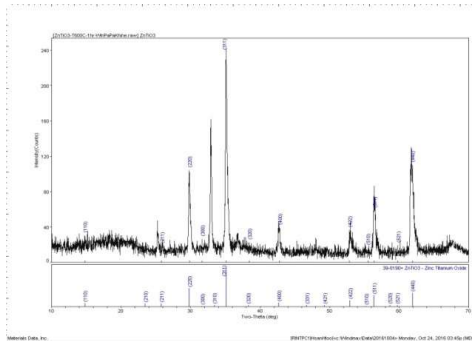


Figure 6 (c). XRD patterns of ZnTiO₃ film at 600 °C

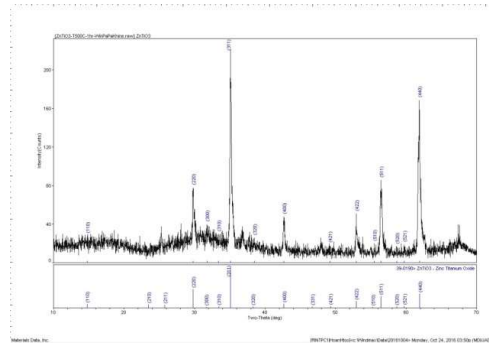


Figure 6 (d). XRD patterns of ZnTiO₃ film at 700 °C

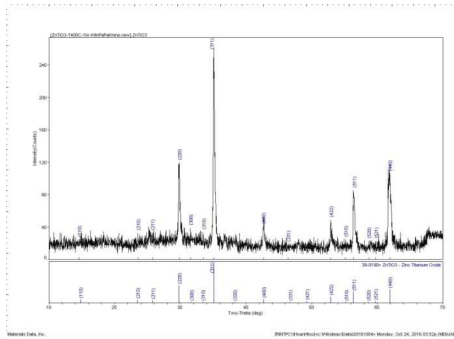


Figure 6 (e). XRD patterns of ZnTiO₃ film at 800 °C

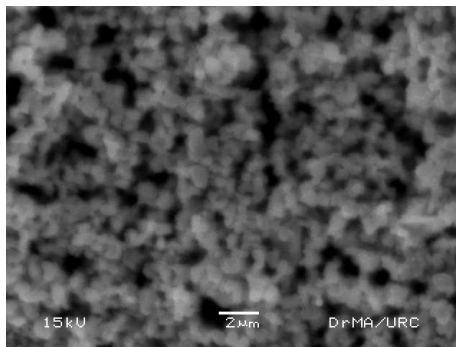


Figure 7(a). SEM analysis of ZnTiO₃ film at 400 °C

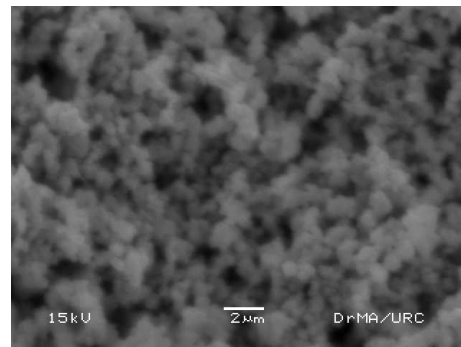


Figure 7(b). SEM analysis of ZnTiO₃ film at 500 °C

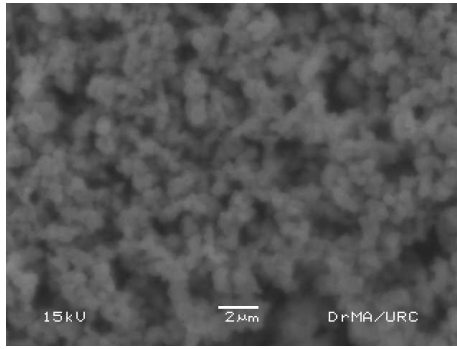


Figure 7(c). SEM analysis of ZnTiO₃ film at 600°C

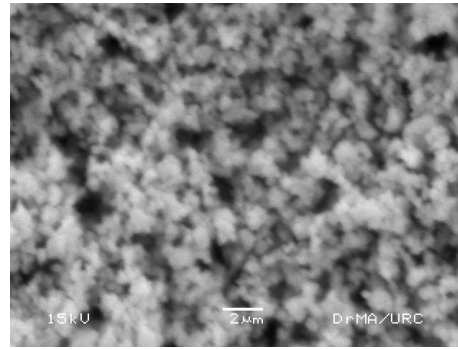


Figure 7(d). SEM analysis of ZnTiO₃ film at 700°C

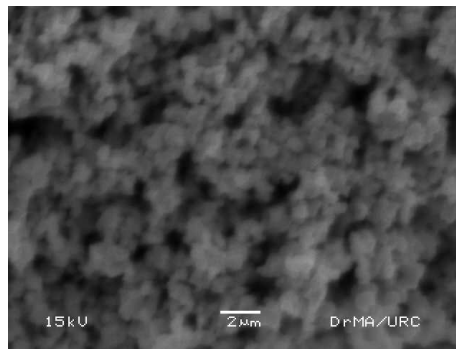


Figure 7(e). SEM analysis of ZnTiO₃ film at 800°C

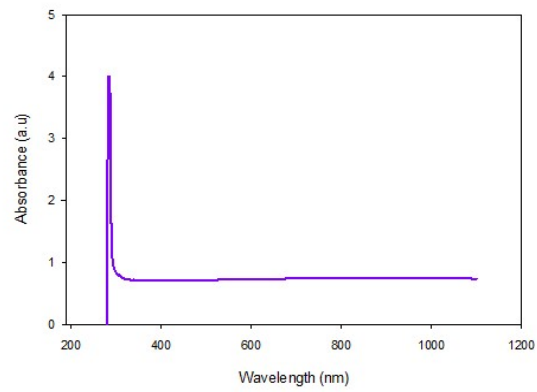


Figure 8(a) UV-VIS spectra of ZnTiO₃

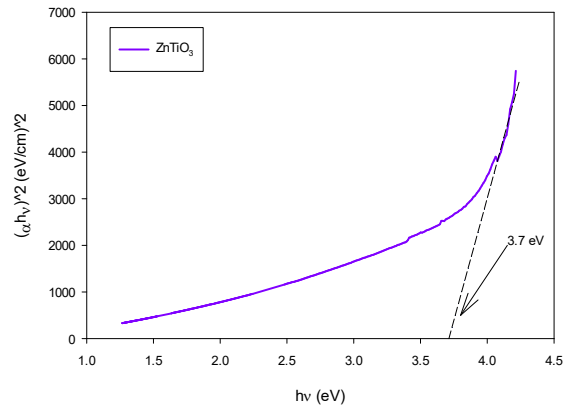


Figure 8(b).Optical energy band gap of ZnTiO₃

Table 1. FWHM and crystalline size of ZnTiO₃ at 850°C

Peaks	FWHM (degree)	Crystallite size (Å)
(220)	0.204	40.254
(311)	0.177	71.144
(422)	0.223	39.767
(511)	0.355	25.361
(440)	0.154	60.116
Average crystalline size		47.328

Table 2. Grain size of ZT at various temperature

Temperature (°C)	Grain Size (nm)
500	228.5
600	287.5
700	285.7
800	406.3
850	400.0

Table 3 .Crystalline size of ZnTiO₃ films at different temperatures

Temperature (°C)	Grain Size (nm)
500	228.5
600	287.5
700	285.7
800	406.3
850	400.0

Table 4 . Grain size of ZnTiO₃films at different temperatures

Temperature(°C)	Grain Size(nm)
400	500
500	550
600	550
700	565
800	588

Table 5. The comparison on band gaps of observed ZnTiO₃and others

Sr.No	Author	Journal	Band gap of ZnTiO ₃ (eV)
1	M.Vishwas et al	Nano-Research for Advanced Materials Technologies	3.15 eV
2	Kuhu Sarkar et al (2014)	Royal Society of Chemistry	4.01 eV
3	R.Hari Krishna (2014)	Asian Ceramic Societies	3.60 eV
4	Bak CHANDRU Yadav et al (2016)	Asian Ceramic Societies	4.01 eV
5	Observed Value		3.70 eV

Conclusion

Perovskite ZnTiO₃ powders can be successfully obtained by the solid state reaction technique and the best conditions for calcination are 850 °C. The annealing temperatures have a strong influence on the crystal structure, percent perovskite phase and the particle size of the ZT powders. Finally, presented SEM and X-ray analyses of ZT-850°C showed advantageous microstructures, with the appropriate pores/ materials ratio and application in the electronic industry as catalysts and color pigments. Heat treatment at 850°C enhanced the atomic mobility and caused the grain growth to result in a better crystallinity. Growth and characterization of ZnTiO₃ films have been studied at different annealing temperatures. As a result of XRD, ZnTiO₃ was absolutely formed onto the Si-substrate at given temperatures. From the SEM results, it was found that all SEM images were porous structures. From UV-VIS spectroscopy measurement, the band gap of ZnTiO₃ was determined to be 3.7eV and it is quite satisfactory and credible compared with others for photovoltaic applications.

Acknowledgements

I would like to thank Professor Dr Khin Khin Win, Head of Department of Physics, University of Yangon, for her kind permission to carry out this work.

I also would like to thank Professor Dr Soe Soe Nwe, Department of Physics, University of Yangon, for her help and advice.

I would like to thank all people who encouraged and supported me during the undertaking of this work.

References

1. Dulin, F.H. et al (1960) Journal of Am. Ceram, Phase equilibria in the system ZnO–TiO₂, Soc. 43 ,125–131.
2. D. Sun, X. Yan, J. Chen, S. Yu, L. Hu and Q. Xue, Chem. Eng. Commun., 13,3905–3909 (2011).
3. F.H. Dulin, D.E. Rase, J. Am. Ceram. Soc. 43 (1960) 125.
4. H. T. Kim, S. H. Kim, S. Nahm, J.D. Byun, and Y. Kim, “Lowtemperature sintering and microwave dielectric properties of zinc metatitanate-rutile mixtures using boron,” *Journal of the American Ceramic Society*, vol. 82, no. 11, pp. 3043–3048, 1999.
5. H.T. Kim, Y. Kim, M. Valant, D. Suvorov, J. Am. Ceram. Soc. 84 (2001) 1081.
6. J. Burschka, N. Pellet, S. Moon, R. Humphry-Baker, P. Gao, M. K. Nazeeruddin, and M. Grätzel, *Sequential deposition as a route to high-performance perovskite-sensitized solar cells*, **Nature** **499**, pp. 316–319, 2013.
7. Kim, H.T. et al (1999) journal of Am. Ceram, Low-fired (Zn, Mg) TiO microwave dielectrics, Soc. 82 (12) 3476–3480.
8. M. Liu, M. B. Johnston, and H. J. Snaith, *Efficient planar heterojunction perovskite solar cells by vapour deposition*, **Nature** **501**, pp. 395–398, 2013.
9. Q. Wang, Y. Shao, Q. Dong, Z. Xiao, Y. Yuan, and J. Huang, Large fill-factor bilayer iodine perovskite solar cells fabricated by low-temperature solution-process, *Energy Environ. Sci.* 7 (7), pp. 2359–2365, 2014. doi:10.1039/C4EE00233D.
10. S.F. Bartram, R.A. Slepety, J. Am. Ceram. Soc. 44 (1961) 493.
11. U. Steinike, B. Wallis, *Cryst. Res. Technol.* 32 (1997) 187.

STUDY ON DIELECTRIC PROPERTIES AND CHARGE CONDUCTION MECHANISM OF ZINC SULPHIDE FILMS BY CHEMICAL BATH DEPOSITION METHOD

Hnin Thu Zar¹, Swe Swe Thein², Than Than Win³
and Yin MaungMaung⁴

Abstract

ZnS films were prepared by chemical bath deposition (CBD) technique at 80°C for 4h. The composite film was characterized by using LCR meter. Comparative study on dielectric and charge conduction properties of ZnS films (1:1), (2:1) and (3:1) were investigated. Dielectric properties of films significantly obtained and indicated the photovoltaic behavior of fabricated films. Dielectric constant (ϵ_r), loss tangent ($\tan\delta$) and capacitance (C) were measured different at frequency modes. The charge conduction mechanism was identified by $1/C^2$ -V characteristics. The dopant concentration for p-type conductivity (N_a), the depletion layer width (W) and barrier height (ϕ) were determined from $1/C^2$ -V characteristic.

Keywords: ZnS, PVA, Dielectric, Chemical Bath Deposition(CBD)

Introduction

Zinc Sulphide (ZnS) is II-VI group semiconductor material. ZnS is one of the most attractive semiconductors. ZnS has two types; hexagonal wurtzite and cubic zinc blende depending on synthesis conditions. It has a wide band gap of 3.5 eV to 3.8 eV. ZnS is an important inorganic material for a variety of applications including photoconductors, solar cells, optical coatings and light-emitting materials [Ben Nasr, T. et al 2006], [Hasanzadeh, J. et al 2013], [Daixun Jiang et al 2009]. Typically, the stable structure at room temperature is the zinc blende, with few observations of stable wurtzite ZnS. There have been various studies thin film characteristics of ZnS including optical and electrical properties [Nada M. Saeed 2011]. Moreover, Polyvinyl alcohol (PVA) was used with ZnS because it is water soluble that has been well studied [Koski, A. et al 2004]. Polyvinyl alcohol has a melting point of 180°C to 190°C. Water solutions of polyvinyl alcohol are also stable and other

¹ PhD candidate, Department of Physics, University of Yangon

² Lecturer, Department of Physics, University of Yangon

³ Associate Professor, Department of Physics, Mandalay University of Distance Education

⁴ Associate Professor, Department of Physics, University of Mandalay

properties such as the transparency over the whole visible spectrum. Moreover, different researchers employed different techniques, such as atomic layer deposition (ALD) [Shin and Sun, 2004], pulsed electrochemical deposition (ECD), chemical vapour deposition (CVD) [Zhenyi et al., 2002], Chemical bath deposition (CBD) [Cheng et al. 2003] and Spray pyrolysis [Afifi et al. 1995]. Among these methods CBD method is frequently used as it is simple, cheap, and convenient for larger area deposition of the film. Chemical bath deposition (CBD), which is well known as a prevalent low – temperature aqueous technique for depositing large – area thin films of semiconductors, has been recognized as the simplest and most economical one. The present work was described the deposition of ZnS and PVA thin films by CBD method.

Experimental Procedure

ZnS films were prepared by chemical bath deposition. CBD, which is well known as a prevalent low-temperature aqueous technique for depositing large-area thin films of semiconductors, has been recognized as the simplest and most economical one. CBD is a technique in which ZnS and PVA were deposited on glass substrates immersed in distilled water. Firstly, (sample A) was prepared by dissolving 1g PVA and 1g ZnS in 150ml of distilled water. The mixture solution was thoroughly stirred by using a magnetic stirrer (Fig.1) for 5h until the polymer become completely soluble. And then, we used 1cm² glass substrate. It was immersed into the mixture solution. For the growth solutions films was formed by multiple layers deposition at a temperature for 4h at 80°C by using hot plate(Fig.2).These mixture were deposited onto glass substrates. And then, filter paper was used and dried in air. Homogeneous films were obtained after drying at room temperature in order to remove residual distilled water. Continuously, (sample B) and (sample C) were prepared 1g PVA , 2g ZnS and 1g PVA, 3gZnS in 150ml of distilled water, respectively. The flow chart of ZnS films preparation was shown in (Fig.3).



Figure1. Photograph of ZnS and PVA solution with magnetic stirrer



Figure 2. Photograph of ZnS and PVA solution by using hot plate at 80°C

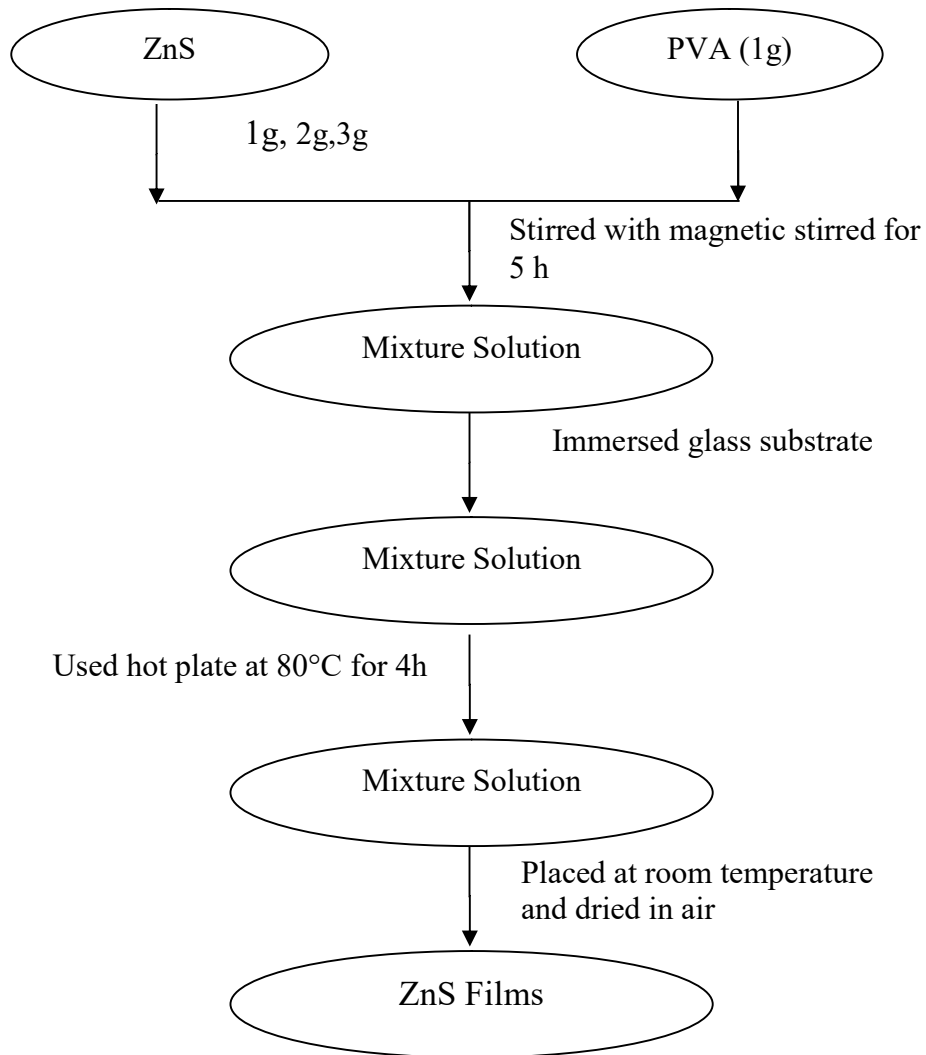


Figure 3. The flow chart of ZnS films

Results and Discussion

Dielectric Characterization

The dielectric properties (ϵ_r -f), (C-f) and ($\tan\delta$ -f) for PVA/ZnS films on glass substrate were examined by LCR meter. The measured values for dielectric properties were listed in Table 1.

Table 1. The Frequency Dependent of Dielectric Properties for PVA/ZnS films

PVA/ZnS films	Frequency (kHz)	Capacitance (pF)	Dielectric loss tangent ($\tan \delta$)	Dielectric constant (ϵ_r)
ZnS:PVA (1:1)	1	9.2342	0.1316	0.0642
	10	6.9542	0.0010	0.0481
	20	6.7262	0.0033	0.0464
	50	6.8972	0.0015	0.0481
	100	6.8972	0.0025	0.0481
ZnS:PVA (2:1)	1	13.5810	0.0517	0.1147
	10	10.2276	0.0004	0.0860
	20	9.8923	0.0012	0.0828
	50	10.1438	0.0006	0.0860
	100	10.1438	0.0010	0.0860
ZnS:PVA (3:1)	1	14.9440	0.0412	0.0849
	10	11.2541	0.0003	0.0637
	20	10.8852	0.0010	0.0613
	50	11.1619	0.0004	0.0637
	100	11.1619	0.0008	0.0637

The variation of capacitance (C), dielectric loss tangent ($\tan\delta$) and dielectric constant (ϵ_r) for the three different ZnS contents were plotted in Fig.4(a), (b) and (c).The realistic characterization of (C-f)variation and (ϵ_r -f) variation for PVA/ZnS films were almost the same nature. The highest values of capacitance (C) and dielectric constant (ϵ_r) were found at (1 kHz) frequency for ZnS: PVA (3:1). The dielectric loss tangent ($\tan\delta$) values varied with applied frequency for the three different ZnS contents were similar.

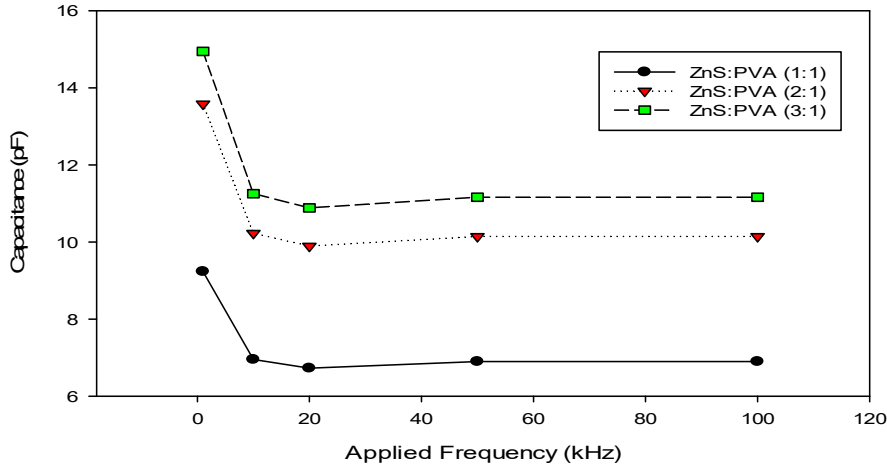


Figure. 4(a) Capacitance and frequency characteristic of ZnS/PVA films

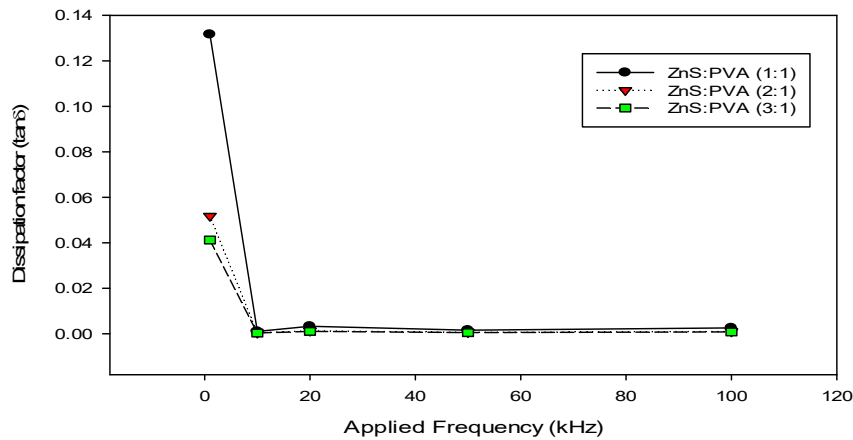


Figure. 4(b) Dissipation factor and frequency characteristic of ZnS /PVA films

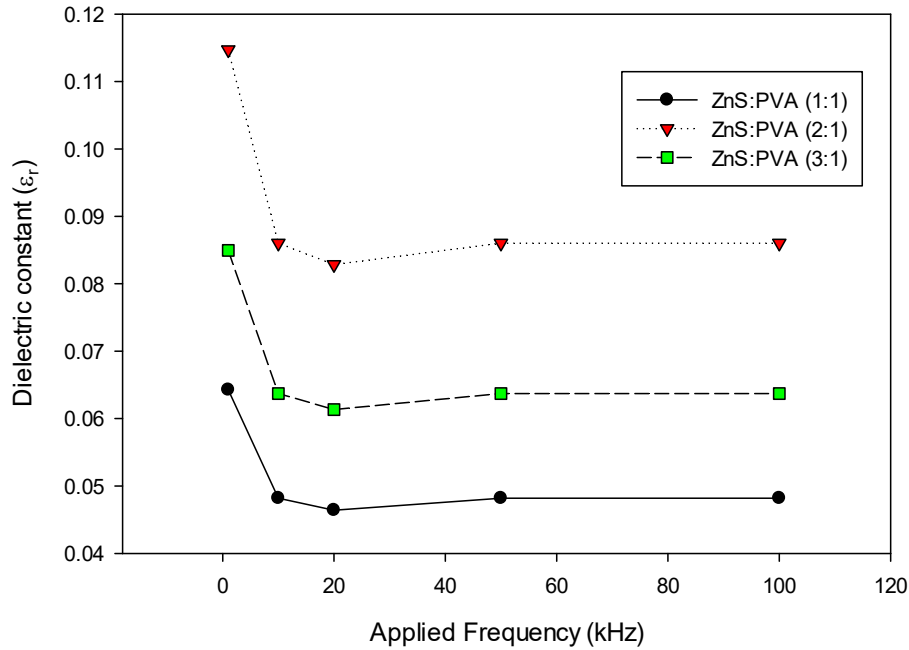


Figure. 4(c) Dielectric constant and frequency characteristic of ZnS /PVA films

Charge Conduction Characterization

The charge conduction mechanism was interpreted by means of $1/C^2$ -V characteristics of 100 kHz. Only the reverse voltage was applied and recorded the value of “C” by impedance analyzer. The step voltage was set 0.2V and delay time was 1 min to avoid transient response. The slow rate was 0.2V/min. The $1/C^2$ -V graphs were shown in Fig. 5(a, b and c). Linear relations with different orientations were clearly formed on $1/C^2$ -V graph. This fact showed the homogeneous and uniform film formation on glass coating substrate. Moreover the ZnS/PV films were successfully deposited on this substrate. All build-in-voltage (V_{bi}) was examined to be positive value and less than unity. The change in slope, $(1/C^2)_{max}$ and V_{bi} were collected in Table 2. And the values of N_a , W , and ϕ at different ZnS/PVA films were calculated in Table 3.

Table 2. The slope, $(1/C^2)_{\max}$ and $V_{bi}(V)$ at different ZnS/PVA films

ZnS/PVA films	Slope (F^{-2}/V)	Capacitance $(1/C^2)_{\max}$ (F^{-2})	Build-in-voltage $V_{bi}(V)$
ZnS:PVA (1:1)	5.41×10^{18}	7.15×10^{20}	0.6340
ZnS:PVA (2:1)	5.91×10^{18}	7.06×10^{20}	0.2672
ZnS:PVA (3:1)	6.23×10^{18}	7.14×10^{20}	0.4672

Table 3. The values of N_a , W and ϕ at different ZnS/PVA films

ZnS/PVA films	Acceptor concentration N_a (cm^{-3})	Depletion layer width W (cm)	Barrier height(ϕ)(eV)
ZnS:PVA (1:1)	2.20×10^{20}	2.808×10^{-6}	0.680
ZnS:PVA (2:1)	2.02×10^{20}	2.790×10^{-6}	0.316
ZnS:PVA (3:1)	1.91×10^{20}	2.805×10^{-6}	0.518

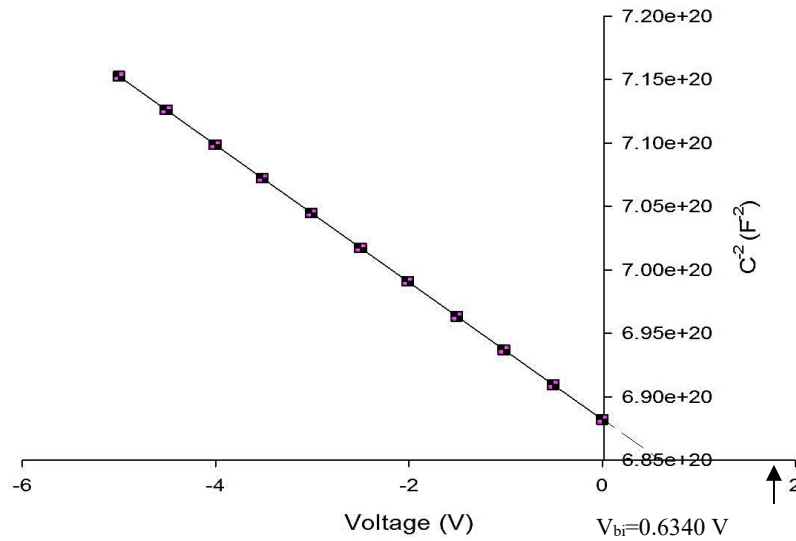


Figure.5 (a) $1/C^2$ - V characteristic of fabricated film with ZnS:PVA (1:1)

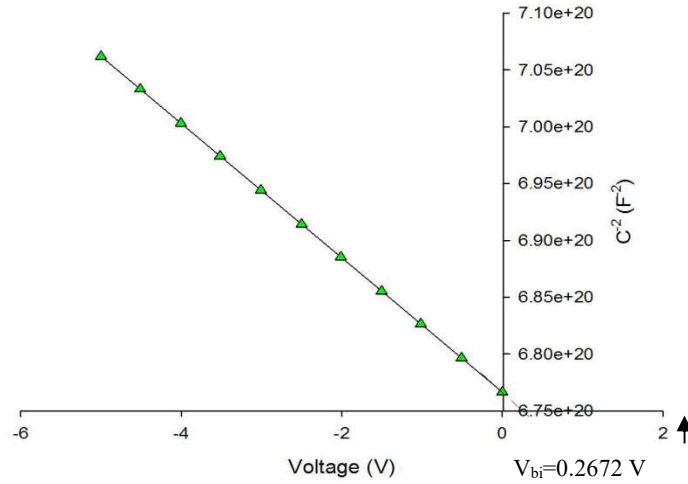


Figure. 5 (b) $1/C^2$ -V characteristic of fabricated film with ZnS:PVA (2:1)

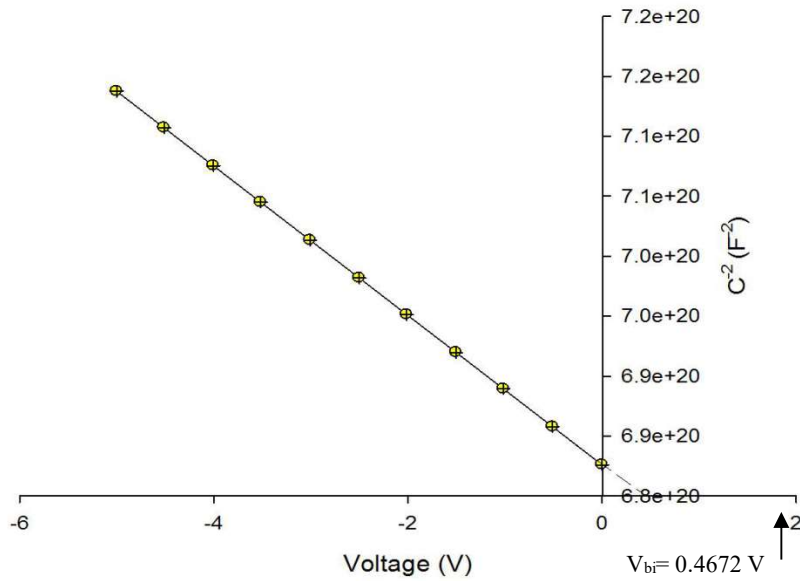


Figure.5 (c) $1/C^2$ -V characteristic of fabricated film with ZnS:PVA (3:1)

Conclusion

Comparative study on dielectric and charge conduction properties of ZnS /PVA films has been investigated. The dielectric properties of films significantly obtained and indicated the photovoltaic behavior of fabricated films. According to the $1/C^2$ -V characteristics curves, the technique used in this work was quite feasible for thin film growth technology. Therefore, glass coating implied the best film quality. The $1/C^2$ -V graph showed the Mott-Schottky relationship. All films were said to be homogeneous because of the linear relationship of $1/C^2$ -V graph.

Acknowledgements

I would like to thank Professor Dr Khin Khin Win, Head of Department of Physics, University of Yangon, for her kind permission to carry out this work.

I also would like to thank Professor Dr Soe Soe Nwe, Department of Physics, University of Yangon, for her help and advice.

I would like to thank all people who encouraged and supported me during the undertaking of this work.

References

1. Afifi, Ashour. A, Mahmoud S.A, (1995), Structural study of ZnS thin films prepared by spray pyrolysis, *Thin Solid Films*, 263 (2), 248-251
2. A.Taherkhani,J. Hasanzadeh, M. Ghorbani, (2013), Luminescence and Structural Properties of ZnS:Cu Nanocrystals Prepared using a Wet Chemical Technique, *Chinese Journal of Physics*, vol.51 (3), pp. 540 –550
3. Bohua Dong, Daixun Jiang, Ge Su, Hau Qu, JMaster Sci, Lixin Cao, Wei Liu, Yuanguang Sun,(2009), *JOSR Journal of Applied Physics*,44, 2792-2795
4. Cheng, Ji.,Dongbo., Fan, Wang Hao., (2003), Chemical bath deposition of crystalline ZnS thin films, *Semiconductor Science and Technology*,18(7), 676-679
5. Nada M. Saeed, (2011), Structural and Optical Properties of ZnS Thin Films Prepared by Spray Pyrolysis Technique, *Journal of Al – Nahrain University*,14 (2), 86 – 92
6. N.Kamoun, M. Kanzari, R. Bennaceur, T. Ben Nasr,(2006), Effect of pH on the properties of ZnS thin films grown by chemical bath deposition, *Thin Solid Films*,500, pp.4-8
7. Shin K.Y. and Sun, Y. J.(2004), Studies on polycrystalline ZnS thin films grown by atomic layer deposition for electroluminescent applications, *Applied Surface Science*,229 (1-4), 105-111
8. Yichao, C., Yongliang, H., Zhenyi, F., (2002), CVD growth of bulk polycrystalline ZnS and its optical properties, *Journal of Crystal Growth*, 237 (3), 1707-1710

FABRICATION MECHANISM AND OPTICAL PROPERTIES OF PURE ZnO AND ZnS-ZnO NANOCOMPOSITE FILMS

Moe Swe¹, May Hnin Thant², ThanThan Win³, and Yin Maung Maung⁴

Abstract

The film of pure ZnO and ZnS – ZnO nanocomposite films have been prepared by chemical deposition method by varying the concentration ratio of pure ZnO and ZnS – ZnO nanocomposite powder. The preparation of these films grown on glass substrates were reported in this work. The optical properties of the samples were characterized by UV- Vis spectroscopy within wavelength range of 190 nm and 1100 nm. ZnS – ZnO nanocomposite (90 % - 10%) exhibited the maximum degree of optical band gap (3.295 eV) why the lowest band gap (2.749 eV) was obtained by ZnS – ZnO nanocomposite film (50% - 50 %).

Keywords : ZnO , ZnS – ZnO nanocomposite powder, 2 – methoxyethanol, Optical badd gap.

Introduction

Zinc sulfide (ZnS) is important II-VI semiconductor material for the development of various modern technologies and photovoltaic applications. II-VI semiconductors such as zinc sulfide (ZnS) have attracted growing interest owing to their possible in optoelectronics, it is important semiconductor material for the development of various modern technologies of solid-state devices such as laser diodes and solar cells. [Skwok K et al 1998] [Antony A et al 2005].

As important II-VI semiconductor, ZnO and ZnS contain only earth-abundant elements and have been intensively studied in a wide range of UV sensors, lasers, field emitters, nanogenerators, solar cells, photocatalysis, etc. [Huang X et al 2013]. Unfortunately, both ZnO and ZnS had a large band gap ($E_g=3.37\text{eV}$ and 3.67 eV for ZnO and ZnS, respectively), and thus there is

¹ PhD candidate, Department of Physics, University of Yangon

² Lecturer, Department of Physics, University of Yangon

³ Associate Professor, Department of Physics, Mandalay University of Distance Education

⁴ Associate Professor, Department of Physics, University of Mandalay

almost no adsorption in the visible light region, which largely limits their application in visible-light-driven water splitting. Recently, the heterostructures of ZnO and ZnS have attracted theoretical and experimental interest because the combination of these two wide band gap semiconductors can yield a novel material with the photoexcitation threshold energy lower than the individual components, leading to improved physical and chemical properties. [Huang X et al 2012] [Chen W et al 2012]. According to our knowledge, apart from ZnS/ZnO hybrid nanowires, few literature was reported on ZnS/ZnO nanocomposites used as effective catalysts for visible light photocatalytic hydrogen production. [Wang M et al 2013] [Shaoo Y et al 2005]. The preparation of reported ZnS/ZnO hybrid nanowires was conducted by a high-temperature hydrothermal method involving the use of expensive and toxic, which makes it difficult to be scaled up and does serious harm to environmental protection and people's health. Therefore, new preparation strategy of ZnS/ZnO heterostructure is greatly desirable to make the best use of ZnO and ZnS for solar energy application. [Aoki T et al 2000] [Jang J et al 2008]

The ZnS/ZnO nanocomposite is easily prepared by the photo deposition of ZnS on the surface of ZnO nanoparticles in photocatalytic process, and ZnO nanoparticles can be abundantly and conveniently obtained by a facile preparation- anneal method using inexpensive and nontoxic inorganic salt and ammonium hydroxide as raw materials. The ZnS/ZnO revealed good catalytic activity and stability in visible-light-driven water splitting and natural sunlight-driven hydrogen evolution. [Nguyen et al 2004] In the present work, chemical deposition method was used because of its advantages like low cost, easy coating of large surfaces with smooth and uniform layers. The present work aims to measure the optical properties by UV-Visible spectroscopy.

Experimental Procedure

Preparation of Solution

In this procedure, ZnO (pure) powders and ZnS – ZnO composite powders were used as starting materials. Firstly, (0.3) g of ZnO(pure) powder was dissolved with 15 ml of 2-methoxyethanol and stirred by magnetic stirrer

at 800 rpm for 5 h. Then, (0.3) g of ZnS – ZnO composite powders were also dissolved with 15 ml of 2- methoxyethanol in different ratios ZnS (10%)-ZnO(90%) ZnS(20%)-ZnO(80%), ZnS(30%)-ZnO(70%), ZnS(40%)-ZnO(60%), ZnS(50%)-ZnO(50%) . It was stirred by magnetic stirrer at 800 rpm for 5 h. All samples were dissolved to reach homogenous mixture solution in each beaker. Finally, ZnO (pure) solution and ZnS–ZnO solutions were obtained. Fig 1 (a) and Fig 1 (b) show the solution of ZnO (pure) and ZnS – ZnO nanocomposite.

Chemical Deposition Process

ZnO (pure) and ZnS – ZnO composite films were deposited on (1x1inches) glass substrates. The substrates of simple glass were cleaned in deionized water (DIW), acetone and absolute ethanol for 20 minutes in each solvent and then dried at room temperature. For the deposition of thin films, the pre-cleaned glass substrates were immersed into solution for 24 h to obtain a uniform coating. After completion of the film deposition, the samples were taken out immediately dried at room temperature for 2 days. The photographs of ZnO(pure) and ZnS-ZnO composite films were indicated in Fig 1(c).The block diagram of experimental procedure was shown in Fig 1 (d).

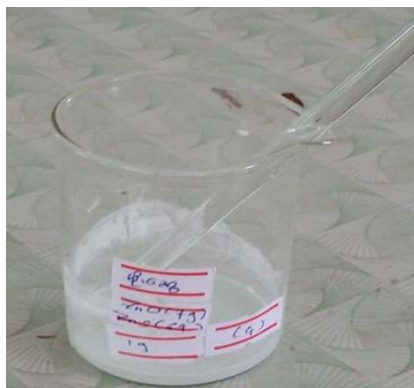


Figure 1 (a) ZnO (pure) Solution

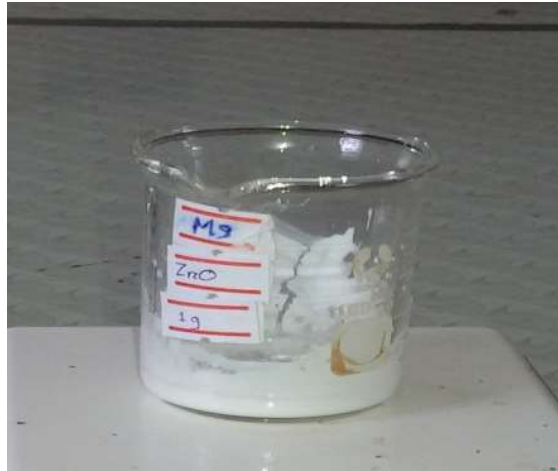


Figure 1 (b) ZnS-ZnO solution



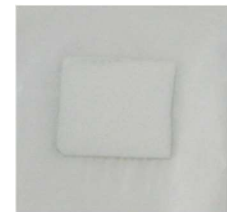
ZnO(pure) film



ZnS(10%)-ZnO(90%) film



ZnS(20%)-ZnO(80%) film



ZnS(30%)-ZnO(70%) film



ZnS(40%)-ZnO(60%) film



ZnS(50%)-ZnO(50%) film

Figure 1 (c) ZnO (pure) film and ZnS-ZnO nanocomposite films

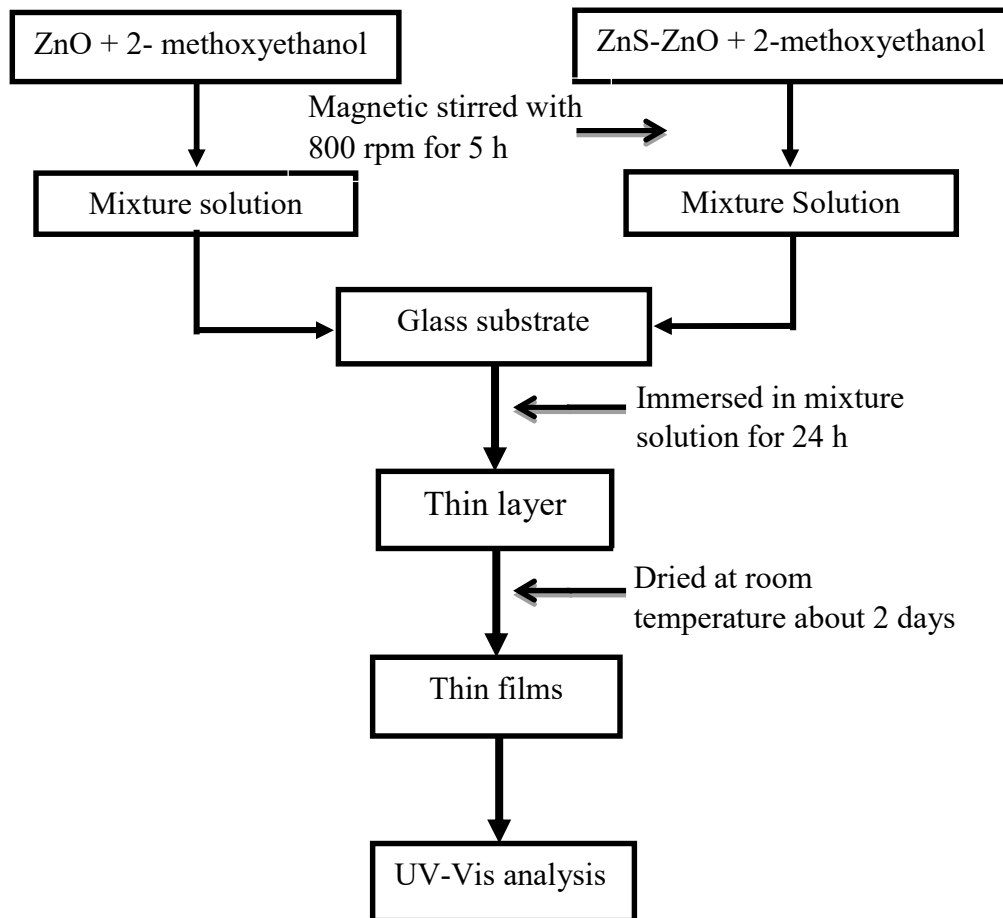


Figure 1(d) Block diagram of ZnO (pure) and ZnS–ZnO nanocomposite films

Results and Discussion

Optical Properties

The optical properties of the ZnO (pure) and ZnS-ZnO films are determined from the transmittance and absorbance measurements in the range 190nm and 1100 nm (UV-Vis IR) by spectrophotometer. Fig 2 (a-f) and Fig 3 (a-f) show the absorption spectra of ZnO (pure) and ZnS-ZnO films for different molar ratios.

Absorption coefficient α associated with the strong absorption region of the films were calculated from absorbance (A) and the thickness (t) using the relation.[Anura Kassim et al 2010][M. singh et al 2013].

$$\alpha = 2.3026A/t$$

where,

α = absorption coefficient

A =absorbance

t =thickness

The absorption coefficient of direct band gap semiconductor is given by,

$$\alpha = A(h\nu - E_g)^{1/2} / h\nu$$

where,

A = constant

$h\nu$ = incident photon energy

E_g = band gap

$(\alpha h\nu)^2 \sim h\nu$ is plotted and the intercepts of the extrapolated straight line at the $(\alpha h\nu)^2=0$ axis gives the value of the E_g of the material.

UV-Vis Analysis

UV-Visible spectroscopy was used for studying the spectral response of ZnO and ZnS. The absorption spectra of ZnO (100%) and ZnS (10%)-ZnO(90%), ZnS(20%)-ZnO (80%) , ZnS (30%)- ZnO (70%), ZnS (40%)-ZnO (60%), ZnS (50%)- ZnO (50%) films were characterized by UV- Vis spectroscopy and shown in Fig 2(a-f) and Fig 3 (a-f).The absorption spectra were observed in the wavelength between 190nm and 1100 nm which is characteristic of ZnO and ZnS. The corresponding calculated band gap values were reported in Table (1).The calculated band gap of pure ZnO was found to be 3.808 eV. The smooth shift of the absorption edge of the ZnS- ZnO different ratios were observed and they were indicated that the band gap values of ZnS (10%)-ZnO(90%), ZnS (20%)-ZnO (80%), ZnS (30%)-ZnO

(70%), ZnS (40%)-ZnO (60%) and ZnS (50%)-ZnO (50%) films were observed 3.393 eV, 3.295eV, 3.106 eV, 2.826 eV and 2.749 eV. The variation of optical band gap with ZnS - ZnO composite was shown in Fig 4.

Table 1. The optical band gap of ZnO (pure) and ZnS-ZnO composite films with different ratios

Film	Band gap (eV)
ZnO (pure)	3.808
ZnS (10%)-ZnO (90%)	3.393
ZnS (20%)-ZnO (80%)	3.295
ZnS (30%)-ZnO (70%)	3.106
ZnS (40%)-ZnO (60%)	2.826
ZnS (50%)-ZnO (50%)	2.749

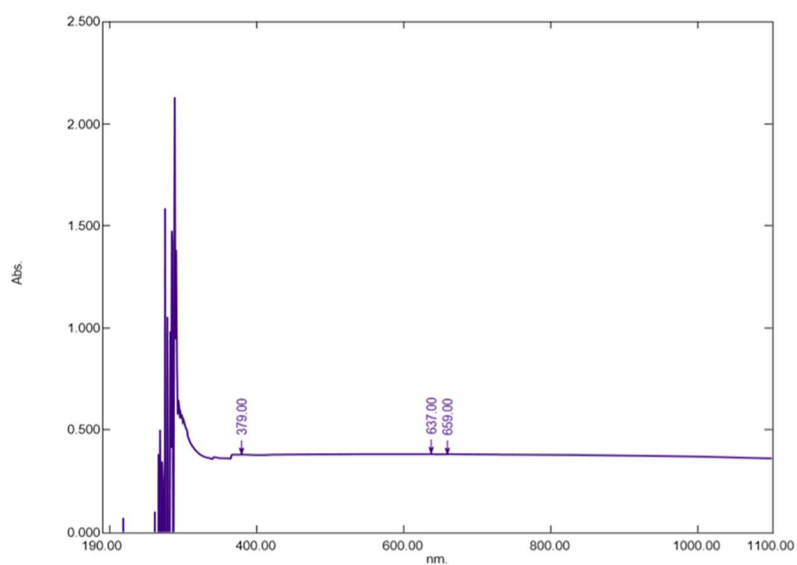


Figure 2 (a) UV-Vis absorption spectrum of ZnO (pure) film

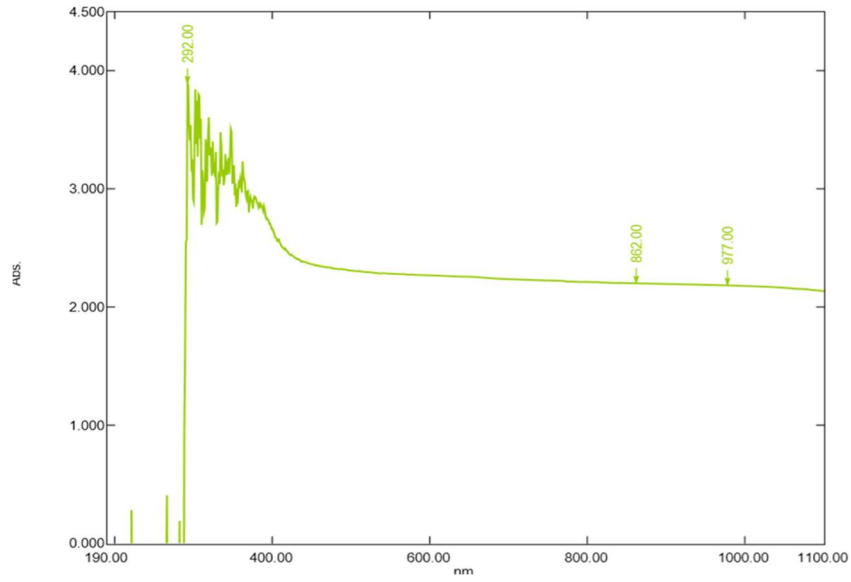


Figure2 (b) UV-Vis absorption spectrum of ZnS(10%)-ZnO(90%) film

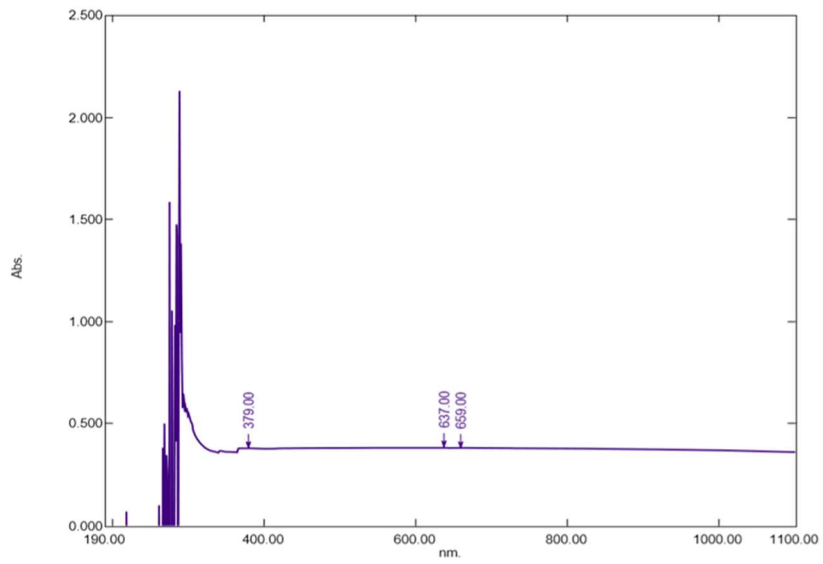


Figure2 (c) UV-Vis absorption spectrum of ZnS(20%) – ZnO(80%) film

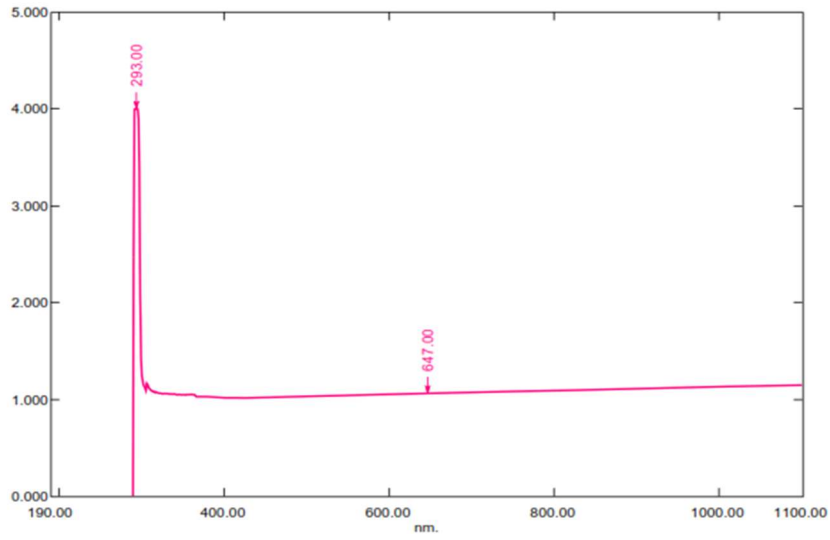


Figure2 (d) UV-Vis absorption spectrum of ZnS(30%)-ZnO(70%)film

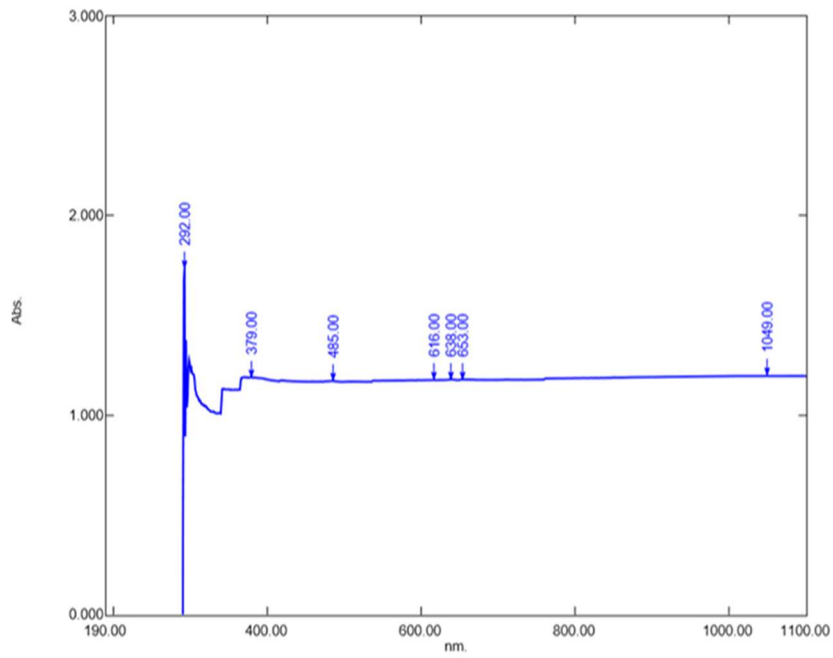


Figure 2 (e) UV-Vis absorption spectrum of ZnS(40%) - ZnO(60%)film

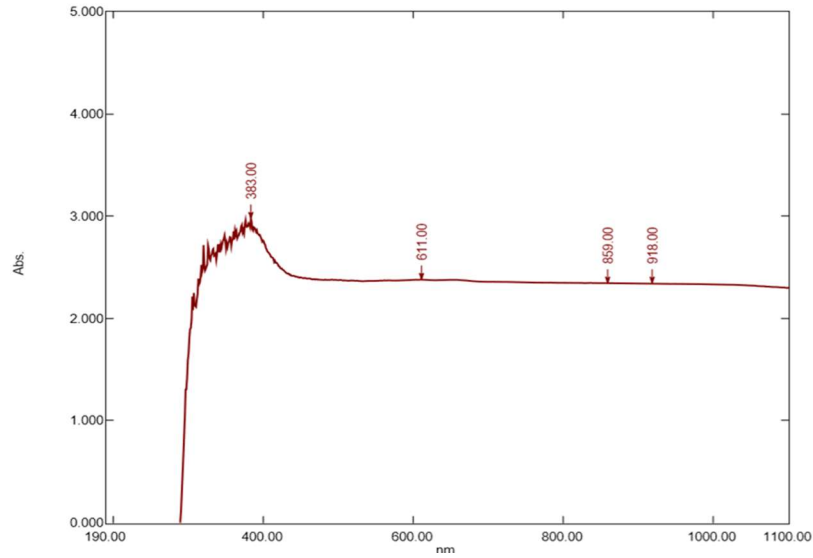


Figure 2 (f) UV-Vis absorption spectrum of ZnS(50%)-ZnO(50%) film

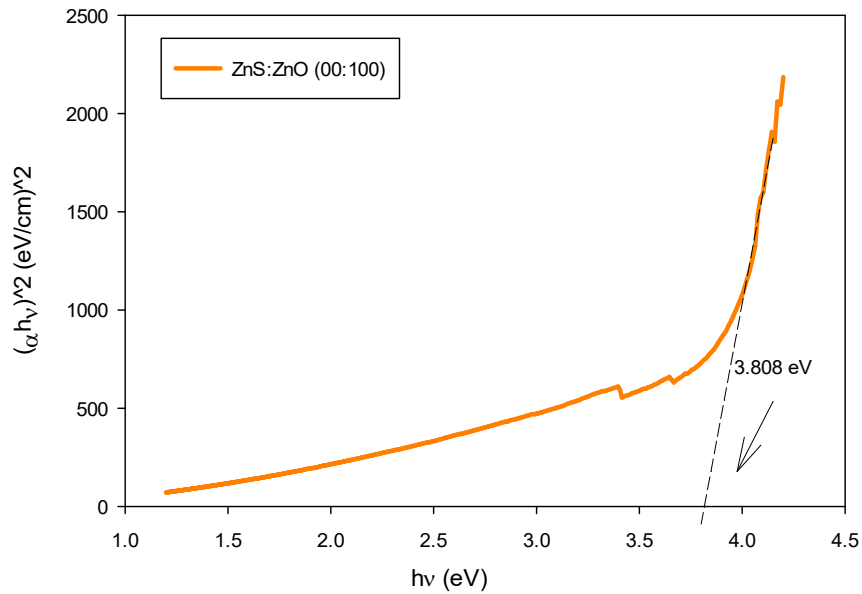


Figure 3 (a) $(\alpha h\nu)^2$ vs $h\nu$ plot for band gap calculation of as grown ZnO film

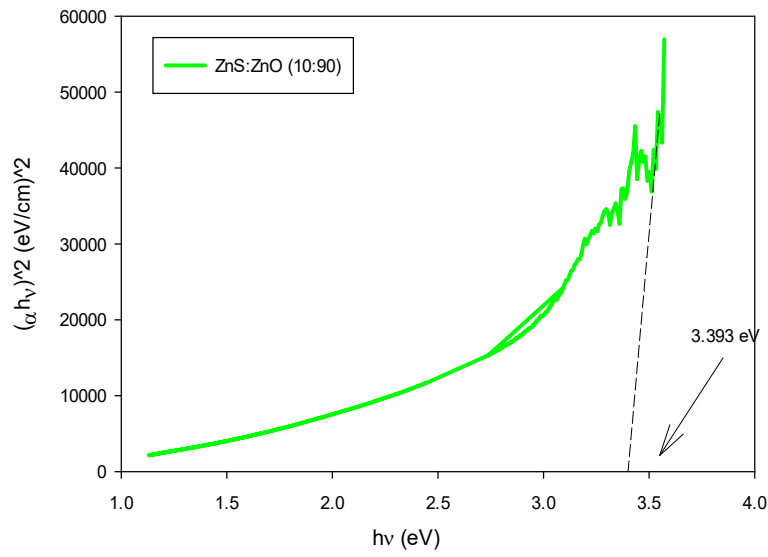


Figure 3(b) $(\alpha h\nu)^2$ vs $h\nu$ plot for band gap calculation of as grown ZnS (10%)-ZnO (90%) film

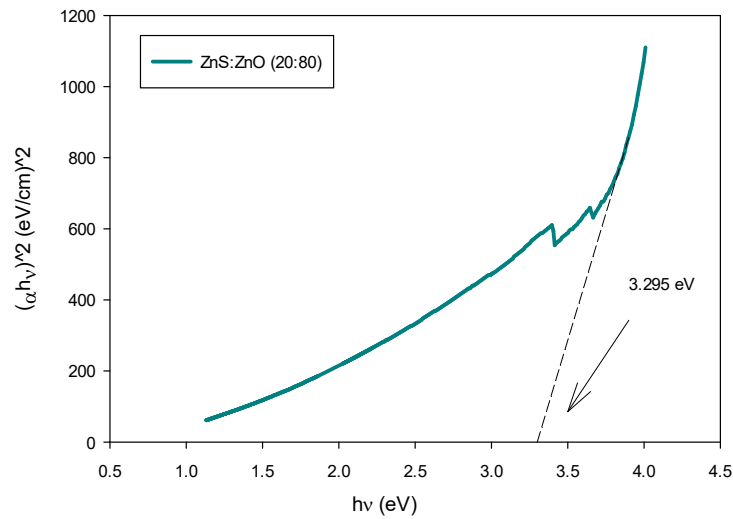


Figure 3 (c) $(\alpha h\nu)^2$ vs $h\nu$ plot for band gap calculation of as grown ZnS (20%)-ZnO (80%)

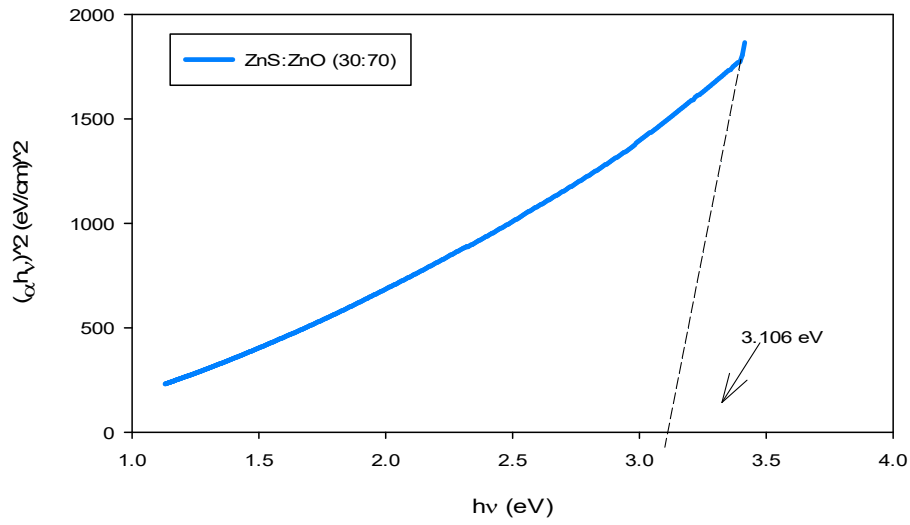


Figure 3 (d) $(\alpha h\nu)^2 Vshv$ plot for band gap calculation of as grown ZnS(30%)-ZnO(70%) film

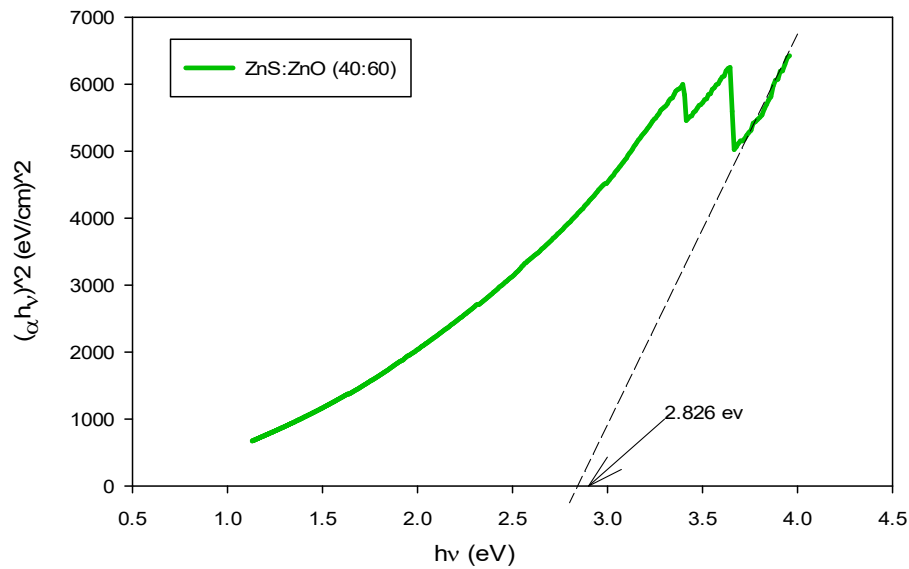


Figure 3 (e) $(\alpha h\nu)^2 Vshv$ plot for band gap calculation of as grown ZnS(40%)-ZnO(60%) film

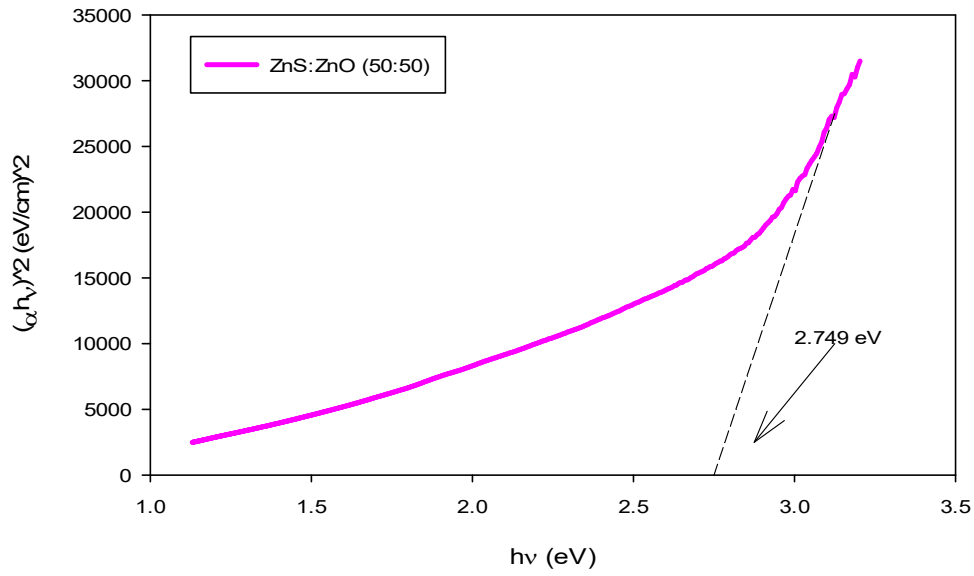


Figure 3 (f) $(\alpha h\nu)^2$ vs $h\nu$ plot for band gap calculation of as grown ZnS(50%)-ZnO(50%) film

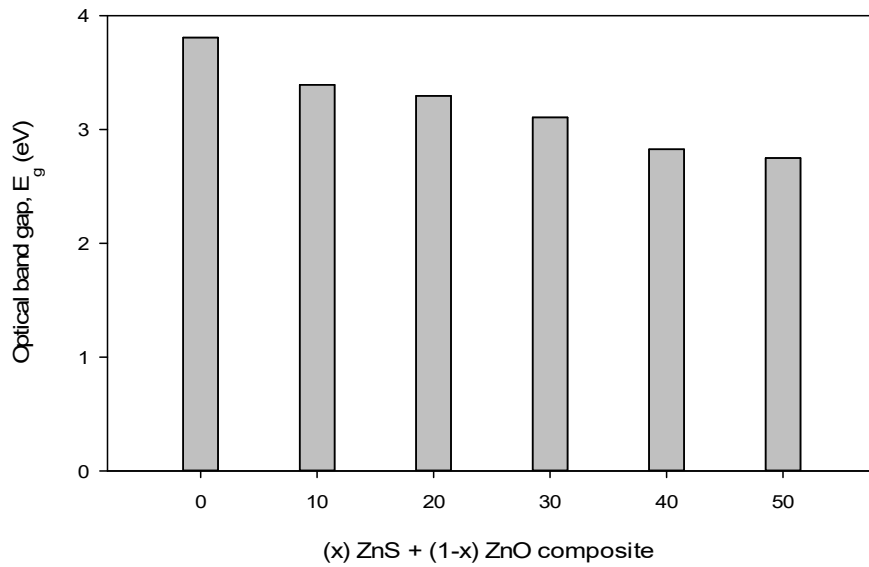


Figure 4. The variation of optical band gap with ZnS – ZnO nanocomposite

Conclusion

Preparation and characterization of ZnS – ZnO composite films have been studied. From the absorbance spectra, the optical band gap values were calculated and the band gap of pure ZnO was found to be 3.808 eV with direct transition. The values of ZnS-ZnO composite films were calculated to be 3.393 eV, 3.295 eV, 3.106 eV, 2.826 eV and 2.749 eV at the different ratios. From the UV-Vis results, it is sure that ZnO and ZnS-ZnO composite films can absorb the light in visible range. When the ZnS composition increased, the energy band gap of composites decreased due to the ability to control the properties of the material decoration through the changes on the synthesis parameters.

Acknowledgements

I would like to thank Professor Dr Khin Khin Win, Head of Department of Physics, University of Yangon, for her kind permission.

I would like to thank Professor Dr Soe Soe Nwe, Department of Physics, University of Yangon, for her valuable advice in the preparation of this paper.

I wish to express thanks to my Supervisor Dr May Hnin Thant, Lecturer, Department of Physics, University of Yangon, for her valuable suggestion to carry out this work.

A special thank to my Co-supervisor Dr Than Than Win, Associate professor Department of Physics, University of Distance Education Mandalay, for her dedicated supervision.

References

1. Antony. A., Mirali. K. V., Manoj.R.J., Jayaraj. M.K., Mater., Cem. Phys,(2005) Vol.90
2. Aoki.T.,Hatanaka.Y., Look. D. C., (2000) Appt. Phys. Lett . 76 3257
3. AnuraKassim.,Tan Wee Tee.,Ho Soon Min., Shanthi Monohorn., Saravanan Nagalingam (2010) Effect of bath temperature on the chemical bath deposition by pbse thin films journal of science engineering and technology,pp 126-132
4. Choudhary. K. R.,Sahoo. Y., Parasad. P. N., (2005) Adv.Mater.17 2877
5. Gu. F. N., Yue M. B., Wu. Z. Y., Sun. L.b., Wang. Y., Zhu. J. H., (2008) "Enhanced Blue Emission From ZnS-ZnO Composite Confine" in SBA-15, 128: 1148-1154
6. Jang. J., Yu. C.J., Choi. S. H., Ji. S. M., Kim. E.S., Lee. J. S., (2008) "Topotactic Synthesis of Mesoporous ZnS and ZnO Nanoplate and Their photocatalytic Activity", J. Catal 254: 144-155
7. M.singh.,k.cbahahada., y.kvijay., (2013) variation of optical band gap in oblique deposited selenium thin film Indian journal of pure and applied physics rajasthan Jaipur vol.55,pp 129-219
8. K. Skwok and X . Sun., "Thin Solid Films" (1998) Vol .335, P .229NgH. T., Han. J., Yamada. T., Nguyen. P., Chen. Y. P., Meyyappan. M., (2004) Nano Let t. 4. 1247
9. W. Chen., H.Ruan., Y. Hu.. D. L..Z.Chen., J. Xian., J. Chen., X. Fu.. Y. Shoo and Y. Zheng., CrysEngComm., (2012)., 6295-6305 RSC
10. X. Huang, M .Wang L. Shoo ., M.G. WillingerC. S. Lee and X.M.Meng., J.Phys. Chem.Lett ., (2013) , 4,740-744 Cross ReF CAS
11. X.Huang., M. Wang., M. G .Willinger., L. Shoo., D. S. Su and X. M. Meng., ACS Nano (2012) 6 , 7333-7339 CrossReF CAS PubMed
12. Zhang. W. H., Shi. J. L., Chen. H. R., Hua. Z. L., Yan. D. S., (2011) "Synthesis and Charactrrization of Nanosize ZnS Confined in Ordered Mesoporous Silica"., Chem . Mater 13: 648-654

SYNTHESIS, STRUCTURAL AND OPTICAL PROPERTIES OF ZnO-TiO₂-GO NANOCOMPOSITE

Su Su Lwin¹, May Hnin Thant², Than Than Win³ and Yin Maung Maung⁴

Abstract

Graphene oxide (GO) nanoparticles were synthesized by Hummer's method and the synthesized graphene oxide was analyzed by X-ray diffraction (XRD), energy dispersive X-ray (EDX), fourier transform infrared spectroscopy (FTIR), UV-Vis spectroscopy and field emission scanning electron microscopy (FESEM). The XRD pattern revealed a (001) diffraction peak, signifying the successful synthesis of GO. The elemental composition of GO was characterized by EDX analysis. The mass ratio of C/O is 2.26. The results of FT-IR showed that C-O bond, O-H group with water molecules and C=C bond with graphene oxide. UV-Vis spectra of GO exhibited maximum absorption peak at 290 nm. And then, ZnO-TiO₂nanocomposite was prepared by simple mechanochemical activation method and the ZnO-TiO₂-GOnanocomposite was prepared by simple mechanical stirring followed by ultra-sonication. X-ray diffraction (XRD) technique was employed to examine the crystal structure and phase analysis of ZnO-TiO₂ and ZnO-TiO₂-GO nanocomposite. The elemental composition of ZnO-TiO₂ and ZnO-TiO₂-GOnanocomposite were characterized by EDX analysis. The optical properties of ZnO-TiO₂ and ZnO-TiO₂-GO nanocomposite were identified by ultraviolet-visible spectroscopy. UV-Vis spectra of ZnO-TiO₂ nanocomposite exhibited maximum absorption peak at 289 nm and 372 nm. For ZnO-TiO₂-GO nanocomposite, the maximum absorption peak are 543 nm and 645 nm. The particles sizes and the surface structure were examined by atomic force microscope (AFM) analysis and field emission scanning electron microscope (FESEM) analysis.

Keywords: Graphene oxide, Nanocomposite, Atomic force microscope, Hummer's method

¹ Demonstrator, Department of Physics, Myeik University

² Lecturer, Department of Physics, University of Yangon

³ Associate Professor, Department of Physics, Mandalay University of Distance Education

⁴ Associate Professor, Department of Physics, University of Mandalay

Introduction

Nanomaterial have found widespread applications in many devices including photo detectors, surface acoustic, wave devices, UV nanolaser, varistors, solar cells, gas sensors, biosensor, ceramics, nanogenerators, and field emission devices. However, the characteristics, especially the band gap of semiconductors are influenced mostly by the transition of particle size from bulk into the nanometer lever scale. Among the semiconductors, the conducting oxides (COs) (e.g. ZnO, SnO₂, TiO₂ etc.) have been researched and investigated the most for their possible use as photocatalysts. The organic dyes are notorious environmental pollutants which could be degraded under sunlight using the COs as photocatalysts. Among these different COs photocatalysts, TiO₂ and ZnO are important nanomaterials owning fascinating physico-chemical characteristics [Hameed Ullah et al (2014)]. Two metal oxides ZnO and TiO₂ are an important in terms of materials technology and have various applications in different industries [Majid jafan et al (2014)]. Zinc oxides of particle size in nanometer range have been paid more attention for their unique properties. They are widely used for solar energy conversion, non-linear optics, catalysis, varistors, pigments, gas sensors, cosmetics. Zinc oxide (ZnO) is an unexpansive, n-type semiconductor with a wide band gap having optical transparency in the visible range [S. Jurablu et al (2015) and P. M. Aneesh (2007)]. Nano titanium dioxide powder has many good functions and features, such as stable properties, non-toxic, high activity of photo catalysis, low cost and good at resisting chemical attack. It is also a nice photo catalyst, disinfectant and antiseptic [Ziquanliu et al (2013)]. ZnO is a direct band gap semiconductor and TiO₂ is an indirect band gap with an energy band gap of 3.0 eV (anatase) or 3.2 eV (rutile) [Yuan Zhi-Hao et al (2001)]. To prevent the reduction of the zinc oxide, zinc oxide is combined with other metal oxides such as: TiO₂, Fe₂O₃, Al₂O₃, etc. In order to improve photocatalytic activity of TiO₂ and ZnO, a popular route is to form composite. ZnO–TiO₂ based sorbents appear to have the fewest technical problems. TiO₂ reacts with ZnO at high temperatures forming zinc titanates and form Zn₂TiO₄, ZnTiO₃ or Zn₂Ti₃O₈, depending on ZnO/TiO₂ molar ratio and on the preparation and calcination conditions.[Majid Jafan (2014)]. Graphene oxide is a wonder material, also offers new avenues in nano composites when combined with these wide band gap semiconductors. Excellent optical

transparency, mechanical strength and electrical conductivity have led to its use in numerous applications. Its chemical stability renders its use as nanocomposite with other materials. With its high optical transparency and specific surface area, it has been investigated with the aim of replacing indium based transparent conducting oxide, potentially opening way for flexible substrates [Muhammad Imran Ahmed et al and C. Pragathiswaran et al]. TiO_2 , Fe_3O_4 and ZnO have been investigated as nanocomposite with GO, offering properties superior to individual materials [Wan-Kuen et al] ZnO -GO composites have been reported for applications like corrosion protection, photocatalysis, batteries, field emission prosperities and for incorporation in polymer solar cells [Muhammad Ali Johar et al]. In this study, ZnO - TiO_2 nanocomposite was synthesized by ball milling at room temperature. A stoichiometric mixture of nano ZnO and TiO_2 powders in 1:1 molar ratio. The graphene oxide (GO) was added to the ZnO - TiO_2 nanocomposite by simple mechanical stirring followed by ultra-sonication. The resulting powders were analyzed by XRD, EDX, FTIR, UV-Vis, FESEM and AFM.

Experimental Procedure

Preparation of Graphene Oxide (GO)

In this research, Graphite, Sulphuric acid (H_2SO_4), Sodium nitrate (NaNO_3), Phosphoric acid (H_3PO_4), Potassium permanganate (KMnO_4) and Hydrogen Peroxide (H_2O_2) were used as starting materials. The block diagram of sample preparation was described in figure 1. All chemicals were analytically pure and directly used as received without further purification. Graphene oxide (GO) was prepared according to the Hummer method. In detail, 500 ml beaker was filled with 108 ml of H_2SO_4 , 5 g of graphite, 2.5 g of NaNO_3 and 12 ml of H_3PO_4 were added into the beaker. The suspension was stirred in an ice bath for 10 min (fig 2). Next, 15 g of KMnO_4 was added to the suspension. The rate of addition was carefully controlled to keep the reaction temperature below 5°C and stirred in ice bath for 3 h (fig 3). Then the mixture was put in a 40°C water bath for 60 min. The temperature of the mixture was adjusted to a constant 98°C for 60 min while water was added continuously. The color of the mixture was changed into yellow. Deionized water was further added so that the volume of the suspension was 400 ml.

15 ml of H₂O₂ was added after 5 min. The reaction product was washed by rinsing and centrifugation with 5 % HCl (fig 4 & 5) then deionized (DI) water for several times to reach pH 5-7. Finally, the product was dried at 60 °C for 24 h in a vacuum oven. The obtained samples were characterized by X-ray diffraction (XRD) using (Rigaku RINT 2000) and energy dispersive X-ray (EDX). Fourier transform infrared spectroscopy (FTIR). UV-Vis spectrometer (UV-Vis; UV-1800) was used to measure the optical absorption properties of GO. The nano structure was confirmed by field emission scanning electron microscope (FESEM).

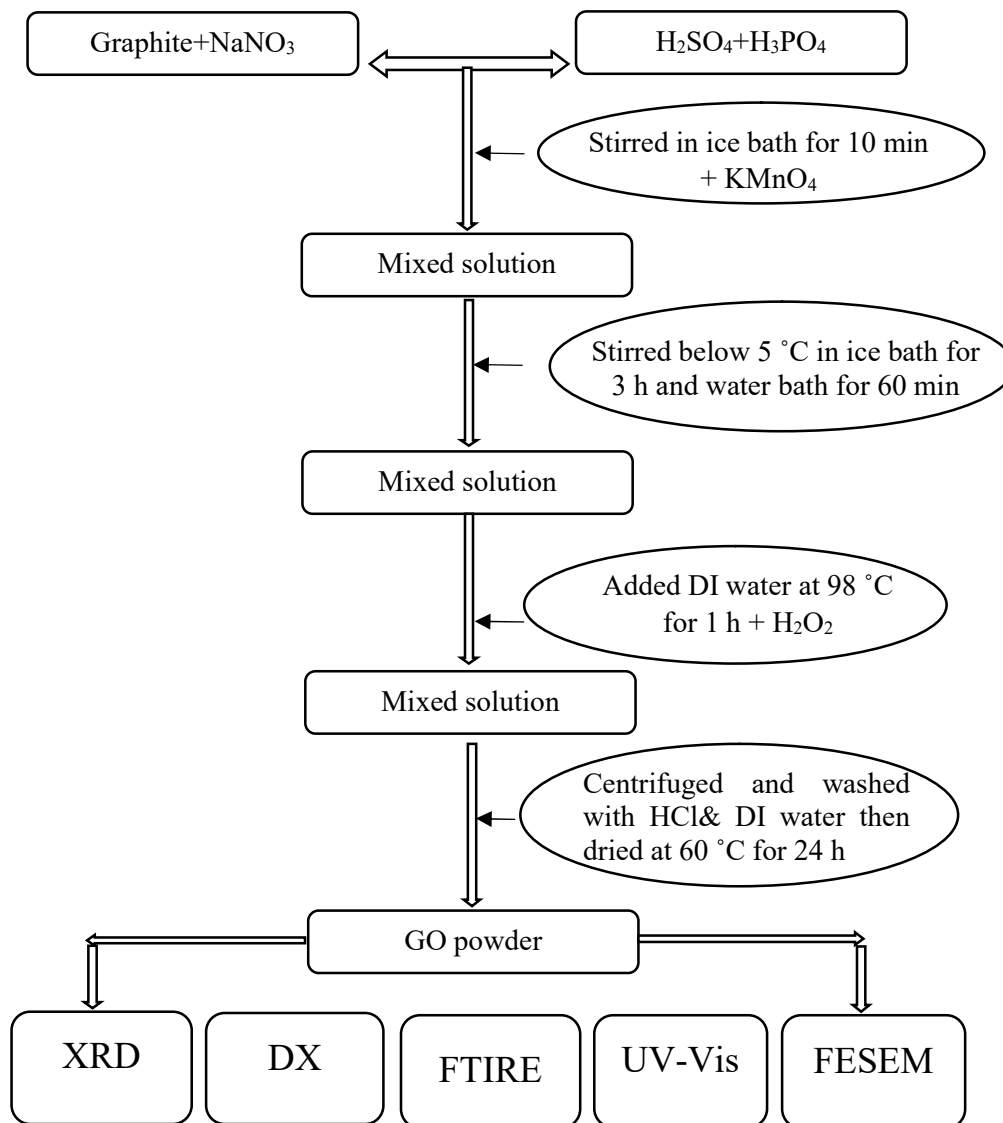


Figure 1. Block diagram of preparation of graphene oxide powder



Figure 2. Graphite, NaNO_3 and H_3PO_4 mixture was stirred in ice bath



Figure 3. Water bath



Figure 4. Centrifuge



Figure 5 . After centrifuging

Preparation of ZnO-TiO₂ nanocomposite

In this case, ZnO and TiO₂ were used as the starting materials. Firstly, ZnO and TiO₂ powder with stoichiometry ZnO: TiO₂=1:1 molar ratio were mixed. Then the mixture was milled with the ball milling machine for 10 h to reduce the particle size. Three stage mesh-sieving was employed to get the uniform particle size. After the sample had calcined at 400°C for 1 h. The block diagram of sample investigation was described in figure 6. The obtained sample was characterized by the X-ray diffraction (XRD) using (Rigaku RINT 2000) and wavelength dispersive X-ray spectroscopy EDX (Bruker Tiger S). Optical absorption spectra of the sample were taken with UV-1800 UV-Vis Spectrometer. The microstructure of the samples were examined by atomic force microscope AFM (Bruker N8 Rados) and field emission scanning electron microscope (FESEM).

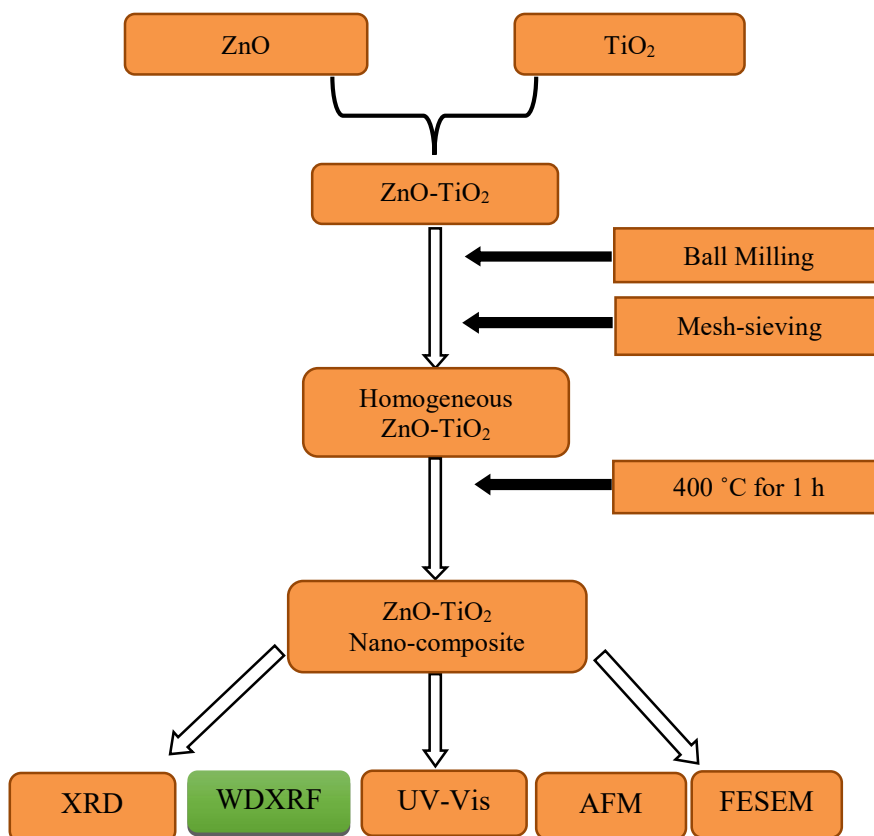


Figure 6 The block diagram of ZnO-TiO₂ nanocomposite

Preparation of ZnO-TiO₂-GO nanocomposite

ZnO-TiO₂-GO nanocomposite was prepared by added to the ZnO-TiO₂ nanocomposite by simple mechanical stirring followed by ultra-sonication. Firstly, 1 g of graphene oxide was added in 100 ml of distilled water and stirred by magnetic stirrer for 1 h. After stirring, the GO solution was ultrasonicated for 1 h. Then 2 g of ZnO-TiO₂nanocomposite was added into the solution and the mixture was ultra sonicated for 1 h again (figure7). The mixture was stirred by magnetic stirrer at 80 °C for 6 h. The mixture was then centrifuged and washed with ethanol for several times to remove the undecorated particle and unreacted chemicals (figure 8). Finally, the product was dried in an air oven at 80 °C for 6 h before characterization. Block diagram for the preparation of ZnO-TiO₂-GO nanocomposite are shown in figure 9.



Figure 7 Ultra-sonication



Figure 8. After centrifuging

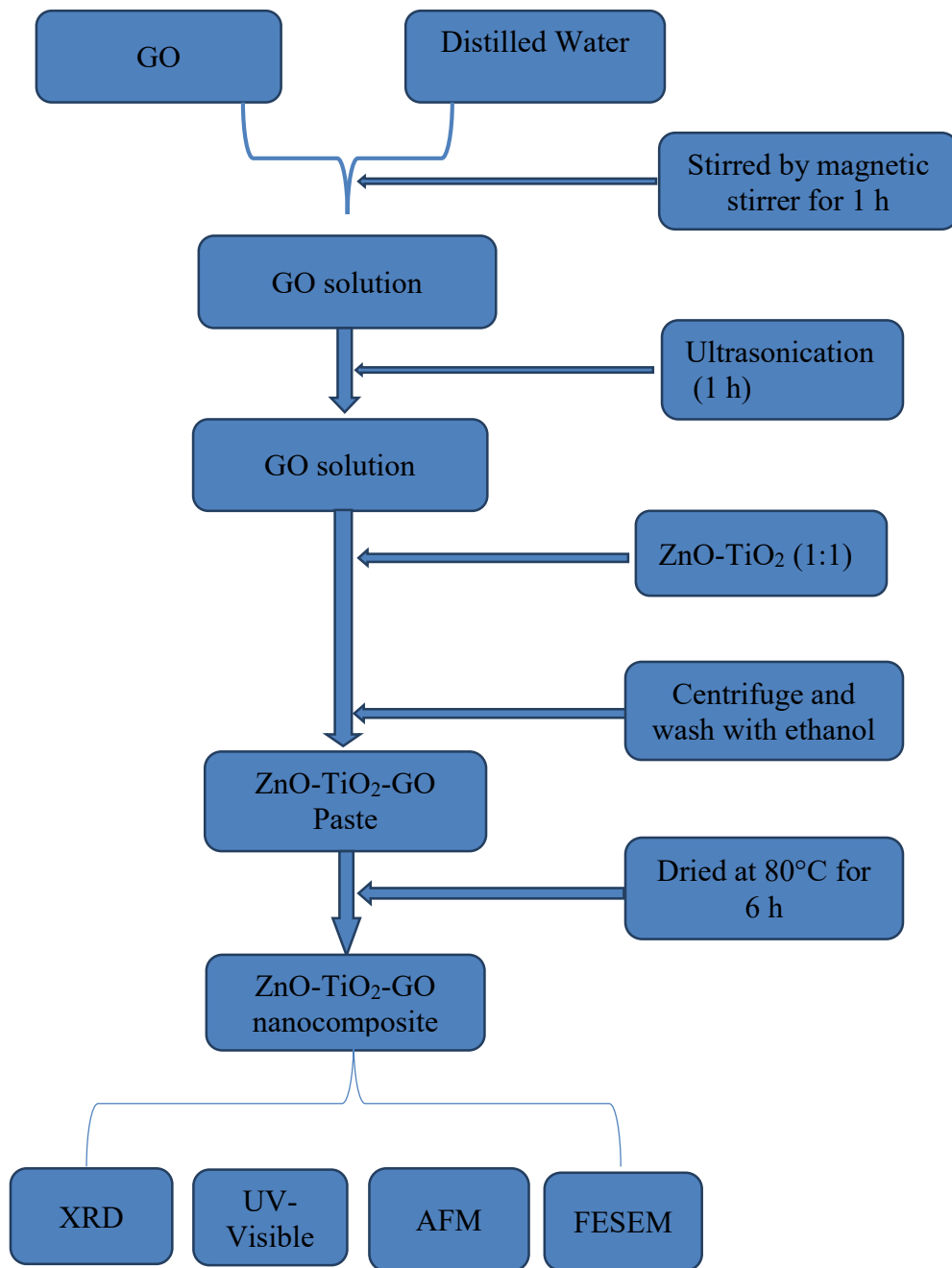


Figure 9. Block diagram for the preparation of ZnO-TiO₂-GO nanocomposite

Results and Discussion

XRD analysis

X-ray diffraction is used to determine crystallinity of polymeric materials. XRD uses the total X-ray scattering both the crystalline and amorphous phases to determine the crystallinity. The phase analysis of GO, ZnO-TiO₂ and ZnO-TiO₂-GO powders were determined by using a X-ray Diffractometer (Rigaku RINT 2000). XRD was performed using monochromatic CuK α radiation ($\lambda = 1.54056 \text{ \AA}$) operated at 40 kV (tube voltage) and 40 mA (tube current). Sample was scanned from 5° to 70° in diffraction angle 2θ with a step-size of 0.02°. The XRD pattern of graphite, graphene oxide, ZnO-TiO₂ and ZnO-TiO₂-GO nanocomposite were shown in figures 10, 11, 12 and 13. According to the XRD pattern of graphite, which showed a strong and sharp diffraction peak at $2\theta = 26.61^\circ$ has the interplanar distance of 0.334 nm. The graphene oxide were matched with standard library file 03-065-1528. GO shows an intense and sharp peak at $2\theta = 11.07^\circ$ has the interplanar distance of 0.799 nm. The increase in interplanar distance of GO is due to the existence of oxygen functional groups. In figure 12, The TiO₂ anatase (PDF-89-4921) and ZnO (PDF-89-0511) phased are observed in the X-ray spectra of mechanochemically activated ZnO-TiO₂ nanocomposite samples with molar ratio of ZnO and TiO₂ as 1:1. ZnO-TiO₂ nanocomposite X-ray patterns is present the higher crystallinity degree of investigated materials. In figure 13 the Graphene Oxide (GO) shows the diffraction peak at 2θ value of 11.07°. In composite the TiO₂ anatase and ZnO phased are clearly observed but the main diffraction peak of GO is absent and it probably lead to partial reduction of GO to graphene and a weak peak at $2\theta = 26.50^\circ$ appears (see in figure 13). It may be due to the low amount and relatively low diffraction intensity of GO in comparison with the diffraction intensity of ZnO-TiO₂ nanocomposite [C.Pragathiswaran et al]. Moreover the other possibility is due to the intercalation of metal oxide after ultrasonic treatment [S Mathialagin et al]. The comparison between the XRD pattern of ZnO-TiO₂-GO composite in international journals and my observed sample are shown in table 1.

Table 1. The XRD patterns of ZnO-TiO₂-GO composite in international journals

No.	Author and Journal name	XRD pattern
1	Mathialagin et al, jornal of Scientific.	
2	Guru Nisha Narayanan et al, I.Journals Chem Tech.	
3	Václav Štengl et al, Chemistry Central Journal.	
4	C.Pragathiswaran et al, Journal of applicable Chemistry	

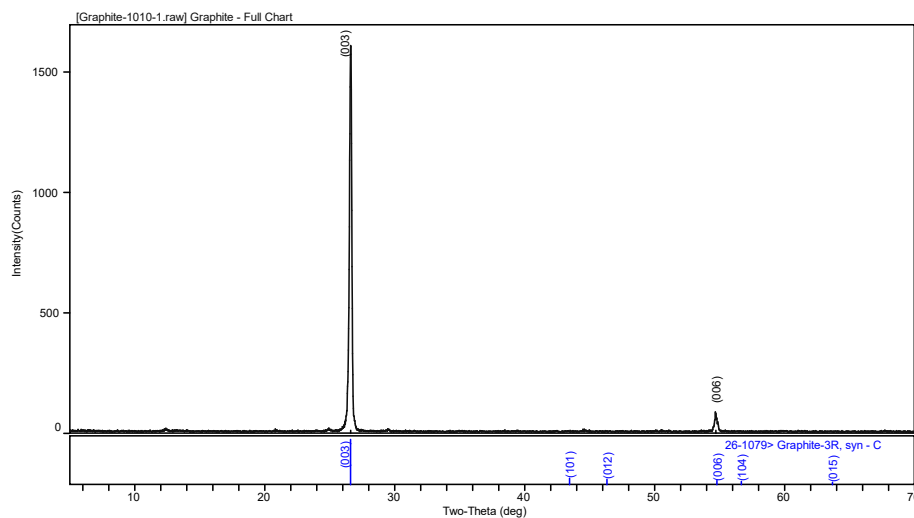


Figure 10. XRD pattern of graphite

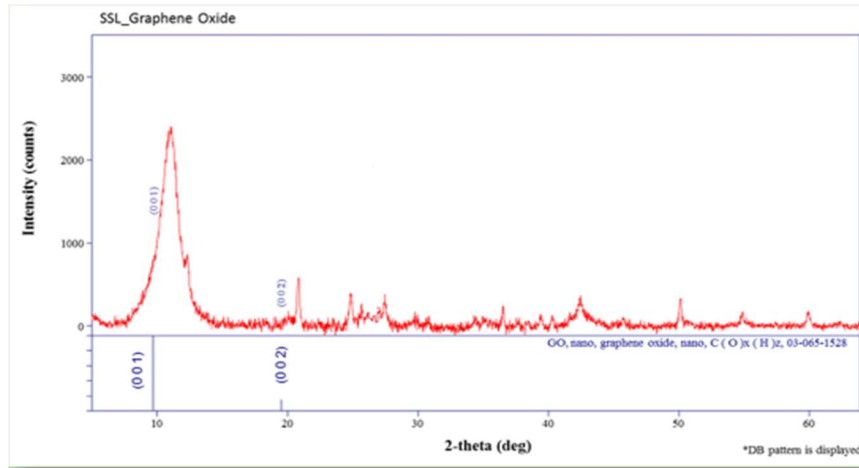


Figure 11. XRD pattern of graphene oxide

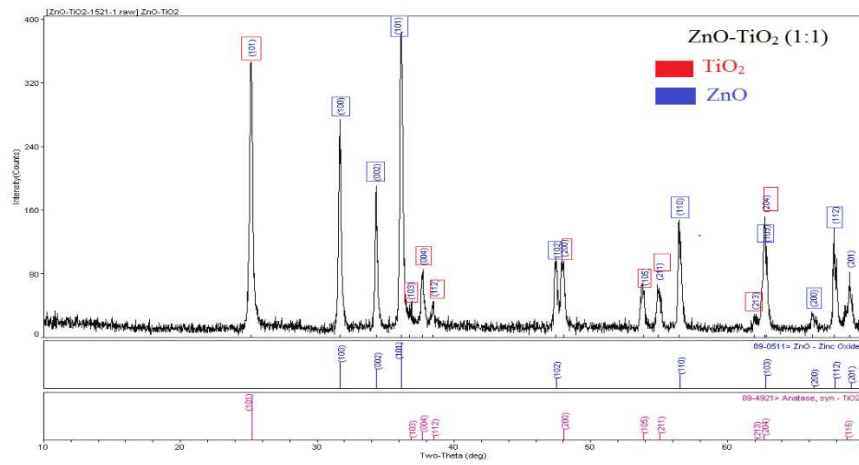


Figure 12. XRD pattern of ZnO-TiO₂ nanocomposite at 400 °C

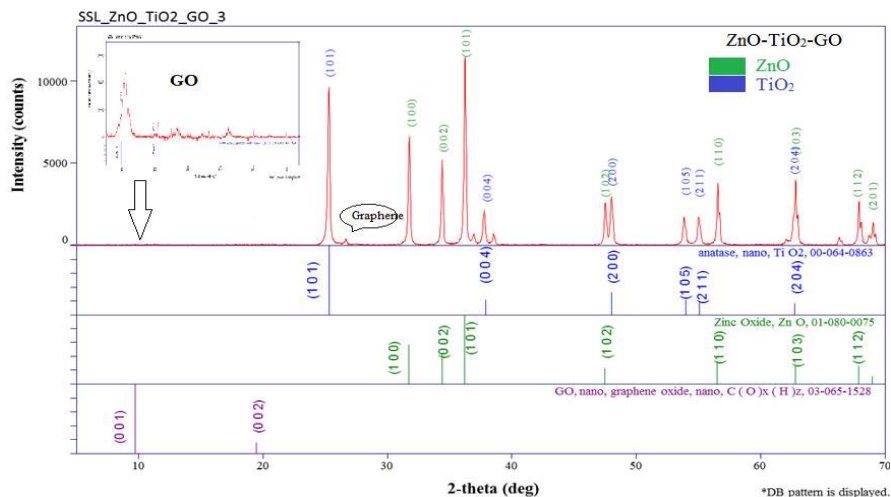


Figure 13. XRD pattern of ZnO-TiO₂-GO nanocomposite at 80 °C.

EDX analysis

The EDX figure of graphene oxide and the results of the EDX elemental for C and O elements of GO are describe in figure 14. The content of C is 67.35 % and the content of O is 29.75%. The mass ratio of C/O is 2.26. The international result of EDX for graphene oxide list in table 2. The EDX spectrum and elemental composition of ZnO-TiO₂ nanocomposite and ZnO-TiO₂-GO nanocomposite are also being described in figure15 and 16by EDX analysis.

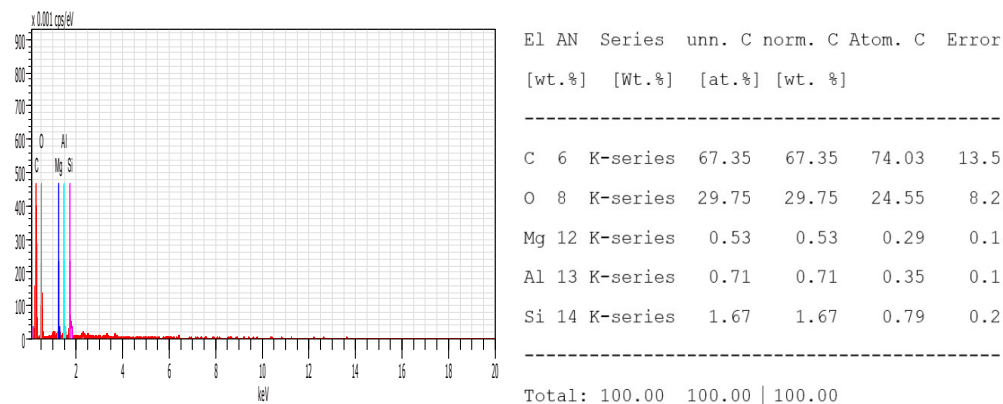
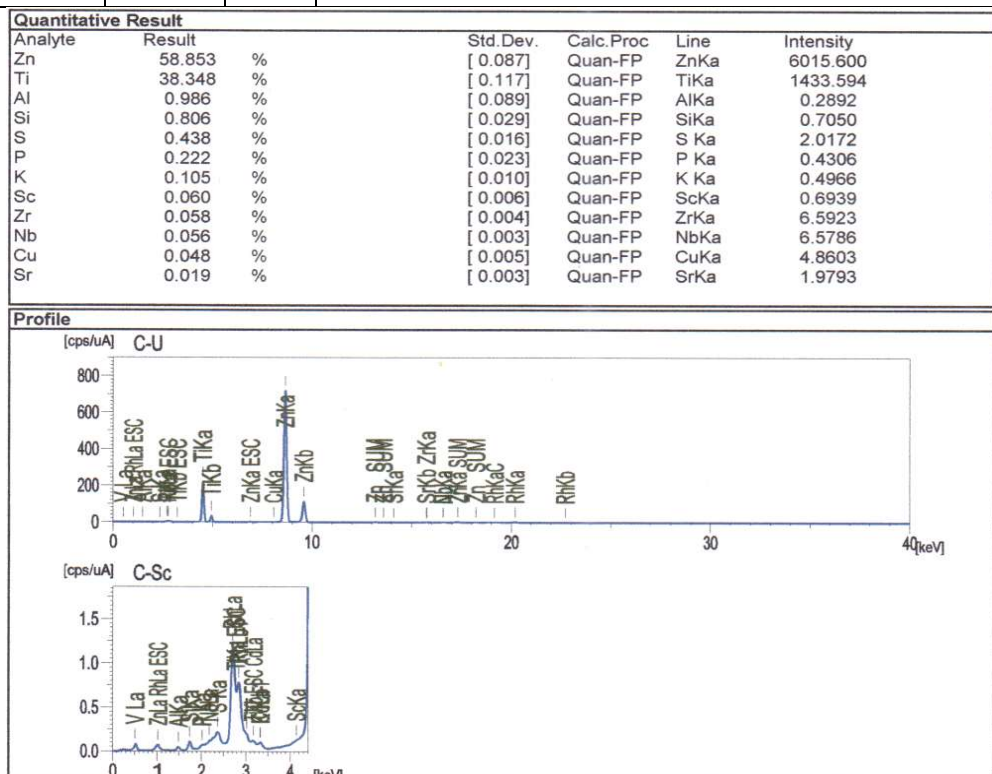


Figure14. EDX spectrum and elemental microanalyses for C and O elements graphene oxide

Table 3. The EDX elemental microanalyses for C and O elements in international journals

Element (wt. %)		C/O	International Journals
C	O		
51.32	44.27	1.15	Won-Chun Oh et al 2010 Journal of the Korean Physical Society, Vol. 56, No. 4, pp. 1097~1102
65.47	35.53	1.84	YunxianPiao et al 2011 The Royal Society of Chemistry
67.35	29.75	2.26	Observed sample

**Figure 15.** EDX spectrum and elemental composition of ZnO-TiO₂ nanocomposite

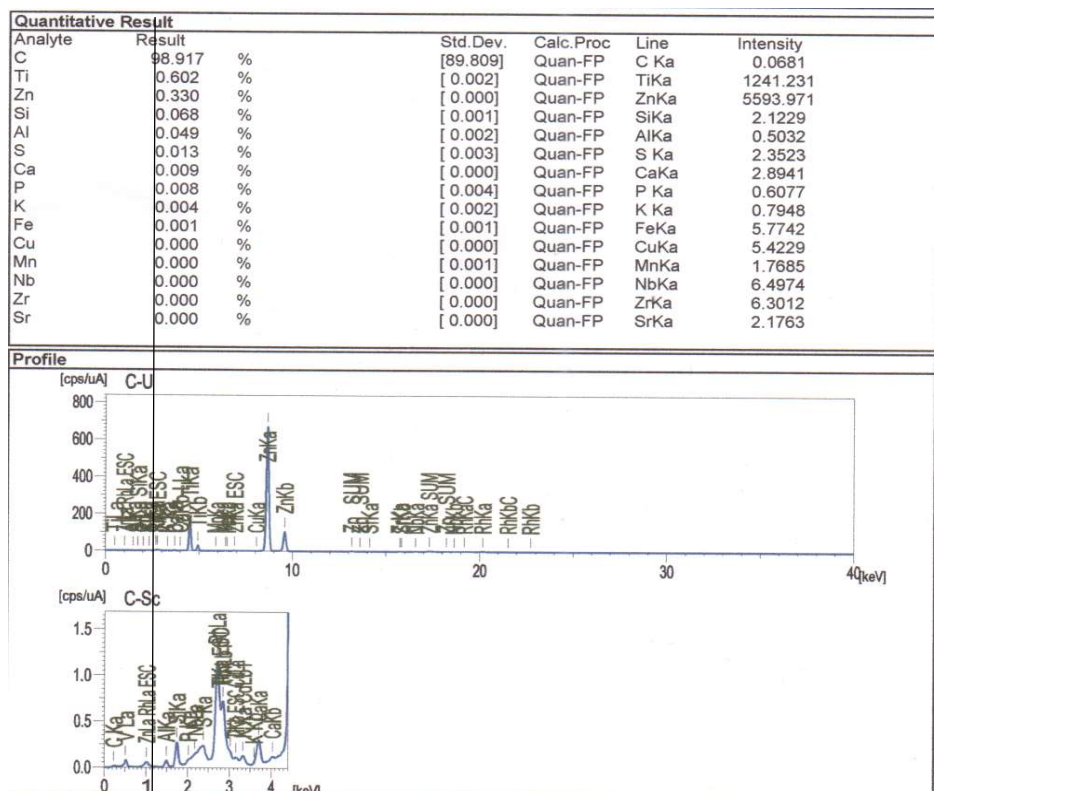


Figure 16. EDX spectrum and elemental composition of ZnO-TiO₂-GO nanocomposite

FTIR analysis of Graphene Oxide

Infrared absorption spectrum diagram (FTIR) of graphene oxide was shown in figure 17. FTIR analysis allows qualitative discussion of the structure of graphene oxide. According to the FTIR analysis the peak at 1082.10 cm⁻¹ and 1384.94 cm⁻¹ which are attributed to the C-O bond, confirming the presence of oxide functional groups after the oxidation process. The peak at 1626.05 cm⁻¹ can be attributed to the stretching vibration of C=C bond. The 3408.33 cm⁻¹ correspond to O-H group of water molecules absorbed on graphene oxide. The presence of these oxygen containing groups reveals that the graphite has been oxidized.

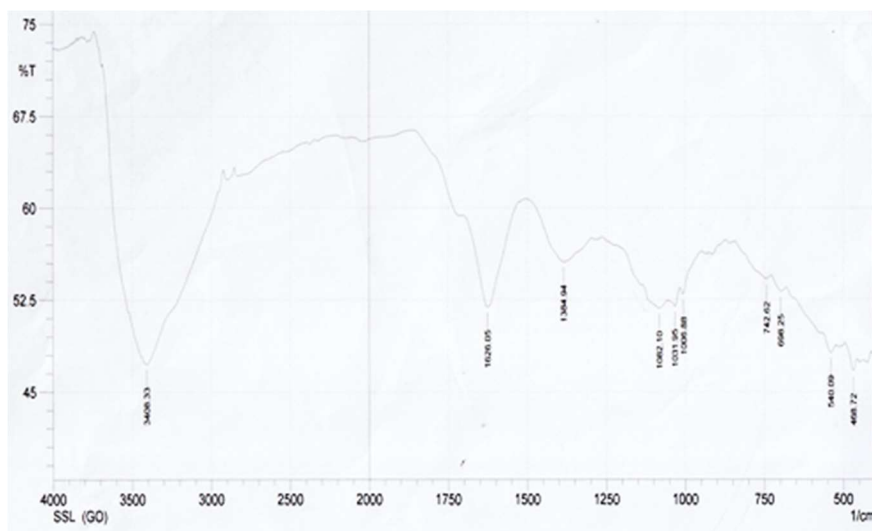


Figure 17. FTIR spectrum of graphene oxide

UV-Visible analysis

The UV-Vis spectra of GO, ZnO-TiO₂ nanocomposite and ZnO-TiO₂-GO nanocomposite powders were recorded with respect to the glass substrate placed in the reference beam using beam spectrometer in the range 190 to 1100 nm. The absorption spectrum of GO, ZnO-TiO₂, ZnO-TiO₂-GO deposited on glass substrate were shown in figure 18, 19 and 20. The GO shows high absorption coefficient in the UV region (290 nm). [In aqueous suspension, measurements reveal strong optical absorption in the UV (Mark Lundie et al)]. UV-Vis spectra of ZnO-TiO₂ nanocomposite exhibited at 289 nm and 372 nm and ZnO-TiO₂-GO was 543 nm and 645 nm respectively. The optical band energy (E_g) of the semiconductor is calculated from the relation.

$$\alpha h\nu = A (h\nu - E_g)^n \text{ ————— (1)}$$

where α is the absorption coefficient, A is a constant (independent from ν), n is the exponent that depends upon the quantum selection rules for the particular material, h is the planck's constant and E_g is the energy band gap. A plot of $(\alpha h\nu)^2$ versus $h\nu$ shows intermediate linear region, the extrapolation of the linear part can be used to calculated the E_g from intersect with $h\nu$ axis as shown in figure 21, 22 and 23. The resultant values of E_g for pure GO is found

to be about 3.93 eV and Zn-TiO₂ nanocomposite is 3.8 eV. The value of E_g for ZnO-TiO₂-GO nanocomposite is found to be 4.083 eV.

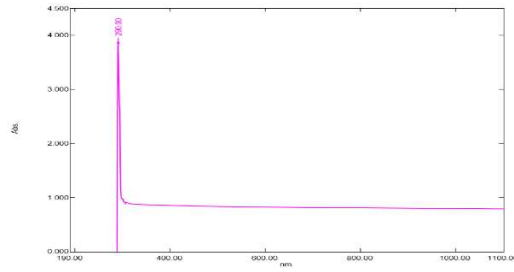


Figure 18.The absorption spectrum of graphene oxide

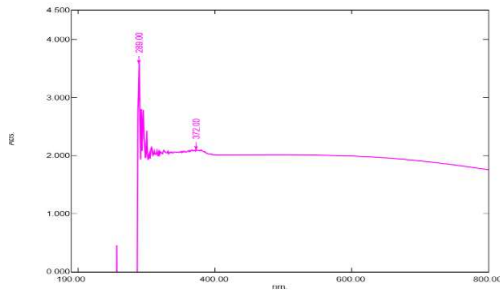


Figure 19

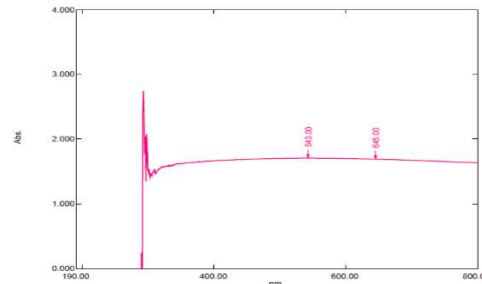


Figure 20

The absorption spectrum of (Fig.19) ZnO-TiO₂, (Fig.20) ZnO-TiO₂-GO nanocomposites

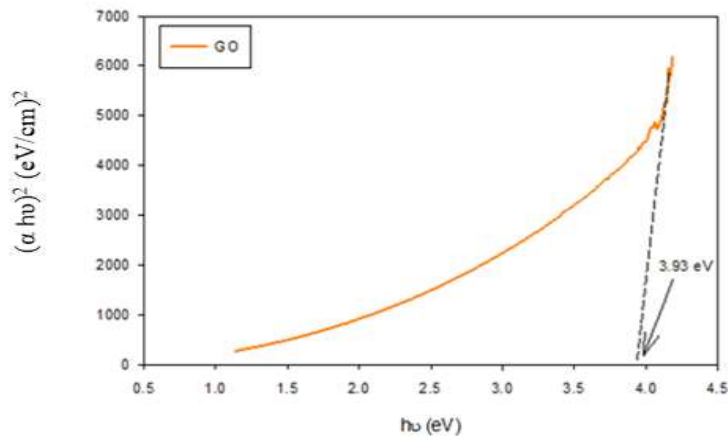


Figure 21. Plot of $(\alpha h\nu)^2$ vs photon energy ($h\nu$) for graphene oxide

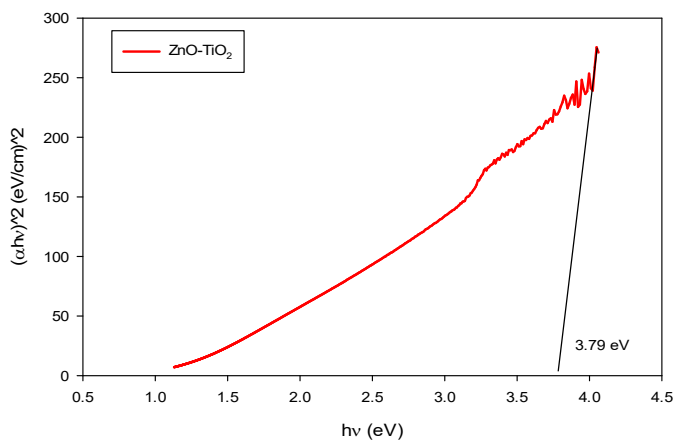


Figure 22. Plot of $(\alpha h\nu)^2$ vs. photon energy ($h\nu$) for ZnO-TiO₂ nanocomposite

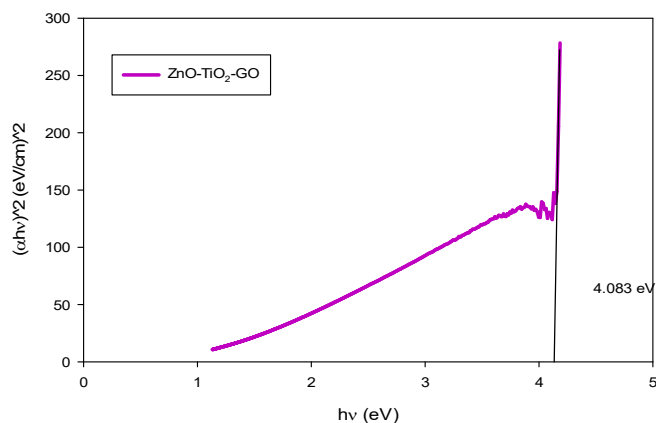


Figure 23. Plot of $(\alpha h\nu)^2$ vs. photon energy ($h\nu$) for ZnO-TiO₂-GO nanocomposit

AFM analysis

The AFM figures of topography, the amplitude, the 3D image and line profile of ZnO-TiO₂ and ZnO-TiO₂-GOnanocomposite are shown in figure 24 and 25. The particles sizes of ZnO-TiO₂ nanocomposites are estimated from particles height to avoid tip-convolution effects. According to the amplitude line profile most of the particles are agglomerate and the average particles sizes of ZnO-TiO₂ nanocomposite are about 78 nm. In ZnO-TiO₂-

GO nanocomposite, it is observed that ZnO-TiO₂ nanocomposites are well attached onto the surface of GO sheet. The average particles sizes are also estimated from the particles height and the average particles sizes are about 30 nm- 50 nm.

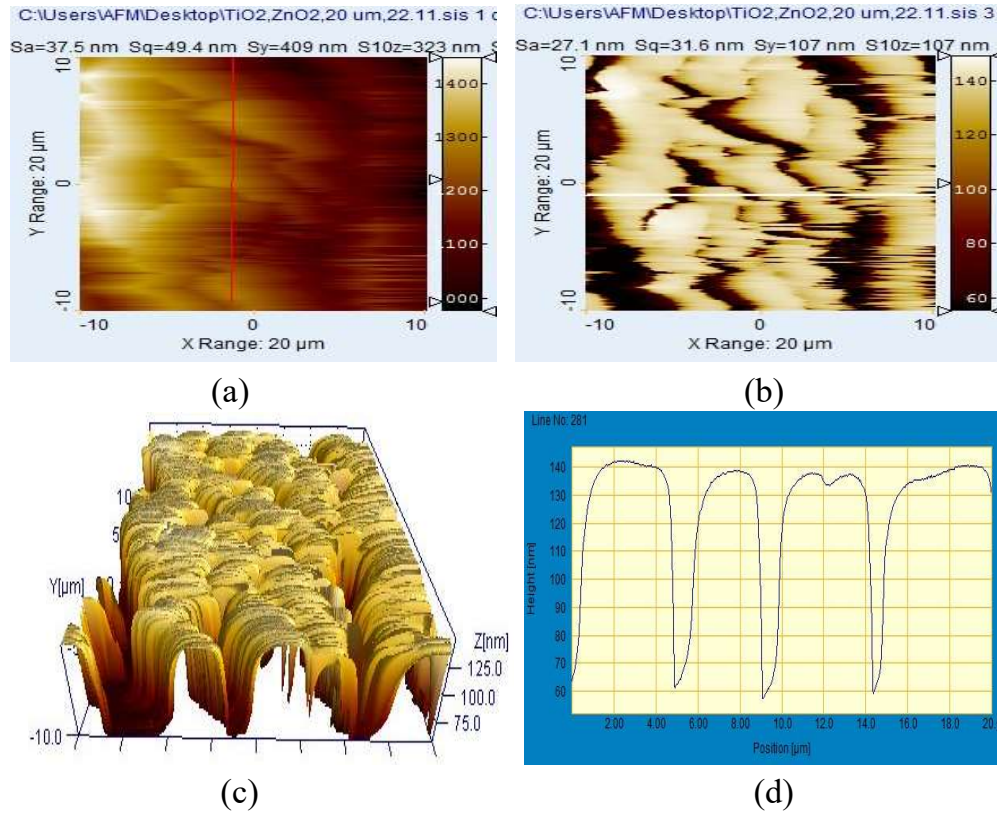
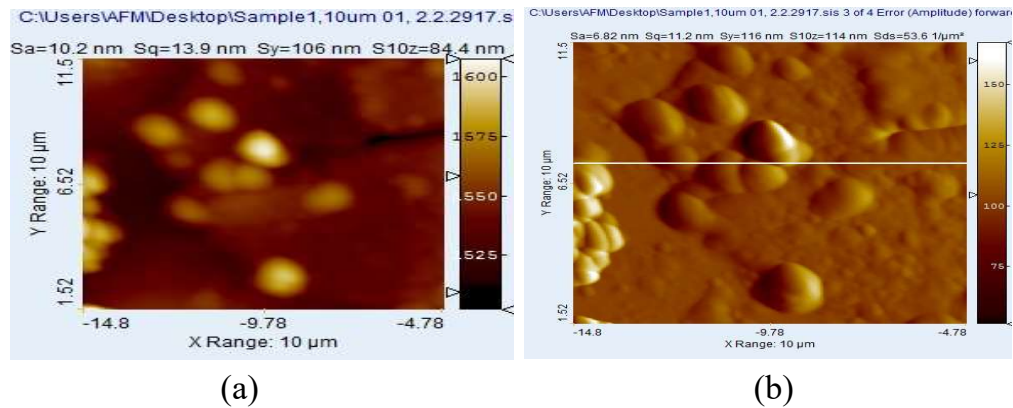
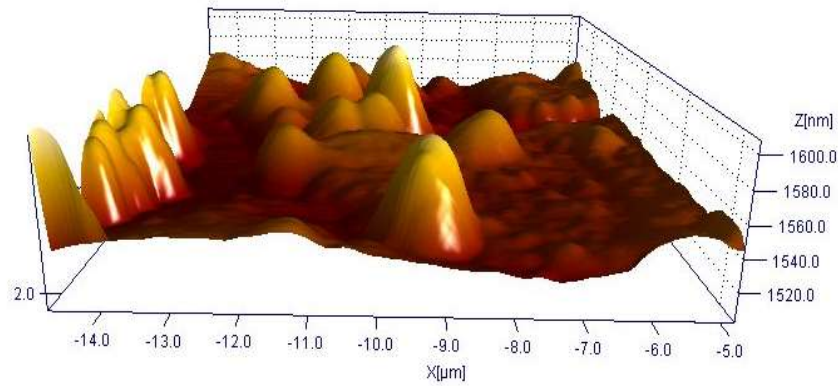


Figure 24. The topography (a), the amplitude (b), the 3D image (c) and line profile for ZnO-TiO₂nanocomposites (d)





(c)



(d)

Figure 25. The topography (a), the amplitude (b), the 3D image (c) and line profile for ZnO-TiO₂-GO nanocomposites (d)

FESEM analysis

The surface structure was estimated again by the field emission scanning electron microscope (FESEM). The FESEM images of GO, ZnO-TiO₂ and ZnO-TiO₂-GO nanocomposite was shown in figure 26, 27 and 28. In figure 26, surface of the graphene oxide was rough with some crumpling and agglomeration, which may be attributed to the residual oxygen containing

functional groups (e.g. -OH). According to the FESEM image of ZnO-TiO₂nanocomposite (figure 27), the nanocomposite particles are also agglomerated and non-uniformed in size. Differentiation between ZnO and TiO₂ in the composites was not possible by FESEM owing to the similar electron density of Zn and Ti. The FESEM image of ZnO-TiO₂-GO nanocomposite was shown in figure 28and according to the SEM image, it is clearly seen that the GO sheets are decorated by ZnO-TiO₂ nanocomposite particles. The GO nanosheets act as a bridges for the connection between different ZnO-TiO₂ nanocomposite particles.

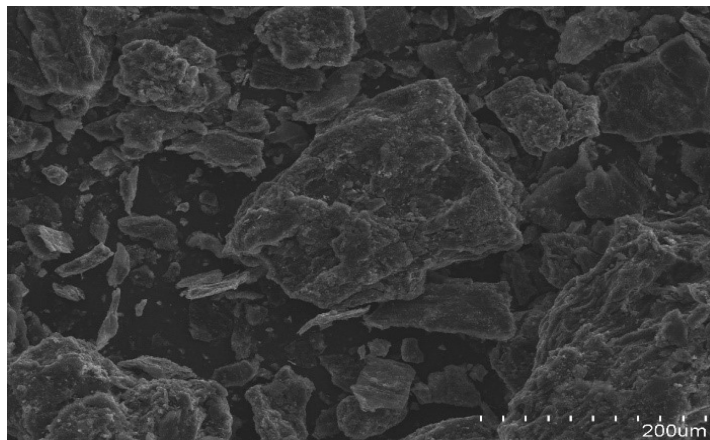


Figure 26. FESEM image of Graphene Oxide

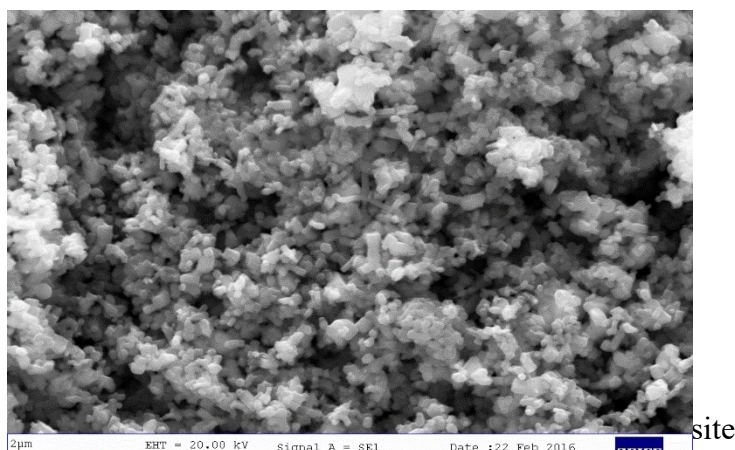


Figure 27. FESEM image of ZnO-TiO₂ nanocomposite

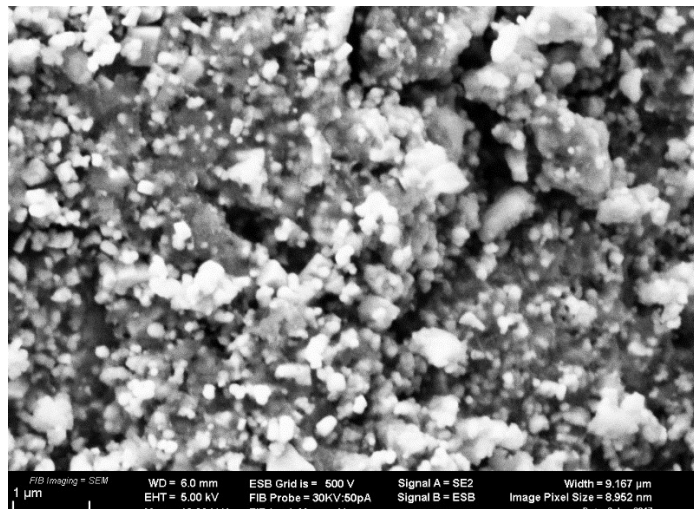


Figure 28. FESEM image of ZnO-TiO₂- GO nanocomposite

Conclusion

Graphene oxide (GO) was prepared by Hummer method. And then, ZnO-TiO₂ nanocomposite was prepared by simple mechanochemical activation method and the ZnO-TiO₂-GO nanocomposite was prepared by simple mechanical stirring followed by ultra-sonication. The XRD results of GO shows 2θ of 11.07° with the interplanar distance of 0.799 nm. Graphite, which showed a strong and sharp diffraction peak at $2\theta=26.61^\circ$ has the interplanar distance of 0.334 nm. The increase in interplanar distance of GO is due to the existence of oxygen functional groups. In ZnO-TiO₂-GO nanocomposite, the main diffraction peak of GO is absent and it probably lead to partial reduction of GO to graphene and a weak peak at $2\theta = 26.50^\circ$ appears. This might be due to the low amount and relatively low diffraction intensity of GO in comparison with the diffraction intensity of ZnO-TiO₂ nanocomposite. Moreover the other possibility is due to the intercalation of metal oxide after ultrasonic treatment. In EDX analysis, the content of C is 67.35 % and the content of O is 29.75% in GO. The mass ratio of C/O in GO is 2.26. According to the FTIR analysis, the -OH groups were be found and the presence of these oxygen containing groups reveals that the graphite has been oxidized. UV-Vis spectra of GO exhibited maximum absorption peak at 290 nm, ZnO-TiO₂ nanocomposite exhibited at 289 nm

and 372 nm and ZnO-TiO₂-GO was 543 nm and 645 nm respectively. The value of E_g for GO, ZnTiO₂ and ZnO-TiO₂-GO are found to be about 3.93 eV, 3.8 eV and 4.083 eV respectively. According to the AFM analysis, the particles in ZnO-TiO₂ nanocomposite are agglomerate and the average particles sizes are about 78 nm. In ZnO-TiO₂-GO nanocomposite, ZnO-TiO₂ nanocomposite are well attached onto the surface of GO sheet and the average particles sizes are about 30 nm- 50 nm. In FESEM image, GO sheets are decorated by ZnO-TiO₂ nanocomposite particles. The GO nanosheets act as a bridge for the connection between different ZnO-TiO₂ nanocomposite particles and can be concluded it has the good behavior of nanocomposite.

Acknowledgements

I wish to express my profound thanks to Dr Si Si Hla Bu, Rector of Myeik University for her kind permission to carry out this work. Moreover, I am greatly indebted to Professor Dr Myint Myint Moe, Head of Department of Physics, Myeik University, for her help with Experimental work and discussion. The author also acknowledge the Support of Professor Dr Khin Khin Win, Head of Department of Physics, University of Yangon.

References

1. A. Stoyanova, H. Hitkova, (2012) "Synthesis and Antibacterial Activity of TiO₂-ZnO Nanocomposites prepared Via Nonhydrolytic Route", *Journal of Chemical Technology and Metallurgy*, **48**, 154-156.
2. C. Pragathiswaran and B. Mahin Abbubakkar (2015) "Synthesis of TiO₂ and ZnO Nano Composites With Graphene Oxide", *Journal of Chemistry*, **42**, 213.
3. Hameed Ullah, Kabeer Ahmad Khan, Wasid Ullah Khan, (2014) "ZnO/TiO₂ Nano-Composite Synthesized by Sol Gel from Highly Soluble Single Source Molecular Precursor", *Chinese Journal of Chemical Physics* **27**, 5.
4. Katerina Zaharieva, Katya Milenova, (2014) "Physicochemical and Photocatalytic Investigations of Mechanochemically Treated TiO₂-ZnO composite", *Journal of ISP*, **8**, 1314-7269.
5. Majid Jafari, Sanaz Razavein, (2014), "Synthesis and Characterization of TiO₂-ZnOxAl₂O₃ Nano-composite Via Sol-Gel Method", ISBN **16**, 153-158.
6. Muhammad Ali Johar, (2015) "Photocatalysis and Bandgap Engineering" Hindawi, 34587.

7. Muhammad Imran Ahmed (2016) "Low resistivity ZnO-GO electron transport layer solar cell AIP ADVANCES,6, 065303
8. P.M. A nesh, K.A.Vanaja, (2007), "Synthesis of ZnO nanoparticles by Hydrothermal method" Nanophotonic Materials, 663966390J-1.
9. R. Iordanova, A. Bachvarova-Nedelcheva, (2011), "Mechanochemical synthesis and photocat- alytic properties of zinc titanates",BCC 43 3.
10. S. Jurablu, M. Farahmandjou, (2015), "Sol-Gel Synthesis of Zinc Oxide(ZnO) Nanoparticles: Study of Structural and Optical Properties", Journal of Science 263.
11. Wan-Kuen, Santosh Kumar, (2016) "Cobalt promoted TiO₂/GO for the photocatalytic degradation ofoxytetracycline" Elsevier, 201 159-168.
12. Yuan Zhi-Hao, Tang Chum, (2011), "Optical Absorption of Sol-Gel Derived ZnO-TiO₂ Nano-Composite Films", Chin.Phys.Lett, 18 11.
13. Ziquan Liu, Rumming Wang,(2014), "Synthesis and Characterization of TiO₂ Nanoparticles" Asian Journal of Chemistry, 26 3.

STUDIES ON EFFECT OF YTTERBIUM SUBSTITUTION IN ZINC FERRITE

Zar Zar Myint Aung¹, Soe Soe Han², Aye Aye Thant³

Abstract

Rare earth, ytterbium doped Zinc ferrites ($Zn(Yb_xFe_{1-x})_2O_4$) with $x=0.0000, 0.0125, 0.0250, 0.0375$ and 0.0500 have been prepared by the solid state method. The raw materials such as ytterbium oxide, zinc oxide and ferrite oxide have been used as the source materials. The spinel ferrite structure, cubic morphology, and the identification of functional groups of the ytterbium doped zinc ferrite have been analyzed systematically using several analytical tools. The resistivity decreases in the sample without RE dopants for both frequency regions of (10 kHz-100 kHz) and (1MHz-10MHz). Moreover, rare-earth doped samples exhibit high conductivity than undoped zinc ferrite. The electrical conductivity at room temperature is directly proportional to the reaction rate of samples.

Keywords: *X-ray diffraction, Scanning electron microscopy, electrical properties*

Introduction

Spinel ferrites are interesting materials owing to their wide range of applications in modern science and technology. They have recently attracted considerable research interest on their structural, magnetic and electrical properties. These structures are attractive for microwave applications, magnetic sensors and catalytic materials owing to their great magnetic permeability and dielectric constant, low dielectric loss, high Curie temperature as well as mechanical strength and chemical stability at low frequencies. In addition, their magnetic properties can be controlled and tailored to practical applications through the appropriate choice from a number of divalent cations in their structure.

Zinc Ferrite has many applications in high- frequency devices, and they play a useful role in technological and magnetic applications.

¹ PhD Candidate, Demonstrator, Physics Department, Lashio University

² Dr, Lecturer, Physics Department, University of Yangon

³ Dr, Professor, Physics Department, Myeik University

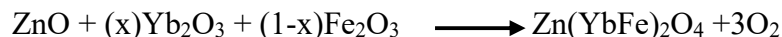
The electrical conductivity and dielectric behavior of spinel ferrites are very sensitive to the type of substituent and sintering conditions, such as temperature, time and heating rate. The aim of the present work was to study the effect of preparation conditions on ZnFe_2O_4 by solid state method in the first step. In the second step, RE ytterbium ions have been doped in ZnFe_2O_4 and investigate the effect of RE ytterbium ions on the properties of zinc ferrite.

Material and Method

Experimental procedure

Rare earth doped Zinc ferrites have been prepared ($\text{Zn}(\text{YbxFe}_{1-x})_2\text{O}_4$) with $x=0, 0.0125, 0.0250, 0.0375$ and 0.0500 by the solid state method. The raw materials such as ytterbium oxide, zinc oxide and ferrite oxide were used as the source materials. The required amount of the ZnO , Yb_2O_3 and Fe_2O_3 has been weighed with digital balance. The raw materials of ZnO , Yb_2O_3 and Fe_2O_3 have been taken in stoichiometric proportions.

These oxide materials were mixed with standard weight percentages according to their stoichiometric calculation by using the following equation.



All compositions have been mixed in an Agate mortar and ground for 4 h. After mixing and grinding, the mixture has been pre sintered at 900°C for 5 h in a furnace with heating rate of $20^\circ\text{C}/\text{min}$ and cooled to room temperature with the same rate. After that, the powder and the mixture has been ground with an Agate motor for 1h. Then, the powder has been pressed into pellets and toroids by uniaxial hydraulic press at a pressure of 5ton. The pellets have been well polished for further characterizations.

The other publication papers were $\text{MgZnFe}_2\text{O}_4$, $\text{NiZnFe}_2\text{O}_4$, $\text{CuZnFe}_2\text{O}_4$ and ZnFe_2O_4 ferrites prepared by their different temperatures. The $\text{MgZnFe}_2\text{O}_4$ was presintered at 800°C for 3 hours and final sintered at 1225°C for 6 hours in a furnace. The $\text{NiZnFe}_2\text{O}_4$ was presintered at 1100°C for 4 hours and final at 1275°C for 30mins. The $\text{CuZnFe}_2\text{O}_4$ presintered was 900°C for 3 hours and final was 1000°C for 6 hours. According to this ferrites

papers, zinc ferrite has been obtained a single phase in the temperature range of 900 °C – 1200 °C.

In addition, the solid state process requires sintered temperature more than 750 °C for phase formation and sintering temperature more than 1000 °C to achieve better densification. The influence of rare earth ions like Yb, Er, Dy, Tb, Gd, Sm substitution on structure, magnetic and electrical properties of (Zn) Yb Fe₂O₄ ferrites. Thus, ZnYbFe₂O₄ was chosen presintered at 900 °C for 5 hours and final sintered for 1000 °C and 1100 °C. The various final sintered of the sample with rare earth(pellets) dopants have been characterized by XRD and SEM. The experimental results of (Zn(Yb_xFe_{1-x})₂O₄) with x=0, 0.0125, 0.0250, 0.0375 and 0.0500 are compared to the undoped and ZnFe₂O₄ their electrical properties are investigated.

Rare Earth Elements

The rare earth elements include 15 lanthanides with the atomic numbers 57 to 71 in the periodic table. In the Figure (1) Ytterbium is a chemical element with symbol Yb and atomic number 70, which is the basis of the relative stability of its 2⁺ oxidation state. Ytterbium can be used as a dopant to help improve the grain refinement, strength, and other mechanical properties stainless steel.



Ytterbium oxide



Zinc ferrite mixture

Figure 1. Ytterbium oxide and zinc ferrite mixed

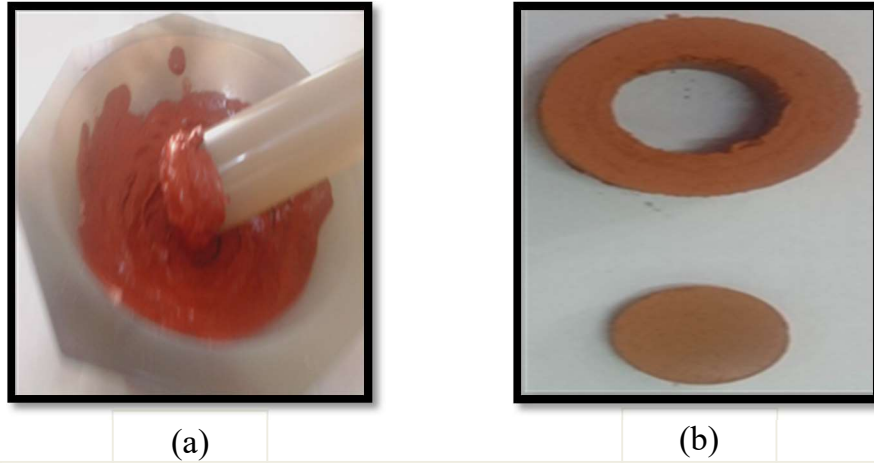


Figure 2(a) Ytterbium oxide and zinc ferrite applied with agate motor and pestle

(b) The pellets and toroids prepared by uniaxial hydraulic press at a pressure of 5tons

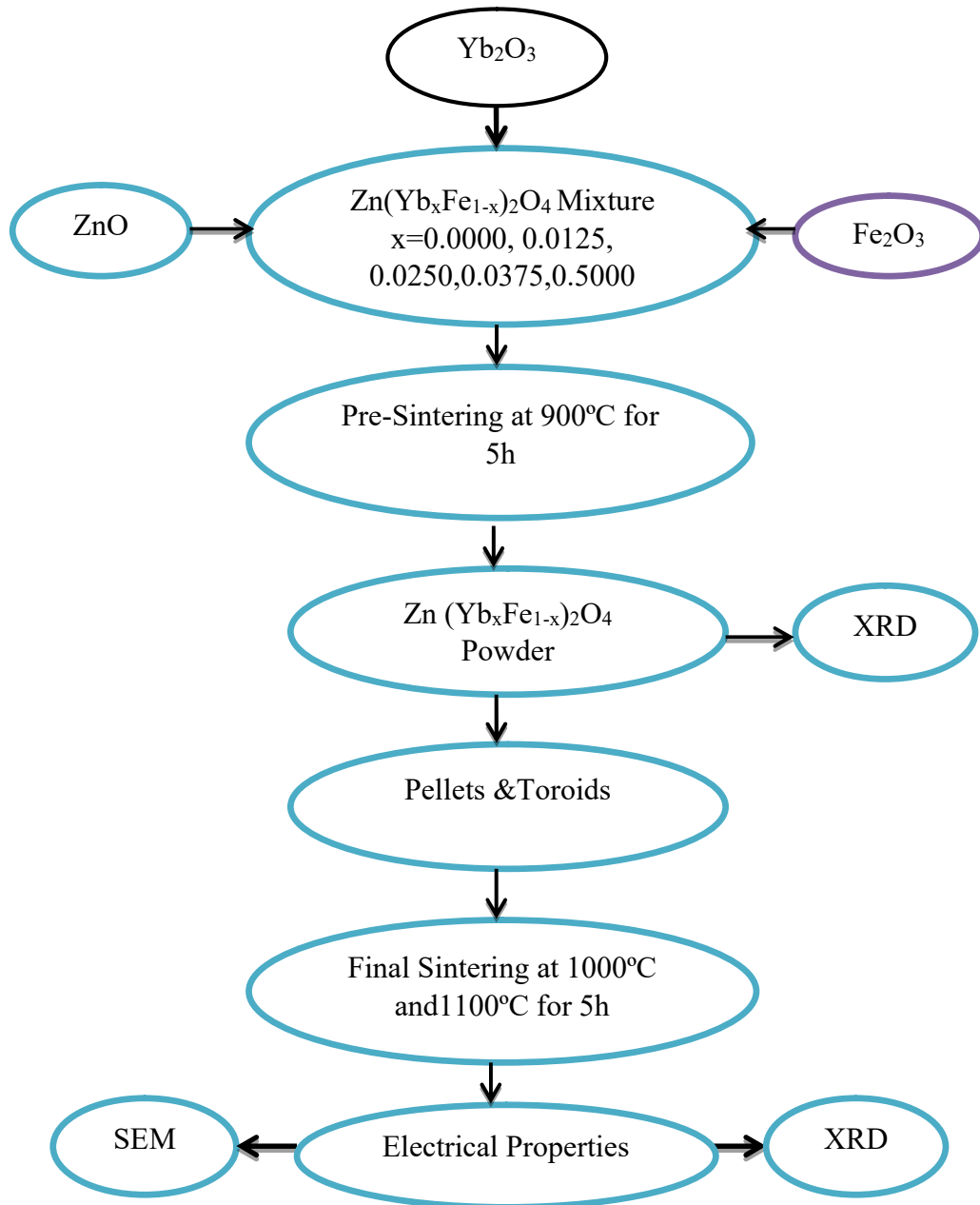


Figure 3. Flow chart of the sample preparation for Yb doped zinc ferrite

Results and Discussion

XRD Analysis

Figure 4 to 5 show XRD patterns of the as prepared and sintered samples of $\text{ZnYbFe}_2\text{O}_4$ nano particles respectively. The XRD peaks indicate the occurrence of pure spinel ferrite structure, which is represented by the reflections from the (2 2 0), (3 1 1) and (4 0 0) planes and it was compared with standard JCPDS patterns. The crystallite sizes of the $\text{ZnYbFe}_2\text{O}_4$ nanoparticles sintered at different temperatures were calculated using the Scherrer's formula, and are listed in table 1. As expected, the crystallite size increased with increasing heat treatment temperature

(1000 °C and 1100 °C) for all sample examined, ranging from 36 to 51 nm. The increasing crystallite size with increasing calcinations temperature agrees well with earlier results.

Figure 6 shows the morphology of the $\text{ZnYbFe}_2\text{O}_4$ nanoparticles at different temperatures. The micrographs clearly indicate the cubic morphology of the nanocrystals. In addition, both the crystallite size and the degree of particle agglomeration increased with increasing sintered temperature, probably because of the disappearance of the polymer at high temperatures, which is in good agreement with XRD results.

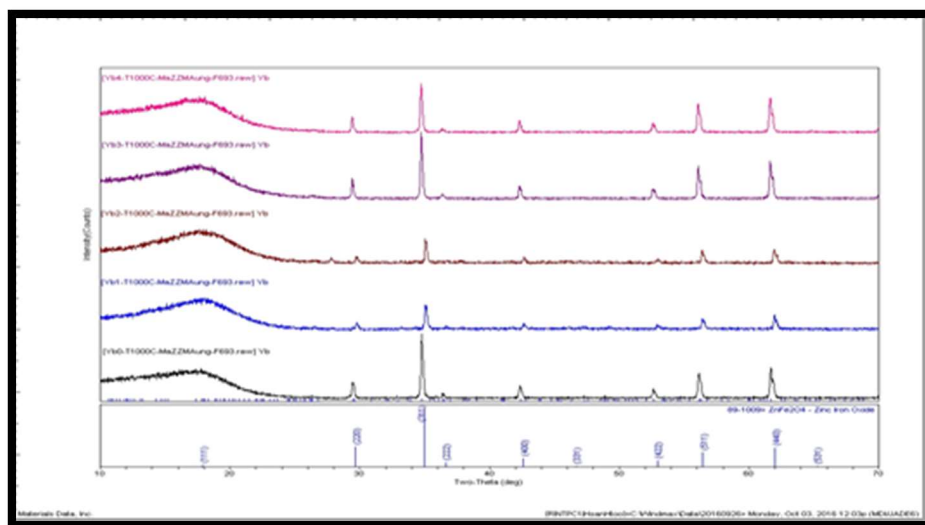


Figure 4. XRD pattern nano-particles of $\text{ZnYbFe}_2\text{O}_4$ at 1000 °C

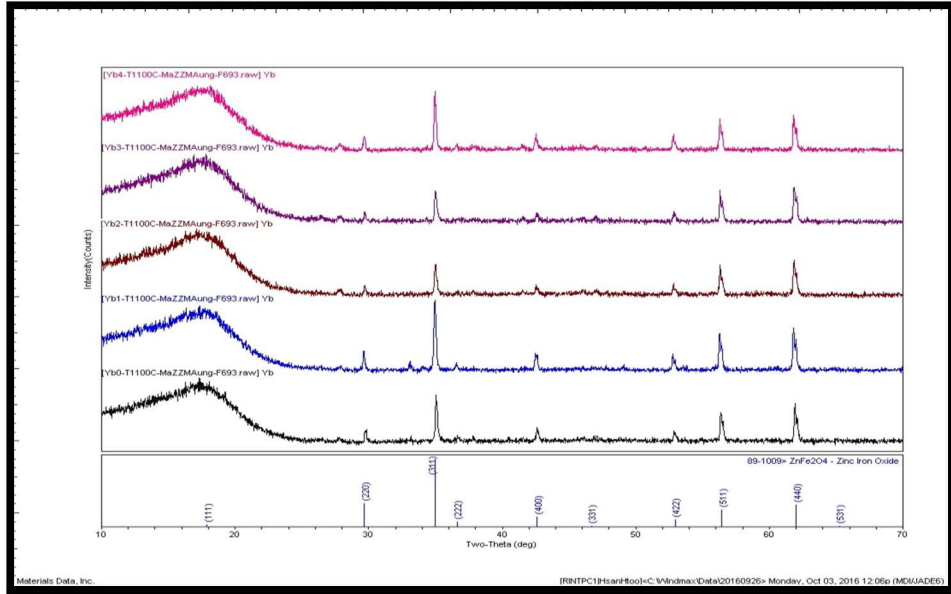


Figure 5. XRD pattern nano-particles of ZnYbFe₂O₄ at 1100 °C

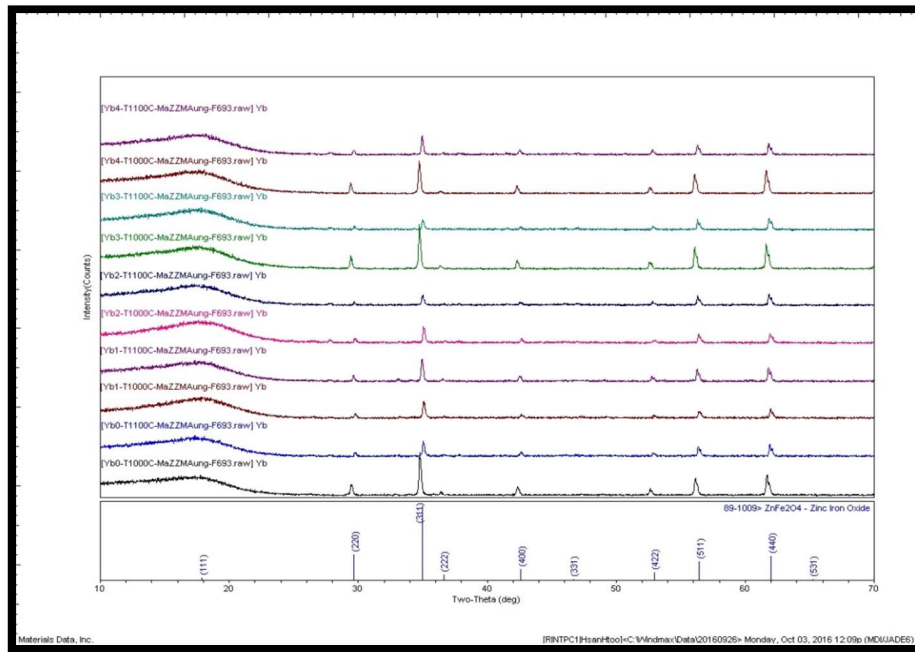


Figure 6. XRD pattern of the ZnYbFe₂O₄ samples at different temperatures

Table 1. Crystallite size of the ZnYbFe₂O₄ samples at different temperatures

Sample	Temperature (°C)	Crystallite size (nm)
x = 0.0000	1000	44.02
	1100	42.46
x = 0.0125	1000	36.78
	1100	43.80
x= 0.0250	1000	44.29
	1100	44.76
x = 0.0375	1000	47.30
	1100	41.18
x = 0.0500	1000	51.77
	1100	49.91

SEM analysis

The SEM images of undoped and rare earth (ytterbium) doped ZnFe₂O₄ pellets are shown in figures with various temperature. The pellets sintered at 1000°C showed an average particle size in the range from 0.9231µm to 7.2910µm in figure 7 whereas for the pellets sintered at 1100°C, the average particle size was in the range from 0.8056µm to 1.03125µm in figure 8. The particle size correlation of the results obtained by XRD and SEM indicates that the agglomerates are made of nanosized particles. Thus, the above discussion confirms the formation of ZnYbFe₂O₄ phase particles between temperatures of 1000°C and 1100°C. The estimate values of average grain size are presented in Table 3 and 4. It is observed that the grain size of undoped- ZnFe₂O₄ is the biggest in all samples. The grain size of Yb doped ZnFe₂O₄ ferrites are gradually decreased until x= 0.0500.

Table 2.The average grain size of the $\text{YbZnFe}_2\text{O}_4$ pellets at 1000 °C temperatures

Composition of rare earth ions	Grain Size
x = 0.0000	7.2910 μm
x = 0.0125	5.4062 μm
x = 0.0250	4.4313 μm
x = 0.0375	3.7669 μm
x = 0.0500	0.9231 μm

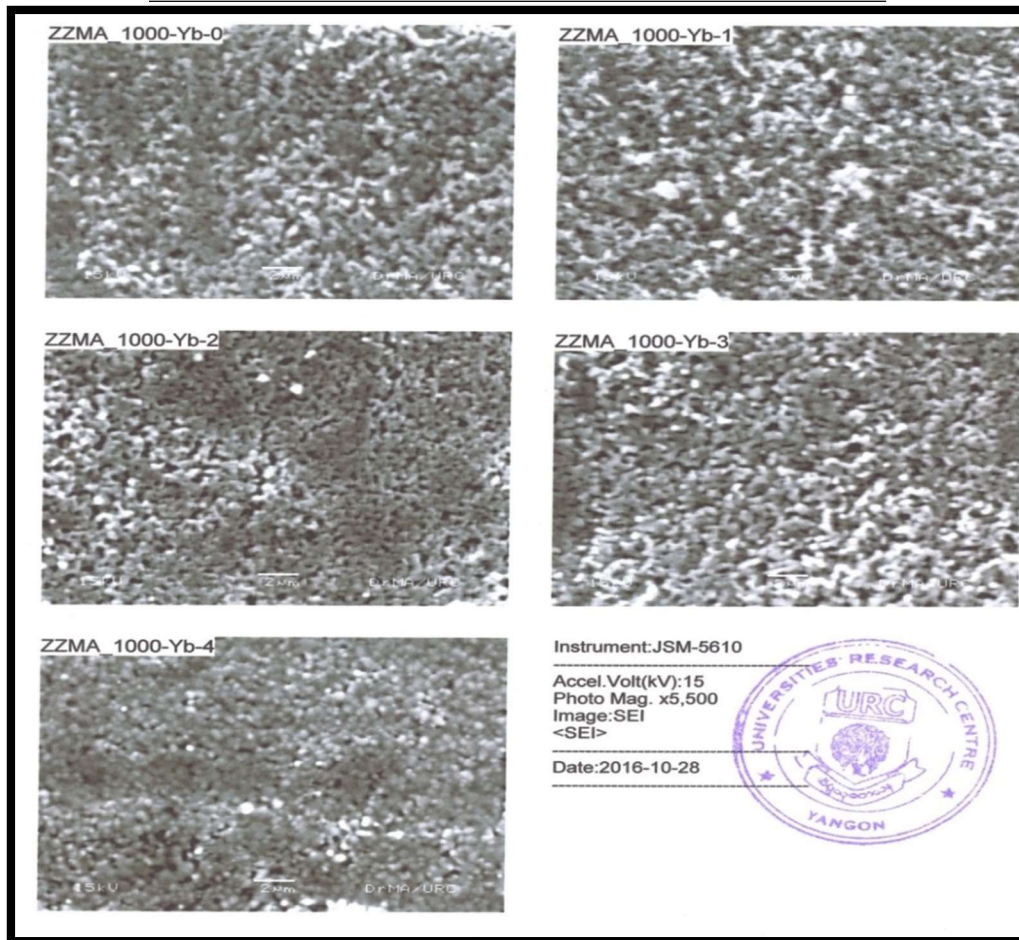


Figure 7. The SEM photograph of the $\text{YbZnFe}_2\text{O}_4$ pellets at 1000 °C temperature

Table 3. The average grain size of the $\text{YbZnFe}_2\text{O}_4$ pellets at 1100 °C temperatures

Composition of rare earth ions	Grain Size
x= 0.0000	1.03125 μm
x= 0.0125	0.8056 μm
x= 0.0250	0.8772 μm
x= 0.0375	0.8116 μm
x= 0.0500	0.6867 μm

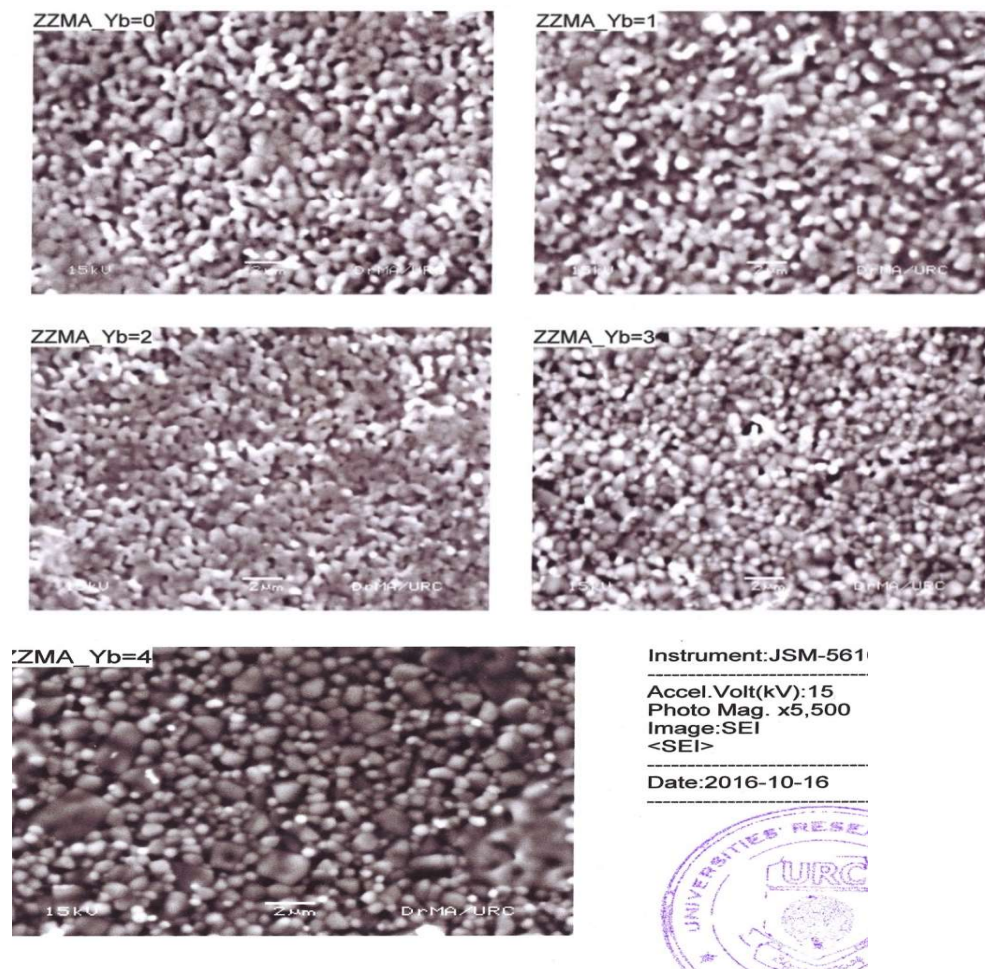


Figure 8. The SEM photograph of the $\text{YbZnFe}_2\text{O}_4$ pellets at 1100 °C temperature

Electrical Properties

Variation of Resistivity with Frequency and Sintered Temperature

The frequency dependent variation of DC resistivity (the inverse of conductivity) for all samples which are sintered at 1000 °C at lower frequency range (10kHz-100kHz) and higher frequency range (1MHz-10MHz) are shown in Fig 9 and Fig 10 respectively. It was found that the resistivity decreases in the sample without RE dopants in both frequency regions. The resistivity increases with increasing RE doping in the sample.

Again the frequency dependent variation of DC resistivity for all samples which are sintered at 1100 °C at lower frequency range (10 kHz-100 kHz) and higher frequency range (1MHz-10MHz) are shown in Fig 11 and Fig 12 respectively. The variation of resistivity shows the same trend as the result in the samples which are sintered at 1000 °C.

By comparing resistivity for different sintering temperatures, it is worth to note that the resistivity decreases with increase in sintering temperature. It has been attributed that the grains becomes bigger at higher sintering temperature and provide higher conductivity.

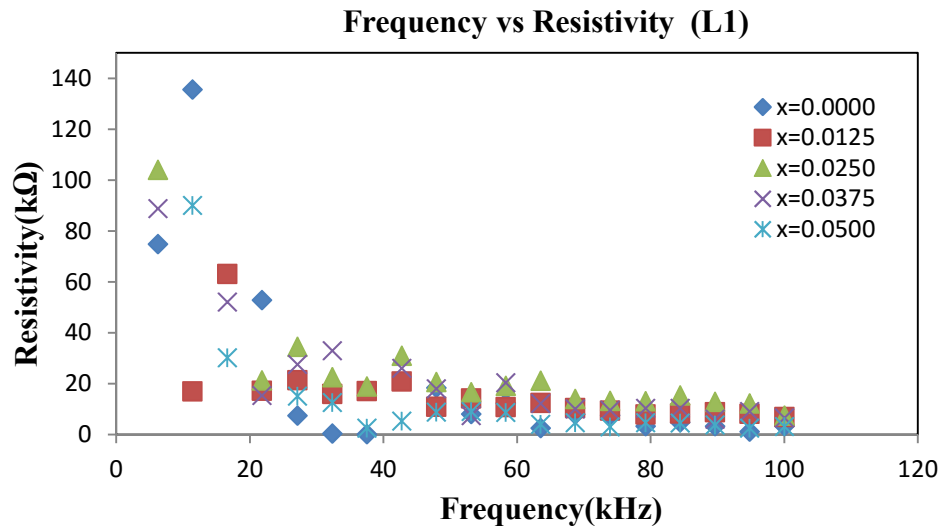


Figure 9. Frequency (10 kHz-100 kHz) dependent resistivity curves for ZnYbFe₂O₄ with different Yb content at 1000°C

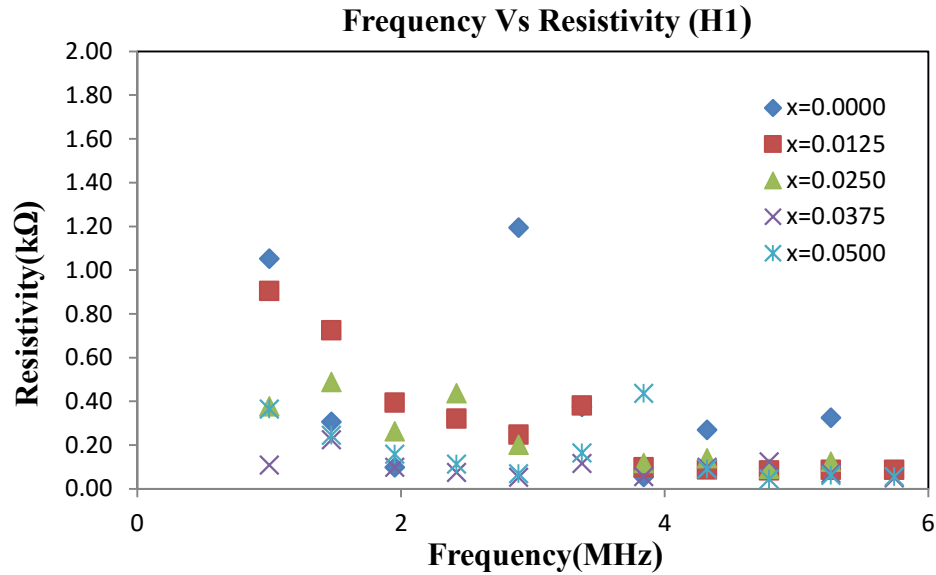


Figure 10. Frequency (1MHz-10MHz) dependent resistivity curves for $\text{ZnYbFe}_2\text{O}_4$ with different Yb content at 1000°C

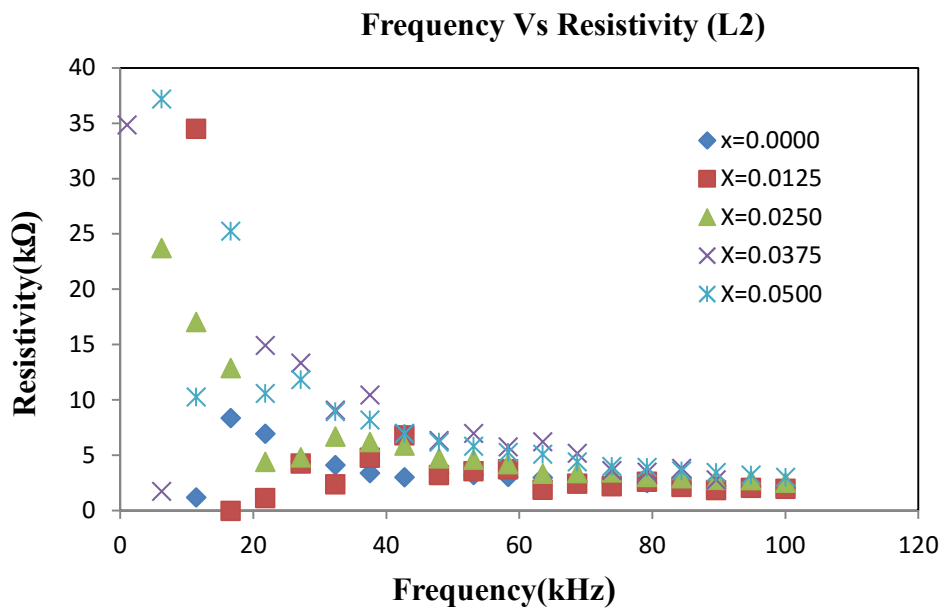


Figure 11. Frequency (10 kHz-100 kHz) dependent resistivity curves for $\text{ZnYbFe}_2\text{O}_4$ with different Yb content at 1100°C

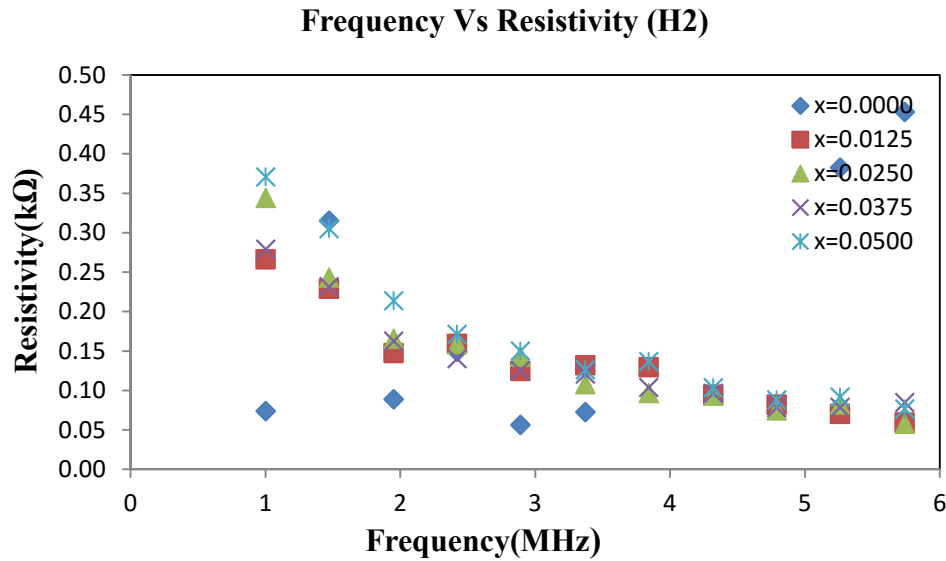


Figure 12. Frequency (1MHz-10MHz) dependent resistivity curves for ZnYbFe₂O₄ with different Yb content at 1100°C

Conclusion

From the above experimental results, it is clearly evident that the nano size of the ferrite particles in Yb doped zinc ferrite ZnFe₂O₄ has been obtained by using solid state method. The microstructure with fine grains has been observed to evaluate the applicability of the ferrite. Moreover, the grain size which is less than 1µm confirmed the formation of the smaller grains under the sintering temperature of 1000°C and 1100°C. Therefore, it is concluded that ZnFe₂O₄ with the homogeneous microstructure has been formed for further investigation with RE dopants.

In this work has been reported a study on the influenced of ytterbium doped on structure, morphology and electrical properties of the Zn (Yb_xFe_{1-x})₂O₄ (x=0.0000, 0.0125, 0.0250, 0.0375 and 0.0500). The resistance and capacitor have been measured in the frequency ranges (10 kHz-100 kHz) and (1MHz-10MHz) with different temperatures 1000°C and 1100°C respectively. The resistivity decreases in the sample without RE dopants in both frequency regions. The resistivity increases with increasing RE doping in

the sample. Moreover, the resistivity decreases with increase in sintering temperature. It has been attributed that the grains becomes bigger at higher sintering temperature and provide higher conductivity. This is proved that the substitution of small amount of RE ions in ferrite can tune the electrical properties.

Acknowledgement

This research was totally done at Department of Physics in University of Yangon, Myanmar (2016-2017).

References

1. A. B. Gadkari, T. J. Shinde, P. N. Vasambekar, (2011) "Structural analysis of Sm³⁺ doped nanocrystalline Mg-Cd ferrites prepared by oxalate co-precipitation method, *Materials Characterization* " 60 1328-1333.
2. A. Goldman, (1990) "Modern Ferrite Technology," Van Nostrand, New York.
3. A.M. Movahedian, Seid Mohammadi, Assadi Iran, (2009) "Comparison of different advanced oxidation processes degrading p-chlorophenol in aqueous solution," *J. Environ. Health. Sci. Eng.*6: 3 153-160.
4. Anu Rana, O. P. Thakur, Vinod Kumar, (2011) " Effect of Gd³⁺ substitution on dielectric properties if nano cobalt ferrite," *Material letters* 65 3191-3192.
5. A. Zhihui, Y. Peng., L. Xiaohua., (2005) "Degradation of 4-chlorophenol by a microwave assisted photo catalysis method ," *J. Hazard. Mater B.* 124 147–152. 6. E Sahinkaya., F. B. Dilek, (2006), "Biodegradation of 4-CP and 2, 4-DCP mixture in a rotating biological contactor (RBC), " *Biochemical Engineering* 31 141–47.
7. E. Sahinkaya, E., F. B. Dilek, (2007) " Biodegradation kinetics of 2, 4-dichlorophenol by acclimated mixed cultures. ," *Biotechnology* 127 716–726.
8. Ferrite material science and technology, (1990) Viswanathan B, Murthy VRK, , New Delhi:Narosa Publishing House, p6,.
9. F. Muthafar, Al-Hilli, Sean Li, Kassim S. Kassim , (2011) " Gadolinium substitution and sintering temperature dependent electronic properties of Li-Ni ferrite, " *Material Chemistry and Physics* 128 127-132.
10. G. Busca, E. Finocchio, V. Lorenzelli, M. Trombetta, S. A. Rossini, (1996) "IR study of alkene allylic activation on magnesium ferrite and alumina catalysts," *J.Chem. Soc, Faraday Trans.* 92 4687-4693.

11. Ge-Liang Sun, Jian-Bao Li, Jing-Jing Sun, Xiao-Zhan Yang , (2004) “The influences of Zn^{2+} and some rare-earth ions on the magnetic properties of nickel–zinc ferrites ,” *Journal of Magnetism and Magnetic Materials* 281: 2–3 173-177.
12. K. B. Modi, H. H. Joshi, R. G. Kulkarni, (1996) “ Magnetic and electrical properties if Al^{3+} substituted $MgFe_2O_4$,” *Journal of materials science* 31 1311-1317.
13. Lijun Zhao, Hua Yang, Xueping Zhao, Lianxiang Yu, Yuming Cui, Shouhua Feng, (2006) “Magnetic properties of $CoFe_2O_4$ ferrite doped with rare earth ion,” *Materials Letters* 60: 1
14. M. A. Ahmed, E. ateia , S.I. El-Dek, (2003) “Rare earth doping effect on the structural and electrical properties of Mg-Ti ferrite,” *Materials letters* 57 4256-4266.
15. M. A. Khan, M. U. Islam, M. Ishaque, I. Z. Rahman, A. Genson and S. Hampshire, (2009) “Structural and physical properties of Ni–Tb–Fe–O system,” *Material Characterization* 60(1) 73-78
16. M. Y.Ghaly, G.Hartel, , R. Mayer, Haseneder, Roland., (2001) “ Photochemical oxidation of p-chlorophenol by UV/H₂O₂ and photo-Fenton process- A comparative study,” *Waste Management.* 21 41-47.
17. N Rezlescu, E Rezlescu, C Pasnicu and M L Craus, (1994) “ Effects of the rare-earth ions on some properties of a nickel-zinc ferrite”, *J. Physics.: Condensed Matter* 6 5707.
18. P. J.Binu, Smitha Thankachan, Sheena Xavier and E. M. Mohammed, (2011) “ Effect of Gd^{3+} doping on the structural and magnetic properties of nanocrystalline Ni-Cd mixed ferrite,” *Physica Scripta* 84 045702-08.
19. P. J.Binu, Smitha Thankachan, Sheena Xavier, E.M. Mohammed, (2012) “Dielectric behavior and AC conductivity of Tb^{3+} doped $Ni_{0.4}Zn_{0.6}Fe_2O_4$ nanoparticles,” *Journal of Alloys and Compounds* 541 29–35.
20. Qi Chen, Adam J Rondinone, Bryan C. Chakoumakos, Z John Zhang, (1999) “ Synthesis of super paramagnetic $MgFe_2O_4$ nanoparticles by co precipitation,” *Journal of Magnetism and Magnetic Materials* 194: 1–3 1-7.
21. Qi Chen, Z. John Zhang, (1998) “Size-dependent super paramagnetic properties of $MgFe_2O_4$ spinel ferrite nanocrystallites,” *Appl Phys Lett* 73:3 156.
22. S.A. Oliver, R.J. Willey, H.H. Hamdeh, G. Oliveri and G. Busca, (1995) “Structure and magnetic properties of magnesium ferrite fine powders,” *Scripta Metallurgica et Materialia*, 33 1695-1-6

LASER RAMAN, FTIR SPECTROSCOPIC INVESTIGATION AND INFRARED LIGHT TESTING OF M_2SO_4 (M = K, NH_4 , Li) DOPED TRIGLYCINE SULPHATE(TGS) CRYSTALS

Ei Cherry Hlaing¹, Moe Thida Aye¹, San Htar Oo² & Win Kyaw³

Abstract

In this paper, crystals of undoped Triglycine Sulphate, $(NH_2CH_2COOH)_3.H_2SO_4$, (abbreviated as TGS) and M_2SO_4 (where M = K, NH_4 , Li) doped TGS have been grown by solution growth method. The grown crystals were characterized by laser Raman and FTIR spectroscopy to study the vibrational characteristics of the various functional groups present in the crystals. Laser Raman spectra were observed by Ocean Optics QE65000 Visolator Raman Spectrophotometer. FTIR spectra were observed by using Perkin-Elmer Spectrum-100 FTIR Spectrophotometer. Vibrational characteristics and mode assignments of constituent molecules of SO_4^{2-} , COO^- , C—C, $CO_2-CH_2-CH_2$, $NH-NH_3$, NH_3 and CO_2 were reported. Furthermore, infrared (IR) light transmission experiments were tested by using laboratory-prepared IR driving circuit to show the IR windows materials.

Keywords: Undoped and M_2SO_4 doped TGS crystals, laser Raman, FTIR, various functional groups, IR windows materials

Introduction

Triglycine Sulphate, $(NH_2CH_2COOH)_3.H_2SO_4$, crystal is considered as one of the potential materials for its wide range of applications, namely, UV tunable laser, second harmonic generation, and pyroelectric infrared sensors due to its high pyroelectric coefficient, optical transmission, and reasonably low dielectric constant (Choudhury, 2008; Krishnakumar, 2011). It is a hydrogen bonded ferroelectric crystal having a typical second-order phase transition at Curie temperature of $49^\circ C$ (Andriyevsky, 2007). TGS has a major

¹ Dr, Demonstrator, Department of Physics, Bago University

² Dr, Lecturers, Department of Physics, Bago University

³ Dr, Associate Professor, Department of Physics, Sagaing University

disadvantage that it depolarized by thermal, mechanical, and electrical means. In order to overcome this difficulty, several studies have been attempted with different organic and inorganic dopants to achieve effective internal bias to stabilize the domains and desired pyroelectric and ferroelectric properties of TGS crystals (Arunmozhi, 2002; Bajpai, 2008).

Alkali halides such as NaBr and KBr-doped TGS crystals were grown, and the effects of the dopant have been investigated. Metal ion dopants have been added to modify the properties of TGS crystal (Khanum, 2012; Renugadevi, 2013). Due to the vast applications of TGS crystal, in this work, single crystals of undoped TGS and M_2SO_4 ($M = K, NH_4, Li$) doped TGS have been grown by slow evaporation method and their molecular vibrational characteristics were studied by laser Raman and Fourier Transform Infrared (FTIR) spectroscopic method. Furthermore, IR radiation and the crystals interaction experiments were tested by using laboratory-prepared IR driving circuit.

Experimental Details

Growth of Crystals

The crystals of triglycine sulphate have been grown by slow evaporation method. Analar (AR) grade glycine and concentrated sulphuric acid were dissolved in deionized water with the molar ratio of 3:1. The solution was heated at 50°C to obtain synthesized TGS crystal. The synthesized salt was again dissolved in triple distilled water and then recrystallized by natural evaporation process. This process was repeated three times to improve the purity of the material. The seed crystals of pure TGS were prepared by natural evaporation method. The chemical reaction for obtaining TGS salt is as follows:



To obtain M_2SO_4 ($M = K, NH_4, Li$) doped TGS crystals, each of the 1 mole% K_2SO_4 , $(NH_4)_2SO_4$ and Li_2SO_4 was added to the saturated mother solution. Transparent and homogeneous crystals were obtained within four weeks. At room temperature, the undoped TGS and M_2SO_4 doped TGS

crystals are colourless. Photographs of the as-grown crystals are shown in Figures 1(a- d). Crystal growth process is shown in Figure 2.

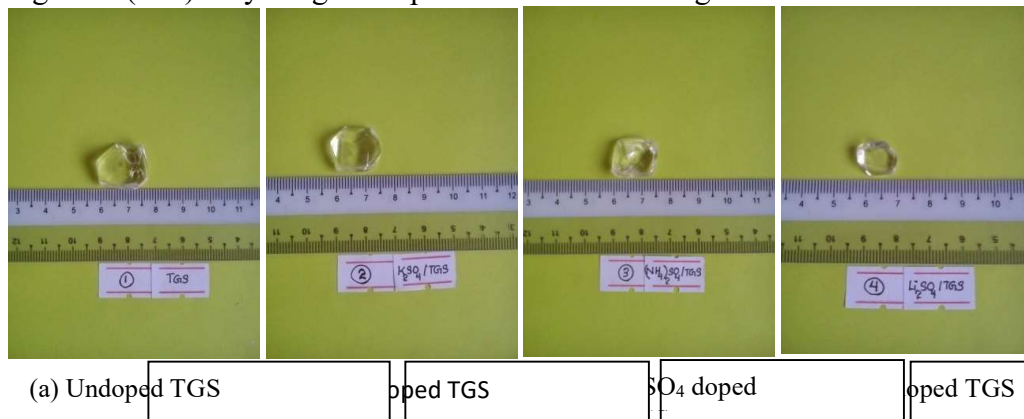


Figure 1. Photographs of (a) undoped TGS, (b) K_2SO_4 doped TGS, (c) $(NH_4)_2SO_4$ doped TGS and (d) Li_2SO_4 doped TGS crystals

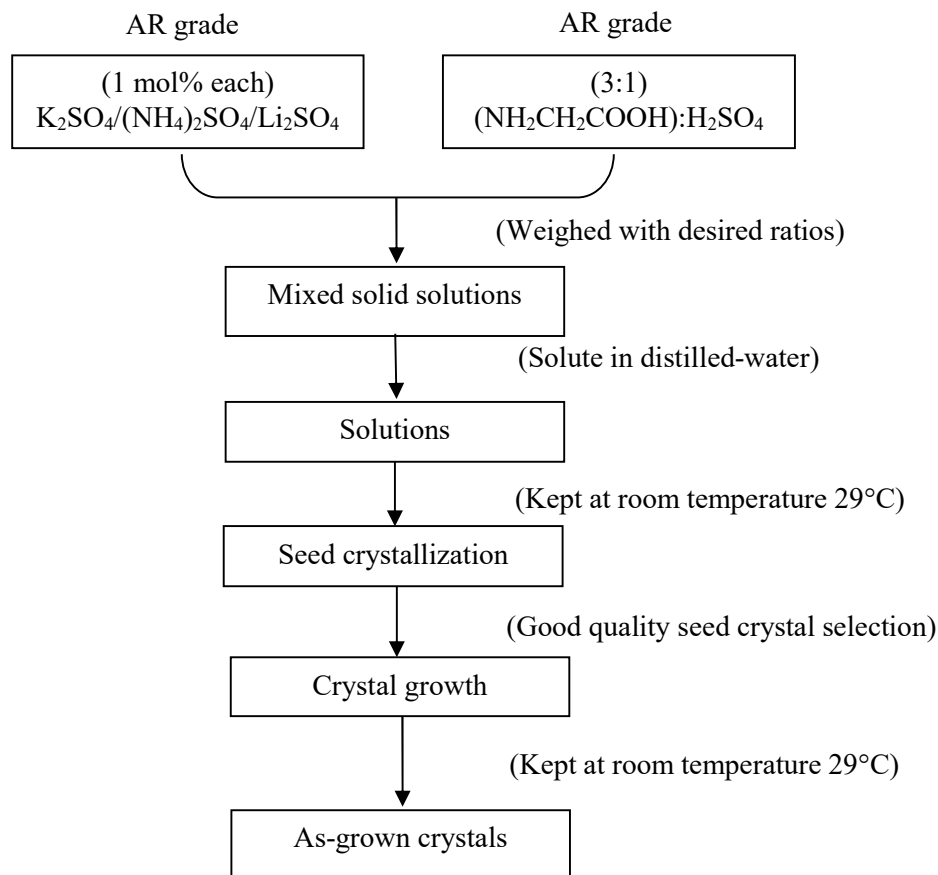


Figure 2. Flow diagram of the crystal growth process

Raman and FTIR Measurements

The vibrational frequencies of a molecule can be probed by using infrared and Raman spectroscopy [Stuart, (1996)]. In all spectroscopic methods, there is a mechanism by which the incident radiation interacts with the molecular energy levels. Raman Spectroscopy can be used to study the vibrational properties of crystals, powders, polymers and even coloured samples (solutions). Raman Scattering is an inelastic scattering of light from molecules. Raman spectroscopy, the mechanism has its origins in the general phenomenon of light scattering, in which the electromagnetic radiation interacts with a pulsating, deformable (polarizable) electron cloud. In the

specific case of vibrational Raman scattering, this interaction is modulated by the molecular vibrations.

Raman spectra of the as-grown crystals were collected on PC controlled Ocean Optics QE65000 Visolator Laser Raman Spectrometer (Institute of Advanced Energy, Kyoto University, Kyoto, Japan) in the Raman shift range of 400 cm^{-1} – 2000 cm^{-1} region.

Infrared (IR) spectroscopy is an important relatively inexpensive and efficient analytical method for characterizing materials. IR spectroscopy is used for obtaining an abundance of information such as thermodynamic data, bond length and diffusion data. On the other hand IR spectroscopy is limited in the ability to obtain accurate quantitative measurements and the range of inorganic and organic materials that are IR visible. The spectrum that is obtained from IR spectroscopy is due to the vibrational modes of the molecules. FTIR transmission spectra of the crystals were observed by using Perkin-Elmer Spectrum-100 FTIR Spectrophotometer (MIR & IR Spectroscopy Laboratory, Kyoto University, Kyoto, Japan) in the wave number range of 500 cm^{-1} – 3500 cm^{-1} region. Photographs of the Ocean Optics QE 65000 Visolator laser Raman spectrometer and Perkin-Elmer Spectrum-100 FTIR Spectrophotometer are shown in Figures 3(a) and (b).

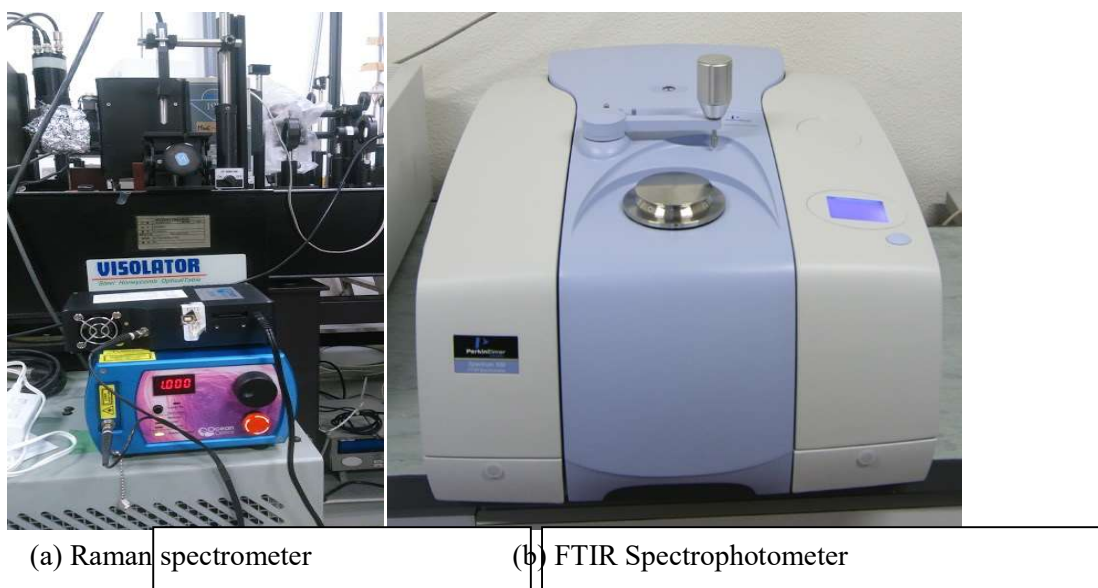


Figure 3. Photographs of (a) Ocean Optics QE65000 Visolator Laser Raman Spectrometer and (b) Perkin-Elmer Spectrum-100 FTIR Spectrophotometer

Infrared (IR) Light Testing Experiments

For the applications of IR windows materials, IR light testing experiments were also performed in this work. Experimental conditions were as follows:

Experimental work is mainly two parts;

- (i) IR testing experiments of IR driver circuit without sample (crystal) and
- (ii) IR testing experiments of IR driver circuit with sample (crystal).

In IR testing experiments,

- IR driver circuit power “ON”.
- The as-grown crystal was polished with the filtered-paper to get smoothing surface.
- The crystal was placed at the IR beam in the IR driver circuit (LED).

Photographs of IR testing experiments without samples and with samples are shown in Figures 4(a – s).

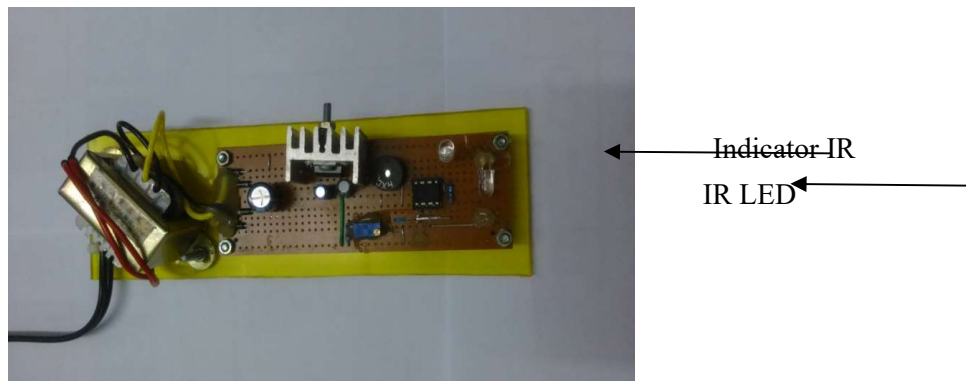


Figure 4.(a) IR driver circuit (Power OFF)

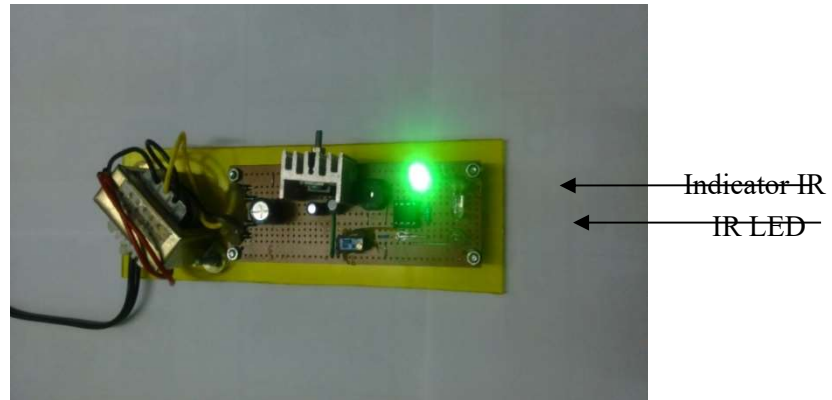


Figure 4.(b) IR driver circuit (Power ON) (Top-view)

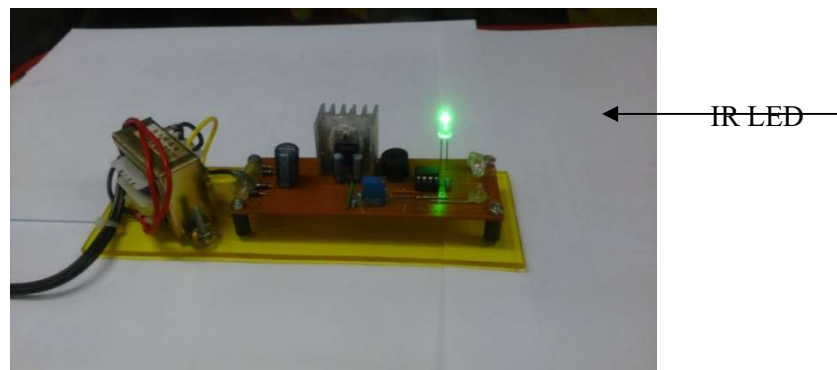


Figure 4.(c) IR driver circuit (Power ON) (Side-view / transmitted IR light source as an electrically ceramic light source)

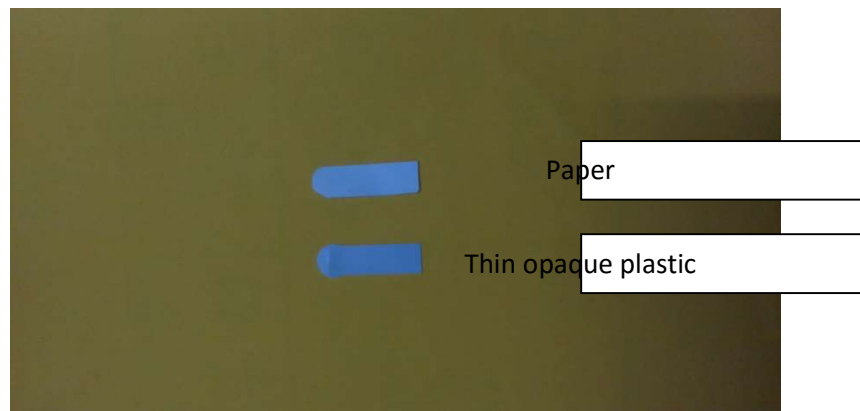


Figure 4.(d) Filters (upper - paper) and (lower – thin opaque plastic)

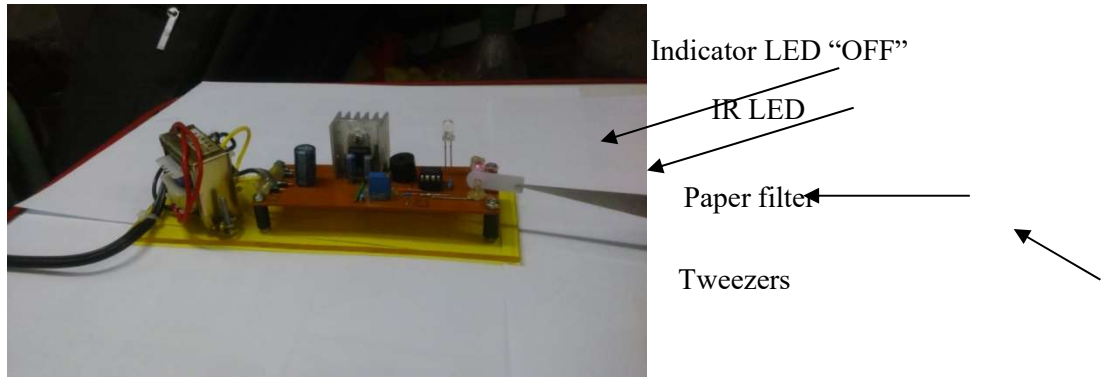


Figure 4(e). Testing of paper as an IR-filter

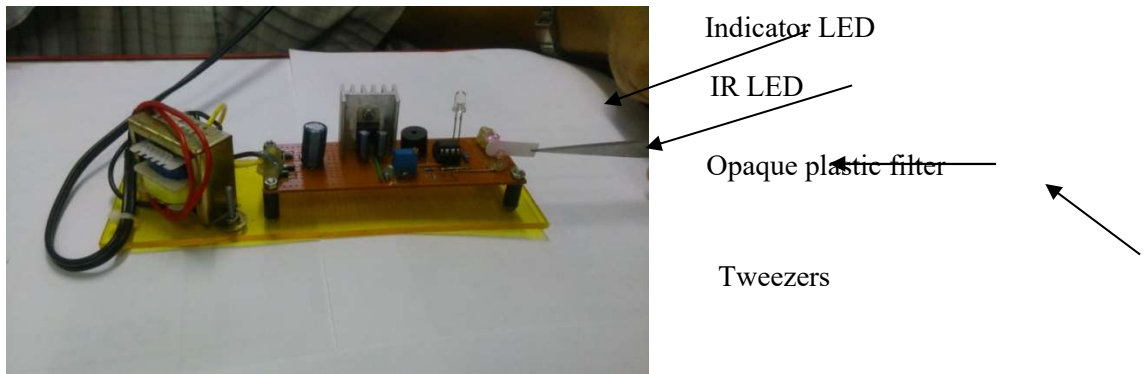


Figure 4.(f) Testing of thin opaque plastic as an IR-filter

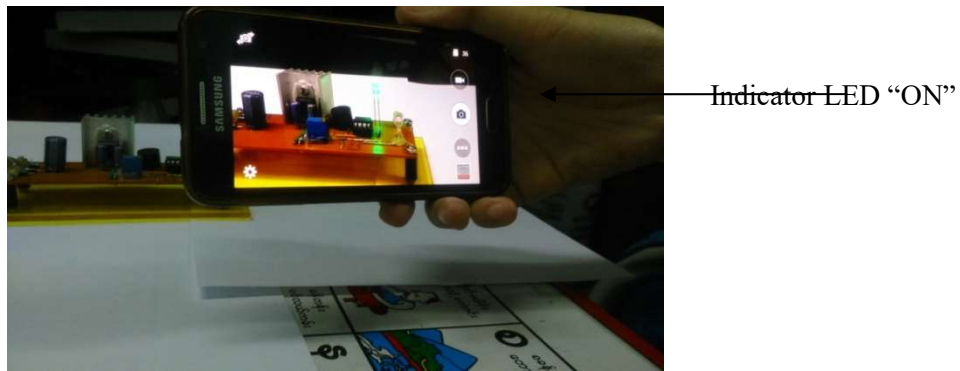


Figure 4(g).Testing of cell-phone camera with interaction of IR (indicator LED "ON")



(h) Length of undoped TGS

(i) Thickness of undoped TGS

Figure 4.(h) Length and (i) thickness of undoped TGS crystal

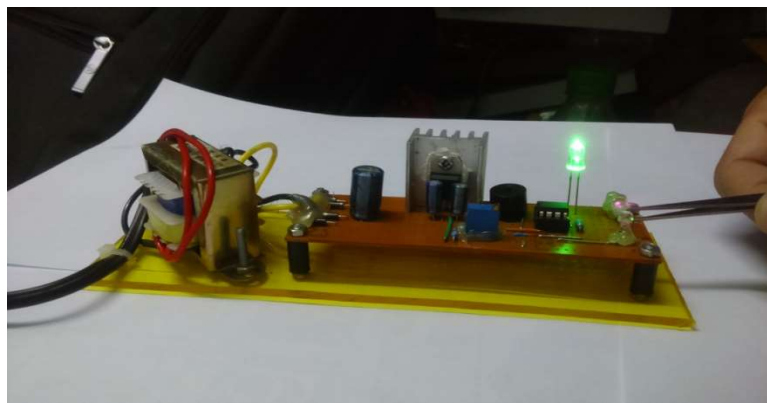


Figure 4.(j) Testing of IR windows material of undoped TGS crystal



(k) Length of K_2SO_4 doped TGS

(l) Thickness of K_2SO_4 doped TGS

Figure 4.(k) Length and (l) thickness of K_2SO_4 doped TGS crystal

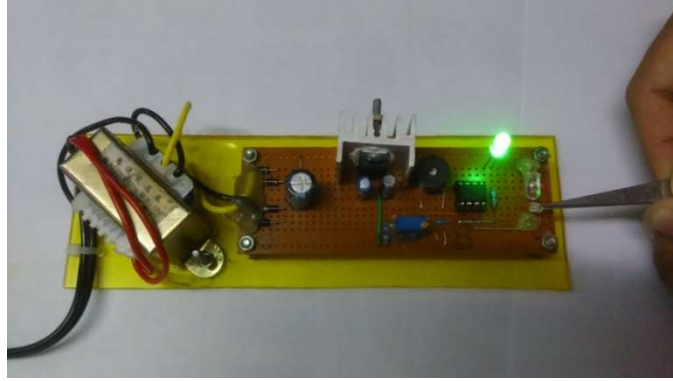


Figure 4.(m) Testing of IR windows material of K_2SO_4 doped TGS crystal



(n) Length of $(NH_4)_2SO_4$ doped TGS

(o) Thickness of $(NH_4)_2SO_4$ doped TGS

Figure 4.(n) Length and (o) thickness of $(NH_4)_2SO_4$ doped TGS crystal

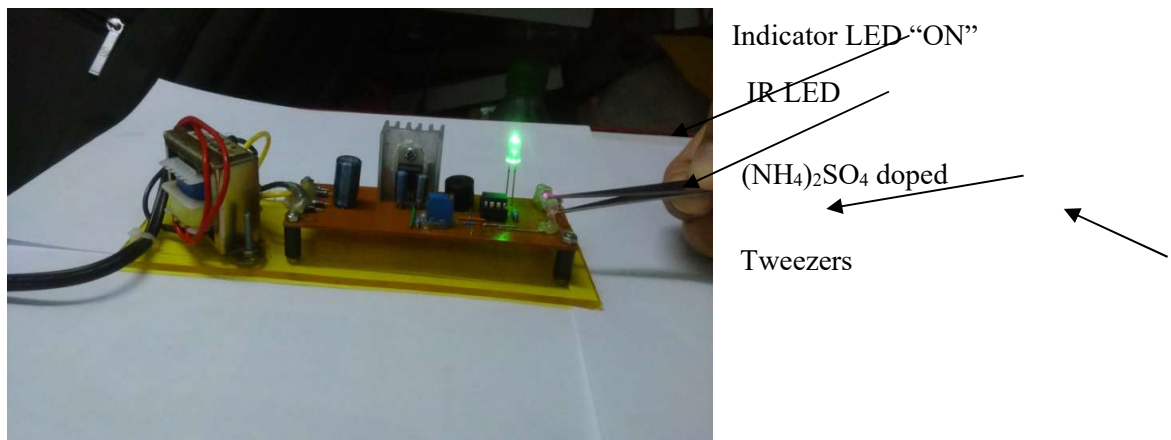


Figure 4.(p) Testing of IR windows material of $(NH_4)_2SO_4$ doped TGS crystal



(q) Length of Li_2SO_4 doped TGS

(r) Thickness of Li_2SO_4 doped TGS

Figure 4.(q) Length and (r) thickness of Li_2SO_4 doped TGS crystal

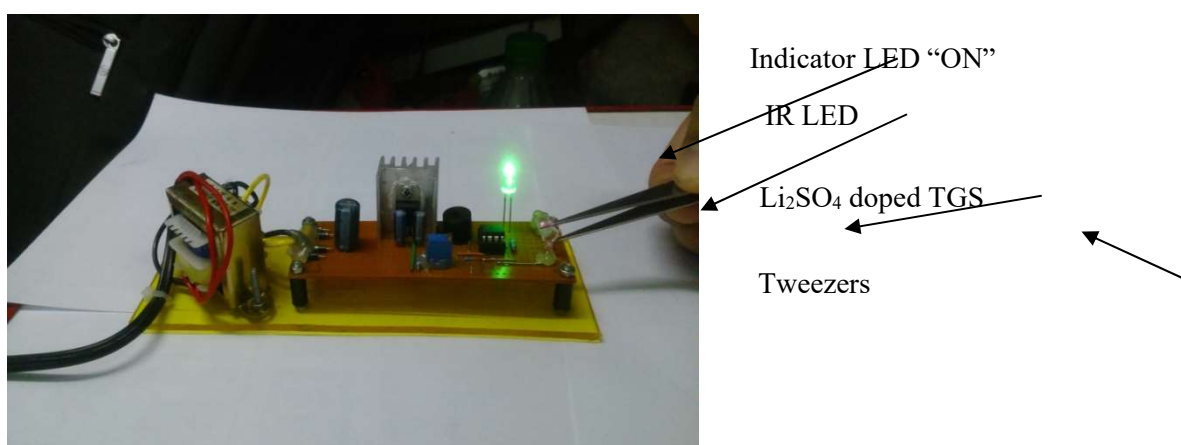


Figure 4.(s) Testing of IR windows material of Li_2SO_4 doped TGS crystal

Results and Discussion

Raman Study

According to FTIR theory, the mid-infrared spectrum can be divided into four regions and nature of a group frequency may be generally determined by the region in which it is located. These regions are normally as follows;

- (i) The X—H stretching region ($2500\text{ cm}^{-1} - 4000\text{ cm}^{-1}$)
- (ii) Triple bond region ($2000\text{ cm}^{-1} - 2500\text{ cm}^{-1}$)
- (iii) Double bond region ($1500\text{ cm}^{-1} - 2000\text{ cm}^{-1}$)
- (iv) Fingerprint region ($400\text{ cm}^{-1} - 1500\text{ cm}^{-1}$). [Stuart, (1996)]

According to vibrational analysis using factor group theory, the sulphate, SO_4^{2-} molecule in free-state is tetrahedral-pyramidal type T_d -symmetry and it processes four normal modes of vibrations. These four normal modes are $\nu_{\text{vib}} = A_1 + E + 2F_2$ and namely; $\nu_1(A_1)$ -symmetric stretching, $\nu_2(E)$ -bending, $\nu_3(F_2)$ -dipole and $\nu_4(F_2)$ -polarization respectively [Ross, 1972]. In general, most of the cases, SO_4^{2-} molecule may be distorted from the ideal T_d symmetry due to their crystalline environments or dopant effects.

Triglycine Sulphate, $(\text{NH}_2\text{CH}_2\text{COOH})_3\cdot\text{H}_2\text{SO}_4$, (TGS), of course, is an organic-inorganic molecules. Frequencies of organic compounds are generally appeared in the regions of over the frequency 1500 cm^{-1} . These frequencies are often shifted into the low and high frequency regions. In the present work, the absorption lines at over the frequency 1400 cm^{-1} were indicated that the organic molecules in TGS crystal.

Raman spectra of the crystals are shown in Figures 5(a – d). As shown in figures, four normal vibrations were appeared in all Raman spectra. In all spectra, the Raman line at 978 cm^{-1} indicates the ν_1 -mode (symmetric-stretching) is influence on others three types of vibrations because this it is a very strong Raman active mode. The ν_3 -mode (dipole character) of SO_4^{2-} at room temperature phase is often splitting. In the present work, the Raman lines at about 1045 cm^{-1} and 1113 cm^{-1} or 1043 cm^{-1} and 1115 cm^{-1} assigned as the ν_3 -mode of SO_4^{2-} . The ν_2 -mode and ν_4 -mode are not clearly changed in the undoped and doped crystals. Raman spectra of the crystals are shown in Figure 6. The observed Raman shift and vibrational characteristics are tabulated in Table 1.

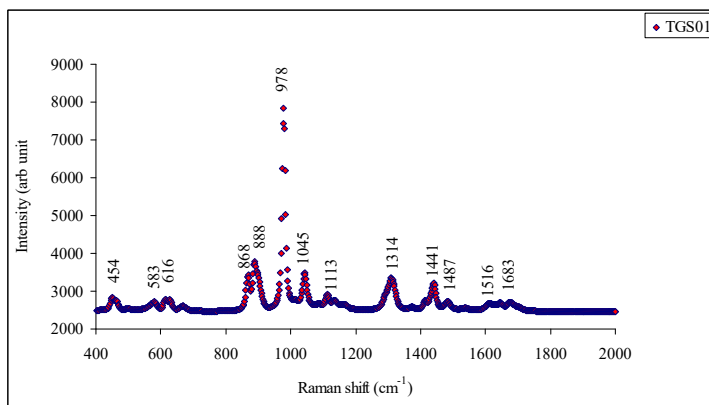


Figure 5.(a) Raman spectrum of undoped TGS crystal

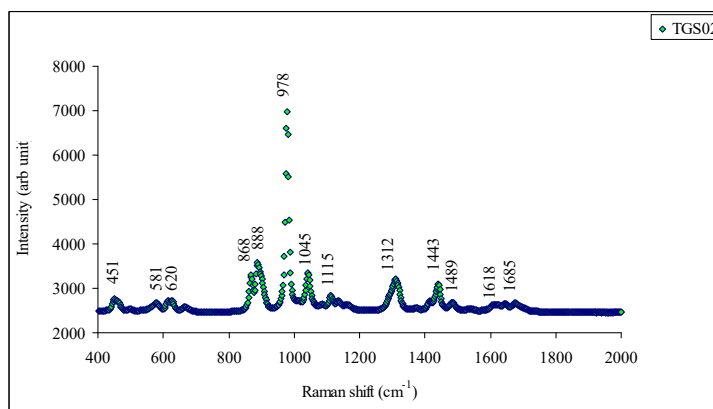


Figure 5.(b) Raman spectrum of K₂SO₄ doped TGS crystal

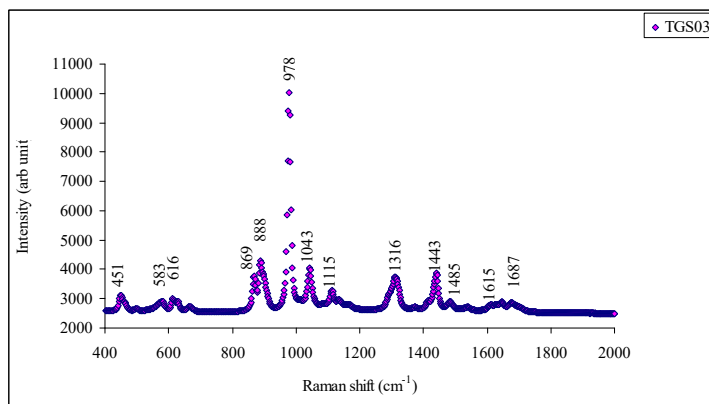


Figure 5.(c) Raman spectrum of (NH₄)₂SO₄ doped TGS crystal

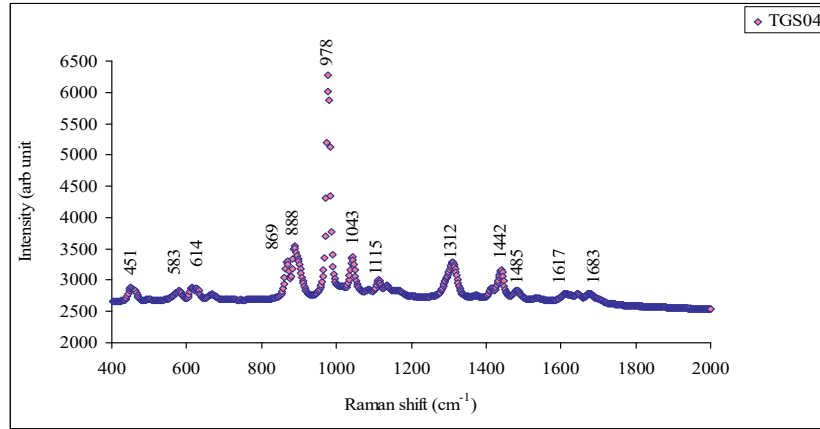


Figure 5.(d) Raman spectrum of Li_2SO_4 doped TGS crystal

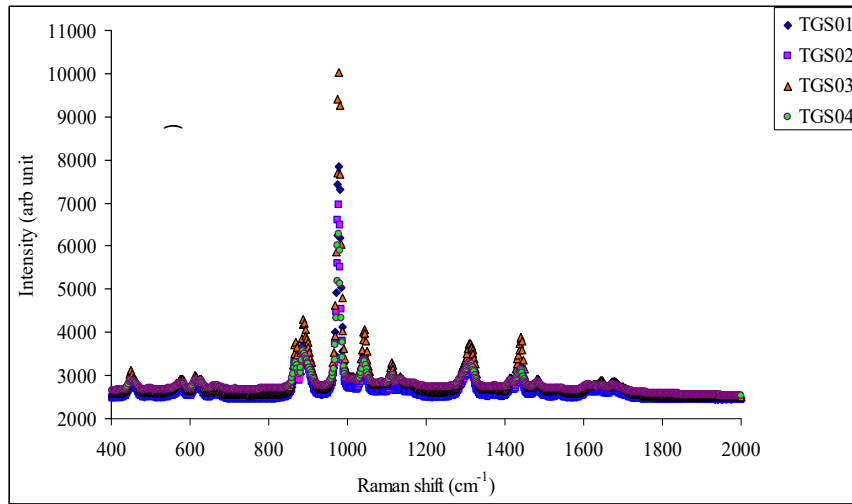


Figure 6. Raman spectra of undoped and M_2SO_4 ($\text{M} = \text{K}, \text{NH}_4, \text{Li}$) doped TGS crystals

Table 1. Raman shifts and corresponding vibrational mode assignments of undoped and M_2SO_4 ($M = K, NH_4, Li$) doped TGS crystals

Raman shift (cm^{-1})				Assignment
TGS	$K_2SO_4/$ TGS	$(NH_4)_2SO_4/$ TGS	Li_2SO_4/TGS	
1683	1685	1687	1683	CO_2 -bending
1616	1618	1615	1617	NH_3 -asymmetric bending
1487	1489	1485	1485	NH -in plane bending + (NH_3)-symmetric bending
1441, 1314	1443, 1312	1443, 1316	1442, 1312	CO_2 -symmetric stretching+ CH_2 -twisting+ CH_2 -bending
1113, 1045 978	1115, 1045 978	1115, 1043 978	1115, 1043 978	ν_3 -mode (SO_4 -dipole) ν_1 -mode (SO_4 -symmetric) stretching
888, 868	888, 868	888, 869	888, 869	C—C- stretching
672	672	672	672	COO-scissoring
616	620	616	614	ν_4 -mode (SO_4 -polarization)
583	581	583	583	COO-rocking
454	451	451	451	ν_2 -mode (SO_4 -bending)

FTIR Study

FTIR transmission spectra of the crystals are shown in Figures 7. (a – d). In this work, the observed wavenumbers can be assigned. In the FTIR spectra, only one normal mode of SO_4^{2-} was found. In Figure 7(a), the collected wavenumbers of undoped TGS crystal matches with the data reported by other authors [Krishnakumar, (2011)]. FTIR transmission spectra of undoped TGS and M_2SO_4 (where $M = K, NH_4, Li$) doped TGS crystals with stack are shown in Figure 8. The collected wavenumbers and their vibrational mode assignments are given in Table 2. The band observed in the wavenumber range of about $3000\text{ cm}^{-1} - 3500\text{ cm}^{-1}$ showed the stretching bands H_2O and the band appeared in each of the spectrum.

Discussion of Infrared (IR) Light Testing Experiments

From IR testing experiments without samples, it can be discussed as follows:

- In IR testing with cell-phone camera, the output green coloured indicator LED indicates “ON” and also IR light (from IR LED) is also emitted.
- In IR testing with paper, the output green coloured indicator LED indicates “OFF” and also IR light (from IR LED) is not emitted.
- In IR testing with thin opaque plastics, the output green coloured indicator LED indicates “OFF” and also IR light (from IR LED) is not emitted.

From IR testing experiments with samples, it can be discussed as follows:

- In this experiment, the output green coloured indicator LED is “ON” and also IR light transmits from the circuit (IR LED). It is found that the crystals are exhibited as IR transmitters or IR windows materials. The crystals can be applied as the IR windows materials of IR transmission measurements for the vibrational characteristics of liquid and gas molecules samples.

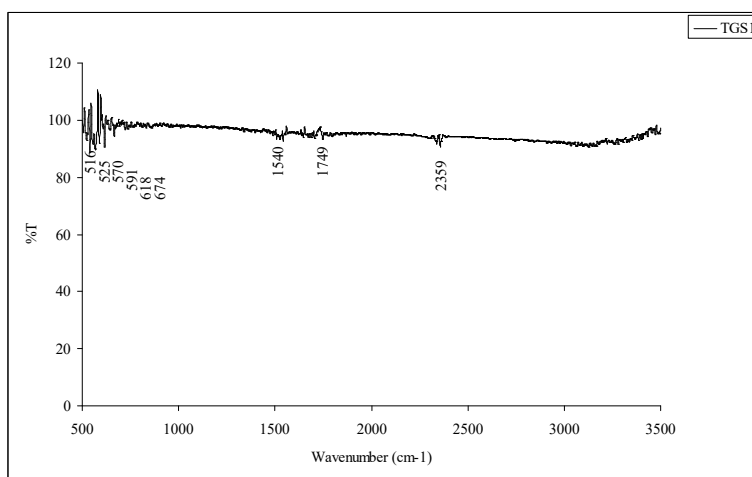


Figure 7.(a) FTIR transmission spectrum of undoped TGS crystal

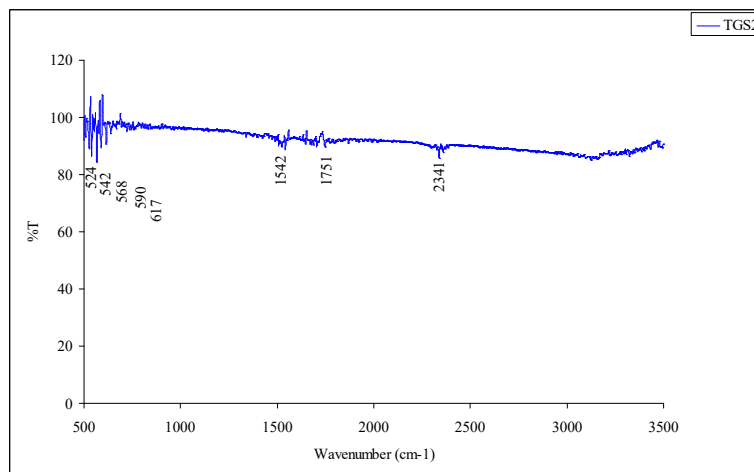


Figure 8.(b) FTIR transmission spectrum of K₂SO₄ doped TGS crystal

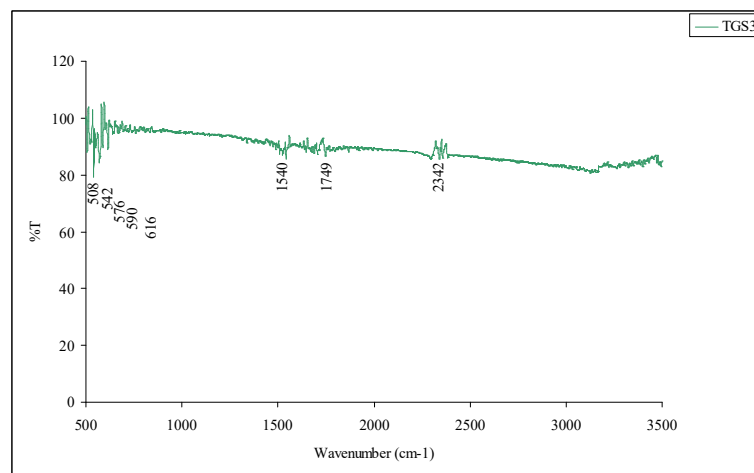


Figure 7.(c) FTIR transmission spectrum of (NH₄)₂SO₄ doped TGS crystal

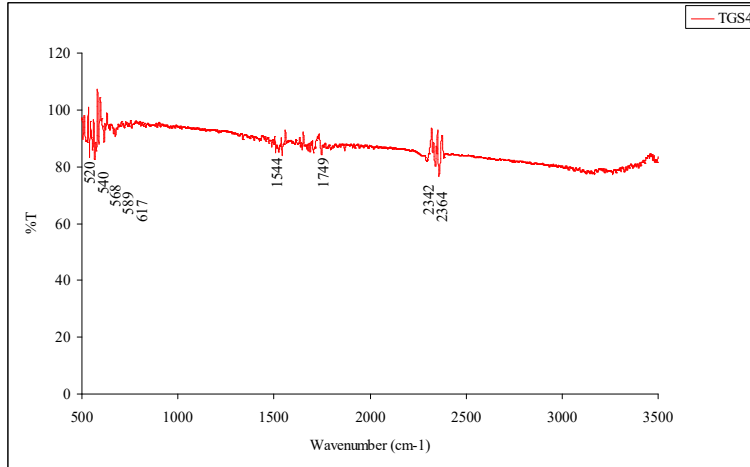


Figure 7.(d) FTIR transmission spectrum of Li₂SO₄ doped TGS crystal

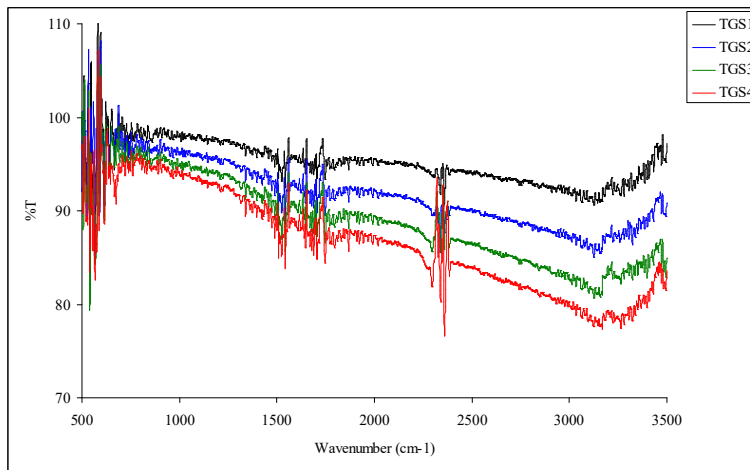


Figure 8. FTIR transmission spectra of undoped and M₂SO₄ (where M = K, NH₄, Li) doped TGS crystals

Table 2. The observed wavenumbers and corresponding vibrational mode assignments of undoped TGS and M_2SO_4 ($M = K, NH_4, Li$) doped TGS crystals

Wavenumber (cm^{-1})				Assignment
TGS	K_2SO_4/TGS	$(NH_4)_2SO_4/TGS$	Li_2SO_4/TGS	
2359	2341	2342	2342, 2364	CO_2 - bending
1749	1751	1749	1749	Combination band
1540	1542	1540	1544	NH_3 -asymmetric bending
674	-	-	-	COO -scissoring
618	617	616	617	SO_4 -polarization
570, 591	568, 590	576, 590	568, 589	COO -rocking
516, 525	524, 542	508, 542	520, 540	COO -twisting

Conclusion

Crystals of undoped and M_2SO_4 ($M = K, NH_4, Li$) doped TGS have been grown by slow solution growth method. The as-grown crystals were characterized by Raman and FTIR spectroscopy. Furthermore, for the applications of IR windows materials, experiments were performed in which the crystals were used as IR transmitters. Experimental results were concluded as follows:

- Raman spectra showed that four normal modes of SO_4^{2-} and vibrational characteristics of organic molecules such as COO^- , $C-C$, $CO_2-CH_2-CH_2$, $NH-NH_3$, NH_3 and CO_2 were observed and assigned in this work.
- FTIR spectra were found to be the same in patterns and most of the wavenumbers of absorption lines were the same in values. Only one normal modes of T_d -symmetry type SO_4^{2-} were found and assigned in this work. Others vibrational modes of organic molecules were found and assigned by molecular vibrational theory.
- The observed Raman lines were agreement with the wavenumbers of FTIR spectra. From the experimental results, the samples responded to infrared (IR) radiation because the wavelength of laser in Raman spectrometer was

1064 nm (monochromatic and/or IR-laser) due to the appearance of Raman lines of the crystals and the wavelength range FTIR Spectrophotometer were 20000 nm – 2857 nm (or wavenumber range of $\sim 500 \text{ cm}^{-1}$ - 3500 cm^{-1}). It showed that the crystals exhibited as the IR response materials or IR sensing materials. From the IR light testing experiments, the crystals exhibited as the IR transmitters or IR windows materials. According to experimental results, the crystals of undoped TGS and M_2SO_4 ($\text{M} = \text{K}, \text{NH}_4, \text{Li}$) doped TGS can be applied as the IR sensing materials and IR windows materials.

Acknowledgements

The authors would like to acknowledge Professor Dr Khin Khin Win, Head of Department of Physics, University of Yangon, for her valuable suggestion and comments for this work. The authors would like to acknowledge Support from JST Sakura Science Program & Japan Asia Youth Exchange Program in Science, Japan and thank to Professor Dr Hideaki Ohgaki, Institute of Advanced Energy Laboratory, Kyoto University, Kyoto, Japan for the laser Raman and FTIR spectroscopic measurements of my research materials.

References

1. Andriyevsky, B., Piecluch-Trojanek, W. and Patryn, A. (2007) "Effect of hydrostatic pressure on structural and electronic properties of TGS crystals (first-principle calculations)", *Condensed Matter Physics*, 10, pp. 33–38.
2. Arunmozhi, G., Lanceros-Mendez, S. and Gomes, E. M. (2002) "Antiferroelectric ADP doping in ferroelectric TGS crystals", *Materials Letters*, 54, pp. 329–336.
3. Bajpai, P.K., Shah, D. and Kumar, R. (2008) "SHI irradiation induced nano scale surface micro-relief's in the polar (010) cleavage of pure and doped TGS crystals", *Indian Journal of Engineering and Materials Sciences*, 15, pp. 334–342.
4. Choudhury, R.R. and Chitra, R. (2008) "Single crystal neutron diffraction study of triglycinesulphate revisited", *Journal of Physics*, 71, pp. 991–995.
5. Gaultz, G. and Vo-Dinh, T. (2003) "Handbook of Spectroscopy", Wiley, New York.
6. Khanum, F. and Podder, J. (2012) "Synthesis, Growth, and Electrical Transport Properties of Pure and LiSO_4 -Doped Triglycine Sulphate Crystal", *International Journal of Optics*, 12, pp. 1–6.
7. Krishnakumar, V., Rajabopathi, M. and Nagalakshmi, R. (2011) " MgCl_2 added triglycine sulphate crystals", *Advanced Materials Letters*, 2, pp. 163–169.
8. Renugadevi, R., Kanchana, G. and Kesavasamy, R. (2013) "Growth and Characterization of Triglycine Sulphate (TGS) Single Crystals", *Elixir Crystal Growth*, 55A, pp. 13033–13035.
9. Stuart, B. and Ando, D. J. (1996) "Modern Infrared Spectroscopy", Wiley, New York.
10. Yadav, M. S. (2003) "A Textbook of Spectroscopy", Anmol, New Delhi.

STUDY ON HUMIDITY SENSITIVE ELECTRICAL PROPERTIES OF BARIUM FERRITE

July Oo¹, Myo Nyunt¹, Tun Aye² & Win Kyaw³

Abstract

Barium ferrites, BaFe₂O₄, were prepared by solid state reaction method. The X-ray diffraction (XRD) method was used for qualitative phase analysis of the samples and to estimate the crystallite sizes of the samples. Scanning Electron Microscope (SEM) was used to examine the morphological features of the samples. The powders were made into circular shape pellets and their humidity sensitive electrical properties of the samples were studied in the relative humidity range of 50 RH% – 98 RH%. The sensitivities of the samples were compared with each other for humidity sensor application.

Keywords: Barium ferrites, XRD, SEM, humidity sensitive electrical properties, sensitivities

Introduction

Spinel type AB₂X₄ compounds exist in a large variety of combinations of cations (A,B) and several different anions (X) such as oxygen (O), sulphur (S), or selenium (Se). This leads to compounds with a wide range of physical properties, although they all have the same structure [Nowosielski, (2007); Pathan, (2010)]. The highly stable spinel structure allows different cations to be located on the same type of site, and owing to the site preference of the cations, many selective magnetic substitutions and various degrees of magnetic dilutions in the two sublattices may be obtained [Patil, (2013); Praveena, (2013)].

Barium ferrites are well known hard magnetic materials, which are based on iron oxide. They are also called as ferrite magnets and could not be easily replaced by any other magnets [Gul, (2007); Joshi, (2003)]. Cubic barium ferrite having the chemical formula of BaFe₂O₄ are widely used

¹. PhD Candidates, Department of Physics, University of Yangon

². PhD Candidate, Assistant Lecturer, Department of Physics, Patheingyi University

³. Dr., Associate Professor, Department of Physics, Sagaing University

in magnetic recording media, microwave devices and electromagnetic shielding fields. Barium ferrite possesses relatively high Curie temperature and magnetic anisotropy field, as well as its excellent chemical stability and corrosion resistivity [Maria1, (2013); Rezlescu, (2002)]. In this work, Barium ferrites, BaFe_2O_4 , were prepared by solid state reaction method. Structural and microstructural characteristics were investigated by XRD and SEM. Humidity sensitive electrical properties of the samples were also reported.

Materials and Method

Preparation of Barium Ferrites, BaFe_2O_4

For synthesis of Barium ferrite, BaFe_2O_4 , the mixture of Barium Carbonate (BaCO_3) and Iron Oxide (Fe_2O_3) powder were used with stoichiometric composition. Analytical Reagent (AR) grade of the raw materials were used in this work. The powder sample was milled by using laboratory-made ball-milling machine for 5 h to be homogeneous and to obtain fine powders. The milling process was carried out in a rotatory mill, which generated vibrations of the balls and milled material inside the container. The weight ratio of balls to milled material was 5:1. After milling process the powders were heated at 900°C , 950°C and 1000°C for 1 h each in vacuum chamber by using thermal resistive heating coil. DELTA A Series DTA4896 and K-type thermocouple were used as the temperature controller and temperature sensor. The obtained as-prepared ferrites were reground in a rotatory mill for 3 h. Figure 1 shows the block diagram of the Barium ferrites samples preparation process. Photographs of the Barium ferrite, BaFe_2O_4 , preparation are shown in Figures 2(a – m) respectively.

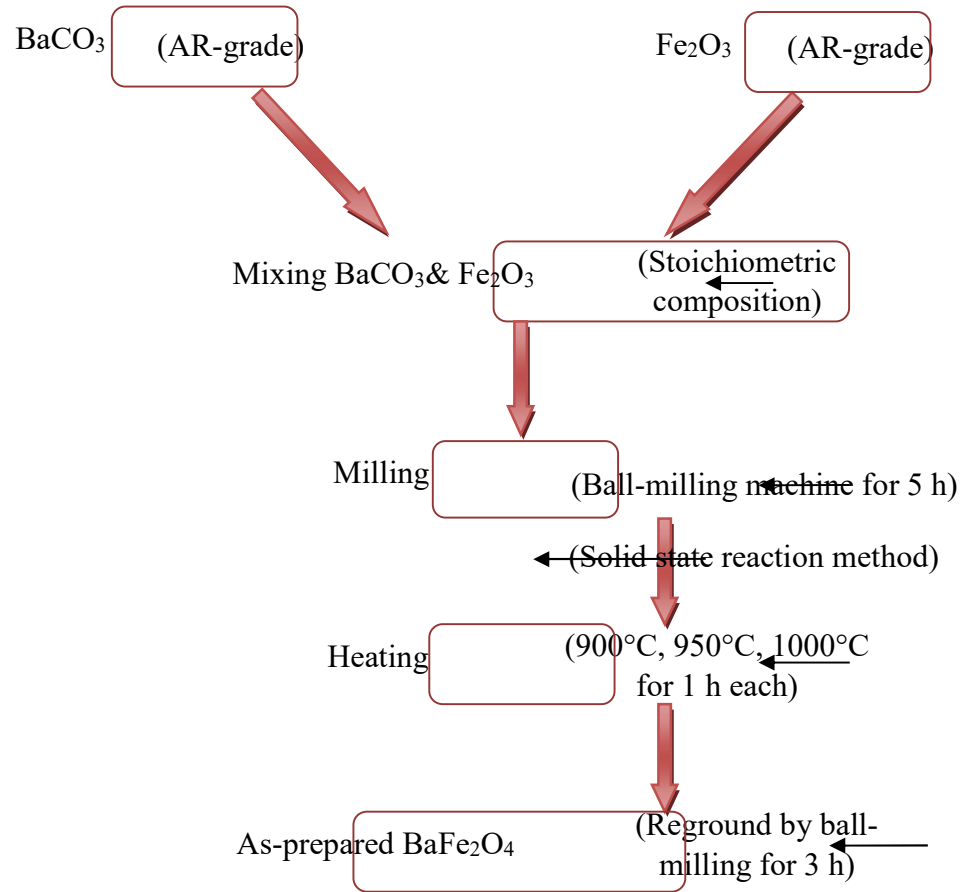


Figure1. Block diagram of the Barium ferrite sample preparation process



Figure 2.(a) Photograph of the weighed starting materials of Fe₂O₃ and BaCO₃



Figure2.(b) Photograph of the mixed weighed starting materials of Fe_2O_3 and BaCO_3



Figure 2.(c) Photograph of the uncoated stainless-steel ball



Figure 2.(d) Photograph of the plastic-coated stainless-steel ball



Figure 2.(e) Photograph of the laboratory-made ball-milling machine



Figure 2.(f) Photograph of the precursor solid solution to prepare BaFe_2O_4

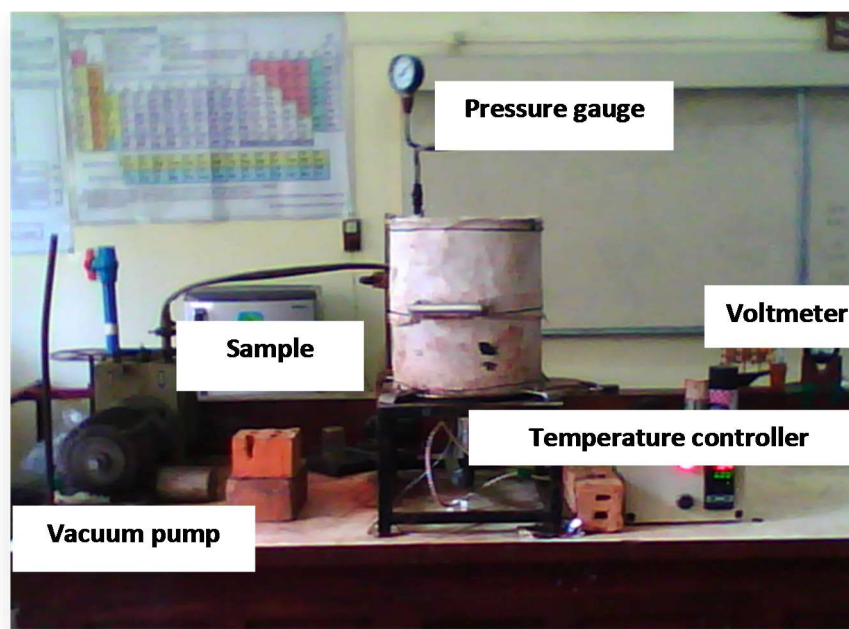


Figure 2.(g) Photograph of the experimental setup of sample preparation system



Figure2. Photographs of the (h) DELTA A Series Temperature Controller DTA4896 at 900°C and (i) as-prepared BaFe₂O₄ prepared at 900°C



Figure 2. Photographs of the (j) DELTA A Series Temperature Controller DTA4896 at 950°C and (k) as-prepared BaFe₂O₄ prepared at 950°C



Figure 2. Photographs of the (l) DELTA A Series Temperature Controller DTA4896 at 1000°C and (m) as-prepared BaFe₂O₄ prepared at 1000°C

XRD and SEM Measurements

The structural characteristics of the samples were investigated by RIGAKU MULTIFLEX X-ray Diffractometer using CuK_α radiation. The lattice parameters were calculated from XRD data using the following

formula, $a = \frac{\lambda \sqrt{(h^2 + k^2 + l^2)}}{2 \sin \theta}$ where 'a' is the lattice parameter (Å), 'λ' is the

wavelength of the X-ray (Å), 'θ' is the Bragg's angle (°) and (h k l) is Miller indices. The average crystallite size of the particles was estimated from the

XRD spectrum by applying Scherrer's formula, $D_{\text{crystallite}} = \frac{0.9\lambda}{B \cos \theta}$ where

'D' is the crystallite size (nm), 'λ' is the wavelength of the X-ray (Å), 'B' is the full width at half maximum (rad) and 'θ' is the angle of diffraction (°).

Scanning electron microscopy (SEM) is a technique whereby a beam of energetically well-defined and highly focused electrons is scanned across a material (sample). Microstructural characteristics of the samples were investigated by using JEOL JSM-5610LV SEM with the accelerating voltage of 15 kV, the beam current of 50 mA and 5500 times of photo magnification.

Humidity-Sensitive Electrical Properties Measurement

Humidity sensitive electrical properties of the Barium ferrites, BaFe_2O_4 were prepared by conventional solid state reaction method at 900°C, 950°C and 1000°C for 1 h each were investigated in the relative humidity range of 50 RH% - 98 RH%.

Firstly, the as-prepared ferrites were made circular shape pellets by using SPECAC hydraulic press with the pressure 5 ton (~70 MPa). Then the pellet was polished by using filtered-paper to get the smoothing surface. Thickness and area of the each of the sample were as 2.95 mm $1.14 \times 10^{-4} \text{ m}^2$. The sample was then fixed on glass plate and silver contacts were made over the sample to ensure good electrical contact.

In this measurement, XSW TDK 0302 Humidity Meter was used as the humidity sensing element. Humidity sensitive electrical resistance and voltage of the sample were observed by two probe method by using FLUKE

189 digital multimeter. The refrigerator (TOSHIBA) was used as the humidity generator. Photographs of the experimental setup of humidity sensitive electrical property measurement are shown in Figures3(a) and (b).

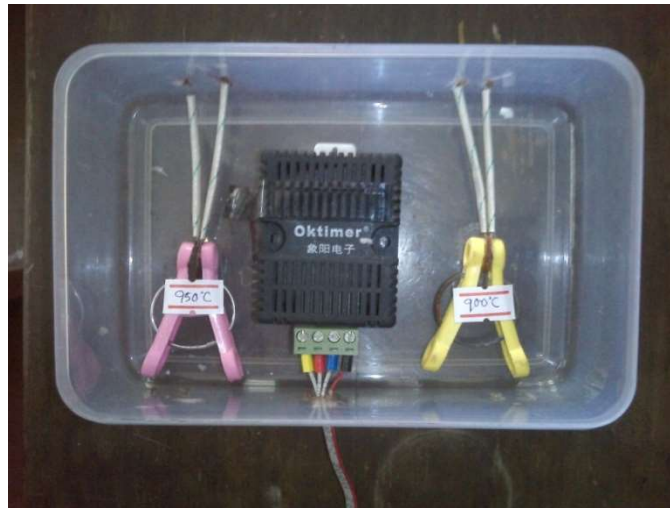


Figure 3.(a) Photograph of the sample and sensor placed in the same condition



Figure 3.(b) Photograph of the experimental setup of humidity sensitive electrical properties measurement

Results and Discussion

XRD Analysis

Powder X-ray diffraction patterns of Barium ferrites, BaFe₂O₄, with different preparation temperatures of 900°C, 950°C and 1000°C for 1 h each are shown in Figure 4(a – c). The observed XRD lines were compared with JCPDS data library file of Cat. No. 46-0113 BaFe₂O₄, Barium Iron Oxide, to identify the qualitative phase analyses of powder samples. The observed XRD patterns were found to be agreed with JCPDS. The appearance of the diffraction peaks demonstrates the single-phase Barium ferrites, BaFe₂O₄, powders.

According to XRD patterns, BaFe₂O₄ belongs to cubic structure at room temperature. The lattice parameters were evaluated by using the equation $\frac{\sin^2 \theta}{(h^2 + k^2 + l^2)} = \frac{\lambda^2}{4a^2}$. The lattice parameters of the sample are tabulated in Table 1. Comparison of the lattice parameters of the samples at different preparation temperatures are shown in Figure 5(a). The lattice parameters of the sample prepared at 950°C was the longest and at 1000°C was the shortest among the samples.

The crystallite sizes of each of the sample are estimated by using the Scherrer formula, $t = \frac{0.9\lambda}{B \cos \theta}$, where "t" is the crystallite size (nm), "λ" is wavelength (Å), "θ" is diffraction angle of the peak under consideration at FWHM (°) and "B" is observed FWHM (radians). In the present work, the obtained crystallite sizes are also presented in Table 5.1. Comparison of the crystallite sizes of the samples at different preparation temperatures are shown in Figure 5(b). As shown in Figure 5(b), the crystallite sizes of the samples increased with increase in annealing temperature.

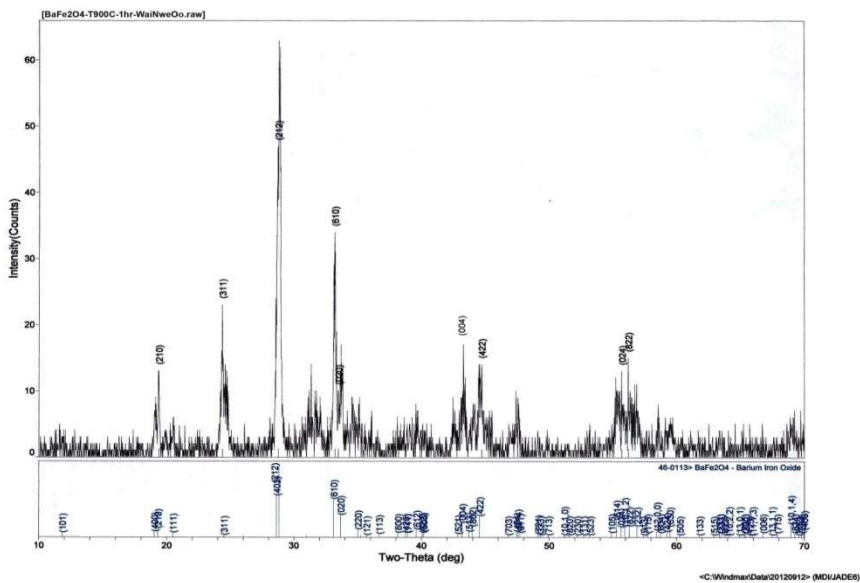


Figure 4.(a) XRD pattern of BaFe₂O₄ prepared at 900°C

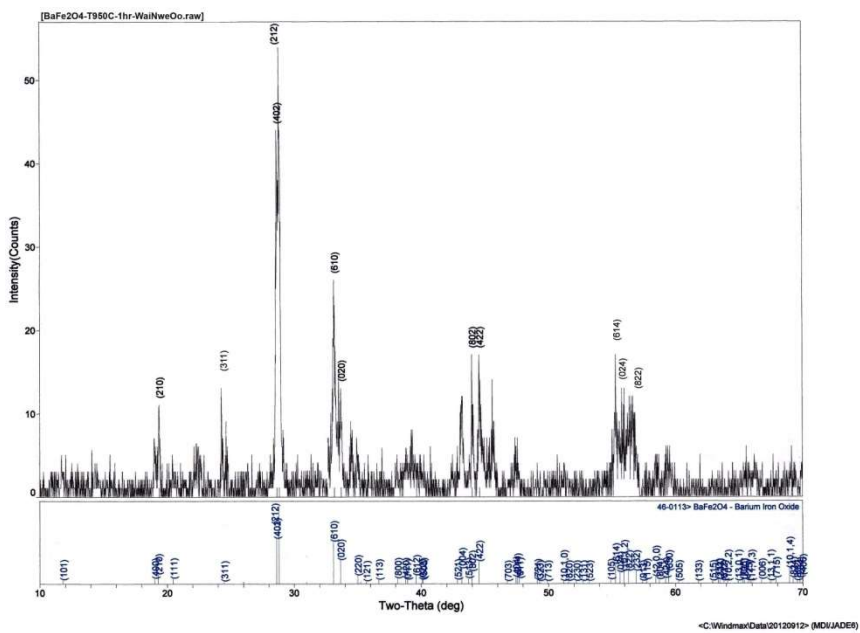


Figure 4.(b) XRD pattern of BaFe₂O₄ prepared at 950°C

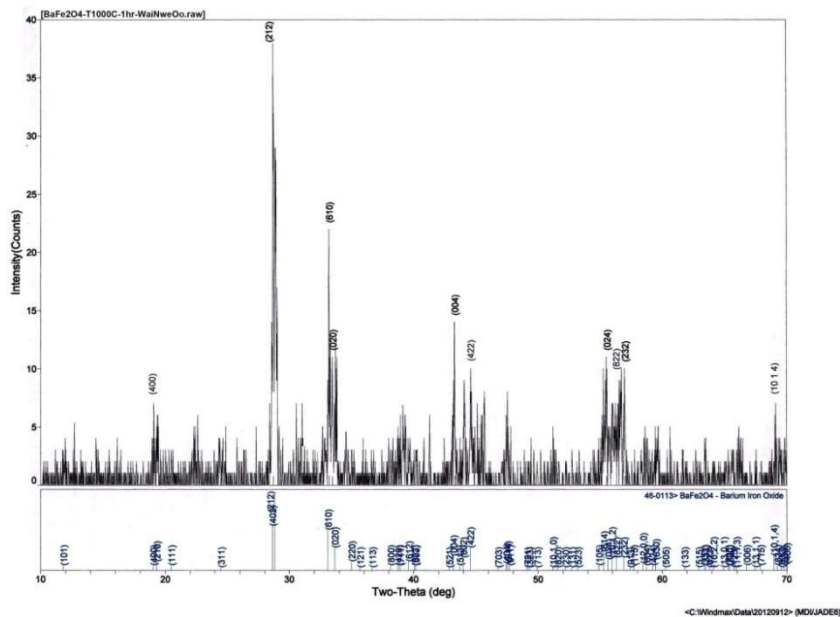


Figure 4.(c) XRD pattern of BaFe_2O_4 prepared at 1000°C

Table 1. The lattice parameters and average crystallite sizes of BaFe_2O_4 at different preparation temperatures

Sr No	Preparation Temperature ($^\circ\text{C}$)	Lattice parameter (Å)	Crystallite size (nm)
1	900	10.5500	25.3315
2	950	12.0170	32.0367
3	1000	8.9103	53.9454

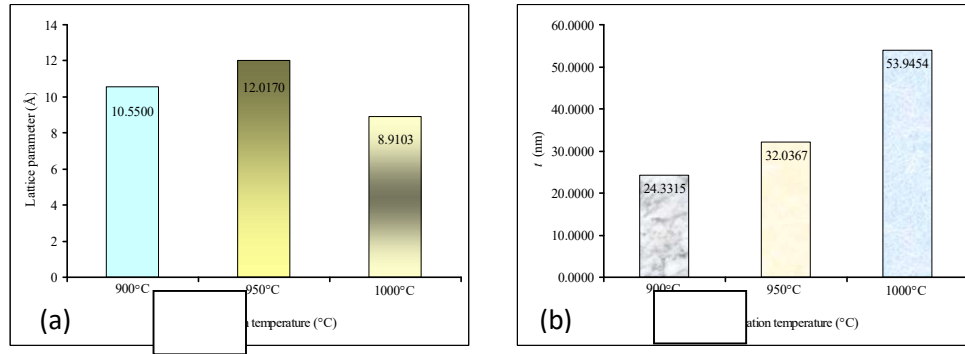


Figure 5. Comparisons of the (a)lattice parameters and (b) crystallite sizes of the BaFe₂O₄ with different preparation temperatures

SEMAnalysis

Material examination by SEM can yield the morphological information of the shape and size of the particles making up the object. Figures6(a – c) show the SEM images of Barium ferrite, BaFe₂O₄, powder of different preparation temperatures of 900°C, 950°C and 1000°C.

As shown in figures, the grain shapes of the samples are uniform block and the obtained samples are found to be clear grain boundary. Some pores are also found in each of the image and these are increased with increase in preparation temperatures. The grain sizes of the samples are listed in Table 2. The largest pore area occurred in the BaFe₂O₄ sample prepared at the temperature of 950°C but the smallest pore area occurred in the sample prepared at the temperature of 900°C.

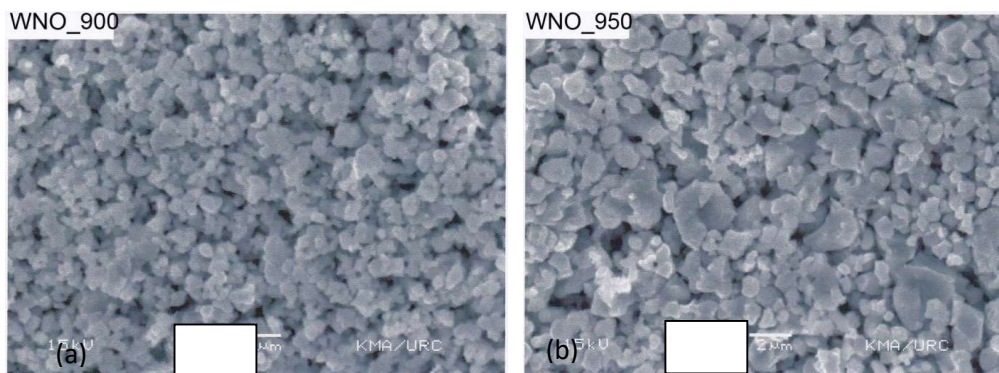


Figure 6.SEM micrographs of BaFe₂O₄prepared at(a) 900°C and (b) 950°C

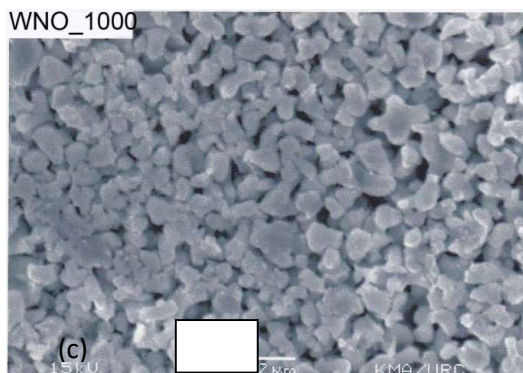


Figure 6.(c)SEM micrograph of BaFe₂O₄ prepared at 1000°C

Table 2. The grain sizes of the BaFe₂O₄ at different preparation temperatures

Sr No	Preparation Temperature (°C)	Grain size (μm)
1	900	0.40 - 1.60
2	950	0.40 - 2.30
3	1000	0.40 - 2.20

Humidity Sensitive Electrical Properties Study

Humidity sensitive electrical resistances R_H versus relative humidity RH%, and dc voltage V_H and capacitance C_H versus relative humidity RH% of the investigated BaFe₂O₄ prepared at three different temperatures of 900°C, 950°C and 1000°C for 1 h each are shown in Figures 7(a – c) and Figures 8 (a – c) respectively.

As shown in RH versus RH% graphs, the electrical resistance of the BaFe₂O₄ sample decreased with increased in relative humidity and the obtained R_H versus RH% curves were fitted with linear type to examine the sensitivity of the sample. The slope of the R_H versus RH% graph can be taken as the sensitivity of the sample. The sensitivities of the samples are tabulated in Table 3. The sensitivity of the BaFe₂O₄ sample prepared at 950°C is the most sensitive material among the candidate samples. The resistance changes in porous spinel type ferrites with increasing of the humidity level occur

because of adsorption and capillary condensation of water [(2004). *Humidity Measuring Technology*.].

The sensitivity factor “S_f” of the sample can be evaluated by using the following relation,

$$S_f = R_{50\%}/R_{98\%}$$

where R_{50%} and R_{98%} are the electrical resistances of the BaFe₂O₄ sample at the relative humidity 50 RH% (start point) and 98 RH% (end point) respectively.

According to the above relation, for BaFe₂O₄ ferrite prepared at 900°C,

$$S_{f(900^\circ\text{C})} = R_{50\%}/R_{98\%} = 16.781 \text{ M}\Omega/12.00 \text{ M}\Omega = 1.3981$$

for BaFe₂O₄ ferrite prepared at 950°C,

$$S_{f(950^\circ\text{C})} = R_{50\%}/R_{98\%} = 50.020 \text{ M}\Omega /17.840 \text{ M}\Omega = 2.8038$$

for BaFe₂O₄ ferrite prepared at 1000°C,

$$S_{f(1000^\circ\text{C})} = R_{50\%}/R_{98\%} = 24.945 \text{ M}\Omega /19.959 \text{ M}\Omega = 1.2498$$

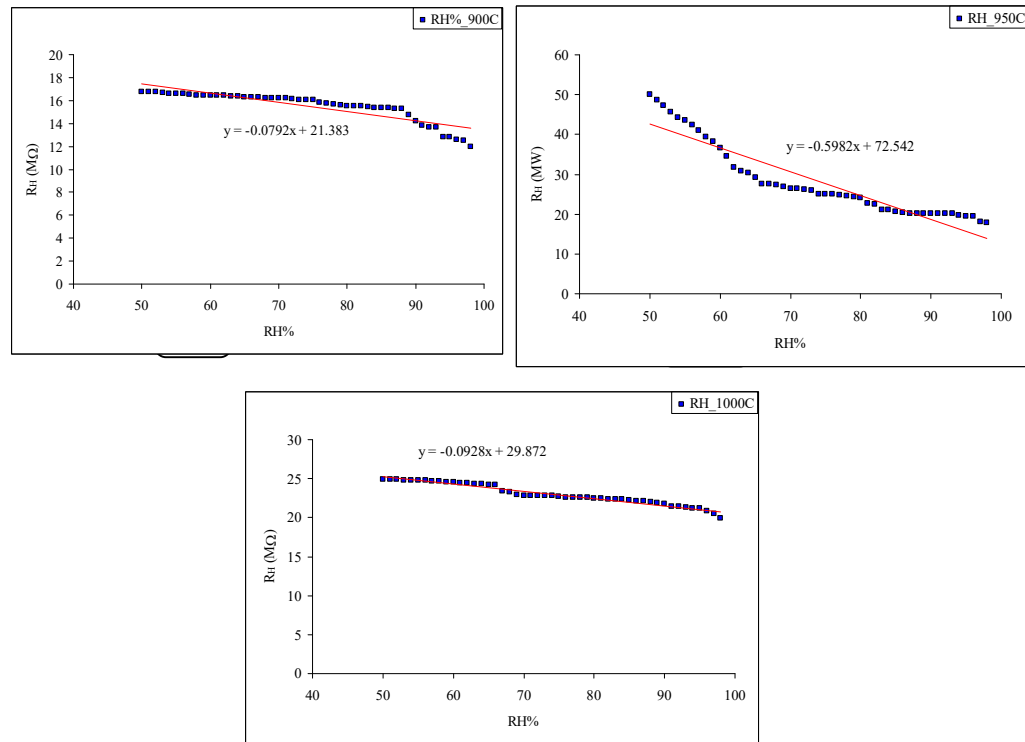


Figure 7. Humidity sensitive electrical resistances of BaFe₂O₄ prepared at (a) 900°C, (b) 950°C and (c) 1000°C for 1 h each

Table 3. Sensitivities and sensitivity factors of the BaFe₂O₄ prepared at three different preparation temperatures of 900°C, 950°C and 1000°C for 1 h each

Sr No	Sample Preparation temperature (°C)	Sensitivity (MΩ/RH%)	Sensitivity factor
1	900	0.0792	1.3981
2	950	0.5982	2.8038
3	1000	0.0928	1.2498

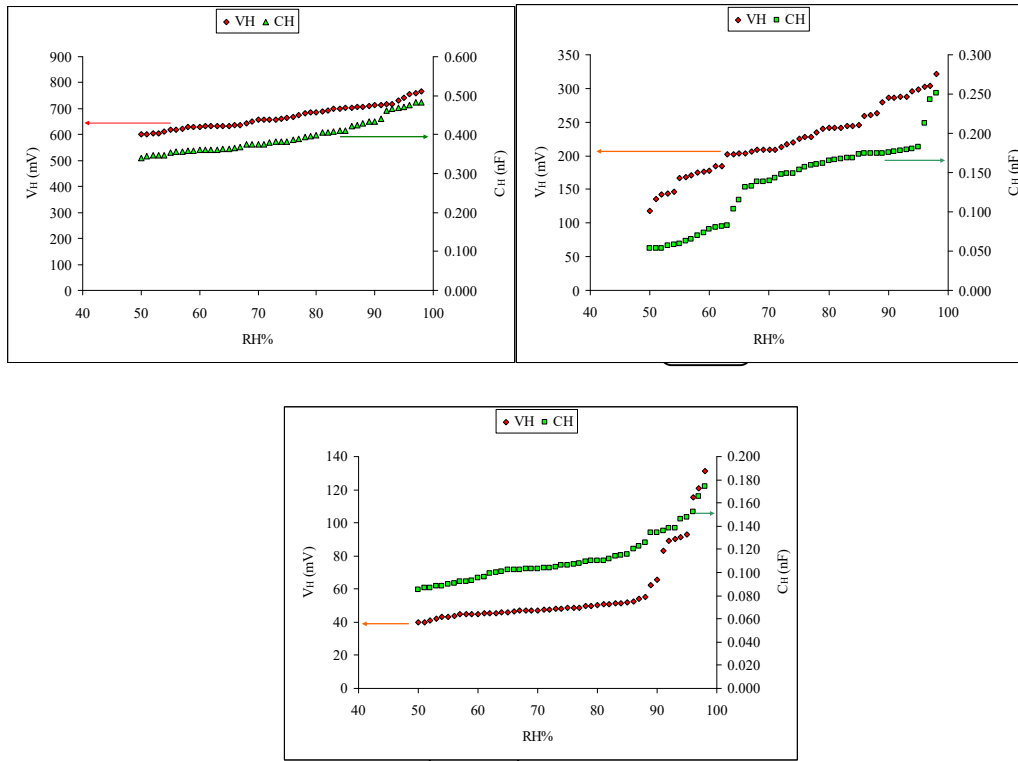


Figure 8. Humidity sensitive dc voltages and capacitances of BaFe₂O₄ prepared at (a) 900°C, (b) 950°C and (c) 1000°C for 1 h each

The obtained sensitivity factors are also presented in Table 3. As presented in Table 3, the sensitivity and sensitivity factor of the sample prepared at 950°C were found to be the largest one. It can be suggested that microstructure (porosity, grain size, structural defects) has a great role on the electrical resistivity. Smaller grains imply an increase of the grain boundary surface which normally account for high resistivity of a polycrystalline material. The larger the specific surface area and porosity of the specimens the more water vapors can be physically adsorbed, resulting in a larger decrease of the resistivity [(2011).*The Humidity/Moisture Handbook*.]. One can see that the sample prepared at 950°C is the most sensitive material to humidity change. As shown in Figures 8(a – c), the dc voltage and capacitance of the samples increased with increase in relative humidity. Experimental data of the humidity sensitive electrical properties measurements are presented in Table 4(a – c).

Conclusion

Barium ferrites, BaFe_2O_4 , were prepared at three different temperatures 900°C, 950°C and 1000°C for 1 h each by using solid state reaction method. The X-ray diffraction investigations of BaCO_3 and Fe_2O_3 annealed at 900°C, 950°C and 1000°C enabled the identification of BaFe_2O_4 phases. The estimated crystallite sizes were found to be increased with increase in annealing temperature and the smallest crystallite size was obtained for powders annealed at temperature of 900°C. The SEM images and distribution of powder particle size showed that the morphological features of BaFe_2O_4 powder particles. From the humidity sensitive electrical properties measurements, the electrical resistance decreased with increase in humidity and sensitivity of the sample also determined. The sensitivity factor was also evaluated. The sensitivity and sensitivity factor of the sample prepared at 950°C were found to be the largest one. The sensitivity and sensitivity factor were decreased with preparation temperature and thus they depend on preparation temperature. According to experimental results, Barium ferrite, BaFe_2O_4 , samples can be used as the humidity sensors in which the sample prepared at 950°C is the most suitable than others.

Table 4.(a) Experimental data of humidity sensitive electrical properties measurement of BaFe₂O₄ prepared at 900°C for 1 h

RH%	R_H(MΩ)	V_H(mV)	C_H(nF)
50	16.781	600.000	0.341
51	16.744	600.900	0.344
52	16.738	603.300	0.346
53	16.704	605.800	0.346
54	16.617	612.300	0.346
55	16.616	619.300	0.353
56	16.592	619.300	0.356
57	16.510	623.300	0.356
58	16.482	627.600	0.358
59	16.482	628.000	0.358
60	16.481	630.300	0.360
61	16.439	631.200	0.361
62	16.428	631.400	0.361
63	16.397	633.400	0.362
64	16.343	633.400	0.363
65	16.300	634.200	0.364
66	16.296	635.800	0.366
67	16.287	636.700	0.369
68	16.236	643.600	0.374
69	16.202	650.500	0.375
70	16.198	655.700	0.376
71	16.196	656.900	0.376
72	16.123	657.300	0.379
73	16.064	658.400	0.381
74	16.045	661.000	0.382
75	16.038	663.000	0.383
76	15.837	669.500	0.387
77	15.760	673.300	0.390
78	15.690	682.300	0.394
79	15.591	684.900	0.396

RH%	R_H(MΩ)	V_H(mV)	C_H(nF)
80	15.525	686.800	0.398
81	15.514	688.000	0.405
82	15.485	691.900	0.406
83	15.420	698.100	0.408
84	15.395	698.500	0.409
85	15.372	702.700	0.411
86	15.338	702.900	0.422
87	15.302	705.400	0.424

Table 4.(a) (Continue) Experimental data of humidity sensitive electrical properties measurement of BaFe₂O₄ prepared at 900°C for 1 h

RH%	R_H (MΩ)	V_H (mV)	C_H (nF)
88	15.259	706.300	0.429
89	14.756	711.000	0.433
90	14.211	712.000	0.433
91	13.814	715.300	0.441
92	13.670	716.900	0.462
93	13.636	718.100	0.467
94	12.807	733.000	0.469
95	12.781	740.800	0.471
96	12.614	755.500	0.475
97	12.481	758.900	0.482
98	12.003	767.000	0.484

Table 4.(b) Experimental data of humidity sensitive electrical properties measurement of BaFe₂O₄ prepared at 950°C for 1 h

RH%	R_H(MΩ)	V_H(mV)	C_H(nF)
50	50.020	117.370	0.053
51	48.700	135.300	0.053
52	47.200	142.240	0.054
53	45.600	143.570	0.057
54	44.300	147.000	0.058
55	43.600	166.970	0.059
56	42.400	168.040	0.063
57	41.100	170.500	0.065
58	39.400	174.810	0.070
59	38.200	176.010	0.073
60	36.600	178.020	0.078
61	34.500	184.130	0.080
62	31.800	184.910	0.081
63	30.900	201.580	0.082
64	30.400	202.040	0.103
65	29.100	203.020	0.115
66	27.569	203.950	0.131
67	27.559	206.500	0.132
68	27.404	208.410	0.138
69	26.833	208.440	0.138
70	26.524	208.790	0.140
71	26.457	209.110	0.143
72	26.277	213.100	0.148
73	26.046	217.530	0.149
74	25.065	220.030	0.149
75	25.041	224.660	0.153
76	24.966	228.150	0.157
77	24.821	228.310	0.159
78	24.511	234.450	0.161
79	24.373	240.040	0.162

RH%	R_H(MΩ)	V_H(mV)	C_H(nF)
80	24.006	241.010	0.165
81	22.651	241.030	0.166
82	22.541	241.110	0.167
83	21.135	244.620	0.169
84	21.020	244.640	0.169
85	20.538	245.400	0.173
86	20.493	258.700	0.174
87	20.250	260.270	0.175

Table 4.(b) (Continue) Experimental data of humidity sensitive electrical properties measurement of BaFe₂O₄ prepared at 950°C for 1 h

RH%	R_H(MΩ)	V_H(mV)	C_H(nF)
88	20.249	263.410	0.175
89	20.173	279.890	0.175
90	20.151	285.840	0.176
91	20.147	286.720	0.177
92	20.090	287.460	0.178
93	20.074	287.740	0.179
94	19.791	296.130	0.180
95	19.446	298.430	0.183
96	19.359	302.010	0.213
97	18.180	304.380	0.243
98	17.840	321.760	0.251
99	17.583	323.570	0.277

Table 4.(c) Experimental data of humidity sensitive electrical properties measurement of BaFe₂O₄ prepared at 1000°C for 1 h

RH%	R_H(MΩ)	V_H(mV)	C_H(nF)
50	24.945	40.000	0.085
51	24.921	40.113	0.087
52	24.890	40.846	0.087
53	24.767	41.880	0.088
54	24.760	43.196	0.088
55	24.758	43.256	0.090
56	24.756	43.512	0.091
57	24.706	44.855	0.092
58	24.672	44.908	0.092
59	24.589	44.997	0.093
60	24.573	45.030	0.095
61	24.483	45.233	0.096
62	24.463	45.532	0.099
63	24.330	45.573	0.100
64	24.324	45.948	0.101
65	24.265	46.090	0.102
66	24.258	46.390	0.102
67	23.365	47.090	0.102
68	23.248	47.112	0.103
69	22.987	47.191	0.103
70	22.875	47.227	0.103
71	22.799	47.362	0.104
72	22.782	47.545	0.104
73	22.764	48.320	0.105
74	22.761	48.359	0.106
75	22.755	48.545	0.106
76	22.643	48.563	0.107
77	22.613	48.579	0.108
78	22.595	49.600	0.109
79	22.553	49.920	0.110

RH%	R_H(MΩ)	V_H(mV)	C_H(nF)
80	22.462	50.107	0.110
81	22.450	50.864	0.110
82	22.397	50.880	0.112
83	22.389	51.231	0.114
84	22.384	51.337	0.115
85	22.290	51.888	0.116
86	22.119	52.589	0.120
87	22.091	54.012	0.123

Table 4.(c) (Continue) Experimental data of humidity sensitive electrical properties measurement of BaFe₂O₄ prepared at 1000°C for 1 h

RH%	R_H(MΩ)	V_H(mV)	C_H(nF)
88	22.038	55.200	0.126
89	21.940	62.080	0.134
90	21.721	65.500	0.134
91	21.438	83.000	0.136
92	21.371	88.900	0.138
93	21.305	90.300	0.138
94	21.181	91.400	0.146
95	21.150	93.200	0.148
96	20.848	115.200	0.152
97	20.550	120.900	0.166
98	19.959	131.200	0.174

Acknowledgement

The authors would like to acknowledge Professor Dr Khin Khin Win, Head Department of Physics, University of Yangon, for her valuable discussions and comments on this work.

References

1. Gul, I.H., Abbasi, A.Z., Amin, F., Anis-Ur-Rehman, M. & Maqsood, A. (2007). Structural, Magnetic and Electrical Properties of $\text{Co}_{1-x}\text{Zn}_x\text{Fe}_2\text{O}_4$ Synthesized by Co-precipitation Method. *Journal of Magnetism and Magnetic Materials*, 311, pp. 494-499.
2. Joshi, G.P., Saxena, N.S., Mangal, R., Mishra, A. & Sharmar, T.P. (2003). Band gap determination of Ni-Zn ferrites. *Bulletins Materials Science*, 26, pp. 387-389.
3. Maria1, K.H., Choudhury S. & Hakim, M.A. (2013). Structural phase transformation and hysteresis behavior of Cu-Zn ferrites. *International Nano Letters*, 3, pp. 1-10.
4. Nowosielski, R., Babilas, R., Dercz, G., Pajak, L. & Wrona, J. (2007). Structure and properties of barium ferrite powders prepared by milling and annealing. *Archives of Materials Science and Engineering*, 28(12), pp. 735-742.
5. Pathan, A.N., Sangshetti, K. & Pangal, A.A.G. (2010). Synthesis and Moussbauer Studies on Nickel-Zinc-Copper Nanoferrites. *Nanotechnology and Nanoscience*, 1(1), pp. 13-16.
6. Patil, S.N. & Ladgaonkar, B.P. (2013). Synthesis and Implementation of $\text{NiZnFe}_2\text{O}_4$ Ferrites to Design Embedded System for Humidity Measurement. *International Journal of Advanced Research in Electrical, Electronics and Instrumentation Engineering*, 19, pp. 3813-3821.
7. Praveena, K., Sadhana, K. & Murthy, S.R. (2013). Elastic behaviour of Sn doped Ni-Zn ferrites. *International Journal of Scientific and Research Publications*, 3, pp. 1-4.
8. Rezlescu, N., Rezlescu, E., Popa, P. & Tudorache, F. (2002). ON THE HUMIDITY SENSITIVITY OF A CERAMIC ELEMENT. STRUCTURE AND CHARACTERISTICS. *Journal of Institute of Technical Physics*, 8, pp. 89-97.
9. (2011). *The Humidity/Moisture Handbook*. Machine Applications Corporation.

DYE-SENSITIZED SOLAR CELL BASED ON TiO₂-MgO COMPOSITE ELECTRODES BY USING COMBINED DYE

Shwe Yee Win¹, Moe Moe Aye², Than Than Win³ and Yin Maung Maung⁴

Abstract

This research focused on improving the methodology of producing dye-sensitized solar cell (DSSCs) by the process of amalgamation with natural dyes. In this research, the *Sansevieria Trifasciata* dye as chlorophyll and *Gardenia* yellow dye as anthocyanin have been prepared and mixed these dyes. The combination of natural dyes by the ratio (1:1) used in the DSSCs as sensitizer. Next the titanium dioxide (TiO₂) and magnesium oxide (MgO) composite materials were mechanochemically prepared. And TiO₂ and MgO were mixed in different ratios as TiO₂ (pure), TiO₂ (95%)-MgO(5%) and TiO₂(90%)-MgO(10%). Then, the TiO₂ – MgO powder were prepared to be paste and they were deposited onto ITO/glass substrate by rolling method and immersed in the mixed dye solution to get dye cells. The dyed TiO₂-MgO-ITO/glass cells were offset with ITO/glass cell coated with adhesive carbon paste. The photovoltaic properties of prepared TiO₂-MgO DSSCs were investigated by J-V measurements. The results showed that the efficiency and fill factor (FF) were acceptable for industrial requirement and they are inexpensive candidates for DSSCs fabrication.

Keywords: *composite powders, ITO/glass, natural dye extract, carbon counter electrode*

Introduction

A solar cell which also known as photovoltaic cell is one of the promising options of renewable energy. Solar cell is divided into two groups which are the crystalline silicon and thin film. The dye-sensitized solar cells (DSSCs) which belong to the thin film groups, emerged as a new class of low cost energy conversion devices with simple manufacturing procedures (Mical G 2003). Dye-sensitized solar cell (DSSCs) is the third generation of solar cell which has been developed by O'Regan and Gratzel in 1991 (Suriati S et al 2015). The principal of operation of DSSCs is based on sensitization of a wide

¹ PhD Candidate, Demonstrator, Department of Physics, Kyaukse University, Myanmar

² Dr, Lecturer, Department of Physics, University of Yangon, Myanmar

³ Dr, Associate Professor, Department of Physics, Mandalay University of Distance Education, Myanmar

⁴ Dr, Associate Professor, Department of Physics, Mandalay University, Myanmar

band-gap metal oxide semiconductor to the visible light region by an adsorbed molecular dye (Lijian M et al 2015). In the fabrication of DSSCs, the choice material and the transparent electrode is crucial to obtain efficient light harvesting, charge separation and extraction. Improving the efficiency of the DSSCs can be achieved by coating a thin film of oxide layers on the TiO₂ electrode such as MgO, ZnO, Al₂O₃, Nb₂O₅, CaCO₃ and SrTiO₃ etc (Helin N et al 2014).

One of the probably best investigated photocatalysts is titanium dioxide (TiO₂). TiO₂ is a wide band gap oxide and it has been used as a photoelectrode in DSSCs. Because of its high specific surface area that allows the absorption of a large number of dye molecules (Kun C C et al 2014). TiO₂ has proved to be one of the most promising materials for various applications such as solar energy conversion, fuel cells, paints and photo catalysts, due to its high chemical stability, availability and low cost. Magnesium oxide (MgO) is another interesting material to catalyses oxidation reaction. Manganese compounds act as photocatalysts with oxygen as oxidative agent. For this reason, many attempts have to be performed to combine materials, titanium and manganese oxide, to get a composite material with advantageous catalytic activity (Boris M et al 2013). The sensitizers used in DSSCs were divided into two types: inorganic dye (includes metal complex, such as polypyridyl complexes of ruthenium and osmium) and organic dye (includes natural organic dyes and synthetically organic dye) according to the structure. Dye from the organic material is very interesting to develop because of the abundant natural (Suriati S et al 2015). Natural dye compounds generally contain anthocyanin, chlorophyll and carotenoids. The advantages of natural dyes are their low cost, easy extraction, non-toxicity and environmental benign nature. The energy conversion efficiency DSSCs is increased by adding a dye that absorbs light with wavelengths in the visible light range of the solar spectrum (Mounir A et al 2012).

Experimental Procedure

Preparation of TiO₂-MgO composite powders

Titanium dioxide (TiO₂) and magnesium oxide (MgO) were used in this work and they were prepared by using agate mortar, mesh-sieving and ball-milling method. Firstly, the TiO₂ was put in the agate mortar and it was ground for 3h to reduce the particle size. Then, the TiO₂ was applied by ball-milling method. The milling time interval was set for 3h. After ball-milling, the TiO₂ was also mesh-sieved with 3 step mesh to get uniform and the lightest particles. The ultrafine TiO₂ powder was heated by 800 °C for 1h. Finally, the undoped TiO₂ powder was obtained.

Next, the TiO₂ and MgO were prepared in different ratios. Firstly, the 95% of TiO₂ and 5% of MgO were mixed together. And they were prepared by using agate mortar, mesh-sieving and ball-milling method. Finally, the homogeneous TiO₂ (95%)-MgO(5%) powder was obtained. The next one of 90% of TiO₂ and 10% of MgO were obtained in similar way. Finally, the homogeneous undoped TiO₂ and the different ratios of TiO₂-MgO composite powders were obtained.

TiO₂-MgO paste preparation

Firstly, 3 g of undoped TiO₂ powder was dissolved in 15 ml of acetic acid. During this preparation, detergent was added into it as a surfactant. Finally, the undoped TiO₂ paste was obtained. Similarly, TiO₂-MgO composite powders were prepared and TiO₂-MgO paste was formed. The undoped TiO₂ and TiO₂-MgO paste were coated on conducting side of ITO glass using rolling method. In order to be dried and strengthen the undoped TiO₂ and TiO₂-MgO paste coating, the plates were calcined 450 °C for 1h. Finally, the undoped TiO₂ and TiO₂-MgO films (active area = 1cm x 1cm) were formed on ITO/glass substrate.

Preparation of dye sensitizer

The anthocyanins pigments were extracted from *Gardenia yellow* and the chlorophyll were obtained from *Sansevieria Trifasciata*. First of all, *Gardenia yellow* was dried at room temperature for one week and they cut a

small piece. After that, they were mixed with ethanol to eliminate the piquancy. After mixing, it was annealed at 80°C for 1h with water-bath and extract solution was formed. After cooling, it was filled with filter paper and the pH level was 6.3 and the colour was found to be yellow. Secondly, *Sansevieria Trifasciata* was cut to become small pieces and they were mixed with ethanol. After mixing, it was annealed at 80°C for 1h with water-bath and the dark green ethanol solution obtained from this procedure is filtered according to the same procedure previously. Then, the pH level was 6.25. After preparing these two dyes solution, they were combined with ratio (1:1) and the pH level was 6.3. And the combined dye solution was obtained. The process was shown in Fig 1.

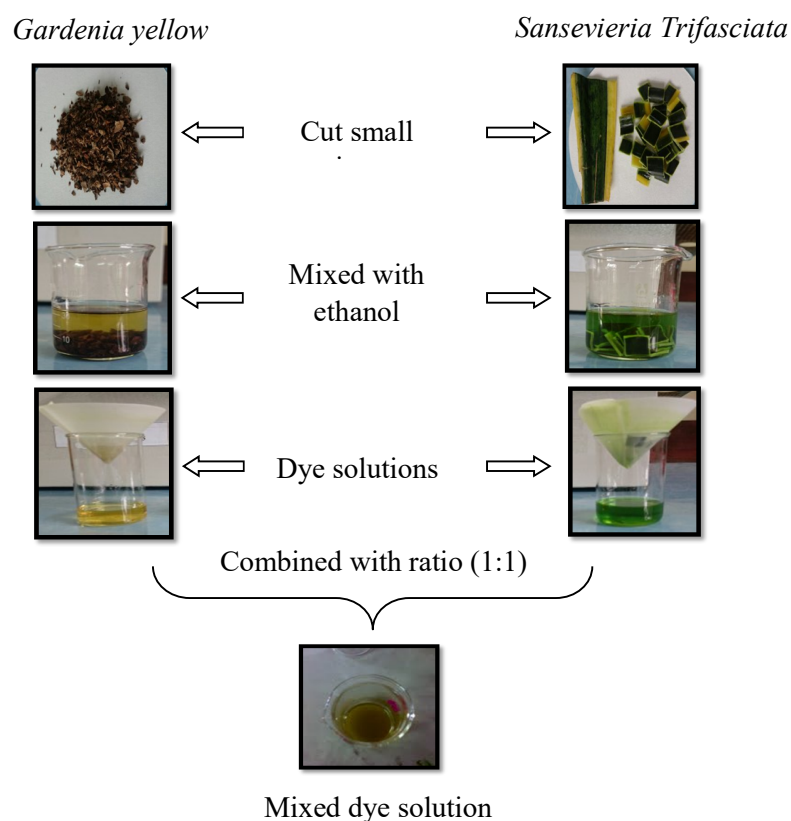


Figure 1. Process of dye solution preparation

Preparation of carbon catalyst

First of all, the KOH (16 ml) and ethanol (8 ml) were mixed together. Then, the carbon powder and the black carbon powder were dispersed into this mixture solution. After dispersion, carbonxylmethylcellulose (0.24 g) was also added and adhesive carbon paste was formed. It was coated onto ITO/glass substrate (active area = 1 cm x 1 cm) by rolling and annealed at 180°C for 1 h.

Assembling of DSSCs

The undoped TiO₂ and TiO₂-MgO electrodes were immersed in mixed dye solution for 1 day and they were calcined at 200 °C for 30 min. Fig 2 showed the carbon coated and TiO₂-MgO coated electrodes.

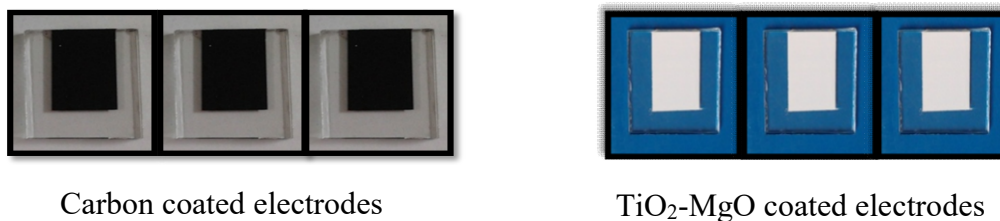


Figure 2. Carbon coated and TiO₂-MgO coated electrodes

Preparation of the positive and negative electrodes were completed, 1-2 drops of mediator were placed on the negative electrode. Two prepared glass slides were set together and the sandwiching of the two plates were offset so that each one had a small position exposed so that an alligator clip could be attached and indicated in Fig3.

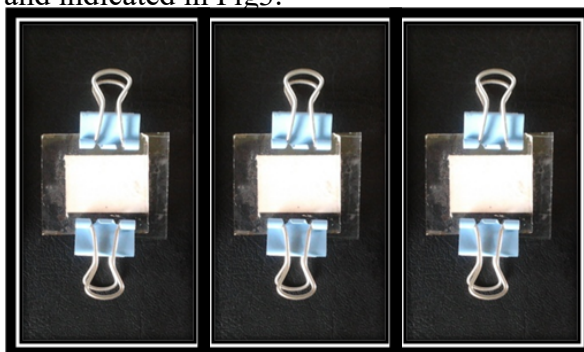


Figure 3. DSSCs with alligator clip

Results and Discussion

Characterization of TiO₂-MgO composite powder

The XRD analysis of the undoped TiO₂ and the different ratios of TiO₂-MgO composite powders were shown in Fig 4(a-c). All the peaks height and peak position were in good agreements with standard JCPDF library file. On the undoped TiO₂ XRD pattern, five peaks were clearly observed. The (101) reflection peak becomes more intense and sharper and the crystal structure of undoped TiO₂ was tetragonal. According to XRD analysis, the crystalline phase of the composite was tetragonal structure, depending mainly on the Mg content and it was found that MgO was influential as composite at this temperature.

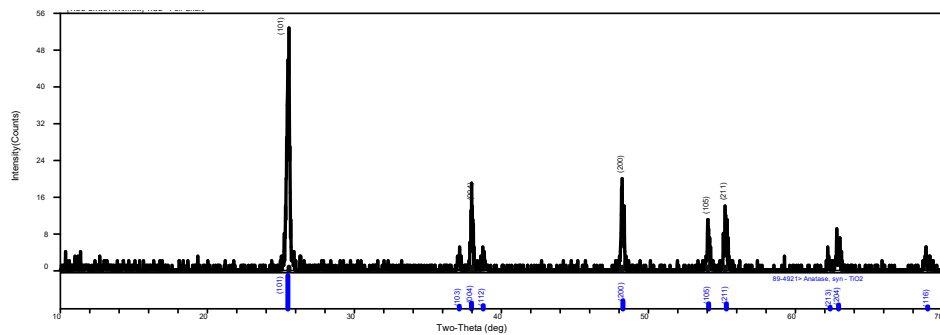


Figure 4(a). XRD patterns of undoped TiO₂ powder at 800°C

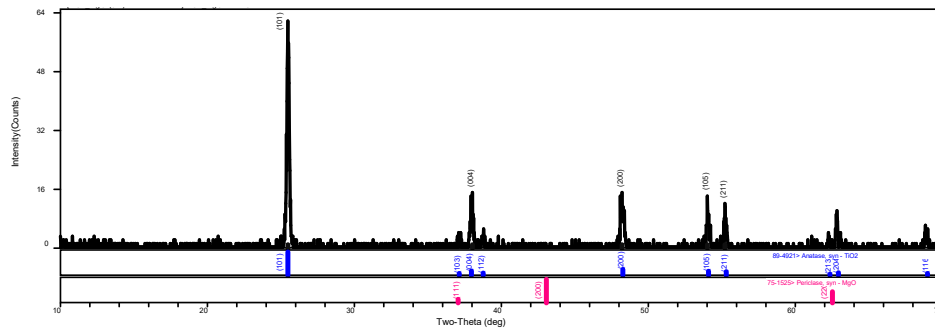
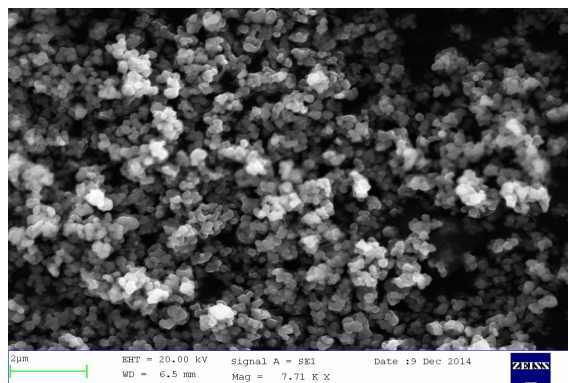
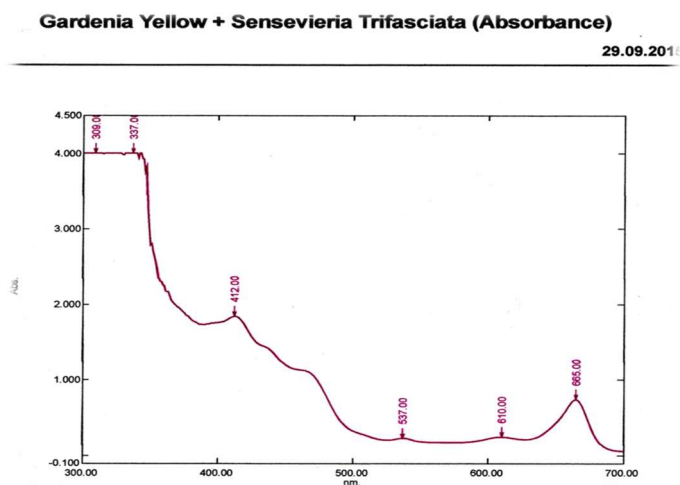


Figure 4(b.) XRD patterns of TiO₂(95%)–MgO(5%) at 800°C

(c) TiO₂(90%)-MgO(10%)**Figure 5.** FESEM image

Optical Analysis

The absorption spectrum of mixed dyes was obtained from UV-Vis spectroscopy. The wavelength range of spectrum lay between 300 nm and 700 nm. . In this absorption spectrum, it was observed that the wide range absorption peaks and all of absorption peaks were within visible region. The energy band gap (E_g) for sample was 2.7526 eV. The UV-Vis absorbance spectra of mixed dye solution with ethanol were shown in Fig 6.

**Figure 6.** UV-Vis absorbance spectra of mixed dye solution with ethanol

Solar Cell Evolution

Fig 7(a-c) showed the change in photocurrent as a function of voltage with mixed dye solution. Photovoltaic cell parameters such as open-circuit voltage V_{oc} , the short-circuit current density J_{sc} , the fill factor (FF) and conversion efficiency were depicted in Table 1.

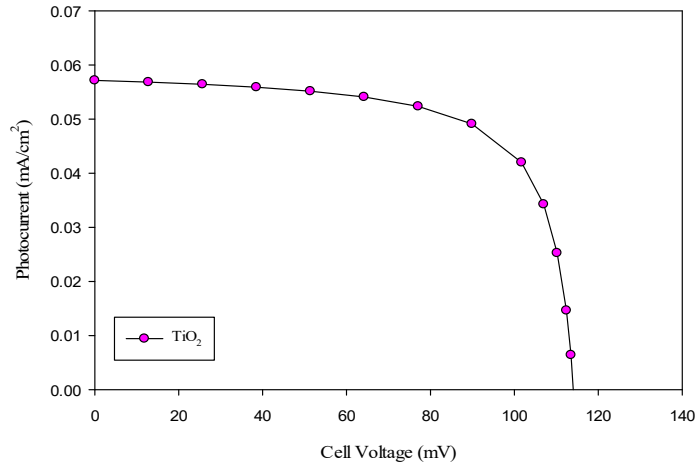


Figure 7(a). Current voltage characteristic curve of undoped TiO₂ cell

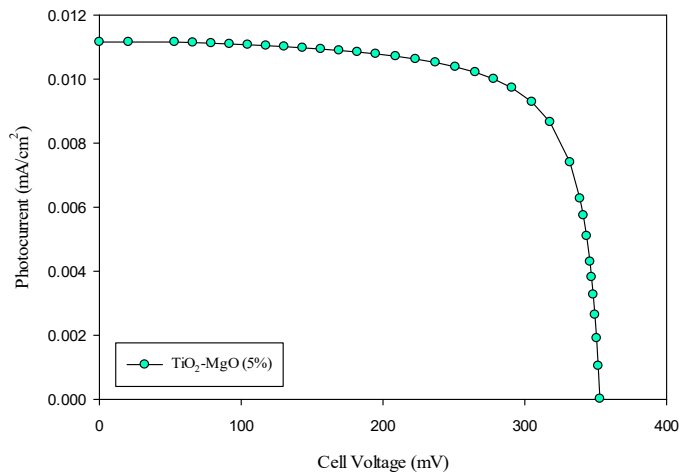


Figure 7(b). Current voltage characteristic curve of TiO₂(95%)-MgO(5%) cell

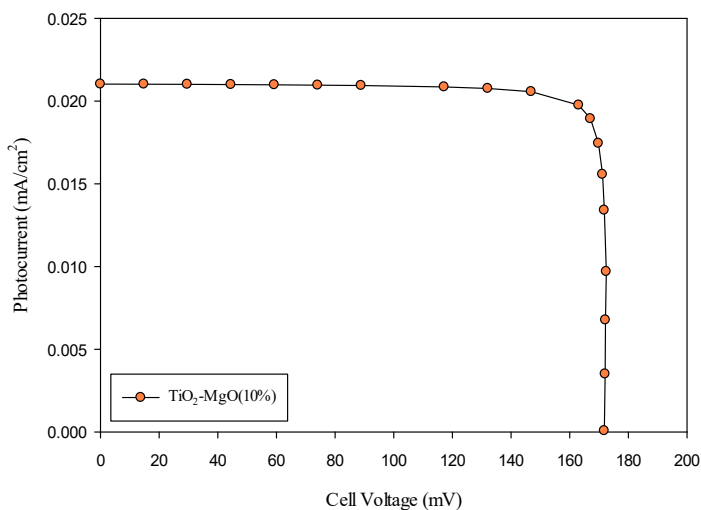


Figure 7(c). Current voltage characteristic curve of TiO₂ (90%)-MgO(10%) cell

Table 1. Photovoltaic parameters of all DSSCs cells with mixed natural dye sensitizer extract

Cell	J _{sc} (mAcm ⁻²)	V _{oc} (mV)	FF	η(%)
undoped TiO ₂	0.048	114	0.67	0.348
TiO ₂ (95%)-MgO(5%)	0.009	178	0.72	0.236
TiO ₂ (90%)-MgO(10%)	0.029	172	0.88	0.259

Conclusion

Preparations of undoped TiO₂ and TiO₂-MgO composite electrode with combined dye extract have been implemented. The XRD studies confirmed that magnesium oxide coated titanium oxide fine powder was totally formed at given temperature. FESEM results indicated that the grain sizes for these powders were 0.233 μm, 0.215 μm and 0.135 μm, also tended to nano-sized grain. The optical absorbance spectrum for a combination of

dyes (*Gardenia yellow* and *Sansevieria Trifasciata*) with mixing ratios (1:1) shows two absorption peaks in the visible region at the wavelength 537 nm (anthocyanine) and 610 nm (chlorophyll). Consequently, the combination of anthocyanine and chlorophyll gives a good absorption range for each of the red, green and blue wavelength. And the energy band gap (E_g) for a combined dye is 2.7526 eV. From I-V variation under illumination, it was significant that V_{OC} - J_{SC} (open-circuit voltage – short-circuit current) behavior was formed for all fabricated films. So, undoped TiO_2 , TiO_2 (95%)-MgO (5%) and TiO_2 (90%)-MgO (10%) nanocomposite films exhibited the photovoltaic properties. As a result of photovoltaic evaluation, the undoped TiO_2 film possessed the best conversion efficiency as 0.348%. The fill factors of both DSSCs were found to be within the range of accepted value for industrial purposes. The research done is certainly said to be of low cost and by simply technique. Thus, the experimental data resulted from this research are quite promising, credible and applicable in use for DSSCs with combined dye sensitizer.

Acknowledgement

I would like to thank to Professor Dr Khin Myat Thu, Head of Department of Physics, Kyaukse University, for her kind permission to carry out this research. This research was totally done at Department of Physics in University of Yangon, Myanmar (2016-2017).

References

1. Boris. M., et al (2013) "Manganese/ TiO_2 Composite Prepared and Used for Photocatalytic Active Textiles". CROATICA CHEMIC ACTA **86** 143
2. Helin. N., et al (2014) "Visible-Light Active and Magnetically Recyclable Nanocomposites for the Degradation of Organic Dye". Materials **7** 4034
3. Kun. C. C., et al (2014) " A Study of Mixed Vegetable Dyes with Different Extraction Concentrations of Use as a Sensitizer for Dye-Sensitized Solar Cells". International Journal of Photoenergy **1**
4. Kartika. S. et al (2011) "Characterization of Optical Properties of the *Sansevieria trifasciata* Extract as Dye Sensitized Solar Cells (DSSC)". International Journal of Basic Applied Science IJBAS-IJENS **11** 10

5. Liberty. L. M et al (2012) "Effect of Calcination Temperature and MgO Crystallite Size on MgO/TiO₂ Catalyst System for Soybean Transesterification". World Academy of Science, Engineering and Technology **64** 889
6. Lijian. M., et al (2015) "Preparation and characterization of Dye-sensitized TiO₂ nanorod solar cells". Thin Solid Films **557** 103
7. Mounir. A., et al (2012) "Studying of Natural Dyes Properties as Photo-Sensitizer for Dye Sensitized Solar Cells (DSSC)" Journal of Electron Devices **16** 1369
8. Mical. G. et al (2003) "Dye sensitized solar cells". Journal of Photochemistry C: Photochemistry Review **4** 145
9. Mark. L, et al (2014) "Analysis of energy gap opening in graphene oxide", 012003 (526)
10. Novoselov K.S, et al (2004) "Electric field effect in atomically thin carbon films" *Science* **306** 666–669
11. Suriati. S. et al (2015) "Materials for Enhanced Dye-Sensitized Solar Cell Performance: Electrochemical Application" International Journal of Electrochemical Science **10** 2859
12. Sungjin. P. et al (2009) "Chemical methods for the production of Graphene", Natural nanotechnology 132
13. Totao. Q, et al (2013) "Facilely prepared Polypyrrole reduced graphene oxide composite with crumpled surface for high performance supercapacitor electrode", ESI